18 June 2010 | $10

Science

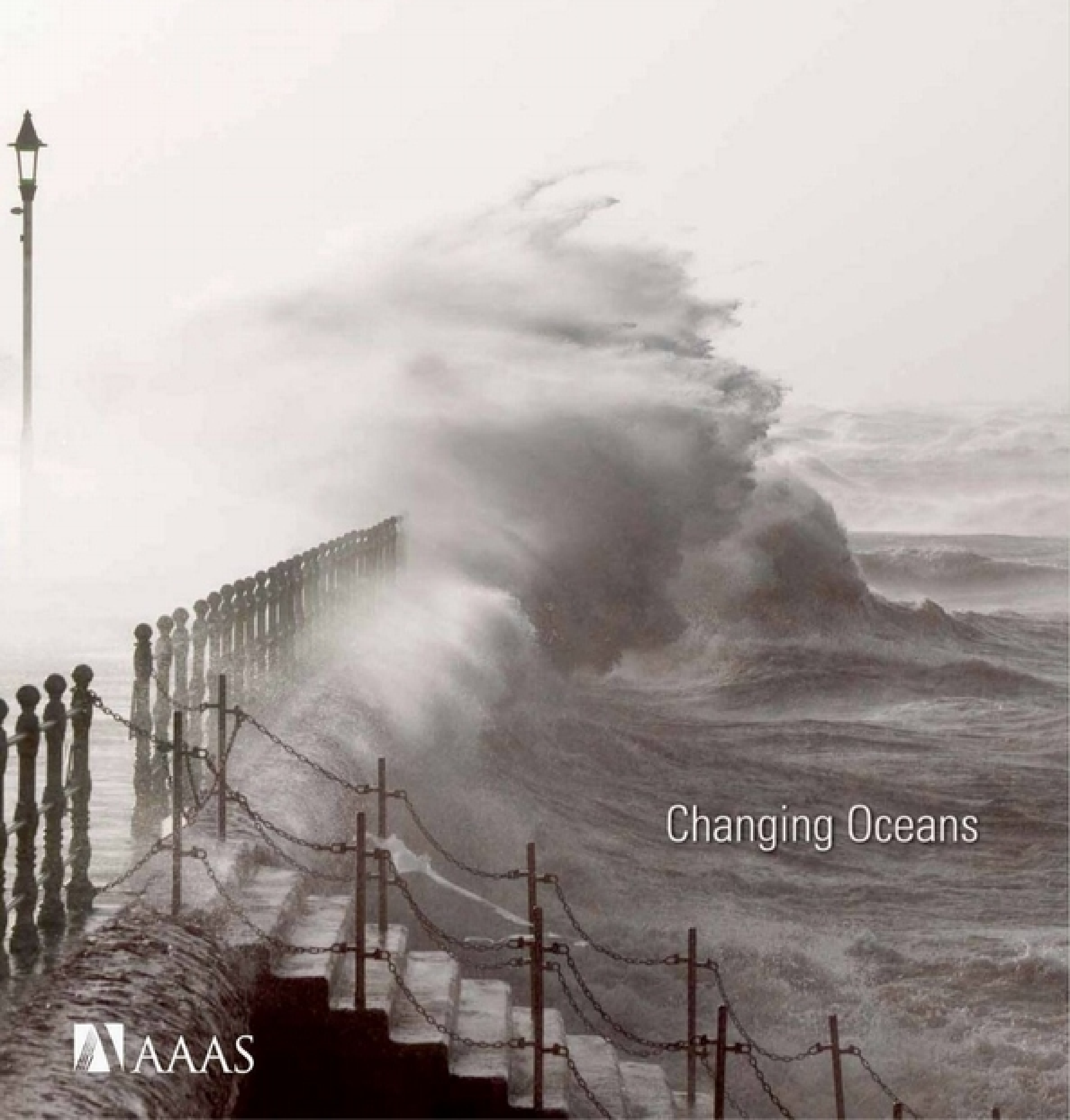

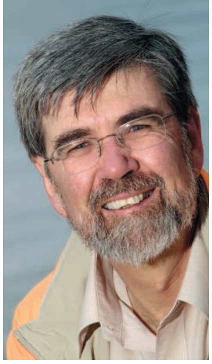

John Church is a chief research scientist at the Centre for Australian Weather and Climate Research, a partnership between the Commonwealth Scientific and Industrial Research Organisation and the Bureau of Meteorology. E-mail: john.church@csiro.au

The Changing Oceans

THE EVOLVING DISASTER OF THE GULF OF MEXICO OIL SPILL REMINDS US THAT OUR WELFARE depends on a healthy marine ecosystem and that the oceans are vulnerable to human activities. The oceans sustain a vast wealth of biological diversity, deliver critical ecosystem services, supply valuable natural resources, and are a central component of the climate system. It is therefore critical that the current ocean-observing system be extended to cover a wider range of ocean properties.

The oceans slow the rate of climate change by absorbing over a quarter of the carbon dioxide released by the burning of fossil fuels and by storing over 90% of the excess heat accumulating in the climate system. These two changes, together with nutrient input into the oceans from fertilizer use and other pollution, are affecting the marine ecosystem by increasing the acidity of the oceans, decreasing subsurface oxygen concentrations, and increasing coastal nutrient loads. At the same time, ocean changes affect the terrestrial environment, being the primary source of the water vapor that drives global rainfall patterns. Changes in ocean temperatures and currents and in the oceans' interaction with the atmosphere are already altering the frequency, intensity, and distribution of storms, droughts, floods, heat waves, and cold spells. And by 2100, rising sea levels from ocean thermal expansion and increasing ocean mass (from melting glaciers, ice caps, and the Greenland and Antarctic ice sheets) will expose an additional tens of millions of people annually to the risk of coastal flooding.

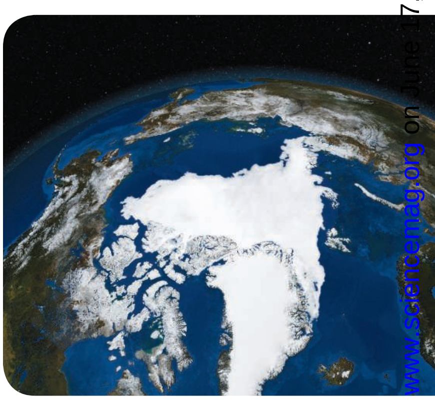

The result of these relationships between the ocean, atmosphere, and land is that the world will experience climate and ocean changes that continue for centuries. In addition, continuing greenhouse gas emissions are increasing the risk of crossing critical thresholds, with poorly understood consequences. If society is to reduce the risk of major ice-sheet contributions to sea-level rise and of profound changes in marine ecosystems, a sustained reduction of greenhouse gas emissions is an urgent priority. However, society has thus far failed to heed the clear warnings about continuing greenhouse gas emissions, making the need to adapt to climate and ocean changes unavoidable. This adaptation will become increasingly challenging for many people around the world, particularly the poor, those living in vulnerable coastal communities, those subject to substantial changes in rainfall, and those with few resources or options. Environmental refugees will become a major social challenge.

Adaptation will require a much improved understanding of the oceans, underpinned by long-term sustained measurements. Satellite observations and automated in situ upper-ocean temperature and salinity observations have improved dramatically in recent years. However, the records are short and both spatially and temporally incomplete. Needed, but rare to nonexistent, are long time series—including data from the deep oceans; under-ice measurements; and geochemical, biological, and ecosystem parameters. The ocean-climate communities throughout the world have benefited tremendously from the formulation of a single coordinated ocean-observing plan. Realistic options for completing this plan, for filling in the gaps, and for extension to a wider range of ocean properties, including ecosystem parameters, are required. There also is a need for greater engagement by marine scientists in addressing climate and ocean variability and change, including their impacts on ecosystems, biodiversity, and fisheries, as well as for improved communication of the importance and urgency of their findings.

Finally, it is essential to sustain global-scale ocean-observing systems and to compile available data into quality-controlled, easily accessible databases. At present, almost all ocean observations are supported by short-term research funding that is subject to changes in research priorities. Long-term funding for sustained observations is absolutely critical. An important step would be mandating and funding existing or new national institutions with responsibility to collect the critical environmental observations, backed by an international legal framework to ensure the free, timely, and open sharing of ocean information for all.

– John A. Church

10.1126/science.1192996

CREDITS: (TOP) BRUCE MILLER; (RIGHT) NASA/GODDARD SPACE FLIGHT CENTER SCIENTIFIC VISUALIZATION STUDIO

FOOD SECURITY

Water Shortages Loom as Northern China's Aquifers Are Sucked Dry

BEIJING—When Luo Yiqi visited the Inner Mongolia region of northern China 3 years ago, he was in for a surprise. In recent years, overgrazed grasslands had withered and turned to desert. Luo had been expecting that. But what stunned the ecologist from the University of Oklahoma, Norman, were the rice fields along a desiccated riverbed. Farmers were pumping water from deep aquifers to cultivate one of the thirstiest crops on the planet. "Apparently, farmers did not get enough scientific guidance," says Luo.

Of all China's environmental woes, the biggest threat to livelihoods and food security may be looming water shortages. China's freshwater resources amount to 2220 cubic meters per person, just a quarter of the world average. For years, the central government focused on declining river flows and rising pollution, largely ignoring what has now become an acute problem: vanishing groundwater. "It was a question of 'out of sight, out of mind,' " says environmental scientist Chen Jining, vice president of Tsinghua University here.

The outlook is especially dire on the North China Plain (NCP), an area encompassing six provinces and the Beijing and Tianjin metropolitan areas. Over the past 40 years, NCP's water table has fallen steadily as some 120 billion cubic meters more water has been pumped from the land than the amount replaced by rainfall, says Liu Changming, a hydrologist at the Institute of Geographical Science and Natural Resource Research of the Chinese Academy of Sciences (CAS) here. Many wells are expected to run dry in the coming decades; when this happens, warns Lester Brown, president of the Earth Policy Institute in Washington, D.C., "China will lose the ability to feed about 10% of its 1.3 billion people."

Until recently, the government was banking on a massive engineering solution. The $75 billion South-to-North Water Diversion Project, now under construction, would bring water from the Yangtze basin to the parched north (*Science*, 25 August 2006, p. 1034). But that remedy is no longer deemed sufficient. "Faced with an escalating crisis, the government is calling for stepped-up monitoring and scientific advice on groundwater management," says Liu. This year, the Ministry of Science and Technology launched a $4.4 million, 5-year project to better understand China's subterranean water resources. The project "is the latest sign of the government's changing attitude," says Pang Zhonghe, a hydrogeologist at CAS's Institute of Geology and Geophysics here. An even bigger effort should get under way soon: a $250 million initiative to drill scientific observation wells to monitor groundwater levels and quality.

China has largely brought its water problems on itself. The classic novel *Outlaws of the Marsh*, written more than 600 years ago, describes the reedy wetlands of the Haihe River Basin, NCP's northern section. The fertile region has been a major target of development; augmenting water drawn from rivers, NCP went from 1800 powered wells in the 1960s to more than 700,000 such wells by 2000, says Liu. The Water Rush paid big dividends, such as turning NCP into the country's wheat and corn belts, says Liang Shunlin, a geographer at the University of Maryland,

U.S. ASTRONOMY

Arecibo to Stay Open Under New NSF Funding Plan

Three years ago, the Arecibo Observatory in Puerto Rico was a telescope with a shining legacy and a dim future. An expert panel had just recommended that its chief supporter, the National Science Foundation (NSF), cut its funding sharply to make room for new astronomy projects. That step, the panel warned, could mean closing the facility—home to the world's largest radio telescope—in 2011 if it couldn't find other backers.

Now, after much hand-wringing, NSF has decided to keep the observatory going until at least 2016 with help from the foundation's geosciences directorate and from NASA. The new funding partners will lead to more atmospheric science and asteroid tracking for the radio telescope—and a new lease on life.

"We're relieved that closure is off the table," says Donald Campbell, director of the National Astronomy and Ionosphere Center at Cornell University, which manages the observatory on NSF's behalf. Under the new funding arrangement, he says, "there will be a more even mix of atmospheric science, asteroid tracking, and astronomy at the observatory than in the past."

Stay tuned. Arecibo will keep monitoring the heavens.

CREDIT: COURTESY OF THE NAIC, ARECIBO OBSERVATORY, A FACILITY OF THE NSF

Built in 1963, the 300-meter telescope made possible storied discoveries such as detection of a binary pulsar system, which led to a Nobel Prize, and the first planets outside the solar system. But in November 2006, an outside panel led by astrophysicist Roger Blandford of Stanford University declared that Arecibo was not as scientifically important as other NSF-funded telescopes (*Science*, 10 November 2006, p. 904). The review recommended that the agency's astronomy division reduce its funding from $10.5 million in

Published by AAAS

The soul of an old violin
1468

A matter of taste
1471

College Park, and Beijing Normal University.

Across the Haihe Basin, each year about 50% more shallow groundwater is consumed than recharged by rainfall. And the surfeit of wells is exhausting deeper phreatic water in the saturated zone that takes much longer to replenish. As NCP is sucked dry, it is shriveling and fissuring, and subsidence now averages more than 1 meter. A few years ago, Liu's team, using radiocarbon dating, found to its astonishment that phreatic water now being drawn from NCP is as much as 30,000 years old. It would take that long, Liu says, to replenish the deep aquifer.

To save water and maintain food security, researchers have proposed improved water conservation, better water pricing policies, and rational agricultural practices. Growing crops and raising livestock account for nearly 66% of China's total water consumption, Liu says. Water-saving measures in agriculture that could be implemented right away include drip and sprinkler irrigation and no-till farming, which reduces evaporation, says Xiao Xiangming, a landscape ecologist at the University of Oklahoma, Norman. Liang adds that researchers should strive to develop crops that lose less water to evaporation and better resist drought.

The south-north diversion may provide temporary relief when the central and eastern lines are completed in 2014. "We can store some of the transferred water underground and take it when we need it," says Qian Yi, a professor in the Department of Environmental Science and Engineering at Tsinghua University. But any water from the diversion project should be viewed as a "supplementary" resource, Liu says: "The first step is to use local water efficiently."

On hostile ground. An engineer surveys a fissure caused by overexploitation of groundwater in northern China's Hebei Province.

A comprehensive solution may depend on better information. Reliable data on aquifer storage, recharge, and water use are notoriously difficult to obtain, says Li Wenpeng, chief engineer at the China Institute of Geological Environmental Monitoring here. For a half-century, the government has relied heavily on data from nonstandardized farmers' wells. To address this shortcoming, the land and water ministries have devised a project, now in final review and expected to start this year, in which more than 20,000 monitoring wells would be drilled across the country, with a focus on northern regions. Each well would track water level, temperature, and water quality, and more than half would also test for pollutants and other contaminants. Remote sensing could augment this effort, Liang says.

"It is time to take action," says Yuan Daoxian, a hydrogeologist at the Institute of Karst Geology in Guilin, China. Unless the government acts quickly to rein in groundwater consumption, Liu adds, "the problem will be impossible to solve." **–LI JIAO**

Li Jiao is a writer in Beijing.

2006 to $4 million and that Arecibo be closed in 2011 if it could not find $4 million from other sources by that date.

Its dire fate has been averted by NSF's own Division of Atmospheric and Geospace Sciences (AGS) and NASA, as well as by modifying the recommendations of the review panel. The new funding plan was unveiled in a 29 April solicitation for proposals to manage the observatory after Cornell's contract ends next year. The solicitation (NSF 10-562) describes how AGS will increase its annual contribution to Arecibo from $2.3 million to $3 million in 2011 and reaching $4 million by 2015. Support from the astronomy division will drop from $8 million in 2010 to $6 million in 2011 and, eventually, to $4 million in 2015. NASA, which stopped contributing to the observatory in 2003, will chip in $2 million a year starting this fall.

Blandford says he's glad that NSF has found a way "to keep a fine facility going." He says the funding levels spelled out in NSF's solicitation seem to be "roughly following the spirit of our recommendations."

Maybe so, says Campbell, but the observatory traveled a bumpy road to get there. "We went through a 20% staff reduction after the review," says Campbell. "Now the staff is overworked, definitely overextended, and we'll be struggling mightily to maintain our research programs." The observatory received $3.1 million last year as part of the massive federal stimulus funding package, which helped to ease its pain, and the Puerto Rican government floated a $3 million bond to pay for needed maintenance. But scientists remain skittish. "Some of the astronomers are worried that our jobs could be on the line," says one researcher who did not wish to be named. "There is still uncertainty."

The lifelines thrown by NASA and AGS could raise the profile of atmospheric studies and asteroid-detection efforts at the observatory, presumably at some cost to astronomical observations. A NASA press release says the agency expects Arecibo to allocate "at least 500 hours per year of telescope operations for planetary radar research supported by NASA, and at least 300 hours of that dedicated to near-Earth objects [NEO] research." Last year's lineup devoted 300 hours to planetary radar, including 170 hours for NEOs.

Robert Robinson, program officer for Arecibo in the AGS division, hasn't laid down any requirements for observing time. However, "we would expect to have more flexibility in the use of the telescope," he says, including being given priority during geophysically interesting events like a solar storm.

Cornell hopes to continue to operate the center. But it will have at least one competitor: SRI International, a nonprofit with a history of managing research and development projects, has said it also plans to bid for the 5-year contract. **–YUDHIJIT BHATTACHARJEE**

CREDIT: CNSPHOTO

ENERGY RESEARCH

Fusion 'Consolation Prize' Gears Up for Show Time

ROKKASHO, JAPAN—Strolling into a massive chamber surrounded by thick concrete walls, fusion engineer Pascal Garin beams like a proud parent as he describes the unique particle accelerator that will be assembled in this empty facility to test novel materials for future fusion reactors. In another vacant building across the campus, physicist Yoshikazu Okumura of the Japan Atomic Energy Agency (JAEA) boasts how the vast hall will soon host the fastest supercomputer in Japan; a stone's throw away, other labs will soon be off-limits to visitors as researchers start experiments on toxic and radioactive materials.

These disparate facilities are all part of a plan to bring fusion energy a step closer to reality. They are proceeding in parallel with the single most important experiment for the future of fusion power, the $12 billion International Thermonuclear Experimental Reactor (ITER). Now under construction in Cadarache, France, ITER is meant to show that it is possible to harvest energy from magnetically contained plasma burning at immense temperatures. But ITER will not fully test fuel production for the plasma envisioned for future reactors, and it will not investigate the advanced materials they require. That's where the $900 million research effort here in Rokkasho, called the Broader Approach, comes in. The project, funded by Japan and six European nations, passed a major milestone on 27 April when its buildings opened on schedule. The Broader Approach is going "rather well," Garin says. That stands in contrast to ITER, which is running late and facing a €1.4 billion shortfall (*Science*, 14 May, p. 798).

The Broader Approach is a child of ITER. In late 2004, ITER's partners at the time—China, the European Union, Japan, South Korea, Russia, and the United States—were split on whether to build the reactor at Cadarache or Rokkasho. Japan and the European Union both had offered to foot half the cost. During the tense stalemate, negotiators crafted a consolation prize for the runner-up. Fusion proponents had long envisioned a Fusion Demonstration Reactor (DEMO) as a steppingstone from ITER to commercial fusion power plant prototypes. But DEMO would require new radiation-resistant materials and extensive engineering studies not on the ITER agenda. "There is still limited knowledge of the physics and engineering requirements for fusion power plants," says JAEA engineer Masanori Araki. Starting these efforts in tandem with ITER would speed the transition to DEMO. The Broader Approach was "a very clever" way to break the impasse, says Garin.

The ITER partners finally tilted to Cadarache. Then in February 2007, Japan and Euratom agreed on a plan for the Broader Approach, under which they would share costs. The project has three ambitious programs. The first is to develop a new type of particle accelerator needed for a future facility to test materials for DEMO. Whereas ITER's vacuum vessel will be made of stainless steel, that won't do for DEMO, which must withstand far greater irradiation damage. Engineers are eyeing reduced activation ferritic steel, a kind of stainless steel that resists irradiation.

To bombard this material with the radiation expected in DEMO, engineers want to build the International Fusion Materials Irradiation Facility (IFMIF), whose site has not yet been chosen. This facility will accelerate two beams of deuterons—nuclei of deuterium, a hydrogen isotope that will merge and smash into flowing liquid lithium, producing a neutron beam aimed at material targets. Whereas current accelerators rev up handfuls of particles to high energies, IFMIF will need a continuous stream of particles at a lower energy. Starting in about 2 years, the Broader Approach will develop and test key components of this future accelerator. Garin, project leader for the accelerator facility and related activities, expects experiments to be completed by 2015. To gain experience controlling the flow of liquid lithium, a test facility will be built at JAEA's labs in Oarai, about 100 kilometers northeast of Tokyo, where the staff has expertise handling highly corrosive materials. Meanwhile, engineers scattered around the world will work on the IFMIF design. As with ITER, the design must go forward even though IFMIF's site will be decided later.

The second leg of the Broader Approach is the International Fusion Energy Research Centre, a grab bag of projects. One is a supercomputer designed to simulate and model ITER, DEMO, and other fusion reactors. It will also aid research on novel materials. Reactors would generate energy by fusing deuterium and a second hydrogen isotope, tritium. Deuterium is abundant in seawater, but tritium is rare. For DEMO and commercial reactors, tritium would be made in the reactor by capturing neutrons from the plasma in a so-called blanket lining the vacuum vessel. There, reactions will multiply the neutrons and steer them toward

Off the ground. Buildings to house Broader Approach research activities were recently completed in Rokkasho, at the northern tip of Japan's Honshu Island.

PHOTO CREDIT: JAPAN ATOMIC ENERGY AGENCY

the lithium; the collisions will produce tritium to feed back into the plasma. This fuel cycle is critical to making fusion energy efficient, says Garin. Starting later this year, the center will begin to develop blanket module materials and radiation-resistant silicon-carbide composites that might supersede ferritic steel in commercial fusion reactors.

Finally, the Broader Approach includes the Satellite Tokamak Program, which will fit Japan's aging JT-60 tokamak in Naka with superconducting magnets. The overhauled tokamak will be used to refine operational protocols "so that experiments on ITER go more smoothly," says Shinichi Ishida, the project leader. They will also be "looking beyond ITER," he says, at plasma experiments relevant to DEMO's design. The new magnets are now being fabricated; experiments on the souped-up JT-60SA (for superadvanced) are expected to start in 2016.

Although the Broader Approach infrastructure is well on track, one big challenge remains: attracting talent. "There is no community of accelerator specialists here," says Garin, who estimates that he needs to hire a few dozen scientists for experiments on the accelerator and a group of 15 to 20 to coordinate and manage IFMIF design activities. All told, the Broader Approach must recruit up to 200 people in Rokkasho, and more for other planned JAEA fusion facilities, Okumura says. The problem is that relocating here is a hard sell. Rokkasho is a cluster of six villages with a population of 11,500 on a peninsula at the northern tip of Japan's main island, Honshu. The snowy, isolated region may be famous for seafood, but it's hard to find good wine or cheese, says Garin, a self-described city lover from southern France who admits that his 3 years so far in Rokkasho have been a big adjustment.

Others enjoy being far from the madding crowd. "In winter, I go skiing every weekend and hiking and fishing in spring and summer," says Okumura. Having lived in rural France, accelerator physicist Christophe Vermare says that he and his wife and two young children "like being near the ocean and the countryside." They also like the attention lavished on children at Rokkasho's new international school, where four teachers oversee just seven pupils. "We have extraordinarily strong support from local authorities to ease our life here," Garin says. "I have less difficulty bringing Europeans to Rokkasho than Japanese," he says. That may be due to Japan's academic culture, in which young researchers feel pressure to land permanent positions early in their careers. The Broader Approach is supposed to wind up in 10 years.

The short horizon raises other issues. "Investing so much money for a few months of experiments is nonsense," Garin says. The time limit could leave a number of key questions unanswered. For instance, the Broader Approach crew won't be able to run the accelerator long enough to verify its reliability for the long-term continuous use needed for IFMIF. The current agreement also does not call for experiments on the interaction between neutron beams and liquid lithium. Garin plans to propose that the accelerator experiments be continued beyond the expiration of the current agreement in 2017. Likewise, Okumura argues that it would make sense to run the supercomputer and other Rokkasho facilities in support of ITER's experimental program, scheduled to start in 2018 and go for 20 years.

According to Okumura, Japan and its European partners could easily extend the Broader Approach. The big question is whether there would still be money for fusion research after paying for ITER. Like all parents of a newborn, Okumura and Garin realize it takes more than 10 years—and heaps of cash—to raise a child.

–DENNIS NORMILE

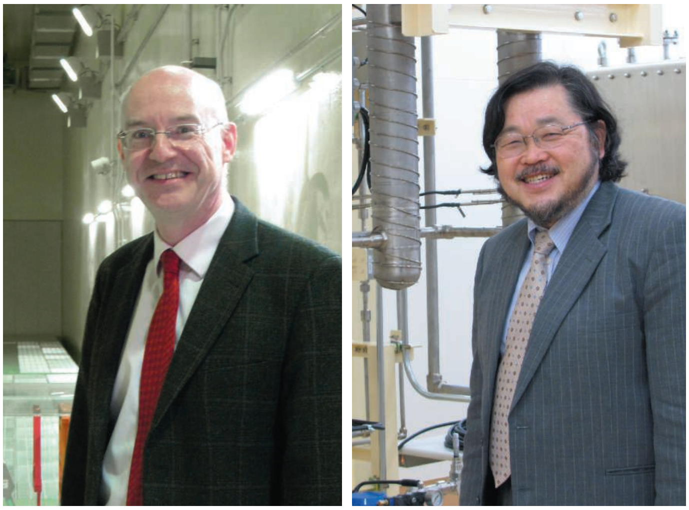

Fatherly pride. With the Broader Approach on track so far, fusion scientists Pascal Garin (*left*) and Yoshikazu Okumura have plenty to smile about.

CREDITS: D. NORMILE/*SCIENCE*

*Science*Insider

From the *Science* Policy Blog

The U.S. Senate rejected a resolution last week that would have blocked the Environmental Protection Agency from **regulating carbon dioxide emissions** based on its finding that they endanger human health. Opponents say Congress, which is deeply divided on the issue, should have responsibility for regulating greenhouse gases. http://bit.ly/epa-greenhouse

Director Francis Collins says the National Institutes of Health needs to revise its **rules designed to prevent conflicts of interest** among researchers after *The Chronicle of Higher Education* reported that a scientist banned by one university from applying for NIH grants for 2 years is free to seek funding after changing jobs. http://bit.ly/nih-director

UNESCO has shelved a planned ceremony this month to award a prize sponsored by the controversial president of Equatorial Guinea amid growing concern that accepting the gift may tarnish its reputation. http://bit.ly/unesco-review

The University of California (UC) system is threatening to boycott Nature Publishing Group's journals to protest what the university is calling an "exorbitant and unreasonable" **increase in subscription fees** and what the publisher says is a necessary adjustment after years of "unfair" discounts. http://bit.ly/uc-boycott

As part of our team coverage of the oil spill in the Gulf of Mexico (see http://news.sciencemag.org/oilspill), we reported that:

- A research cruise hopes to study a modern-day analog to **violent outflows of methane gas** from the sea floor that might have caused the planet's temperature to spike about 55 million years ago. Methane makes up about 40% by mass of what's spewing out of the BP well.

- Scientists want to divert less water **from the Mississippi River** to protect Louisiana's wetlands. Increasing the flow through the delta should help keep oil at bay for longer.

See the full postings and more at **news.sciencemag.org/scienceinsider**.

Published by AAAS

ENVIRONMENT

Endosulfan's Exit: U.S. EPA Pesticide Review Leads to a Ban

After a lengthy scientific review, the United States last week decided to ban the use of endosulfan, an inexpensive organochlorine pesticide that builds up in the environment. The U.S. Environmental Protection Agency (EPA) ruled that the compound—which has a variety of uses from Florida's tomato crops to California's cotton—should be phased out on a schedule to be negotiated with the manufacturer. More than 60 other countries have already opted for a ban; the holdouts—including India and China—argue that the pesticide should continue to be permitted where farmers cannot afford substitutes.

Exposed. A review by EPA found potential health risks for farm workers coming in contact with endosulfan.

EPA concluded that endosulfan poses a hazard to both wildlife and humans, citing evidence of fish deaths downstream from treated areas and indications of neurodegenerative impacts in animals, with implications for humans, particularly farm workers. Among recent data cited by EPA is a study published online earlier this year in *Ecotoxicology* showing that fish at lower trophic levels in the Everglades may retain endosulfan in tissues and pass it on to wading birds that feed on them. (Compounds that collect in tissues and are passed to predators up the food chain are said to "bioaccumulate.") Previous studies have detected low levels of endosulfan in Arctic animals' tissues, a key indicator of bioaccumulation. Other studies have found traces of endosulfan in human breast milk.

The current EPA review began after Bayer, endosulfan's patent holder and original maker, received permission to reregister the product in 2002, with a request for updated toxicity data from EPA. Bayer's test results, submitted in 2006, showed evidence of developmental neurotoxicity in rats and toxicity at low levels in the fetuses of pregnant rats; the agency subsequently opened its review for the withdrawal of certain uses. The next year, Bayer stopped selling endosulfan in the United States and pledged to stop selling it internationally by the end of this year. The only remaining U.S.-registered endosulfan maker today is Makhteshim Agan, an Israeli manufacturer with a branch in North Carolina.

Starting in 2007, EPA gathered public comment on endosulfan's ecotoxicological impacts and on potential economic impacts on U.S. farmers if the pesticide were banned. Last week, EPA announced that it will seek a voluntary phaseout with Makhteshim Agan.

The EPA decision seems to have already had repercussions abroad. The Australian Pesticides and Veterinary Medicines Authority, which allows some restricted uses of endosulfan, issued a statement last week saying that it does not know of any human health impacts in Australia. But the agency says it is in contact with EPA and other Australian authorities to see if it, too, should take further action on endosulfan.

Some advocates of a global ban are pushing for controls through the Stockholm Convention, which restricts the use of long-lived compounds. Endosulfan is similar in some ways to the "Dirty Dozen" persistent organic pollutants (POPs)—including chlordane and dieldrin—that were restricted when the convention went into force in 2004. Last year, the convention's scientific advisory group, the POPs Review Committee (POPRC), recommended that endosulfan be considered a POP under the treaty's definition—but they encountered dissent.

India's representative at last year's annual meeting of POPRC argued that endosulfan is not toxic to humans or the environment at levels currently detected. India also questioned whether Indian users were the source of "long-range transport."

Although research shows unquestionably that endosulfan travels far afield, questions do remain over whether the bioaccumulated levels in animals are high enough to be toxic, says Bert Volger of Ceres International LLC, who represented Makhteshim Agan as an observer at the 2009 POPRC meeting. The company disagrees with EPA's scientific assessment but said in a press release last week that, given the high cost of challenging EPA's decision, it will cooperate with the proposed U.S. phaseout.

When POPRC holds its next meeting in October to consider the socioeconomic impacts of restricting endosulfan use, India is expected to make the argument that a ban would harm poor farmers. (The Indian government owns the country's main producer of endosulfan, Hindustan Insecticides Ltd.) Environmental groups say China, another major endosulfan manufacturer and user, is likely to support India's position.

EPA considered economic impacts alongside environmental ones when it evaluated a ban in the United States. It concluded that a switch to safer replacements would not harm farmers' bottom lines. Alternatives like the insect-attacking bacterium *Bacillus thuringiensis* and a family of synthesized plant compounds known as pyrethroids are less toxic to humans. Many farmers in China have already made the switch to these substitutes, according to a report to the Stockholm Convention from two observing environmental activist groups, Pesticide Action Network International and the International POPs Elimination Network (IPEN). Still, China may not be ready to list endosulfan under the Stockholm Convention, according to Joe DiGangi of IPEN.

DiGangi, who has been monitoring the POPRC conversations, says IPEN has pushed these alternatives for India as well. He argues that EPA's decision could influence policies abroad in a couple of ways. DiGangi says it will add new studies to the toxicity data available to decision-makers, and it could persuade other countries that "a Stockholm Convention listing is on the horizon." The impact on endosulfan manufacturers such as India will be limited, however, he says: "The U.S. ban will not affect the Indian industry economically," for example, but it will make the defense of endosulfan "even more difficult."

–NAOMI LUBICK

Naomi Lubick is a writer in Zurich, Switzerland.

CREDIT: LUIS M. ALVAREZ/AP PHOTO

ScienceNOW

From *Science*'s Online Daily News Site

False Peepers Frighten Predators Is that a snack or a snake? To small tropical birds foraging on the rainforest floor, those two scowling eyes peering back at them from between the leaves could be a predator. But they could also belong to one of the hundreds of caterpillar species that have evolved eyelike spots and patterns to trick feasting birds. The patterns don't need to be highly detailed to work. Even the mere suggestion of eyes is enough to shoo a bird away, suggesting that the birds are reacting to hard-wired, predator-avoidance instincts, researchers report in the *Proceedings of the National Academy of Sciences*. http://bit.ly/false-eyes

Did a Deep Sea Once Cover Mars?

Once upon a time, a deep ocean covered one-third of Mars. Then, billions of years ago, it dried up, leaving the arid, rocky planet we see today. It's a provocative idea, but is it true?

In a new study, Gaetano Di Achille and Brian Hynek of the University of Colorado, Boulder, considered 52 martian deltas—piles of river-borne sediment—that formed at the level of some body of standing water, as the Mississippi delta is forming at the level of the Gulf of Mexico. One-third of the deltas are at the same elevation ±177 meters (one standard deviation), the pair reports in *Nature Geoscience*. The simplest explanation, the researchers say, is that all of these deltas formed around the same ocean about 3.5 billion years ago.

But planetary fluvial geologist Rossman Irwin of the Planetary Science Institute in Tucson, Arizona, is somewhat skeptical, pointing to some deltas and valley networks that lie well below the team's favored sea level, a physical impossibility if an ocean that deep existed at the time they formed. Even so, he thinks it's likely that some sort of northern ocean once existed, even if it's difficult to prove. http://bit.ly/mars-sea

Genetic Map of Autism Comes Into Focus

A new study of nearly 1000 people with autism has confirmed that the genetics of the disease are much more idiosyncratic than some had thought. Rather than a few genes that raise the risk of autism throughout the population, scientists are finding dozens of genes that spur disease, many of them in just one or two people.

Researchers scanned the genomes of 996 children with autism-spectrum disorders, a group of conditions that affect social and communication skills, at high resolution and compared them with the genomes of the children's parents and those of 1287 people without the disease. Just over 5% of those affected had at least one copy-number variant—a deletion or duplication of stretches of DNA that can encompass many genes—that was not present in their parents. And copy-number variants inherited from parents were also much more common in the autistic cohort: Overall, rare copy-number variants were 19% more likely to disrupt genes in autistic children than in controls, the team reports in *Nature*.

Deletions of genes had a big effect. Nearly all of these were extremely rare, showing up in, at most, a handful of families. "Most individuals that have autism will have their own rare form," genetically speaking, concludes senior author Stephen Scherer, a geneticist at the Hospital for Sick Children in Toronto, Canada.

However, the team found that genes deleted in autistic patients tended to perform similar tasks. Many were involved in aspects of cell proliferation, such as organ formation. A number participated in development of the central nervous system and others in maintaining the cytoskeleton, which protects the cell and helps it move. http://bit.ly/autism-genes

Read the full postings, comments, and more at **news.sciencemag.org/sciencenow**.

Was the New World Settled Twice?

Were the primary ancestors of today's Native Americans really the first people to set foot in the New World? Genetic evidence suggests so, but ancient skeletons tell a different story.

In an attempt to settle the debate, a team of paleoanthropologists compared the skulls of several dozen Paleoamericans, which date back to the early days of migration 11,000 years ago, with those of more than 300 Amerindians, which date to 1000 years ago. The researchers found clear differences in the shapes and sizes of the Paleoamerican and Amerindian samples. That suggests that more than one group of individuals migrated to the Americas from Asia, the team reports in *PLoS ONE*. And due to the age of the skeletons, the researchers say, this other group of individuals arrived before the primary ancestors of today's Native Americans.

The work is "solid" and "perhaps the most sophisticated analysis of craniofacial traits undertaken to date," says Theodore Schurr, a molecular anthropologist at the University of Pennsylvania. But he warns that the small sample sizes leave the door open to other interpretations. http://bit.ly/new-world

CREDITS (TOP TO BOTTOM): D. H. JANZEN *ET AL., PNAS EARLY EDITION* (2010); LEEH-IB-USP

Sublime. Ilya Kaler plays the Vieuxtemps, crafted by Guarneri del Gesù in 1741.

Probing the Secrets Of The Finest Fiddles

Violinmakers take up the tools of science in a study of Guarneri del Gesù's Vieuxtemps and other great violins

CHICAGO, ILLINOIS—Ilya Kaler, a renowned soloist, gazes admiringly at the 269-year-old violin. He has just played four other great old Italian instruments in an invitation-only recital in the cramped quarters of Bein and Fushi Inc., violin dealers whose shop looks out over Chicago's famous Michigan Avenue. Now Kaler holds the star of the 7 April event, a fiddle named the Vieuxtemps after a previous owner and crafted by Bartolomeo Giuseppe Antonio Guarneri, also known as Guarneri del Gesù, who, along with Antonio Stradivari, is widely considered the best violinmaker ever to have lived.

"This is one of the greatest instruments in existence, no doubt, one of two, maybe three," says Kaler, who, with his easy smile and a crimson handkerchief tucked into the breast pocket of his tuxedo, exudes the unassailable confidence of a virtuoso. Then he reconsiders that count. "Three is too many," he says.

For sale for $18 million, the Vieuxtemps is a superior instrument, a piece of 18th century art, a potential investment, a legend. It's also the subject of scientific study. With the permission of its owner and dealer Geoffrey Fushi, a team of violinmakers and scientists has put the Vieuxtemps and three of the other violins in the recital through tests including computed tomography (CT) scans and acoustic measurements. They hope to pinpoint traits that distinguish a great violin from a good one or a Stradivarius from a Guarneri.

The project also highlights an emerging trend within violinmaking. For decades, the instrument has fascinated a small community of scientists and engineers. Now, even as the scientific experts age and retire, some leading violinmakers are adopting their conceptual tools and experimental methods and taking a decidedly more scientific approach to their centuries-old craft.

Online
sciencemag.org
Podcast interview with author Adrian Cho.

"Violinmaking involves a lot of sitting around and scraping pieces of wood, and if you want to have a life of the mind, you want to be thinking about these [technical] things," says Joseph Curtin, a violinmaker from Ann Arbor, Michigan, who proposed the study to Fushi. But so far, science cannot tell the best fiddles from the merely good ones, cautions James Woodhouse, an acoustics engineer at the University of Cambridge in the United Kingdom who has studied the violin for 35 years. "We know pretty well how to distinguish a really bad instrument from a really good one. What distinguishes a pretty good instrument from a stratospheric instrument, I think we still don't know."

As Kaler plays, however, it's hard to believe that distinction will forever defy scientific analysis. The brilliance of another Guarneri del Gesù, the Sennhauser, slices through as he moves from the introspective andante to the skipping allegro of a sonata by Handel. The darker sound of a violin made by Giovanni Battista Guadagnini in 1752 conjures an image of molasses as the soloist wrings emotion from Schumann's melancholy *Romance in A*, and the Cathedral Stradivarius sings sweetly as he bows Gluck's soaring *Mélodie*.

Finally, the Vieuxtemps rings out almost painfully bright in three pieces including the playful *Rondino* by 19th century Belgian violinist Henri François Joseph Vieuxtemps, who once owned the fiddle. The violins speak with voices as distinct as people's, and it seems impossible that science cannot quantify the differences.

Scientists seduced

The violin has captivated scientists for more than a century. In 1862, German physicist Hermann von Helmholtz cobbled a stroboscope from a tuning fork to decipher the motion of a bowed string. A single kink zips back and forth between the "bridge," the stanchion on the violin's belly over which the strings run, and the spot where the player pins the string to the fingerboard. The vibrations pass through the bridge and into the violin's body, whose arched top is carved from a slab of spruce and whose back and sides are made of maple. Since the 1930s, researchers have learned much about how the violin converts those vibrations to sound.

To move a lot of air and sing loudly, a violin must vibrate readily, or "resonate," like a tuning fork. But whereas a tuning fork has a single soundmaking resonance at a sharply defined frequency, a violin has hundreds of resonances that overlap, enabling it to respond at pitches ranging from 196 hertz (open G) to above 20,000 hertz. Yet it should not ring equally at all pitches, as it would then sound lifeless. "It's not a loudspeaker with a flat-spectrum response," says George Stoppani, a violinmaker in Manchester, U.K. Instead, the spectrum with which a violin radiates

CREDIT: EUGENE SCHENKMAN, *THE STRAD DIMENSION*

sound resembles a mountain range, with each peak corresponding to a pattern of motion, or "mode," of the body (see figure, below).

One way to study the spectrum and the modes is by thwacking the bridge with a small hammer and measuring the violin's output and motion. Around 280 hertz lies the A0 mode, in which air flows in and out of the "f holes" on the violin's belly. The B1– and B1+ modes, identified in the 1980s, lie around 480 hertz and 550 hertz. Around 2500 hertz lies a thicket of modes called the "bridge hill," long thought to be due to motion of the bridge. Each mode can be complex, as the violin's symmetrical exterior hides its asymmetrical interior. Under one foot of the bridge, a beam called the bass bar reinforces the top; beneath the other foot, a pillar called the sound post connects top and back.

Much work has focused on the radiation spectrum, which varies among violins a bit like the way fingerprints vary among people. In 1991, German physicist Heinrich Dünnwald reported on the spectra of 700 violins including 53 old Italians, dividing them into six bands that he claimed are associated with qualities of sound. For example, Dünnwald said, a violin that radiates more strongly between 650 hertz and 1300 hertz than in the neighboring bands sounds "nasal," whereas one that pumps out more energy from 4200 hertz to 6400 hertz than at lower frequencies sounds "harsh."

Dünnwald defined a quality index according to which 92.5% of the old Italians ranked as superior, compared with 19% of quality instruments made after 1800. But some researchers question the simple association of frequency bands with sound qualities and the conceptual value of such correlations. "Of course, the old Italians were on top of the list, and that's not that interesting to me because it doesn't tell you how a violin works," says Gabriel Weinreich, a physicist retired from the University of Michigan, Ann Arbor, who has studied the violin since 1978.

Scientists continue to probe the violin in ever greater detail, teasing out the interplay of modes and showing, for example, that the bridge hill does *not* stem from a simple rocking of the bridge. Until recently, however, their work attracted little interest from violinmakers. That's changing, says Woodhouse. "There's a lot of research going on, but it's driven by makers," he says. "And they're top makers, not marginal makers who everybody laughs at."

A revolution in the making

The meeting of minds hasn't come easy, says Samuel Zygmuntowicz, a violinmaker from New York City who made a violin that sold at auction for $130,000, a record for a living maker. Scientists responded tepidly a few years ago when he presented work at an acoustics meeting at Cambridge, he says. "They were trying to explain to me how to do better measurements, and I was trying to explain the phenomena I thought I was discovering," he says. "We couldn't get past it." But Zygmuntowicz boned up on physics and says a meeting in Cambridge last September went much better.

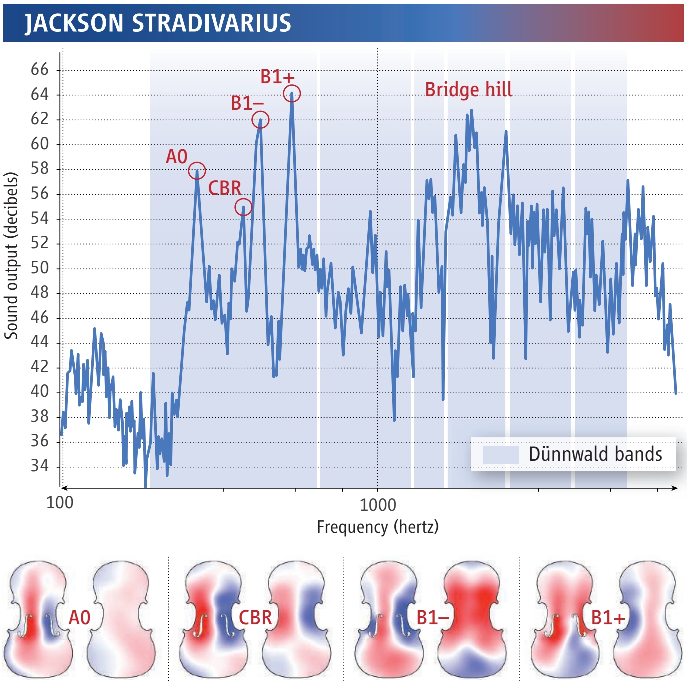

Sonic fingerprint. Each peak in a violin's spectrum corresponds to a mode of vibration. Red and blue denote motion in opposite directions.

Working with scientists has given violinmakers access to tools far more sophisticated than the chisels and calipers they traditionally use. As early as the 1980s, researchers put violins through CT x-ray scanners, to trace an instrument's internal structure and look for defects and repairs. High-resolution scans may also provide insight into a long-debated issue of whether the wood in the old instruments differs from that in newer ones, perhaps because it was treated in some way.

Terry Borman, a violinmaker from Fayetteville, Arkansas, and Berend Stoel, a computer scientist working on image processing at Leiden University Medical Center in the Netherlands, took high-resolution scans of three Guarneri del Gesùs, two Stradivariuses, and eight modern violins. They found no difference between the average densities of the wood in the tops of old and new violins. Within the old tops, however, the density varied less between the light grains produced as trees grow during the warmer months and the dark grains produced during colder months, they reported 2 July 2008 in *PLoS ONE*. "So the old violins were a lot more homogeneous," Borman says.

Conversely, teaming with leading makers gives scientists access to rare old instruments. George Bissinger, a physicist at East Carolina University in Greenville, North Carolina, has studied the violin since 1969. But it wasn't until he teamed with Zygmuntowicz in 2006 that he was able to put a Guarneri del Gesù and two Stradivariuses through testing in a project called Strad3D. He and eight violinmakers, a radiologist, and an engineer used a three-dimensional laser vibrometer to map the fiddles' mode, an anechoic chamber to analyze their spectra, and CT scans to probe their guts.

The study has provided no simple way to separate the good violins from the bad ones, however. For example, the spectra of fine old violins differ from those of poorer new ones only in a few subtle ways, Bissinger says. The old Italians have slightly more uniform spectra and slightly greater damping than 14 lesser violins, Bissinger reported in the *Journal of the Acoustical Society of America* in September 2008. They also have stronger A0 modes. "That's the one robust difference between a good and a bad violin," he says.

The current study suggests that the Vieuxtemps sings in a way that other fiddles do not. In fact, that observation was the impetus for the project. Curtin had heard that Fushi had the fiddle and talked his way into making some measurements. As other analysts do, he uses a tiny automated impact hammer to strike the bridge from the side. But Curtin also tapped it from the top. "I found an acoustical feature that showed up spectacularly well in the Vieuxtemps, in fact more so than with any other violin I've seen," he says.

Curtin had pinged other instruments that way and saw signs of a second bridge hill above 3500 hertz. But when its bridge is struck

CREDITS: GEORGE STOPPANI

Like new. Typical patches and repairs show up as light spots in the CT scan of a 1730s violin (*right*). The Vieuxtemps (*center*) is spotless.

vertically, the Vieuxtemps resonates sharply at 4125 hertz, Curtin explains a few days after the recital. In his quiet studio off a dirt road outside Ann Arbor, he shows several plots—made with software written by Stoppani. The Vieuxtemps's spectrum shows a peak about 5 decibels high that is absent in the spectrum of the Cathedral Strad. The Jarnowich Guarneri del Gesù shows a smaller feature, so the resonance may be common to Guarneri del Gesùs, says Curtin, who wants to trace its origin.

Spurred by that observation, Curtin talked Fushi into letting him conduct more tests and assembled a team including Borman, Stoel, Stoppani, Weinreich, and Woodhouse. The researchers are still analyzing their data, but one fact is already clear. Most old instruments have been repaired multiple times and patched near the bridge and sound post. A CT scan shows that the Vieuxtemps is pristine (see figures, above), Borman says. So compared with other old Italians, it may sound more like its maker intended.

What difference?

But can subtle density variations or spectral features explain the supposedly superior qualities of Strads and Guarneris or distinguish between them? Cambridge's Woodhouse has doubts. Acoustically speaking, researchers can now say why a violin sounds like a violin and not a guitar, he says, but they struggle to make finer distinctions. "If you chose any particular feature, you can probably find two million-dollar violins that differ from each other in that one feature as much as the million-dollar ones differ from a good $10,000 modern one," Woodhouse says.

In fact, Woodhouse and Claudia Fritz, a psychoacoustician at Pierre and Marie Curie University in Paris, have studied how big the changes in a violin's spectrum must be before listeners can tell the difference. To do that, Fritz digitized the spectrum of a violin to create a "virtual violin." When a violinist plays, say, an A, the string vibrates at 440 hertz and multiples of that frequency, or "harmonics." The violin's spectrum then determines how strongly it radiates at each of those frequencies. With the virtual violin, Fritz can change that spectrum, raising and lowering peaks or shifting their frequencies.

Not surprisingly, musicians have proved much more sensitive than nonmusicians to small changes in the spectrum, as Fritz and colleagues reported in December 2007 in the *Journal of the Acoustical Society of America*. When comparing single notes, musicians could tell if the strength of a resonance like the A0 or B1+ changed by about 4 decibels—slightly more than a doubling in intensity. They could tell if the frequency of the resonance was shifted by about 5%, roughly the difference between, say, C and C-sharp. Curtin says the Vieuxtemps's B1+ resonance is about 10% higher in frequency than those of the Strads. Listeners could detect smaller changes in a Dünnwald band.

The researchers also tested the correlations between subjects' perceptions and the relative strengths of the Dünnwald bands, which are used as guides by makers, and came up with some surprises. For example, some people thought notes with stronger low-frequency components sounded nasal, whereas others thought just the opposite. "When violinmakers are talking about the nasal band, they should be careful," Fritz says, "because there is no nasal band at all."

Such results further complicate an already confusing situation. Yet, collaborations between scientists and violinmakers seem likely to continue, as they offer makers greater insight into their creations, which for centuries they have crafted by copying excellent old instruments. "I think the best way to make a great violin is to understand what makes an instrument great and what's peripheral," Curtin says. "When we copy, we tend to copy everything."

Moreover, the fact that so far tests have identified no obvious difference between great and good violins may actually be telling researchers something. Most studies have been made on violins in pristine isolation, typically suspended by rubber bands from a mount. Of course, when played, a fiddle lies clamped beneath a violinist's jaw, its neck cradled in the musician's hand, its strings worked by the bow. The instrument's defining qualities may show through only in that interaction.

"I can tell you that the violinist is the big deal," Bissinger says. "A great violinist can make even a bad violin sound good." Zygmuntowicz agrees but warns that researchers may struggle to get reliable data on the working violin. "The situations that a violin operates in are really contaminated circumstances for testing," he says. "Science has shied away from that interaction because it doesn't make good papers yet."

To hear Kaler tell it, the violin-violinist interaction is subtle. Asked what distinguishes the Vieuxtemps, he cites its resonance and ease of response. Then he adds, "If a violin responds too easily, it limits the possibility of a performer to produce many colors or to put his or her own imprint on the instrument because the instrument anticipates your desires too much." So a violin must resist just enough to make the violinist work for what he wants, he says.

If the Vieuxtemps resists Kaler, it doesn't show. He closes the recital on the Vieuxtemps with Alexander Glazunov's dreamy *Meditation*, its luminous last note, a seemingly impossibly high D, hanging in the air like twilight. To the scientifically minded, it whispers, "Explain my beauty!" But doing so may be as difficult as grasping the fading reverberations of the music itself. **–ADRIAN CHO**

CREDITS (LEFT TO RIGHT): EUGENE SCHENKMAN; *THE STRAD DIMENSION*; BEREND STOEL AND TERRY BORMAN

Published by AAAS

PROFILE: LINDA BARTOSHUK

A Taste for Controversy

After discovering "supertasters," Linda Bartoshuk is pushing to change how psychologists evaluate subjective experiences such as taste and pain

GAINESVILLE, FLORIDA—After just a glance at her graduate student's notes, Linda Bartoshuk knows that the results of today's experiment will have to be thrown out. The concentration of quinine—a bitter chemical used in this study of taste perception—is one-tenth of what it should be. The student, Adilia Blandon, suddenly realizes her mistake. Blandon had given the quinine to a team of undergraduate assistants to gauge volunteers' sensitivity to different flavors, but with the wrong standard for bitterness, she can't compare these data with previous results. Blandon turns to Bartoshuk with a cringe and groan. Behind her, the doomed experiment continues.

Moments like these test a busy scientist's patience. But without missing a beat, Bartoshuk nods and says, "Don't worry. This is why we call it a pilot study. Now is the time to catch mistakes." Blandon perks up like a sail catching a fresh breeze and heads back into the lab.

Bartoshuk, a professor here at the University of Florida (UF), Gainesville, wasn't just being nice. "I tell my students that if you're not making mistakes in science, you're not taking enough risk." It was an oversight similar to Blandon's that led to Bartoshuk's most famous discovery: supertasters, people with extreme taste sensitivity. But Bartoshuk's research has illuminated more than the human mouth, says Anthony Jack, a psychologist at Case Western Reserve University in Cleveland, Ohio: "She has helped lead the movement to study subjective experience, considered off-limits for a long time."

That leadership has paid off in many high-profile publications, election to the National Academy of Sciences, and last year, the presidency of the Association for Psychological Science (APS). Her career hasn't come without controversy, however. The concept of supertasters still ignites debate. And Bartoshuk is making waves again. Her latest passion is nothing short of overturning one of the central methods of her entire field, the subjective scales on which generations of psychologists have built their careers.

How not to keep a girl out of science

As a girl born in mostly rural South Dakota in 1938, science was not high on the list of career options for Bartoshuk. But after reading every science-fiction book she could get her hands on, the young Bartoshuk dreamed of astronomy. Her high school had other plans for her. "They forced me to take secretary classes," she recalls with a wry smile. They did accede to Bartoshuk's request to take trigonometry, physics, and chemistry. "I was the only girl in the class, and I was as surprised as anyone when I got the highest grades." It helped her win a scholarship to attend Carleton College in Northfield, Minnesota—her family couldn't afford the tuition otherwise—and it was science ever after.

Bartoshuk says she abandoned astronomy when she learned that "women weren't allowed to use the big telescopes." She switched to the field that would become the scientific love of her life: psychophysics, the study of how physical stimuli from the environment—sugar on your tongue, vibrations in your ear, heat on your skin—lead to the mysterious phenomenon called subjective experience. It may be a branch of psychology, says Bartoshuk, but "psychophysics has a lot in common with astronomy." Like the stars in a distant galaxy, the minds of other people are ultimately "untouchable," she says. The only way to bridge the gap is with rigorous experimental observation and mathematical analysis.


CREDIT: J. BOHANNON

Taste explorer. After unlocking the mystery of taste sensitivity, Linda Bartoshuk is now hunting for the "perfect tomato."

Already as an undergraduate, Bartoshuk decided to study taste. "The tongue was unexplored territory in sensory research," she says. As a first-year graduate student at Brown University, she wanted to work with Carl Pfaffmann, one of the leading taste researchers and the first to identify the nerves that send taste signals from the mouth to the brain. She vividly recalls her first conversation with the man who would become her Ph.D. adviser. "Pfaffmann told me point-blank that he didn't want women in his lab," says Bartoshuk. And why? "They're always crying and washing their hair."

Bartoshuk dresses plainly, but she does wear big, bright emotions. When she laughs, which is often, she shakes with it. And when she recalls the troubles with Pfaffmann, the sting is suddenly visible in her face, 5 decades later. Lewis Lipsitt, a psychologist at Brown University, says that Pfaffmann was not an easy man. "[He] could be

Published by AAAS

blunt and he was by nature not an effusive, congratulating kind of person."

Bartoshuk's emotions and hair care didn't prevent her from winning over Pfaffmann. One day, Bartoshuk says, she finally became "one of the boys." An experiment was going badly, with nerve fibers drying out. "I had an idea for a solution, but Pfaffmann was completely dismissive," she says. So she stormed out and returned with a contraption she'd made out of wire to keep the fibers suspended in mineral oil. It worked. "He told me, 'I guess you're pretty good at this.' "

Five years later, when Bartoshuk was settled as a scientist at Yale University, the phone rang. It was Pfaffmann. "I was still mad at him," she recalls, but he had an astonishing proposal. Calling her from a hospital bed, he wanted Bartoshuk to study him; a viral infection had damaged Pfaffmann's nervous system, knocking out taste sensation from one side of his tongue.

Intrigued by this rare opportunity, for months Bartoshuk conducted experiments on her former mentor. By "painting" taste solutions across his tongue in different directions—either from the "dead" side to the "live" side or vice versa—she was able to test conflicting theories for taste perception. "We proved that the taste-transmitting nerves do not poach across the midline of the tongue," says Bartoshuk. "We confirmed that taste follows touch paths on the tongue, which wasn't known." And by tracking the intensity of tastes as Pfaffmann's nerves healed, they discovered "unexpected" aspects of how the nerve signals add up to subjective taste perception. "He turned into one of the best data sets at the time," says Bartoshuk.

Then, Pfaffmann suffered a stroke and slowly died. Bartoshuk published a short abstract version of the results and put the data away. "I was too sad to work on it," she says. But all these years later, some of the work is still new to science. Bartoshuk intends to publish it, with Pfaffmann as lead author, "if people agree that it's ethical."

Supertasters

In 1990, Bartoshuk noticed something strange in her latest study of people's sensitivity to bitterness. Like researchers before her, she observed that people differ in sensitivity to identical solutions of a bitter chemical called PTC. The underlying genetics were well understood. The expression in taste buds of a protein receptor for PTC was required, and you either had it or you didn't. Over the years, she had been using the same test subjects for other taste experiments, and she suddenly realized that "some of the same people who were the most sensitive to bitterness were also the most sensitive to sweetness and sourness."

For the most part, sensitivity to what was known as the "basic tastes"—bitter, sweet, sour, salty—were thought to be independent. But what if they weren't? Bartoshuk's subjects were judging the intensity of bitter solutions in relation to a control solution of saline. "I realized that if some people are more sensitive to every taste, salt included, then that is no control at all."

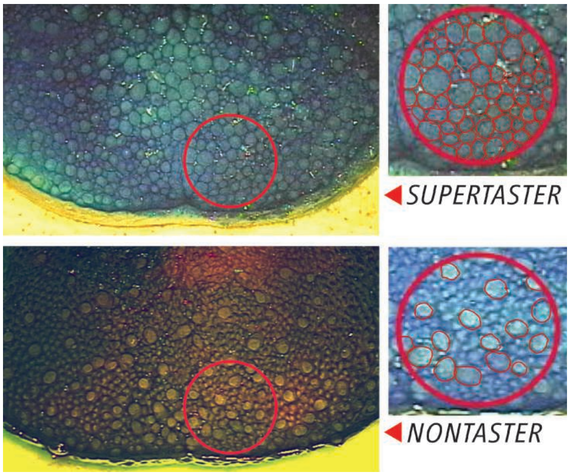

Rosetta stone. Supertasters have far more fungiform papillae, bumps on the tongue that house the taste buds.

To try to get around the problem, Bartoshuk asked her subjects to put the intensity of tastes they experienced on a scale based on a totally different sense. "I used sound," she says. At the bottom of the scale was silence; at the top was "the loudest sound you have ever heard." Because people's sensitivity to taste and sound should be independent, this could be a way to identify people with highly tuned tongues.

A striking pattern emerged from the data. About 25% of people she studied were highly sensitive—as high as triple the average—to every taste. "These are people who live in a different taste world," says Bartoshuk. "If our tastes are painted in pastel colors, theirs are painted in neon." She dubbed them "supertasters."

The term soon became a household name, and Bartoshuk was inundated with requests for interviews. Bartoshuk didn't mind the attention, but she quickly regretted the term, especially as confusion about the phenomenon spread. "It's not actually true that their taste is super," she acknowledges. "It's just different." She says that, for example, vegetables from the Brassicaceae family of plants—cabbage, broccoli, kale—taste bitter to supertasters so they tend to avoid them. On the other hand, they also tend to eat fatty and salty foods sparingly, "so they are less likely to be obese."

And what makes someone a supertaster? "It turns out to be simple," says Bartoshuk, who regrets that she is not one of them. "Supertasters have far more taste buds than the rest of us." Bartoshuk has administered the test for taste-bud density—counting those bumps in a fixed area of a blue-dyed tongue—to thousands of people. Realizing that taste-bud density determined the intensity range of taste "was like discovering a Rosetta stone for the senses," she says.

Not everyone agrees with Bartoshuk that people are born with fixed food preferences, and it seems that most who disagree do so sharply. "People learn to like or dislike bitter foods," says Tom Baranowski, a psychologist at Baylor College of Medicine in Houston, Texas. "There's no relationship between those preferences and whether or not you're a supertaster." Baranowski says he had hoped supertaster status would be "a lever" for improving public health. But now he calls it "a waste of time." Several other researchers have also failed to reproduce correlations between supertaster status and behavioral or health trends.

Partly because of the media blitz, a scientific "feud" over supertasters may have been inevitable, says Beverly Tepper, a psychologist at Rutgers University in New Brunswick, New Jersey. "Some of [Bartoshuk's] colleagues have felt that she oversold supertasters." Tepper says that further research has supported the supertaster effects—that Bartoshuk was right after all, she believes—but that "a lot of people have gotten soured to this field because there are a lot of confusing results." There is even disagreement over how to diagnose someone as a supertaster. The most widespread diagnostic method continues to be high sensitivity to bitterness, frustrating Bartoshuk. "Initially, lots of people accepted that definition," she says, although taste-bud density turned out to be a more reliable marker. "I think we were sloppy about it."

Regardless of the disputes, says Tepper, Bartoshuk "really launched this whole area, and it has helped psychophysics to see individual differences" between people.

You taste tomato, I taste …

Bartoshuk pops a bright red wedge into her mouth. "Oh! These are delicious," she says, munching on one of the different varieties

CREDITS: COURTESY OF LINDA BARTOSHUK

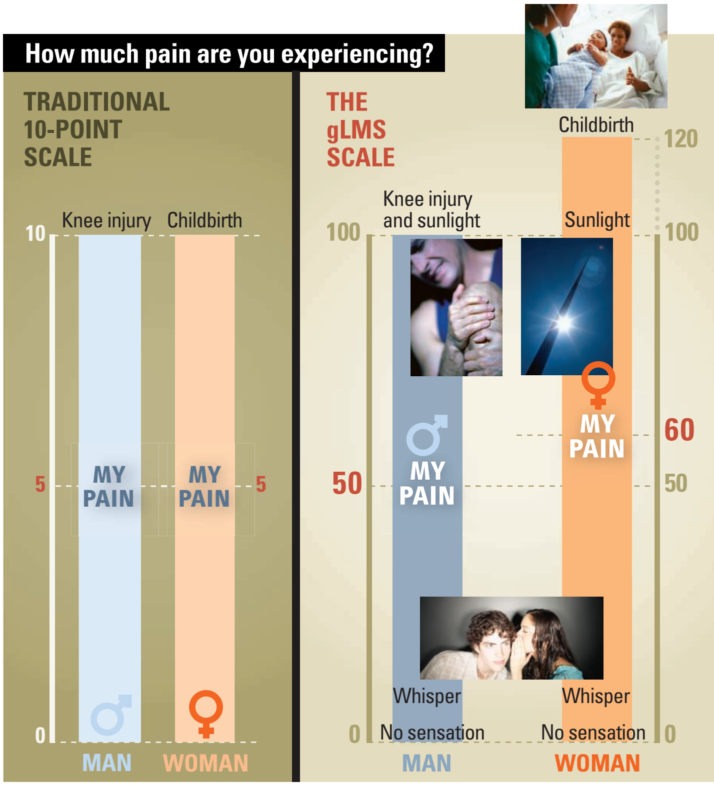

Same pain? On the traditional scale (*left*), the pain reported by a man and woman may end up equal. Bartoshuk's method uses a personalized scale built of each person's experiences from various senses. In this case, the calibrated scale indicates the woman's injury is more painful than the man's.

of tomatoes that have just been sliced and distributed into plastic sample cups. In the coming weeks, hundreds of people will eat similar tomato wedges, scoring various aspects of the taste experience. "The goal is to find the perfect tomato," she says.

Improving people's diet is the aim of this interdisciplinary study. The taste of tomatoes and other fruits "have degraded because of the pressures of the market," says Harry Klee, a plant biologist at UF who collaborates on the project. As supermarkets have demanded fruit that can withstand shipping and rapidly ripen, taste has been unintentionally bred out of tomatoes. Klee believes that the genes for tastiness, most of which is determined by the dozens of aroma molecules that tomatoes produce, can be put back into supermarket varieties. But the challenge is to nail down what exactly people like about "good" tomatoes.

Bartoshuk is drawing on a lesson from her supertaster research by reconceiving how to use sensory scales. She has decided that to make sure the subjective taste data from different people can be compared, each subject must build a personalized scale. It is a complex process, beginning with a strange task: "Please identify the strongest sensation of any kind that you have ever experienced." For most people, says Bartoshuk, the strongest is some kind of pain. Among women, for example, it is usually childbirth. That defines the top of a sensory ladder, and the intensity of various non-taste sensations—loud sounds, bright lights—define the intermediate rungs.

Bartoshuk says that this method, called the general labeled magnitude scale (above), helps her avoid a serious mistake. "If I want to compare the taste experiences of different people, how do I know they're using the scale the same way?" she says. On a 10-point scale of sweetness, "if you say this tomato is 6, and I also say it's a 6, how do we know it's the same sensation? Your 6 might actually be equivalent to a 3 for me."

She first noticed the scaling problem in taste research, but Bartoshuk says that it goes far deeper: "Anytime you want to compare subjective experience across different subjects, you run into the scaling problem." She says the error casts doubt on decades of psychophysics research, as well as studies in other fields that have misused subjective scales, such as in neuroscience in which subjects report experiences as their brains are mapped. Nor does it end with academia. The same scaling methods are still used to compare subjective experience between potential customers—billions of dollars are spent on market research—and by physicians, particularly for assessing pain.

It's not just that the traditional subjective scales produce noisy data, says Bartoshuk: "They can produce misleading results." The worst of these are "reversal artifacts." Bartoshuk says she encountered one of those with supertasters. "If you use the old 10-point scale, you can make it seem as if supertasters are less sensitive to salt than normal people, which of course is the opposite of reality."

One convert is Ann Berger, a clinical pain researcher at the National Institutes of Health Clinical Center in Bethesda, Maryland, who worked with Bartoshuk in the 1990s on oral pain. "I use [Bartoshuk's] scale and it works," says Berger. "It's most important for assessing chronic pain." Berger says that data collected from traditional 10-point scales "are meaningless," and as a result "patients are incorrectly medicated." The tradeoff with the new scaling method is that "it does take longer to do," she says, "but it's crucial." Berger would like to see Bartoshuk's scale adopted as the standard method for pain assessment. The problem, she says, is that "these bad scales were made mandatory by the Joint Commission," the organization responsible for accrediting health care organizations in the United States. "Now we're stuck with them."

In recent years, Bartoshuk has pushed to get the word out on the problem of subjective scaling; it was the sole focus of her plenary lecture at last year's annual APS conference. She has discovered that the issue has a history. R. Duncan Luce, a psychologist at the University of California, Irvine, had described problems with subjective scaling in a 1983 paper in the economic journal *Theory and Decision*. "The [traditional] 10-point scale is really easy to use, but it's also useless," says Luce. "A lot of people dismiss this problem as the concern of a few theoreticians. But it is serious."

One veteran researcher who dismisses it is Adam Drewnowski, director of the Nutritional Sciences Program at the University of Washington, Seattle. "There is no reversal artifact," the epidemiologist says. "All these scales work in a similar way and get you approximately similar results." Nonetheless, Drewnowski says that new computer-aided techniques allow him to avoid numbered scales altogether. "We now use visual analog scales" on which subjects "point and click" relative positions. "It's much faster," he says, but "you can use any scale."

Some agree with Bartoshuk but have varying degrees of optimism that her alternative scaling method will catch on. "There is huge inertia involved in changing a system that seems to work," says John Prescott, a psychologist at the University of Newcastle in Ourimbah, Australia. "In fact, this success is illusory, based on the fact that scale results are consistent with previous scale results, without any consideration of whether the scale measures what it is supposed to measure."

Of course, it could be that Bartoshuk's concern about the subjective scaling error is itself an error. After thinking it over, she lays down a verdict. "It would be wonderful," she says. "Making conceptual mistakes can be an incredible window into new insights."

–JOHN BOHANNON

CREDITS: (IMAGES) PHOTOS.COM

Published by AAAS

Survivor. Debbie Motts, cured of Hodgkin's lymphoma at 18, learned at 47 that the treatment likely caused breast cancer.

CANCER RESEARCH

Childhood's Cures Haunted By Adulthood's 'Late Effects'

As the number of cancer survivors climbs into the many millions, researchers are trying to learn why some acquire treatment-related diseases and others do not

Every weekday for nearly 3 months, 13-year-old Debbie Motts pressed a Tic Tac mint to her nose as she made her way through the lobby, down the elevator, and along the halls to the radiation clinic for her Hodgkin's lymphoma treatment. She hated the smell of the hospital; the Tic Tac helped. Now, nearly 40 years later, she hates the smell of Tic Tacs. They conjure up memories of her treatment: the sick days, the hair loss, the constant metallic taste in her throat.

At 18, Motts was declared cancer-free. She regained a normal life, got married, and had two children. But in 2007, a routine mammogram led to the detection of cancer cells in her right breast. Doctors said it was most likely a late-emerging side effect of the radiation she received as a child. The cure, they believed, had caused the cancer.

There are 11.4 million cancer survivors living in the United States, according to the National Cancer Institute, a cohort that has tripled over the past 3 decades. Some, like Motts, were treated as children or teenagers; almost 80% of children treated for cancer today live at least 5 years after diagnosis.

But roughly 40% of these survivors will develop life-threatening health problems within 30 years of their initial cancer diagnosis, according to a 2006 study published in *The New England Journal of Medicine*. The list of cancer therapy's late effects is long and troubling. It includes not just second cancers but strokes, bone damage, and obesity. Lungs can scar and stiffen, making it hard to breathe. Heart muscles can weaken and become flabby, unable to pump blood. Not everyone develops problems, however; 25% remain healthy.

As the number of survivors has grown, so has the field of late-effects research. Several U.S. hospitals have opened centers devoted exclusively to cancer survivors. St. Jude Children's Research Hospital has amassed a rich database on adult survivors of pediatric cancer called the Childhood Cancer Survivorship Study, launched in 1993.

TREATMENT	GENE	ASSOCIATED EFFECT
Alkylating agents/ topoisomerase inhbitors	*GST, RAD*	leukemia
Anthracyclines	*CBR1, CBR3*	heart failure
Cisplatin	*COMT, TPMT*	hearing loss
Radiation	*LEPR*	obesity
Thiopurines	*TPMT*	leukemia
Thiopurines + alkylating agents	*TPMT*	leukemia
Thiopurines + radiation	*TPMT*	brain tumors
Thiopurines + topoisomerase inhibitors	*TPMT*	leukemia

Vulnerabilities. Researchers have linked a growing number of genes to a higher risk of harm from cancer therapy.

But many questions remain. Few childhood cancer survivors have been followed for more than 30 years. Little research has been done on cancer survivors diagnosed as adults. Also unknown are the molecular mechanisms that cause many late effects.

A small number of researchers have turned to genetics to help untangle the problem. Recent work on chemotherapy, for example, has identified a gene variant linked to heart problems that appear long after anthracycline drug treatment. Other scientists interested in late effects recently formed an international group to pool data on gene variants that increase the risks for patients who carry them. Their goal is to develop a stronger grasp on the biology behind these late effects, identify the cancer patients who are predisposed, and tailor their treatments accordingly.

Subtle toxicity

Smita Bhatia keeps a tidy office at California's City of Hope cancer center in the foothills of the San Gabriel Mountains, with a "Cancer-Free Kids" sticker pasted to a filing cabinet and pictures of her own grown daughters on the shelves. A pediatric oncologist and chief of population genetics, she has sifted through hundreds of genes for those that predict certain late effects.

In 2004, Bhatia decided to concentrate on the *carbonyl reductase* (*CBR*) gene. It encodes a drug-metabolizing enzyme that breaks down anthracyclines, considered the backbone of childhood cancer treatment and used to treat about one-half of all cancer patients. Anthracyclines are usually administered intravenously and disrupt the DNA of rapidly dividing cancer cells. Nearly one-third of patients who receive a moderate dose develop congestive heart failure later on, a condition in which the heart no longer pumps enough blood. Most who develop the disease die from it.

Doctors have known about the problem for years now but haven't understood until recently the irregular pattern of harm. "Some patients who have congestive heart failure have received a very low dose" of anthracycline, Bhatia explains. "And others have received high, high doses and have escaped congestive heart failure." That led her to look for susceptibility linked to a metabolic response.

CREDITS (TOP TO BOTTOM): COURTESY OF DEBBIE MOTTS; (TABLE SOURCE) SMITA BHATIA AND MARY RELLING/ST. JUDE CHILDREN'S RESEARCH HOSPITAL

Published by AAAS

The CBR protein, which is expressed in the liver and brain, as well as the heart, breaks anthracyclines down into an alcohol metabolite. Lab studies on human heart cells have shown that high-risk forms of two variants of the gene—known as *CBR1* and *CBR3*—metabolize the drug more efficiently, causing larger-than-normal amounts of metabolites to collect. In the heart, studies have shown that the cells die off when these metabolites build up to a high level, doing permanent damage to the muscle.

After a pilot study in 2008 indicated that anthracycline-treated children with a variant of the *CBR3* gene had a higher risk for heart problems, Bhatia and her group scaled up their research. They matched 165 patients who had been treated with anthracyclines as children and had later developed heart failure with 323 controls: childhood cancer patients with identical treatment but no heart failure. Javier Blanco, a pharmaceutical scientist at the University at Buffalo in New York, genotyped the blood and saliva samples.

When Bhatia's group crunched the numbers back at the City of Hope, they found confirmation of the pilot study. Patients with the high-risk variant of the *CBR1* or *CBR3* gene who were exposed to 250 mg or less of anthracyclines, a common dose for cancers like Hodgkin's lymphoma and acute lymphoblastic leukemia, were 4.8 times more likely to develop congestive heart failure. (Patients treated with a higher dose were at high risk regardless of their *CBR* status.) Blanco, who presented the study at the American Society of Clinical Oncology's 2010 annual meeting on 7 June, cautions that the results still need to be replicated. The next step will be to apply the findings to patients at risk. Bhatia hopes to start a clinical trial within 2 years that would use different chemotherapy treatments or a "cardioprotectant" drug.

Daniel Mulrooney, a pediatric oncologist at the University of Minnesota, Twin Cities, and leader in research linking low doses of radiation and chemotherapy to an increased risk of heart disease in survivors, calls the CBR study fascinating. "So much of cancer survivorship has been describing the epidemiology," he says. "What this does is it helps us understand why these things happen. And moving from describing late effects to understanding the mechanism of why these things happen is crucial to treating them."

Expanding the search

The CBR finding is one of a handful to identify genetic risk factors for late effects. Variants in the *COMT* and *TPMT* genes,

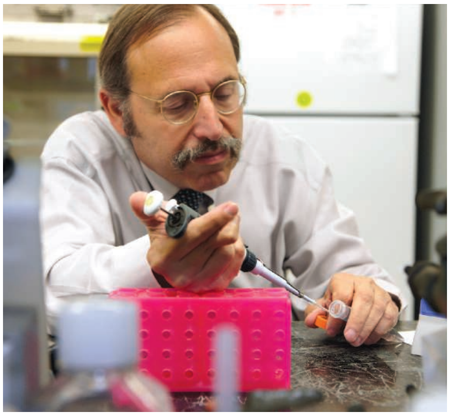

Wider net. Smita Bhatia and Barry Rosenstein are involved in an international search for the causes of therapy-related late effects.

CREDITS (TOP TO BOTTOM): PHILIP CHANNING/CITY OF HOPE; © 2010 MOUNT SINAI MEDICAL CENTER

which affect metabolism, have been associated with hearing loss among cancer survivors treated with cisplatin, a platinum-based chemotherapy drug. The leptin-receptor gene has been linked to obesity among female survivors of acute lymphoblastic leukemia.

Some researchers have devoted their careers to the subject and unearthed surprisingly little, partly because the cost of genome sequencing is high. But as costs drop, it will become increasingly easy for researchers to study multiple genes, says Joseph Neglia, co-leader of the Cancer Outcomes and Survivorship Research Program at the University of Minnesota's Masonic Cancer Center and also an author of the CBR study.

Studying multiple genes is essential to understanding the pathology of a disease, says Neglia: "The concept that there's a single gene that's the master controller for a single drug is just fundamentally wrong." Bhatia agrees. She thinks the future of this research lies in probing groups of carefully selected candidate genes believed to be involved in late-effects pathways. The CBR story, although exciting, is only part of a bigger genetic picture, she says.

To help fill out that picture, Bhatia is heading up the largest ever multi-institutional, case-control study on late effects of chemotherapy and radiation and studying genes among 1175 childhood cancer survivors who developed heart disease, stroke, bone damage, or a second cancer after their initial treatment.

At the Mount Sinai Medical Center in New York City, Barry Rosenstein, a radiation biologist, has helped to organize another search. Rosenstein has studied genetic predictors for radiation-induced late effects for 12 years. (He calls it "radiogenomics.") He published nearly 20 findings on candidate genes that appeared to be linked to disease, including a 2006 paper on a genetic marker for skin fibrosis among breast cancer patients. But many of his studies had limitations: Results were not consistently validated, or relative risks were too low to be useful in the clinic. The skin fibrosis finding, for example, was replicated in some studies but not others. "We came to a bit of a dead end," he says: "Nothing was good enough to serve as a predictive assay."

He has shifted his focus to genomewide studies, teaming with Catharine West, a professor of radiation biology at the University of Manchester in the United Kingdom, to create an international "Radiogenomics Consortium" of biologists, oncologists, epidemiologists, and geneticists. He says, "It's kind of an agnostic approach. We're going to give every gene a chance."

In the clinic, considering late effects during the initial cancer treatment can be difficult. "We can't sacrifice successful treatment of the primary cancer," Neglia says. "But it's a tough balance. I'm sitting here, looking at a picture on my desk of a teenager who was treated for Hodgkin's disease who may be looking at a hip replacement … because of steroid side effects. And she's 18. We appear to have cured Hodgkin's disease, but there's a cost."

It is a Faustian bargain: winning freedom from one cancer in youth in exchange for the specter of a different disease in adulthood. The pervasiveness of bad outcomes is what "makes us so committed to trying to understand what happened, so we can prevent it in the future," Bhatia says. This future, researchers hope, will include increasingly personalized cancer treatments designed to minimize the risks of late effects or arrest them at their earliest stage. It's about restoring what cure really means, says Neglia: "getting the child back to who they were before the diagnosis of cancer."

–JENNY MARDER

Jenny Marder is a writer in Washington, D.C.

Published by AAAS

MARINE BIOGEOCHEMISTRY

The Invisible Hand Behind A Vast Carbon Reservoir

A key element of the carbon cycle is the microbial conversion of dissolved organic carbon into inedible forms. Can it also serve to sequester CO_2?

XIAMEN, CHINA—For simple sea creatures, dissolved organic carbon (DOC) is the staff of life. Much of it, however, is as unpalatable as chaff and accumulates in the water column. Scientists are unraveling how organic matter in the marine food chain is converted into forms that less readily relinquish carbon in the form of carbon dioxide (CO_2). "The existence of this 'inedible' organic carbon in the ocean has been known for quite some time. But its role in the global carbon cycle has been recognized only recently," says Michal Koblizek, a microbiologist at the Institute of Microbiology in Trebon, Czech Republic.

New findings are unmasking the invisible processes that suspend immense amounts of carbon just below the ocean waves. "It's really huge. It's comparable to all the carbon dioxide in the air," says Jiao Nianzhi, a microbial ecologist here at Xiamen University. He and others are exploring the tantalizing prospect of sequestering CO_2 in this reservoir. It's too early to say whether the vast pool will respond to geoengineering, says Dennis Hansell, a marine biogeochemist at the University of Miami in Florida. However, he says, "I expect the light to come on over heads and we'll experience an 'ah ha!' moment."

Data from several research cruises have yielded a broad-brush view of what Jiao has dubbed the microbial carbon pump (MCP): the microbe-driven conversion of bioavailable organic carbon into difficult-to-digest forms known as refractory DOC. This summer, the European Project on Ocean Acidification is carrying out a slate of experiments in Arctic waters that includes probing the MCP. Then in October, Jiao's team heads to the opposite thermal extreme: They will explore the mechanisms of the MCP and CO_2 sequestration in the equatorial Indo-Pacific Warm Pool, the warmest marine waters in the world. The MCP will also be featured next month at a Gordon Research Conference on marine microbes, and it is outlined in a paper in press at *Nature Reviews Microbiology*. The concept "could revolutionize our view of carbon sequestration," says Markus Weinbauer, a microbial oceanographer at Laboratoire d'Océanographie de Villefranche in France.

The ocean surface is like a planet-sized set of lungs that inhale and exhale CO_2. As a global average, the oceans take up about 2% more of the gas than they release. Some CO_2 dissolves into the water column, forming carbonic acid. As atmospheric CO_2 levels rise, ocean pH decreases, a phenomenon called acidification that could endanger corals and other creatures by slowing the growth of carbonate skeletons (see p. 1500). Carbon also enters the seas through the food web: During photosynthesis, phytoplankton fixes CO_2 to organic carbon—as much as 60 gigatons of carbon per year, roughly the same amount fixed on land. "The carbon is not captured for long," says Koblizek. Most new marine biomass is consumed in days and returned to the air as CO_2. Some, however, ends up in the deep ocean sink, when remains of dead organisms fall to the sea floor. Each year, this biological pump deposits roughly 300 million tons of carbon in the seabed.

Even more massive amounts of carbon are suspended in the water column as DOC. The oceans hold an estimated 700 billion tons of carbon as DOC—more than all land biomass put together (600 billion tons of carbon) and nearly as much as all the CO_2 in the air (750 billion tons of carbon). About 95% of organic carbon is bound up as refractory DOC: "the largest pool of organic matter in the ocean," says Farooq Azam, a microbiologist at Scripps Institution of Oceanography in San Diego, California. In the December 2009 issue of *Oceanography*, a team led by Hansell and Craig Carlson of the University of California, Santa Barbara, compiled the first global map of DOC distribution. Carbon-14 studies suggest that refractory compounds swirl in this microbial eddy for more than 6000 years, several times the circulation time of the ocean.

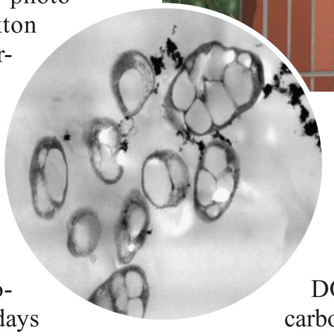

DOC doc. Jiao Nianzhi formulated the MCP concept based on his studies of AAPB, an unusual kind of photosynthetic bacteria (*left*).

The realization that refractory DOC is a key element in the global carbon cycle has lit a fire under efforts to figure out what the stuff is and where it comes from. Researchers now know that refractory DOC consists of thousands of compounds, such as complex polysaccharides and humic acids. A team led by Xosé Antón Álvarez Salgado of the Instituto de Investigaciones Marinas in Vigo, Spain, has tracked the conversion of some forms of bioavailable carbon to refractory carbon by observing changes in their optical properties: Humic substances absorb UV light and re-emit it as blue fluorescence at specific wavelengths.

The origins of most refractory DOC are a black box. Some is produced when light degrades organic matter near the ocean surface. Oil seeps contribute to the pool. "The oil spill in the Gulf of Mexico is just one drastic example of how this material is released into the ocean," says Meinhard Simon, a microbial oceanographer at the University of Oldenburg in Germany. Other compounds are likely forged in underwater vents or in wildfires and swept into the sea. For the most part, however, says Azam, "we lack understanding of the mechanisms of its formation or variations in its magnitude and composition."

CREDITS: COURTESY OF JIAO NIANZHI

Azam and others credit Jiao with a key insight: the recognition that microbes play a dominant role in "pumping" bioavailable carbon into a pool of relatively inert compounds. Some refractory DOC hangs in the upper water column, while some gets shunted to the deep ocean interior via the biological pump. The MCP "may act as one of the conveyor belts that transport and store carbon in the deep oceans," says Chen-Tung "Arthur" Chen, an ocean carbonate chemist at National Sun Yat-sen University in Kaohsiung, Taiwan. The MCP also appears to function in deep waters, where bacteria adapted to the high-pressure environment may have "a special capacity" to degrade refractory DOC, says Christian Tamburini, a microbiologist at the Centre d'Océanologie de Marseille in France.

It took sharp sleuthing to uncover the microbial connection with refractory DOC. In a landmark paper in 2001, Hiroshi Ogawa of the University of Tokyo and colleagues showed that marine microbes are able to convert bioavailable DOC to refractory DOC (*Science*, 4 May 2001, p. 917). Then a month later, Zbigniew Kolber, now at the Monterey Bay Aquarium Research Institute in Moss Landing, California, and colleagues reported that in the upper open ocean, an unusual class of photosynthetic bacteria called AAPB accounts for 11% of the total microbial community (*Science*, 29 June 2001, p. 2492). AAPBs seemed to be plentiful everywhere, according to measurements of infrared fluorescence from the microbe's light-absorbing pigments.

It turned out, though, that other organisms were throwing the AAPB estimates way off the mark. Using a new technique, Jiao's group determined that the fluorescent glow of phytoplankton was masking the glow of the target microbes. "Just like when the moon is bright, less stars are visible," Jiao says. He put the new approach through its paces in 2005, when China's *Ocean 1* research vessel conducted campaigns to mark the 600th anniversary of Admiral He Zheng's historic voyages. The observations "turned things upside down," Jiao says. His group found that AAPBs are more abundant in nutrient-rich waters than in the open ocean, indicating that AAPB population levels are linked with DOC, not light.

Next, Jiao found that AAPBs are prone to viral infection, and he isolated the first phage that's specific for these bacteria. Phages rip apart their hosts, spilling their guts, including organic carbon, into the water. This viral shunt acting on many marine bacteria "may be a significant player in the accumulation of refractory DOC compounds" in the water column, says Steven Wilhelm, a microbiologist at the University of Tennessee, Knoxville. Pulling together several strands—the ubiquity of AAPBs, their low abundance but high turnover rate, the tight link to DOC, and their susceptibility to infection—Jiao proposed that AAPBs and other microbes are a key mechanism for the conversion of bioavailable DOC to refractory DOC. That may seem counterintuitive, as microbes do not set out to produce refractory DOC; rather, the compounds are a byproduct of their demise. "This process is not beneficial to the cell," says Simon.

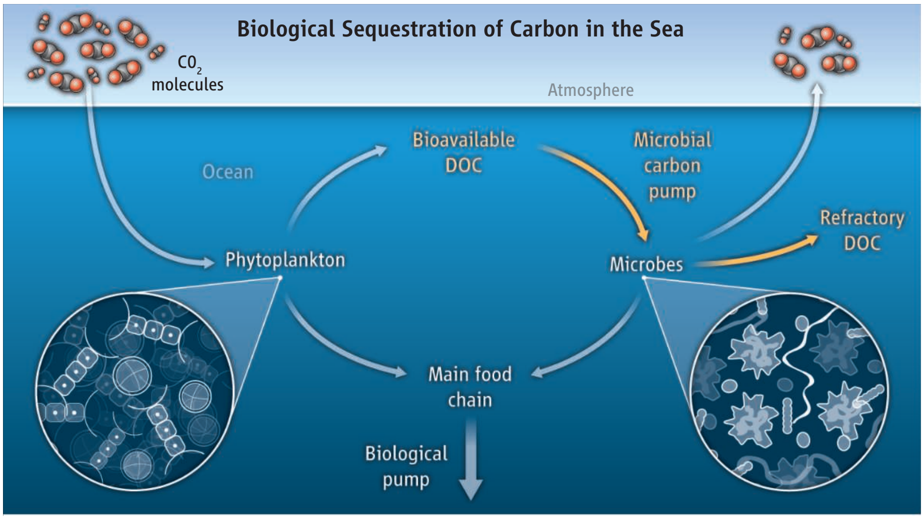

Double-barrel pump. Each year, the biological pump deposits some 300 million tons of carbon in the deep ocean sink. Even more massive amounts are suspended in the water column as dissolved organic carbon, much of which is converted into refractory forms by the microbial carbon pump.

CREDIT: C. BICKEL/*SCIENCE*

Because the buildup of refractory DOC in the water column is accidental, it will be a challenge to coax microbes to sequester more carbon. For decades, researchers have been tinkering with the biological pump to store more carbon in the deep ocean by seeding seas with iron fertilizer. The iron triggers phytoplankton blooms that suck more CO_2 from the air. That should also drive more carbon into the refractory pool, Koblizek says.

Even tweaking the MCP could have a profound effect. The water column holds on average 35 to 40 micromoles of carbon from refractory DOC per liter. An increase of a mere 2 to 3 micromoles per liter would sock away several billion tons of carbon, says Nagappa Ramaiah, a marine microbial ecologist at the National Institute of Oceanography in Goa, India. "We have to investigate any and all means to help sink the excess carbon," he says.

Two billion years ago, when bacteria ruled Earth, the oceans held 500 times as much DOC as today, most likely generated by the MCP, Jiao says. Ecosystem dynamics have changed immensely since then, but the microbial sequestration potential could still be huge, he argues. No chemical equilibrium would limit conversion of bioavailable DOC to refractory DOC, which in turn would not exacerbate ocean acidification, says Jiao, who is planning pilot experiments this summer. Ramaiah, meanwhile, says he is looking for enhanced sequestration potential in select marine bacteria strains.

There's no simple recipe—and some scientists are not convinced that it's feasible or even safe. "I do not think it is possible to enhance carbon sequestration by the MCP. We have no handle on any controls" of how refractory DOC is generated, says Simon. With the present knowledge, any sequestration effort, argues Weinbauer, "could come back like a boomerang and worsen the problem." At the same time, humans may already be "inadvertently stimulating the MCP," says Salgado. Global warming is increasing stratification, reducing deep convection, and stimulating microbial respiration—all of which favor the MCP, he says.

The MCP concept should help address critical issues, such as whether ocean acidification and warming will significantly alter carbon flux into refractory DOC, says Azam, who with Jiao chairs the Scientific Committee on Oceanic Research's new working group on the role of MCP in carbon biogeochemistry. The upcoming research cruises should fill in more details of how the MCP governs carbon cycling and how it may respond to climate change. As Wilhelm notes, "We are just at the dawn of developing this understanding."

–RICHARD STONE

Published by AAAS

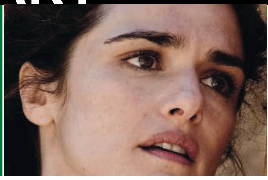

LETTERS

edited by Jennifer Sills

Forests and Climate: A Warming Paradox

E. ROTENBERG AND D. YAKIR ("CONTRIBUTION OF SEMI-ARID FORESTS TO THE CLIMATE SYSTEM," Reports, 22 January, p. 451) showed that forestation may not be an effective tool for climate change mitigation. They found that in a semi-arid landscape, the warming potential of a forest due to changes in the surface albedo and the longwave radiation emission far outweighs the cooling effect due to carbon sequestration. However, their analysis did not address the fact that the radiation balance of the surface is not the same as the radiation balance of the climate system. The atmosphere retains a significant portion of the longwave radiation emitted and the shortwave radiation reflected by the surface. Globally, only 10% of the surface longwave radiation escapes the atmosphere to the outer space (*1*). The escape fraction over Rotenberg and Yakir's site is probably higher due to low cloud cover, but not by much: The outgoing longwave radiation for a clear sky at the top of the atmosphere suggests a maximum of 20% (*2*). Similarly, because of atmospheric absorption and cloud reflection, the local albedo at the top of the atmosphere is lower than the surface value. By not taking into account this energy redistribution, Rotenberg and Yakir may have substantially overestimated the warming effect of forestation (and the cooling effect of desertification).

A deeper issue, also related to energy redistribution, is whether it is accurate to combine the CO_2 radiative forcing and the surface radiation change for the purpose of analysis. To help policy discussions, the greenhouse effects are often expressed as climate sensitivity (*3*), estimated at ~0.8°C increase in the surface temperature per W m^{-2} increase in the radiative forcing (*4*). The surface exchange process does not work that way. Rotenberg and Yakir's paradoxical result—that the forest, being an efficient convector, is much cooler despite more radiation loading than the shrubland—provides a powerful argument against combining the two quantities. In humid climates, forests also cool the surface by removing its latent heat, which is released above the atmospheric boundary layer by cloud condensation.

XUHUI LEE

School of Forestry and Environmental Studies, Yale University, New Haven, CT 06511, USA. E-mail: xuhui.lee@yale.edu

References

1. K. E. Trenberth *et al.*, *Bull. Am. Meteorol. Soc.* **90**, 331 (2009).
2. S. K. Yang *et al.*, *J. Clim.* **12**, 477 (1999).
3. V. Ramanthan, G. Carmichael, *Nat. Geosci.* **1**, 221 (2008).
4. IPCC, Summary for Policymakers (SPM), in *Climate Change 2007: The Physical Science Basis: Contribution of Working Group I to the Fourth Assessment Report of the Intergovernmental Panel on Climate Change*, S. Solomon *et al.*, Eds. (Cambridge Univ. Press, New York, 2007).

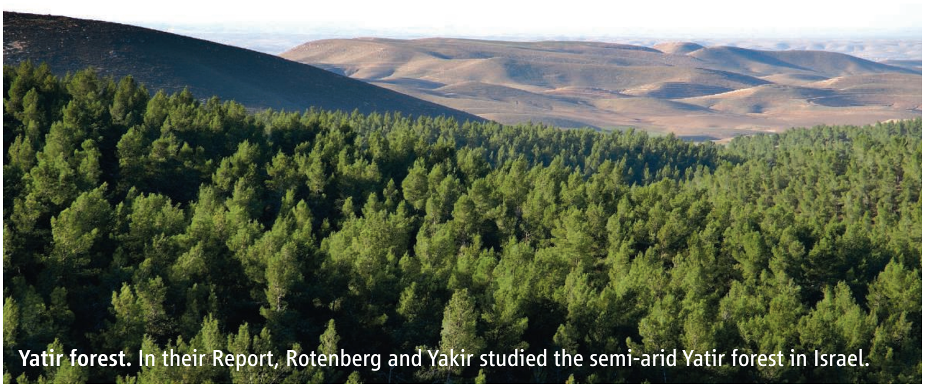

Yatir forest. In their Report, Rotenberg and Yakir studied the semi-arid Yatir forest in Israel.

CREDIT: THE WEIZMANN INSTITUTE

Forests and Climate: The Search for Specifics

E. ROTENBERG AND D. YAKIR ("CONTRIBUTION of semi-arid forests to the climate system," Reports, 22 January, p. 451) demonstrate that dryland afforestation amplifies global warming and that desertification has resulted in net global cooling. However, the climatic impact of desertification warrants a more detailed analysis.

First, Rotenberg and Yakir's results from Yatir forest [located at the arid/semi-arid transition zone (*1*)] cannot be extrapolated to all areas undergoing desertification. Modeling the climatic effects of land-use change must account for diverse climate sensitivities dependent on various combinations of plant communities and climate (*2*).

Second, the spectral properties of infrared radiation reflected from green vegetation are fundamentally different from those of exposed soil (*3*). Unlike the radiation generated by soil, vegetation-derived shortwave infrared radiation (700 to 2000 nm) hardly interacts with the major absorption bands of CO_2, H_2O, and methane and dissipates substantial amounts of energy to space that are not accounted for by conventional analysis of albedo effects.

Third, common dryland ecosystems (open woodlands, savannas, and grasslands) differ from the pine forest analyzed by Rotenberg and Yakir. Such ecosystems have higher albedo than pine forest and produce an average 7 tons of biomass per hectare and year (*4*). Drylands support high biodiversity and provide livestock fodder, woody biomass, or high-value agricultural products (*5*, *6*). Desertification may have benefits in terms of increasing albedo, but those come at a cost: fossil fuel use, progressive further land degradation, and a shift to intensive irrigation agriculture that will result in high additional energy costs and greenhouse gas emissions.

We must address these questions before rendering final judgment on the climate sensitivity of desertification processes.

STEFAN LEU

The Jacob Blaustein Institutes for Desert Research, and MOP Judea, Ben Gurion University, Sde Boker, 84990, Israel. E-mail: louiss@bgu.ac.il

References

1. Y. Shachnovich, P. R. Berliner, P. Bar, *J. Hydrol*. **349**, 168 (2008).
2. R. A. Pielke Sr. *et al*., *Tellus* **59B**, 587 (2007).
3. C. J. Tucker, *Remote Sensing Environ*. **8**, 127 (1979).
4. U. Safriel, Z. Adeel, in *Ecosystems and Human Well-Being: Current State and Trends* (Island Press, Millennium Ecosystem Assessment Series, 2005), vol. 1; www.millenniumassessment.org/documents/document.291.aspx.pdf.
5. J. S. Samra, M. K. Vishwanatham, A. R. Sharma, *Agroforest. Syst.* **46**, 197 (1999).
6. K. Abu Rabia, E. Solowey, S. Leu, *J. Environ. Manage*. **19**, 353 (2008).

Response

WE AGREE WITH LEE THAT TRANSLATING OUR radiative forcing (RF) results into temperature change is complex. In our Report, we warned that "[t]he *RF* values in this context should be interpreted with caution and are used here as a convenient way [a metric] to compare the magnitude of biogeophysical and biogeochemical forcing."

It is clear that RF alone does not have a direct relation to temperature change at Earth's surface (*1–4*). Temperature sensitivity to RF associated with atmospheric CO_2 can be three times that associated with albedo (*5*). Temperature can also change in response to nonradiative effects, such as evapotranspiration efficiency or surface roughness (*3*, *4*). Indeed, the massive sensible heat flux generated in the semi-arid forest could, if associated with sufficiently large forested area, modify atmospheric circulation and consequently local-to-regional climate more than any of the RF parameters [such as by influencing the depth of the planetary boundary layer, development of convective conditions, and cloud cover (*6*, *7*)].

Regardless of the uncertainty in translating RF to temperature change, the results from the semi-arid site showed large and robust effects. The local RF associated with the semi-arid land cover changes is about 50 W m^{-2} (divided mainly between short- and longwave radiation effects). This is important when considering that as much as ~20% of the thermal radiation (or ~5 W m^{-2}, which is further enhanced by shortwave reflected light) can radiate straight out to space under the mostly cloudless conditions in this region, contributing to the planetary climate system. Although a local effect, it is still significant compared to the global top-of-atmosphere RF associated with doubling of atmospheric CO_2 concentrations, estimated at about 4 W m^{-2}.

Whereas we estimated local RF on the basis of field measurements, the intricate translation of such RF estimates into temperature change (or even just into top-of-atmosphere RF) must rely on models and satellite observations. At present, it is still a challenge, even for the best models, to sum up measurable RF and other nonradiative effects and provide a reliable climate-change forecast (*8*). The continuous exchange between models and observations is critical to advancing the field and ultimately providing useful information for policy discussions (*4*).

Leu highlights the difficulties in developing appropriate and reliable metrics to assess factors that influence the climate system. Referencing a paper by Pielke *et al*. (*9*), Leu points out that surface temperature differs depending on the presence of different land use and plant communities. Our use of the RF metric cannot be directly related to Pielke's arguments on the suitability of surface temperature to assess climate change. We indicate the large impact on surface RF of the primary conversion of mostly bare surface to vegetated land cover, and vice versa, in the semi-arid zone. This research, in turn, should motivate more detailed investigations, including the consideration of different plant communities, soils, and geographical characteristics, as suggested by Leu.

The additional issue of unique plant reflectivity in the near-infrared (NIR) range, which may have climatic consequences, clearly deserves further investigation. But this effect can be assessed using our existing experimental setup because reflectivity measurements in this study included shortwave radiation (S) (305 to 2800 nm), complemented by photosynthetic active radiation (PAR) [400- to 700-nm range (*10*, *11*)], with the difference predominantly representing the NIR range (700 to 2800 nm). The results indicated that in going from sparse shrubs to open canopy forest, reflectivity decreased on average to 0.55, 0.53, and 0.57 for the S, PAR, and NIR, respectively. Although some enhanced reflectivity in the NIR range is indeed indicated, this is a relatively small effect and would be further diluted because of the overall higher atmospheric absorption in this spectral range (*12*), and the general increase in the diffusive nature of reflected radiation.

Finally, as pointed out by Leu, desertification and afforestation in the semi-arid and other dry regions have wide range of implications, including economic, societal, and climatic, all of which should be considered in management, policy- and decision-making processes.

DAN YAKIR AND EYAL ROTENBERG

Environmental Sciences and Energy Research, Weizmann Institute of Science, Rehovot 76100, Israel. E-mail: dan.yakir@weizmann.ac.il

References

1. R. A. Betts *et al.*, *Agric. Forest. Meteorol*. **142**, 216 (2007).
2. J. Pongratz *et al.*, *Geophys. Res. Lett.* **36**, L02709 (2009).
3. E. L. Davin, N. de Noblet-Ducoudre, *Am. Meteor. Soc.* **23**, 97 (2010).
4. Climate Research Committee, National Research Council, *Radiative Forcing of Climate Change: Expanding the Concept and Addressing Uncertainties Committee on Radiative Forcing Effects on Climate* (National Academies Press, Washington, DC, 2005).

CORRECTIONS AND CLARIFICATIONS

News of the Week: "Five questions on the spill" by R. A. Kerr *et al*. (21 May, p. 962). The third author of the story was Lauren Schenkman, not Laura Schenkman. The name is correct in the online HTML version.

News Focus: "Animal communication helps reveal roots of language" by M. Balter (21 May, p. 969). The chimpanzee Washoe, who learned to communicate using American Sign Language, was mistakenly referred to as a male. Washoe was a female.

TECHNICAL COMMENT ABSTRACTS

Comment on "Deep-Sea Temperature and Ice Volume Changes Across the Pliocene-Pleistocene Climate Transitions"

Jimin Yu and Wally S. Broecker

Sosdian and Rosenthal (Reports, 17 July 2009, p. 306) used magnesium/calcium ratios in benthic foraminifera from the North Atlantic to reconstruct past bottom-water temperatures. They suggested that both ice volume change and ice-sheet dynamics played important roles during the late Pliocene and mid-Pleistocene climate transitions. We present evidence that their record of deep ocean temperature is not reliable, thus raising doubts about their conclusions.

Full text at www.sciencemag.org/cgi/content/full/328/5985/1480-c

Response to Comment on "Deep-Sea Temperature and Ice Volume Changes Across the Pliocene-Pleistocene Climate Transitions"

S. Sosdian and Y. Rosenthal

Yu and Broecker argue that the paleoceanographic interpretation of our 3.2-million-year record of North Atlantic deep-sea temperature hinges on the determination of whether temperature or carbonate saturation is the primary driver of benthic foraminiferal magnesium/calcium ratios from the North Atlantic. Here, we present evidence supporting our argument that bottom-water temperature variability is the primary control on benthic foraminiferal Mg/Ca at our site.

Full text at www.sciencemag.org/cgi/content/full/328/5985/1480-d

5. E. L. Davin *et al., Geophys. Res. Lett.* **34**, L13702 (2007).
6. D. D. Baldocchi, C. A. Vogel, *Tree Physiol.* **16**, 5 (1996).
7. A. D. Culf, *Bound. Layer Meteorol*. **58**, 1 (1992).
8. K. E. Trenberth, J. T. Fasullo, *Science* **328**, 316 (2010).
9. R. A. Pielke *et al., Tellus* **59B**, 587 (2007).
10. CarboEuropeIP, Ecosystem Component Database (http://gaia.agraria.unitus.it/database/carboeuropeip/).
11. K. J. McCree, in *Encyclopedia of Plant Physiology, Vol. 12A*, O. L. Lange, P. S. Nobel, C. B. Osmond, H. Ziegler, Eds. (Springer, Berlin, 1981), pp. 41–55.
12. E. Pettit, *The Sun and Stellar Radiation in Astrophysics*, J. Hynek, Ed. (McGraw-Hill, New York, 1951).

Letters to the Editor

Letters (~300 words) discuss material published in *Science* in the previous 3 months or issues of general interest. They can be submitted through the Web (www.submit2science.org) or by regular mail (1200 New York Ave., NW, Washington, DC 20005, USA). Letters are not acknowledged upon receipt, nor are authors generally consulted before publication. Whether published in full or in part, letters are subject to editing for clarity and space.

Call for Science to Clear Whaling Confusion

NEGOTIATIONS ON THE FUTURE OF THE International Whaling Commission (IWC) may culminate in a decision at the annual meeting in Morocco from 21 to 25 June that would suspend the current moratorium on commercial whaling and allow commercial catches of fin, minke, sei, and Bryde's whales in the North Atlantic, Southern Ocean, and North Pacific. Proposals from the Chair for a consensus decision to allocate ad hoc catch quotas close to current levels of whaling for a 10-year period have been criticized for sidelining science ("Deal to legalize whaling would sideline science," V. Morell, News of the Week, 30 April, p. 557). In response, a press release issued 7 May (revised 11 May) expressed the intention that catches would be within limits calculated according to the IWC's agreed, science-based, and "extremely conservative" Revised Management Procedure (RMP) (*1*). Unfortunately, this intent is not reflected in the wording of the actual proposal, which allows sufficient room for interpretation to potentially allow much higher catches than would be considered sustainable in the long term according to the agreed and published specification of the RMP (*2*). This confusion can only be resolved by explicit adoption of the published procedure into the IWC Schedule and instructions to the IWC Scientific Committee to perform the relevant calculations. Calculations of sustainable catch levels using the procedure and performed by the Scientific Committee, which includes scientists nominated by both whaling and non-whaling governments in addition to a number of independent experts, would be transparent, documented, and verifiable. Without such advice from the Scientific Committee, many of the 88 member nations of the IWC will not have the scientific resources themselves to assess the validity of the proposed catches amid the inevitable claims and counterclaims that are being made.

JUSTIN COOKE,[1]* SIDNEY HOLT,[2] RUSSELL LEAPER,[3] VASSILI PAPASTAVROU[4]

[1]Centre for Ecosystem Management Studies, Hoellenbergstrasse 7, 79312 Windenreute, Germany. [2]Voc Palazzetta 68, Paciano PG, 06060, Italy. [3]School of Biological Sciences, University of Aberdeen, Aberdeen AB24 2TZ, UK. [4]Department of Biology, University of Bristol, Bristol BS8 2LR, UK.

*To whom correspondence should be addressed. E-mail: jgc@cems.de

References

1. Revised Press Release: IWC Chair and Vice-Chair: "If you really care about whale conservation, give our proposal a fair reading" (11 May 2010); www.iwcoffice.org/_documents/commission/future/RevisedPressReleaseMay10.pdf.
2. IWC, *J. Cetacean Res. Manage.* **1** (suppl.), 251 (1999).

Published by AAAS

Comment on "Deep-Sea Temperature and Ice Volume Changes Across the Pliocene-Pleistocene Climate Transitions"

Jimin Yu* and Wally S. Broecker

Sosdian and Rosenthal (Reports, 17 July 2009, p. 306) used magnesium/calcium ratios in benthic foraminifera from the North Atlantic to reconstruct past bottom-water temperatures. They suggested that both ice volume change and ice-sheet dynamics played important roles during the late Pliocene and mid-Pleistocene climate transitions. We present evidence that their record of deep ocean temperature is not reliable, thus raising doubts about their conclusions.

Sosdian and Rosenthal (*1*) used magnesium/calcium (Mg/Ca) ratios in the benthic foraminifera *Cibicidoides wuellerstorfi* (epifaunal) and *Oridorsalis umbonatus* (infaunal) to derive a 3.2-million-year record of bottom-water temperatures (BWTs) for the deep North Atlantic. Combined with benthic oxygen isotope ratios ($\delta^{18}O$), this allowed them to calculate deep seawater $\delta^{18}O$ values, which provide an estimate of ice volume changes. Based on this, they concluded that the increase in ice volume during the late Pliocene transition was caused by global cooling, whereas an additional change in ice-sheet dynamics was likely to have induced the shift to 100,000-year cycles at the mid-Pleistocene transition. Here, we argue that their reconstructed down-core BWTs are not reliable, and therefore their conclusion is not substantiated and should be considered with caution.

The regional Mg/Ca-temperature calibration [Mg/Ca = 0.15 × BWT + 1.16 (Eq. 1)] used in (*1*) is defined by the regression of two data points: their core-top Mg/Ca and modern BWT versus Mg/Ca and an estimated BWT during the Last Glacial Maximum (LGM). We use published core-top and down-core data to demonstrate that this method is not valid. Because of incomplete information about past deep water conditions, a baseline is that a robust BWT reconstruction method should produce BWTs for core-top samples from extensive geographic regions closely matching modern values within the cited error. It is not acceptable to obtain seemingly reasonable results for only one core. Equation 1 does not fit core-top *C. wuellerstorfi* and *O. umbonatus* samples from global oceans (*2*–*4*) (Fig. 1A). Applying Eq. 1 to these two species shows large BWT deviations from expected temperatures (*5*) (Fig. 1B). The difference is not randomly distributed and is up to 5°C with an average estimation error of ±2.7°C, significantly larger than the ±1.1°C error quoted in (*1*). Application of Eq. 1 to a 2-km water depth core BOFS 11K, which is located at the same region as the cores used in (*1*), yields a ~2°C warmer BWT at the LGM than that during the Holocene, clearly at odds with benthic $\delta^{18}O$ and colder LGM BWT estimated by porewater measurements (*6*) (Fig. 1D). Therefore, Eq. 1 used by (*1*) lacks support from both core-top and down-core data sets.

Different from the planktonic foraminiferal and inorganic carbonates, *C. wuellerstorfi* and *O. umbonatus* from global oceans show no clear relationship between their Mg/Ca and growth BWTs in the range of –1°C to 4°C (*2*–*4*) (Fig. 1A). The elevated Mg/Ca in shells from the deep Norwegian Sea highlights an influence of the degree of carbonate ion saturation (ΔCO_3^{2-}) on benthic foraminiferal Mg/Ca (*2*, *3*) (Fig. 1C). The larger scatter of *O. umbonatus* (Fig. 1C) may indicate a complication from porewater chemistry associated with this species. The residual Mg/Ca for core-top *C. wuellerstorfi* after removing the ΔCO_3^{2-} effect shows a

Lamont-Doherty Earth Observatory of Columbia University, 61 Route 9W, Post Office Box 1000, Palisades, NY 10964–8000, USA.

*To whom correspondence should be addressed. E-mail: jiminyu@ldeo.columbia.edu

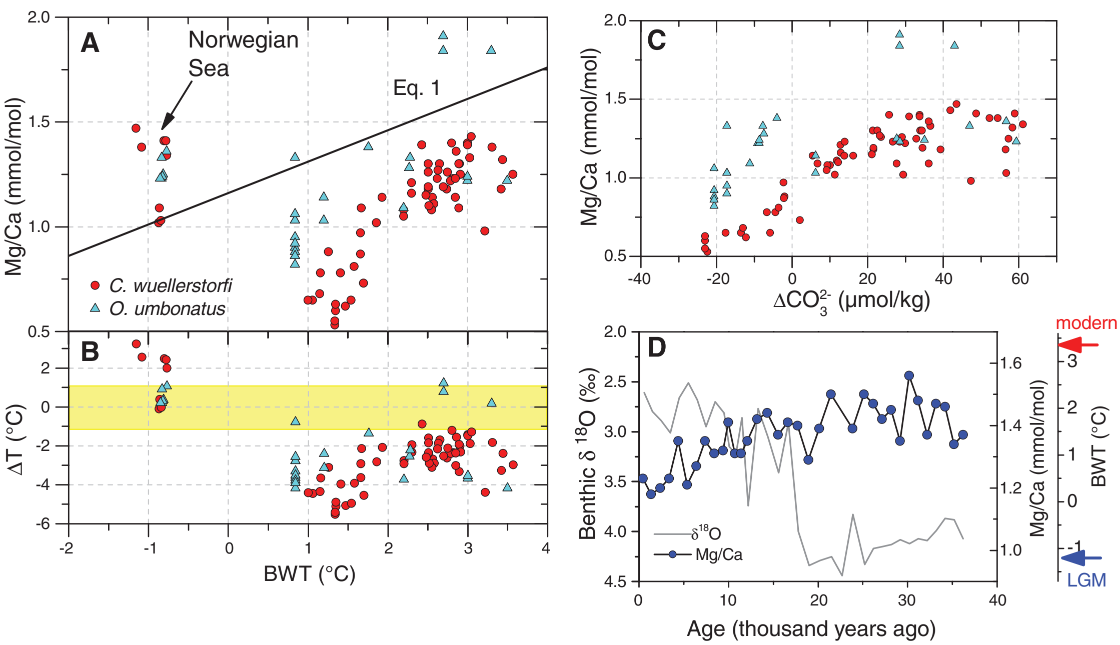

Fig. 1. Mg/Ca (**A**) and ΔT (**B**) versus BWT for global core-top *C. wuellerstorfi* (*2*) and *O. umbonatus* (*3*, *4*). ΔT = BWT by Eq. 1 – BWT estimated from modern hydrographic data (*5*). The shaded bar in (B) indicates the ±1.1°C error quoted in (*1*). A constant interspecies offset in Mg/Ca of 0.16 mmol/mol (*1*) is applied before converting *O. umbonatus* Mg/Ca to BWTs using Eq. 1. (**C**) Mg/Ca in *C. wuellerstorfi* (*2*) and *O. umbonatus* (*3*, *4*) versus deep water ΔCO_3^{2-}. (**D**) *C. wuellerstorfi* Mg/Ca derived BWT using Eq. 1 for BOFS 11K (55.2°N, 20.4°W, 2004 m) compared with benthic $\delta^{18}O$ (*2*). Also shown are BWTs at modern and LGM periods for a nearby core ODP 981 (55.48°N, 14.65°W, 2184 m) estimated by porewater measurements (*6*). Mg/Ca in *O. umbonatus* from the Norwegian Sea are corrected by 0.2 mmol/mol to account for cleaning effect (*3*). All other Mg/Ca values were measured using the same cleaning procedure (*2*–*4*).

negligible dependence on BWTs (*2*). Based on a comprehensive sensitivity test on a sequence of cores from 1- to 4-km water depth in the North Atlantic, it has been shown that it is not possible to use *C. wuellerstorfi* Mg/Ca for down-core BWT reconstructions even with the information about deep water ΔCO_3^{2-} from an independent proxy (*2*). Deep North Atlantic waters (>~3 km water depth) are expected to have high ΔCO_3^{2-} during the interglacial and low values during glacial periods (*2*). This ΔCO_3^{2-} change could partially explain the lowered benthic Mg/Ca during glacial periods observed in cores used in (*1*).

Obtaining BWT and ice volume changes is important for understanding the mechanisms responsible for climate changes in the past. The precondition is to use a robust method and fully consider possible complicating factors. The fact that Eq. 1 proposed by Sosdian and Rosenthal (*1*) fails to yield reasonable BWTs for core-top and down-core samples casts doubt on the validity of their BWT and ice volume reconstructions involving Mg/Ca in benthic foraminifera.

References

1. S. Sosdian, Y. Rosenthal, *Science* **325**, 306 (2009).
2. J. M. Yu, H. Elderfield, *Earth Planet. Sci. Lett.* **276**, 129 (2008).
3. H. Elderfield, J. M. Yu, P. Anand, T. Kiefer, B. Nyland, *Earth Planet. Sci. Lett.* **250**, 633 (2006).
4. C. H. Lear, Y. Rosenthal, N. Slowey, *Geochim. Cosmochim. Acta* **66**, 3375 (2002).
5. R. M. Key *et al.*, *Global Biogeochem. Cycles* **18**, GB4031 (2004).
6. J. F. Adkins, K. McIntyre, D. P. Schrag, *Science* **298**, 1769 (2002).

30 December 2009; accepted 4 June 2010
10.1126/science.1186544

Response to Comment on "Deep-Sea Temperature and Ice Volume Changes Across the Pliocene-Pleistocene Climate Transitions"

S. Sosdian[1,2]* and Y. Rosenthal[1]

Yu and Broecker argue that the paleoceanographic interpretation of our 3.2-million-year record of North Atlantic deep-sea temperature hinges on the determination of whether temperature or carbonate saturation is the primary driver of benthic foraminiferal magnesium/calcium ratios from the North Atlantic. Here, we present evidence supporting our argument that bottom-water temperature variability is the primary control on benthic foraminiferal Mg/Ca at our site.

Over the past 10 years, magnesium/calcium (Mg/Ca) ratios in benthic foraminifera have provided new insights into the Cenozoic history of deep ocean temperature and continental ice volume on various time scales. Yu and Broecker (*1*) question the reliability of our 3.2.-million-year record (*2*) of ocean temperature in the deep North Atlantic based on such ratios because of the confounding influence of carbonate ion saturation (ΔCO_3).

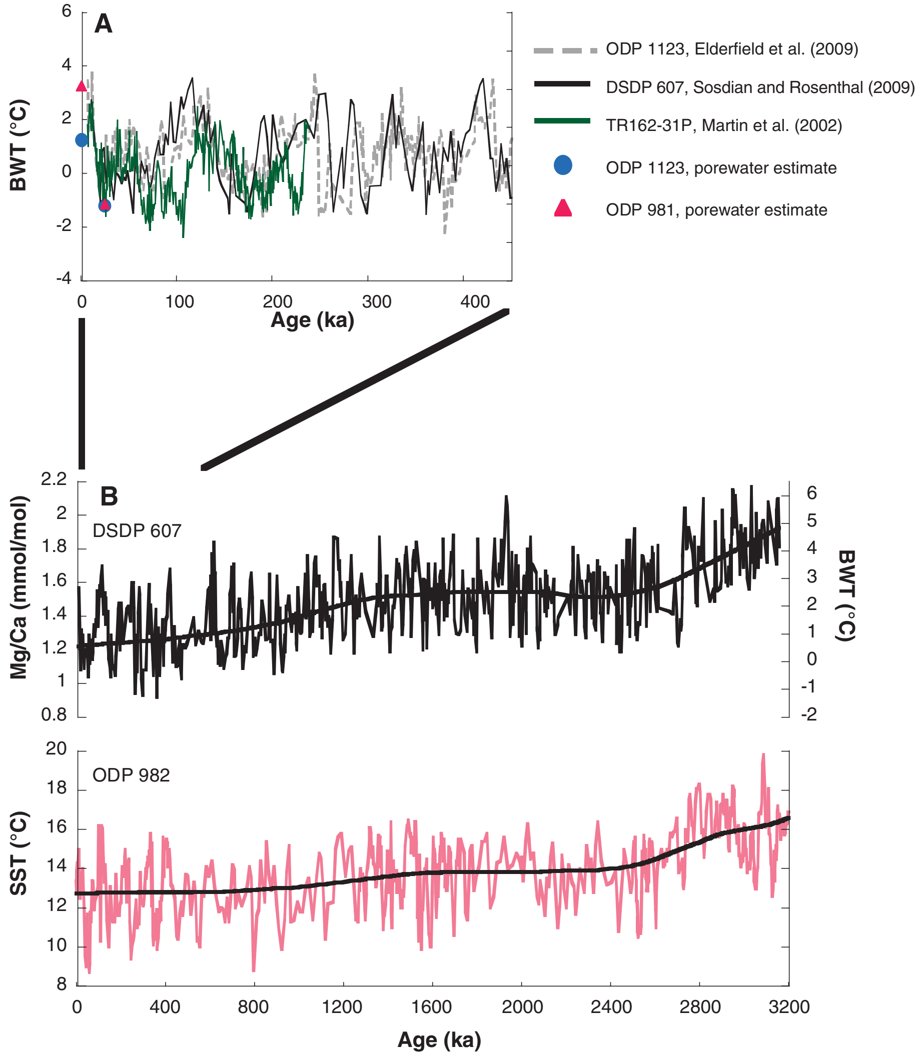

Fig. 1. Comparison of the Mg/Ca-derived BWT record from DSDP site 607 with (**A**) late Pleistocene BWT records derived from *Uvigerina* Mg/Ca from the southern Pacific Ocean (*12*), eastern equatorial Pacific [(*11*); recalculated using calibration from *12*)], and porewater estimates for the North Atlantic (triangles) and South Pacific Ocean (circles) (*6*). Note the consistency among all the records, suggesting that during glacial maxima BWTs were similar and close to freezing in all sites, in agreement with conclusions derived from porewater data for the LGM. (**B**) Alkenone-derived SST record from the high-latitude North Atlantic ODP site 982 exhibits significant coherency in both the long-term trend and G-I variability (*16*).

Current calibrations suggest a dominant temperature control on benthic foraminiferal Mg/Ca above 5°C with a sensitivity of ~0.12 mmol mol^{-1} per °C (*3*). At temperatures below 4°C, a decrease in deep water ΔCO_3 below 20 µmol kg^{-1} leads to an increasingly higher offset of Mg/Ca data from the expected warm-temperature calibration line (*4*, *5*). Deep Sea Drilling Program (DSDP) site 607 (41°N, 32°W; water depth 3427 m), which we studied in (*2*), is characterized by modern bottom-water temperature (BWT) = 2.6°C and ΔCO_3 = ~33 µmol kg^{-1} and therefore is currently minimally affected by the [CO_3] ion effect (*4*, *5*). This was likely also the case for other interglacials, and hence the uncertainty in reconstructing interglacial BWTs is relatively small. The largest uncertainty in our reconstruction (*2*) is, therefore, associated with reconstructing BWTs during the late Pleistocene glacial

[1]Rutgers University, Institute of Marine and Coastal Sciences, New Brunswick, NJ 08901, USA. [2]School of Earth and Ocean Sciences, Cardiff University, Main Building, Park Place, Cardiff CF10 3YE, UK.

*To whom correspondence should be addressed. E-mail: SosdianS@cardiff.ac.uk

intervals when the presence of nutrient-rich, low [CO_3] Antarctic Bottom Water at this site could have biased Mg/Ca estimates of BWT. Based on an estimated decrease of ~20 μmol kg^{-1} during the Last Glacial Maximum (LGM) from a nearby site (*5*) and Mg/Ca-ΔCO_3 sensitivity of 0.0085 mmol mol^{-1} per μmol kg^{-1}, we calculated ~0.17 mmol mol^{-1} LGM-to-Holocene (HL) change in Mg/Ca due to lower saturation state. Considering that 0.17 out of the measured 0.54 mmol mol^{-1} LGM-HL increase in Mg/Ca at site 607 was due to the increase in [CO_3], we calculated an LGM-HL change of ~3.1°C, based on the temperature sensitivity of 0.12 mmol mol^{-1} per °C (*3*). This estimate is entirely consistent with the benthic foraminiferal oxygen isotope ($\delta^{18}O_b$) record showing an LGM-HL change of about –1.5 per mil (‰) in the companion piston core [Chain 82-24-23PC; 43°N, 31°W; water depth 3406 m (*2*)] assuming –0.8‰ change in LGM seawater composition in the North Atlantic (*6*). In contrast, if entirely due to the saturation effect, the site 607 Mg/Ca record would imply a >60 μmol kg^{-1} LGM-HL change in [CO_3], which is larger than current estimates of 10 to 25 μmol kg^{-1} (*7*–*9*). In our report (*2*), we accounted for the [CO_3] ion effect by using apparently greater temperature sensitivity of ~0.15 mmol mol^{-1} per °C, which yields similar LGM-HL change of 3.3 ± 1.1°C.

The above comparison demonstrates that ~70% of the LGM-HL Mg/Ca signal at site 607 is attributable to changes in BWT, in contrast to Yu and Broecker's contention that carbonate ion changes primarily influence the Mg/Ca record at site 607 whereas BWT has only a weak effect. Nonetheless, we agree with Yu and Broecker that additional estimates of changes in [CO_3] saturation could reduce the uncertainty in our BWT reconstruction (estimated at ±1.1°C). In the absence of these, we validate our 3.2-million-year reconstruction by comparing it to other climate records. Our temperature record suggests that climate cooling over the past 3.2 million years occurred primarily through two distinct events associated with the late-Pliocene and mid-Pleistocene shifts in the global $\delta^{18}O_b$ record (*2*). BWT variations generally covary and are coherent with the $\delta^{18}O_b$ record in frequency, average long-term trend, and glacial-interglacial (G-I) amplitude, and are consistent with the low-resolution ostracod temperature record from this site (*10*). In contrast, the lack of coherency and synchronicity between Mg/Ca, $\delta^{13}C$ (as a nutrient/[CO_3] analog) and deep Atlantic dissolution records across the Pleistocene suggests that saturation changes do not dominate the Mg/Ca variability at this site (*2*). Furthermore, our BWT reconstruction is consistent with other late-Pleistocene benthic foraminiferal Mg/Ca-derived BWT records from the Atlantic, Southern, and Pacific Oceans despite different carbonate histories in each basin (Fig. 1A) (*11*, *12*) and with estimates based on $\delta^{18}O_b$ in benthic foraminifera, suggesting G-I temperature variability of 2 to 4.5°C (*13*, *14*). Of particular interest is the coherency and synchronicity (relative to $\delta^{18}O_b$) with the BWT record from Southern Ocean ODP (Ocean Drilling Program) site 1123. This record is derived from the benthic foraminifer *Uvigerina sp.*, a species that is allegedly "free" of [CO_3] ion effect (*12*), and thus supports the application of our site-specific calibration.

The timing and magnitude of temperature change in our BWT record (*2*) show strong similarity with high-latitude sea surface temperature (SST) records across the Pliocene-Pleistocene climate transitions and on G-I time scales, indicating that our BWT record is indeed capturing variations in the temperature of high-latitude source waters (Fig. 1B) (*15*, *16*). Notably, the agreement holds for both interglacial (when [CO_3] effect is minimal) and glacial (when [CO_3] effect is the largest) intervals. These lines of evidence and the consistency between our results and other late Pleistocene sea-level reconstructions (*2*) suggest that we are correctly accounting for changes in carbonate saturation and that therefore, within the quoted errors, our BWT reconstruction is valid.

References

1. J. Yu, W. Broecker, *Science* **328**, 1480 (2010); www.sciencemag.org/cgi/content/full/328/5985/1480-c.
2. S. Sosdian, Y. Rosenthal, *Science* **325**, 306 (2009).
3. T. M. Marchitto, S. P. Bryan, W. B. Curry, D. C. McCorkle, *Paleoceanography* **22**, PA1203 (2007).
4. H. Elderfield, J. Yu, P. Anand, T. Kiefer, B. Nyland, *Earth Planet. Sci. Lett.* **250**, 633 (2006).
5. J. Yu, H. Elderfield, *Earth Planet. Sci. Lett.* **276**, 129 (2008).
6. J. F. Adkins, K. McIntyre, D. P. Schrag, *Science* **298**, 1769 (2002).
7. T. M. Marchitto, D. W. Oppo, W. B. Curry, *Paleoceanography* **17**, 1038 (2002).
8. D. M. Anderson, D. Archer, *Nature* **416**, 70 (2002).
9. J. Yu, H. Elderfield, *Earth Planet. Sci. Lett.* **258**, 73 (2007).
10. G. Dwyer *et al.*, *Science* **270**, 1347 (1995).
11. P. Martin *et al.*, *Earth Planet. Sci. Lett.* **198**, 193 (2002).
12. H. Elderfield *et al.*, *Quat. Sci. Rev.* **29**, 160 (2010).
13. L. Labeyrie, J.-C. Duplessy, P. Blanc, *Nature* **327**, 477 (1987).
14. C. Waelbroeck *et al.*, *Quat. Sci. Rev.* **21**, 295 (2002).
15. W. F. Ruddiman, M. E. Raymo, D. G. Martinson, B. M. Clement, J. Backman, *Paleoceanography* **4**, 353 (1989).
16. K. T. Lawrence, T. D. Herbert, C. M. Brown, M. E. Raymo, A. M. Haywood, *Paleoceanography* **24**, PA2218 (2009).

26 January 2010; accepted 27 May 2010
10.1126/science.1186768

SCIENCE IN FILM

Better Reception in Europe?

Stuart Firestein

Agora
Alejandro Amenábar, director
Mod Producciones, Himenóptero, and Telecinco Cinema, Spain, 2009. 126 minutes.
http://agorathemovie.com/

Sometime in the career of every scientist there is a moment when he or she asks "Why, really, am I doing this? Who cares?" Imagine how much more intense that feeling might have been for ancient astronomers trying to fathom why some stars wandered through the heavens in predictable but incomprehensible paths—gazing up each night at a star-filled sky and wondering what it all meant.

Spanish director Alejandro Amenábar's film *Agora* captures this passion and how it often borders on lunacy. The film is set against a panoramic history of the struggle between the faith demanded by religion and the incessant questioning of the scientist (even if the two world views coalesce on many things). Amenábar has chosen early 5th century Alexandria for his place and a female Greek philosopher, Hypatia, as his heroine. Neither is perfect, because the history is blurred. But both are powerful as metaphor, with just enough historical fact to be curiously, and frighteningly, contemporary.

When the film begins, the cult of Christianity is on the rise in Alexandria, whose great library houses the largest extant collection of classical writings. In fact, this was probably only the daughter library, the Serapeum, as the main library seems to have been destroyed earlier (Julius Caesar is often blamed). No matter, the library is the repository of ancient knowledge and the center of the intellectual life of the pagan Greeks who governed the city and practiced an early form of science.

Only slightly less historically blurred is the character of Hypatia (played with grace and passion by Rachel Weisz), a brilliant female philosopher, mathematician, astronomer, and teacher, whose existence has been verified although none of her writings have survived. Among her multiple interests seems to have been conical curves, the geometrical method of finding the four main curves (circle, ellipse, parabola, and hyperbola) within different cuts of a cone. She is portrayed as courageous: Besides disregarding the political dangers she faces, she insists on not settling for the easy answers (at that time, the ungainly but predictively powerful Ptolemaic system of circles within circles).

One of the many beauties of the film is its seamless interplay between the personal and the panoramic, in both time and space. Amenábar uses shots of Earth from space and of the city-state of Alexandria from high overhead to frame the self-important and antic-looking activities of individuals scurrying about trying to understand a world they can never quite grasp. This visual metaphor captures the futile, foolish, beautiful, and inevitable faces of science. At one point, Hypatia remarks that if only she could unravel a little more and know what governs the "wanderers" (the observable planets), she could go to her grave happy. It is a deeply touching moment because you, we, know how much there is she will in fact never know. And we can't help think, are we any different?

Amenábar's film surprisingly and unflinchingly dives into the tension between science and religion, and the view he offers is not black and white. The "scientific" Greeks are just as devoted to their pagan gods as the new Christians are to their savior. The Greeks are blind to the truth of planetary movement because they cannot imagine Earth moving or the heavens being governed by anything but perfect circles. Science can be as blind as religion, and the results can be almost as devastating.

In a particularly compelling cinematic moment, as the Christian mobs sack the library, scrolls are ripped from their shelves, torn apart, and flung into the air. The camera slowly pans from the roof to the floor; gravity seems disjointed as papers fly in all directions and rationality is chased out the door, not to return for another ten or so centuries. How unsettling to watch the world turned over so easily, by a mob, by politicians manipulating a crowd.

Hypatia, working her way through the mechanisms of the heavens while nearly blind to the far more complicated mechanisms of humankind, makes the leap to a heliocentric universe and planetary orbits guided by ellipses, not perfect circles. If perfect circles aren't the rule in the heavens, why should we expect perfection here on Earth? Her realization comes just as she is seized and murdered by a mob of Christian zealots, convinced she is a witch for espousing crazy ideas about God's creation and for not accepting her subordinate role as a woman.

Because this is the movies, Hypatia is given the moment when she realizes that elliptical orbits are the solution to her paradoxical observations and that Earth indeed moves through the heavens, it is just another wanderer. While there is no record that she had this epiphany, her study of conical curves makes it plausible. In any case, it would be another 1200 years before Johannes Kepler, a devout Christian, demonstrated the elliptical paths of the planets and changed our view once and for all.

CREDIT: FROM AGORA, BY TERESA ISASI/COURTESY NEWMARKET FILMS

Agora is a movie you don't want to miss. Released last year in Europe to considerable acclaim, it won the Sloan Foundation award for best science film at the Hamptons International Film Festival (2009) and has finally found an American distributor, after a year-long search. See it, take your students to see it, take your mother to see it. It is a profoundly affecting film.

Another European film did not fare so well in its Atlantic crossing. I recently had the opportunity to see two versions of Jacques Perrin and Jacques Cluzaud's *Océans*. The French original was released in January to popular and critical acclaim. The Disney-distributed version debuted in the United States on Earth

The reviewer is at the Department of Biological Sciences, Columbia University, New York, NY 10027, USA. E-mail: sjf24@columbia.edu

Océans
Jacques Perrin and Jacques Cluzaud, directors
Galatée Films, France, 2009. 100 minutes. www.oceans-lefilm.com/

Oceans
Jacques Perrin and Jacques Cluzaud, directors
Disneynature, USA, 2010. 87 minutes. http://disney.go.com/disneynature/oceans/

Day. It is no secret that the two versions are quite different, with the Disney release marked by several cuts, and that some of the sponsoring organizations had their affiliations removed from the American version.

In one omitted scene, a young boy and an older man walk through a natural history museum of extinct marine animals. Another missing scene shows them standing in front of an admittedly beautiful aquarium exhibit while the narrator remarks "but if this is all there was it would be … a sad reflection of the real world" we are destroying. The suspicious may see the deletion of this touching scene as an egregious act of corporate self-interest (Disney being a big player in the marine theme park biz).

In the U.S. version, Pierce Brosnan drones on with an insipid narration, full of platitudes and often unwarranted optimism. The more powerful original has little narration and leaves the viewer undisturbed to experience the beauty of the oceans without being told what to think. The worst transgression of all may occur in an unlikely place: the credit roll. In the original, a thoughtful warning about the state of the globe from the older man and his young companion dissolves into the credits. These roll to a slow and pensive ballad while haunting footage, mostly from earlier scenes, maintains the sense of humility appropriate to thinking about the oceans and what we are doing to them. In the Disney version, a nonsensical upbeat derivative rock song, "Make a Wave," accompanies shots of the cameramen and others actually making the movie—as if the whole thing were just some more Hollywood pretend.

Now it may be that once Disney becomes a film's American distributor, one has to expect concessions for the children who will now be the target audience. And perhaps a case can be made that getting to young children and making them environmentally conscious will serve an important future function. But public policy about the environment is being decided now by adults who are uninformed or misinformed—not by children who in 30 years might feel good about the oceans because they saw this movie when they were 8.

To me, a larger question is why there is no adult market in the United States for an environmentally sensitive and demanding film with an informed and important scientific message. Did potential American distributors turn down Amenábar's star-filled, award-winning, historical action film because it had a cogent scientific theme? Why are films like *Océans* and *Agora* finding strong, sophisticated, adult audiences in Europe and failing to attract attention in America?

10.1126/science.1192783

FILM: ENVIRONMENT

Takes on Hunters and Roads

Once again, we took advantage of the annual Environmental Film Festival in the Nation's Capital to sample movies that "celebrate the wonder of the natural world and illuminate the growing challenges to life on Earth." This year's festival (the 18th) featured 155 films, many of which explored links between our foods and the environment. Some works addressed the ecological implications of various human activities; others focused on green practices and potential solutions to the problems we face. A few—such as the four-part *Rauta–Aika* (*The Age of Iron*) (1982), filmed from poet Paavo Haavikko's interpretation of the Finnish national epic, *Kalevala*—seemed hard to link to the environment under even the most inclusive approach. The screenings were often enhanced through discussions with the filmmakers and involved experts and activists. Brief descriptions of all of the films can be found at www.dcenvironmentalfilmfest.org/films.php. Here are comments on several that we managed to catch.

Lords of Nature: Life in a Land of Great Predators. Karen Anspacher-Meyer and Ralf Meyer, directors. Green Fire Productions, USA, 2009. 60 minutes. www.lordsofnature.org

The early-20th-century extirpation of wolves from Yellowstone National Park was followed by pronounced changes in vegetation. Elk browsing on young trees had a drastic impact on willow, cottonwood, and aspen. After wolves were reintroduced to Yellowstone in the 1990s, recruitment of these trees rebounded (elk became more skittish and shifted their feeding habits). The wolves also had other effects: their kills supported more scavengers; beaver recolonized streams, feeding on the flourishing willows; pronghorn lost fewer calves to coyote; reestablished streamside vegetation retarded erosion and provided cover for birds, fish, and invertebrates. Yellowstone serves as the film's prime example of the ecological importance of top predators, and the Meyers highlight research carried out there by Bill Ripple and Bob Beschta. *Lords of Nature* follows the scientists to Zion National Park, where they record data on the similar effects of cougars on ecological diversity and resilience.

Recognizing that the large predators can only persist when they are tolerated by humans, the filmmakers visited livestock producers in Minnesota (home to more wolves than any state except Alaska) and Idaho. These cattle farmers and sheepherders describe nonlethal approaches (such as trained guard dogs, fencing flocks at night, and spooking predators) that they have successfully used to reduce their losses to (and conflict with) wolves.

The film returns several times to the experiences and reflections of wildlife biologist Aldo Leopold. While working for the Forest Service, he had helped

CREDITS (TOP TO BOTTOM): © GALATÉE FILMS; © LARRYTHORNGREN.COM

eradicate wolves from New Mexico. In wolf-free Wisconsin, he witnessed the effects of overabundant deer. And through his classic conservation writings he argued for a land ethic that preserved the integrity and stability of biotic communities, including their crucial predators. As Meyer and Meyer intended, *Lords of Nature* should motivate viewers to help us achieve Leopold's goals.

–Sherman J. Suter

Seed Hunter. Sally Ingleton, director. 360 Degree Films, Australia. 2008. 59 minutes. www.seedhunter.com

Despite some hyperbole (e.g., Australian scientist Ken Street as "the Indiana Jones of agriculture"), Ingleton has put together an appealing and informative adventure story. Street and an international team travel the world collecting "ancient" seeds to use in breeding new crop strains. The rationale is that modern crops have been selected for certain qualities (such as rapid growth or good taste) but may not be able to withstand changes in temperature, moisture, and pathogens that accompany climate change. Varieties that were never (or are no longer) cultivated could harbor genes that will be important for future agriculture. Journeying to remote parts of Tajikistan, the team collects an assortment of seeds and searches for the wild chickpea, which Street describes as "poor man's meat." One problem they encounter is that well-meaning aid workers have distributed modern seed strains to poor farmers and many older varieties have already disappeared. They eventually locate cautious farmers who had held on to their old seeds (wheat, barley, and others) and even find their "Holy Grail," the wild chickpea. The final scenes show Street depositing seeds for safekeeping in the gene bank at Svalbard and presenting some drought-resistant seed to a farmer in Syria whose wheat crops have failed for lack of rain.

–Barbara Jasny

The Last Days of Shishmaref. Jan Louter, director. Miroir Film, Netherlands. 2008. 91 minutes. www.thelastdaysofshishmaref.com

Many of the Inupiaq who live in Shishmaref, an Alaskan village just north of the Bering Strait, are hunter-gatherers, for whom caribou, walrus, and seal serve as primary food sources. Louter's depiction of their subsistence lifestyle under normal circumstances is stark and definitely not prettified. Howling dogs and roaring winds are repeated elements in the film. Villagers chop ice for water (there are no water or sewer lines), and they deplore the fact that the government ignores their requests for assistance. Although they carve whalebone and ivory, the filmmaker shows them as hanging on to life rather than as artists. Nonetheless, interviews with families make clear that this is the place and the way of life they have chosen. Now they find they may lose the little they do have as a result of climate change. Rising temperatures are thawing the permafrost beneath the village, leading to increased erosion and greater vulnerability to storm surges. As homes collapse into the sea, the villagers face evacuation further inland. In a surreal scene, one family huddles around a television watching a special news program explain that the village will disappear within 10 years. *The Last Days of Shishmaref* is not uplifting, but it is a poignant film. **–Barbara Jasny**

A Road Not Taken. Christina Hemauer and Roman Keller, directors. Switzerland, 2010. 66 minutes. www.roadnottaken.info/

In 1979, Jimmy Carter installed solar panels on the roof of the White House. Seven years later, Ronald Reagan had them dismantled. Unity College, Maine, later refurbished 16 and used some of them on its cafeteria. Hemauer and Keller's documentary follows up on their fate. The filmmakers journey from Maine (where many panels remain in a barn), to Washington, DC (where a lack of paperwork initially precludes donating a panel to the Smithsonian Institution), to Georgia (Carter's presidential library), and back to Washington (where the National Museum of American History formally accepts a panel). Interspersed interviews and film clips fill in some historical details and suggest current perspectives.

A Road Not Taken clearly delivers its principal message, that the United States moved away from the national conservation policy and development of alternative energy sources that Carter desired. However, by relying mainly on unplanned actions and uninformed interviews, the narrative sags. More coverage of the decision to remove the panels would have been interesting. Or the movie might have gone further into some of the themes it hints at, such as connections between energy and the conflicts in Iraq and Afghanistan, recent progress toward Carter's goals, and how we might jump from our current path to a greener one. **–Laura Zahn**

Division Street. Eric Bendick, director. Frogpondia Films, USA, 2009. 53 minutes.

The landscape of the United States has been carved up by a surface transportation network that includes some 6.5 million km of roadways. The farthest one can roam from a road in the contiguous 48 states is 35 km. With two friends, Bendick embarked on a backpacking trip to that most remote site, a hillside in the Thorofare valley of Yellowstone National Park. *Division Street* interweaves scenes and scenery from their wilderness pilgrimage with considerations of the undesired effects of highways and of some of the approaches being taken to mitigate those. Collisions flatten fauna and occasionally kill people. Roadways form barriers that fragment habitats, thus increasing the rate of loss of local populations. The film showcases the provision of wildlife corridors under or above the roadbed that allow animals to avoid traffic—offering examples from the Canadian Rockies, a Montana Indian reservation, and Florida. Other segments of the film touch on urban sprawl, city planning, and "green transportation." Bendick effectively presents the perspectives of people who are trying to reshape our highways in order "to save the remaining wild places in between them." **–Sherman J. Suter**

10.1126/science.1191554

CREDITS (TOP TO BOTTOM): HEMAUER & KELLER; SALLY INGLETON; MIROIR FILM; FROGPONDIA FILMS

SCIENCE POLICY

Proposed U.S. Policy for Ocean, Coast, and Great Lakes Stewardship

Regional planning bodies would implement coordinated, ecosystem-based approaches to coastal and marine spatial planning.

Jane Lubchenco[1]* and Nancy Sutley[2]

The Deepwater Horizon–BP oil spill in the Gulf of Mexico is a stark reminder of the intimate dependence of coastal communities on healthy coastal and oceanic ecosystems and of the urgent need to revise policies to ensure wise stewardship of coasts, oceans, and Great Lakes. In the Gulf, and around the world, scientific evidence indicates that coastal and oceanic ecosystems are being disrupted and depleted, with serious consequences for human well-being (*1*, *2*). Oil spills are but one threat. Overfishing, destructive fishing gear, nutrient and chemical pollution, habitat loss, and introduction of nonnative species threaten the health of these ecosystems. Climate change and ocean acidification interact with and exacerbate the impacts of these stressors. The result is the loss of many benefits that humans want and need from these ecosystems, including healthy seafood, clean beaches, resilient economies and jobs, cultural and recreational opportunities, vibrant coastal communities, protection against hurricanes, abundant wildlife, provision of drinking water, and the oxygen that we breathe (*2*).

Although the United States has laws to address many individual issues (e.g., water quality, fishing, and shipping), the historical sector- and issue-based management does not ensure good stewardship across the plethora of uses. Furthermore, the sector-by-sector approach is inadequate to incorporate current scientific knowledge about the interconnectedness among habitats, species, and ecosystems, or between healthy ecosystems and human health and economic and social well-being (*1*, *3*). The need for science-based solutions and forward-thinking, holistic approaches to management has never been greater (*4*–*6*).

An Ecosystem-Based Approach

President Obama in June 2009 constituted his Interagency Ocean Policy Task Force and charged it with developing a national ocean policy and recommending actions that include "a comprehensive, ecosystem-based framework for the long-term conservation and use of our resources" (*7*).

The task force sought input from citizens and proposed a national ocean policy, a coordinating structure, and priority areas, outlined in the interim reports released in September 2009 (*8*) and December 2009 (*9*). Public comments on each report have been deliberated by the task force to finalize recommendations for the president. Recommendations (*8*–*10*) incorporate the fundamental changes consistently emphasized previously (*4*–*6*) as essential to addressing the heretofore "failure of understanding" and "failure of governance" to achieve the stewardship for continued, sustainable use of oceans, coasts, and the Great Lakes. If adopted, the proposed National Ocean Policy (NOP) would, for the first time, constitute a cohesive, national approach to enhancing this stewardship. The NOP would send the resounding message that healthy oceans matter and that policies will now reflect the goal of ensuring healthy, productive, and resilient ecosystems.

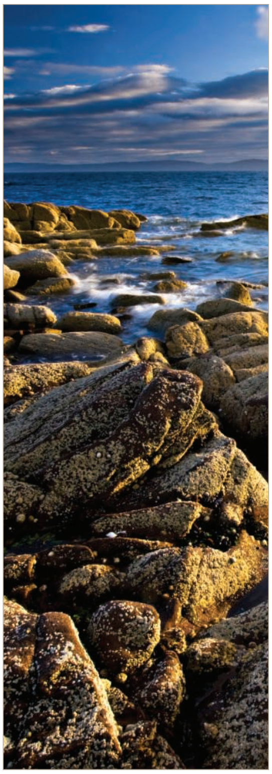

CREDIT: ISTOCKPHOTO.COM

The recommendations incorporate ecosystem approaches to management and complement innovative state and regional efforts, such as coastal governors' agreements for regional ecosystem-based management (EBM) (*9*, *11*). EBM is a place-based, ecosystem approach to management that considers connections between people and ecosystems, as well as connections among ecosystem components (*3*). The recommendations draw on experiences with EBM and coastal and marine and spatial planning (CMSP) from Australia, New Zealand, the European Union, and Canada (*12*).

The proposed NOP encompasses a diversity of activities and ecosystem services, including freedom of navigation; access to traditional and renewable energy sources; promotion of human health; provision of food; protection of coasts from flooding and erosion; maintenance of military readiness; support for recreational activities (e.g., boating, fishing, and surfing); respect of cultural heritage; enhancement of homeland security; and support for maritime commerce and coastal economies. A core principle unifying these diverse interests is the protection and restoration of the productivity, biodiversity, and resilience of ecosystems. A consistent priority is the maintenance and recovery of ecosystem integrity and the continual provision of the range of valuable ecosystem services that humans depend on.

The proposed NOP includes a series of regional planning bodies (RPBs), consisting of federal, state, and tribal agencies in each region, to develop and implement EBM through comprehensive coastal and marine spatial plans within their existing statutory and regulatory authorities (*9*). Through CMSP, they can identify areas suitable for specific types of activities in order to reduce user conflicts, minimize environmental impacts, facilitate compatible uses, and preserve critical ecosystem functioning and services (*13*, *14*).

Linking Science and Management

Two fundamental tenets of the NOP are that (i) cross-sectoral EBM is a mature governance concept, and (ii) the science supporting EBM is sufficiently developed to address the complex issues inherent in managing simultaneous pressures (*3*, *15*). Although many governance and scientific challenges have yet to be resolved, it is clear that EBM is not only feasible, it is the only logical approach to reconcile the inherent trade-offs when managing for multiple uses and conserving the ability of ecosystems to sustain-

[1]Under Secretary of Commerce for Oceans and Atmosphere and Administrator of the National Oceanic and Atmospheric Administration, Washington, DC 20230, USA. [2]Chair of the Council on Environmental Quality and the Interagency Ocean Policy Task Force, Washington, DC 20500, USA.

*Author for correspondence. E-mail: jane.lubchenco@noaa.gov

Published by AAAS

ably produce services (*16*). EBM represents a fundamental shift toward more comprehensive, integrated techniques that acknowledge the interconnected components of ecosystems, including linkages between humans and the natural environment. By emphasizing these connections, the EBM approach sets up decisions to incorporate a wider range of ecosystem services than are inherent in the sector-by-sector approach. Contrary to sector-by-sector management, EBM specifically allows cross-sectoral trade-offs to be considered (*3*). Although ecosystem approaches are already being pursued incrementally within current statutes (*15*), a more explicit, comprehensive policy is needed for EBM to be fully operational and effective at a national scale.

The proposed NOP supports a broad portfolio of scientific research, mapping, monitoring, observation, and assessment to provide critical knowledge to inform EBM decisions. Scientific information—such as species and habitat distributions, human-use patterns, and knowledge of key ecosystem processes—is essential for the development of decision-support tools for effective implementation of EBM and CMSP within an integrated ecosystem framework (*3*, *17*). Priority gaps need to be filled to conduct assessments and forecasts, develop models, and create visualization and valuation tools. Observational and monitoring systems and indicators of the natural and socioeconomic characteristics of these ecosystems need to be expanded to support the wide array of activities called for in the NOP.

Sustainably managing ecosystems requires an understanding of the functional connections between living and nonliving components, the position of nonlinear thresholds, and ways in which ecosystems could change under different management scenarios. Precaution is needed to avoid unintentional losses of ecosystem resilience or diversity. Increased knowledge of complex relations takes on real value when ecosystems can be managed sustainably, without reaching or exceeding critical tipping points (*18*). The proposed NOP supports precautionary, adaptive, and integrated management approaches to enhance understanding of how ecosystems respond to cumulative human impacts. RPBs will be responsible for developing science-based coastal and marine spatial plans that follow national principles and require the development and evaluation of alternative future-use scenarios and trade-offs. The solutions will not be immediate. Reaching the desired outcomes of CMSP will take time, commitment, and the understanding that a continuous learning process will be necessary for all parties involved.

The overarching new NOP is based upon societal choices about goals (e.g., the desire to have healthy oceans, secure and healthy citizens, and minimal conflicts among users). Science informs the approaches and tools (EBM, CMSP, regional focus, and stakeholder engagement) to achieve the goals and identify constraints on trade-offs. So too must science inform each RPB's analyses and decisions. Accomplishing the priorities of the proposed NOP (*8*, *9*) will require effective, two-way communication between scientists and information users, including decision-makers, resource managers, and the general public. Therefore, stakeholder and user group engagement is embedded in every step of the CMSP process, and their input will help to build the socioeconomic knowledge base and understanding of societal values. These efforts will benefit from the integration of social and natural sciences, including the development of tools to evaluate and communicate the full range of provisioning, supporting, regulating, and cultural ecosystem services, and the trade-offs in services associated with different decisions (*16*–*18*).

Making the Vision a Reality

Achieving the comprehensive vision of the proposed NOP will challenge federal agencies with ocean-related mandates to better coordinate their activities and to engage more effectively with partners and stakeholders. A proposed National Ocean Council, co-chaired by the Council for Environmental Quality and the Office of Science and Technology Policy and composed of senior administration officials from 24 departments and agencies, would spearhead the development of initial plans, structures, and dispute-resolution mechanisms. The vision outlined by the Interagency Ocean Policy Task Force would unfold in a series of specific implementation plans for the task force's nine priority objectives (*10*).

This framework embodies flexible, adaptive management, where new knowledge continually informs and improves management and policy decisions. In addition, the acknowledgment that sustainable land practices benefit coastal and oceanic water quality emphasizes the links between land and sea. Finally, the objectives identify the need to protect and restore ecosystems through sustainable management in order to build resilience to climate change and ocean acidification.

A charge to enact a NOP could not be more timely, as the country tackles the challenges of dealing with the unprecedented dimensions of the BP oil spill in the Gulf. The large scale of the impacts and the diversity of sectors affected emphasize the need for a more holistic, integrated approach to ocean management, one that acknowledges the interconnectedness of human and natural systems. Oil spill responses benefit from the planning, thought, and assessment that occur before the event. Under the proposed CMSP framework (*9*), regional plans would enhance preparedness, consider risks posed by all ocean uses, and inform the implementation of a comprehensive national energy policy.

The vision of the proposed National Ocean Policy priority objectives will be achieved through enhanced coordination and integration across the federal government and its local, state, tribal, and regional partners. Although this policy applies specifically to the waters of the United States, given the interconnectedness of the global ocean, it is a vision that our nation will pursue in its relationships and deliberations with international partners.

References and Notes

1. Millennium Ecosystem Assessment, *Ecosystems and Human Well-Being: Synthesis* (Island Press, Washington, DC, 2005).
2. U.N. Environment Programme (UNEP), *Marine and Coastal Ecosystems and Human Well-Being: A Synthesis Report Based on Findings of the Millennium Ecosystem Assessment* (UNEP, Nairobi, 2006).
3. K. L. McLeod, H. M. Leslie, Eds., *Ecosystem-Based Management for the Oceans* (Island Press, Washington, DC, 2009).
4. Pew Oceans Commission, *America's Living Ocean: Charting a Course for Sea Change* (Pew Trusts, Washington, DC, 2003); www.pewtrusts.org/our_work_report_detail.aspx?id=30009.
5. U.S. Commission on Ocean Policy, *An Ocean Blueprint for the Twenty-First Century: Final Report* (Washington, DC, 2004); http://oceancommission.gov/.
6. The Joint Ocean Commissions Initiative was developed by the chairs and members of the Pew and U.S. Ocean Commissions to maintain momentum for implementation of their recommendations; www.jointoceancommission.org/.
7. B. Obama, memorandum, 12 June 2009; www.whitehouse.gov/sites/default/files/page/files/2009ocean_mem_rel.pdf.
8. Council on Environmental Quality, *Interagency Ocean Policy Task Force Interim Report* (White House, Washington, DC, 2009); www.whitehouse.gov/administration/eop/ceq/initiatives/oceans/interimreport/.
9. Council on Environmental Quality, *Interagency Ocean Policy Task Force Interim Framework for Effective Coastal and Marine Spatial Planning* (White House, Washington, DC, 2009); www.whitehouse.gov/administration/eop/ceq/initiatives/oceans/interim-framework.
10. Priority objectives are listed on p. 26 of (*8*).
11. E. Stokstad, *Science* **326**, 1618 (2009).
12. A. A. Rosenberg *et al.*, in (*3*), pp. 294–313.
13. L. B. Crowder *et al.*, *Science* **313**, 617 (2006).
14. F. Douvere, *Mar. Policy* **32**, 762 (2008).
15. S. Murawski, *Mar. Policy* **31**, 681 (2007).
16. G. Daily *et al.*, *Issues Ecol.* **2**, 1 (1997).
17. S. E. Lester *et al.*, *Biol. Conserv.* **143**, 576 (2010).
18. J. Lubchenco, L. E. Petes, *Oceanography* **23**, 115 (2010).

19. We thank President Obama for his commitment to our oceans, coasts, and the Great Lakes; our colleagues on the Interagency Ocean Policy Task Force; Americans who provided input to the Task Force; the U.S. Commission on Ocean Policy, Pew Oceans Commission, and the Joint Ocean Commission Initiative; and S. Murawski, L. Petes, J. Lukens, P. Levin, M. Ruckelshaus, C. Harvey, and A. Guerry for their assistance.

10.1126/science.1190041

NEUROSCIENCE

A Kantian View of Space

The animal brain is able to represent space without prior experience of exploring a location.

Linda Palmer and Gary Lynch

How does the brain represent space? Is this representation entirely the result of learning from experience? In his *Critique of Pure Reason*, Immanuel Kant argued that there must be certain "a priori conditions" of cognition, which could not be derived from experience but must instead be given prior to it. His theory includes two "a priori pure forms" of space and of time, regarded as constraints of thought rather than results of investigation or experience (*1*, *2*). On pages 1576 and 1573 of this issue, Langston *et al*. (*3*) and Wills *et al*. (*4*) both refer to Kant's theory and report that critical components of the brain's spatial representation systems are already in place when an animal first encounters an extended environment. This supports the view that spatial representation indeed includes an innate component prior to experience.

In both studies, the researchers placed electrodes in the hippocampal formation of freely moving 14-day-old rat pups (a remarkable technical achievement), and recorded the activity ("firing" of electrical impulses) of individual neurons at 16 days after birth and up to 2 weeks afterward. They were thus able to sample three classes of cells with distinctly different spatial coding characteristics when the pups leave their nest to first explore the outside world (see the figure). The studies agree that two of these cell types—one that discharges when the animal's head points in a particular direction relative to the environment ("direction cells") (*5*) and a second that fires when the rat moves through a particular location within the environment ("place cells") (*6*)—are present at day 16, only 2 days after the eyes have opened. Both studies indicate that the direction cells in the rat pups are already adultlike, whereas the place cells increase in number and undergo considerable refinement with age and experience.

The two studies disagree regarding a third class of spatial neurons. These "grid cells" fire in repeated discrete locations as the animal moves around its environment, forming the vertices of a polygonal grid that covers the environment (*7*). Langston *et al*. describe rudimentary grid cells at day 16, whereas Wills *et al*. emphasize their appearance in appreciable numbers, and a more mature form, at day 20. Grid cells mature rapidly according to Wills *et al*. but more slowly as determined by Langston *et al*. The discrepancy underscores a debate between the two laboratories about how the developmental program unfolds: which cell types prompt the development of others, and what is primary and what is derived in spatial representation.

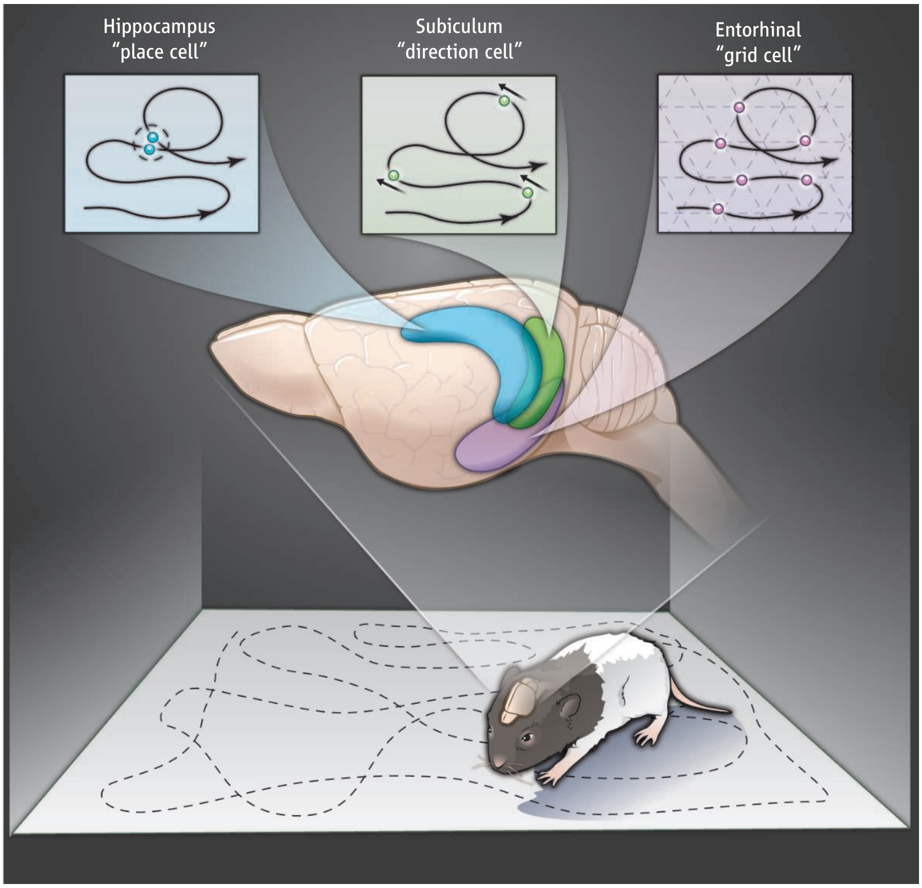

Exploring a new environment. In rat pups, a given place cell in the hippocampus fires whenever the animal traverses a particular location within the environment; a given direction cell fires whenever the animal's head faces in a certain direction relative to its environment; and a given grid cell fires at the vertices of a regular, repeating grid that covers the environment. The direction and place cells are present when pups make their first such exploration; the time of grid cell appearance is disputed.

Department of Anatomy and Neurobiology, University of California, Irvine, CA 92697, USA. E-mail: lcpalmer@uci.edu

The results for place and grid neurons raise the question of the role of learning, as opposed to the onset of preformed neuronal network operations, in the emergence of these cell types during first exploration of an environment. Both studies addressed this issue by testing animals at different ages in unfamiliar surroundings, reasoning that older first explorers will have more adultlike cells if maturation plays the dominant role. This was the case: The number of neurons encoded to location increased steadily as a function of the age at first exposure, rather than number of exposures.

But the case is not quite closed. Long-term potentiation, a form of synaptic plasticity associated with memory formation, appears in the hippocampus by age 11 days in rats and then undergoes a maturation that extends through the third week after birth (*8*). Possibly, then, the efficiency of learning increases with age, allowing the older first explorers to more quickly and easily form spatial-encoding cells. However, another discovery in the two studies indicates that an expanded role for learning would not greatly detract from the central conclusion that spatial representation is partly innate. Direction, place, and grid

Published by AAAS

cells in adults predominate (for the most part) in different regions of the brain. Both reports describe compelling evidence that the three types of neuronal activity observed predominate in their appropriate subdivisions in the youngest rats tested. It follows that the defining features of the neurons' firing characteristics depend on the unique circuit designs, distributions of neurotransmitters and cell types, and input-output relationships characteristic of the regions in which they are found which are largely in place before the eyes open.

What would Kant think of these experiments? For philosophers, "a priori" means necessarily true, as in logic and mathematics, and as such is distinct from "innate"; for example, instincts and drives may be innate, but not a priori. Kant believed he had established the a priori (and not merely innate) status of space as a "transcendental condition" of our representation of the world. This is, however, quite compatible with the existence of a neurobiological substrate of the mental functions he identifies (*9*), so he would likely be fascinated and delighted by these investigations.

References

1. I. Kant, *Kritik der Reinen Vernunft* (Hartknoch, Riga, Latvia, 1781).
2. H. E. Allison, *Kant's Transcendental Idealism* (Yale Univ. Press, New Haven, CT, 2004).
3. R. F. Langston *et al.*, *Science* **328**, 1576 (2010).
4. T. Wills *et al.*, *Science* **328**, 1573 (2010).
5. J. S. Taube *et al.*, *J. Neurosci.* **10**, 420 (1990).
6. J. O'Keefe, J. Dostrovsky, *Brain Res.* **34**, 171 (1971).
7. T. Haftin, M. Fyhn, S. Molden, M. Moser, E. I. Moser, *Nature* **436**, 801 (2005).
8. E. A. Kramár, G. Lynch, *Neuroscience* **118**, 387 (2003).
9. L. Palmer, *Gen. Rev. Psychol.* **12**, 105 (2008).

10.1126/science.1191527

ATMOSPHERIC SCIENCE

Tilting at Connections, from Pole to Equator

Over the past 3 million years, how did variations in sunlight near the poles cause sea surface temperatures near the equator to fluctuate?

S. George Philander

After the demise of the dinosaurs some 65 million years ago, Earth experienced irregular global cooling because of processes associated with the drifting of continents (*1*). About 3 million years ago, glaciers formed in high northern latitudes, surface waters cooled in parts of the equatorial Atlantic and Pacific Oceans (*2*), and climate sensitivity to variations in obliquity (the tilt of Earth's axis) increased substantially. Since that time, changes in sunlight associated with obliquity variations at a period of 41,000 years induced variations in global ice volume and equatorial sea surface temperatures (SST). In general, variations at the equator occurred a few thousand years before those in high latitudes and thus could not have been a direct consequence of the waxing and waning of glaciers. How did the changes in sunlight, which were large mainly near the poles, affect the tropics? Two papers in this issue, on pages 1550 and 1530 (*3, 4*) shed light on the matter.

Researchers have learned much about the factors that determine equatorial SST from studies of El Niño and La Niña. These events involve an adiabatic, horizontal redistribution of warm surface waters along the equator (see the figure, panel B). Because the thermocline, the interface between the warm surface water and the colder deeper water, is so shallow, a mere change in its slope affects SST. Surface temperatures, in turn, influence the winds that determine the thermocline's slope. The positive feedbacks implied by this circular argument affect the global climate, as is evident during an intense El Niño. The impact on climate would be even larger if extreme SST patterns were to persist for prolonged periods, not merely for a few months as in the case of El Niño. That is because SST patterns determine the extent of the stratus clouds that cover cold surface waters in low latitudes, and also the atmospheric concentration of water vapor, a powerful greenhouse gas (*5*).

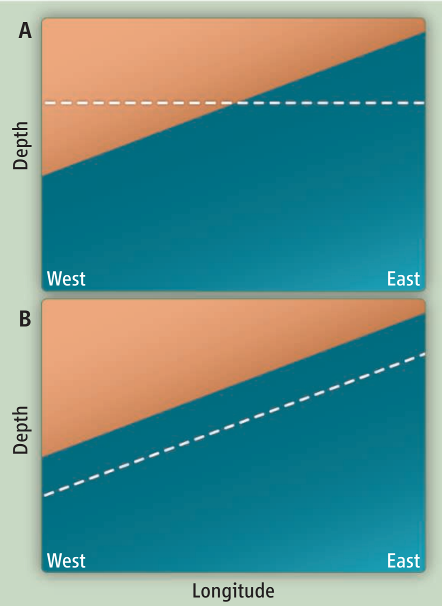

Shifting seas. Shifts in winds, sea surface temperatures, and the ocean's heat budget can induce shifts in the distribution of warm (red) and cool (blue) waters along the equator in the Pacific Ocean. In the shift from La Niña to El Niño (**A**), adiabatic processes change the slope of the thermocline (solid to dashed line). The very different diabatic change in (**B**) requires changes in the ocean heat budget, which can be induced by variations in obliquity.

A mechanism that could induce extreme, long-lasting SST changes involves the vertical movements of the thermocline (see the figure, panel B). This diabatic mechanism requires changes in the heat budget of the oceans. Today, the oceans gain large amounts of heat from sunlight in equatorial regions where surface waters are cold. Currents transport that heat to higher latitudes where it is lost to the atmosphere. The loss depends on atmospheric conditions; it occurs mainly in winter, when cold continental air blows over the warmer ocean. If that high-latitude loss decreased while the gain at the equator continued, then warm water would accumulate in low latitudes and the thermocline would deepen (panel B). Studies with ocean models corroborate this hypothesis that the oceanic loss of heat in high latitudes controls the depth of the thermocline in low latitudes (*6*). Philander and Fedorov (*7*) propose that, as the globe and the deep ocean cooled over the past tens of millions of years, the initially deep equatorial thermocline shoaled (moved closer to the surface). A threshold was reached about 3 million years ago when cold water appeared at the surface in the tropical Pacific and Atlantic. This altered the ocean's heat budget and circulation (*8*), allowed conditions in high latitudes to influence tropical SST by vertically shifting the thermocline,

Princeton University, Princeton, NJ 08540, USA, and University of Cape Town, South Africa. E-mail: gphlder@princeton.edu

Published by AAAS

and introduced climate feedbacks.

Over the past 3 million years, the climate feedbacks have amplified the response to obliquity forcing and have also accelerated the cooling trend that started much earlier. The obliquity cycles are evident in SST changes in the eastern and western equatorial Pacific. The cooling trend, however, appears only in the east, not the west, so that the SST gradient along the equator in the Pacific increased as we approached the present. This difference between the eastern and western Pacific is a consequence of a long-term shoaling of the thermocline; because of its downward slope to the west, it affected SST strongly in the east but not the west. Superimposed on this trend were vertical oscillations of the thermocline (see the figure, panel B). Obliquity cycles at times caused the thermocline to be sufficiently shallow to affect SST all along the equator, in the east and west. At such times, the tongue of cold water along the equator stretched far west of the dateline. The thermocline has a complex spatial structure and, even though it can be shallow all along the equator, it usually remains deep near 4°N. That is why measurements that cover the last ice age, across the equator along 95°W, show practically no change in SST at 4°N but large changes at the equator and further south (*9*). (A section across the equator in the far western Pacific, to determine whether SST changes there are similar to those along 95°W, would be valuable.)

The observations of Martínez-Garcia *et al*. (*3*) and of Herbert *et al*. (*4*) corroborate the hypothesis that oceanic links can translate obliquity forcing in high latitudes into SST response in low latitudes, but several questions remain unanswered. Researchers have thus far considered the waxing and waning of glaciers, and the SST fluctuations in the tropical Pacific, as two unrelated facets of the response to obliquity variations. The challenge now is to determine how the two facets are connected, and why, over the past 0.7 million years, cycles of about 100,000 years became dominant. Further questions concern the effect of variations in the atmospheric concentration of carbon dioxide on climate. The arguments of Herbert *et al*. (*4*), which suggest that this greenhouse gas played an important role in producing similar tropical SST variations in different regions, are undermined by the striking differences between the eastern and western equatorial Pacific, between the regions north and south of the equator along 95°W, and between the equatorial Pacific and Atlantic. In the Atlantic, obliquity signals appear to be secondary to those induced by precession of Earth's axis, for reasons yet to be explored.

References and Notes

1. J. Zachos *et al.*, *Science* **292**, 686 (2001).
2. About 3 million years ago, surface waters cooled in the tropics, zonal SST gradients were established along the equator, and the tropical pool of warm surface waters contracted in the north-south direction (meridionally), but the precise timing varied from place to place (*3–6*).
3. A. Martínez-Garcia *et al.*, *Science* **328**, 1550 (2010).
4. T. D. Herbert *et al.*, *Science* **328**, 1530 (2010).
5. C. M. Brierley *et al.*, *Science* **323**, 1714 (2009).
6. A. V. Fedorov *et al.*, *Science* **312**, 1485 (2006).
7. S. G. Philander, A. V. Fedorov, *Paleoceanography* **18**, 1045 (2003).
8. The threshold about 3 million years ago signaled a change in how the ocean absorbed heat in the tropics and transported it poleward. Previously, vertical mixing (perhaps involving hurricanes) was important. Afterward, the wind-driven circulation acquired a meridional overturning component with much stronger upwelling at the equator (*10*).
9. K. Horikawa, M. Minagawa, M. Murayama, Y. Kato, H. Asahi, *Geophys. Res. Lett.* **33**, L13605 (2006).
10. A. V. Fedorov, C. M. Brierley, K. Emanuel, *Nature* **463**, 1066 (2010).

10.1126/science.1189748

ANTHROPOLOGY

Dating Pharaonic Egypt

Hendrik J. Bruins

Radiocarbon dating and modeling of Egyptian dynasties are strengthening the links between historical chronology and archaeological associations.

Ancient literary sources of Pharaonic Egypt constitute the historical cornerstone of time in the eastern Mediterranean region during the Bronze and Iron Ages (the third to first millennia B.C.E.). Historical chronologies for ancient Egypt are based on abundant but fragmentary written sources, and various chronological interpretations exist (*1–5*). Radiocarbon dating has the potential to verify those interpretations (*6*). On page 1554 of this issue, Bronk Ramsey *et al*. (*7*) present a comprehensive and sophisticated radiocarbon dating study on the chronology of Pharaonic Egypt, involving 211 samples. The short-lived plant samples for ^{14}C dating were selected from individual funerary contexts in various museum collections. Each sample could be associated with the reign of a particular Pharaoh or with a specific section of the historical chronology.

Ben-Gurion University of the Negev, Jacob Blaustein Institutes for Desert Research and Department of Bible, Archaeology and Ancient Near Eastern Studies, Sede Boker Campus, 84990, Israel. E-mail: hjbruins@bgu.ac.il

Bronk Ramsey *et al*. developed three separate multiphase models for each major period—Old Kingdom, Middle Kingdom, and New Kingdom—to obtain high-precision ^{14}C chronologies. The ^{14}C model results for the Old Kingdom have an average calendrical precision of 76 years and correspond with the historical consensus chronology according to Shaw (*4*). The Middle Kingdom results have an average calendrical precision of 53 years, also favoring the conventional historical chronology. The New Kingdom results, based on 128 ^{14}C dates with an average calendrical precision of 24 years, however, do not support the younger (low) historical chronology options (*1*, *5*), but are nearest to the consensus chronology (*4*) with the 18th Dynasty beginning in 1550 B.C.E. The model actually favors a slightly older beginning of the New Kingdom at ca. 1560 B.C.E.

The enormous volcanic eruption at Santorini in the Aegean Sea during the Late Minoan IA period (*8*, *9*) is a key stratigraphic time marker in the eastern Mediterranean region during the second millennium B.C.E. However, a vexing time difference exists of ~100 to 150 years between archaeo-historical dating and radiocarbon dating of the eruption (see the figure).

Concerning ^{14}C dating, how do the new results for dynastic Egypt (*7*) relate to the Minoan Santorini eruption? The most precise radiocarbon date of the eruption is 1627 to 1600 B.C.E., obtained by wiggle matching of a sequence of ^{14}C-dated tree rings from an olive tree found on Thera, buried in tephra (*10*). Radiocarbon dates from the archaeological site of Akrotiri (Thera) (*8*) on short-lived plant remains related to the Minoan Santorini eruption yielded an average date (uncalibrated) of 3350 ± 10 years before the present (^{14}C yr B.P.) (*11*). Remarkably similar ^{14}C dates were obtained from Crete on animal bones found at Palaikastro in Late Minoan IA context with volcanic ash of the Minoan Santorini eruption and related tsunami deposits: 3350 ± 25 yr B.P. along the promontory and 3352 ± 23 yr B.P. at the inland archaeological site (*12*). By comparing these ^{14}C dates (*10–12*) with the new radiocarbon-based chronol-

Published by AAAS

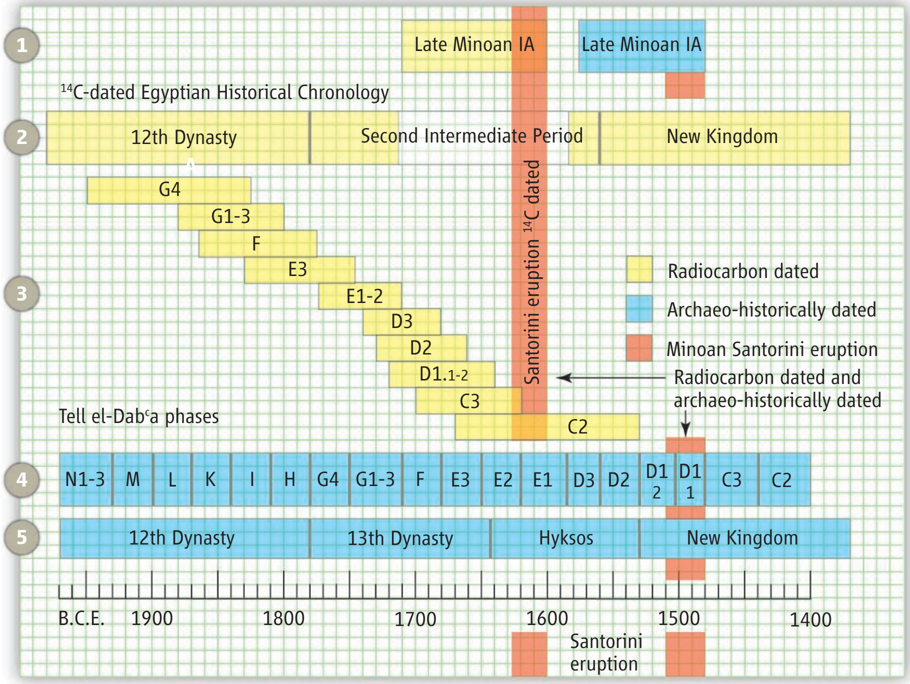

Setting on a date. Dating and association complexities regarding Egyptian dynastic chronology in the second millennium B.C.E. From top to bottom: (1) Radiocarbon dating (yellow) (*16*) and archaeo-historical dating (blue) (*13–15*) of the Aegean Late Minoan IA period in relation to the ^{14}C-dated (*10*) and archaeo-historical dated (*13–15*) Santorini eruption (red). (2) The new radiocarbon and modeling results (yellow) by Bronk Ramsey *et al.* of Egyptian dynastic chronology over the selected time interval. A large part (blank) of the Second Intermediate Period was not investigated owing to the lack of secure samples. (3) The ^{14}C results (yellow) (*14*) of various archaeological phases of Tell el-Dabᶜa. (4) The much younger archaeo-historical dating (blue) by Bietak of the same phases (*13*, *14*). (5) The association of the Tell el-Dabᶜa phases (*13*, *14*) with the young (low) Egyptian historical chronology (blue).

ogy for dynastic Egypt (*7*), it emerges that the Minoan Santorini eruption is older than the ^{14}C dates (both uncalibrated and calibrated) for the beginning of the New Kingdom (see the figure).

However, according to archaeo-historical dating, the eruption took place during the New Kingdom (18th Dynasty), around 1500 B.C.E. (*13–15*). The discrepancy between the two dating methodologies is also reflected by the two alternative dates for the Aegean Late Minoan IA archaeological period: (i) ca. 1710 to 1600 B.C.E. by ^{14}C dating (*16*) and (ii) ca. 1575 to 1480 B.C.E. according to archaeo-historical dating (*13–15*). The two deviating chronologies for the crucial Late Minoan IA period, during which the Santorini eruption occurred, show that one has to be very careful not to mix dates from one methodology (^{14}C) with the other (archaeo-historical), as it may lead to inaccurate archaeological and historical associations (*12*).

Tell el-Dabᶜa, situated in the eastern Nile Delta, is a key archaeological site, having a detailed sequence of phases associated, respectively, with the Middle Kingdom, the 13th Dynasty, the Hyksos Period, and the 18th Dynasty (*13*, *14*) (see the figure). From the radiocarbon dating of short-lived plant material from many archaeological phases of Tell el-Dabᶜa, a graphic overview of the calibrated ^{14}C results, after sequencing, was presented in relation to the stratigraphy (*14*). Comparison of these ^{14}C results with the ^{14}C investigation by Bronk Ramsey *et al.* of dynastic Egypt gives rise to a problem. Phases D1.2-1.1 of Tell el-Dabᶜa are associated with the beginning of the New Kingdom, dated by Bietak (*13*, *14*) on historical-archaeological considerations to ca. 1530 to 1480 B.C.E. However, the calibrated ^{14}C age range for these strata, after sequencing, is ca. 1720 to 1640 B.C.E. (*14*), which is much older than the results by Bronk Ramsey *et al.* for the beginning of the New Kingdom, ca. 1550 to 1560 B.C.E. Hence, a time difference of ~90 to 170 years exists between two investigations for the beginning of the 18th Dynasty.

What is erroneous here—the ^{14}C dates by one study (*7*) or the other (*14*)? or the associations between the Tell el-Dabᶜa archaeological phases and dynastic history, as the ^{14}C results from Tell el-Dabᶜa are systematically older by ca. 100 to 200 years than the Egyptian historical chronology (*13*, *14*)? or the associations between the various funerary archaeological contexts from museum collections and dynastic history (*7*)? The last possibility seems unlikely, given the coherence between the ^{14}C dating results from multiple archaeological sources. On the other hand, Tell el-Dabᶜa has detailed archaeological linkages with the Aegean and the Near East (*13*, *14*). Therefore, not only Tell el-Dabᶜa is involved in this enigma, but the Middle and Late Bronze Age archaeology of the Aegean and the Levant as well.

The systematic investigation by Bronk Ramsey *et al.* marks a great step forward in the corroboration and refinement of Egyptian dynastic chronology with radiocarbon dating. However, much of the Second Intermediate Period, including the Hyksos Period, was not included in the above investigation, as secure samples are rare. Given the enigmatic ^{14}C dates from Tell el-Dabᶜa, a key site in relation to the Second Intermediate Period and the beginning of the New Kingdom, it would be very important to conduct systematic radiocarbon research of multiple-source samples from the 13th Dynasty and the Hyksos Period. Moreover, ^{14}C dating of other Middle and Late Bronze Age archaeological sites in the region will enable association of archaeological strata with the new radiocarbon-dated Egyptian historical chronology (*7*), which may lead to a solution of the complex multidisciplinary problems in establishing a chronology for the second millennium B.C.E.

References

1. R. Krauss, *Sothis und Monddaten, Studien zur astronomischen und technischen Chronologie Altägyptens* (Pelizaeus-Museum, Hildesheim, Germany, 1985).
2. K. A. Kitchen, *World Archaeol.* **23**, 201 (1991).
3. J. von Beckerath, *Chronologie des Pharaonischen Ägypten* (Verlag Ph. von Zabern, Mainz, Germany, 1997).
4. I. Shaw, Ed., *The Oxford History of Ancient Egypt* (Oxford Univ. Press, Oxford, 2000).
5. E. Hornung, R. Krauss, D. A. Warburton, Eds., *Ancient Egyptian Chronology* (Brill, Leiden, the Netherlands, 2006).
6. F. A. Hassan, S. W. Robinson, *Antiquity* **61**, 119 (1987).
7. C. Bronk Ramsey *et al.*, *Science* **328**, 1554 (2010).
8. C. G. Doumas, *Thera: Pompeii of the Ancient Aegean* (Thames and Hudson, London, 1983).
9. H. Sigurdsson *et al.*, *AGU* **87**, 337 (2006).
10. W. L. Friedrich *et al.*, *Science* **312**, 548 (2006).
11. C. B. Ramsey, S. W. Manning, M. Galimberti, *Radiocarbon* **46**, 325 (2004).
12. H. J. Bruins, J. van der Plicht, J. A. MacGillivray, *Radiocarbon* **51**, 397 (2009).
13. M. Bietak, in *The Synchronisation of Civilisations in the Eastern Mediterranean in the Second Millennium BC II*, M. Bietak, Ed. (Verlag der Österreichischen Akademie der Wissenschaften, Vienna, 2003), pp. 23–33.
14. M. Bietak, F. Höflmayer, in *The Synchronisation of Civilisations in the Eastern Mediterranean in the Second Millennium BC III*, M. Bietak, E. Czerny, Eds. (Verlag der Österreichischen Akademie der Wissenschaften, Vienna, 2007), pp. 13–23.
15. J. A. MacGillivray, in *Time's Up! Dating the Minoan Eruption of Santorini*, J. Heinemeier, W. L. Friedrich, Eds. (Monographs of the Danish Institute at Athens, vol. 10, Athens, 2009), pp. 154–170.
16. S. W. Manning *et al.*, *Science* **312**, 565 (2006).

10.1126/science.1191410

PHYSICS

A Drop of Quantum Matter

Studies of a quantum object—a Bose-Einstein condensate—in free-fall conditions may provide high-precision tests of general relativity.

Paulo Nussenzveig and João C. A. Barata

Physics in the 20th century witnessed two major revolutions, relativity and quantum mechanics. General relativity relies on the equivalence principle. When an object in a gravitational field undergoes free fall, it is indistinguishable from the same object in an inertial reference frame—it acts as if it were weightless in outer space. A popular account of a free-fall environment was given by the thought experiment of "Einstein's elevator" (*1*) (see the figure, panel A). General relativity is mainly formulated in terms of classical objects. On page 1540 of this issue, van Zoest *et al*. (*2*) describe an intriguing experiment that brings together fundamentals of general relativity and quantum mechanics. They follow the evolution of a prototypical quantum object, a Bose-Einstein condensate (BEC), under free-fall conditions (see the figure, panel B). The use of BECs in atom interferometers should allow for more sophisticated tests of general relativity.

Some predictions of Einstein's general relativity involve the so-called frame-dragging effects, which can be viewed as manifestations of Mach's principle, a term coined by Einstein in reference to the statement, or conjecture, that all accelerated motions are relative to the reference frame provided by the overall distribution of matter in the universe. As Einstein wrote in a letter to Mach, "inertia originates in a kind of interaction between bodies" (*3*). In this spirit, inertial reference systems must be affected by the motion of distant as well as nearby matter. A gyroscope in free fall in Earth's orbit experiences both the de Sitter, or geodetic, effect and the Lense-Thirring effect (*4*), which cause slight changes in its precessional motions relative to distant stars. The geodetic effect is caused by the orbital motion of the gyroscope in the curved spacetime around Earth (or Earth's motion around the gyroscope). The much smaller Lense-Thirring effect is caused by Earth's rotation around its own axis, which adds a twist to the curvature of space.

Einstein himself expressed doubts about the possibility of measuring such small effects (*5*). Nevertheless, experimental tests of the geodetic effect, with accuracy on the order of 6×10^{-3}, have been reported in measurements of the Moon's orbit (*6*) and (with smaller accuracy) on binary pulsars (*7*). Precise measurements of satellite orbits around Earth (*8*) or the detection of anomalous precessional motions of gyroscopes in Earth's orbit (*9*) provided information about both the geodetic and the Lense-Thirring effects, albeit with smaller precision (10^{-1}) for the latter.

Instituto de Física, Universidade de São Paulo, Post Office Box 66318, São Paulo, SP 05314-970, Brazil. E-mail: nussen@if.usp.br; jbarata@fma.if.usp.br

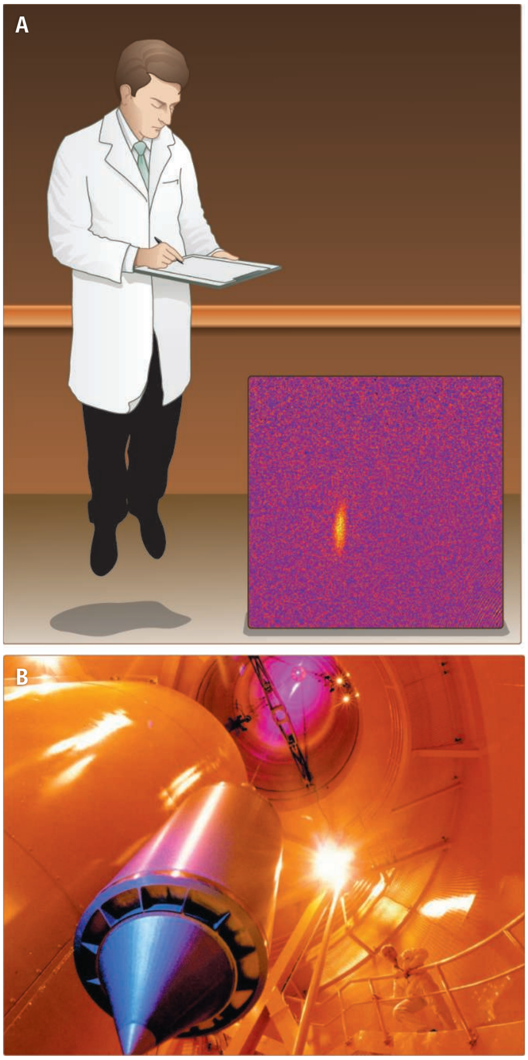

Free falling. (**A**) A rendition of the experiment, as an "Einstein elevator" in free fall containing a human observer and the Bose-Einstein condensate of van Zoest *et al*. The enclosed elevator prevents the observer from knowing if the sensation of weightlessness is caused by free fall in a gravity field, or if the elevator is in outer space. (**B**) The ZARM drop tower in Bremen and the capsule into which van Zoest *et al*. fit their entire experiment. The capsule was dropped from a height of 120 m, in vacuum. Residual gravity was on the order of 10^{-6} of the local value of Earth's gravity.

PHOTO CREDIT: (PANEL B) ZARM/UNIVERSITY OF BREMEN

One way to achieve much higher precision in tests of general relativity is to use atom interferometers (*10*), replacing macroscopic man-made objects by atoms as the test masses. Quantum-mechanical matter waves are used to measure changes in distance or time. Just as in many light-based interferometers, incoming matter waves are split so that they travel over two paths, and interference fringes are observed when the waves recombine. Typically, matter waves are split and recombined by means of atom-light interaction: An atomic transition causes the atom's momentum to change and deflects it. Atoms traveling along the ensuing spatially separated paths experience different gravitational fields or inertial effects, accumulating different phase shifts, which can be measured with high precision.

Atom interferometers have been used to test aspects of general relativity such as time dilation in a gravity field (*11*). However, just as with light interferometers, greater sensitivity results when coherent sources, such as lasers, are used. For atom interferometers, the equivalent of a laser is a BEC. The atoms in a BEC act like one particle—they form a cloud that can be contained within one matter wavelength—and have very low velocities, taking a longer time to traverse the interferometer, which leads to better precision (*12*). The formation of such condensates is possible because bosons—particles with integer spin—can all be "packed" into the same quantum state. Tests of the equivalence principle with BECs are expected to achieve accuracies as high as 1 part in 10^{16} (*12–14*).

To create a BEC, van Zoest *et al*. started with a very cold and dense sample of bosonic particles, in this case, rubidium-87 atoms. The sample was laser cooled and trapped down to microkelvin temperatures and then evaporatively cooled into the nanokelvin regime (*15*). Normally this procedure requires a lab full of fancy lasers, delicate optics very

Published by AAAS

carefully aligned and placed on vibration-isolated tables, vacuum chambers and pumps, and delicate control electronics. For a free-fall study on Earth, all of this equipment was fit into a capsule of 60 cm by 60 cm by 215 cm. The lasers had to retain their frequency and intensity stability upon release. The capsule dropped more than 120 m, and after it experienced a deceleration of up to 50 times Earth's gravity upon landing, the data on the expansion of the BEC in free fall were retrieved. The experiment is a proof-of-principle that such setups can achieve the robustness and reliability required for future experiments in space.

Many challenges will have to be faced before putting BECs into interferometers and using them in space. The BEC expansion that van Zoest *et al*. observed for 1 s agreed with the underlying many-body theory only by taking into account tiny magnetic field curvatures. Such stray fields will have to be dealt with in order to achieve ultrahigh precision. There are other interesting aspects of performing quantum tests of general relativity. Gravity may act differently on bosons than it does on fermions, particles with half-integer spin that must all reside in different quantum states (*16*). Comparison with ultracold Fermi gases could reveal if differences indeed exist.

To summarize the importance of the experiment by van Zoest *et al*., we list some directions for future studies. The equivalence principle can be tested by comparing BEC atom interferometers in free fall on Earth to similar ones in outer space. Interferometers in Earth's orbit can be used to measure frame-dragging effects with high precision (achieved by the ultracold atomic samples), and comparisons between gravitational effects on bosonic and fermionic atomic species can be performed in space experiments. The dynamics of many-body systems in microgravity are interesting in themselves. The robustness and extreme control demonstrated here give a good indication that such perspectives may come true.

In his book *Imagined Worlds* (*17*), Dyson mentions two kinds of scientific revolutions: concept-driven revolutions and tool-driven revolutions. General relativity is certainly of the first kind, whereas the 50-year-old invention of the laser can be attributed to the second kind. BECs present for atomic interferometry the same kind of perspective as lasers do for interferometry with light. By dropping BECs in free fall, we may very well land upon new revolutions in the study of gravitational properties of quantum matter.

References

1. A. Einstein, L. Infeld, *The Evolution of Physics* (Simon and Schuster, New York, 1938).
2. T. van Zoest *et al*., *Science* **328**, 1540 (2010).
3. A. Einstein, Letter to Ernst Mach, Zürich, 25 June 1913, quoted in C. Misner, K. S. Thorne, J. A. Wheeler, *Gravitation* (Freeman, San Francisco, 1973).
4. S. Weinberg, *Gravitation and Cosmology* (Wiley, New York, 1972).
5. H. Pfister, *Gen. Relativ. Gravit.* **39**, 1735 (2007).
6. J. G. Williams, S. G. Turyshev, D. H. Boggs, *Phys. Rev. Lett.* **93**, 261101 (2004).
7. I. H. Stairs, S. E. Thorsett, Z. Arzoumanian, *Phys. Rev. Lett.* **93**, 141101 (2004).
8. I. Ciufolini, *Nature* **449**, 41 (2007).
9. S. Buchman *et al*., *Adv. Space Res.* **25**, 1177 (2000).
10. A. D. Cronin, J. Schmiedmayer, D. E. Pritchard, *Rev. Mod. Phys.* **81**, 1051 (2009).
11. H. Müller, A. Peters, S. Chu, *Nature* **463**, 926 (2010).
12. G. Varoquaux *et al*., http://arxiv.org/abs/0705.2922v2 (2007).
13. W. Ertmer *et al*., *Exp. Astron.* **23**, 611 (2009).
14. S. Dimopoulos, P. W. Graham, J. M. Hogan, M. A. Kasevich, *Phys. Rev. Lett.* **98**, 111102 (2007).
15. M. H. Anderson *et al*., *Science* **269**, 198 (1995).
16. J. D. Barrow, R. J. Scherrer, *Phys. Rev. D Part. Fields Gravit. Cosmol.* **70**, 103515 (2004).
17. F. J. Dyson, *Imagined Worlds* (Harvard Univ. Press, Cambridge, MA, 1998).

10.1126/science.1191666

OCEANS

The Great Indo-Pacific Communicator

Warm water flowing through the Indonesian archipelago from the Pacific to the Indian Ocean influences the climate of the surrounding regions.

Delia W. Oppo[1] and Yair Rosenthal[2]

A complex ocean current system weaves its way through a network of passages, shallow seas, and deep basins between the Indonesian islands (*1*). Every second, this Indonesian Throughflow (ITF) carries ~15 million m^3 of warm, relatively low-salinity water from the tropical Pacific to the Indian Ocean (*1–3*). The ITF eventually makes its way to the Atlantic Ocean (see the figure), thus contributing to global ocean circulation (*1*). Through complex but poorly understood feedbacks, including heat and water exchange with the atmosphere, the ITF is influenced by and modulates climate in the Indo-Pacific region (*1–4*). A shift in the climate regimes of the tropical Pacific and Indian oceans in the mid-1970s—perhaps in response to global warming (*5*)—highlights the possible importance of the ITF and its connection to climate phenomena such as the monsoons, the El Niño–Southern Oscillation (ENSO), and the Indian Ocean Dipole (IOD).

The ITF's influence depends on its temperature, salinity, and volume transport (*1*, *3*). These properties change seasonally in association with the monsoons and interannually in response to basin-scale variations in tropical winds associated with ENSO and the IOD (*1–3*). Surface winds typically flow from east to west in the tropical Pacific. Consequently, warm water piles up in the western Pacific, thickening the warm surface layer. This deepens the thermocline and elevates the surface of the western Pacific, driving a strong ITF flow into the Indian Ocean. During an El Niño event, the tropical Pacific easterly winds relax, the western Pacific thermocline shoals, and warm water moves from the western Pacific toward the central and eastern Pacific. The thermocline cooling and shoaling extends to the Indonesian Seas, and the ITF cools and weakens (*1*). During a La Niña event, the opposite conditions prevail: Tropical easterly winds are stronger, the western Pacific thermocline warms and deepens, and the ITF is warmer and stronger.

The Pacific climate regime is not, however, the only control on ITF transport. Like ENSO, the IOD—an interannual oscillation characterized by anomalous sea surface temperatures in the Indian Ocean—influences climate on an almost global scale (*6*). During the positive phase of an IOD, easterly winds in the tropical Indian Ocean off the south Java coast are anomalously strong. Opposite conditions characterize a negative IOD event. The flow of the warm surface ITF appears to increase during a positive IOD (*2*), consistent with studies suggesting that the direction of winds off the south Java

[1]Department of Geology and Geophysics, Woods Hole Oceanographic Institution, Woods Hole, MA 02543, USA. [2]Institute for Marine and Coastal Sciences and Department of Earth and Planetary Sciences, Rutgers University, New Brunswick, NJ 08901, USA. E-mail: doppo@whoi.edu

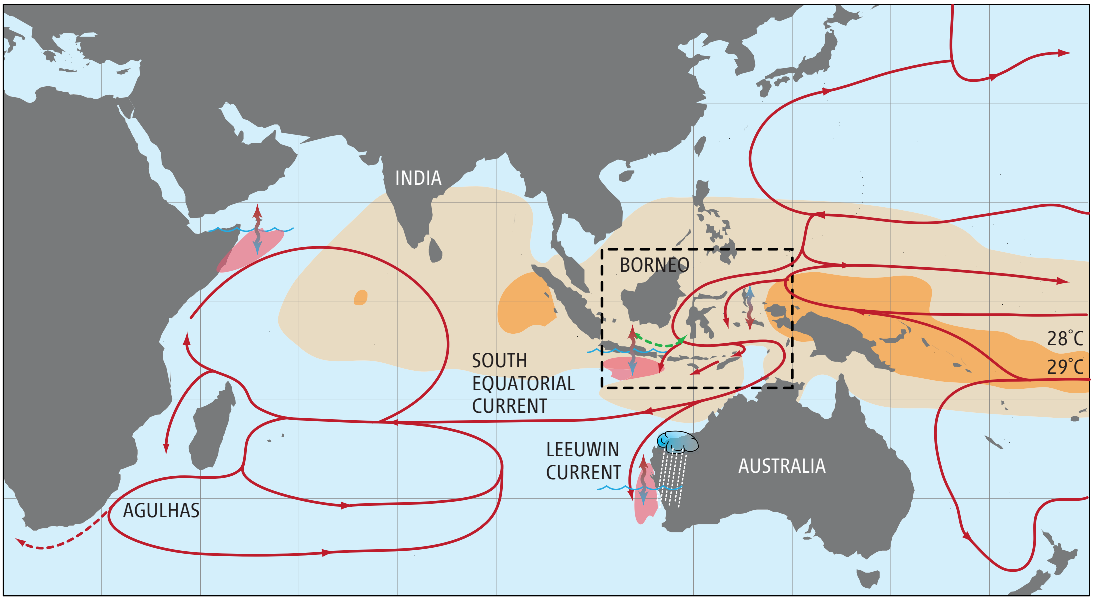

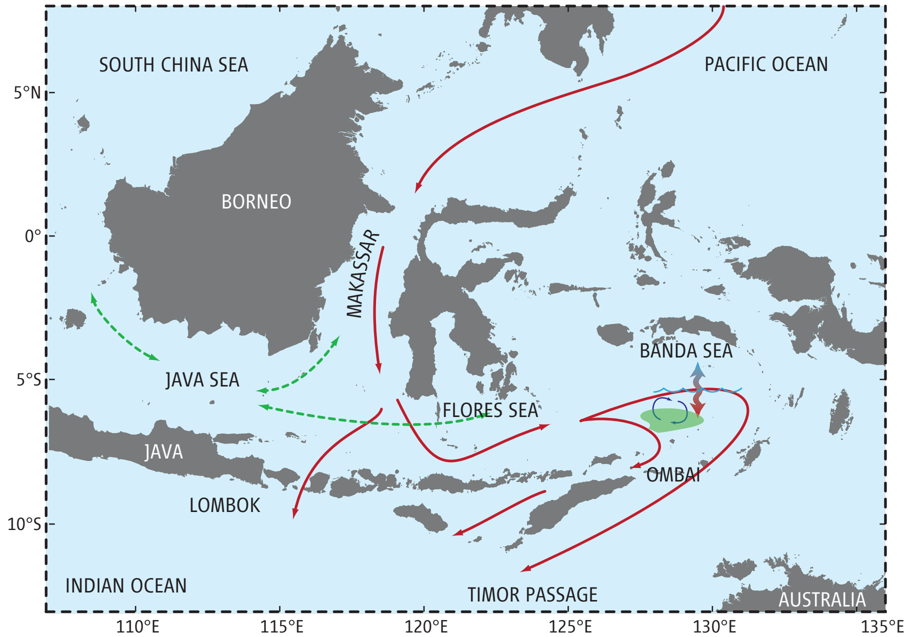

The Indonesian Throughflow (ITF) and its climatic effects. Most of the ITF flows through the Makassar Strait. Some of its waters enter the Indian Ocean through the Lombok Strait, but most flow eastward into the Banda Sea, where they cool and freshen (see the text). This modified ITF enters the Indian Ocean through the Ombai Strait and the Timor Passage (*1*). From here, some ITF flows southward in the Leeuwin Current (*15*), bringing heat and moisture to western Australia, but most joins the South Equatorial Current and transits across the Indian Ocean. At the African coast, most joins the south-flowing Agulhas Current (*1*). This current, now containing ITF water, turns eastward and recirculates in the Indian Ocean, but some of it rounds the Cape of Africa and flows into the Atlantic (*16*). Green arrows denote seasonal reversal in surface exchange with the Java Sea. Pink denotes upwelling areas that are warmer than they would be without the ITF. Two-way vertical arrows indicate air-sea exchange. Low-salinity water and heat are mixed downward in the Banda Sea while cold water is mixed upward.

CREDIT: MAPS ADAPTED FROM (5, 9)

coast strongly affects the ITF and may even modulate the ENSO influence (*4*). More data are needed to understand the links among the ITF, IOD, and ENSO and their implications for climate variations in, for example, Indonesia and western Australia.

The Austral-Asian monsoon also dramatically influences the ITF (*1*–*3*). Seasonal wind reversals drive variations in the input of relatively fresh Java Sea surface water to the southern Makassar Strait. Fresh water from the Java Sea appears to be an important factor inhibiting the southward flow of warm surface water within the Strait during boreal winter (*1*). The winds also contribute to ITF modification in the Banda Sea, where air-sea exchange, intense vertical mixing fueled by tidal energy, and wind-driven upwelling of colder waters cool and freshen the ITF (*3*) and appear to control the direction and strength of the ITF flow between the Banda Sea and the exit passages (*2*, *3*). The ITF in turn may influence sea surface temperatures in the monsoon-driven upwelling areas of the Indian Ocean (see the figure), thus modulating the monsoons' impacts (*1*, *3*).

Despite decades of research, fundamental questions remain about the ITF and its variability (*7*). There are few simultaneous observations within the many ITF passages, and those that do exist (*2*, *3*) span too short a period to assess whether the emerging picture of the ITF and its variability are as accurate estimates of climate mean conditions (*7*). Recent climate trends in the Indo-Pacific region include diminished Pacific easterly wind strength (*8*) and changes in IOD (*9*) and ENSO (*10*) variability. Whether these trends are a response to natural variability or are related to global warming remains a matter of debate (*11*), but it is likely that the ITF is also changing.

Geologic records of past changes in the ITF and surrounding areas can provide evidence of tropical climate change on longer time scales and in a warmer world. Such records also provide information on how sensitive the tropics are to natural climate variability. Preliminary evidence from the Timor Sea suggests that the ITF was stronger and/or warmer ~7000 years ago (*12*), when western tropical Pacific sea surface temperatures were ~1°C higher than today (*13*). If geological evidence from other ITF portals confirms this result, it will help to determine how sensitive the ITF is to potential future climate change.

What drove these past changes? Do they relate to large-scale wind changes in the Pacific or Indian Ocean, changes in surface freshwater distribution, or mixing and air-sea exchange in the Indonesian Seas? And how did the ITF and regional climate vary during the last millennium, which included the Medieval Warm Period (when western tropical Pacific sea surface temperatures were similar to today) and the Little Ice Age

(when the western Pacific sea surface was ~ 1°C colder and much fresher) (*14*)? Although the nature of tropical interannual variability during these recent intervals is still uncertain, comprehensive data collection and modeling efforts can provide insights into the long-term behavior and climatic impacts of this complex system in response to future climate change.

References and Notes

1. A. L. Gordon, *Oceanography* **18**, 14 (2005).
2. J. Sprintall, S. E. Wijffels, R. Molcard, I. Jaya, *J. Geophys. Res.* **114**, C07001 (2009).
3. A. L. Gordon *et al.*, *Dyn. Atmos. Oceans* 10.1016/j.dynatmoce.2009.12.002 (2009).
4. J. T. Potemra, N. Schneider, *J. Geophys. Res.* **112**, C05035 (2007).
5. K. E. Trenberth, *Bull. Am. Meteorol. Soc.* **71**, 988 (1990).
6. N. H. Saji, T. Yamagata, *Clim. Res.* **25**, 151 (2003).
7. A. L. Gordon *et al.*, in *Proceedings of the OceanObs'09: Sustained Ocean Observations and Information for Society Conference, vol. 1, Venice, Italy, 21–25 September 2009,* J. Hall, D. E. Harrison, D. Stammer, Eds. (ESA Publication WPP-306, 2010).
8. G. A. Vecchi *et al.*, *Nature* **441**, 73 (2006).
9. W. Cai, T. Cowan, A. Sullivan, *Geophys. Res. Lett.* **36**, L11705 (2009).
10. M. J. McPhaden, D. Zhang, *Nature* **415**, 603 (2002).
11. E. Guilyardi, *Clim. Dyn.* **26**, 329 (2006).
12. J. Xu, A. Holbourn, W. Kuhnt, Z. Jian, H. Kawamura, *Earth Planet. Sci. Lett.* **273**, 152 (2008).
13. L. D. Stott *et al.*, *Nature* **431**, 56 (2004).
14. D. W. Oppo, Y, Rosenthal, B. K. Linsley, *Nature* **460**, 113 (2009).
15. R. L. Smith *et al.*, *J. Phys. Oceanogr.* **21**, 323 (1991).
16. A. L. Gordon, *Nature* **421**, 904 (2003).
17. We thank A. Gordon and F. Gibbons for comments on the manuscript. Supported by NSF grants OCE-0726829 (D.W.O.) and OCE-0902977 (Y.R) and by the Woods Hole Oceanographic Institution's Ocean and Climate Change Institute.

10.1126/science.1187273

MOLECULAR BIOLOGY

Paring MiRNAs Through Pairing

The extent of base-pairing between a microRNA and RNA affects both RNA translation and stability of the microRNA itself.

Amy E. Pasquinelli

MicroRNAs (miRNAs) repress gene expression by forming base pairs with specific sequences in protein-coding messenger RNAs (mRNAs). The degree of complementarity between a miRNA and its target mRNA determines the mechanism of posttranscriptional regulation (*1*). Nearly perfect pairing induces cleavage of the target mRNA, whereas partial pairing results in translational repression and mRNA decay through deadenylation pathways. On pages 1534 and 1563 of this issue, Ameres *et al*. (*2*) and Cazalla *et al*. (*3*) reveal that, surprisingly, the extent of base-pairing also affects stability of the miRNA itself.

MiRNAs function in many essential cellular pathways, and deviations in mature miRNA amounts have been linked to human diseases (*4*). MiRNA transcripts undergo multiple processing steps to produce the functional, 22-nucleotide, mature species that are bound by Argonaute (Ago) proteins in RNA-induced silencing complexes (RISCs) (*5*). There is a growing list of factors that control miRNA synthesis and processing, but less is known about mechanisms that determine miRNA stability. The half-lives of mature miRNAs range from hours to days, and their stability can be regulated by the cell division cycle or extracellular signals through pathways that are yet to be elucidated (*5*).

In animals, miRNAs typically do not form extensive numbers of base pairs with target sites in mRNAs. Yet the introduction of reporter mRNAs that have perfect complementarity to endogenous miRNAs results in decreased abundance of the target mRNAs in cells. What has not been previously recognized is that extensive base-pairing also results in decreased amounts of the miRNA. Ameres *et al*. analyzed the fate of miRNAs in cultured fruit fly (*Drosophila melanogaster*) cells after introducing miRNA "sensors" that contain multiple sequences complementary to endogenous miRNAs. MiRNAs with perfect complementarity to target sites underwent 3′ end "trimming" (removal of nucleotides) and untemplated nucleotide additions, or "tailing" (see the figure). This remodeling of mature miRNAs was also demonstrated in cultured mammalian cells transfected with antagomirs, chemically modified RNAs designed to bind to specific miRNAs. Although remodeling of the miRNA correlated well with the extent of base-pairing, as many as seven mismatches between the 3′ end of the miRNA and its target RNA still elicited substantial trimming and tailing of

Department of Biology, University of California, San Diego, La Jolla, CA 92093, USA. E-mail: apasquinelli@ucsd.edu

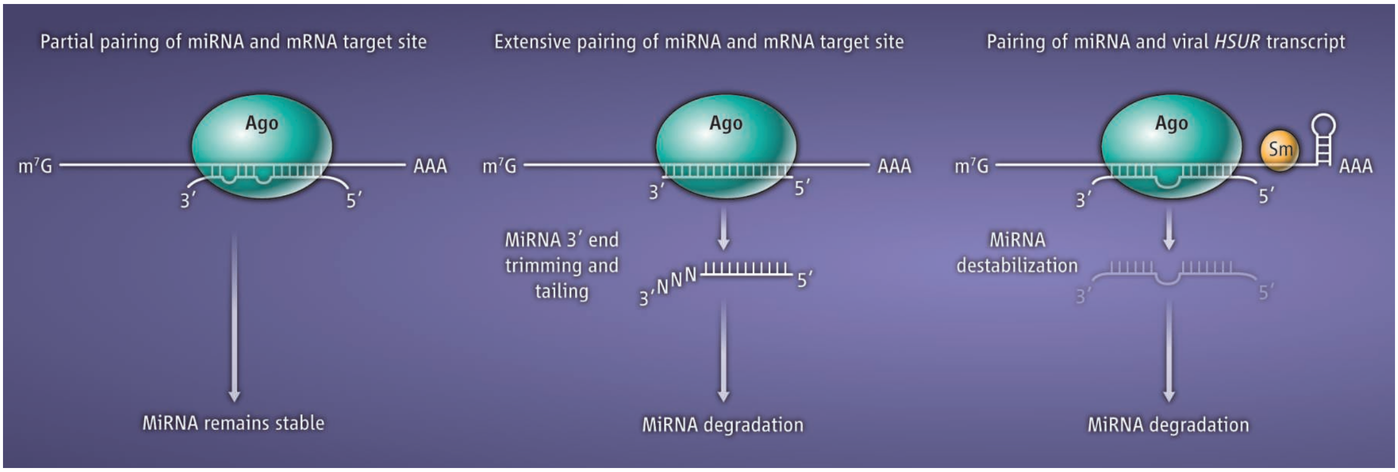

Pairing and stability. In animals, miRNAs often recognize target mRNAs through partial complementarity **(left)**. This prevents decay mechanisms that act on miRNAs or siRNAs that form extensive base pairs with targets **(middle)**. The viral small RNA *HSUR 1* targets cellular *miR-27*, triggering its destabilization **(right)**.

the miRNA in vitro. This raises the question of how often natural miRNA-RNA pairs that do not form perfect complementary pairs, but do have strong 3′ end complementarity, might result in altered miRNA levels.

Ameres *et al*. further show that trimming and tailing of RISC-loaded small RNAs that pair extensively with target RNAs are prevented by the addition of 2′-*O*-methyl groups to their 3′ ends. In *Drosophila*, small interfering RNAs (siRNAs) of exogenous or endogenous origin typically load into Ago2 through a pathway that includes 3′ end methylation by the enzyme Hen1 (*6*). MiRNAs, on the other hand, are incorporated into Ago1 complexes without the 3′ end modification step. This small RNA sorting mechanism allows siRNAs to regulate targets through extensive base-pairing interactions without triggering siRNA remodeling; partial complementarity is sufficient for unmodified miRNAs to function and evade trimming and tailing. However, miRNAs and siRNAs are incorporated into the mammalian Agos 1 to 4 somewhat indiscriminately and do not receive protective 3′ end modifications (*6*). Thus, natural expression or ectopic introduction of RNAs with extensive complementarity to specific miRNAs could have profound effects on the steady-state levels of endogenous miRNAs.

Cazalla *et al*. show that one function of the noncoding uridine-rich RNAs (HSURs) of the virus *Herpesvirus saimiri* is to bind and modulate the amounts of a specific host cell miRNA. *HSUR 1* and *2* contain highly conserved sequences predicted to pair with three host cell miRNAs (*miR-142-3p*, *miR-27*, and *miR-16*), and the viral RNAs and miRNAs were found to associate in ribonucleoprotein complexes. However, only the amount of *miR-27* was consequently affected by this interaction. Notably, *miR-27* can form extensive base pairs with *HSUR 1*, whereas *miR-142-3p* and *miR-16* exhibit much weaker complementarity to the HSURs. The authors demonstrate that a decrease in the amount of *miR-27* occurs at the level of mature miRNA stability, but the mechanism of decay is yet to be elucidated.

The extensive base-pairing between *miR-27* and *HSUR 1* suggests that destabilization of the miRNA could be associated with 3′ end trimming and tailing events, comparable to the fate of miRNAs targeted by antagomirs shown by Ameres *et al*. The enzymes that act on miRNAs associated with complementary RNAs are not yet known. Conversely, interaction of miRNAs with target RNA sequences is thought to increase miRNA half-life by preventing its release from Ago and subsequent destabilization (*7*). Thus, the steady-state amounts of specific miRNAs could depend largely on the number of complementary sequences and the extent of base-pairing between miRNAs and target RNAs.

HSURs are like cellular small nuclear RNAs (snRNAs) in that they associate with Sm ribonucleoproteins and contain trimethylated cap structures, features that direct nuclear localization of RNAs (*8*). Although Cazalla *et al*. identified *miR-27* in a complex with Sm-bound *HSUR 1*, it is unclear whether the interaction occurs in the nucleus or in the cytoplasmic phase of HSUR biogenesis. Nuclear residence of a miRNA has been shown to result in its destabilization (*9*), opening the possibility that recruitment of *miR-27* to the nucleus through its interaction with *HSUR 1* could make it vulnerable to a similar decay pathway.

Although many cellular RNA target-miRNA pairings might not be extensive enough to trigger trimming and tailing of the miRNA, the introduction of foreign RNA into cells could offer target sites that do engage this miRNA decay pathway. The ability of *HSUR 1* to bind and destabilize *miR-27* illustrates how the presence of a viral transcript can disrupt the expression of multiple endogenous genes normally regulated by this miRNA. The knowledge that extensive base-pairing between a siRNA and target RNA site can reduce the half-life of the siRNA should guide the design of RNA interference tools with greater potency in vivo.

References

1. M. Chekulaeva, W. Filipowicz, *Curr. Opin. Cell Biol.* **21**, 452 (2009).
2. S. L. Ameres *et al*., *Science* **328**, 1534 (2010).
3. D. Cazalla, T. Yario, J. Steitz, *Science* **328,** 1563 (2010).
4. Q. Jiang *et al*., *Nucleic Acids Res.* **37** (Database issue), D98 (2009).
5. Z. S. Kai, A. E. Pasquinelli, *Nat. Struct. Mol. Biol.* **17**, 5 (2010).
6. T. A. Farazi, S. A. Juranek, T. Tuschl, *Development* **135**, 1201 (2008).
7. S. Chatterjee, H. Großhans, *Nature* **461**, 546 (2009).
8. S. I. Lee, S. C. Murthy, J. J. Trimble, R. C. Desrosiers, J. A. Steitz, *Cell* **54**, 599 (1988).
9. H. W. Hwang, E. A. Wentzel, J. T. Mendell, *Science* **315**, 97 (2007).

10.1126/science.1191531

MEDICINE

HDL *miR*-ed Down by *SREBP* Introns

Michael S. Brown, Jin Ye, Joseph L. Goldstein

MicroRNAs that reduce cholesterol export from cells are encoded in the same genes that increase cholesterol synthesis.

Animal cells must maintain a membrane cholesterol-to-phospholipid ratio within tight limits for normal function. Elaborate mechanisms control the cellular input of cholesterol from endogenous synthesis or uptake from plasma lipoproteins. Much less is known about the factors that regulate the output of cholesterol from cells. On pages 1566 and 1570 of this issue, Najafi-Shoushtari *et al*. (*1*) and Rayner *et al*. (*2*) show that cholesterol output is controlled by the same genes that regulate cholesterol input, but in a reciprocal manner and through an unexpected mechanism.

The regulatory genes in question direct the synthesis of sterol regulatory element-binding proteins (SREBPs), which are membrane-bound transcriptional activators (*3*). Vertebrates have two *SREBP* genes. *SREBP-2* preferentially activates the synthesis and uptake of cholesterol, whereas *SREBP-1* preferentially activates the synthesis of fatty acids (*4*). Najafi-Shoushtari *et al*. and Rayner *et al*. reveal that both genes also encode, within their introns, a microRNA (*miR-33*) that has the reciprocal effect. *miR-33* blocks the egress of cholesterol from cells by reducing the mRNA and protein levels for ABCA1, a transporter in the plasma membrane that secretes cholesterol from cells (*5*). When cells are depleted of cholesterol, both the transcription of *SREBP*s and the intron-encoded *miR-33* rise modestly.

SREBP-1 and *SREBP-2* encode *miR-33b* and *miR-33a*, respectively, which differ in only 2 of 19 nucleotides that constitute the mature microRNA. Both *miR-33* isoforms target for destruction several mRNAs—most prominently the mRNA encoding ABCA1—that contain a highly conserved target sequence in their 3′-untranslated regions. When cultured mammalian cells were transfected with *miR-33*, the amount of mRNA encoding ABCA1 decreased, whereas the

Department of Molecular Genetics, University of Texas Southwestern Medical Center, Dallas, TX 75390, USA. E-mail: mike.brown@utsouthwestern.edu; joe.goldstein@utsouthwestern.edu

opposite occurred when cells were transfected with RNA molecules that specifically reduced *miR-33* levels.

ABCA1 functions most prominently in macrophages and hepatocytes (*5*). In macrophages, it excretes cholesterol that accumulates as a result of the uptake of oxidized cholesterol-carrying lipoproteins. In liver, ABCA1 is essential for the production of the precursor forms of high-density lipoprotein (HDL). Indeed, Najafi-Shoushtari *et al*. and Rayner *et al*. show that delivery of a *miR-33* antagonist leads to a small but significant increase in plasma HDL. So far, the most remarkable feature of the *miR-33a/b* story is the pattern of evolutionary conservation. The precursor for mature *miR-33a* is found within the same intron of *SREBP-2* from many animal species, including large and small mammals, chickens, and frogs. There is even a perfectly conserved mature form of *miR-33a* in the single *SREBP*-like gene of the fruit fly *Drosophila melanogaster*. The latter is most remarkable because insects do not synthesize sterols. Their single *SREBP* gene controls fatty acid production (*6*). Moreover, the fruit fly genome does not contain *ABCA1*, so the target of *miR-33a* in *Drosophila* is unknown.

In contrast to the uniform conservation of *miR-33a* in *SREBP-2*, there is a gap in the evolutionary conservation of *miR-33b* in *SREBP-1* (according to the U.S. National Center for Biotechnology Information database). The *SREBP-1* genes from large mammals encode *miR-33b*, but there is no trace of *miR-33b* in the *SREBP-1* genes of small mammals (rats and mice) or chickens.

Although the amount of mature *miR-33a* rises and falls in concert with *SREBP-2* mRNA, the amplitude of variation is quite small in the systems studied by Najafi-Shoushtari *et al*. and Rayner *et al*. This is likely because variations in cellular cholesterol levels cause relatively minor changes in the transcription of the *SREBP* genes. Cholesterol regulates SREBP activity most profoundly at the level of protein processing (*3*). SREBPs are synthesized as membrane proteins in the endoplasmic reticulum and transported to the Golgi complex, where they are proteolyzed to release active fragments that enter the nucleus. There, they enhance transcription of cholesterol-synthesizing genes, such as those encoding 3-hydroxy-3-methylglutaryl coenzyme A (HMG CoA) synthase and HMG CoA reductase. When cells are depleted of cholesterol, the level of nuclear SREBP-2 increases by orders of magnitude owing to increased proteolytic processing, and mRNAs encoding HMG CoA synthase and reductase increase correspondingly (*4*). By contrast, the mRNA encoding SREBP-2 increases by less than a factor of 2, explaining why *miR-33a* also shows relatively small changes. Whether or not such small changes influence plasma HDL in humans is yet to be determined.

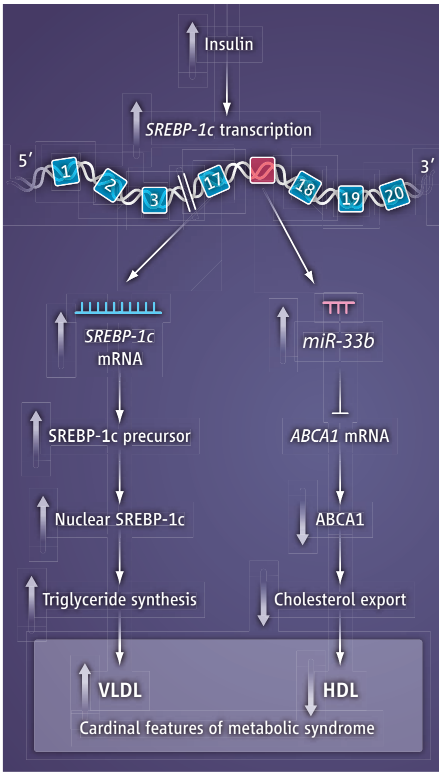

Potential dual role of SREBP in metabolic syndrome. In obese subjects with metabolic syndrome, insulin resistance leads to elevated insulin, which activates transcription of *SREBP-1c* in the liver. This leads to increased VLDL triglycerides and decreased HDL cholesterol in the blood. *miR-33b* is encoded in intron 17 (red); exons are in blue.

One circumstance in which transcription of an *SREBP* gene is profoundly regulated in vivo and where changes in *miR-33* are likely to be important clinically is in the liver (see the figure). Hepatocytes produce two alternatively spliced transcripts of *SREBP-1*, called *SREBP-1a* and *SREBP-1c*. The promoter and first exon of *SREBP-1c* differ from those of *SREBP-1a*, the isoform that predominates in most nonhepatic tissues (*7*). Transcription of *SREBP-1c* in liver is enhanced by insulin, working in concert with nuclear liver X receptors (*8*, *9*). When insulin levels are high, *SREBP-1c* is transcribed at extremely high levels, and the resultant nuclear SREBP-1c activates genes necessary to produce fatty acids, which are incorporated into triglycerides (*4*). As a result, in states of hyperinsulinemia, the liver becomes engorged with fat, and plasma triglyceride levels rise. The usual cause of hyperinsulinemia is peripheral insulin resistance, which leads to hyperglycemia and enhanced insulin secretion. Inasmuch as *miR-33b* is encoded in human (but not in rodent) *SREBP-1c*, the hepatic level of *miR-33b* would be predicted to be markedly elevated in insulin-resistant states in humans, but not in mice and rats.

In humans, insulin resistance is a hallmark of metabolic syndrome, which is provoked by obesity (*10*). In addition to hyperinsulinemia, hyperglycemia, and fatty liver, cardinal features of metabolic syndrome include an increase in plasma triglyceride levels, owing to elevated very-low-density lipoproteins (VLDL), and a decrease in plasma HDL. Low HDL is believed to contribute to the increase in coronary heart disease in these subjects. Evidence suggests that the hypertriglyceridemia is caused by the insulin-induced increase in *SREBP-1c* mRNA and protein. Is it possible that the reduction in HDL is caused by a decrease in ABCA1, owing to the increased production of *miR-33b* from the insulin-stimulated *SREBP-1c* gene?

Unfortunately, this question cannot be answered by study of hepatic *miR-33b* in the usual models of insulin resistance in obese rats or mice, because the *SREBP-1c* genes of these model animals lack *miR-33b*. This is consistent with the observation that obese insulin-resistant mice manifest all of the cardinal features of metabolic syndrome except a reduction in HDL (*11*). Here is a situation where geneticists may come to the rescue, by searching for mutations in *miR-33b* in patients with metabolic syndrome who manifest inappropriately elevated HDL. Alternatively, the hypothesis can be tested by treating metabolic syndrome subjects with agents that antagonize *miR-33b* and testing for increased HDL.

References and Notes

1. S. H. Najafi-Shoushtari *et al*., *Science* **328**, 1566 (2010); published online 13 May 2010 (10.1126/science.1189123).
2. K. J. Rayner *et al*., *Science* **328**, 1570 (2010); published online 13 May 2010 (10.1126/science.1189862).
3. M. S. Brown, J. L. Goldstein, *Cell* **89**, 331 (1997).
4. J. D. Horton, J. L. Goldstein, M. S. Brown, *J. Clin. Invest.* **109**, 1125 (2002).
5. A. D. Attie, *Trends Biochem. Sci.* **32**, 172 (2007).
6. A. S. Kunte, K. A. Matthews, R. B. Rawson, *Cell Metab.* **3**, 439 (2006).
7. I. Shimomura, H. Shimano, J. D. Horton, J. L. Goldstein, M. S. Brown, *J. Clin. Invest.* **99**, 838 (1997).
8. J. J. Repa *et al*., *Genes Dev.* **14**, 2819 (2000).
9. G. Chen, G. Liang, J. Ou, J. L. Goldstein, M. S. Brown, *Proc. Natl. Acad. Sci. U.S.A.* **101**, 11245 (2004).
10. G. M. Reaven, *Cell Metab.* **1**, 9 (2005).
11. A. J. Kennedy, K. L. J. Ellacott, V. L. King, A. H. Hasty, *Dis. Model Mech.* **3**, 156 (2010).

12. Supported by NIH grant HL20948.

10.1126/science.1192409

INTRODUCTION

Changing Oceans

THE OCEAN IS A DYNAMIC AND RAPIDLY EVOLVING ENVIRONMENT, A LONG-appreciated truth which becomes increasingly apparent as we observe it ever more carefully. Some of the transformations that we see are ones we are causing, and some are new to us only because we are looking in greater detail and with more sophisticated tools. This special issue contains a series of Reviews and News pieces that highlight some of the ways in which we see our oceans changing. Lozier (p. 1507) discusses how recent studies have challenged our view of large-scale ocean circulation as a simple conveyor belt, by revealing a more complex and nuanced system that reflects the effects of ocean eddies and surface atmospheric winds on the structure and variability of the ocean's overturning. Next, Doney (p. 1512) reviews how the chemistry of the oceans is changing, mostly due to human fossil fuel combustion, fertilizer use, and industrial activity. Nicholls and Cazenave (p. 1517) present an overview of recent sea-level rise, its impacts on coastal regions, and how adaptation may lessen those impacts. Two pieces examine how climate change is affecting marine biological systems: Schofield *et al*. (p. 1520) illustrate and discuss the role of ocean-observation techniques in documenting how marine ecosystems in the West Antarctic Peninsula region are evolving, and Hoegh-Guldberg and Bruno (p. 1523) present a more global view of the ways in which marine ecosystems are being affected by rapid anthropogenic variations.

Several News pieces provide even more information about current ocean trends. Kerr (p. 1500) discusses the certainty of ocean acidification and the uncertainty surrounding acidification's effects on marine life. Malakoff (p. 1502) takes on ocean noise, which is increasing because of ever-expanding ship traffic. Stokstad (p. 1504) covers improvements in shrimp aquaculture, and Kaiser (p. 1506) sets the record straight on the ocean's garbage patches. Information on where and how researchers are keeping tabs on the sea is supplied as a graphic (p. 1498). In News Focus, a story by Stone (p. 1476) looks at the ocean's microbial carbon pump. On *Science* Careers (www.sciencecareers.org), Fields has profiled human geographer Joshua Cinner, whose work informs coral reef management.

In a related Policy Forum, Lubchenco and Sutley (p. 1485) propose an approach to safeguard U.S. ocean, coastal, and Great Lakes ecosystems from the increasingly numerous and intense stresses that human activities are causing.

Together, these pieces provide an introduction to some of the important discoveries we have made recently about our oceans, underscore how human activities are changing them, and identify some of the challenges we must face if we are to continue to enjoy their vast but finite resources.

– JESSE SMITH, NICK WIGGINTON, CAROLINE ASH, JULIA FAHRENKAMP-UPPENBRINK, ELIZABETH PENNISI

CONTENTS

News

Reviews

See also News Focus p. 1476; Policy Forum p. 1485; Science *Podcast; and* Science *Careers at www.sciencecareers.org*

CREDIT: THINKSTOCK

Science

Published by AAAS

NEWS

Keeping Tabs on the Sea

Efforts to monitor the ocean are getting bigger and more sophisticated, but vast swaths of the marine world remain unknown

Scientists have been probing the sea for centuries, using everything from humble buckets and nets to sophisticated buoys, submarines, and satellites. Charted on a map, these efforts "can look impressive; it looks like the ocean is well sampled," says oceanographer Timothy Cowles of the nonprofit Consortium for Ocean Leadership in Washington, D.C. "But that's not true; the ocean remains vastly undersampled for its size." He and others are trying to change that by building better global networks for collecting and sharing data and deploying more capable instruments that can operate for years without human tending. Below, a brief look at some new and existing programs to better "see" the sea.

–DAVID MALAKOFF

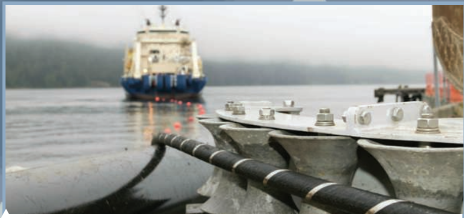

CABLED SEA-FLOOR OBSERVATORIES

Fiber-optic cables strung from shore across the ocean floor are enabling researchers to keep a close watch on the bottom of the sea. Off Canada's Vancouver Island, for instance, the NEPTUNE project's 800 kilometers of cable will provide power and data flow for sensors that will collect information on everything from crustal dynamics to deep-sea ecosystems. The United States, Japan, Taiwan, and the European Union have begun to build or plan similar cabled instruments.

DRIFTING BUOYS

Ocean currents carry some 4500 drifting science buoys, collecting data on everything from water temperatures to wind speeds. Many simply float on the surface and last just weeks or months. But about 3300 Argo floats do more. Currently concentrated in the green-shaded regions of the map, these 2-meter-long robots can survive for 4 years at sea. Every 10 days they sink up to 2 kilometers, then pop back to the surface to relay temperature and water conductivity profiles to satellites. First deployed in 2000, they now collect more than 100,000 profiles annually, giving scientists unprecedented insight into ocean dynamics.

SHIP-BASED SAMPLING

Ships remain a mainstay of ocean science, from hauling trawl nets across the sea floor, to censusing marine life, to using sonar to map the depths. Increasingly, researchers are trying to coordinate their efforts, for instance, by having science vessels from different nations repeat measurements along similar tracks so that scientists can detect changes over time. Researchers also train ferry and cargo vessel crews to tow plankton-collecting nets or grab water samples (*Science*, 12 December 2008, p. 1627). But work such as drilling into the sea floor or tending special deep-sea submersibles requires specially built ships.

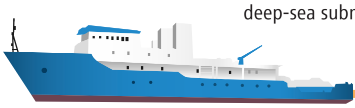

Sources: The Global Ocean Observing System (gosic.org/ios/GOOS-Main-page.htm); National Science Foundation; The Consortium for Ocean Leadership.

IMAGE CREDITS (TOP TO BOTTOM): NEPTUNE CANADA; ALICIA NAVIDAD/CSIRO

OCEAN OBSERVATORIES INITIATIVE

At a cost of more than $380 million, the new U.S. Ocean Observatories Initiative is one of the most ambitious sea-science programs ever. By 2015, the National Science Foundation plans to have more than 1000 sensors installed at six sites along North and South America. The automated observatories will include a mix of buoys, sea-floor sensors, and mobile robots and will collect a wide range of geological, biological, and oceanographic information. First up: the Endurance Array off Oregon and Washington states.

SATELLITE IMAGERY

There's nothing like the view from space to get the big picture of a changing ocean. Although orbiting sensors often can't penetrate below the sea's surface, they've become increasingly important for tracking shifting sea ice, plankton blooms, and oil spills. By measuring sea-surface heights and temperatures, they've also become a big part of climate science. Researchers, however, say they still need to get their feet—and instruments—wet to get a complete understanding of what the satellites are showing them.

MOORED BUOYS

Battered by waves and rusted by salt water, large buoys chained to the sea floor are the nitty-gritty workhorses of marine science. Nearly 400 moored buoys—most at the surface, some submerged—routinely collect data on everything from wave heights to current speeds. Newer models also measure carbon dioxide levels. The Global Tropical Moored Buoy Array (blue diamonds) is one of the biggest networks, with more than 100 buoys girdling the equator.

IMAGE CREDITS (TOP TO BOTTOM): ILLUSTRATION BY JACK COOK, WOODS HOLE OCEANOGRAPHIC INSTITUTION; IMAGE COURTESY OF THE OCEANSITES PROGRAM; NASA GODDARD'S SCIENTIFIC VISUALIZATION STUDIO; NOAA

NEWS

Ocean Acidification Unprecedented, Unsettling

Humans are caught up in a grand planetary experiment of lowering the ocean's pH, with a potentially devastating toll on marine life

ASIDE FROM THE DINOSAUR-KILLING asteroid impact, the world has probably never seen the likes of what's brewing in today's oceans. By spewing carbon dioxide from smokestacks and tailpipes at a gigatons-per-year pace, humans are conducting a grand geophysical experiment, not just on climate but on the oceans as well.

Over the past 4 years, there's been a crescendo of concern that the ocean experiment may be scarier than its climate counterpart (http://news.sciencemag.org/sciencenow/2006/07/05-01.html). Now the geochemists are weighing in, and they are not mincing words: The physics and chemistry of adding an acid to the ocean are so well understood, so inexorable, that there cannot be an iota of doubt—gigatons of acid are lowering the pH of the world ocean, humans are totally responsible, and the more carbon dioxide we emit, the worse it's going to get. Unconstrained emissions growth is likely to leave the current era of human planetary dominance "as one of the most notable, if not cataclysmic, events in the history of our planet," geochemist Lee Kump of Pennsylvania State University, University Park, and colleagues wrote last December in a special issue of *Oceanography*. The geochemical disruption will reverberate for tens of thousands of years.

It's less clear how marine life will fare. "We can detect these changes [in ocean acidity], but we still don't have a good idea of how ecosystems would change," says marine biologist Victoria Fabry of California State University, San Marcos. With nothing in the geologic record as severe as the ongoing plunge in ocean pH, paleontologists can't say for sure how organisms that build carbonate shells or skeletons will react. In the laboratory, corals always do poorly. The lab responses of other organisms are mixed (http://news.sciencemag.org/sciencenow/2009/12/01-01.html). In the field, researchers see signs that coral growth does slow, oyster larvae suffer, and plankton with calcareous skeletons lose mass. There are enough alarming signs that global oceanic acidification "is an experiment we would not choose to do," says Fabry.

Nothing like it

Strictly speaking, the ocean, now at a pH of 8.1, will not turn into an acid, as its pH will not drop below 7.0. But on dissolving into the ocean, carbon dioxide instantly forms bicarbonate ions (HCO_3^-) and hydrogen ions—the H^+ of pH. The "acidification" resulting from the current carbon dioxide emissions is massive and rapid, a combination that is "almost certainly unprecedented in Earth history," says earth systems modeler Andrew Ridgwell of the University of Bristol, United Kingdom.

The closest analog in the geologic record to the present acidification appears to be the Paleocene-Eocene Thermal Maximum (PETM) 55.8 million years ago. At its start, anywhere from 2000 to 7000 gigatons of carbon were released as methane and carbon dioxide, the methane quickly oxidizing to carbon dioxide. Where it all came from—volcanoes, icy sea-floor methane hydrates, marshy peat, or a combination—no one is sure, but almost all of it would eventually have gone into the ocean. PETM's carbon gush was on a par with what burning the 2180 gigatons of carbon in the world's fossil fuel reserves would produce, notes Kump and his colleagues.

The difference this time around is speed. Today, "you could argue the rate of release is 10 times faster [than at the PETM], if not faster," says paleoceanographer James Zachos of the University of California, Santa Cruz. Whereas nature took a few thousand years to spout out thousands of gigatons of carbon, he notes, humans could be doing it in a few centuries.

And speed makes a big difference. It takes the ocean about 1000 years to flush carbon dioxide added to surface waters into the deep sea where sediments can eventu-

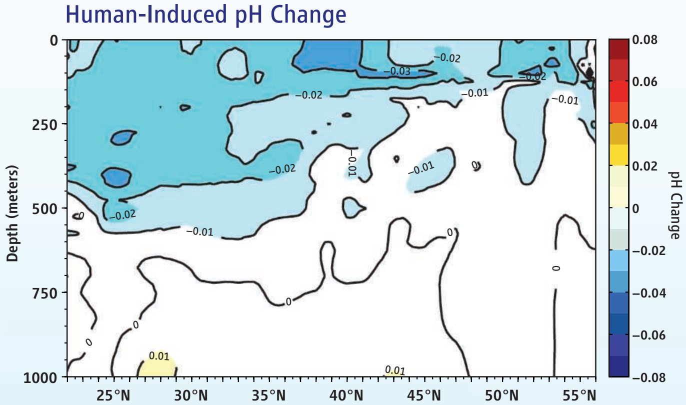

Blue, blue, blue. Measurements to 1000 meters deep across the North Pacific revealed that in 15 years carbon dioxide emissions drove down pH (blues) in all surface waters and as deeply as 550 meters.

First victims? Corals appear to be particularly vulnerable to falling pH caused by rising carbon dioxide.

CREDITS (TOP TO BOTTOM): R. H. BYRNE ET AL., GEOPHYSICAL RESEARCH LETTERS 37 © 2010 AMERICAN GEOPHYSICAL UNION; PHOTOS.COM

ally neutralize the added acid. The PETM release appears to have been slow enough that no biological catastrophe struck in the upper ocean, only an extinction among tiny shell-forming organisms living on the deep sea floor. But today's emissions are so rapid that they are piling up in surface waters.

And the acid flows

The latest evidence of raging acidification of surface waters comes in the first direct, basinwide observation of plunging pH. Marine chemist Robert Byrne of the University of South Florida in St. Petersburg and colleagues reported 20 January in *Geophysical Research Letters* that the pH of surface waters along a line running 3200 kilometers north from near the island of Hawaii fell between 1991 and 2006 (see figure, p. 1500). The pH decline attributable to human activities over the 15 years was 0.026 pH unit, a drop Byrne calls "startling" in its rapidity. Overall, researchers estimate there has been a 0.1-pH-unit decline for the global ocean since industrialization began a couple of centuries ago. In logarithmic pH units, the change may seem tiny, but in absolute terms, that translates into a 30% increase in surface-ocean acidity.

Now ocean pH is lower than it's been for 20 million years, and it's going to get lower, says marine chemist Richard Feely of the National Oceanic and Atmospheric Administration's (NOAA's) Marine Environmental Laboratory in Seattle, Washington. He and his colleagues have modeled future pH based on what he calls the irrefutable chemistry of acidification. The model assumes a business-as-usual growth in carbon dioxide emissions. As they report in the same *Oceanography* issue, the modeling predicts a drop from a pre-industrial pH of 8.2 to about 7.8 by the end of this century. That would increase the surface ocean's acidity by about 150% on average.

Living with acid

The future of marine life in an acidifying ocean is far less clear than the chemistry of acidification but nonetheless looks bleak for many organisms. Falling pH has two effects on species that build shells or skeletons of calcium carbonate. These organisms include tropical corals, echinoderms, mollusks, microscopic foraminifera floating in surface waters, and certain algae. When the hydrogen ion concentration of seawater gets high enough, the calcium carbonate in these organisms begins to dissolve.

Colder waters with a greater capacity for carbon dioxide will be affected first. Feely's modeling projects that by midcentury, all Arctic waters will corrode the most vulnerable crystal form of calcium carbonate, called aragonite. By the end of the century, all of the Southern Ocean and parts of the North Pacific will be corrosive to sea snails called pteropods and other aragonitic organisms.

The other effect of falling pH is already at work. As hydrogen ion concentrations go up, more and more of the ocean's carbonate ions—the building block of all carbonate shells and skeletons—combine with hydrogen ions to form bicarbonate, driving down the concentration of the essential carbonate. Organisms have a harder time extracting the carbonate they need from the surrounding water.

In a compilation of controlled acidification studies, marine chemist Scott Doney of the Woods Hole Oceanographic Institution in Massachusetts and his colleagues found that all 11 species of tropical coral studied under falling pH slowed their aragonite production. Among noncoral calcifiers, most also slowed their carbonate building, though a few, such as certain coralline red algae and echinoderms, increased it.

So far, field observations tend to support the deleterious effects of falling pH. In the 2 January 2009 issue of *Science* (p. 116), marine scientists Glenn De'ath, Janice Lough, and Katharina Fabricius of the Australian Institute of Marine Science in Townsville reported on their broad survey of coral across the Great Barrier Reef of Australia. Reading the rate of growth recorded in coral skeletons, the group found that calcification across the Great Barrier Reef had declined 14.2% since 1990. And they found no sign that such a "severe and sudden decline" had occurred in the past 400 years. Although the group could not pin down what caused the slower growth, they pointed to a rise in ocean temperatures combined with declining pH.

Planktonic foraminifera also seem to be

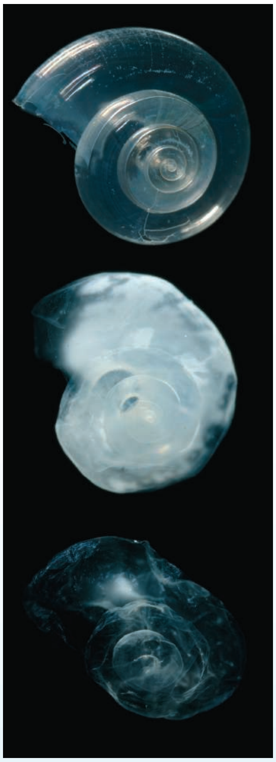

Going, going, … In seawater of the pH that may prevail by the century's end, the shell of a pteropod dissolves in a matter of weeks (*top to bottom*).

CREDIT: © DAVID LITTSCHWAGER/NATIONAL GEOGRAPHIC STOCK

suffering in this lower pH environment. Paleoceanographer Andrew Moy and his colleagues at the Antarctic Climate and Ecosystems Cooperative Research Centre in Hobart, Australia, found that the shells of one type of foram growing in today's Southern Ocean are 30% lighter than those of the same species from the past few thousand years. In a paper published online 8 March 2009 in *Nature Geoscience*, they point to acidification as the cause because they find a correlation between higher atmospheric carbon dioxide and lower shell weight in a 50,000-year-long Southern Ocean sediment record.

Curtailed shell growth may be fatal for some organisms. Water naturally low in pH wells up along the coast of Oregon and sometimes floods into Netarts Bay, from which the Whiskey Creek Shellfish Hatchery in Tillamook draws its water. Alan Barton, now of Bear Creek Shellfish Hatchery in North Carolina; Sue Cudd of Whiskey Creek Shellfish Hatchery in Tillamook, Oregon; and chemical oceanographer Burke Hales of Oregon State University, Corvallis, found a strong correlation between corrosively high concentrations of carbon dioxide in hatchery water and mass mortality of oyster larvae forming their first partially aragonitic shells. "We're getting a window into the future of what the open ocean will be like in 100 years," says Hales.

In April, the National Research Council (NRC) pointed out in a report that getting a clearer view through that window will take more time and money, which governments are starting to spend. For the European Project on Ocean Acidification, a 27-institute research consortium is expanding the monitoring of ongoing acidification and examining biological effects. The 2009 Federal Ocean Acidification Research and Monitoring Act got interagency coordination going in the United States, and $5.5 million in NOAA's fiscal year 2010 budget has boosted research in that agency. But the NRC report also concluded that "development of a National Ocean Acidification Program will be a complex undertaking." They got that right. **–RICHARD A. KERR**

Published by AAAS

NEWS

A Push for Quieter Ships

Although sonar and air guns have grabbed headlines, researchers say the cacophony from ships creates far more ocean noise

A shifting soundscape. Increased shipping has made the ocean noisier, potentially disrupting communication among whales and other marine life.

FROM A DRIFTING BOAT, THE OCEAN OFF Massachusetts can seem like one of the quietest places on Earth. But Leila Hatch isn't fooled. Over the past 4 years, the marine ecologist has helped lead studies at the Gerry E. Studds Stellwagen Bank National Marine Sanctuary that are documenting how human activities are ramping up the region's undersea noise—and highlighting just how difficult it may be to turn down the volume.

"We're getting a much better understanding of how much sound is in the sanctuary and where it's coming from," says Hatch, who works for the U.S. National Oceanic and Atmospheric Administration. Sophisticated acoustic sensors, for instance, have enabled researchers to assemble a detailed "noise budget" for the 2200-square-kilometer preserve. It includes the musical calls of whales and fish and the rumbles created by wind and rain. But it also documents the mechanical thrashing of giant ships steaming into nearby Boston Harbor.

Those ships "can actually double the noise levels in some parts of the sanctuary," notes Hatch, swamping the low-frequency wavelengths that whales and other sea creatures use to communicate, find mates, and navigate their watery world. Researchers worry that the cacophony is making it even harder for these creatures to overcome the numerous human threats—from toxic pollution to overexploitation—that have already pushed some to the edge of extinction.

Stellwagen's monitoring program, one of the world's most intensive, has implications well beyond the marine sanctuary. It has helped focus attention on the growing acoustic clutter created by the world's nearly 100,000 large commercial ships. Although other sources of ocean noise—including military sonar, pile drivers, and the undersea air guns that scientists and energy companies use to map the sea floor—have generated more controversy because of the risks to sea life (*Science*, 11 January 2008, p. 147), researchers say everyday ship traffic is arguably the sea's most pressing sound problem. Over the past 50 years, the growing trade fleet has contributed to a 32-fold increase in low-frequency noise in some parts of the ocean; that's a doubling of the din every decade. "Shipping may be responsible for 90% of the sound energy we add to the ocean, but it seems like we spend most of our time talking about the other 5 or 10% of the problem," says Brandon Southall, a former leader of U.S. government efforts to study and regulate ocean noise and now a consultant with SEA Inc. in Santa Cruz, California. In part, that's because ships typically aren't covered by the world's few laws that deal with ocean noise.

The conversation, however, is shifting. Recently, a group of shipping industry officials, scientists, and government regulators began to examine strategies for slashing low-frequency shipping noise. Engineers say such a reduction is technologically feasible, but the costs—and opposition from some shipping companies—could be formidable. Still, "shipping noise is an issue that is getting more attention," says acoustician Arthur Popper of the University of Maryland, College Park, who studies the effects of sound on fish and is organizing a major international conference* on ocean noise set for Ireland in August.

Sound pollution

The Stellwagen sanctuary's innovative monitoring effort is sure to get attention at the meeting. Almost from the moment the U.S. government preserve was created in 1992, its managers have moved to understand how ocean noise might be influencing Stellwagen's animals, particularly endangered humpback and right whales. In 1996, researchers began their first efforts to measure noise levels and by 2004 had dotted the sanctuary's waters with acoustic buoys and sea floor–mounted instruments. In part, the devices—many built at Cornell University—were designed to listen to the thousands of tugs, tankers, and cargo carriers that ply the Boston shipping channel, which cuts through the sanctuary. Other researchers

*Second International Conference on the Effects of Noise on Aquatic Life, Cork, Ireland, 15–20 August 2010.

On the same frequency. Large ships produce sounds in the same bandwidths that fish and some marine mammals use (*right*). The acoustic clutter can be intense in heavily traveled sea lanes (*far right*) of the Boston Harbor channel as it passes through the Stellwagen marine sanctuary off Massachusetts.

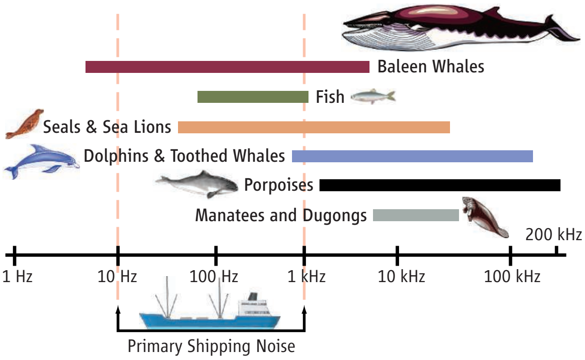

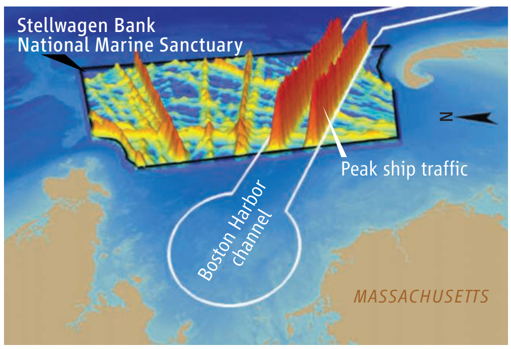

CREDITS: (TOP) JOHN CALAMBOKIDIS/CASCADIA RESEARCH, WWW.CASCADIARESEARCH.ORG; (BOTTOM, LEFT TO RIGHT) ADAPTED FROM B. SOUTHALL/NMFS/NOAA, JUPITERIMAGES; ADAPTED FROM NOAA/STELLWAGEN BANK NATIONAL MARINE SANCTUARY

Published by AAAS

have attached sensitive electronic "ears" to some of Stellwagen's humpback whales so as to understand how the whales respond to different kinds of sounds. And last year, scientists from Cornell and the Woods Hole Oceanographic Institution in Massachusetts unveiled a unique network of 10 buoy-mounted sensors that are specially tuned to pick up the calls of right whales and then warn passing ships in a bid to prevent deadly collisions.

Together, such efforts have provided an unusually detailed sound portrait of this small sliver of ocean. Researchers, for instance, now know how the sanctuary's soundscape can vary by place, time of day, and ocean conditions. And they can track both passing ships and whales.

The data are unsettling. One potential problem is that shipping noise consistently occurs at levels loud enough—and within frequencies low enough (between 10 and 1000 hertz)—to make it hard for whales to maintain acoustic contact, Hatch and her colleagues concluded in a 2008 paper in *Environmental Management*.

The study, which combined acoustic data and individual ship movements, found that large tankers produced twice the acoustic signal of cargo ships and were more than 100 times noisier than research ships (which tend to be smaller and designed to be quieter). Because saltwater is such an efficient conductor of low-frequency sound, the researchers calculated that a single large vessel could transmit its sound throughout most of the sanctuary.

One worry is that the din is essentially deafening North Atlantic right whales, of which fewer than 400 remain. In a quiet ocean, one whale's calls might be discernible to a mate or family member swimming 20 or more kilometers away. In noisy Stellwagen, however, that range is reduced, possibly down to just a kilometer or two, estimates a team led by acoustician Christopher Clark of the Cornell Lab of Ornithology (see figure, above). The whale's "communication space"—the three-dimensional bubble in which it can hear and be heard—"is seriously compromised by noise from commercial shipping traffic," they concluded last year in an ocean noise special issue of *Marine Ecology Progress Series*.

So far, it's hard to know if the cacophony has harmed the whales. Drawing on studies of chronic noise's impacts on land-dwelling mammals, however, some researchers predict shipping noise is increasing the animals' stress levels. A few studies have also shown that the whales call less in noisy areas. They may also

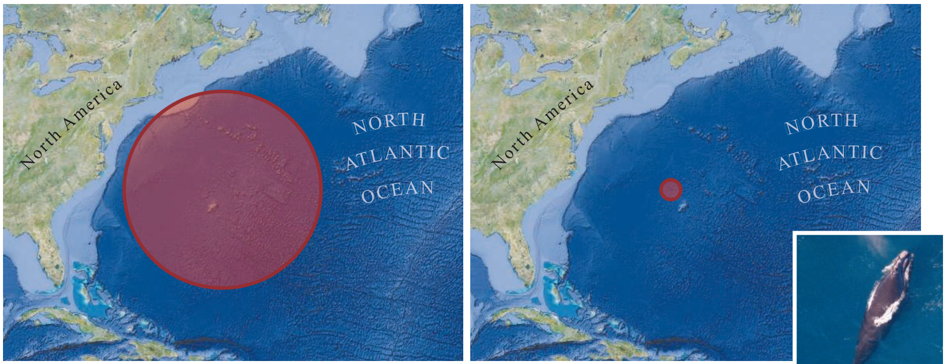

Hear me? Shipping noise may reduce the communication range (red circle) of some baleen whales, such as the North Atlantic right whale (*inset*), by 90% (*top right*).

be retuning their calls in a bid to be heard. Over the past several decades, for instance, the fundamental frequency of "contact calls" made by North Atlantic right whales has risen by about an octave, according to studies by bioacoustician Susan Parks of Pennsylvania State University, University Park. Although such adjustments might seem minor, researchers say they could carry significant survival costs if they even modestly reduce breeding or hunting success. Some fish may be similarly affected, but assessing noise effects in the wild is "extremely difficult," says Popper.

Silencing ships

Despite the uncertainty, some parts of the shipping industry are taking the issue seriously. At a 2008 meeting in Hamburg, Germany—a hub for world shipbuilders—the Darmstadt-based Okeanos Foundation for the Sea persuaded several industry leaders to declare vessel noise "a global problem" and set a goal of freezing it at current levels within 10 years and then reducing it by several-fold within 30 years. In particular, the leaders called on the International Maritime Organization (IMO)—a United Nations group that oversees shipping—to convene a working group to explore technical options for quieting ships.

Online
sciencemag.org
An interview with a scientist studying ocean noise.

The United States has since tapped Stellwagen's Hatch to advise its member of the panel. "The goal is to take a holistic approach to the rising level of ambient shipping noise, which everyone agrees is real," she says. "If we can push down that overall level, we know we can increase the communication space for a lot of animals."

There are plenty of ways to make ships quieter, shipping experts have told IMO in written comments. The biggest need, they say, is to reduce the tendency of ship propellers to "cavitate," or produce noise when tiny air bubbles that form around the blades burst. By redesigning the propellers—and changing the way water is funneled into them—shipbuilders could drastically cut sound production under normal operating conditions. Other gains could come from mounting noisy engines and machinery on sound-insulating platforms, streamlining boxy hulls now optimized for storage, and slowing cruising speeds. In addition to reducing noise, the experts say those changes would help companies reduce fuel use and pollution.

"Essentially, a noisy ship is an inefficient ship," says Hatch. "Until now, there haven't been good enough financial and environmental reasons not to drive a shoebox through the ocean. Now, there are a lot of good ones."

Retrofitting existing ships would be costly, however, according to an analysis commissioned by the International Fund for Animal Welfare in Geneva, Switzerland. Quieting an oil tanker, for instance, could cost $2.8 million, an expense the highly decentralized and often financially precarious shipping industry is unlikely to pay without new regulations. Yet few observers see new rules coming anytime soon. Silencing advocates say it may be easier to encourage shipbuilders to start building quieter vessels, especially if IMO can come up with some clear guidelines. But that could be "a decades-long process to update the current fleet," says Hatch.

Despite the slow pace, she's happy to see her field move beyond simply documenting the ocean-noise problem to trying to solve it. "We clearly need more science," Hatch says. "But I think we can also start finding better ways of doing what we need to do in the ocean without creating unnecessary noise." Like everyone, she's just seeking a little more peace and quiet. **–DAVID MALAKOFF**

David Malakoff is a writer in Alexandria, Virginia.

CREDITS: ADAPTED FROM C. W. CLARK/CORNELL UNIVERSITY; (MAP SOURCE) GOOGLE EARTH; (INSET) NOAA

New leaf. Shrimp farms have caused environmental problems such as the destruction of mangrove forests (*above*), but research in breeding and other areas has led to more productive farms that pollute less.

NEWS

Down on the Shrimp Farm

Can shrimp become the new chicken of the sea without damaging the ocean?

THE BLUE WATERS OF KUNG KRABAEN BAY in southwest Thailand are fringed with lush mangroves. Yet just a few hundred meters behind the trees are more than 200 small ponds teeming with shrimp that once threatened to cause severe environmental harm. What has been happening in Kung Krabaen Bay illustrates the peril and promise of farming shrimp, which have become the world's biggest marine aquaculture product.

In the 1980s, poor rice farmers cut down many of the mangroves and dug out ponds to take advantage of an expanding market. Densely stocked, the ponds accumulated a sludge of feces and undigested feed that the farmers flushed into the bay, threatening to choke it. It looked like the farmers were "going to pollute themselves out of business," recalls Claude Boyd of Auburn University in Alabama, who has studied shrimp farming and water quality in Thailand and elsewhere.

Sludge dumping, along with other environmentally harmful practices, gave shrimp farming a bad reputation. But in the past 15 years, many shrimp farmers have been cleaning up their act. Although motivated more by economics than environmental concerns, they have made substantial strides in many places to reduce their toll on the marine world, both locally and globally.

With the help of researchers at the Kung Krabaen Bay Royal Development Study Center, for example, farmers in the bay have replanted the mangroves and switched to a new system for raising shrimp that releases far less pollution into the surrounding water. "It's really quite impressive," Boyd says. Researchers around the world are refining this system, called biofloc technology, which relies on cultivating microbes to recycle nutrients and reduce waste.

Academics and companies are also striving to improve processed shrimp feed and replace the fish meal it contains with other protein sources, a change that could help prevent further depletion of fish species at the base of oceanic food webs. Ultimately, by making shrimp aquaculture more productive—through breeding programs and perhaps high-tech inland farms—some researchers hope they can grow cheaper, more plentiful shrimp while sparing marine habitats altogether. "We can take shrimp farming out of the coastal zone," predicts Addison Lawrence of Texas A&M University, Corpus Christi.

Much remains to be done. Many of these improvements haven't reached smaller, poorer farms, which raise most of the world's shrimp. And because demand for seafood is going up dramatically, the overall impact on the oceans might still increase. Earlier this month, researchers and others gathered in Bangkok to draft a global strategy for sustainability in aquaculture production, which the Food and Agriculture Organization of the United Nations says will need to almost triple by 2050 to meet demands for freshwater fish and seafood. The challenge is how to do that with minimal environmental harm.

Growing pains

Shrimp farming has been going on in Asia for hundreds of years, but in the past 3 decades it has expanded exponentially. Worldwide production rose from less than 100,000 metric tons in 1980 to more than 3 million metric tons in 2007. Shrimp are now one of aquaculture's biggest products, exceeded in volume by only a few freshwater species, carp and tilapia.

Much of the groundwork for modern shrimp farming was laid in Asia. In the 1950s and '60s, Japanese researchers made key steps toward raising the kuruma prawn (*Penaeus japonicus*) in captivity—not an easy task given the complex life cycle of shrimp: They reproduce in the ocean and mature in estuaries. Researchers in Taiwan later discovered that the tiger prawn (*P. monodon*) grows especially fast and was suited for commercial operations.

Another advance was inducing spawning. Research in the 1970s showed that snipping just one eyestalk lowered the amount of a gonad-inhibiting hormone and coaxed females to spawn. Growing these broodstock in hatcheries eliminated the need to collect wild broodstock by trawling, which was depleting populations of wild shrimp and catching other marine life.

CREDITS (LEFT TO RIGHT): GEORGE CHAMBERLAIN/GLOBAL AQUACULTURE ALLIANCE; ALFREDO QUARTO, MANGROVE ACTION PROJECT, WWW.MANGROVEACTIONPROJECT.ORG

Published by AAAS

Collateral damage from shrimp farming ramped up in the 1980s, when farmers sought cheap coastal land for new shrimp farms. Some governments encouraged the conversion of mangrove forests to ponds, and countless square kilometers of this productive coastal ecosystem were lost. Environmental groups protested, and farmers themselves soon discovered that mangrove forests were not a good place for shrimp farms because the soil was too acidic. Remaining mangroves are now largely spared, although destruction still occurs in some developing countries, says Steve Trent, who directs the Environmental Justice Foundation in London.

The more serious problem has been shrimp farming's effect on water quality. As farms proliferated and production intensified—large farms in Ecuador have even used crop-dusters to feed shrimp—they released more and more effluent. Inefficient feeding methods compound the problem; unstable, low-quality feed breaks down before the shrimp eat it all. Farmers use more than needed, and the unused nutrients are washed out to sea.

In 2007, Xie Biao and Yu Kaijin of the Nanjing Institute of Environmental Science in China reported in *Ocean & Coastal Management* that 43 billon tons of wastewater from shrimp farms enter China's coastal waters annually, compared with 4 billion tons of industrial wastewater. "Everyone agrees now that careless development of aquaculture has a dramatic impact on the environment," says Yoram Avnimelech of Technion, the Israel Institute of Technology, in Haifa. "It has led to massive eutrophication."

Two cures in one

A devastating shrimp disease helped shrimp farming turn a corner. In 1993, an outbreak of white spot syndrome virus (WSSV)—which can wipe out entire farms—caused production to collapse in China. After spreading through Asia, the pandemic reached South and Central America in 1999. WSSV and other viruses "forced tremendous change in the shrimp farming business," says George Chamberlain of the Global Aquaculture Alliance, a trade group based in St. Louis, Missouri.

One of those changes is the use of disease-free broodstock raised in biosecure hatcheries, reducing the pressure to collect wild shrimp for broodstock. Another disease-fighting advance: reducing water exchange between shrimp ponds and the environment, which spreads the virus. Research in the 1990s showed that water exchange could be eliminated if the ponds were aerated to provide the shrimp with oxygen.

In aerated ponds, beneficial bacteria flourish and help supplement the shrimp's diet by recycling nutrients already in the pond. With the addition of a carbon source, such as wheat flour, these bacteria convert ammonium from shrimp waste into protein. The microbes glom onto floating particles, creating nutritious masses called biofloc that shrimp eat. Biofloc can reduce the need for protein supplements by as much as 50%.

The technique is used fairly widely in intensive systems in Asia, where farms with higher yields can afford to aerate the water with internal pumps or paddlewheels. Even at more traditional farms, where aeration is too expensive, farmers can boost production with biofloc, says Avnimelech.

Future farms

Biofloc can reduce the need for protein in shrimp feed but not eliminate it. And that protein demand has had an environmental impact that extends beyond the shrimp farmer's local bay or coast.

Shrimp consume 28% of the fish meal used in aquaculture. Demand for fish meal is depleting some of the world's stock of so-called forage fish. "Fish meal is a global issue," says Craig Browdy, manager of aquaculture research at Novus International, a feed manufacturer based in St. Charles, Missouri. Researchers are pushing to use fish waste from canneries or to come up with land-based alternatives.

Feed manufacturers have already created shrimp food based on soybean meal and other sources of vegetable proteins. A decade ago, shrimp feed consisted on average of about 20% to 30% fish meal; now it's between 10% and 20%. "That is a tremendous success story," says Lawrence. Fish-free feeds are not cheaper, however, because of the expense of removing compounds that affect digestibility and then adding nutritional supplements.

Despite the progress, skeptics worry that the net expansion of aquaculture will swamp the improvements. In terms of overall impact on ocean ecosystems, shrimp farmers are "not making any gains," says Peter Bridson of the Monterey Bay Aquarium in California. The solution, according to aquaculture advocates, is not only to improve feed substitutes and intensify production even more but, ultimately, to move shrimp farming out of the coastal zone into concrete raceways covered with greenhouses.

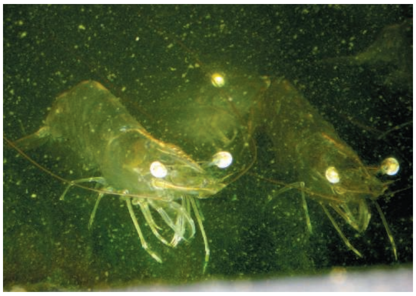

Waste not. High-tech farms (*top*) enable microbes to convert shrimp feces into protein-rich biofloc (white flecks, *left*) consumed by shrimp.

Experimental prototypes, and a handful that are in early phases of commercial operation, can reach yields of 100 tons per hectare per year—10 times the typical yield today. These superintensive biofloc systems could produce fresh shrimp year-round in temperate climates, but they require sophisticated engineering to control water temperature, oxygen levels, and water quality. How to do this and compete on price is a difficult question, given the cost of land, labor, and energy.

Lawrence is optimistic, however, that research and engineering will lead to shrimp that are as cheap as chicken while less polluting. If the industry can do that, then it really will have earned a new reputation.

–ERIK STOKSTAD

CREDITS (TOP TO BOTTOM): THOMAS JAMES; GEORGE CHAMBERLAIN/GLOBAL AQUACULTURE ALLIANCE

NEWS

The Dirt on Ocean Garbage Patches

Their biological impact is uncertain and their makeup, misunderstood

Catch of the day. Plastic bits in the ocean (*top*) and collected from plankton tows in the Great Pacific Garbage Patch.

CHANCES ARE YOU'VE HEARD OF THE GREAT Pacific Garbage Patch. It is, according to countless press and TV reports, a "trash vortex," "the world's largest rubbish dump," and a "vast mass of floating debris" midway between Hawaii and California. According to Charles Moore, a sailor-turned-scientist who discovered the patch in 1997 and has been interviewed on *The Oprah Show*, the *Late Show with David Letterman,* and *Good Morning America*, it is a plastic soup twice the size of Texas.

Although many media stories conjure up a chunky soup of bottles and tires, it is mostly an unstrained consommé of small bits of floating plastic. And the patch Moore found isn't the only one. A similar accumulation of plastic particles—which include weathered fishing line, Styrofoam, wrappers, and raw resin pellets—has shown up in the North Atlantic Ocean. But the potential harm to marine life is far from clear. "We just don't know the importance," says biological oceanographer James Leichter of the Scripps Institution of Oceanography in San Diego, California, who points out that "there's a lot more water than plastic."

Accumulating tiny plastic debris was first discovered in 1972, when researchers at the Woods Hole Oceanographic Institution in Massachusetts found plastic particles up to 0.5 centimeters in diameter in their surface plankton nets in the North Atlantic's Sargasso Sea (*Science*, 17 March 1972, p. 1240). Since then, there have been a dozen or so similar reports mainly from the North Atlantic and the North Pacific.

It was Moore who brought the problem to public attention. In 1997, he sailed from Hawaii to Long Beach, California, across a notoriously calm area, where for a solid week he spotted at least one bottle or piece of plastic every hour, he says. Moore went back with some scientists and a plankton tow net. In a 2001 paper in *Marine Pollution Bulletin*, they reported the highest average plastic count on record in the Pacific—334,271 pieces per square kilometer—and a startling 6:1 ratio of plastic to zooplankton by weight. They worried that the plastic was exposing animals to toxins, pointing to a Japanese study showing that polypropylene pellets can suck up pollutants from seawater.

Independent Seattle oceanographer Curtis Ebbesmeyer, known for using spilled shipments of shoes and rubber ducks to study ocean currents, suggested that Moore had found a "garbage patch" within the North Pacific subtropical gyre—one of several major ocean gyres, or large, wind-driven, circular current systems with a quiet center.

While scientists commend Moore's efforts to raise public awareness of marine pollution, some question the 6:1 ratio he came up with. Doubts have also been raised about the patch's size.

Nevertheless, there's clearly a lot of plastic out there. When graduate students from Scripps spent 19 days in the same area last summer sampling sea life, they snagged plastic on every one of 126 plankton tows. Often, the half-liter jar of residue strained from a single 0.5-kilometer tow contained so many plastic chips that the jar "looked like a snow globe," says graduate student Miriam Goldstein, who led the trip. "That is not normal."

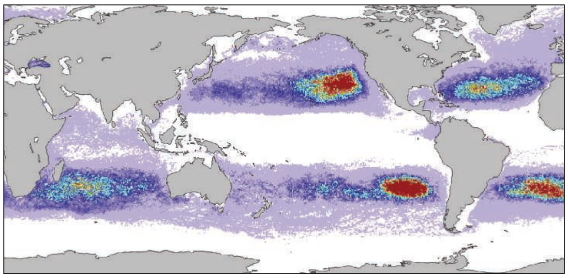

Trash traps. A modeler has predicted the spots (red, yellow) within five gyres where oceanic debris will wind up.

Similar findings have come from off the U.S. East Coast. Last winter, the Sea Education Association (SEA), a nonprofit in Falmouth, Massachusetts, that takes students on sailing research trips, reported high—but consistent year-to-year—microplastic counts over a 1450-kilometer transect in the western North Atlantic Ocean that SEA has been sampling for 22 years. Oceanographic modeler Nikolei Maximenko of the University of Hawaii, Manoa, had predicted this patch's location; he has pinpointed other likely patches in the Indian Ocean, South Pacific, and South Atlantic.

Whether the plastic is damaging marine ecosystems is, however, an open question. In the past, researchers have mostly focused on larger threats: abandoned fishing nets that trap turtles and seals; plastic bags that block the digestive tracts of turtles; and the toothbrushes and bottle caps that seabirds mistake for food, sometimes starving as a result or dying from a blockage. But toxin-laden microplastics may add another risk to marine life. Benthic worms, mussels, krill, sea cucumbers, and birds will ingest tiny plastic particles, according to various studies, some by marine ecologist Richard Thompson of the University of Plymouth in the United Kingdom. "There's quite a lot of signals out there that we need to be concerned," says Thompson. But nobody has yet confirmed that significant amounts of chemicals wind up in animals' tissues.

Nor does anyone know where all this plastic ultimately goes. Does it simply get too small to trap with a net? Does it sink to the sediments? Wash onto shore? (Large numbers of microplastics have been found on a Hawaii beach.) One worrisome find from the Scripps trip: a hatchetfish, a midwater dweller, with a plastic chip in its stomach. "It's going somewhere," says SEA oceanographer Kara Lavender Law. She and others would like to find out where.

–JOCELYN KAISER

CREDITS (FROM TOP): SCRIPPS INST. OF OCEANOGRAPHY; D. LAURSEN/ALGALITA MARINE RESEARCH FOUND.; J. LEICHTER/SCRIPPS; N. MAXIMENKO, P. NILLER, J. HAFNER

REVIEW

Deconstructing the Conveyor Belt

M. Susan Lozier

For the past several decades, oceanographers have embraced the dominant paradigm that the ocean's meridional overturning circulation operates like a conveyor belt, transporting cold waters equatorward at depth and warm waters poleward at the surface. Within this paradigm, the conveyor, driven by changes in deepwater production at high latitudes, moves deep waters and their attendant properties continuously along western boundary currents and returns surface waters unimpeded to deepwater formation sites. A number of studies conducted over the past few years have challenged this paradigm by revealing the vital role of the ocean's eddy and wind fields in establishing the structure and variability of the ocean's overturning. Here, we review those studies and discuss how they have collectively changed our view of the simple conveyor-belt model.

A single measurement of deep-ocean temperatures taken by the captain of a British slave-trade ship in 1751 was the catalyst for Count Rumford's supposition, nearly 50 years later, that ocean waters overturned, with high-latitude water "deprived of a great part of its heat by cold winds" descending to the ocean floor, spreading equatorward and necessitating a "current at the surface in an opposite direction" (*1*). In the following two centuries, as deep water masses were meticulously cataloged and surface currents were mapped across the globe, a long line of oceanographers worked to trace the route of the overturning waters from disparate observations (*2*). Despite these efforts, our modern conceptualization of the ocean's overturning and our understanding of its climatic importance coalesced only in the past few decades as a result of the work of two prominent oceanographers: one who provided a theoretical framework for the route of the deep waters that constitute the lower limb of the overturning, and another who provided a climatic context for the overturning itself.

Fifty years ago, Henry Stommel theorized that recently ventilated waters of high-latitude origin must be transported equatorward at depth along western-intensified boundary currents (*3*). Assuming that water masses formed via deep convection in isolated regions in the northern North Atlantic and near Antarctica essentially fill the abyssal ocean, Stommel surmised that the deep ocean exports these waters via a distributed upwelling to the surface. Furthermore, he suggested that because such upwelling produces a stretching of the water column that induces a loss of angular momentum, the deep interior waters must compensate by flowing poleward toward regions of higher angular momentum. Thus, the equatorward transport of deep water masses was confined to the western boundaries of the basins. Stommel's theory gave the ocean's overturning, previously amorphous in its third dimension, a structure: Deep waters are transported equatorward in a steady, continuous deep western-intensified boundary current from their formation sites at high latitudes (Fig. 1) (*4*). The interior flow, much weaker, moves poleward and upward. Another important element emerged from Stommel's study: The deep western boundary currents (DWBCs) of the global ocean are connected, linked across hemispheres and basins to form a continuous stream of deep waters spreading through the abyss. Later work (*5*) applied this theoretical construct to the actual ocean flow field, linking distant currents into a coherent overturning.

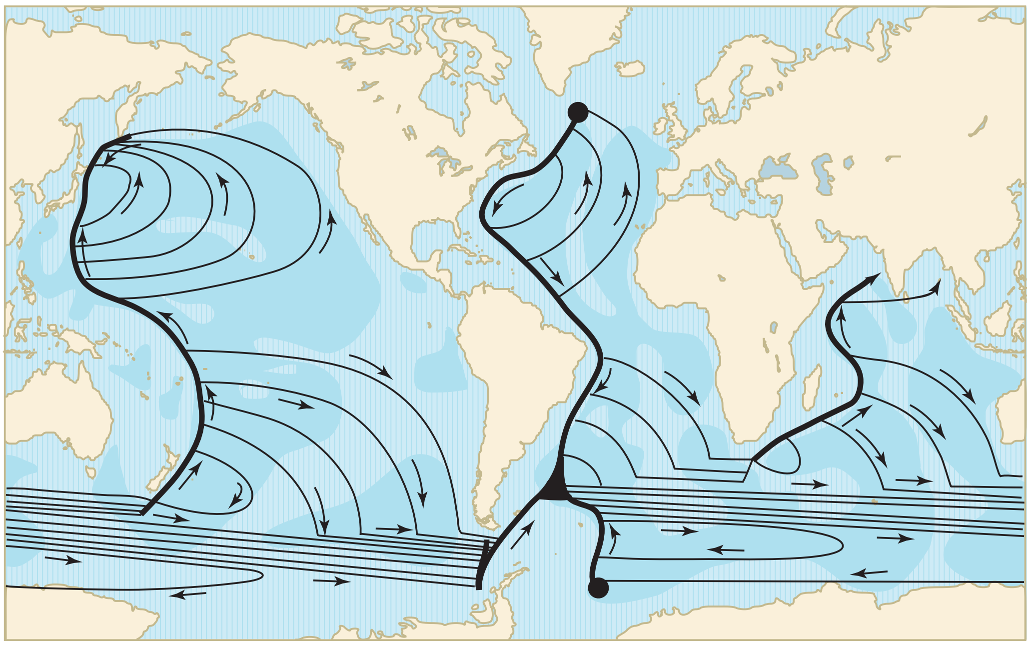

Fig. 1. The abyssal flow field, as theorized by Stommel in 1958 (*4*). Water mass source regions in the northern North Atlantic and Antarctica are denoted by black dots. These water masses are spread equatorward by interconnecting western intensified boundary currents (thick lines) that feed the poleward interior circulation (thin lines). Arrows indicate direction of flow. [Reprinted from (*4*), with permission from Elsevier]

Almost 25 years after Stommel's conceptualization, work by Broecker and colleagues suggested that the ocean's overturning was responsible for the rapid climate fluctuations experienced during Earth's last glacial period (*6*). Using a moniker first introduced in the early 1980s (*7*) and popularized with an illustration appearing in *Natural History* (Fig. 2) (*8*), Broecker suggested that the "great ocean conveyor belt" flipped on and off during the last glacial period in response to strong freshwater forcing, presumed to result from melting of the continental ice sheets. Though the importance of the ocean's overturning to Earth's climate had previously been understood, Broecker's work essentially cemented the role of the conveyor belt as an agent of climate change. Thus, just as Stommel's work gave spatial structure

Division of Earth and Ocean Sciences, Nicholas School of the Environment, Duke University, Durham, NC 27708, USA. E-mail: mslozier@duke.edu

to the overturning, Broecker's provided a temporal context.

Since these efforts, oceanographers have collectively supported the paradigm that the ocean "conveyor belt" transports recently ventilated waters from the subpolar North Atlantic along the "lower limb" of the conveyor belt to the rest of the global ocean, where the waters are upwelled and then transported along the "upper limb" back to deepwater formation sites. This conveyor belt is assumed to operate continuously along western boundary currents in the deep ocean, be vulnerable to changes in deepwater production at high latitudes due to variable buoyancy forcing, and provide a continuous supply of relatively warm surface waters to deepwater formation sites. Since its inception, oceanographers have understood that the conveyor model grossly oversimplifies the mechanics and pathways of the overturning: No one expects a water parcel tagged at the surface in the northern North Atlantic to be swept along the conveyor belt unimpeded in its equatorward, surfaceward, and ultimately poleward progress. However, this conceptual model has still fostered expectations for the response of the ocean's circulation to a warming climate: If high-latitude surface waters warm or freshen, deepwater production would diminish or cease. Because the conveyor belt is assumed to be driven by deepwater production, it would share this same fate. Northern Europe, robbed of the heat that prevailing westerlies gain at the expense of surface waters returning northward, would cool.

After decades as a dominant paradigm, some major features of the conveyor belt have recently been called into question. One study finds that most of the subpolar-to-subtropical exchange in the North Atlantic occurs along interior pathways (*9*), another that the DWBC breaks up into eddies at 11°S (*10*), another that there is little meridional coherence in the overturning transport from one gyre to the next (*11*), and another that wind forcing, rather than buoyancy forcing, can play a dominant role in changing the transport of the overturning (*12*). All told, the sum of these studies calls for a revamping of our conceptual model of the ocean's overturning. Added impetus for revamping comes from a recent study (*13*) revealing a considerable reservoir of anthropogenic CO_2 in the deep North Atlantic, surmised to result from the production of high-latitude water masses and their subsequent equatorward spread. Clearly, an improved understanding of the pathways of the upper and lower limbs of the ocean's overturning will aid assessments of the ocean's role in the uptake, transport, and storage of heat and CO_2, crucial components of Earth's climate system. This review, with a focus on the Atlantic because of the preponderance of observations in that basin, examines whether the ocean conveyor-belt model is an appropriate framework for that assessment.

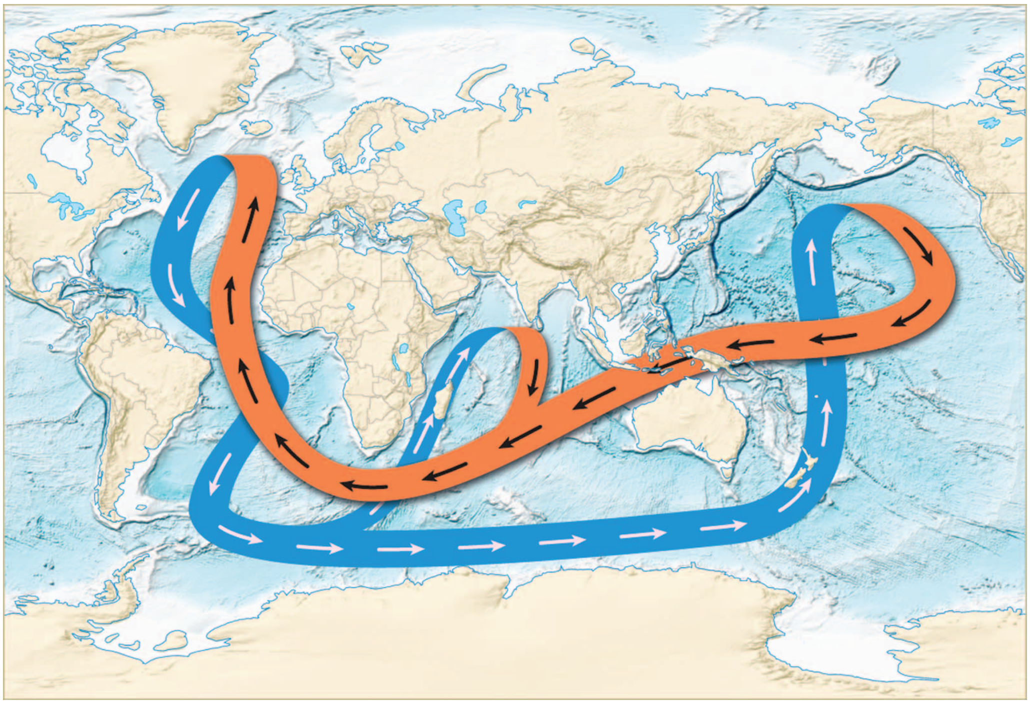

Fig. 2. Schematic of the ocean conveyor belt. Arrows indicate direction of flow. Orange, the warm, shallow waters of the upper limb of the conveyor belt; blue, the cold, deep waters of the deep limb. [Adapted from (*8*)] [Credit: Joe LeMonnier]

What Is the Conveyor Belt?

A critical examination of the conveyor-belt model has actually been under way for a number of years. As pointed out in 2002 (*14*), the conveyor belt is only loosely defined as flow that carries heat and salt from high to low latitudes and vice versa: It has never had an operational definition with mathematical rigor. Today, oceanographers refer to the meridional overturning circulation (MOC) as the two-dimensional (2D) flow field with a transport defined as the zonally integrated meridional flux of mass. However, despite the precise definition, many of the suppositions held for the conveyor belt have carried over to the meridional overturning; namely that overturning waters are principally carried in boundary currents and that overturning transport is continuous in space and time, yet susceptible in the main to changes in deepwater production in the northern North Atlantic. These suppositions are revisited below.

Are Western Boundary Currents Continuous Conduits of Recently Ventilated Deep Waters?

Early and strong evidence for the existence of DWBCs followed on the heels of Stommel's theory (*1*). Measures of water-mass properties and geochemical tracers have consistently revealed that North Atlantic Deep Water (NADW), the conglomeration of recently ventilated waters from the Nordic and Labrador Seas, is carried along a narrow corridor of the continental slope from the North Atlantic subpolar basin to the subtropics and equatorward (*15*, *16*). Although the geochemical tracers in this DWBC confirmed the presence of recently ventilated waters, they also raised a conundrum. The age of boundary-current waters is greater than that calculated from a simple model of advection along the boundary current (*17*, *18*). To explain this mismatch, it was conjectured that boundary-current waters mix with older interior waters as they transit downstream. Indeed, confirmation of such mixing came from a study of deep floats purposely seeded in the DWBC downstream of the Tail of the Grand Banks (*19*). These floats revealed a pattern of detrainment and reentrainment as they flowed equatorward, providing a visualization of along-stream aging. Thus, the notion of continuous flow along the ocean's deep limb of the conveyor

belt was modified to include the role of eddies in essentially diluting the boundary-current waters.

Eddies were elevated from a supporting role in the transport of waters along the lower limb of the overturning circulation to a starring role with the publication of an observational and modeling study of the DWBC in the South Atlantic (*10*). In this study, the southward transport of deep waters at 8°S, off the Brazilian coast, was shown to be carried entirely by migrating coherent eddies: Direct velocity measurements showed no evidence for a continuous, mean flow at the depth of the NADW. An accompanying modeling analysis attributed the generation of eddies to the instability of the DWBC. This study provided the first evidence that not only do eddies disrupt the transport of deep waters along the western boundaries, but, at least at this one locale, they constitute the transport. The ubiquity of this phenomenon remains unknown.

Is the DWBC a Unique Path for the Transport of Recently Ventilated Deep Waters?

Stommel's theorized structure for the western intensified DWBC was based on steady-state, large-scale dynamics. At the time, there was little to no appreciation for the ubiquity and strength of the eddy field, which is hardly surprising because the flow field was vastly undersampled. In Stommel's theory, the DWBC was needed to satisfy a steady, poleward interior flow. Though the expectation of this poleward flow has largely been abandoned, repeated confirmation of a DWBC continues to fuel our expectation that it is the primary conduit for the transport of recently ventilated waters. However, profiling floats released in the Labrador Sea during the 1990s (*20*), including those placed directly in the southward-flowing boundary current (*21*), exited the basin by either recirculating back into the Labrador Sea or heading eastward along the North Atlantic Current. Surprisingly, no floats were exported from the subpolar basin to the subtropics along the DWBC.

A follow-up study using dozens of acoustically tracked RAFOS floats (to avoid possible biases in deep pathways due to intermittent surfacing) placed in the DWBC at the depth of the Labrador Sea Water over a period of 3 years successfully revealed the export of subpolar waters to the subtropics (*9*). However, the primary route for this export was via interior pathways, not along the DWBC. In fact, only 8% of the floats launched in the DWBC stayed within the current as it transited the subtropics; all others were detrained along its length, particularly so at topographic "choke points" (*9*). The detrained floats subsequently drifted generally southward within the basin interior. An accompanying analysis using an ocean general-circulation model (*22*) quantitatively partitioned the export of Labrador Sea Waters into those that made the transit along the DWBC and those that transited the interior. The latter transport far outweighed the former, revealing the interior as the primary route for the equatorward transport of deep waters. Though the observational program with RAFOS floats and the companion modeling study were focused on waters of Labrador Sea origin, an analysis of the pathways of the Nordic Sea overflow waters within the same ocean-circulation model reveals similar results: Floats launched within the DWBC at 53°N do not follow a continuous boundary current, but instead take multiple paths to the subtropics, including interior pathways far removed from the DWBC (Fig. 3).

The fact that these recent float observations and modeling results directly contradict the predicted dominance of the DWBC theorized by Stommel is reconciled by considering the effect of eddies on the deep flow. Early modeling work in the 1970s (*23*), when the ocean eddy field was receiving deserved attention, demonstrated how eddies, generated from instabilities of mean currents, could drive deep mean flow in the form of strong recirculations adjacent to energetic boundary currents. Subsequent theoretical work linked eddy-driven flow with a signature of homogenized potential vorticity (*24*). This link-

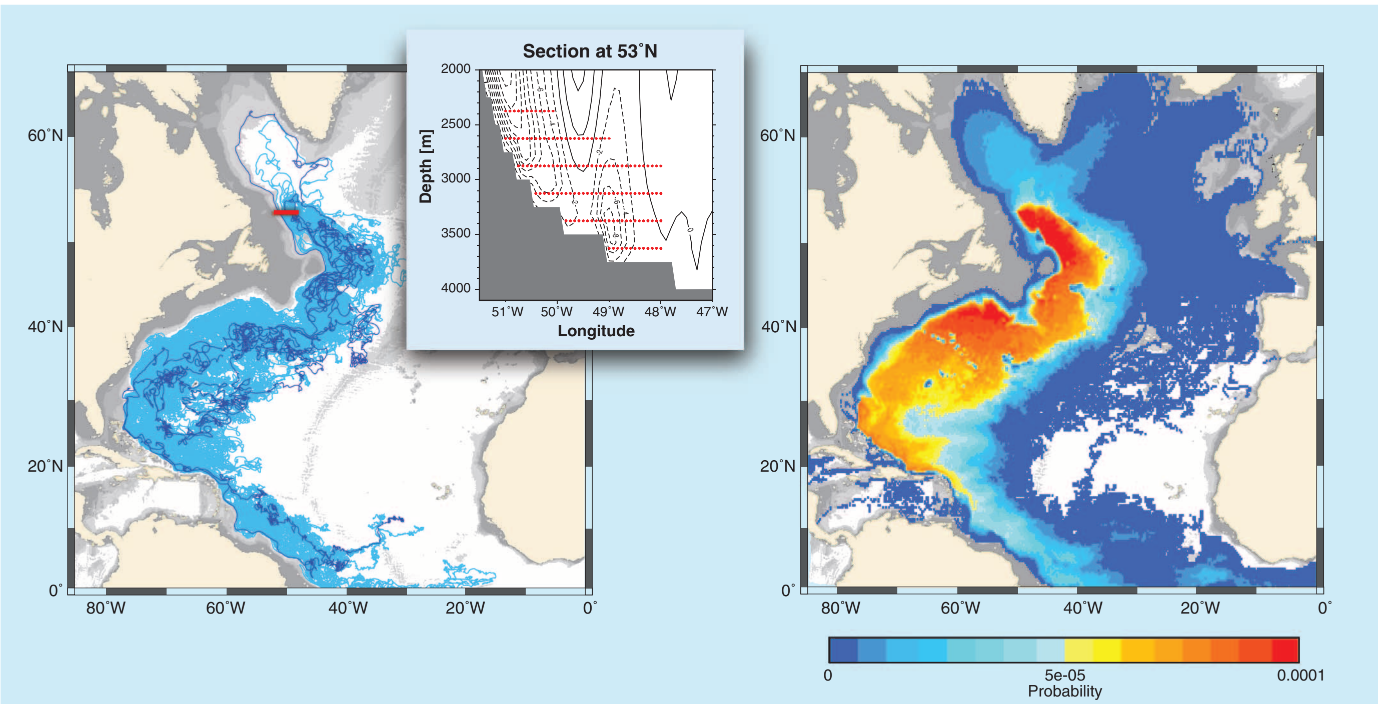

Fig. 3. (**Left**) Fifty-year trajectories of 50 e-floats randomly selected from a total of ~18,000 deployed within an eddy-resolving ocean general-circulation model (*9*, *22*) at the depth of the Nordic Seas overflow waters. Floats were launched at 53°N in the southward-flowing DWBC (inset) with mean launch locations marked with red bars. The meridional velocity is contoured at 2-cm/s increments, with solid and dashed lines indicating northward and southward flow, respectively. The model's DWBC structure compares favorably with the observed flow at 53°N (*40*). Launches were made only if the temperature was ≤2.3°C at the time of the launch. Three selected trajectories (dark blue) highlight the interior pathway. (**Right**) A 2D probability map of float locations from the entire set of e-floats over 50 years.

age, coupled with an analysis of hydrographic data that revealed extensive homogenization of potential vorticity in the deep waters adjacent to the Gulf Stream/North Atlantic Current, prompted the conjecture that eddy-driven recirculations provide an alternate pathway for the export of deep waters from the subpolar to the subtropical basin (*25*). Attribution of this pathway to eddy-driven recirculations was recently made explicit by model simulations (*9*) that reveal equatorward flow in the ocean interior, opposite that theorized 50 years ago when ocean flow at depth was presumed steady. Thus, there is now an observational, modeling, and theoretical basis for discarding the notion that DWBCs provide a continuous and unique pathway for the deep limb of the MOC. Though most observational and modeling studies to date have focused on the North Atlantic, there is little reason to suspect that other DWBCs are not similarly affected by the presence of eddies and, consequently, that alternate pathways exist for the spreading of the deep waters. The North Atlantic does not hold a monopoly on energetic eddy fields at depth (*10*).

In sum, the impact of eddies on our concept of a continuous lower limb for the ocean's overturning has evolved from an understanding that eddies can detrain and entrain fluid along the DWBC to the recognition that the DWBC can, at certain locales and perhaps certain times, be a series of migrating eddies, to the realization that eddy-driven flow provides an alternate pathway for deep waters to spread globally. This impact of the eddy field on pathways for recently ventilated waters has clear implications for the interpretation of the age, transport, and variability of the waters that compose the DWBC. With large-scale recirculations whose extent and strength vary in depth (*25*), the age of boundary-current waters will be a strong function of local physics, potentially overriding the imprint of upstream source characteristics (*26*). The diversion of floats from the DWBC into the interior at multiple locations implies that the DWBC will not have a continuous throughput of recently ventilated water and that coherence in transport along the DWBC will be weak. Finally, if eddies are the product of the instabilities of the swift boundary currents, themselves driven principally by the wind field, a simple deduction leads to the suggestion that recirculations, and the alternate pathways they create, must also be dependent on wind forcing and its temporal variability. Thus, a varying transport of a water mass in a boundary current cannot simply be interpreted as varying upstream export. The disconnect goes even further: Studies of convection in the Labrador basin (*27*, *28*) have demonstrated that variable export is largely divorced from variable deepwater production in that basin, breaking another long-standing expectation of the conveyor belt.

Is the Upper Limb of the Overturning Continuous?

Concurrent with surprising turns of the deep limb, two recent studies have found unexpected pathways in the upper ocean. An analysis of hundreds of surface drifters that transited the Gulf Stream from 1990 to 2002 (Fig. 4) (*29*) revealed that only one followed a pathway to the subpolar gyre. This result was identified as a conundrum because a sizable portion (~20 to 25%) of Gulf Stream waters are expected to flow northwestward into the subpolar basin as the MOC upper limb. Possible explanations for the missing throughput include insufficient drifter lifetimes, insufficient sampling, and the influence of a strong southward Ekman transport that inhibits exchange across the subtropical/subpolar boundary. A follow-up study (*30*), however, suggests another possible mechanism for the missing throughput. Using an expanded drifter data set that is subdivided by temporal periods, this study suggests that throughput to the subpolar ocean is temporally variable, controlled by large-scale winds. Though it remains to be seen whether undersampling can indeed be discounted as a factor and/or whether the expected exchange is found beneath the near-surface layer, the suggestion of variable exchange finds support from a study of property fields in the eastern subpolar gyre (*31*), where the relative proportion of salty subtropical water entering the subpolar latitudes was found to be highly variable, a function of winds that control the shape, extent, and strength of the ocean gyres.

Collectively, these studies raise questions similar to those asked of the lower limb: Is the upper-limb transport continuous in time? If not, what mechanism principally controls its variability and what are the dominant time scales for this variability? Though answers to these questions have not yet been ascertained, there are indications that wind-driven gyre dynamics plays a strong role in the determination of the exchange of mass and heat across gyre/gyre boundaries. These indications include a discontinuity in the meridional coherence of transport anomalies at gyre/gyre boundaries in the surface waters of the North Atlantic (*11*) and MOC changes in that basin with a gyre-specific pattern (*12*).

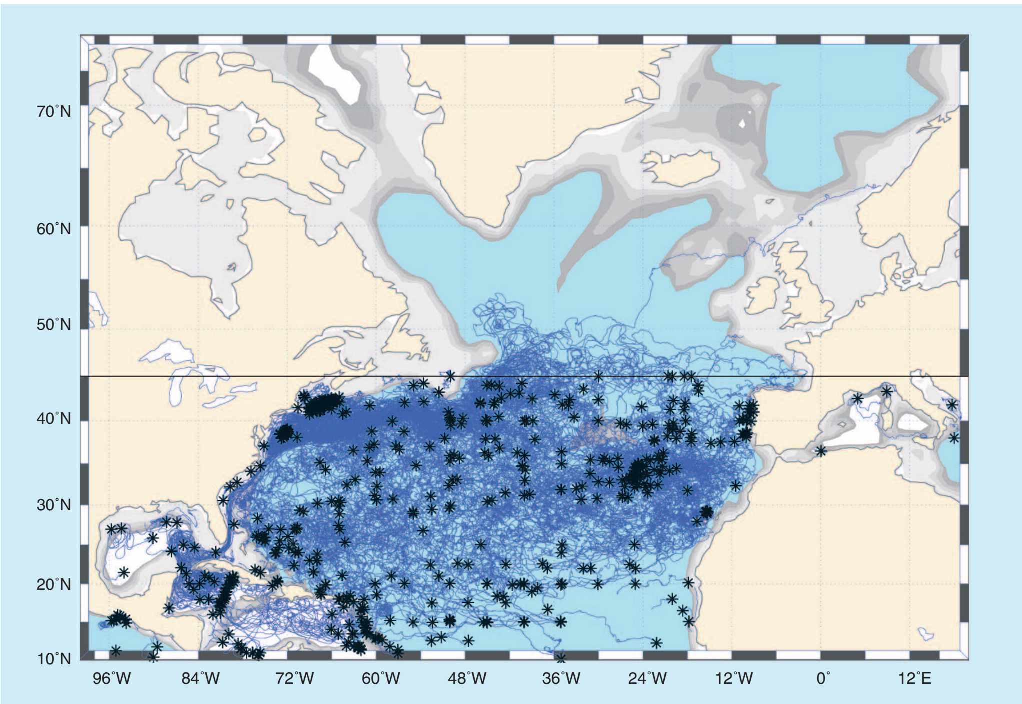

Fig. 4. Trajectories of surface drifters deployed in the North Atlantic from 1990 to 2002. Only drifters deployed south of 45°S (black line) are shown, with asterisks marking the deployment locations. [Reprinted from (*29*), with permission from the American Geophysical Union]

What Forces the Overturning?

The question of whether and how wind forcing affects the pathways of the upper and lower limbs of the overturning is inextricably linked to the question of what drives the overturning itself. Although many past studies have invoked buoyancy forcing at high latitudes as the driving mechanism for the overturning, other studies over the past decade have pointed to the possibility that wind forcing—by creating surface mass

fluxes and/or by providing the mixing needed to return deep waters to the surface—is instead the dominant mechanism (*14*). These opposing hypotheses for the forcing of the overturning have been neatly summarized as "push" or "pull" views of this circulation feature (*32*). The question of which forcing controls the variability of the overturning may depend crucially on time scale: A recent study that isolated the impact of buoyancy and wind forcing on MOC transport in the North Atlantic found the latter dominated on interannual to decadal scales, whereas the former dominated on longer, centennial time scales (*12*). Of course, this neat categorization may not hold if climate variability brings changes to the strength and position of the large-scale wind fields, as suggested by recent modeling studies (*33*, *34*). Furthermore, historical assumptions about the conveyor belt and its operation are being overturned on other fronts: A recent study shows that MOC transport in the subtropical North Atlantic is susceptible to variability in the "leakage" of warm and salty Agulhas Current water into the South Atlantic (*35*). Because this variability is remotely forced and because it depends on wave propagation and eddy processes, it elegantly illuminates the progression of our understanding of the overturning's complexity.

What Are the Open Questions About the Overturning?

Recent evidence that the ocean's overturning limbs are not spatially and temporally continuous should not cast a shadow on the certainty of the overturning itself: There is clear and abundant evidence that ocean waters overturn. Deep water masses, primarily from the North Atlantic, spread to other ocean basins, with a concomitant surface mass flux of ~20 sverdrups. Considerably less certain is the 3D structure of the overturning. Global pathways for the waters in the lower and upper limbs and the mechanisms governing their spatial and temporal variability remain unknown. Equally uncertain are the dominant mechanisms governing the overturning transport and its accompanying property transports. Such uncertainty surrounding the mean forcing of the overturning presents a cornucopia of possibilities for the forcing that creates overturning changes: High-latitude warming and/or freshening, as well as local and/or remote wind variability, all remain plausible.

Of all questions surrounding the MOC, one looms largest: What is the importance of MOC variability to the meridional transport of heat compared with other forcing? Clear and convincing evidence that sea-surface temperature changes in the North Atlantic impact the climate of northern Europe is coupled with an unproven supposition that overturning changes will create such temperature changes. Though ocean models have repeatedly demonstrated that high-latitude freshening will lead to a diminution of the overturning (*36*)—and, thus, a substantial change in North Atlantic sea-surface temperatures—no observational study to date has been able to successfully link sea-surface temperature changes with overturning changes. Presumably, this link is difficult to establish because of the strength of the ocean's eddy and/or wind field, but that too has yet to be made evident.

How Are These Questions Being Addressed?

Since 2004, a monitoring array for MOC volumetric and heat transport has been in place at 26°N in the North Atlantic. Results from this array are providing an unprecedented view of the temporal variability of the overturning (*37*) and the challenges accompanying such variability (*38*). Interestingly, the overturning transport showed more range over the course of one year than had previously been expected for decades of change. In the context of an ocean conveyor belt, such a result would have been surprising, but with the emerging understanding of the contributions from the ocean's wind and eddy field to the transport of mass and heat in the ocean, such a result is decidedly unsurprising. Though the array at 26°N was initially envisioned to monitor the overturning circulation of the entire Atlantic, studies showing little to no coherence across gyre boundaries have prompted interest in monitoring the overturning circulation in the South Atlantic and the subpolar North Atlantic. Clearly, the connectivity of the overturning and, more importantly, of the meridional heat transport from one basin to the next can no longer be assumed on interannual time scales. To complement current and planned direct observations of the overturning, new methods to estimate the transport with profiling floats and satellite products are yielding promising results (*39*).

Summary

Though appealing in its simplicity, the ocean conveyor-belt paradigm has lost luster over the years, precisely because it has overdistilled the complexity of the ocean's overturning. This complexity has slowly been revealed as the ocean has increasingly been observed at finer scales in space and time and in places previously only sparsely sampled. As discussed, the ocean's eddy field, unaccounted for just decades ago and now uncovered by measures at appropriate scales, figures prominently in the dismantling of the conveyor-belt paradigm. Another player in this dismantling is the ocean's wind field. The traditional assignation of surface ocean gyres to wind-forcing and overturning to buoyancy forcing has ignored the vital impact of winds on overturning pathways and mechanics. As the study of the modern ocean's role in climate continues apace, the conveyor-belt model no longer serves the community well—not because it is a gross oversimplification but because it ignores crucial structure and mechanics of the ocean's intricate global overturning.

References and Notes

1. B. A. Warren, in *Evolution of Physical Oceanography*, B. Warren, C. Wunsch, Eds. (MIT Press, Cambridge, MA, 1981), pp. 6–41.
2. P. Richardson, *Prog. Oceanogr.* **76**, 466 (2008).
3. N. Hogg, R. X. Huang, Eds., *Collected Works of Henry M. Stommel*, vol. 2 (American Meteorological Society, Boston, 1995), pp. 307–709.
4. H. Stommel, *Deep-Sea Res.* **5**, 80 (1958).
5. A. L. Gordon, *J. Geophys. Res.* **91**, 5037 (1986).
6. W. S. Broecker, *Oceanography* **4**, 79 (1991) and references therein.
7. W. S. Broecker, T.-H. Peng, *Tracers in the Sea* (Lamont-Doherty Earth Observatory, Palisades, NY, 1982).
8. W. S. Broecker, *Nat. Hist.* **10**, 74 (1987).
9. A. S. Bower, M. S. Lozier, S. F. Gary, C. W. Böning, *Nature* **459**, 243 (2009).
10. M. Dengler *et al.*, *Nature* **432**, 1018 (2004).
11. R. J. Bingham, C. W. Hughes, V. Roussenov, R. G. Williams, *Geophys. Res. Lett.* **34**, L23606 (2007).
12. A. Biastoch, C. W. Böning, J. Getzlaff, J. M. Molines, G. Madec, *J. Clim.* **21**, 6599 (2008).
13. C. L. Sabine *et al.*, *Science* **305**, 367 (2004).
14. C. Wunsch, *Science* **298**, 1179 (2002).
15. W. M. Smethie, R. A. Fine, A. Putzka, E. P. Jones, *J. Geophys. Res.* **105**, 297 (2000).
16. R. S. Pickart, *Deep-Sea Res.* **39**, 1553 (1992).
17. D. R. Watts, Ed., in *Equatorward Currents in Temperatures 1.8-6.0 °C on the Continental Slope in the Mid-Atlantic Bight* (Elsevier, Amsterdam, 1991), pp. 183–196.
18. M. Rhein, *Deep-Sea Res.* **41**, 263 (1994).
19. A. S. Bower, H. D. Hunt, *J. Phys. Oceanogr.* **30**, 784 (2000).
20. K. L. Lavender, R. E. Davis, W. B. Owens, *Nature* **407**, 66 (2000).
21. J. Fischer, F. A. Schott, *J. Phys. Oceanogr.* **32**, 573 (2002).
22. K. C. Getzlaff, C. W. Böning, J. Dengg, *Geophys. Res. Lett.* **33**, L21S08 (2006).
23. W. R. Holland, L. B. Lin, *J. Phys. Oceanogr.* **5**, 642 (1975).
24. P. B. Rhines, W. R. Young, *J. Fluid Mech.* **122**, 347 (1982).
25. M. S. Lozier, *Science* **277**, 361 (1997).
26. M. S. Lozier, *Geophys. Res. Lett.* **26**, 219 (1999).
27. R. S. Pickart, M. A. Spall, *J. Phys. Oceanogr.* **37**, 2207 (2007).
28. F. Straneo, *J. Phys. Oceanogr.* **36**, 1822 (2006).
29. E. Brambilla, L. D. Talley, *J. Geophys. Res.* **111**, C07026 (2006).
30. S. Hakkinen, P. B. Rhines, *J. Geophys. Res.* **114**, C04005 (2009).
31. H. Hátún, A. B. Sandø, H. Drange, B. Hansen, H. Valdimarsson, *Science* **309**, 1841 (2005).
32. M. Visbeck, *Nature* **447**, 383 (2007).
33. T. Delworth, F. Zeng, *Geophys. Res. Lett.* **35**, L20708 (2008).
34. A. Biastoch, C. W. Böning, F. U. Schwarzkopf, J. R. E. Lutjeharms, *Nature* **462**, 495 (2009).
35. A. Biastoch, C. W. Böning, J. R. E. Lutjeharms, *Nature* **456**, 489 (2008).
36. R. J. Stouffer *et al.*, *J. Clim.* **19**, 1365 (2006).
37. S. A. Cunningham *et al.*, *Science* **317**, 935 (2007).
38. C. Wunsch, *Nat. Geosci.* **1**, 165 (2008).
39. J. K. Willis, *Geophys. Res. Lett.* **37**, L06602 (2010).
40. J. Fischer, F. A. Schott, M. Dengler, *J. Phys. Oceanogr.* **34**, 1548 (2004).

41. I would like to acknowledge S. Gary's aid in the construction of Fig. 2, helpful comments on the manuscipt from B. Corliss and P. Baker, and insightful discussions with A. Bower and R. Williams. Support from the NSF is also gratefully acknowledged.

10.1126/science.1189250

REVIEW

The Growing Human Footprint on Coastal and Open-Ocean Biogeochemistry

Scott C. Doney

Climate change, rising atmospheric carbon dioxide, excess nutrient inputs, and pollution in its many forms are fundamentally altering the chemistry of the ocean, often on a global scale and, in some cases, at rates greatly exceeding those in the historical and recent geological record. Major observed trends include a shift in the acid-base chemistry of seawater, reduced subsurface oxygen both in near-shore coastal water and in the open ocean, rising coastal nitrogen levels, and widespread increase in mercury and persistent organic pollutants. Most of these perturbations, tied either directly or indirectly to human fossil fuel combustion, fertilizer use, and industrial activity, are projected to grow in coming decades, resulting in increasing negative impacts on ocean biota and marine resources.

The ocean plays a pivotal role in the global biogeochemical cycles of carbon, nitrogen, phosphorus, silicon, and a variety of other biologically active elements and chemical compounds (*1*, *2*). Human fossil-fuel combustion, agriculture, and climate change have a growing influence on ocean chemistry, both regionally in coastal waters and globally in the open ocean (*3*–*5*) (Fig. 1). Some of the largest anthropogenic impacts are on inorganic carbon (*6*), nutrients (*4*, *7*), and dissolved oxygen (*8*, *9*), which are linked through and affect biological productivity. Seawater chemistry is also altered, some times quite strongly, by the industrial production, transport, and environmental release of a host of persistent organic chemicals (*10*) and trace metals, in particular mercury (*11*), lead (*12*), and perhaps iron (*13*).

Marine biogeochemical dynamics is increasingly relevant to discussions of ecosystem health, climate impacts and mitigation strategies, and planetary sustainability. Human-driven chemical perturbations overlay substantial natural biogeochemical cycling and variability. Key scientific challenges involve the detection and attribution of decadal and longer trends in ocean chemistry as well as more definitive assessments of the resulting implications for ocean life and marine resources.

The biogeochemical state of the sea reflects both cycling and transformations within the ocean, much of which are governed by biological dynamics, and fluxes across the ocean boundaries with the land, atmosphere, and sea floor (*2*, *14*). For most chemical species, seawater concentrations are governed more by kinetics—the rates of net formation and transport processes—than by chemical equilibrium with particles and sediments. Clear exceptions are dissolved gases such as carbon dioxide (CO_2) and oxygen (O_2), which are driven to solubility equilibrium with the partial pressure of gases in the atmosphere in the surface ocean by air-sea gas exchange.

Phytoplankton in the ocean surface plays a crucial biogeochemical role, converting CO_2 and nutrients into particulate organic and inorganic matter via photosynthesis and releasing O_2 in the process. The rate of marine primary production is governed by temperature, light (strongly influenced by surface turbulent mixing depths), and limiting nutrients, most notably nitrogen, phosphorus, iron, and silicon for some plankton. Some fraction of the biologically produced particulate matter subsequently sinks into the subsurface ocean and is consumed by microbes and macrofauna, releasing CO_2 and nutrients and consuming subsurface O_2. Export production thus maintains strong vertical gradients in biogeochemical tracers over the water column.

The global biologically driven export flux of ~10 Pg of C year^{-1} must be balanced by a supply of "new" nutrients brought up from below by ocean circulation, input by rivers, or deposited from the atmosphere. With sufficient iron and phosphorus, some diazotrophic microbes can produce "new" nitrogen in situ through nitrogen fixation that converts inert nitrogen gas into biological reactive nitrogen. Marine microbes produce and consume a number of trace gases that can influence climate, for example CO_2, nitrous oxide (N_2O), methane (CH_4), and dimethylsulfide (DMS).

Ocean upwelling and mixing bring water with elevated CO_2 and nutrients to the surface and replenish subsurface O_2, with ventilation time scales of years to a few decades in the main thermocline (upper 1 km of the water column) and many centuries for deep waters. Natural ocean-atmosphere climate modes (e.g., El Nino–Southern Oscillation and Pacific Decadal Oscillation) generate substantial interannual to interdecadal variability in ocean biogeochemistry. The major external source terms to the ocean are typically river inputs and atmospheric deposition of dust,

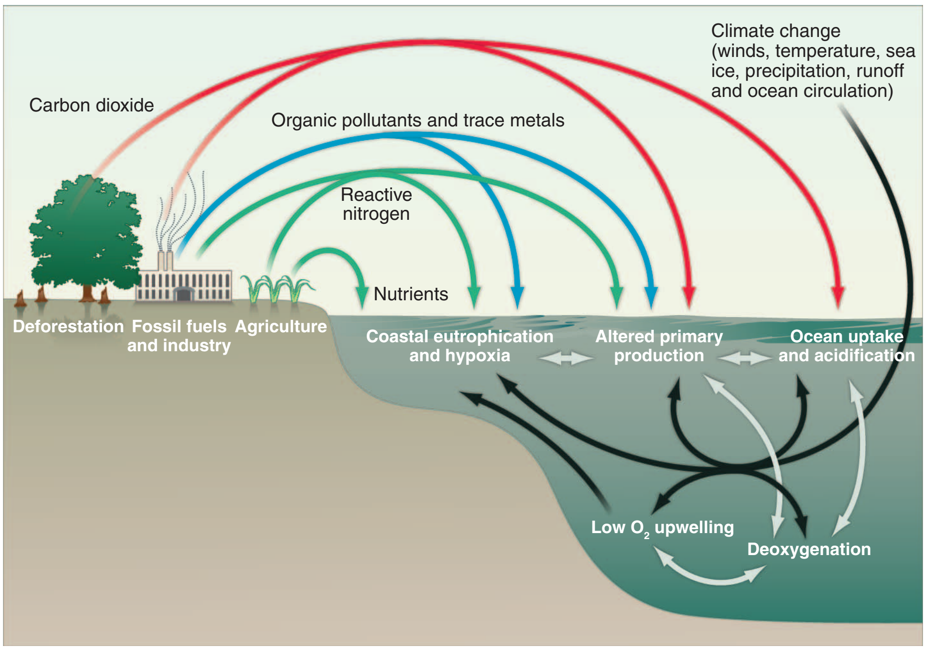

Fig. 1. Schematic of human impacts on ocean biogeochemistry either directly via fluxes of material into the ocean (colored arrows) or indirectly via climate change and altered ocean circulation (black arrows). The gray arrows denote the interconnections among ocean biogeochemical dynamics. Note that many ocean processes are affected by multiple stressors, and the synergistic effects of human perturbations is a key area for further research.

Marine Chemistry and Geochemistry Department, Woods Hole Oceanographic Institution, Woods Hole, MA 02543, USA. E-mail: sdoney@whoi.edu

aerosols, and precipitation. These source terms are balanced mostly by losses to the seafloor via the burial of the small fraction (<1% of organic matter) of sinking particulate matter that is not destroyed either in the water column or in surface sediments.

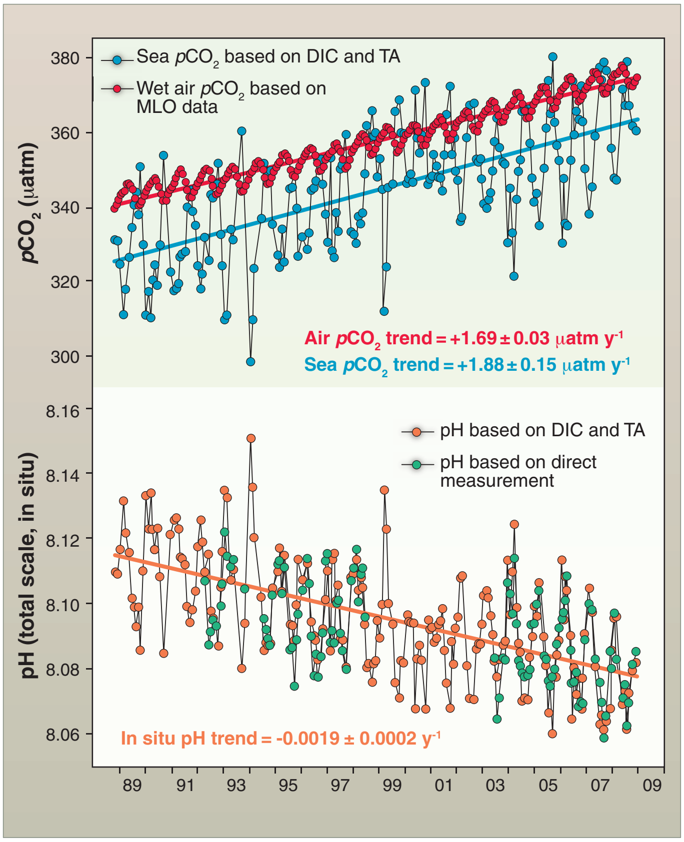

Fig. 2. Time series of (**top**) atmospheric CO_2 and surface ocean pCO_2 and (**bottom**) surface ocean pH at the atmospheric Mauna Loa Observatory (MLO) on the island of Hawai'i and Station ALOHA in the subtropical North Pacific north of Hawai'i, 1988–2008. [Adapted from (*26*)]

Human Drivers on Biogeochemical Cycles and Ocean Climate

For most of history, it was inconceivable that humankind could directly influence ocean chemistry other than in local and inconsequential manners. That changed after the industrial revolution with the development of modern energy systems, chemical industries, and agriculture that process ever-growing volumes of material, some of which are released either advertently or inadvertently into the environment and eventually reach the ocean. For example, because of human fossil-fuel combustion, deforestation, and land-use change (*3*), global mean atmospheric carbon dioxide (CO_2) has grown by almost 40% from about 280 parts per million (ppm) in the preindustrial era to nearly 388 ppm by 2010 (*15*). The invention of the Haber-Bosch process, which converts N_2 gas into fixed nitrogen for agricultural fertilizer, has had an even greater proportional impact on the global nitrogen cycle, approximately equaling the annual production of reactive nitrogen from natural sources (*4*). Comparable amplifications of a factor of 2 to 3 have occurred in the emissions of reactive phosphorus (*16*) and mercury (*17*) to the atmosphere and hydrosphere.

Indirect human effects on ocean chemistry can also occur, mainly through climate change. According to the most recent synthesis by the Intergovernmental Panel on Climate Change, warming of the climate system since the mid-20th century is unequivocal and is very likely caused by the increase in anthropogenic greenhouse gas concentrations (CO_2, N_2O, CH_4, and chlorofluorocarbons) (*18*). Documented physical changes relevant to ocean biogeochemistry include upper-ocean warming, altered precipitation patterns and river runoff rates, and sea-ice retreat in the Arctic and the West Antarctic Peninsula. Reduced stratospheric ozone over Antarctica appears to be causing a major shift in atmospheric pressure (more positive Southern Annular Mode conditions), which strengthens and displaces poleward the westerly winds in the Southern Ocean and which also may be increasing ocean vertical upwelling (*19*). Future climate projections indicate continuation, and in many cases acceleration, of these trends as well as other changes such as more intense tropical storms, an ice-free summer in the Arctic, and a very likely reduction in the strength of the Atlantic deepwater formation.

Ocean Uptake of Anthropogenic CO_2

Rising atmospheric CO_2 causes a net air-to-sea flux of excess CO_2 that dissolves in surface seawater as inorganic carbon through well-known physical-chemical reactions. The global uptake rate is governed primarily by atmospheric CO_2 concentrations and the rate of ocean circulation that exchanges surface waters equilibrated with elevated CO_2 levels with subsurface waters. The distribution, global inventory, and decadal trend in anthropogenic CO_2 are well characterized from ship-based observations (*6*, *20*) and models (*3*). Based on a recent synthesis, in 2008 fossil-fuel combustion released 8.7 ± 0.5 Pg of C year^{-1} to the atmosphere primarily as CO_2, contributing to an ocean uptake of 2.3 ± 0.4 Pg of C year^{-1} (*3*). Cumulative ocean carbon uptake since the beginning of the industrial age is equivalent to about 25 to 30% of total human CO_2 emissions (*6*).

Climate change is expected to decrease ocean uptake of anthropogenic CO_2 because of lower CO_2 solubility in warmer waters and slower physical transport into the ocean interior due to increased vertical stratification and reduced deepwater formation (*21*). In contrast, stronger Southern Ocean winds and ocean upwelling may increase future uptake of anthropogenic CO_2 (*22*). Changes in ocean circulation also alter the upward transport of subsurface water enriched in nutrients and dissolved inorganic carbon, and these biogeochemical feedbacks tend to partially offset climate effects on anthropogenic CO_2 uptake. In model estimates for the contemporary Southern Ocean for example, enhanced efflux of natural CO_2 due to stronger winds and upwelling more than compensates for increased anthropogenic CO_2 uptake, leading to a net reduction in global ocean uptake (*19*, *23*). Recent observations of the air-sea difference in the partial pressure of carbon dioxide (pCO_2), the driving force for air-sea CO_2 exchange, indicate a weakening of oceanic uptake in a number of regions, although there remains some debate about whether this signal should be attributed primarily to climate change or decadal climate variability (*3*, *24*).

Ocean Acidification

Ocean uptake of anthropogenic CO_2 also alters ocean chemistry, leading to more acidic conditions (lower pH) and lower chemical saturation states (Ω) for calcium carbonate ($CaCO_3$) minerals used by many plants, animals, and microorganisms to make shells and skeletons (*25*). Seawater acid-base chemistry is buffered largely by the inorganic carbon system, and CO_2 acts as a weak acid in seawater. Processes that add CO_2, like air-to-sea gas flux or bacterial respiration of organic matter, increase the concentration of hydrogen ions (H^+) and thus decrease pH (pH = $-\log_{10}[H^+]$).

Critically for many organisms, the addition of CO_2 reduces carbonate ion (CO_3^{2-}) concentration through the reaction $H^+ + CO_3^{2-} \rightarrow HCO_3^-$, even though the total amount of dissolved inorganic carbon (DIC) goes up (DIC = $[CO_2] + [H_2CO_3] + [HCO_3^-] + [CO_3^{2-}]$). Declining CO_3^{2-} in turn lowers $CaCO_3$ saturation state, $\Omega = [Ca^{2+}][CO_3^{2-}]/K_{sp}$, where K_{sp} is the thermodynamic solubility product that varies with temperature, pressure, and mineral form. Ocean surface waters are currently supersaturated ($\Omega > 1$) for the two major forms used by marine organisms, aragonite (corals and many

mollusks) and calcite (coccolithophores, foraminifera, and some mollusks). Because of pressure effects and higher metabolic CO_2 from organic matter respiration, Ω decreases with depth, often becoming undersaturated (Ω < 1), at which point unprotected shells and skeletons begin to dissolve.

Ocean acidification is documented clearly from ocean time-series and survey measurements over the past two decades (Fig. 2) (*26*, *27*). From preindustrial levels, contemporary surface ocean pH has dropped on average by about 0.1 pH units (a 26% increase in $[H^+]$), and additional declines of 0.2 and 0.3 pH units will occur over the 21st century unless human CO_2 emissions are curtailed substantially (*28*). Surface ocean $CaCO_3$ saturation states are declining everywhere, and polar surface waters will become undersaturated for aragonite when atmospheric CO_2 reaches 400 to 450 ppm for the Arctic and 550 to 600 ppm for the Antarctic (*29*). Subsurface waters will also be affected but more slowly, governed by ocean circulation, with the fastest rates in the main thermocline and high latitudes where cold surface waters sink into the ocean interior. Many coastal waters naturally have low pH, a factor amplified by acid rain (*30*) and nutrient eutrophication (see below).

The rates of change in global ocean pH and Ω are unprecedented, a factor of 30 to 100 times faster than temporal changes in the recent geological past, and the perturbations will last many centuries to millennia. The geological record does contain past ocean acidification events, the most recent associated with the Paleocene-Eocene Thermal Maximum 55.8 million years ago. But these events may have occurred gradually enough and under different enough background conditions for ocean chemistry and biology that there is no good paleo-analog for the current situation (*31*).

On the basis of laboratory experiments and limited surveys across ocean chemistry gradients, ocean acidification will likely reduce shell and skeleton growth by many marine calcifying species including corals and mollusks (*25*). Ocean acidification also may reduce the tolerance of some species to thermal stress. Some studies suggest a threshold of about 550 ppm atmospheric CO_2 where coral reefs would begin to erode rather than grow because of acidification and surface ocean warming; this would negatively affect diverse reef-dependent taxa (*32*). Polar ecosystems also may be particularly susceptible when surface waters become undersaturated for aragonite, the mineral form used by many mollusks.

Some organisms may benefit in a high-CO_2 world, in particular photosynthetic organisms that are currently limited by the amount of dissolved CO_2 in seawater. In laboratory experiments with elevated CO_2, higher photosynthesis rates are found for certain phytoplankton species, seagrasses, and macroalgae, and enhanced nitrogen-fixation rates are found for some cyanobacteria. Indirect impacts on noncalcifying organisms and marine ecosystems as a whole are possible but more difficult to characterize from present understanding.

Climate Change and Trends in Biological Productivity

Primary production by upper-ocean phytoplankton forms the base of the marine food web and drives ocean biogeochemistry through the export flux of organic matter and calcareous and siliceous biominerals from planktonic shells. Satellite observations indicate a strong negative relationship, at interannual time scales, between productivity and warming in the tropics and subtropics, most likely because of reduced nutrient supply from increased vertical stratification (*33*). Numerical models project declining low-latitude marine primary production in response to 21st-century climate warming (*34*). The situation is less clear in temperate and polar waters, although there is a tendency in models for increased production because of warming, reduced vertical mixing, and reduced sea-ice cover. The climate signal in primary production may be difficult to distinguish from natural variability for many decades (*35*).

Changes in atmospheric nutrient deposition also can alter productivity but mostly on regional scales near industrial and agricultural sources. Present anthropogenic reactive nitrogen deposition to the surface ocean (54 ± 23 Tg of N $year^{-1}$) (Fig. 3) supports an export production of ~0.3 Pg of C $year^{-1}$ (~3% of global total) while producing an additional ~1.6 Tg $year^{-1}$ of N_2O (*7*). In much of the North Pacific, equatorial Pacific, and Southern Ocean, phytoplankton are limited by iron, but most of the atmospheric iron deposition is in the form of mineral dust that is not readily bioavailable. Anthropogenic combustion sources and increased cloud-water acidity are increasing soluble iron input to the ocean (*13*, *36*). Models suggest that anthropogenic iron deposition could have a greater positive impact on productivity than anthropogenic nitrogen and also enhance nitrogen fixation, but direct observations are lacking (*37*).

Coastal Hypoxia and Open-Ocean Deoxygenation

Low subsurface O_2, termed hypoxia, occurs naturally in open-ocean and coastal environments from a combination of weak ventilation and/or strong organic matter degradation (*8*, *9*). Dissolved O_2 gas is essential for aerobic respiration, and low O_2 levels negatively affect the physiology of higher animals, leading to so-called "dead-zones" where many macrofauna are absent. Thresholds for hypoxia vary by organism but are ~60 μmol of O_2 kg^{-1} or about 30% of surface saturation. Under suboxic conditions (<5 μmol kg^{-1}), microbes begin to use nitrate (NO_3)

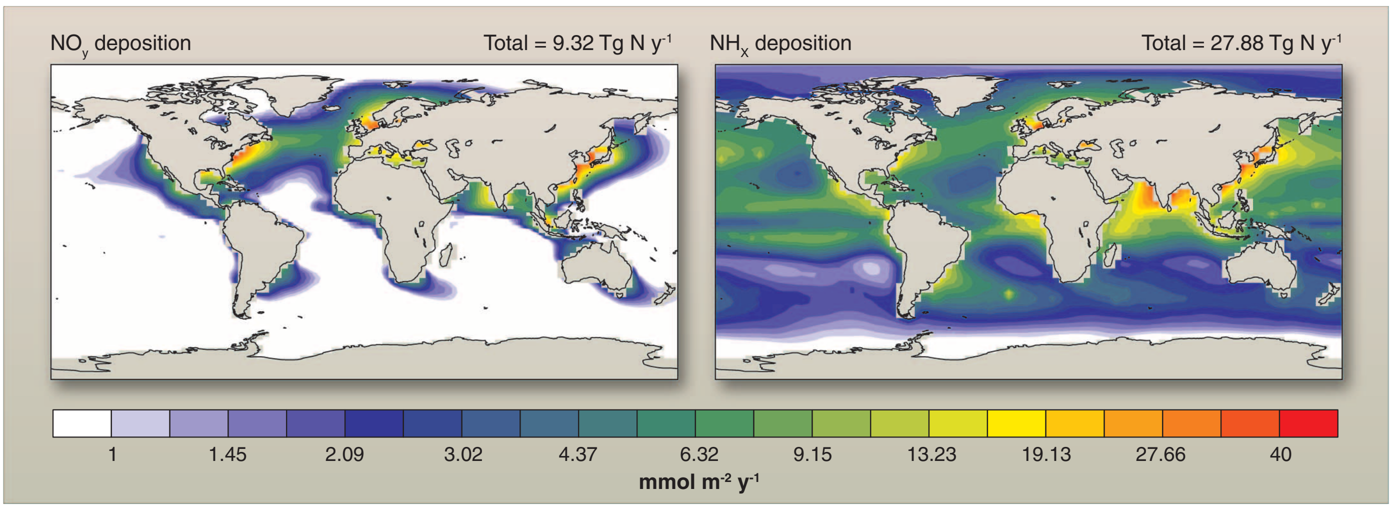

Fig. 3. Model estimated deposition fluxes of anthropogenic reactive nitrogen (mol N m^{-2} $year^{-1}$) to the ocean surface for oxidized forms (NO_y), primarily from fossil fuel combustion sources, and reduced forms (NH_x) primarily from agricultural sources. [Adapted from (*30*)]

rather than O_2 as a terminal electron acceptor for organic matter respiration (denitrification), resulting in reactive nitrogen loss and N_2O production. Toxic hydrogen sulfide (H_2S) production occurs under anoxic (no O_2) conditions. The organic matter respiration that generates hypoxia also elevates CO_2, thus leading to coupled deoxygenation and ocean acidification in a future warmer, high-CO_2 world. The synergistic effects of these multiple stressors may magnify the negative physiological and microbial responses beyond the impacts expected for each perturbation considered in isolation (*38*, *39*).

Fertilizer runoff and nitrogen deposition from fossil fuels are driving an expansion in the duration, intensity, and extent of coastal hypoxia, leading to marine habitat degradation and, in extreme cases, extensive fish and invertebrate mortality (*8*, *40*, *41*). About half the global riverine nitrogen input (50 to 80 Tg of N year^{-1}) is anthropogenic in origin (*4*, *42*), and anthropogenic nitrogen deposition is concentrated in coastal waters downwind of industrial and intensive agricultural regions (*30*). The result is coastal eutrophication and enhanced organic matter production, export, and subsurface decomposition that consumes O_2. Nutrient eutrophication is also associated with increased frequency of harmful algal blooms (*43*).

Worldwide there are now more than 400 coastal hypoxic systems covering an area > 245,000 km^2 (*40*). Population growth and further coastal urbanization will only exacerbate coastal hypoxia without careful land and ocean management. Accelerated hypoxia may also result from climate warming and regional increases in precipitation and runoff that increase water-column vertical stratification; on the other hand, more intense tropical storms could disrupt stratification and increase O_2 ventilation (*8*).

Expanding coastal hypoxia is also induced in some regions by reorganization in ocean-atmosphere physics. Off the Oregon-Washington coast, increased wind-driven upwelling is linked to the first appearance of hypoxia, and even anoxia, on the inner shelf after 5 decades of hypoxia-free conditions (*44*). Further south in the California Current System, the depth of the hypoxic surface has shoaled along the coast by up to 90 m (*45*). The same physical phenomenon, along with the penetration of fossil-fuel CO_2 into off-shore source waters, are introducing waters corrosive to aragonite ($\Omega < 1$) onto the continental shelf (*46*). There is conflicting evidence on how coastal upwelling may respond to climate change, and impacts may vary regionally (*47*).

Extensive deoxygenation is also occurring in the open ocean, most notably in the thermocline of the North Pacific and tropical oceans (*9*, *48*) (Fig. 4). A portion of the observed oxygen change likely reflects decadal variability in ocean circulation, but similar to ocean CO_2 distinct secular trends are apparent at some long-term time series stations (*49*). Models project further reductions of 1 to 7% in the global oxygen inventory and expansions of open-ocean oxygen minimum zones over the 21st century from decreased solubility in warmer waters and slower ventilation rates (*50*).

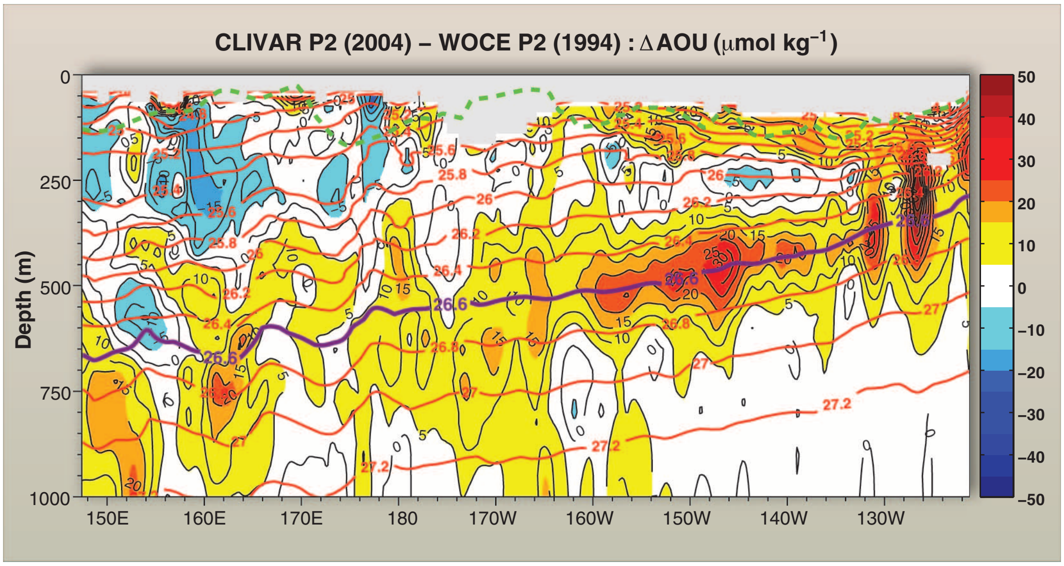

Fig. 4. Decadal change in subsurface O_2 from 1994 to 2004 along 30°N in the North Pacific with positive values indicating an increase in apparent oxygen utilization (AOU) and a decline in O_2 (μmol kg^{-1}); contour plot is overlaid by mixed-layer depths (green line) and potential density surfaces (pink) (*48*). The large AOU increase on the 26.6 potential density anomaly surface (purple line) is a combination of a decadal-time-scale ventilation cycle in the North Pacific and a smaller deoxygenation trend estimated to be about 5 μmol kg^{-1} decade^{-1}) (*48*, *49*). CLIVAR, Climate Variability and Predictability Program; WOCE, World Ocean Circulation Experiment.

The Global Spread of Industrial Pollutants

Points sources of pollution from industrial discharges and oil spills are often highly visible and destructive to the local and regional marine environment (*51*). Perhaps less well known is the global spread of industrial pollutants into what otherwise would appear to be pristine environments. Elevated oceanic levels of persistent organic pollutants (*10*) and methyl mercury, a highly toxic organic form (*11*), raise serious concerns for marine ecosystem health and, potentially, human health through the consumption of contaminated seafood. Many organic and organo-metallic compounds bioaccumulate in the fatty tissues of marine organisms at levels orders of magnitude higher than ambient seawater concentrations. Such pollutants are passed up the food chain and are most concentrated in marine organisms at the higher trophic levels including predatory fish, marine mammals, and seabirds.

Key factors in determining overall biological impacts for a particular pollutant are source magnitudes and locations, physical and biological transport pathways, toxicity, and persistence in the environment. Pollutants exhibit elevated levels near local point sources and in coastal and open-ocean waters because of atmospheric deposition downwind of industrial regions (e.g., western Pacific near East Asia and North Atlantic near North America and Western Europe) (*17*, *52*) (Fig. 3). However, they are also distributed globally, found in even the most remote marine locations, transported through the atmosphere in the vapor phase, aerosols, and soot particles (i.e., black carbon); by ocean currents; and in some cases by migrating animals (*53*).

Elemental mercury (Hg^0), the main chemical form in the ocean, is transformed into the more toxic methyl mercury form by microbes, particularly in reduced environments such as coastal sediments and perhaps oxygen minimum zones (*11*). Although mercury distributions are poorly characterized from direct seawater measurements, time histories reconstructed from numerical models (*17*) and biological samples (e.g., seabird feathers) indicate increasing trends over the 20th century (*11*). It is encouraging that, after the phaseout of leaded gasoline in

North America that began in the mid-1970s, the high levels of anthropogenic lead observed in the North Atlantic declined sharply and are now comparable to those occurring at the beginning of the 20th century (*12*).

Some persistent organic pollutants are synthetic and did not exist in nature before industrial manufacture. Production for some organic pollutants peaked in developed nations in the mid- to late 20th century but is continuing to grow in the developing world. Commonly measured synthetic contaminants include pesticides like DDT, polychlorinated biphenyls, and brominated flame retardants such as polybrominated diphenyl ethers. However, there are many more organic compounds synthesized and used that presumably exist in the ocean but that have not been detected (*54*).

Human activities have also increased levels of naturally occurring compounds such as polycyclic aromatic hydrocarbons, which have sources from petroleum spills and natural oil seeps as well as, primarily, incomplete combustion from wildfires, biomass burning, and fossil fuels (*55*). In a study on the Gulf of Maine downwind of the Northeast United States, another combustion product, black carbon, contributed up to 20% of the total particulate organic carbon in seawater and about half of the "molecularly uncharacterized" fraction (*56*). Environmental samples often contain organic compounds similar in chemical structure to known pollutants but which may be biosynthesized natural products; compound-specific radiocarbon analysis is emerging as a powerful tool for distinguishing between natural and industrial sources (*10*).

Future Research Directions

A deeper understanding of human impacts on ocean biogeochemistry is essential if the scientific community is to provide appropriate and timely information to the public and decision-makers on pressing environmental questions. Although some progress has been made on a nascent ocean observing system for CO_2 (*57*), the marine environment remains woefully undersampled for most compounds. The oceanographic community needs to develop a coordinated observational plan that takes better advantage of in situ autonomous sensors and observation platforms (*58*). Monitoring efforts should be paired with laboratory and field process studies to better elucidate the biological effects of changing chemistry at organism, population, and ecosystem levels.

In particular, more detailed biochemical, system biology, and genomic studies are required to explain mechanistically the responses of cells and organism to external perturbations, supplementing what have often been to date more phenomenological findings. Genomic and physiological research should be embedded in large-scale ecological and biogeochemical spatial surveys and time series to facilitate scaling to ecosystems (*59*). Further work is needed across scales exploring possible synergistic effects among multiple stressors and to assess the potential for biological acclimation and adaptation to human perturbations over decadal to centennial time scales. Lastly, targeted research is needed on the impacts on marine resources and fisheries, potential adaptation strategies, and the consequences for human social and economic systems (*60*).

References and Notes

1. W. H. Schlesinger, *Biogeochemistry: An Analysis of Global Change* (Academic Press, San Diego, CA, 1997).
2. J. L. Sarmiento, N. Gruber, *Ocean Biogeochemical Dynamics* (Princeton Univ. Press, Princeton, NJ, 2006).
3. C. Le Quéré *et al.*, *Nat. Geosci.* **2**, 831 (2009).
4. J. N. Galloway *et al.*, *Biogeochemistry* **70**, 153 (2004).
5. S. D. Donner, C. J. Kucharik, *Proc. Natl. Acad. Sci. U.S.A.* **105**, 4513 (2008).
6. C. L. Sabine *et al.*, *Science* **305**, 367 (2004).
7. R. A. Duce *et al.*, *Science* **320**, 893 (2008).
8. N. N. Rabalais *et al.*, *Biogeoscience* **7**, 589 (2010).
9. R. F. Keeling, A. Körtzinger, N. Gruber, *Annu. Rev. Mar. Sci.* **2**, 199 (2010).
10. C. M. Reddy, J. J. Stegeman, M. E. Hahn, in *Oceans and Human Health: Risks and Remedies from the Seas*, P. J. Walsh, S. L. Smith, H. M. Solo-Gabriele, W. H. Gerwick, Eds. (Academic Press, Burlington, MA, 2008), pp. 121–141.
11. W. F. Fitzgerald, C. H. Lamborg, C. R. Hammerschmidt, *Chem. Rev.* **107**, 641 (2007).
12. A. E. Kelly, M. K. Reuer, N. F. Goodkin, E. A. Boyle, *Earth Planet. Sci. Lett.* **283**, 93 (2009).
13. A. W. Schroth, J. Crusius, E. R. Sholkovitz, B. C. Bostick, *Nat. Geosci.* **2**, 337 (2009).
14. M. J. R. Fasham, Ed., *Ocean Biogeochemistry* (Springer, New York, 2003).
15. National Oceanic and Atmospheric Administration Earth System Research Laboratory, www.esrl.noaa.gov/gmd/ccgg/trends/.
16. E. M. Bennett, S. R. Carpenter, N. F. Caraco, *Bioscience* **51**, 227 (2001).
17. N. E. Selin *et al.*, *Global Biogeochem. Cycles* **22**, GB2011 (2008).
18. S. Solomon *et al.*, in *Climate Change 2007: The Physical Science Basis. Contribution of Working Group I to the Fourth Assessment Report of the Intergovernmental Panel on Climate Change*, S. Solomon *et al.*, Eds. (Cambridge Univ. Press, Cambridge, 2007), pp. 19–91.
19. C. Le Quéré *et al.*, *Science* **316**, 1735 (2007); published online 17 May 2007 (10.1126/science.1136188).
20. C. L. Sabine, T. Tanhua, *Annu. Rev. Mar. Sci.* **2**, 175 (2010).
21. P. Friedlingstein *et al.*, *J. Clim.* **19**, 3337 (2006).
22. J. L. Russell, K. W. Dixon, A. Gnanadesikan, R. J. Stouffer, J. R. Toggweiler, *J. Clim.* **19**, 6382 (2006).
23. N. S. Lovenduski, N. Gruber, S. C. Doney, *Global Biogeochem. Cycles* **22**, GB3016 (2008).
24. A. J. Watson *et al.*, *Science* **326**, 1391 (2009).
25. S. C. Doney, V. J. Fabry, R. A. Feely, J. A. Kleypas, *Annu. Rev. Mar. Sci.* **1**, 169 (2009).
26. J. E. Dore, R. Lukas, D. W. Sadler, M. J. Church, D. M. Karl, *Proc. Natl. Acad. Sci. U.S.A.* **106**, 12235 (2009).
27. R. H. Byrne, S. Mecking, R. A. Feely, X. Liu, *Geophys. Res. Lett.* **37**, L02601 (2010).
28. J. C. Orr *et al.*, *Nature* **437**, 681 (2005).
29. M. Steinacher, F. Joos, T. L. Frölicher, G.-K. Plattner, S. C. Doney, *Biogeoscience* **6**, 515 (2009).
30. S. C. Doney *et al.*, *Proc. Natl. Acad. Sci. U.S.A.* **104**, 14580 (2007).
31. L. R. Kump, T. J. Bralower, A. Ridgwell, *Oceanography* **22**, 94 (2009).
32. J. Silverman, B. Lazar, L. Cao, K. Caldeira, J. Erez, *Geophys. Res. Lett.* **36**, L05606 (2009).
33. M. J. Behrenfeld *et al.*, *Nature* **444**, 752 (2006).
34. M. Steinacher *et al.*, *Biogeoscience* **7**, 979 (2010).
35. S. A. Henson *et al.*, *Biogeoscience* **7**, 621 (2010).
36. C. Luo *et al.*, *Global Biogeochem. Cycles* **22**, GB1012 (2008).
37. A. Krishnamurthy *et al.*, *Global Biogeochem. Cycles* **23**, GB3016 (2009).
38. H. O. Pörtner, A. P. Farrell, *Science* **322**, 690 (2008).
39. P. G. Brewer, E. T. Peltzer, *Science* **324**, 347 (2009).
40. R. J. Diaz, R. Rosenberg, *Science* **321**, 926 (2008).
41. L. A. Levin *et al.*, *Biogeosciences* **6**, 2063 (2009).
42. S. P. Seitzinger, J. A. Harrison, E. Dumont, A. H. W. Beusen, A. F. Bouwman, *Global Biogeochem. Cycles* **19**, GB4S01 (2005).
43. D. M. Anderson, P. M. Glibert, J. M. Burkholder, *Estuaries* **25**, 704 (2002).
44. F. Chan *et al.*, *Science* **319**, 920 (2008).
45. S. J. Bograd *et al.*, *Geophys. Res. Lett.* **35**, L12607 (2008).
46. R. A. Feely, C. L. Sabine, J. M. Hernandez-Ayon, D. Ianson, B. Hales, *Science* **320**, 1490 (2008); published online 22 May 2008 (10.1126/science.1155676).
47. A. Bakun, D. B. Field, A. Redondo-Rodriguez, S. J. Weeks, *Glob. Change Biol.* **16**, 1213 (2010).
48. S. Mecking *et al.*, *Global Biogeochem. Cycles* **22**, GB3015 (2008).
49. F. A. Whitney, H. J. Freeland, M. Robert, *Prog. Oceanogr.* **75**, 179 (2007).
50. T. L. Frölicher, F. Joos, G.-K. Plattner, M. Steinacher, S. C. Doney, *Global Biogeochem. Cycles* **23**, GB1003 (2009).
51. National Research Council, *Oil in the Sea: Inputs, Fates and Effects* (National Academies Press, Washington, DC, 2003).
52. H. von Waldow, M. Macleod, M. Scheringer, K. Hungerbühler, *Environ. Sci. Technol.* **44**, 2791 (2010).
53. R. W. Macdonald *et al.*, *Sci. Total Environ.* **254**, 93 (2000).
54. P. H. Howard, D. C. G. Muir, *Environ. Sci. Technol.* **44**, 2277 (2010).
55. A. L. C. Lima, J. W. Farrington, C. M. Reddy, *Environ. Forensics* **6**, 109 (2005).
56. D. X. Flores-Cervantes, D. L. Plata, J. K. MacFarlane, C. M. Reddy, P. M. Gschwend, *Mar. Chem.* **113**, 172 (2009).
57. S. C. Doney *et al.*, *Deep Sea Res. Part II Top. Stud. Oceanogr.* **56**, 504 (2009).
58. K. S. Johnson *et al.*, *Oceanography* **22**, 217 (2009).
59. S. C. Doney, M. R. Abbott, J. J. Cullen, D. M. Karl, L. Rothstein, *Front. Ecol. Environ.* **2**, 457 (2004).
60. S. R. Cooley, S. C. Doney, *Environ. Res. Lett.* **4**, 024007 (2009).

61. This work was supported by the Center for Microbial Oceanography, Research and Education (C-MORE) (NSF grant EF-0424599) and the W. Van Alan Clark, Sr. Chair for Excellence in Oceanography from the Woods Hole Oceanographic Institution. I thank J. Dore for Fig. 2, I. Lima for Fig. 3, S. Mecking for Fig. 4, and C. Reddy and C. Lamborg for discussions on ocean pollutants.

10.1126/science.1185198

REVIEW

Sea-Level Rise and Its Impact on Coastal Zones

Robert J. Nicholls[1*] and Anny Cazenave[2*]

Global sea levels have risen through the 20th century. These rises will almost certainly accelerate through the 21st century and beyond because of global warming, but their magnitude remains uncertain. Key uncertainties include the possible role of the Greenland and West Antarctic ice sheets and the amplitude of regional changes in sea level. In many areas, nonclimatic components of relative sea-level change (mainly subsidence) can also be locally appreciable. Although the impacts of sea-level rise are potentially large, the application and success of adaptation are large uncertainties that require more assessment and consideration.

The Fourth Assessment Report (AR4) of the Intergovernmental Panel on Climate Change (IPCC) projected that global sea level will rise by up to ~60 cm by 2100 in response to ocean warming and glaciers melting (*1*). However, the recently identified accelerated decline of polar ice sheet mass (*2*–*5*) raises the possibility of future sea-level rise (SLR) of 1 m or more by 2100 (*6*, *7*). Today, low-elevation coastal zones below 10-m elevation contain ~10% of the world population (*8*). Here, non–climate-related anthropogenic processes (such as ground subsidence due to oil and groundwater extraction, or reduced sediment supply to river deltas caused by dam building) often amplify local vulnerability associated with climate-related SLR. The extent of future SLR, the resulting impacts on low-elevation coastal zones, and the ability of society to cope via adaptation remain uncertain. Here, we review current knowledge on the magnitude and causes of contemporary SLR, examine future projections and their uncertainties, and discuss SLR impacts. These impacts are sensitive to how societies prepare for and adapt to SLR.

What Are the Causes of Contemporary Sea-Level Rise?

Although mean sea level remained nearly stable since the end of the last deglaciation [~3000 years ago; e.g., (*9*)], tide gauge measurements available since the late 19th century indicate that sea level has risen by an average of 1.7 ± 0.3 mm/year since 1950 (*10*). Since the early 1990s, SLR has been routinely measured by high-precision altimeter satellites. From 1993 to 2009, the mean rate of SLR amounts to 3.3 ± 0.4 mm/year (Fig. 1) (*11*), suggesting that SLR is accelerating.

Two main factors contribute to SLR: (i) thermal expansion of sea water due to ocean warming and (ii) water mass input from land ice melt and land water reservoirs (*1*). Ocean temperature data collected during the past few decades indicate that ocean thermal expansion has significantly increased during the second half of the 20th century [e.g., (*12*)]. Thermal expansion accounts for about 25% of the observed SLR since 1960 (*13*) and about 50% from 1993 to 2003 (*1*). Since then, upper-ocean warming has been smaller [e.g., (*12*, *14*)], and on average over the satellite altimetry era (1993 to 2009), the contribution of ocean temperature change to the global mean sea level may be ~30% (*15*).

Numerous observations have reported worldwide retreat of glaciers and small ice caps during recent decades, with an appreciable acceleration of this retreat during the 1990s (*1*, *16*). The glacier contribution to SLR from 1993 to 2009 may be ~30% (*1*, *17*). Change in land water storage, due to natural climate variability and human activities (e.g., underground water mining, irrigation, urbanization, and deforestation), contributes little (<10%) to current sea-level change (*18*). By contrast, intensive dam building along rivers during the second half of the 20th century lowered sea level by ~ −0.5 mm/year (*19*).

Since the early 1990s, different remote-sensing tools [airborne and satellite radar and laser altimetry; synthetic aperture radar interferometry (InSAR); and, since 2002, space gravimetry from the Gravity Recovery and Climate Experiment (GRACE) mission] have provided good data on the mass balance of the polar ice sheets. These data indicate that Greenland and West Antarctica mass loss is accelerating [e.g., (*2*)]. Between 1993 and 2003, <15% of the global SLR was due to the ice sheets (*1*). However, since about 2003, their contribution has nearly doubled (*3*–*5*, *20*); increasing glacier and ice sheet mass loss has compensated for reduced ocean thermal

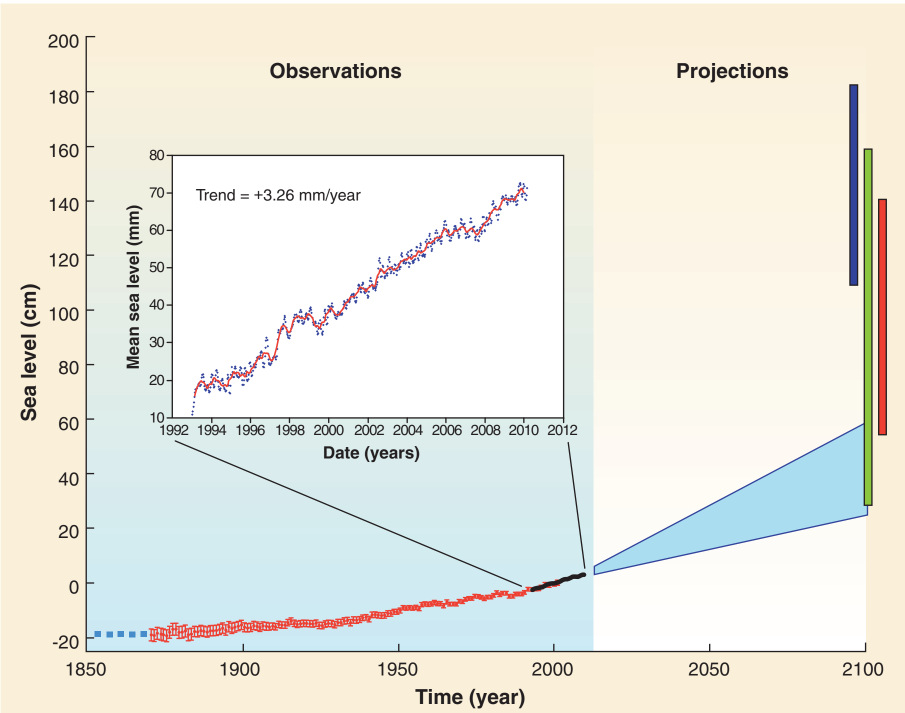

Fig. 1. Global mean sea level evolution over the 20th and 21st centuries. The red curve is based on tide gauge measurements (*10*). The black curve is the altimetry record (zoomed over the 1993–2009 time span) (*15*). Projections for the the 21st century are also shown. The shaded light blue zone represents IPCC AR4 projections for the A1FI greenhouse gas emission scenario. Bars are semi-empirical projections [red bar: (*32*); dark blue bar: (*33*); green bar: (*34*)].

[1]School of Civil Engineering and the Environment and the Tyndall Centre for Climate Change Research, University of Southampton, Southampton SO17 1BJ, UK. [2]Laboratoire d'Etudes en Géophysique et Océanographie Spatiales LEGOS-CNES, Observatoire Midi-Pyrénées, 18 Av. E. Belin, 31401 Toulouse cedex 9, France.

*To whom correspondence should be addressed. E-mail: r.j.nicholls@soton.ac.uk (R.J.N.); anny.cazenave@legos.obs-mip.fr (A.C.)

expansion, such that SLR continues at almost the same rate (Fig. 1). Although not monotonic through time, we estimate that on average over the altimetry era (1993 to 2009), total land ice mass loss explains ~60% of the rate of SLR (*15*).

Accelerated loss of ice sheet mass partly results from rapid outlet glacier flow along some margins of Greenland and West Antarctica where the grounding line is below sea level, and further iceberg discharge into the surrounding ocean [e.g., (*21*–*23*)]. Recent observations suggest that warming of subsurface ocean waters triggers coastal ice discharge (*22*, *24*, *25*). Although surface mass processes (snow accumulation versus surface melting) also contribute to Greenland mass loss (*26*), in West Antarctica mass loss essentially results from ice dynamics [e.g., (*2*, *3*)].

Satellite altimetry shows that sea level is not rising uniformly (Fig. 2). In some regions (e.g., western Pacific), sea level has risen up to three times faster than the global mean since 1993. Spatial patterns in sea-level trends mainly result from nonuniform ocean warming and salinity variations (*1*, *27*), although other factors also contribute, including the solid Earth response to the last deglaciation and gravitational effects and changes in ocean circulation due to ongoing land ice melting and freshwater input (*28*, *29*). Spatial patterns in ocean thermal expansion are not permanent features: They fluctuate in space and time in response to natural perturbations of the climate system (*1*); as a result, we expect that the sea-level change patterns will oscillate on multidecadal time scales. IPCC AR4 projections suggest appreciable regional variability around the future global mean rise by 2100 in response to nonuniform future ocean warming (*1*), but agreement between the models is poor. However, accurate estimates of future regional sea-level changes are required for coastal impact and adaptation assessment.

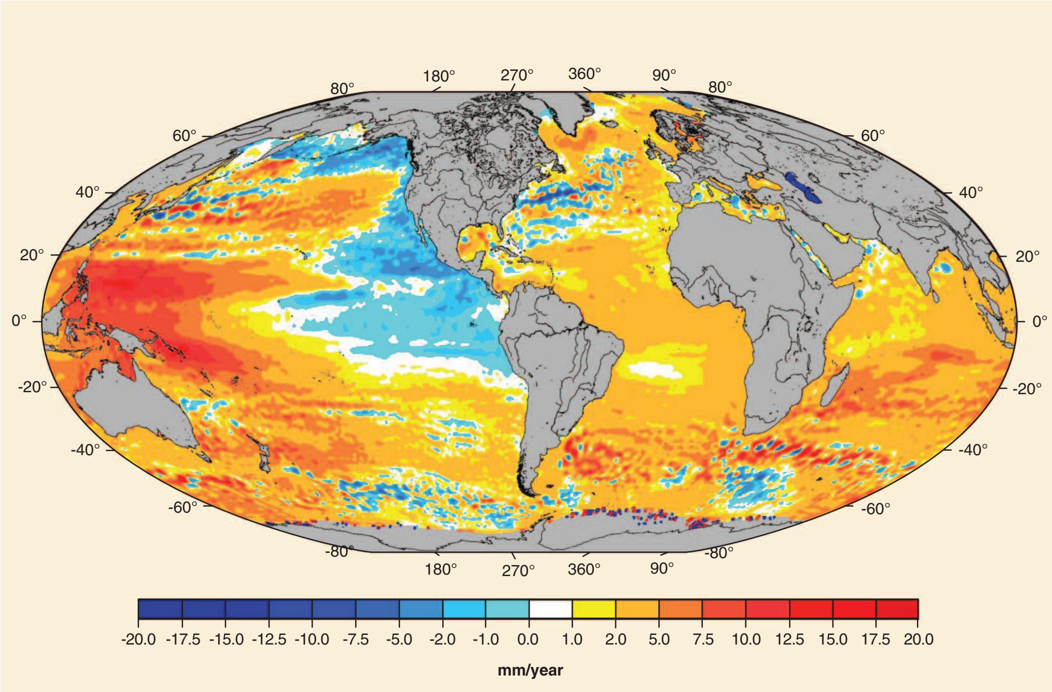

Fig. 2. Regional sea-level trends from satellite altimetry (Topex/Poseidon, Jason-1&2, GFO, ERS-1&2, and Envisat missions) for the period October 1992 to July 2009 (*48*).

How Much Will Global Sea-Level Rise in the 21st Century?

The rapid changes observed in polar regions suggest that the ice sheets respond to current warming on much shorter time scales than previously anticipated [e.g., (*1*)]. However, it is unknown whether these processes will continue into the future, resulting in a partial collapse of the ice sheets after a few centuries, or whether a new equilibrium will be reached (*30*, *31*). For the near term (next decades), the largest unknown in future SLR is the behavior of the ice sheets. Although IPCC AR4 projections did not account for dynamical changes of large ice sheets, simple kinematics and observations of current velocities of marine-terminated glaciers in Greenland and West Antarctica suggest that future ice-dynamics discharge could lead to SLR of about 80 cm by 2100 (*6*). Several groups have developed semi-empirical approaches in which a simple relation between past sea-level rate and temperature or radiative forcing is determined, and then extrapolated through the 21st century using IPCC temperature or forcing projections [e.g., (*32*–*34*)]. Depending on some model variants, these studies yield SLR between ~30 and 180 cm by 2100 (Fig. 1). The upper limit of these estimates is well above IPCC AR4 SLR projections [of ~60 cm for the business-as-usual A1FI greenhouse gas emissions scenario (*1*)].

What Are the Main Impacts of Sea-Level Rise?

The physical impacts of SLR are well known (*35*). The immediate effect is submergence and increased flooding of coastal land, as well as saltwater intrusion of surface waters. Longer-term effects also occur as the coast adjusts to the new conditions, including increased erosion and saltwater intrusion into groundwater. Coastal wetlands such as saltmarshes and mangroves will also decline unless they have a sufficient sediment supply to keep pace with SLR. These physical impacts in turn have both direct and indirect socioeconomic impacts, which appear to be overwhelmingly negative (*35*). Although climate-induced SLR is important, coastal impacts also result from relative (or local) SLR (e.g., from geological processes such as subsidence). For example, relative sea level is presently falling where land is uplifting considerably, such as the northern Baltic and Hudson Bay—the sites of large (kilometer-thick) glaciers during the last glacial maximum. In contrast, relative sea level is rising more rapidly than climate-induced trends on subsiding coasts. In many regions, human activities are exacerbating subsidence on susceptible coasts, including most river deltas [e.g., the Ganges-Brahmaputra, Mekong, and Changjiang deltas (*36*, *37*)]. The most dramatic subsidence effects have been caused by drainage and groundwater fluid withdrawal; over the 20th century, coasts have subsided by up to 5 m in Tokyo, 3 m in Shanghai, and 2 m in Bangkok (*38*). To avoid submergence and/or frequent flooding, these cities now all depend on a substantial flood defense and water management infrastructure. South of Bangkok, subsidence has led to substantial shoreline retreat of more than 1 km, leaving telegraph poles standing in the sea.

These and other human-induced changes in coastal areas (such as coastal defenses, destruction of wetlands, port and harbor works, and reduced sediment supply due to dams) obscure the impacts of climate-induced SLR during the 20th century (*39*, *40*). The nonclimate components of SLR receive much less attention than climate components, because they are considered a local issue. However, they are so widespread that they amount to a global problem warranting more systematic

study, including appropriate mitigation (of human influence) as well as adaptation options.

As the magnitude of climate-induced SLR increases, the impacts will become more apparent (*35*), especially in certain low-elevation coastal zones (Fig. 3). Most countries in South, Southeast, and East Asia appear to be highly threatened because of the widespread occurrence of densely populated deltas, often associated with large growing cities (Fig. 3). Africa also appears highly threatened owing to the low levels of development combined with expectations of rapid population growth in coastal area: Egypt and Mozambique are two "hot-spots" for potential impacts. However, the small island states experience the largest relative increase in impacts, including regions of high islands like the Caribbean. Low islands such as the Maldives or Tuvalu face the real prospect of submergence and complete abandonment during the 21st century (*41*).

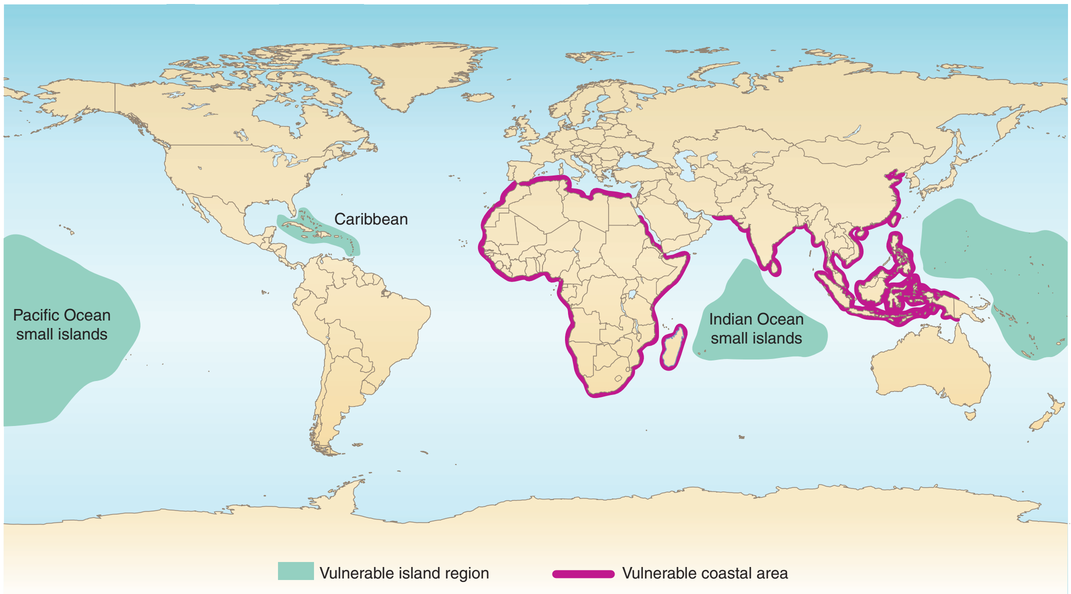

Fig. 3. Several regions are vulnerable to coastal flooding caused by future relative or climate-induced sea-level rise. At highest risk are coastal zones with dense populations, low elevations, appreciable rates of subsidence, and/or inadequate adaptive capacity.

Can Adaptation Help?

Many impact studies do not consider adaptation, and hence determine worst-case impacts [e.g., (*42*)]. Yet, the history of the human relationship with the coast is one of an increasing capacity to adapt to adverse change [e.g., (*43*)]. In addition, the world's populated coasts became increasingly managed and engineered over the 20th century (*35*). The subsiding cities discussed above all remain protected to date, despite large relative SLR. Analysis based on benefit-cost methods show that protection would be widespread as well-populated coastal areas have a high value and actual impacts would only be a small fraction of the potential impacts [e.g., (*44*)], even assuming high-SLR (>1 m/century) scenarios (*45*). This suggests that the common assumption of a widespread forced retreat from the shore in the face of SLR is not inevitable. In many densely populated coastal areas, communities advanced the coast seaward via land claim owing to the high value of land (e.g., Singapore). Yet, protection often attracts new development in low-lying areas, which may not be desirable, and coastal defense failures have occurred, such as New Orleans in 2005. Hence, we must choose between protection, accommodation, and planned retreat adaptation options (*35*). This choice is both technical and sociopolitical, addressing which measures are desirable, affordable, and sustainable in the long term. Adaptation remains a major uncertainty concerning the actual impacts of SLR.

In one of the few strategic plans to respond to SLR, the Netherlands is planning to upgrade protection both for SLR and to provide higher levels of safety (to a nominal chance of failure of 1 in 100,000) by building their North Sea coast seaward using beach nourishment (*46*). The plan stresses how adaptation to SLR must be integrated into wider coastal management and development plans. It also explicitly recognizes that adaptation will continue beyond 2100 (*35*). In most developing countries, the issues are more challenging, and the limits to adaptive capacity will be a key constraint. National development plans will need to address the growing risks of coastal occupancy and identify the most appropriate approaches to coastal management.

Outlook

The extent of future SLR remains highly uncertain—more so than in 2007, when the IPCC AR4 was published. A two-track solution is required to advance the scientific understanding of observed and future climate-induced SLR and develop pragmatic impact and adaptation scenarios that capture the uncertainties of future SLR. The former analysis should focus on understanding the processes that control SLR (e.g., ice sheet instabilities), whereas the latter analysis requires a range of plausible scenarios, including the low probability–high consequence part of the possible SLR range where our understanding is weaker (*7*). More attention must also focus on the nonclimate components of SLR, especially for coasts more susceptible to subsidence, such as deltas. Nonclimate processes tend to be larger where there are high concentrations of people and economic activity, and hence have a high impact potential.

The impacts of SLR can also be divided into two distinct issues: impacts for climate policy, which usually focus on the effects of climate-induced SLR and the incremental benefits of different climate mitigation policies, and impacts for coastal management policy, which must consider all relevant climate and nonclimate coastal drivers. An improved understanding of adaptation is fundamental, because it is one of the biggest determinants of actual rather than potential impacts. Studies such as the World Bank assessment of adaptation costs in developing countries (*47*) are useful starting points to address these problems.

References and Notes

1. IPCC, *Climate Change 2007: The Physical Science Basis, Contribution of Working Group I to the Fourth Assessment Report of the Intergovernmental Panel on Climate Change*, S. Solomon *et al.*, Eds. (Cambridge Univ. Press, Cambridge, 2007).
2. I. Allison, R. B. Alley, H. A. Fricker, R. H. Thomas, R. C. Warner, *Antarct. Sci.* **21**, 413 (2009).
3. E. Rignot *et al.*, *Nat. Geosci.* **1**, 106 (2008).
4. E. Rignot, J. E. Box, E. Burgess, E. Hanna, *Geophys. Res. Lett.* **35**, L20502 (2008).
5. I. Velicogna, *Geophys. Res. Lett.* **36**, L19503 (2009).
6. W. T. Pfeffer, J. T. Harper, S. O'Neel, *Science* **321**, 1340 (2008).
7. J. A. Lowe *et al.*, *UK Climate Projections Science Report: Marine and Coastal Projections* (Met Office Hadley Centre, Exeter, UK, 2009).
8. G. McGranahan, D. Balk, B. Anderson, *Environ. Urban.* **19**, 17 (2007).
9. K. Lambeck, Y. Yokoyama, T. Purcell, *Quat. Sci. Rev.* **21**, 343 (2002).
10. J. A. Church, N. J. White, *Geophys. Res. Lett.* **33**, L01602 (2006).
11. M. Ablain, A. Cazenave, G. Valladeau, S. Guinehut, *Ocean Sci.* **5**, 193 (2009).
12. S. Levitus *et al.*, *Geophys. Res. Lett.* **36**, L07608 (2009).
13. C. Dominguez *et al.*, *Nature* **453**, 1090 (2008).
14. E. W. Leuliette, L. Miller, *Geophys. Res. Lett.* **36**, L04608 (2009).

15. A. Cazenave, W. Llovel, *Annu. Rev. Mar. Sci.* **2**, 145 (2010).
16. M. F. Meier *et al.*, *Science* **317**, 1064 (2007).
17. J. G. Cogley, *Ann. Glaciol.* **50**, 96 (2009).
18. P. C. D. Milly *et al.*, *Understanding Sea Level Rise and Vulnerability*, J.A. Church *et al.*, Eds. (Blackwell, New York, 2010).
19. B. F. Chao, Y. H. Wu, Y. S. Li, *Science* **320**, 212 (2008).
20. J. L. Chen, C. R. Wilson, D. Blankenship, B. D. Tapley, *Nat. Geosci.* **2**, 859 (2009).
21. I. M. Howat, I. R. Joughin, T. A. Scambos, *Science* **315**, 1559 (2007).
22. D. Holland, R. H. Thomas, B. de Young, M. H. Ribergaard, B. Lyberth, *Nat. Geosci.* **1**, 659 (2008).
23. H. Pritchard, R. J. Arthern, D. G. Vaughan, L. A. Edwards, *Nature* **461**, 971 (2010).
24. E. K. Rignot, M. Koppes, I. Velicogna, *Nat. Geosci.* **3**, 187 (2010).
25. F. Straneo *et al.*, *Nat. Geosci.* **3**, 182 (2010).
26. M. van den Broeke *et al.*, *Science* **326**, 984 (2009).
27. C. Wunsch, R. M. Ponte, P. Heimbach, *J. Clim.* **20**, 5889 (2007).
28. G. Milne, W. R. Gehrels, C. W. Hughes, M. E. Tamisiea, *Nat. Geosci.* **2**, 471 (2009).
29. D. Stammer, *J. Geophys. Res.* **113**, C06022 (2008).
30. D. Vaughan, *Clim. Change* **91**, 65 (2008).
31. D. Notz, *Proc. Natl. Acad. Sci. U.S.A.* **106**, 20590 (2009).
32. S. Rahmstorf, *Science* **315**, 368 (2007).
33. M. Vermeer, S. Rahmstorf, *Proc. Natl. Acad. Sci. U.S.A.* **106**, 21527 (2009).
34. A. Grinsted, J. C. Moore, S. Jevrejeva, *Clim. Dyn.* **34**, 461 (2009).
35. R. J. Nicholls *et al.*, in *Climate Change 2007: Impacts, Adaptation and Vulnerability. Contribution of Working Group II to the Fourth Assessment Report of the Intergovermental Panel on Climate Change*, M. L. Parry *et al.*, Eds. (Cambridge Univ. Press, Cambridge, 2007).
36. J. P. Ericson, C. Vorosmarty, S. Dingman, L. Ward, M. Meybeck, *Global Planet. Change* **50**, 63 (2006).
37. J. P. M. Syvitski *et al.*, *Nat. Geosci.* **2**, 681 (2009).
38. R. J. Nicholls *et al.*, *Ranking Port Cities with High Exposure and Vulnerability to Climate Extremes: Exposure Estimates. Environment Working Papers No. 1* (Organization for Economic Co-Operation and Development, Paris, 2008).
39. R. J. Nicholls, P. P. Wong, V. Burkett, C. D. Woodroffe, J. Hay, *Sustainability Sci.* **3**, 89 (2008).
40. R. J. Nicholls, C. D. Woodroffe, V. R. Burkett, in *Climate Change: Observed Impacts on Planet Earth*, T. M. Letcher, Ed. (Elsevier, Oxford, 2009), pp. 409–424.
41. N. L. Mimura *et al.*, in *Climate Change 2007: Impacts, Adaptation and Vulnerability. Contribution of Working Group II to the Fourth Assessment Report of the Intergovernmental Panel on Climate Change*, M. L. Parry *et al.*, Eds. (Cambridge Univ. Press, Cambridge, 2007).
42. S. Dasgupta, B. Laplante, C. Meisner, D. Wheeler, J. Yan, *Clim. Change* **93**, 379 (2009).
43. M. VanKoningsveld, J. P. M. Mulder, M. J. F. Stive, L. VanDerValk, A. W. VanDerWeck, *J. Coast. Res.* **24**, 367 (2008).
44. M. Sugiyama *et al.*, *Estimating the Economic Cost of Sea-Level Rise. MIT Global Change Joint Program Publications, Report 156* (Massachusetts Institute of Technology, Cambridge, MA, 2008).
45. R. J. Nicholls, R. S. J. Tol, A. T. Vafeidis, *Clim. Change* **91**, 171 (2008).
46. Delta Commission, available at www.deltacommissie.com/doc/deltareport_full.pdf (2008).
47. World Bank, *Economics of Adaptation on Climate Change*, Consultation Draft (World Bank, Washington, DC, 2009).
48. AVISO (Archiving, Validation and Interpretation of Satellite Oceanographic data), available at www.aviso.oceanobs.com/.

10.1126/science.1185782

REVIEW

How Do Polar Marine Ecosystems Respond to Rapid Climate Change?

Oscar Schofield,[1]* Hugh W. Ducklow,[2] Douglas G. Martinson,[3] Michael P. Meredith,[4] Mark A. Moline,[5] William R. Fraser[6]

Climate change will alter marine ecosystems; however, the complexity of the food webs, combined with chronic undersampling, constrains efforts to predict their future and to optimally manage and protect marine resources. Sustained observations at the West Antarctic Peninsula show that in this region, rapid environmental change has coincided with shifts in the food web, from its base up to apex predators. New strategies will be required to gain further insight into how the marine climate system has influenced such changes and how it will do so in the future. Robotic networks, satellites, ships, and instruments mounted on animals and ice will collect data needed to improve numerical models that can then be used to study the future of polar ecosystems as climate change progresses.

How does a changing physical ocean environment affect regional and local marine food webs? Many regions, especially polar seas (*1*, *2*), are experiencing changes in atmospheric/ocean circulation (*3*), ocean properties (*4*, *5*), sea ice cover (*6*, *7*), and ice sheets (*8*, *9*). These rapid climatic changes are triggering pronounced shifts and reorganizations in regional ecosystems and biogeochemical cycles (*10*, *11*). However, it remains difficult to link these ecosystem changes to shifts in the physical system. Overcoming this gap is a critical step in establishing any level of predictive skill.

The West Antarctic Peninsula (WAP), northwestern North America, and the Siberian Plateau are exhibiting rapid regional warming (*1*), but only the WAP has a maritime climate. Thus, the WAP is an ideal location to monitor and understand the impacts of rapid climate change on marine ecosystems. Other regions of Antarctica are exhibiting much smaller rates of warming—and some, such as the Ross Sea (*12*), are even experiencing trends in the opposite direction—but climate models predict strong warming and circumpolar sea ice retreat around Antarctica over the next century (*13*). Understanding the response of the WAP ecosystems to climate change will thus help to predict further changes in the polar ecosystem as a whole and will provide insight into the planetary-scale changes that are likely as greenhouse gas–driven warming continues.

[1]Coastal Ocean Observation Laboratory, Institute of Marine and Coastal Sciences, School of Environmental and Biological Sciences, Rutgers University, New Brunswick, NJ 08901, USA. [2]The Ecosystems Center, Marine Biological Laboratory, Woods Hole, MA 02543, USA. [3]Department of Earth and Environmental Sciences, Columbia University, NY 10964, USA. [4]British Antarctic Survey, Madingley Road, Cambridge CB3 0ET, UK. [5]Biological Sciences Department and Center for Coastal Marine Sciences, California Polytechnic State University, San Luis Obispo, CA 93407, USA. [6]Polar Oceans Research Group, Post Office Box 368, Sheridan, MT 59749, USA.

*To whom correspondence should be addressed. E-mail: oscar@marine.rutgers.edu

Physical Changes in the WAP

Changes in the WAP are profound (Fig. 1). Midwinter surface atmospheric temperatures have increased by 6°C (more than five times the global average) in the past 50 years (*14*, *15*). Eighty-seven percent of the WAP glaciers are in retreat (*16*), the ice season has shortened by nearly 90 days, and perennial sea ice is no longer a feature of this environment (*17*, *18*). These changes are accelerating (*19*, *20*).

Ocean warming has been implicated as a major driver for this deglaciation (*21*). The ocean has become warmer in the WAP (*17*). Most of this heat comes from the warm, saline Upper Circumpolar Deep Water (UCDW) that penetrates onto the WAP shelf from the Antarctic Circumpolar Current (ACC) in the adjacent deep ocean. The increased supply of heat from the UCDW is believed to be associated with the strengthening of winds over the Southern Ocean (*22*, *23*). Enhanced upwelling of heat to the WAP is complemented by rising summertime surface-ocean heating (*24*), which is associated with the strong retreats in the seasonal sea ice cover (*7*, *18*).

This atmosphere–ocean-ice interplay at the WAP results in a positive feedback that amplifies and sustains atmospheric warming. Understanding these feedbacks will require better knowledge of the processes at the shelf edge and in the adjacent deep ocean to determine where and when the UCDW intrudes from the ACC onto the WAP shelf. Although the ACC is a major current in the

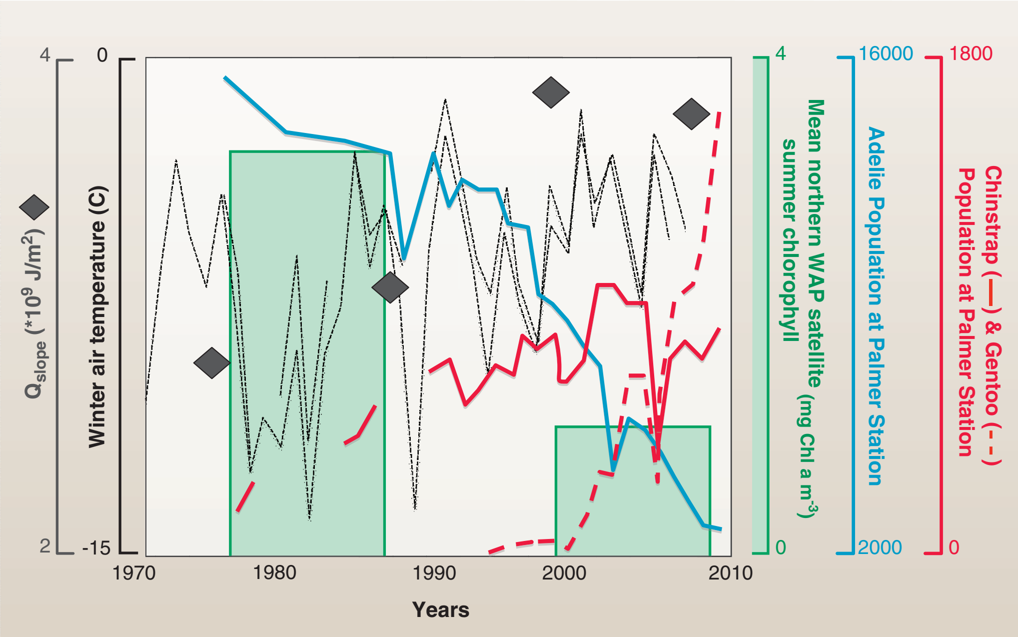

Fig. 1. Changes observed along the WAP over the past 30 years. Annual average air temperatures at Faraday/Vernadsky Station (65°15′S, 64°16′W) and Rothera Station (67°34′S, 68°08′W) have increased. There has been an increase in heat content (relative to freezing) of ACC slope water that had direct access to the WAP continental shelf (black diamonds). Average phytoplankton biomass declined between 1978–1986 and 1998–2006 (between 1987 until 1997, no ocean color satellite imagery was available). There were also large shifts in the penguin populations at Anvers Island from 1975 to 2008.

global ocean circulation system and has undergone substantial warming in recent decades (*25*), coherent sampling of the ACC remains a challenge.

Ecosystem Changes in the WAP

In part because of the heat and nutrients supplied by the UCDW, the WAP hosts an extremely productive marine ecosystem supported by large phytoplankton blooms (*26*). However, over the past 30 years the magnitude of these blooms has decreased by 12% (*27*). The changes have been particularly dramatic in the northern WAP, with declines driven by an increase in cloudy days, deep mixed layers associated with persistently strong winds, and a reduction in the marginal ice zone (*27*). There is evidence that the algal community composition has shifted from large to small cells (*27*, *28*). These changes are not uniform across the Peninsula; areas in the south that were previously mostly covered with ice now have open water, allowing local ocean productivity rates to increase (*27*, *29*). Nevertheless, the net productivity of the WAP appears to have decreased.

The shift in phytoplankton biomass and size has direct consequences for grazer communities, especially Antarctic krill (*Euphausia superba*), which are inefficient at grazing small cells (*30*, *31*). In contrast, tunicates such as the salp (*Salpa thomsoni*) are efficient at grazing the smaller cells. In the WAP, there is evidence that krill are being replaced by salps (*32*, *33*)—a phenomenon that can be magnified over time because salps consume krill eggs and larvae (*34*). The decline in phytoplankton biomass also favors salps, whose filtering apparatus can become clogged when phytoplankton biomass is high (*35*). Lastly, the spawning behavior of Antarctic krill depends on sea ice (*36*). Because krill form a critical trophic link between primary producers and upper-level consumers, the shift in zooplankton community structure suggests that there should be dramatic changes in the higher trophic levels (fish, seals, whales, and penguins and other seabirds) (*37*).

These changes have been documented most dramatically in Antarctic pygoscelid penguins. In the past 30 years in the northern WAP, populations of ice-dependent Adélie penguins (*Pygoscelis adeliae*) have fallen by 90%, whereas those of ice-intolerant Chinstrap (*P. Antarctica*) and Gentoo (*P. papua*) penguins have risen in the northern and mid-Peninsula region (*10*). The latter two species were only recently established at the WAP: The first Chinstraps were observed in 1975, and Gentoos arrived in 1994.

Declines in the polar species have been related to decreasing sea ice cover and its possible effects on prey availability (*10*). Penguins breed in locations with predictably abundant food, allowing them to forage and return to their colonies to feed chicks (*38*). The Adélie penguins breed in locations where deep ocean canyons exist near the land margin; these canyons provide a possible conduit for the warm UCDW to extend to near the land margin (*39*), keeping winter ice low and supporting high primary productivity rates (*26*). The increase in ocean warming has led to lower total ocean productivity and decreased winter sea ice cover, which is a critical habitat for the spawning of krill (*36*) and Antarctic silverfish. Shifts in climate have thus had a cascading effect, with altered sea ice distributions disrupting the evolved life strategies of resident species, leading to changes in community structure and in the abundance of populations, and ultimately altering the nature of local and regional food webs (*40*). These local canyon-associated hot spots provide a singular opportunity to study how global changes that affect the circulation and marine climate in the region of the ACC can ripple through marine food webs. Ecosystem dynamics also reflect top-down effects as many higher trophic levels recover from past whale harvests along the WAP (*41*). The changes along the WAP are just one example of how rapid climate change will affect polar ecosystems, which argues for a polar ocean observational strategy that is capable of studying the interactions and feedbacks between the ocean, the atmosphere, perennial/annual ice, and regional ecosystems.

Toward a New Strategy for Polar Ocean Ecosystem Observation

Cost considerations and the harsh conditions in the polar oceans restrict the coverage that can be provided by research ships. Furthermore, cloud cover is often heavy, hampering remote sensing approaches, whereas sea ice and icebergs make it difficult to deploy surface ocean moorings. To overcome these hurdles, the oceanographic community has been developing technologies that may form the foundation for a coherent observational strategy. The strategy will require a nested multiplatform approach that will enable sustained observations throughout the year in the Southern and Arctic oceans.

Key goals for such a strategy will be to quantify a heat budget for the atmosphere and ocean, understand how the deep ocean is interacting with shelf waters, how this flux changes with time, and how this affects regional marine climate, ice dynamics, and ecology. Achieving these goals will require an expanded number of ocean and atmospheric measurements from automated sensors and long-duration profiling floats (Fig. 2A). Profiling floats are very effective at mapping the properties of the deep ocean. They have, for example, documented the warming of the ACC (*25*). These floats cannot sample in ice or in coastal waters and have a limited capacity to carry chemical/biological sensors. So, the floats need

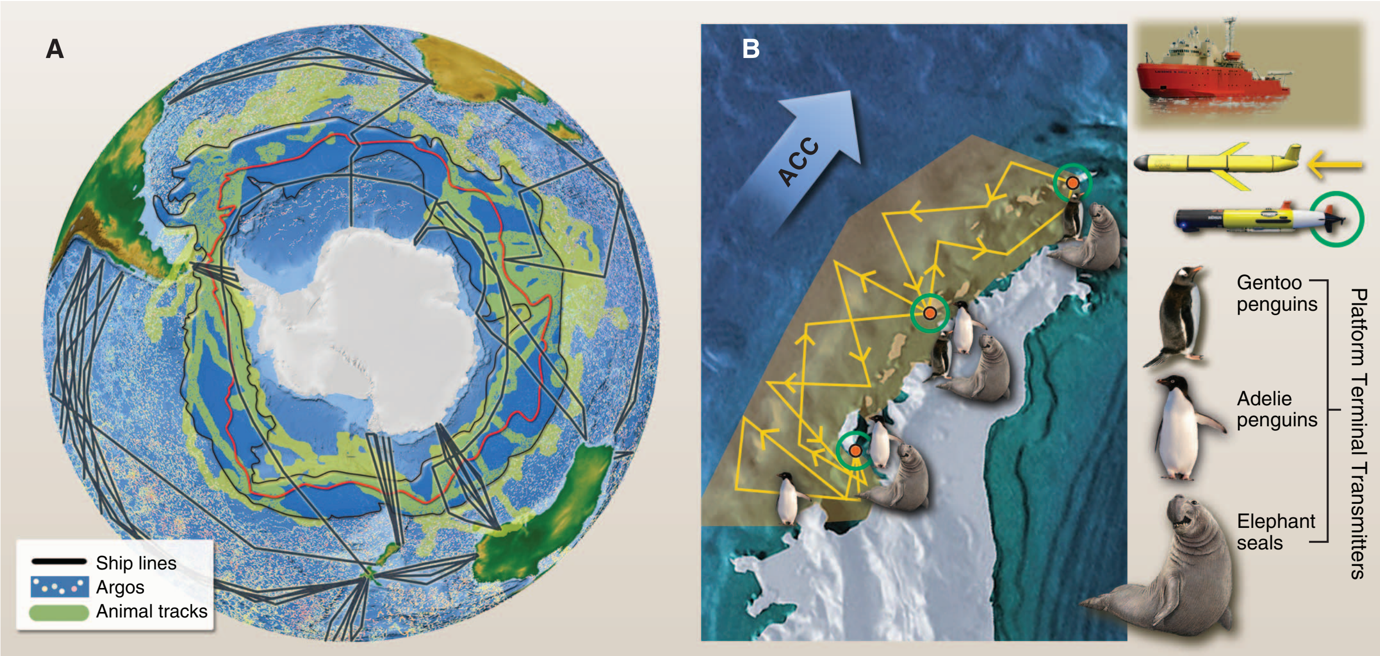

Fig. 2. A potential ocean-observing network for studying the ACC and its role in structuring continental shelf ecosystems. (**A**) The proposed network for studying the ACC (mean current is denoted by a red line, and the bright blue area shows its spatial variability). Hydrography of the ACC will be sampled with profiling floats (colors on the dots indicate individual profiling floats over time) (*25*). Spatial data collected by floats need to be complemented by ships outfitted with automated sensors. Animals (such as whales, seals, and birds) can be outfitted with sensors can also provide spatial data. For example, the bold transparent yellow lines denote the spatial coverage provided by elephant seals [redrawn from data presented in (*43*)]. (**B**) A proposed regional observing network for the West Antarctic Peninsula that could be embedded within the larger ACC-observing network. The system consists of high-resolution sampling conducted by autonomous underwater vehicles and animals outfitted with sensors. These sampling networks will also consist of research vessels and underwater gliders.

to be complemented with data collected by ships through repeat transects or "ships of opportunity" (research vessels, resupply ships, and tourist vessels) that are abundant during the summer months and are increasingly being outfitted with automated sensors that collect atmospheric and ocean data.

Another approach showing promise is the deployment of oceanographic instruments on marine mammals, such as seals, fish, and whales (*42*, *43*). This provides information on animal behavior in relation to oceanographic features and provides vertical profile data to complement the profiling floats. However, instruments deployed on animals can currently only carry a limited set number of sensors; transects by research vessels therefore remain invaluable.

The interaction of the ocean with the cryosphere is a key factor influencing polar marine ecosystems and must be part of any observing system design. Remote sensing techniques can provide regional data on sea ice extent and concentration and have the potential to provide information on sea ice thickness (*44*). In situ measurements are needed to calibrate satellite data and provide detailed local information. For example, ice thickness can be measured with upward-looking sonars, either on fixed moorings to provide time series or on autonomous underwater vehicles for spatial surveys (*45*). Glacial ice also affects the ecosystem response to climate change because glacial ice melt stratify the water column and enhance primary production.

Characterizing how the shifts in the physics alter marine ecosystems is a daunting challenge: Many key species are mobile, requiring sampling networks to span a wide range of spatial and temporal scales. Fortunately, we can prioritize regions to sample by focusing on biological hotspots (*40*, *46*). Many biological hotspots are spatially constrained (~10 to 100 km^2) and distributed throughout polar systems. They are often located near sea mounts, islands, and deep sea canyons that are adjacent to land. The close proximity to land allows a wide range of sampling strategies. Routine shore-based sampling (even during winter) can be augmented with sea-floor cables, which provide high bandwidth and power to sample the benthic communities and the overlying water column (*47*) despite the presence of ice. Time series can then be complemented with spatial data collected by autonomous underwater vehicles and gliders that are capable of providing high-resolution maps of the physics, chemistry, and biology (*48*). Navigation by the mobile platforms would be facilitated by sea floor– and ice-mounted acoustic transponders. Combined, the spatial time series will enable the development of coupled ocean atmosphere–food web numerical models.

Polar Seas in a Changing Climate

The challenges for developing an observing system capable of elucidating the causes and impacts on marine ecosystem changes in polar oceans is not to be underestimated, because these regions are among the harshest in the world. Emerging technology can meet these challenges, because automation will lower the costs associated with ship operations by providing complementary approaches to collecting data. This is fortunate, as there is scientific urgency in deploying such systems given the observed changes in both the Arctic and Southern oceans.

These observational systems will provide insights into potential future ecosystem changes in polar oceans, but their deployment will require international cooperation given the scale of effort required; however, because many of the technologies have been demonstrated to be effective it is not unreasonable to believe that these networks could be deployed in 5 to 10 years. The benefits of better understanding the marine ecosystem, and being better able to predict, protect, and make use of its resources, are strong drivers to make this a reality.

Reference and Notes

1. O. A. Anisimov *et al.*, in *Climate Change 2007: Impacts, Adaptation and Vulnerability. Contribution of Working Group II to the Fourth Assessment Report of the Intergovernmental Panel on Climate Change*, M. L. Parry *et al.*, Eds. (Cambridge Univ. Press, Cambridge, 2007), pp. 655–688.
2. V. Smetacek, S. Nicol, *Nature* **437**, 362 (2005).
3. J. Turner, T. A. Lachlan-Cope, S. Colwell, G. J. Marshall, W. M. Connolley, *Science* **311**, 1914 (2006).
4. S. Häkkinen, P. B. Rhines, *Science* **304**, 555 (2004).

5. M. P. Meredith, J. C. King, *Geophys. Res. Lett.* **32**, L19604 (2005).
6. J. Comiso, C. L. Parkinson, R. Gersten, L. Stock, *Geophys. Res. Lett.* **35**, L01703 (2008).
7. S. E. Stammerjohn, D. Martinson, R. Smith, R. Iannuzzi, *Deep Sea Res. Part II Top. Stud. Oceanogr.* **55**, 2041 (2008).
8. A. J. Cook, A. J. Fox, D. G. Vaughan, J. G. Ferrigno, *Science* **308**, 541 (2005).
9. M. van den Broeke *et al.*, *Science* **326**, 984 (2009).
10. H. W. Ducklow *et al.*, *Philos. Trans. R. Soc.* **362**, 67 (2007).
11. M. A. Moline *et al.*, *Ann. N.Y. Acad. Sci.* **1134**, 267 (2008).
12. J. Turner *et al.*, *Geophys. Res. Lett.* **36**, L08502 (2009).
13. T. J. Bracegirdle, W. M. Connolley, J. Turner, *J. Geophys. Res.* **113**, D03103 (2008).
14. P. Skvarca, W. Rack, H. Rott, T. I. Donángelo, *Polar Res.* **18**, 151 (1999).
15. D. G. Vaughan *et al.*, *Clim. Change* **60**, 243 (2003).
16. A. J. Cook, A. J. Fox, D. G. Vaughan, J. G. Ferrigno, *Science* **308**, 541 (2005).
17. D. G. Martinson, S. Stammerjohn, R. Iannuzzi, R. Smith, M. Vernet, *Deep Sea Res. Part II Top. Stud. Oceanogr.* **55**, 1964 (2008).
18. S. E. Stammerjohn, D. G. Martinson, R. C. Smith, X. Yuan, D. Rind, *J. Geophys. Res.* **113**, C03S90 (2008).
19. E. Rignot *et al.*, *Nat. Geosci.* **1**, 106 (2008).
20. T. A. Scambos *et al.*, *Geophys. Res. Lett.* **31**, L18402 (2003).
21. D. G. Vaughan *et al.*, *Clim. Change* **60**, 243 (2003).
22. D. W. J. Thompson, S. Solomon, *Science* **296**, 895 (2002).
23. G. J. Marshall, *J. Clim.* **16**, 4134 (2003).
24. M. P. Meredith, J. C. King, *Geophys. Res. Lett.* **32**, L19604 (2005).
25. S. T. Gille, *Science* **295**, 1275 (2002).
26. B. B. Prézelin, E. E. Hofmann, M. Moline, J. M. Klinck, *J. Mar. Res.* **62**, 419 (2000).
27. M. Montes-Hugo *et al.*, *Science* **323**, 1470 (2009).
28. M. A. Moline, H. Claustre, T. K. Frazer, O. Schofield, M. Vernet, *Glob. Change Biol.* **10**, 1973 (2004).
29. A. Clarke *et al.*, *Philos. Trans. R. Soc. London Ser. B Biol. Sci.* **362**, 149 (2009).
30. S. McClatchie, C. M. Boyd, *Can. J. Fish. Aquat. Sci.* **40**, 955 (1983).
31. L. B. Quetin, R. M. Ross, in *Antarctic Nutrient Cycles and Food Webs*, W. R. Siegfried *et al.*, Eds. (Springer-Verlag, Berlin, 1985), pp. 372–377.
32. V. Loeb *et al.*, *Nature* **387**, 897 (1997).
33. A. Atkinson, V. Siegel, E. Pakhomov, P. Rothery, *Nature* **432**, 100 (2004).
34. J. Nishikawa *et al.*, *Polar Biol.* **15**, 31 (1995).
35. R. Perissinotto, E. A. Pakhomov, *Mar. Biol.* **131**, 25 (1998).
36. L. B. Quetin, R. M. Ross, *Am. Zool.* **41**, 74 (2001).
37. W. R. Fraser, E. E. Hofmann, *Mar. Ecol. Prog. Ser.* **265**, 1 (2003).
38. W. R. Frazer, W. Z. Trivelpiece, in *Foundations for Ecological Research West of the Antarctic Peninsula*, R. M. Ross *et al.*, Eds. (American Geophysical Union, Washington, DC, 1996), pp. 257–272.
39. J. M. Klinck, E. E. Hofmann, R. C. Beardsley, B. Salihoglu, S. Howard, *Deep Sea Res. Part II Top. Stud. Oceanogr.* **51**, 1925 (2004).
40. O. E. Rhodes, E. P. Odum, in *Population Dynamics in Ecological Space and Time*, O. E. Rhodes *et al.*, Eds. (Univ. of Chicago Press, Chicago, 1996), pp. 1–8.
41. L. Balance *et al.*, in *Whales, Whaling and Ocean Ecosystems*. J. A. Estes *et al.*, Eds. (Univ. of California Press, Berkeley, CA, 2006), pp. 215–230.
42. D. P. Costa, J. Klinck, E. Hofmann, M. Dinniman, J. Burns, *Deep Sea Res. Part II Top. Stud. Oceanogr.* **55**, 323 (2008).
43. M. Biuw *et al.*, *Proc. Natl. Acad. Sci. U.S.A.* **104**, 13705 (2007).
44. A. P. Worby *et al.*, *J. Geophys. Res.* **113**, C05S92 (2008).
45. M. J. Doble, A. L. Forrest, P. Wadhams, B. E. Laval, *Cold Reg. Sci. Technol.* **56**, 90 (2009).
46. R. C. Smith *et al.*, *Oceanography (Wash. D.C.)* **8**, 77 (1995).
47. O. Schofield *et al.*, *J. Oceanic Eng.* **27**, 146 (2002).
48. R. E. Davis *et al.*, in *Technology and Applications of Autonomous Underwater Vehicles*, G. Griffiths, Ed. (Taylor and Francis, London, 2003), pp. 37–58.

49. These efforts were only possible with funding support provided by the National Science Foundation's Office of Polar Programs, the British Antarctic Survey, the Gordon and Betty Moore Foundation, and NASA.

10.1126/science.1185779

REVIEW

The Impact of Climate Change on the World's Marine Ecosystems

Ove Hoegh-Guldberg[1]* and John F. Bruno[1,2]

Marine ecosystems are centrally important to the biology of the planet, yet a comprehensive understanding of how anthropogenic climate change is affecting them has been poorly developed. Recent studies indicate that rapidly rising greenhouse gas concentrations are driving ocean systems toward conditions not seen for millions of years, with an associated risk of fundamental and irreversible ecological transformation. The impacts of anthropogenic climate change so far include decreased ocean productivity, altered food web dynamics, reduced abundance of habitat-forming species, shifting species distributions, and a greater incidence of disease. Although there is considerable uncertainty about the spatial and temporal details, climate change is clearly and fundamentally altering ocean ecosystems. Further change will continue to create enormous challenges and costs for societies worldwide, particularly those in developing countries.

Earth, with its life-filled ocean, is unusual among planets (*1*). Covering 71% of Earth's surface, the ocean nurtured life on our planet and continues to play a dominating role in regulating its climate. Change has been the norm as Earth has swung through a variety of states in which life has prospered, dwindled, or experienced calamitous declines. In the latter case, intrinsic events (e.g., volcanic activity) or extrinsic events (e.g., large meteorite strikes) have sometimes resulted in hostile conditions that have increased extinction rates and driven ecosystem collapse. There is now overwhelming evidence that human activities are driving rapid changes on a scale similar to these past events (*2*). Many of these changes are already occurring within the world's oceans (Figs. 1 and 2), with serious consequences likely over the coming decades.

Our understanding of how climate change is affecting marine ecosystems has lagged behind that of terrestrial ecosystems. This is partly due to the size and complexity of the ocean, but also to the relative difficulty of taking measurements in marine environments. Long-term studies of climate change in the oceans are rare by comparison to those on land (*3*). Here, we review the impacts of anthropogenic climate change on marine ecosystems, revealing that the majority are changing rapidly with an increased risk of sudden nonlinear transformations. Given the overwhelming importance of the ocean to life on our planet, these changes underscore the urgency with which the international community must act to limit further growth of atmospheric greenhouse gases and thereby reduce the serious risks involved.

Rates of Change

Rising atmospheric greenhouse gas concentrations have increased global average temperatures by ~0.2°C per decade over the past 30 years (*4*), with most of this added energy being absorbed by the world's oceans. As a result, the heat content of the upper 700 m of the global ocean has increased by 14×10^{22} J since 1975 (*5*), with the average temperature of the upper layers of the ocean having increased by 0.6°C over the past 100 years (*2*) (Fig. 1, A and B). These changes are ongoing; global ocean surface temperatures in January 2010 were the second warmest on record for the month of January, and the period June to August 2009 reached 0.58°C above the average global temperature recorded for the 20th century, 16.4°C (*6*).

In addition to acting as the planet's heat sink, the oceans have absorbed approximately one-third of the carbon dioxide produced by human activities. The absorption of anthropogenic CO_2 has acidified the surface layers of the ocean, with a

[1]Ocean and Coasts Program, Global Change Institute, University of Queensland, St. Lucia, QLD 4072, Australia. [2]Department of Marine Sciences, University of North Carolina, Chapel Hill, NC 27599, USA.

*To whom correspondence should be addressed. E-mail: oveh@uq.edu.au

steady decrease of 0.02 pH units per decade over the past 30 years and an overall decrease since the pre-industrial period of 0.1 pH units (*7*) (Fig. 1C). Although these increases appear small in terms of pH, they are associated with a substantial decline in the concentration of carbonate ions (Fig. 1D) and represent a major departure from the geochemical conditions that have prevailed in the global ocean for hundreds of thousands if not millions of years (Fig. 1C) (*8*, *9*).

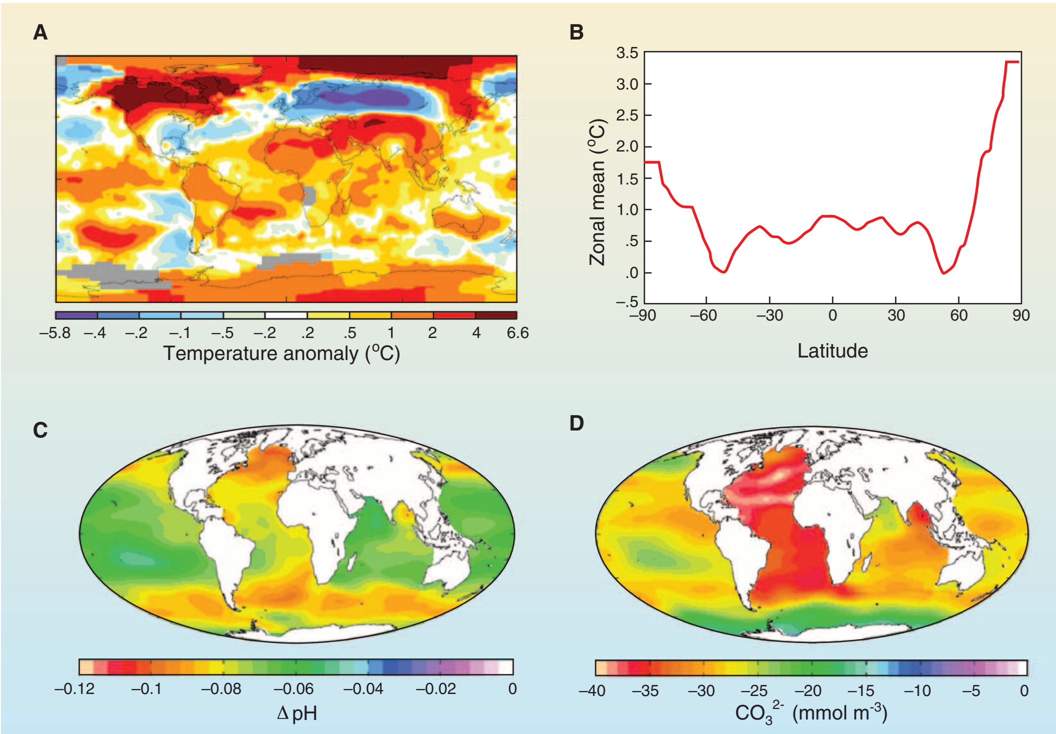

Fig. 1. Recent changes in ocean temperature, acidity, and carbonate ion concentration. (**A**) Surface temperature anomaly for January 2010 relative to the mean for 1951–1980. (**B**) The same data presented in (A) as a function of latitude. (**C**) Estimated change in annual mean sea surface pH between the pre-industrial period (1700s) and the present day (1990s). (**D**) Estimated change in annual mean sea surface carbonate ion concentration between the pre-industrial period (1700s) and the present day (1990s). [Credits: (A) and (B) NASA Goddard Institute for Space Studies; (C) and (D) Global Ocean Data Analysis Project (*57*)]

Increases in the heat content of the ocean have driven other changes. Thermal expansion of the oceans as well as increased meltwater and discharged ice from terrestrial glaciers and ice sheets have increased ocean volume and hence sea level (*10*) (Fig. 2, A and B). Warmer oceans also drive more intense storm systems (*11*) (Fig. 2C) and other changes to the hydrological cycle (*12*). The warming of the upper layers of the ocean also drives greater stratification of the water column, reducing mixing in some parts of the ocean and consequently affecting nutrient availability and primary production. These changes have increased the size of the nutrient-poor "ocean deserts" of the Pacific and Atlantic by 6.6 million km^2, or 15%, over the period 1998 to 2006 (*13*).

General circulation models also predict that oxygen concentrations in the upper layers of the ocean are likely to decrease as a consequence of increasing stratification (*14*); this is supported by recent observations (*15*). There is growing paleological evidence that declining oxygen concentrations have played a major role in at least four or five mass extinction events, driving large amounts of hydrogen sulfide into the atmosphere as a result of deep-ocean anoxia (*16*). In some situations, intensified upwelling resulting from changes in wind strength can lead to a greater flux of organic material into deeper shelf waters, leading to an increase in respiration, hypoxia, and in some cases the eruption of toxic gases such as methane and hydrogen sulfide from deep anoxic sediments (*17*). Changes to wind and ocean currents driven by anthropogenic climate change are consequently likely to interact with overfishing and eutrophication, further increasing the incidence of hypoxic and anoxic events. These events are associated with an increased risk of mass mortalities among some deepwater benthic communities, as has recently been seen along the west coasts of North America (*18*) and southern Africa (*19*).

The uneven distribution of heating (Fig. 1, A and B) also strongly influences the behavior of ocean currents (*20*), which play critical roles in the dynamics, local climates, and biology of the ocean. Slowing of the thermohaline or Meridional Overturning Circulation (MOC) as a result of disproportionate heating in Earth's polar regions has major implications for regional climates. It is very likely that the MOC is changing as a result of higher temperatures in polar regions and a decrease in the salinity of surface waters due to ice sheet melt, and will continue to do so (*21*). Natural variability within the ocean climate system also occurs at various time scales (seasonal to decadal), producing climatic phenomena such as the El Niño–Southern Oscillation (ENSO), North Atlantic Oscillation (NAO), and Pacific Decadal Oscillation (PDO) (*20*). Although our comprehension of how this variability will change over the coming decades remains uncertain, the steady increases in heat content of the ocean and atmosphere are likely to have profound influences on the strength, direction, and behavior of the world's major current systems (*21*). Changes in the behavior of ocean currents have the potential to strongly influence the distribution and abundance of marine ecosystems, as demonstrated by recent impacts of ENSO variability on kelp forests (*22*) and coral reefs (*23*) (Box 1 and table S2).

Some of the most striking impacts of global climate change have appeared in polar oceans, where temperatures and acidities are changing at more than twice the global average (*4*, *21*) (Fig. 1). As a result of the changes, the amount of Arctic sea ice is steadily decreasing, its area being 16.5 million km^2 in March 1979 but reduced to 15.25 million km^2 by March 2009 (Fig. 2D). Summer sea ice (measured in September each year) is projected to disappear completely by 2037 (*24*). The warming of the polar oceans also has important ramifications for the stability of continental ice sheets, such as those in Greenland and in western Antarctica (WAIS), which are sensitive to small increases in global temperature (*25*). Changes in ice sheet volume have important implications for sea level rise, with an overall contribution of up to 12 m to mean sea levels if both Greenland and WAIS ice sheets were to melt completely (*26*). Satellite altimeter data (Fig. 2A) reveal that the average global sea level is changing at a rate of 3.3 ± 0.4 mm/year (over the period 1993–2006), which is consistent with tidal gauge data (*26*) and is tracking the highest projections of the fourth assessment report of the Intergovernmental Panel on

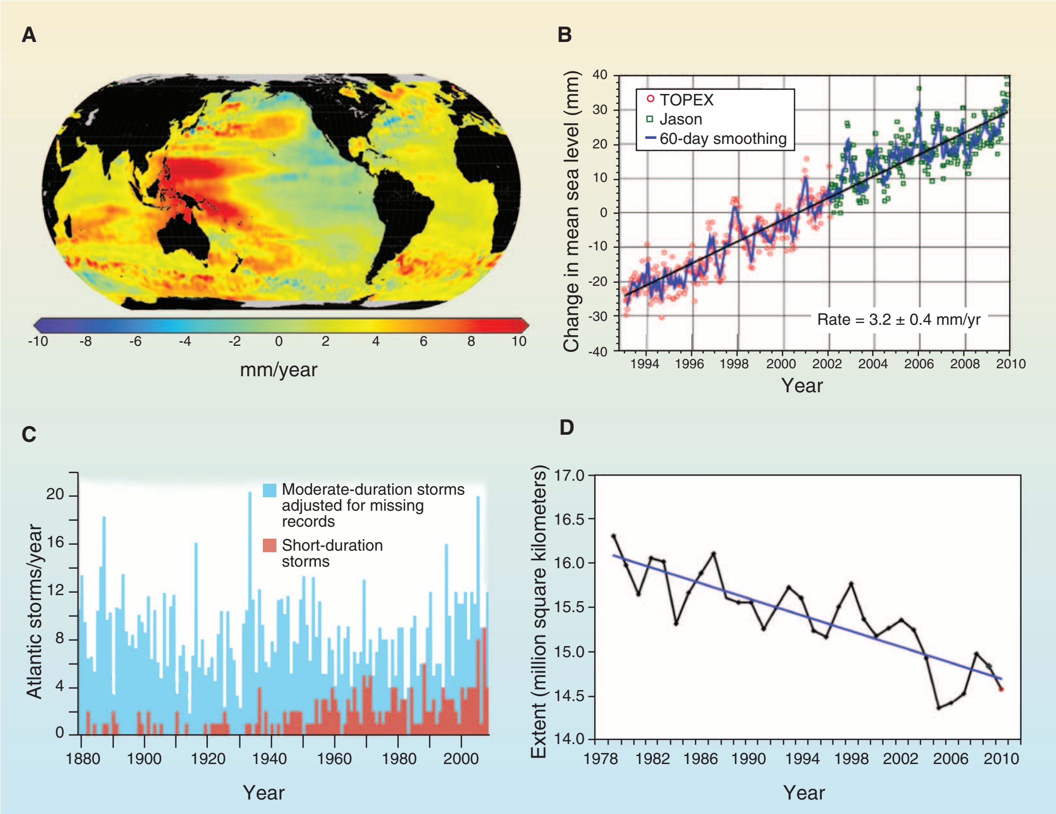

Fig. 2. (**A** and **B**) Average rate of global sea level rise (1993–2010) from TOPEX/Poseidon and Jason satellite altimetry data, shown as a map (A) and as a global mean sea level (B). (**C**) Trends in moderate-duration storms (lasting >2 days) and short-duration storms (<2 days) in the North Atlantic since 1880. (**D**) Average monthly Arctic sea ice extent from February 1979 to February 2010. [Credits: (A) NOAA/Laboratory for Satellite Altimetry; (B) Colorado Center for Astrodynamics Research (http://sealevel.colorado.edu) (*58*); (C) adapted from (*59*) with permission; (D) National Snow and Ice Data Center, Boulder, CO]

Climate Change (IPCC). Current estimates of future sea level rise by 2100 range from 0.5 to 1.2 m (*26*).

Effects on Ecosystem Function

The scale and pace of change in the chemical and physical conditions within the world's oceans have set in motion a wide range of biological responses, with a corresponding rise in the number of studies reporting changes, from 319 published papers in 2000 to more than 1000 papers by 2009. However, papers reporting changes within marine ecosystems remain at only ~5% of the total publications on climate change (table S1 and fig. S1). Rather than revisiting the impacts of climate change on an ecosystem-by-ecosystem basis, here we focus on the impact of rapid anthropogenic climate change on general marine ecosystem processes and services.

Temperature has a fundamental effect on biological processes simply by its influence on molecular kinetic energy (i.e., Maxwell-Boltzmann energy distribution), which determines the rate of fundamental processes such as enzyme reactions, diffusion, and membrane transport (*27*). Moderate increases in temperature increase metabolic rates, which ultimately determine life history traits, population growth, and ecosystem processes (*28*). In this regard, organisms tend to adapt to local environmental temperatures, with optimal physiological responses matching temperatures that are close to the environmental average. Organisms are able to acclimatize to a range of temperatures around these optimal values (*27*). Beyond this range, however, acclimatization fails, mortality risk increases, fitness is reduced, and populations decline or are driven to local extinction (*27*).

Variation in temperature can also have impacts on key biological processes. For example, the distribution and abundance of phytoplankton communities throughout the world, as well as their phenology and productivity, are changing in response to warming, acidifying, and stratifying oceans (*7*, *13*). The annual primary production of the world's oceans has decreased by at least 6% since the early 1980s, with nearly 70% of this decline occurring at higher latitudes (*29*) and with large relative decreases occurring within Pacific and Indian ocean gyres (*13*). Climate variability strongly influences ocean productivity, such as seen in the anomalous conditions of 1998, which that left a clear fingerprint on global ocean phytoplankton productivity and chlorophyll standing stocks (*30*). Overall, these changes in the primary production of the oceans have profound implications for the marine biosphere, carbon sinks, and biogeochemistry of Earth (*31*).

Animal metabolism is temperature-dependent (*27*), and consequently ecological processes such as predator-prey interactions are likely to be altered as warming occurs (*32*). Respiration is also more sensitive than photosynthesis to changes in temperature (*33*), resulting in the caloric demands of consumers being potentially more strongly influenced by increased temperature when compared to the temperature response of primary production (Fig. 3, A to F). Increasing temperatures in mesocosm experiments from 21° to 27°C have shown that the consumer control of primary production is substantially strengthened and reduces both total food web biomass and the ratio of plant to animal biomass (*34*). Large-scale field studies of North Atlantic plankton communities have documented similar temperature–food web relationships (Fig. 3, E and F) (*35*).

These findings have implications for the ability of pelagic systems to capture and store carbon dioxide, with the potential for these critical ocean processes to decline as temperature increases (*33*). Warming has also been found to decrease the size of individual phytoplankton (*35*), further altering the functioning and biogeochemistry of shallow pelagic ecosystems and, in particular, reducing their potential for carbon sequestration.

Changes to ocean conditions also have direct influences on the life history characteristics of marine organisms as varied as invertebrates and sea birds (Fig. 3, G to I, and table S2). The developmental rates of poikilotherms, where body temperatures vary with the environment, increase exponentially with temperature (*28*), with important consequences for a range of ecological attributes including larval dispersal, population connectivity, local adaptation, and speciation (*28*). Reduced developmental times may also result in phenological mismatches between developing larval organisms and the availability of suitable food (*36*), similar to phenological mismatches reported for terrestrial systems (*37*). When combined with changing patterns of primary productivity and metabolic rate, these fundamental

influences have the potential to substantially modify ocean food web dynamics, from coastal to open-ocean ecosystems.

Reduced Habitat Complexity

Among the most clear and profound influences of climate change on the world's oceans are its impacts on habitat-forming species such as corals, sea grass, mangroves, salt marsh grasses, and oysters. Collectively, these organisms form the habitat for thousands of other species. Although some resident species may not have absolute requirements for these habitats, many do, and they disappear if the habitat is removed. For example, mass coral bleaching and mortality, the result of increasing temperatures, is already reducing the richness and density of coral reef fishes and other organisms (*23*).

Coastal angiosperms such as mangroves, sea grass, and saltmarsh communities also face escalating threats from both local and global stresses (table S2). Although mangrove deforestation (1 to 2% per year) represents a greater near-term threat, risks from sea level are increasing, with expected losses of 10 to 20% of mangroves by 2100 (*38*). Impacts on mangrove habitats vary with location; areas with steep coastal inclines or coastal human infrastructure that limit landward migration are most at risk. Mangroves in many areas can adapt to sea level rise by landward migration, but these shifts threaten other coastal habitats such as saltmarsh, which have other important biogeochemical and ecological roles.

Sea ice, like coral reefs and kelp forests, plays a critical role in structuring the biodiversity of polar oceans. The spring melt has a major role in determining the timing of phytoplankton blooms and consequently influences polar marine food web dynamics. In addition, the loss of sea ice will drive additional changes through reductions in food webs that are dependent on sea-ice algae (*39*), which may explain the recent 75 ± 21% per decade decrease in krill (*40*). Sea ice also plays a critical role for a wide range of birds and mammals, functioning as a temporary or permanent platform from which crucial predatory, reproductive, or migratory activities are carried out (*41*). Many arctic mammals face serious declines, with polar bears projected to lose 68% (~700,000 out of 1 million km^2) of their summer habitat by 2100. Ice-dependent Antarctic organisms such as penguins and seals are declining and, in some cases, face an escalating risk of extinction under the current projections for Antarctic warming (*42*).

Ecologically Novel Assemblages, "Exotic" Species, and Disease

One of the inevitable outcomes of differing tolerances for changes in the environment among marine organisms is the development of novel assemblages of organisms in the near future. Such communities will have no past or contemporary counterparts (*43*) and consequently are

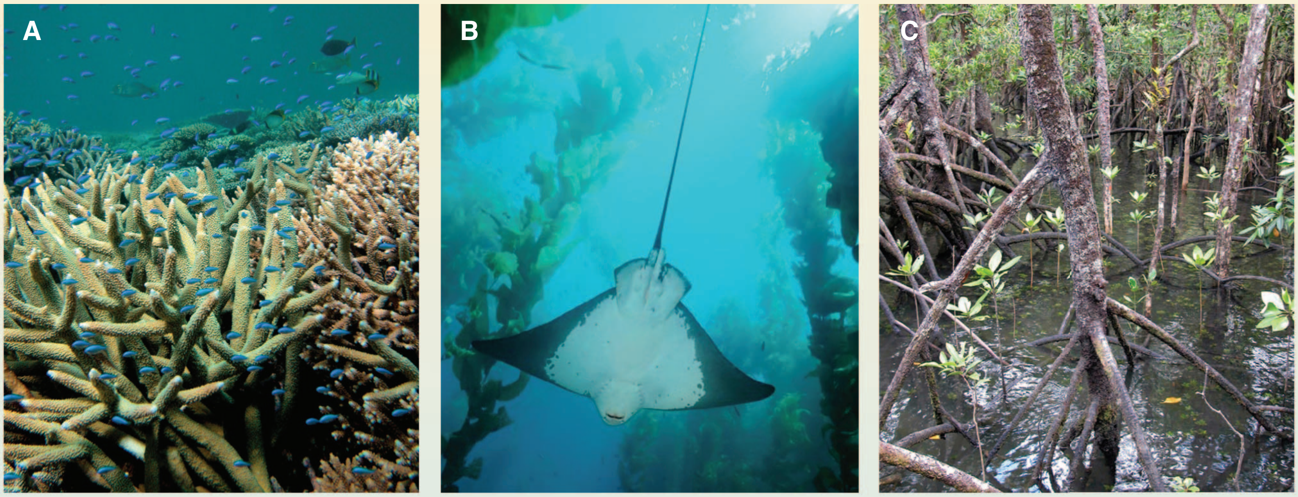

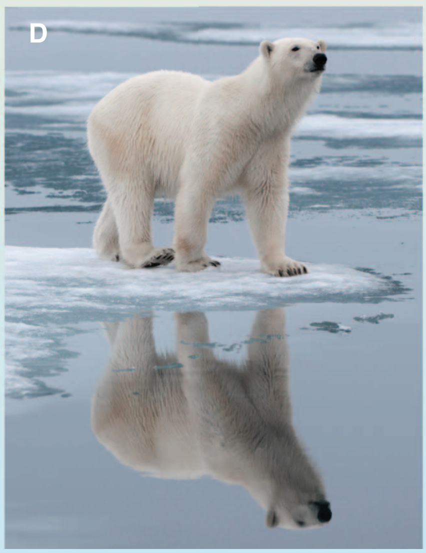

Box 1. Marine ecosystems are already responding to the rapid pace of change in the physical and chemical conditions that surround them (see table S2 for summary of recent literature). One of the most important impacts has been on the organisms and physical processes that create habitat for millions of other species. (**A**) Heron Island, southern Great Barrier Reef. Coral Reef ecosystems are declining because of anomalously warm sea temperatures, which are driving an increased frequency of coral bleaching and mortality. These impacts are combining with local impacts, as well as the slowing of reef accretion due to the impact of ocean acidification. Complex coral-dominated reef ecosystems like this one are likely to be rare by 2050. (**B**) Kelp forest (*Macrocystis pyrifera*, with California bat ray, *Myliobatis californica*) near San Clemente Island, California, USA. Warming ocean temperatures are driving a major contraction in the distribution of kelp forests worldwide. (**C**) Daintree River, northeastern Australia. Mangroves are critically important coastal habitat for numerous coastal species. The loss of 10 to 20% of mangroves is projected if sea levels rise by 1 m above today. (**D**) The loss of summer sea ice by 2040 in the Arctic will have a strong impact on a range of dependent organisms, both above and below the ice. [Credits: (A) and (C) O. Hoegh-Guldberg; (B) Philip Colla, www.Oceanlight.com; (D) Daniel J. Cox, www.NaturalExposures.com]

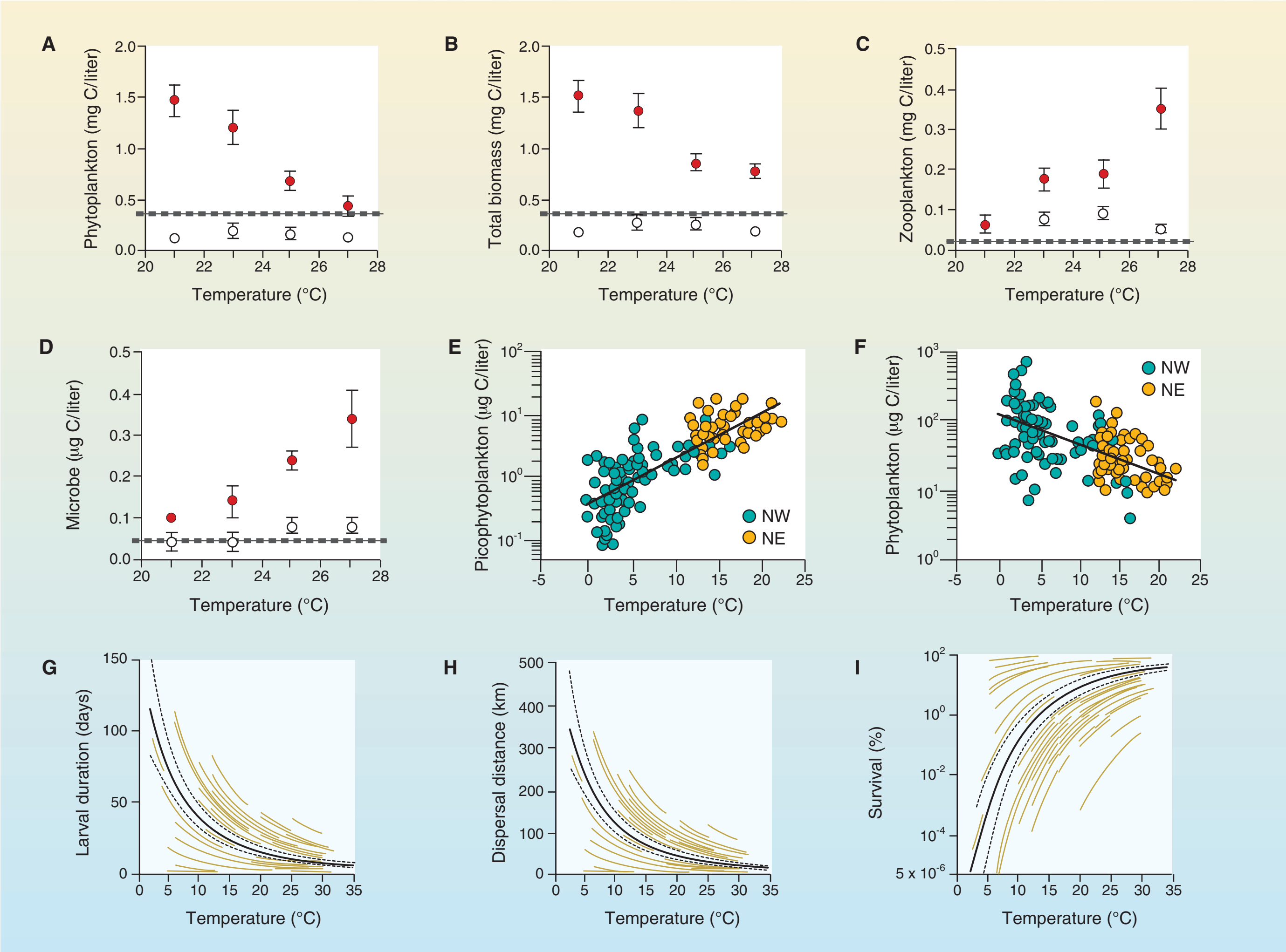

Fig. 3. Effects of climate change on biological processes in the ocean. (**A** to **D**) Experimental mesocosm results demonstrating the effect of temperature on different food web properties. Solid symbols indicate supplemental nutrient addition; open symbols indicate ambient (low) nutrient concentration; dashed horizontal lines denote initial conditions; error bars denote SE. (**E** and **F**) Relationship between temperature and abundance of small phytoplankton (E) and total phytoplankton biomass (F) from large-scale field sampling of the North Atlantic. Black lines are regression lines. (**G**) Relationship between water temperature and planktonic larval duration from published experimental laboratory studies of 72 species (six phyla, including six fish and 66 invertebrates). (**H** and **I**) The predicted effects of temperature on larval dispersal distance (H) and larval survival (I). In (G) to (I), black lines represent the population-averaged responses; brown lines represent species-specific trajectories. [Credits: (A) to (D) from (*34*); (E) and (F) from (*35*); (G) to (I) from (*28*); all figures reprinted with permission of authors and journal]

likely to present serious challenges to marine resource managers and policy makers. The rising number of "exotic" marine species (table S2) provides some insight into the challenges ahead. Over the past several hundred years, the movement of ships and other transport vehicles around the globe has enabled the spread of a large number of marine species. Successful establishment, however, depends on conditions at the destination matching the tolerance range of invading organisms. Recent accelerated warming of high-latitude environments has increased the chances that species being transported from lower latitudes are able to establish themselves and spread (*44*). A rising number of species are expanding their ranges, often with large-scale impacts on ecosystems at the destination. For example, the southeastern Australian sea urchin *Centrostephanus rodgersii* (Diadematidae) has recently expanded its range into Tasmanian waters, where it has transformed macroalgal communities into taxonomically impoverished "urchin barrens" (*22*). Although barrens are a prominent feature of the southeastern Australian mainland normally occupied by *C. rodgersii*, they are relatively novel in Tasmanian waters (*22*).

Climate change has been implicated in recent variation in the prevalence and severity of disease outbreaks within marine ecosystems (*45*). These influences are likely to be a consequence of several factors, including the expansion of pathogen ranges in response to warming, changes to host susceptibility as a result of increasing environmental stress, and the expansion of potential vectors. There are numerous examples that illustrate this effect, including the spread of the oyster parasite *Perkinsus marinus* across a 500-km range of the northeastern United States during pronounced warming in 1990 and 1991 (*46*). Other examples are the strong association of thermal stress and coral cover in predicting disease within reef-building corals (*47*) and the temperature susceptibility of red abalone in California to a fatal rickettsial infection (*48*). A growing number of studies show a rise in marine diseases and has prompted some to conclude that "a warmer world would be a sicker world" (*45*). That said, there are large uncertainties about the interplay between ecological dynamics and potential vectors or disease-causing agents, making it difficult to predict whether the incidence of particular diseases will increase or decrease in a warmer and more acidic world. The potentially large costs of an increasing incidence and prevalence of dis-

ease, however, make a compelling reason for understanding and limiting these changes.

Local-Global Interactions, Synergies, and Thresholds

Although most of the ocean is undergoing impacts from multiple anthropogenic stressors (*49*), little is known about the potential for large-scale synergisms (or antagonisms) (*50*). Even additive effects have great potential to overwhelm key species and entire ecosystems. Coral reefs represent a prominent example where increasing mass coral bleaching and reduced calcification as a result of increasing atmospheric CO_2 are combining with the increasing inputs of sediments, nutrients, and pollution from disturbed coastlines to reduce the ability of these ecosystems to recover from natural and anthropogenic disturbances (*47*). Another example is that of open-ocean ecosystems, where a wide range of factors, including overfishing, increased ultraviolet light exposure, as well as warming and stratifying surface waters, are driving complex changes in community structure and food web dynamics.

Recent evidence suggests that there is now a growing risk that several thresholds will soon be exceeded (*51*). For example, increasing ocean temperatures and acidities associated with atmospheric CO_2 concentrations of 450 parts per million (ppm) represent a serious threat to ecosystems such as coral reefs. In the latter case, temperatures that exceed 2°C above pre-industrial temperatures are very likely to drive an unsustainable frequency of mass coral bleaching and mortality, whereas ocean acidification associated with atmospheric CO_2 above 450 ppm will push coral reefs into a negative carbonate balance (*23*). Similar thresholds (400 to 450 ppm or a +2°C increase in average global temperature above pre-industrial values) have been identified for key ocean components such as aragonite undersaturation of the Southern Ocean (*52*), loss of polar sea ice (*24*), and the melting of the Greenland (*53*) and Western Antarctic (*54*) ice sheets. Specific thresholds (or tipping points) are predicted to have large-scale consequences for coastal and oceanic ecosystems, as outlined above. These drivers add to the complex behavior of ecological systems, increasing the chance of triggering amplifying feedback loops and domino effects. Given the growing evidence that relatively small increases in the concentrations of atmospheric carbon dioxide will trigger a wide array of irreversible changes to critically important marine ecosystems, avoiding any further increases and aiming to reduce the atmospheric concentration of CO_2 below 350 ppm in the long term must be an international imperative (*55*, *56*).

Managing Risk in a Changing World

The rapid ecological shifts that are occurring in the world's oceans present major challenges for managers and policy makers. Understanding and reducing risk exposure will become increasingly important as conditions change and the likelihood of major ecological shifts increases. These changes will decrease the relevance of current models and practices for managing ecological resources and fisheries stocks, leading the management of many marine resources into "uncharted waters." Nonetheless, "no regret" management strategies that reduce the impact of local stresses while maintaining ecological resilience will play an increasingly important role as the climate changes. Actions that reduce the flow of nutrients and sediments from coastal catchments, for example, as well as those that reduce activities such as the deforestation of mangroves and the overfishing of key ecological species (e.g., herbivores), will become increasingly important as the impacts of climate change mount. Natural resource management must also remain flexible in order to absorb the sudden and nonlinear changes that are likely to characterize the behavior of most ecosystems into the future. Overall, however, reducing greenhouse gas emissions remains the priority, not only because it will reduce the huge costs of adaptation but also because it will reduce the growing risk of pushing our planet into an unknown and highly dangerous state.

References and Notes

1. C. Bounama, W. von Bloh, S. Franck, *Astrobiology* **7**, 745 (2007).
2. R. Pachauri, *Climate Change 2007: Synthesis Report* (IPCC Secretariat, Geneva, 2007).
3. C. Rosenzweig *et al.*, *Nature* **453**, 353 (2008).
4. J. Hansen *et al.*, *Proc. Natl. Acad. Sci. U.S.A.* **103**, 14288 (2006).
5. S. Levitus *et al.*, *Geophys. Res. Lett.* **36**, L07608 (2009).
6. National Oceanic and Atmospheric Administration, National Climatic Data Center, State of the Climate Global Analysis (www.ncdc.noaa.gov/sotc/?report=global&year=2010&month=1&submitted=Get+Report), accessed 4 March 2010.
7. S. Doney, V. Fabry, R. Feely, J. Kleypas, *Annu. Rev. Mar. Sci.* **1**, 169 (2009).
8. J. R. Petit *et al.*, *Nature* **399**, 429 (1999).
9. C. Pelejero, E. Calvo, O. Hoegh-Guldberg, *Trends Ecol. Evol.* **25**, 332 (2010).
10. S. Rahmstorf *et al.*, *Science* **316**, 709 (2007).
11. T. R. Knutson *et al.*, *Nat. Geosci.* **3**, 157 (2010).
12. K. Trenberth *et al.*, Eds., *Observations: Surface and Atmospheric Climate Change. Climate Change 2007: The Physical Science Basis. Contribution of Working Group I to the Fourth Assessment Report of the Intergovernmental Panel on Climate Change* (Cambridge Univ. Press, Cambridge, 2007).
13. J. Polovina, E. Howell, M. Abecassis, *Geophys. Res. Lett.* **35**, L03618 (2008).
14. R. J. Diaz, R. Rosenberg, *Science* **321**, 926 (2008).
15. R. Matear, A. Hirst, B. McNeil, *Geochem. Geophys. Geosyst.* **1**, 1050 (2000).
16. L. Kump, A. Pavlov, M. Arthur, *Geology* **33**, 397 (2005).
17. A. Bakun, S. Weeks, *Ecol. Lett.* **7**, 1015 (2004).
18. F. Chan *et al.*, *Science* **319**, 920 (2008).
19. S. J. Weeks, B. Currie, A. Bakun, K. R. Peard, *Deep Sea Res. I* **51**, 153 (2004).
20. J. Alheit, A. Bakun, *J. Mar. Syst.* **79**, 267 (2010).
21. N. L. Bindoff *et al.*, Eds., *Observations: Oceanic Climate Change and Sea Level* (Cambridge Univ. Press, Cambridge, 2007), pp. 387–432.
22. S. D. Ling, *Oecologia* **156**, 883 (2008).
23. O. Hoegh-Guldberg *et al.*, *Science* **318**, 1737 (2007).
24. M. Y. Wang, J. E. Overland, *Geophys. Res. Lett.* **36**, L07502 (2009).
25. T. Naish *et al.*, *Nature* **458**, 322 (2009).
26. A. Cazenave, W. Llovel, *Annu. Rev. Mar. Sci.* **2**, 145 (2010).
27. P. Hochachka, G. Somero, *Biochemical Adaptation: Mechanism and Process in Physiological Evolution* (Oxford Univ. Press, New York, 2002).
28. M. I. O'Connor *et al.*, *Proc. Natl. Acad. Sci. U.S.A.* **104**, 1266 (2007).
29. W. Gregg, M. Conkright, P. Ginoux, J. O'Reilly, N. Casey, *Geophys. Res. Lett.* **30**, 1809 (2003).
30. M. J. Behrenfeld *et al.*, *Nature* **444**, 752 (2006).
31. P. Falkowski *et al.*, *Science* **290**, 291 (2000).
32. E. Sanford, *Science* **283**, 2095 (1999).
33. A. López-Urrutia, E. San Martin, R. P. Harris, X. Irigoien, *Proc. Natl. Acad. Sci. U.S.A.* **103**, 8739 (2006).
34. M. I. O'Connor *et al.*, *PLoS Biol.* **7**, e1000178 (2009).
35. X. A. G. Morán, A. López-Urrutia, A. Calvo-Díaz, W. K. W. Li, *Glob. Change Biol.* **16**, 1137 (2010).
36. J. Durant, D. Hjermann, G. Ottersen, N. Stenseth, *Clim. Res.* **33**, 271 (2007).
37. G. R. Walther *et al.*, *Nature* **416**, 389 (2002).
38. D. M. Alongi, *Estuar. Coast. Shelf Sci.* **76**, 1 (2008).
39. R. Gradinger, *Deep Sea Res. II* **56**, 1201 (2009).
40. A. Atkinson, V. Siegel, E. Pakhomov, P. Rothery, *Nature* **432**, 100 (2004).
41. S. E. Moore, H. P. Huntington, *Ecol. Appl.* **18**, S157 (2008).
42. C. Barbraud *et al.*, *Proc. Natl. Acad. Sci. U.S.A.* **105**, E38, E39 (2008).
43. J. Williams, S. Jackson, *Front. Ecol. Environ* **5**, 475 (2007).
44. J. J. Stachowicz, J. R. Terwin, R. B. Whitlatch, R. W. Osman, *Proc. Natl. Acad. Sci. U.S.A.* **99**, 15497 (2002).
45. D. Harvell, S. Altizer, I. M. Cattadori, L. Harrington, E. Weil, *Ecology* **90**, 912 (2009).
46. S. Ford, R. Smolowitz, *Mar. Biol.* **151**, 119 (2007).
47. J. F. Bruno *et al.*, *PLoS Biol.* **5**, e124 (2007).
48. J. Moore, T. Robbins, C. Friedman, *J. Aquat. Anim. Health* **12**, 26 (2000).
49. B. S. Halpern *et al.*, *Science* **319**, 948 (2008).
50. E. S. Darling, I. M. Côté, *Ecol. Lett.* **11**, 1278 (2008).
51. J. Rockström *et al.*, *Nature* **461**, 472 (2009).
52. B. I. McNeil, R. J. Matear, *Proc. Natl. Acad. Sci. U.S.A.* **105**, 18860 (2008).
53. J. Gregory, P. Huybrechts, S. Raper, *Nature* **428**, 616 (2004).
54. T. Naish *et al.*, *Nature* **458**, 322 (2009).
55. J. Hansen *et al.*, *Open Atmos. Sci. J.* **2**, 217 (2008).
56. J. E. N. Veron *et al.*, *Mar. Pollut. Bull.* **58**, 1428 (2009).
57. R. Key *et al.*, *Global Biogeochem. Cycles* **18**, GB4031 (2004).
58. E. Leuliette, R. Nerem, G. Mitchum, *Mar. Geod.* **27**, 79 (2004).
59. C. Landsea, G. Vecchi, L. Bengtsson, T. Knutson, *J. Clim.* **34**, (2010).

60. We thank O. Pantos for important discussion and preparatory work undertaken for this review, the Coral Reef Ecosystems Laboratory at the University of Queensland's Global Change Institute (www.coralreefecosystems.org), and the ARC Centre for Excellence in Coral Reef Studies. J.F.B. was a sabbatical visitor at the Global Change Institute at the University of Queensland during the preparation of this review. O.H.-G. has not received any additional funds, paid consultancies, or patents pertaining to this work. J.F.B. has no paid consultancies and no other affiliations but was funded by a Commonwealth Scientific and Industrial Research Organisation Climate Adaptations Flagship and by the University of North Carolina for part of this work.

Supporting Online Material

www.sciencemag.org/cgi/content/full/328/5985/1523/DC1
Fig. S1
Tables S1 and S2
References

10.1126/science.1189930

Reassortment of Pandemic H1N1/2009 Influenza A Virus in Swine

D. Vijaykrishna,[1,2]*† L. L. M. Poon,[1]* H. C. Zhu,[1,2] S. K. Ma,[1] O. T. W. Li,[1] C. L. Cheung,[1] G. J. D. Smith,[1,2]† J. S. M. Peiris,[1]‡ Y. Guan[1,2]‡

Pandemic H1N1/2009 influenza virus emerged from swine in Mexico to infect humans and has rapidly spread to more than 200 countries (*1*). This virus was generated by multiple reassortment events, and each of its precursor gene segments has circulated in swine for more than 10 years (*2*, *3*). Infection of swine with H1N1/2009 virus has been observed in multiple countries (*4*). But, because of a paucity of systematic surveillance of swine influenza worldwide, questions remain whether H1N1/2009 will become established in swine and become a reservoir of reassortment that may produce novel viruses of potential threat to public health.

Over the past 10 years, systematic virological surveillance of influenza viruses in swine has been ongoing in a Hong Kong abattoir, wherein over 95% of swine tested originate from adjacent provinces in China (*2*, *5*). A total of 32 H1N1 and H1N2 viruses were isolated in fortnightly surveys from June 2009 to February 2010 (table S1) (*6*). Since 22 October 2009, 10 H1N1/2009 viruses were isolated from four of eight sampling occasions. Phylogenetic analysis shows that all eight genes of these viruses belonged to the H1N1/2009 lineage (fig. S1). Pandemic H1N1/2009 viruses isolated on the same sampling occasion were genetically identical, suggesting transmission of viruses occurred within swine herds. But viruses from different sampling dates were genetically distinct from each other and also from H1N1/2009-like swine viruses isolated in other countries, indicating multiple independent introductions of these viruses from humans to swine. The H1N1/2009 viruses had not been detected in our surveys until October 2009, supporting the contention that this virus lineage did not arise from China (*2*).

Three major lineages of swine H1 influenza viruses have been prevalent in swine in our surveys in the past 10 years: classical swine H1N1 (CS), European "avian-like" H1N1 (EA), and triple-reassortant H1N2 (TRIG) viruses (Fig. 1, A and B) (*2*). The remaining 22 viruses described here include 5 EA H1N1, 1 TRIG H1N2, and 16 reassortant viruses belonging to five different genotypes (Fig. 1C).

On 7 January 2010, a novel reassortant [A/swine/Hong Kong/201/2010 (H1N1)] appeared with an H1N1/2009-like neuraminidase (NA) gene, an EA-like hemagglutinin (HA) gene, and the six internal genes derived from TRIG lineage viruses (Fig. 1 and fig. S1). The TRIG internal gene cassette (with its new EA-derived M gene) therefore continues to be adept at acquiring novel HA and NA genes (*7*). The identity of the novel virus has been confirmed by direct polymerase chain reaction detection of the eight gene segments in the original swab specimen (*6*). The HA gene of A/swine/Hong Kong/201/2010 grouped within the EA swine lineage, in a basal phylogenetic position to the H1N1 and H1N2 swine viruses isolated during the study period (Fig. 1A and fig. S1A). Hemagglutination inhibition titers indicated that neither H1N1/2009 vaccine nor natural infection reliably elicits cross-protective antibody to A/swine/Hong Kong/201/2010 (table S2) (*6*). The NA gene sequence grouped within the H1N1/2009 NA clade (100% boostrap support), indicating that it was derived from H1N1/2009 (Fig. 1B and fig. S1B). Comparison with the consensus of all available H1N1/2009 NA genes showed a single silent nucleotide substitution in A/swine/Hong Kong/201/2010.

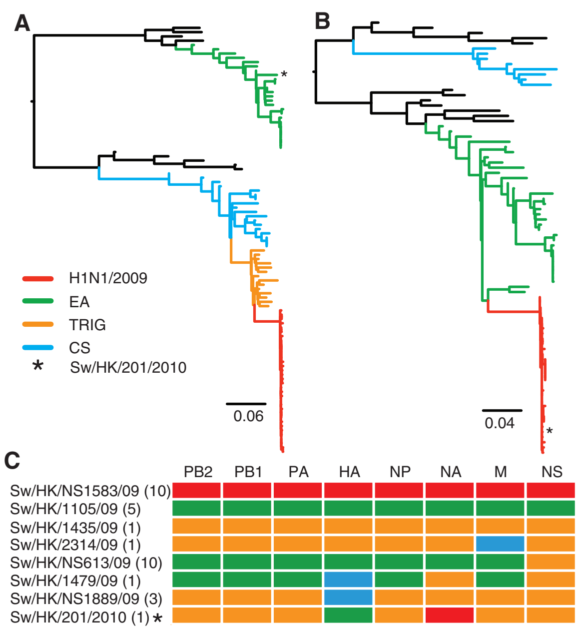

Fig. 1. Maximum-likelihood phylogenies of the influenza (**A**) hemagglutinin and (**B**) neuraminidase genes showing major swine H1 lineages. An asterisk denotes the phylogenetic position of the newly characterized reassortant virus. Identical phylogenies with virus names shown are provided in fig. S1, A and B. Scale bars represent nucleotide substitutions per site. (**C**) Lineages of reassortant swine viruses identified through phylogenetic analyses, with the name of a representative virus and number of each variant isolated listed to the left. Asterisk indicates the newly characterized virus A/swine/Hong Kong/201/2010.

The amino acid sequences of A/swine/Hong Kong/201/2010 showed predicted resistance to the adamantanes but not to oseltamivir, similar to recently described Hong Kong swine viruses (*2*). Experimentally infected swine developed mild illness and seroconverted. Virus shedding was observed for up to 13 days, and there was efficient transmission of infection to contact animals (figs. S2 and S3).

The H1N1/2009 virus has remained antigenically and genetically stable and of relatively low virulence for humans since its detection in humans in April 2009 (*1*). Our results show that the introduction of H1N1/2009 virus to swine has provided it with opportunities for reassortment. Furthermore, H5N1 and H9N2 viruses have been occasionally isolated from swine in Asia (*5*), providing the possibility for the incorporation of avian virus genes into mammalian-adapted viruses. Phylogenetic analyses on the emergence of the 1918, 1957, and 1968 pandemics suggests that all three of these pandemics evolved undetected in an intermediate mammalian host for some years before they were recognized in humans (*8*). The 2009 pandemic, although mild and apparently contained at present, could undergo further reassortment in swine and gain virulence. It is therefore important that surveillance in swine is greatly heightened and that all eight gene segments are genetically characterized so that such reassortment events are rapidly identified.

References and Notes

1. World Health Organization, Pandemic (H1N1) 2009: Update 89, www.who.int/csr/don/2010_02_26/en/index.html (2010).
2. G. J. D. Smith *et al.*, *Nature* **459**, 1122 (2009).
3. R. J. Garten *et al.*, *Science* **325**, 197 (2009); published online 22 May 2009 (10.1126/science.1176225).
4. T. Pasma, T. Joseph, *Emerg. Infect. Dis.* **16**, 706 (2010).
5. J. S. M. Peiris *et al.*, *J. Virol.* **75**, 9679 (2001).
6. Materials and methods are available as supporting material on *Science* Online.
7. N. Bastien *et al.*, *J. Infect. Dis.* **201**, 1178 (2010).
8. G. J. D. Smith *et al.*, *Proc. Natl. Acad. Sci. U.S.A.* **106**, 11709 (2009).
9. This work was supported in part by the National Institute of Allergy and Infectious Diseases (NIAID) contract HHSN266200700005C and the Area of Excellence Scheme of the University Grants Committee (grant AoE/M-12/06) of the Hong Kong SAR Government. We acknowledge the Food and Environmental Hygiene Department of Hong Kong for facilitating this study. Authors declare no conflict of interest. Sequence data generated from this study were deposited in GenBank with accession nos. CY061626 to CY061881.

Supporting Online Material

www.sciencemag.org/cgi/content/full/328/5985/1529/DC1
Materials and Methods
Fig. S1
Tables S1 and S2
References

4 March 2010; accepted 13 May 2010
10.1126/science.1189132

[1]State Key Laboratory of Emerging Infectious Diseases and Department of Microbiology, Li Ka Shing Faculty of Medicine, University of Hong Kong, Hong Kong Special Administrative Region, China. [2]International Institute of Infection and Immunity, Shantou University Medical College, Shantou, Guangdong 515031, China.

*These authors contributed equally to this work.
†Present address: Duke-NUS Graduate Medical School, Singapore.
‡To whom correspondence should be addressed. E-mail: malik@hkucc.hku.hk (J.S.M.P.); yguan@hkucc.hku.hk (Y.G.)

Tropical Ocean Temperatures Over the Past 3.5 Million Years

Timothy D. Herbert,[1] Laura Cleaveland Peterson,[2] Kira T. Lawrence,[3] Zhonghui Liu[4]

Determining the timing and amplitude of tropical sea surface temperature (SST) change is an important part of solving the puzzle of the Plio-Pleistocene ice ages. Alkenone-based tropical SST records from the major ocean basins show coherent glacial-interglacial temperature changes of 1° to 3°C that align with (but slightly lead) global changes in ice volume and deep ocean temperature over the past 3.5 million years. Tropical temperatures became tightly coupled with benthic $\delta^{18}O$ and orbital forcing after 2.7 million years. We interpret the similarity of tropical SST changes, in dynamically dissimilar regions, to reflect "top-down" forcing through the atmosphere. The inception of a strong carbon dioxide–greenhouse gas feedback and amplification of orbital forcing at ~2.7 million years ago connected the fate of Northern Hemisphere ice sheets with global ocean temperatures since that time.

Understanding the links between tropical sea surface temperatures (SSTs) and changes in high-latitude climate across ice age cycles presents a challenge to paleoclimatologists. On the one hand, the tropical oceans should be shielded from processes that produce large temperature sensitivity in the high latitudes, including ice-albedo feedback on land, sea-ice feedbacks, and steering of wind fields by ice sheets. Modeling studies suggest that the direct effects of large continental ice sheets should extend equatorward on a length scale of ~2000 km from the (primarily Northern Hemisphere) edge of polar ice sheets and sea ice (*1*, *2*)—a substantial radius, but not nearly enough to extend climate change throughout the tropics. However, the high latitudes may possess other potent influences on tropical ocean temperatures. High-latitude oceanographic processes determine the properties of subsurface waters that help to determine vertical density stability, mixing, and upwelling in the tropical oceans (*3*–*5*). Most ocean carbon cycle models also give the high-latitude oceans the dominant role in modulating the carbon dioxide (CO_2) greenhouse effect that helps determine global surface temperatures (*6*–*8*).

Changes in tropical ocean SST could in turn lead to large positive feedbacks that enhance the global expression of glacial-interglacial climate cycles (*9*, *10*). The tropical oceans provide the major storage of heat for the global climate system and are also the source of most of the atmospheric water vapor, the single most important greenhouse gas. Evaporation of water from the surface ocean depends directly on SST (*11*). Through their dominant role in the global hydrological cycle, tropical oceans can also exert effects on global cloud cover, on terrestrial vegetation and soil moisture, and on the release of the greenhouse gases methane (CH_4) and nitrous oxide (N_2O) from land (*12*), both of which depend in part on tropical temperatures and hydrology.

The magnitude of tropical ocean temperature change over the course of the Ice Ages has been debated since the inception of modern quantitative paleoclimatology. The first global reconstructions of ocean SST at the heart of the last ice age, the seminal Climate: Long-range Investigation, Mapping, and Prediction (CLIMAP) study based on marine microfossils, suggested that glacial ocean cooling was restricted to mid and high latitudes (some tropical oceanic areas in fact yielded estimates of warmer-than-modern SST) (*13*). Newer geochemically based SST proxies, as well as revisions of microfossil-based SST calibrations, now give a consensus that the CLIMAP result—although qualitatively correct in producing a picture of polar amplification of glacial temperature changes—underestimated tropical cooling during the last ice age (*14*–*17*). It is now clear that substantial glacial-interglacial sensitivity exists in tropical SST over the course of at least the past ~1 million years (My) in every region examined to date (*16*–*20*).

Over the combined ~800-thousand-year (ky) length of the Vostok and European Project for Ice Coring in Antarctica (EPICA) ice core records (*12*, *21*–*24*), tropical SST varies coherently with measured glacial-interglacial variations in the greenhouse gases CO_2, CH_4, and N_2O. Indeed, it has been argued that time series of tropical ocean temperatures may provide one of the best available templates for reconstructing the effect of past greenhouse gas levels on global climate (*14*). This study presents a composite record of tropical SST variations from the mid-Pliocene [3.5 million years ago (Ma)] to the present, a span of time that allows us to assess tropical high-latitude climate linkages over the course of the onset and intensification of cyclic Northern Hemisphere ice ages at 2.7 Ma (*25*). We used the alkenone unsaturation index, recorded at ~3-ky resolution, at each of four tropical ocean sediment sites so as to provide a self-consistent picture of SST changes on both broad and orbital scales. Tropical SST records are synchronized via benthic foraminiferal $\delta^{18}O$ that was measured in the same sediments at the study sites and aligned to the global LR04 (*26*) stack. The benthic oxygen isotope record, which records a combination of deep-ocean temperature changes and variations in continental ice volume over time, also allows us to compare the timing and amplitude of tropical SST changes with climate evolution in the high latitudes.

We argue that the tropical SST data suggest that a coherent, substantial CO_2-glaciation feedback began at about 2.7 Ma, synchronizing to first order the tropical SST variations at the orbital time scale in late Pliocene and all of Pleistocene time. Before 2.7 Ma, the combination of glacial and CO_2 feedbacks may have been much weaker, suppressing the similarity of tropical SST between the different ocean basins and lessening their sensitivity to high-latitude processes.

Evolution of tropical SST over 3.5 million years. We chose to examine four tropical sites located in dynamically distinct regions of the three ocean

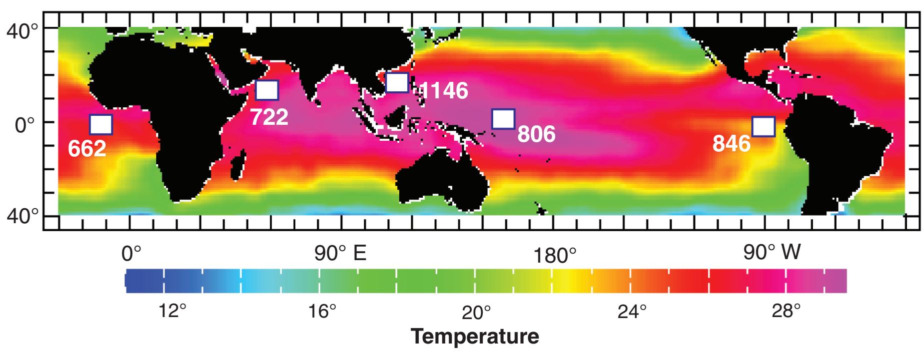

Fig. 1. Location of long sediment cores analyzed for this study in relation to mean annual SST (SOM text). SST estimates from site 806 were made with the Mg/Ca method (*19*); all others were made by use of alkenone paleothermometry.

[1]Department of Geological Sciences, Brown University, Providence, RI 02912, USA. [2]Environmental Studies, Luther College, 700 College Drive, Decorah, IA 52101, USA. [3]Department of Geology and Environmental Geosciences, Lafayette College, Easton, PA 18042, USA. [4]Department of Earth Sciences, The University of Hong Kong, James Lee Science Building, Pokefulam Road, Hong Kong, People's Republic of China.

basins [Fig. 1 and supporting online material (SOM) text S.1]. We produced alkenone SST records at each site over intervals of Plio-Pleistocene time in which supporting stratigraphic data indicate continuous sedimentation. The alkenone paleotemperature proxy relies on the unsaturation index of biomarkers produced by restricted species of coccolithophorid algae, organisms that must live in the photic zone. Modern ecological studies and data from recent sediments support the proposition that alkenone temperature estimates closely approximate mean annual temperature in the surface ocean mixed layer (*27*). By combining alkenone records from widely dispersed tropical locations, we hope to minimize biases from local SST responses and seasonal biases in alkenone production (SOM text S.1). The alkenone proxy reaches saturation at about 28°C, which prevents us from producing records from the "warm pool" locations of the tropical Indo-Pacific and Atlantic basins.

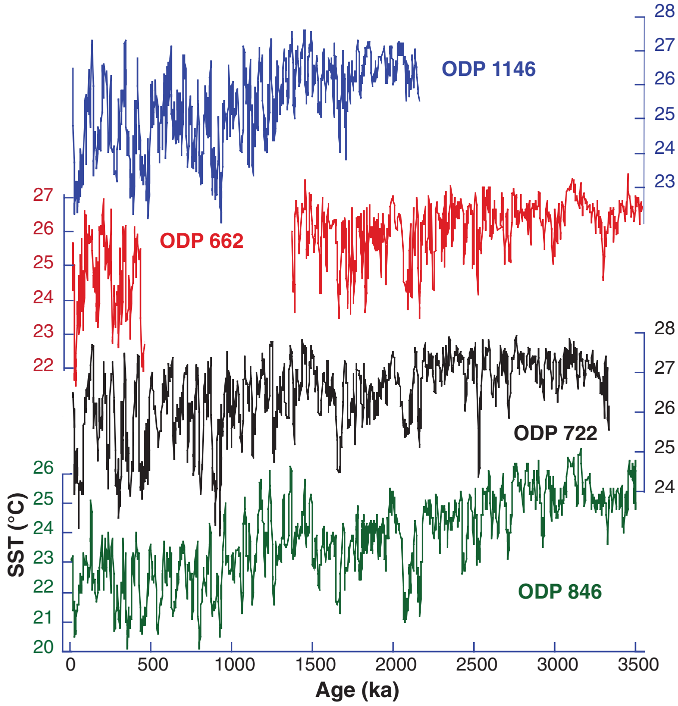

Fig. 2. Estimates of SST at the four sites on the basis of alkenone paleotemperature determinations. The gap in the ODP site 662 record comes from an interval disturbed by slumping that was not sampled. Data are archived at ftp://ftp.ncdc.noaa.gov/pub/data/paleo/contributions_by_author/herbert2010/.

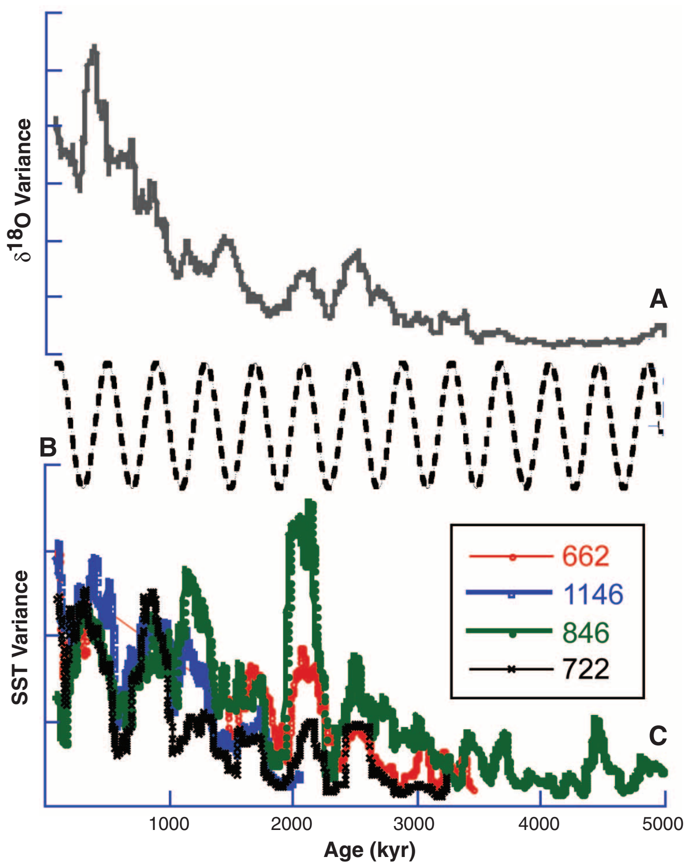

Fig. 3. (**A**) Variance in δ^{18}O, computed in 200-ky moving windows. (**B**) 404-ky eccentricity cycle (inverted). (**C**) Variance in SST, computed in 200-ky moving windows, at the four sites with alkenone paleotemperature estimates.

Our tropical records show very strong similarity to each other and to the pattern of global ice volume and deep-sea temperatures over the course of the Plio-Pleistocene glaciations (Figs. 2 and 3). Within the pattern of rhythmic SST changes, unusually intense coolings punctuate the record at ~2.5, 2.1, and 1.7 Ma at all the sites. The similarity of tropical SST extends beyond the pattern of individual ice age cycles; our data reveal coherent long-wavelength (300 to 500 ky in duration) trends in SST that may be related to orbital forcing (Figs. 2 and 4). The absolute values of SST variance, centered on a 200-ky moving average, appear to converge strongly in the late Pleistocene (past 1 My), which is indicative of an increasingly uniform ice-age tropical SST response as we approach the present (Fig. 3). More surprisingly, changes in SST variance appear timed to the 404-ky component of orbital eccentricity; variance in SST is highest during periods of lower-than-average eccentricity. The existence of eccentricity-related (~100- and 400-ky spectral components) in the δ^{18}O record has long been controversial (*28*–*31*), but this expression in tropical SST variance seems hard to dismiss. Low eccentricity apparently favors prolonged excursions to low temperatures during ice ages, even during the lengthy interval from ~2.7 to 1 Ma when ice age cycles follow the 41 ky obliquity pacing.

The similarity of our tropical SST records led us to construct an averaged representation ("stack") in order to compare the aggregate tropical temperature changes with the global δ^{18}O curve (Fig. 4 and SOM text S.5). We have included a shorter (1.4 My) Mg/Ca–based record from the Pacific warm pool in an effort to better represent the evolution of the warmest regions of the tropical ocean over time. The stack enhances the signal-to-noise ratio of the proxy measurements, emphasizes the common components of tropical temperature trends, and averages the phasing of SST changes in disparate parts of the tropical ocean. It reveals the strong similarity in timing and amplitude of tropical temperature changes in relation to ice age climates, although the SST data contain more long-wavelength (~400 ky) variability and also more intense coolings at ~1.66 and 2.07 Ma (marine oxygen isotope stages 58 and 76, respectively) than would be inferred from the benthic δ^{18}O record of glaciation. The stack estimates only one aspect of the tropical response to glacial cycles over time; other important variables such as the tropical hydrological cycle remain to be reconstructed on Plio-Pleistocene time scales.

The tropical SST records resemble the evolution of high-latitude climate in important ways.

On the long time scale, the rising variance, with an exponential time scale (averaged over the 3 longest SST records) of 0.58 My recalls the pace of the 0.68 My time constant of the exponentially increasing amplitude in $\delta^{18}O$ toward the present (*32*) (Fig. 3). Shifts in spectral content, most notably the mid-Pleistocene transition from 41- to 100-ky cycles, occur in both tropical SST and benthic $\delta^{18}O$ in the interval 1.0 to 0.8 Ma (Figs. 2 and 4, SOM text S.2, and figs. S2 and S3). In detail, the phases of tropical SST with respect to global ice volume do differ between sites by a few thousand years, implicating the operation of regional-scale processes in addition to the common component. In all records, however, phase analysis indicates that tropical SST slightly leads (by about 2 to 5 ky, depending on site and time) glacial cycles as recorded by $\delta^{18}O$. These phase relations indicate that one cannot regard tropical SST as being forced by continental glaciation itself. Because the benthic $\delta^{18}O$ signal is a composite of the relatively slow process of high-latitude ice sheet growth and decay and the potentially much more rapid process of deep ocean cooling and warming on glacial-interglacial cycles (*33*–*35*), the net phase of the $\delta^{18}O$ signal most likely is weighted toward the slow ice sheet component. Our data therefore leave open the possibility that tropical temperatures changed essentially synchronously with those of the deep sea (*35*) over much of the past 2.7 My.

A milestone in climate evolution occurred at ~2.7 Ma, when linkages both between the tropical sites and from the tropics to the high latitudes (represented by the $\delta^{18}O$ curve) increased. The increase in 41-ky SST variance at 2.7 Ma coincides with the appearance of ice-rafted debris in the open North Atlantic and Pacific oceans at the same time, which is widely interpreted to reflect the appearance of large Northern Hemisphere continental ice sheets that would characterize glacial climates from that time onward (*25*, *36*). This obliquity-related component of tropical SST variability not only increases in amplitude beginning at about 2.7 Ma (fig. S3), but becomes highly coherent between the tropical sites at this time (Fig. 5). Other tropical proxies such as the 41-ky pacing of dust delivery to the Arabian Sea (*37*) and an increase in C_4 vegetation in northeast Africa (*38*) also show the incursion of high-latitude signals into the tropics at about the same time. For the next ~2 My, ice age cycles and tropical SST varied coherently at the 41-ky time scale, following the pacing of the earth's orbital obliquity.

Global Connections. The similarity of SST responses in dynamically dissimilar regions of the tropical ocean indicates a common forcing of glacial-scale temperature changes. However, the observed SST changes are opposite in sign to the annual tropical radiation forcing at the obliquity periodicity (*18*) and lack the 23- and 19-ky spectral components that should dominate seasonal insolation forcing of the study regions (*39*). The observed patterns therefore cannot be considered as simple adjustments of tropical SST to solar insolation forcing. Alternative mechanisms for changing SST within tropical climatology (such as changes in the strength of the Easterlies, changes in equatorial thermocline tilt, or changes in the intensity of monsoonal winds) would not produce synchronous responses in the tropical oceans or would produce very different amounts of warming and cooling in different tropical regions. Certain mechanisms, such as a trade wind–induced change in the tilt of the equatorial Pacific thermocline, would produce antiphased SST changes between the East and West that have not been observed [fig. S4 of (*19*) compares the similarity of the alkenone record of SST in the eastern Pacific Ocean Drilling Program (ODP) site 846 to the Mg/Ca record from ODP site 806 in the western Warm Pool].

It seems more than coincidence that both the amplitude of tropical SST cycles, and the coherence of the 41-ky component in tropical SST to orbital pacing rose at the same time that the Northern Hemisphere high latitudes began to sustain major glaciations. Because it is unlikely that Northern Hemisphere ice sheets directly drove the SST responses, a parsimonious interpretation of the climatic changes over the past 3.5 My would instead invoke a common cause for both the intensity of glacial cycles and their expression in the tropics. The most likely candidate lies in high-latitude oceanographic processes tied to the global carbon cycle, which would provide a common driver for global temperature changes and for glaciation. No clear consensus exists yet to explain the late Pleistocene CO_2 and greenhouse gas cycles captured in polar ice cores, but most plausible models concentrate on mechanisms in the high-latitude oceans (such as changes in stratification, wind mixing, or biological productivity) that could sequester CO_2 in the deep sea during ice ages and then release it in interglacial periods (*6*, *8*, *40*). However, a tropical SST change in parallel with CO_2 forcing would provide a powerful positive feedback to glacial-interglacial climate change by enhancing the initial CO_2 greenhouse forcing with additional water vapor effects (*11*, *41*). Tropical temperature feedbacks could easily spill over into forcings on methane and nitrous oxide emissions from tropical wetlands as well, as suggested by the record of these gases in polar ice cores (*12*, *23*).

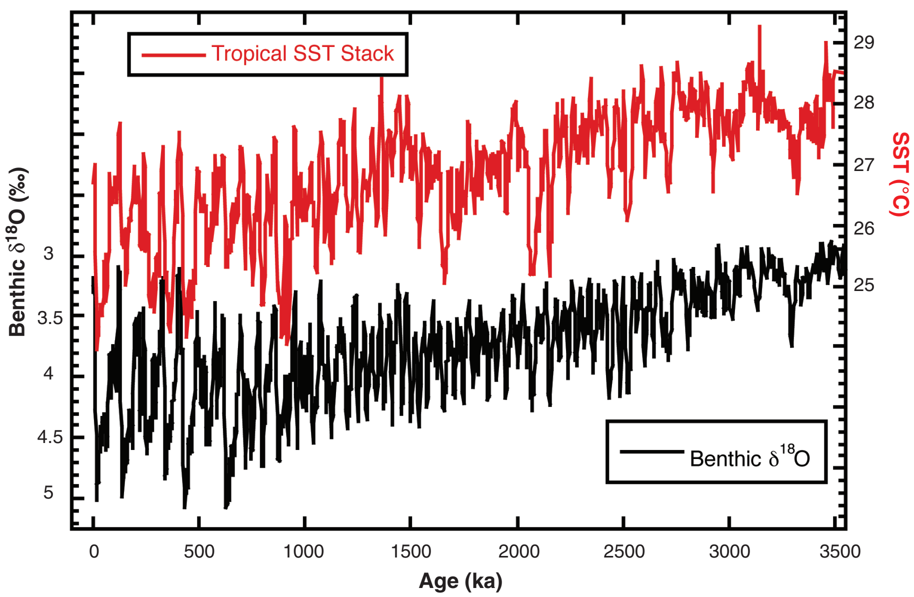

Fig. 4. Comparison of the tropical stack (four alkenone records plus Mg/Ca record from ODP site 806 of Medina *et al.* (*19*) to the global benthic $\delta^{18}O$ stack of Lisiecki and Raymo (*26*).

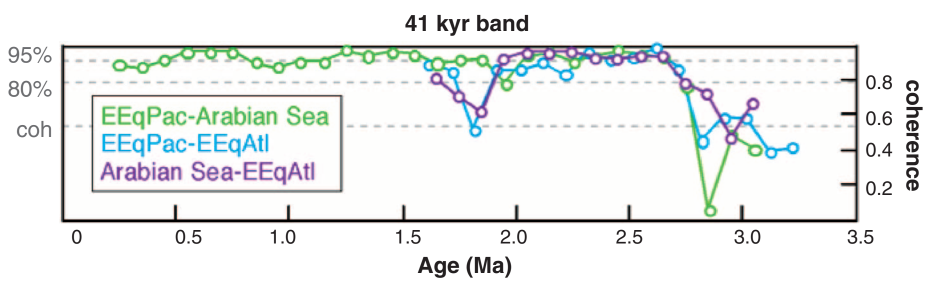

Fig. 5. Coherence between tropical sites at the 41-ky obliquity frequency, across the time span of intensification of Northern Hemisphere glaciation. The coherence at the 41-ky band rises sharply around 2.7 Ma and remains high from that time to the present. Coherence was determined by means of cross-spectral analysis using a 500-ky window with one-half lags.

We therefore used the rhythm and amplitude of the tropical SST stack to infer the following sequence of greenhouse gas–climate relations over the past 3.5 My. Before the onset of cyclic Northern Hemisphere glaciation, CO_2 and tropical temperatures varied dominantly at the ~404-ky cycle, with only modest amplitude. At about 2.7 Ma, poorly understood climatic processes began to couple high-latitude Northern Hemisphere glaciation to deep-ocean CO_2 sequestration at the obliquity pacing, which led to the step-function increase in coherency at the 41-ky obliquity component between the tropical SSTs and also between the tropical records and deep ocean $\delta^{18}O$ (Fig. 5 and fig. S5). Since that time, every glacial cycle was sustained to a large degree by a reduction in CO_2 and other greenhouse gases, as evidenced by the consistent pattern of tropical cooling and warming exhibited in close temporal association with increases and decreases in the $\delta^{18}O$ record. The amplitude and pacing of the greenhouse gas cycles has changed sympathetically with high-latitude climate as well: We would infer that the late Pliocene–early Pleistocene declines in CO_2 were much less severe than those of the late Pleistocene, as evidenced by the smaller drops in tropical SST. The transition from the 41-ky regime to the late Pleistocene 100-ky regime—although it led to deeper glacial extremes—hardly seems like a revolution. Tropical SSTs were strongly coupled to high-latitude change before this transition, and a pervasive ~400-ky (possibly eccentricity-related) modulation of SST variance preceded the spectral shift by at least 1.5 My. The increasingly similar pattern of SST variance (Fig. 3) reflects the imposition of an increasingly powerful greenhouse gas component of tropical SST forcing that overrode potentially divergent regional dynamical responses of tropical SST to the ice ages. The pattern we sketch seems consistent with the less continuous but more direct evidence on the evolution of CO_2 over the past 2 My (*42*) on the basis of the boron isotope proxy in marine plankton shells. As reconstructed in that study, CO_2 excursions also occurred with the ice age cycles of both the "41 ky" and "100 ky" worlds, although their amplitude during the 41 ky world of the early Pleistocene was approximately one half (30 to 40 parts per million) of typical late Pleistocene 100-ky ice age cycles.

If greenhouse gas feedbacks largely coordinated the intensity of the glacial effect on global climates, then how can one explain the evidence to this point that global CO_2 levels have declined by only a very small amount from the mid-Pliocene to the present (*43*–*46*)? The answer seems to us that our view of climate evolution over this time has been confounded by two types of trends in the data. The first is the tendency for glacial cycles after 2.7 Ma to become more intense toward the present, which is evident in both the benthic $\delta^{18}O$ record and in our tropical SST data. Many studies have implicitly assumed that this dynamic represents a second process, a progressive drift toward cooler and more glaciated conditions. Linear fits to long climatic time series appear to support such a drift (Table 1), but they are quite misleading. If we look simply at the long-term trend of extremes of the ice ages and pick the maxima and minima of the benthic $\delta^{18}O$ curve for succeeding glacial and interglacial periods, we see that the behaviors are quite different from each other (Fig. 6A). The depth of glaciations increases almost monotonically toward the present. Interglacials, however, have changed relatively little over the past 3.5 My. After a period of progressive cooling and/or increase in continental ice in the late Pliocene, interglacial climates in fact reached their coldest/most glaciated extent in the early—not late—Pleistocene. This interpretation is consistent with the ice volume reconstruction of (*35*) that suggests more-intense deglaciations for the late as compared with the early Pleistocene. The story from the tropics is quite similar (Fig. 6, B and C). Interglacial cooling has been modest (Fig. 6C). Interglacial temperature decline at our sites has not been uniform but ranges from about 0.15°C per million years to 0.7°C per million years (Table 1). Only the eastern equatorial Pacific cold tongue (represented by ODP site 846) shows a strong progressive cooling over time (we have not tried to model oscillatory components of the data in Fig. 6). Evidence from the Indo-Pacific warm pool based on a different (Mg/Ca) SST proxy suggests essentially no cooling over the past 3.5 My (*19*, *47*, *48*). We therefore estimate the aggregate tropical interglacial cooling to lie in the range of 0.5 to 0.75°C over the past 3.5 My. In contrast, glacial SST cooling has intensified strongly and consistently between the sites (Fig. 6B).

The story of the evolution of global climate in relation to Northern Hemisphere glaciation turns out to concern mostly the ice ages themselves: It is a story of how and why, beginning at about 2.7 Ma, the climate began to plunge ever more deeply into ice ages over time while recovering to a similar interglacial state in between ice ages. A modest (1 to 2°C) change in deep-ocean temperatures over this interval, and essentially no change in interglacial sea levels (*35*), together with the small interglacial tropical ocean surface cooling we estimate above, require only subtle reductions in CO_2 and greenhouse gases in the interglacial state of climate since 2.7 Ma. This picture is consistent with reconstructed glacial-interglacial contrasts in partial pressure of CO_2 (P_{CO_2}) (*42*), which display no systematic reduction in interglacial

Table 1. Statistical analysis of alkenone SST trends shown in (Fig. 6). *T*, temperature in degrees Celsius; *r*, correlation coefficient; *t*, age in millions of years.

Site	Time span	Linear trend of SST (entire series)	Interglacial trend	Glacial trend
ODP 662	0–3.5 Ma	$T = 24.56 + 0.647 \times t$, $r = 0.64$	$T = 26.09 + 0.242 \times t$, $r = 0.47$	$T = 22.95 + 1.02 \times t$, $r = 0.78$
ODP 722	0–3.4 Ma	$T = 25.44 + 0.600 \times t$, $r = 0.60$	$T = 26.85 + 0.156 \times t$, $r = 0.33$	$T = 24.71 + 0.677 \times t$, $r = 0.72$
ODP 846	0–3.5 Ma	$T = 22.01 + 1.00 \times t$, $r = 0.86$	$T = 23.37 + 0.699 \times t$, $r = 0.61$	$T = 21.06 + 1.169 \times t$, $r = 0.82$
ODP 1146	0–2.1 Ma	$T = 23.80 + 1.437 \times t$, $r = 0.65$	$T = 26.46 + 0.224 \times t$, $r = 0.31$	$T = 23.10 + 1.459 \times t$, $r = 0.83$

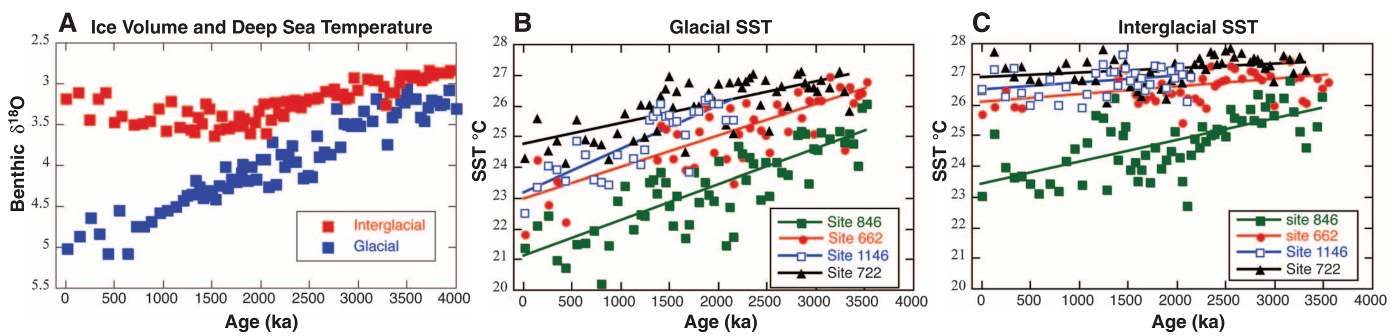

Fig. 6. (**A**) Evolution of benthic $\delta^{18}O$ for interglacial and glacial periods over the past 4 My. (**B**) Evolution of tropical SST for glacial periods over the past 3.5 My, with least squares line fit superimposed. (**C**) Evolution of tropical SSTs for interglacial periods over the past 3.5 My, with least-squares line fit superimposed.

CO_2 levels over the past 2.1 My but rather an intensification of P_{CO_2} drawdown in glacial periods toward the present, as would be inferred from the asymmetrical evolution of our continuous tropical temperature stack (Fig. 3). Provided that consistent, orbital-resolution paleo-CO_2 reconstructions can be obtained in the future, our tropical temperature stack can help to constrain the equilibrium sensitivity of tropical climate to CO_2 forcing over a range of paleo-CO_2 perturbations since the mid-Pliocene (*42–46*).

References and Notes

1. A. J. Broccoli, S. Manabe, *Clim. Dyn.* **1**, 87 (1987).
2. C. S. Jackson, A. J. Broccoli, *Clim. Dyn.* **21**, 539 (2003).
3. D. H. Andreasen, A. C. Ravelo, A. J. Broccoli, *J. Geophys. Res.* **106**, (C1), 879 (2001).
4. S.-Y. Lee, C. J. Poulsen, *Earth Planet. Sci. Lett.* **248**, 238 (2006).
5. S. G. Philander, A. V. Fedorov, *Paleoceanography* **18**, 1045 (2003).
6. D. Archer, A. Winguth, D. Lea, N. Mahowald, *Rev. Geophys.* **38**, 159 (2000).
7. D. M. Sigman, S. L. Jaccard, G. H. Haug, *Nature* **428**, 59 (2004).
8. J. R. Toggweiler, *Paleoceanography* **14**, 571 (1999).
9. M. A. Cane, *Science* **282**, 59 (1998).
10. P. Huybers, P. Molnar, *Clim. Past* **3**, 549 (2007).
11. I. M. Held, B. J. Soden, *J. Clim.* **19**, 5686 (2006).
12. R. Spahni *et al.*, *Science* **310**, 1317 (2005).
13. CLIMAP Project Members, *Science* **191**, 1131 (1976).
14. D. W. Lea, *J. Clim.* **17**, 2170 (2004).
15. A. C. Mix, A. E. Morey, N. G. Pisias, S. W. Hostetler, *Paleoceanography* **14**, 350 (1999).
16. M. S. Kienast, S. Steinke, K. Stattegger, S. E. Calvert, *Science* **291**, 2132 (2001).
17. A. Rosell-Mele *et al.*, *Geophys. Res. Lett.* **31**, L03208 (2004).
18. Z. Liu, T. D. Herbert, *Nature* **427**, 720 (2004).
19. M. Medina-Elizalde, D. W. Lea, *Science* **310**, 1009 (2005).
20. M. W. Schmidt, M. J. Vautravers, H. J. Spero, *Geochem. Geophys. Geosyst.* **7**, Q02P10 (2006).
21. J. R. Petit *et al.*, *Nature* **399**, 429 (1999).
22. U. Siegenthaler *et al.*, *Science* **310**, 1313 (2005).
23. L. A. Loulergue *et al.*, *Nature* **453**, 383 (2008).
24. D. Lüthi *et al.*, *Nature* **453**, 379 (2008).
25. N. J. Shackleton *et al.*, *Nature* **307**, 620 (1984).
26. L. E. Lisiecki, M. E. Raymo, *Paleoceanography* **20**, PA1003 (2005).
27. P. J. Muller, G. Kirst, G. Ruhland, I. von Storch, A. Rossell-Mele, *Geochim. Cosmochim. Acta* **62**, 1757 (1998).
28. J. D. Hays, J. Imbrie, N. J. Shackleton, *Science* **194**, 1121 (1976).
29. J. Imbrie *et al.*, *Paleoceanography* **8**, 699 (1993).
30. S. C. Clemens, R. Tiedemann, *Nature* **385**, 801 (1997).
31. P. Huybers, C. Wunsch, *Nature* **434**, 491 (2005).
32. L. E. Lisiecki, M. E. Raymo, *Quat. Sci. Rev.* **26**, 56 (2007).
33. N. J. Shackleton, *J. Sci.* **217**, 1897 (2000).
34. R. Bintanja, R. S. W. van de Wal, *Nature* **454**, 869 (2008).
35. S. Sosdian, Y. Rosenthal, *Science* **325**, 306 (2009).
36. M. A. Maslin, G. H. Haug, M. Sarnthein, R. Tiedemann, *Geol. Rundsch.* **85**, 452 (1996).
37. J. Bloemendal, P. deMenocal, *Nature* **342**, 897 (1989).
38. S. J. Feakins, P. B. deMenocal, T. I. Eglinton, *Geology* **33**, 977 (2005).
39. A. C. Clement, A. Hall, A. J. Broccoli, *Clim. Dyn.* **22**, 327 (2004).
40. J. L. Sarmiento, J. R. Toggweiler, *Nature* **308**, 621 (1984).
41. R. T. Pierrehumbert, in *Mechanisms of Global Change at Millennial Time Scales,* P. U. Clark, R. S. Webb, L. D. Keigwin, Eds., vol. 112 of *Geophysical Monograph Series* (American Geophysical Union, Washington, DC, 1999), pp. 339–361.
42. B. Hönisch, N. G. Hemming, D. Archer, M. Siddall, J. F. McManus, *Science* **324**, 1551 (2009).
43. M. Pagani, *Philos. Trans. R. Soc. London A* **360**, 609 (2002).
44. J. Van Der Burgh, H. Visscher, D. L. Dilcher, W. M. Kürschner, *Science* **260**, 1788 (1993).
45. P. N. Pearson, M. R. Palmer, *Nature* **406**, 695 (2000).
46. A. K. Tripati, C. D. Roberts, R. A. Eagle, *Science* **326**, 1394 (2009).
47. M. W. Wara, A. C. Ravelo, M. L. Delaney, *Science* **309**, 758 (2005).
48. C. Karas *et al.*, *Nat. Geosci.* **2**, 434 (2009).

49. This research was supported by National Science Foundation (NSF) grants OCE9986760 and OCE-0351599 to T.D.H. and OCE0623487 and OCE0623310 to T.D.H. and K.T.L. and by grants from the Evolving Earth Foundation to K.T.L. This research used samples provided by ODP and the Integrated Ocean Drilling Program (IODP). ODP was sponsored by NSF and participating countries under the management of Joint Oceanographic Institutions. IODP is supported by NSF; Japan's Ministry of Education, Culture, Sports, Science and Technology; the European Consortium for Ocean Drilling Research; and the People's Republic of China, Ministry of Science and Technology.

Supporting Online Material
www.sciencemag.org/cgi/content/full/328/5985/1530/DC1
SOM Text
Figs. S1 to S4
References

2 December 2009; accepted 30 April 2010
10.1126/science.1185435

Target RNA–Directed Trimming and Tailing of Small Silencing RNAs

Stefan L. Ameres,[1] Michael D. Horwich,[1] Jui-Hung Hung,[2] Jia Xu,[2] Megha Ghildiyal,[1] Zhiping Weng,[3] Phillip D. Zamore[1]*

In *Drosophila*, microRNAs (miRNAs) typically guide Argonaute1 to repress messenger RNA (mRNA), whereas small interfering RNAs (siRNAs) guide Argonaute2 to destroy viral and transposon RNA. Unlike siRNAs, miRNAs rarely form extensive numbers of base pairs to the mRNAs they regulate. We find that extensive complementarity between a target RNA and an Argonaute1-bound miRNA triggers miRNA tailing and 3′-to-5′ trimming. In flies, Argonaute2-bound small RNAs—but not those bound to Argonaute1—bear a 2′-*O*-methyl group at their 3′ ends. This modification blocks target-directed small RNA remodeling: In flies lacking Hen1, the enzyme that adds the 2′-*O*-methyl group, Argonaute2-associated siRNAs are tailed and trimmed. Target complementarity also affects small RNA stability in human cells. These results provide an explanation for the partial complementarity between animal miRNAs and their targets.

In *Drosophila melanogaster*, different pathways produce small interfering RNAs (siRNAs) and microRNAs (miRNAs) (*1*). Fly siRNAs associate with Argonaute2 (Ago2) to direct cleavage of target RNAs with extensive complementarity to the siRNA guide [RNA interference (RNAi)], whereas miRNAs typically act with Argonaute1 (Ago1) to decrease the translation and stability of partially complementary mRNAs (*2–5*). In plants, both siRNAs and miRNAs bind target mRNAs through extensive base pairing across the entire small RNA guide (*6*). The reason for the difference between animals and plants in the degree of complementarity between miRNAs and their targets remains enigmatic.

[1]Howard Hughes Medical Institute and Department of Biochemistry and Molecular Pharmacology, University of Massachusetts Medical School, Worcester, MA 01605, USA. [2]Department of Biomedical Engineering, Boston University, Boston, MA 02215, USA. [3]Program in Bioinformatics and Integrative Biology, University of Massachusetts Medical School, Worcester, MA 01605, USA.

*To whom correspondence should be addressed. E-mail: phillip.zamore@umassmed.edu

In flies, a key step in the production of a functional siRNA-Ago2 complex, but not a miRNA-Ago1 complex, is the addition of a 2′-*O*-methyl group to the 3′ end of the small RNA by Hen1 (*7–9*), an *S*-adenosylmethionine–dependent methyltransferase (*10*). Plant Hen1 protects siRNAs and miRNAs alike from 3′-terminal uridylation and degradation (*10–12*). The function of siRNA methylation in flies is unknown.

miRNA sensors affect steady-state miRNA levels. In a set of *Drosophila* cell lines that expressed reporter transgenes with one or more fully complementary sites for miRNAs ("miRNA sensors"), we noted that the steady-state abundance of the corresponding miRNA was decreased (Fig. 1). For example, a stably transformed S2 cell line constitutively expressing *egfp* (enhanced green fluorescent protein) mRNA bearing in its 3′ untranslated region (3′UTR) two sites fully complementary to miR-34 showed a decrease in miR-34, but not other miRNAs, relative to control *egfp* cell lines (Fig. 1A). Treatment of S2 cells with ecdysone induces the expression of *let-7* and miR-125, among other miRNAs (*13*). After ecdysone treatment, the steady-state abundance of *let-7*, but not that of miR-125 [which resides in the same primary transcript (fig. S1)], was lower at both 24 and 48 hours after induction in a stable S2 cell line expressing *egfp* bearing in its 3′UTR four sites fully complementary to *let-7*, compared to cell lines expressing *egfp* with two sites for miR-1 or miR-34 (Fig. 1A). Similarly, a clonal cell line expressing an *egfp* mRNA bearing two sites

complementary to the miRNA, *bantam*, showed reduced levels of *bantam* ($P < 0.001$), but not of miR-277 ($P < 0.26$) or miR-33 ($P < 0.38$), relative to a clonal cell line expressing *egfp* without miRNA-complementary sites (Fig. 1, B and C, and fig. S2) (*14*). Transient expression of a primary RNA containing both *let-7* and miR-1 hairpins in clonal reporter lines producing *egfp* with sites complementary to miR-1 or *let-7* decreased only the miRNA that can bind the complementary target (fig. S3) (*14*). Finally, miR-34 levels were significantly reduced ($P < 0.01$) in four independently derived clonal reporter cell lines expressing *egfp* bearing two miR-34 complementary sites (fig. S4) (*14*). The expression of mRNAs containing sites perfectly complementary to a miRNA did not influence the detection of those miRNAs by Northern hybridization (fig. S5) (*14*).

Target-dependent destabilization of miR-277. *Drosophila* siRNAs and miRNAs partition between Ago1 and Ago2 according to their duplex structure (*15*–*18*). Consequently, some miRNAs, including miR-277, partition into both Ago1 and Ago2 (*19*). Expression of *egfp* bearing two sites fully complementary to miR-277 caused a small but significant reduction in the abundance of that miRNA ($P < 0.018$) when compared to an *egfp*-expressing control cell line (Fig. 2A). We used Ago1 immunoprecipitation as well as oxidation with $NaIO_4$ followed by β-elimination to distinguish between Ago1- and Ago2-loaded miR-277 (Fig. 2B and fig. S6) (*8*). Ago2-loaded small RNAs bear 2′-*O*-methyl–modified 3′ termini, making them refractory to oxidation; Ago1-loaded miRNAs bear 2′,3′-hydroxy 3′ termini, so that oxidation followed by β-elimination removes their final nucleotide, making them 1 nucleotide (nt) shorter. Relative to a control reporter, the miR-277–complementary reporter had a significant effect on Ago1-associated miR-277 ($P < 0.007$) but not Ago2-associated miR-277 ($P < 0.71$; Fig. 2B and fig. S6) (*14*). This is consistent with earlier observations that Ago2, but not Ago1, silences an *egfp* reporter with target sites perfectly complementary to miR-277 (*19*).

Target RNA–dependent remodeling of small RNAs in vitro. To decipher the mechanism by which a complementary target RNA triggers miRNA destabilization, we followed the fate of a miRNA in the presence of a perfectly complementary target RNA. A small RNA duplex comprising 5′ ^{32}P-radiolabeled *let-7* bound to *let-7** was assembled into Ago1 in *Drosophila* embryo lysate (Fig. 3A). When a fully complementary, 7-methylguanosine–capped target RNA was added to the lysate after loading *let-7* into Ago1, the amount of intact *let-7* declined and new longer ("tailed") and shorter ("trimmed") forms of *let-7* appeared; *let-7* was unaffected by addition of a control target (Fig. 3B and fig. S7). Similar results were obtained for a miRNA with different sequence (fig. S8). The added nucleotides in the tailed *let-7* species were adenines (table S1).

Lysates from 0- to 2-hour-old *Drosophila* embryos contain endogenous *bantam* miRNA loaded into Ago1 (*4*). Incubation of these lysates with an in vitro transcribed, 7-methylguanosine–capped target RNA containing one site fully complementary to *bantam* triggered tailing and

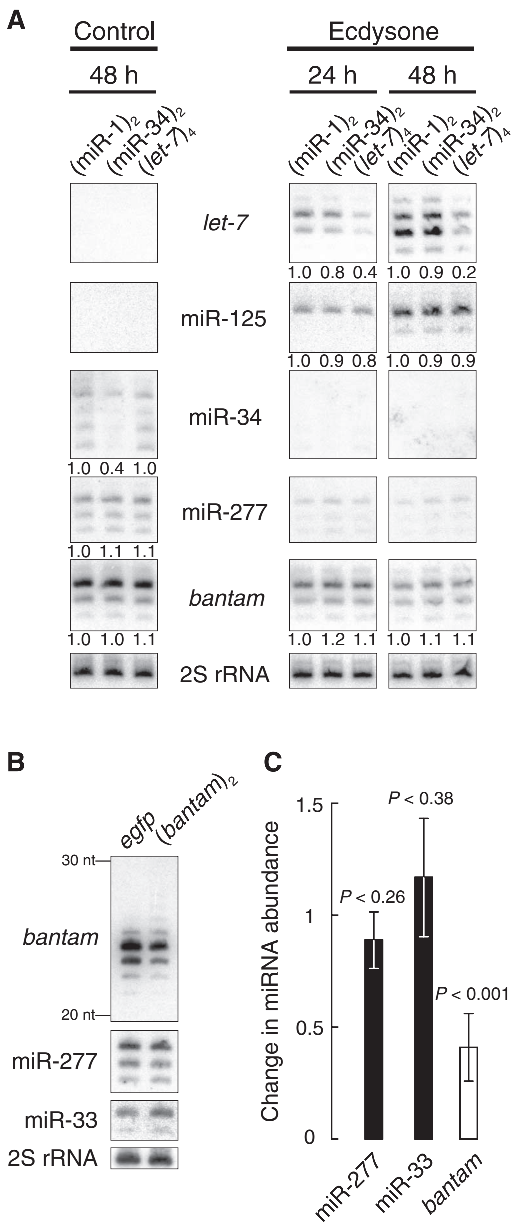

Fig. 1. Target-directed destabilization of miRNAs. (**A**) Northern analysis of total RNA from S2 cells stably expressing *egfp* mRNA bearing in its 3′UTR two target sites for miR-1 [(miR-1)$_2$] or miR-34 [(miR-34)$_2$] or four target sites for *let-7* [(*let-7*)$_4$]. Time of ecdysone (right panels) or control treatment (left panel) is indicated. Relative levels of the miRNAs are indicated below the lanes. (**B**) Representative Northern analysis of total RNA from a clonal S2 cell line expressing *egfp* mRNA bearing in its 3′UTR two target sites for *bantam* [(*bantam*)$_2$] and a clonal control cell line expressing sole *egfp* mRNA. (**C**) Means ± SD for three biologically independent replicates of the experiment in (B). Levels of each miRNA were first normalized to the 2*S* rRNA loading control.

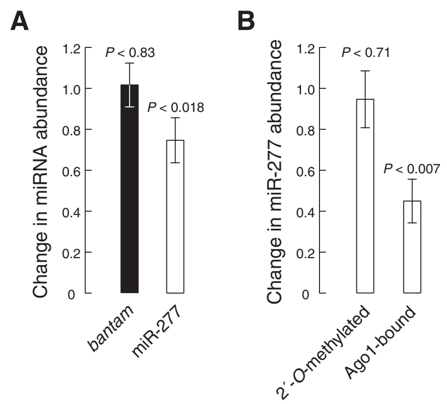

Fig. 2. Target-dependent destabilization of miR-277. (**A**) Change in miR-277 or *bantam* abundance in total RNA from a clonal S2 cell line expressing *egfp* mRNA bearing in its 3′UTR two target sites for miR-277 [(miR-277)$_2$], relative to a clonal control cell line expressing sole *egfp* mRNA. Before comparison, miRNA levels were normalized to the 2*S* rRNA loading control. (**B**) Change in 2′-*O*-methylated (estimated by resistance to oxidation and β-elimination) and Ago1-associated miR-277 (determined by immunoprecipitation) [see fig. S6 and (*14*) for details]. In all experiments, at least two technical replicates of three biologically independent measurements were used to determine means ± SD.

trimming of *bantam*, whereas a control target did not alter *bantam* length or abundance (Fig. 3C). Thus, fully complementary target RNAs triggered tailing and trimming in vitro for both an exogenous miRNA assembled into Ago1 in vitro (*let-7* and *bantam*) and an endogenous miRNA (*bantam*) assembled in vivo, before the lysate was prepared.

To determine whether 3′-terminal 2′-*O*-methylation—a modification found on Ago2- but not Ago1-associated small RNAs (*8*)—influences target-directed miRNA tailing or trimming, we used a *let-7*/*let-7** duplex to assemble *let-7* bearing a 2′-*O*-methyl–modified 3′ end into Ago1 in embryo lysate; the 2′-*O*-methyl–modified *let-7* was loaded normally into Ago1 (fig. S9). The presence of a methyl group at the 2′ position of the 3′-terminal nucleotide blocked tailing and trimming of Ago1-bound *let-7* (Fig. 3D). A 3′-terminal, 3′-deoxy modification also inhibited target-directed effects (fig. S10). siRNAs, which load into Ago2 in embryo lysate, were not affected (Fig. 3, E and F). However, in extracts prepared from embryos of homozygous mutant *hen1^{f00810}* flies (*8*, *9*), the Ago2-bound siRNA became susceptible to target-dependent tailing and trimming (Fig. 3F). These data suggest that methylation of small RNAs by Hen1 renders them resistant to the small RNA modifying and trimming enzymes recruited by a small RNA-bound complementary target RNA.

Sequence requirements for miRNA remodeling. Relative to plant miRNAs, animal miRNAs are generally less complementary to their target sites (*20*). To determine the extent of complementarity required to elicit tailing and trimming, we analyzed a set of target RNAs with various different degrees of complementarity to a ^{32}P-radiolabeled miRNA loaded into Ago1 in embryo lysate (Fig. 4A). Target sites that resembled the majority of natural miRNA binding sites in animals—including sites paired only to the miRNA seed region or to both the seed and a small patch of 3′ sequence identified as a miRNA-binding determinant (*20*)—did not trigger tailing and trimming (Fig. 4B and fig. S11). Targets with eight or fewer mismatches with the 3′ end of the miRNA triggered tailing and trimming (Fig. 4, A and B, and fig. S11). Moreover, a small central bulge of 3 nt, flanked by fully complementary sequence, triggered tailing and trimming, but 5- or 7-nt central bulges did not. We conclude that in vitro, target RNA–directed tailing and trimming of a miRNA requires extensive but not complete complementarity, whereas the canonical animal miRNA binding sites described previously do not alter miRNA stability.

Hen1 protects Ago2-bound small RNAs. We sequenced 18- to 29-nt small RNAs from heterozygous or homozygous mutant *hen1^{f00810}* heads (tables S2 and S3). Consistent with the idea that Hen1 does not act on Ago1-associated small RNAs, the absence of Hen1 in the mutant flies altered neither the abundance nor the length of most miRNAs (Fig. 5A). The most abundant class of Ago2-bound small RNAs are endogenous siRNAs (endo-siRNAs), and they are fully or extensively complementary to cellular or transposon-derived mRNAs (*21*–*24*). The length heterogeneity of perfectly genome-matching endo-siRNA reads increased in *hen1^{f00810}* mutant heads relative to the heads of their heterozygous siblings (Fig. 5B, upper panel, and fig. S15). In contrast, endo-siRNA reads that contain 3′ nontemplated nucleotide additions (prefix reads) increased in the *hen1* mutant heads (Fig. 5B, lower panel). The sequences of prefix reads correspond to the reference fly genome for their first ≥15 nt, then contain a short tail of 3′ nucleotides not found in genomic sequence. The majority of prefix reads contained a single 3′ uridine tail; the

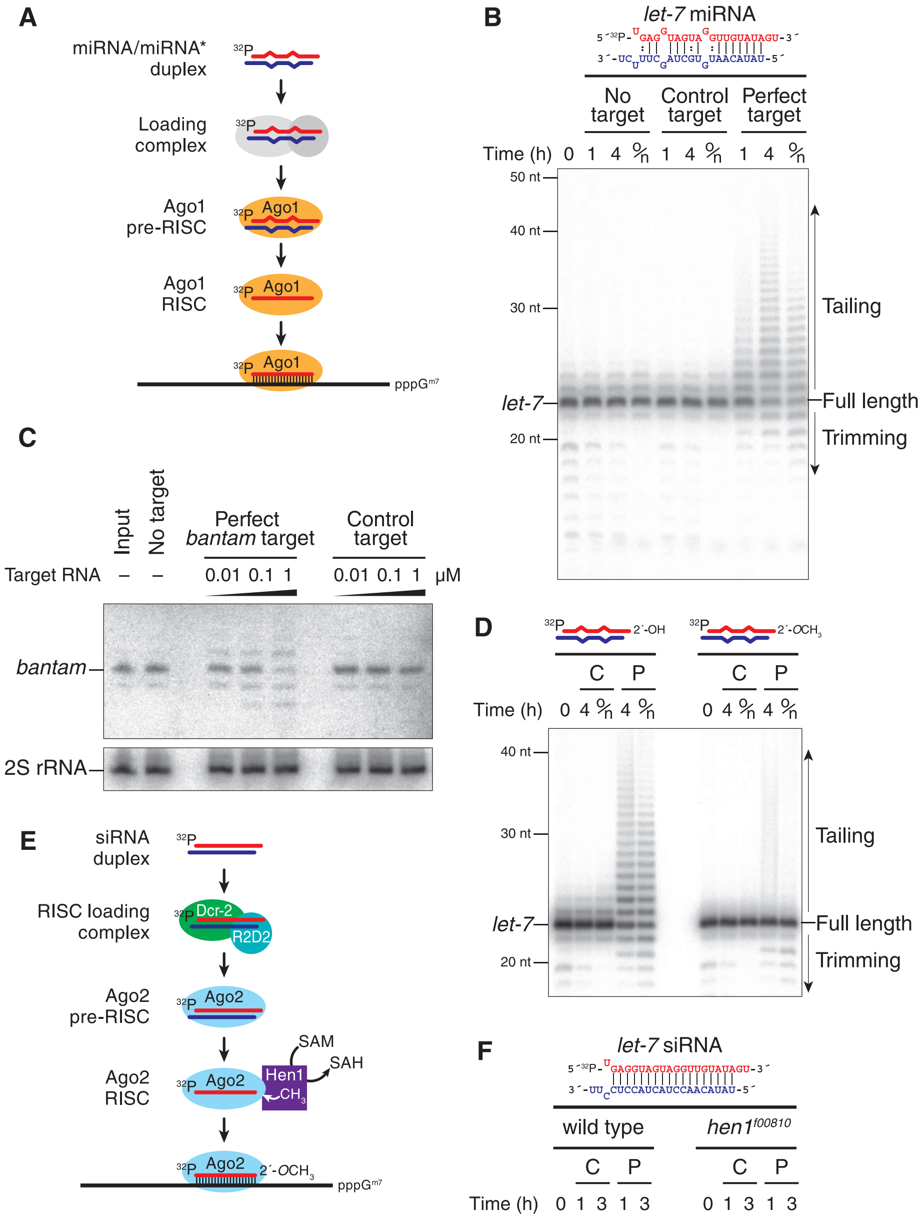

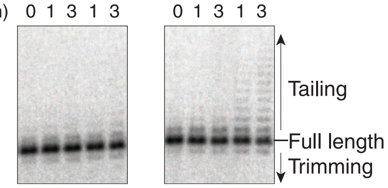

Fig. 3. Terminal 2′-*O*-methyl modification and Argonaute protein identity control small RNA stability. (**A**) The in vitro miRNA stability assay used in (B) and (D). (**B**) In the presence of a fully complementary target RNA, but not an unrelated control RNA, *let-7* was tailed and trimmed. (**C**) Endogenous *bantam* miRNA was tailed and trimmed when *Drosophila* embryo extract was incubated overnight with a fully complementary target RNA, but not a control target. *bantam* and 2S rRNA were detected by Northern blotting. (**D**) 2′-*O*-methyl modification of an Ago1-loaded miRNA blocked tailing and trimming. (**E**) The in vitro siRNA stability assay used in (F). (**F**) A fully complementary target RNA directed tailing and trimming of an Ago2-loaded siRNA in the absence of Hen1. C, control target RNA; P, perfectly complementary target RNA; o/n, overnight.

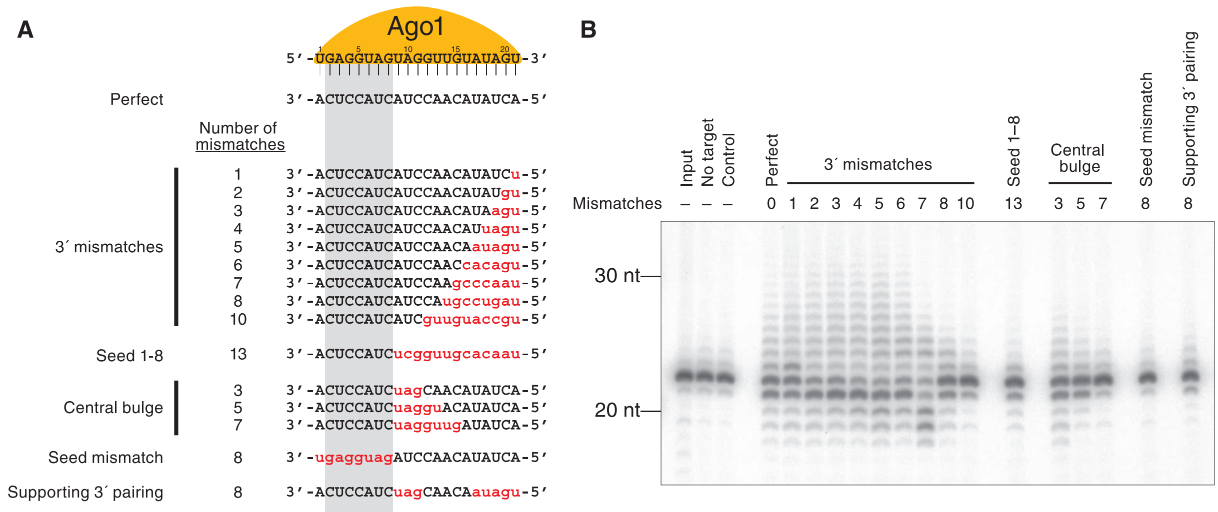

Fig. 4. Target sequence requirements for miRNA tailing and trimming. (**A**) Target RNAs assayed for their ability to direct tailing and trimming in vitro. Mismatches are indicated with red lowercase letters. The miRNA seed sequence is highlighted in gray. (**B**) Seed pairing plus extensive central and 3′ pairing between the miRNA and the target was required for efficient tailing and trimming. The miRNA duplex was assembled into Ago1 by incubation in *Drosophila* embryo lysate, then the target RNA was added and the reaction incubated overnight.

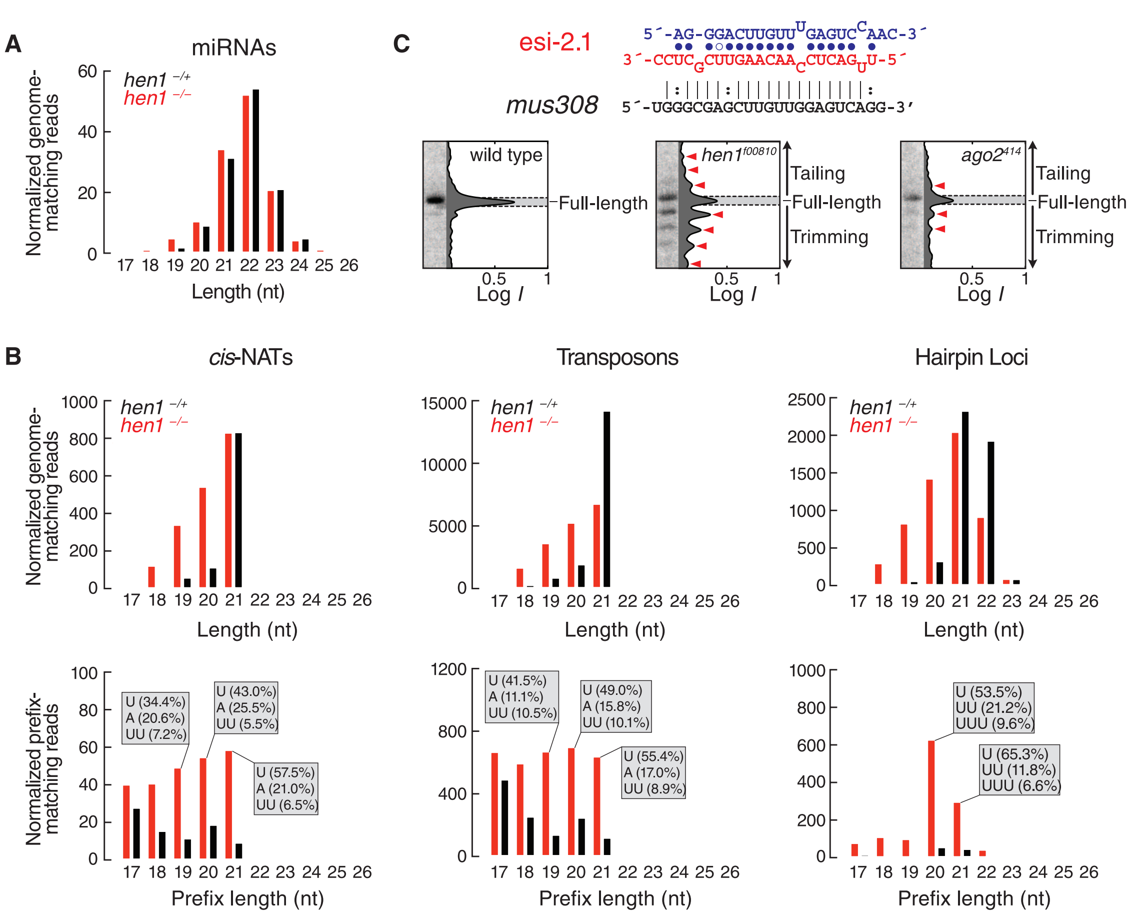

Fig. 5. Small RNA tailing and trimming in vivo. (**A**) Length distribution of miRNAs from heterozygous (black) or homozygous (red) *hen1*^{f00810} fly heads. For each annotated pre-miRNA, reads were normalized to sequencing depth, then normalized miRNA reads for each distinct pre-miRNA were weighted equally to eliminate the influence of differences in transcriptional rates. (**B**) Length distribution of endo-siRNA sequence reads perfectly matching the fly genome (top panels) or matching only within a 5′ prefix (bottom panels) for heterozygous (black) or homozygous (red) *hen1*^{f00810} heads. The three classes of endo-siRNAs were analyzed separately: siRNAs derived from natural antisense transcripts (cis-NATs), from transposons, or from hairpin loci (esiRNAs). The most frequent non–genome-matching nucleotide additions are indicated in the gray boxes as the percentage of all nontemplated additions for specific prefix lengths. Reads are in parts per million (ppm). (**C**) The sequence of the esi-2.1 duplex and its cellular mRNA target, *mus308*. Northern analysis was used to detect esi-2.1 in total RNA from whole Oregon R (wild type), *hen1*^{f00810}, or *ago2*^{414} mutant flies, and absolute signal intensities (*I*, $\log_{10}$ scale) were determined for each lane. Tailing and trimming products are marked with red arrowheads.

second most abundant nucleotide added was adenine. Longer tails comprising more than one non–genome-matching addition were rare but nearly always corresponded to homopolymeric stretches of uridines (Fig. 5B, lower panel). Such uridine tails are found on small RNAs in plants lacking Hen1 and are believed to tag siRNAs and miRNAs for destruction (*12*).

In vivo, endo-siRNAs from long hairpin transcripts (esiRNAs) associate predominantly with Ago2, but a minor fraction can be detected bound to Ago1 (*22*, *23*, *25*). In the absence of Hen1, esiRNAs generally became shorter (Fig. 5B). In particular, esi-2.1 (also termed hp-CG4068B and esiRNA-sl-1)—the most abundant hairpin-derived endo-siRNA—was less abundant, tailed, and trimmed in both *hen1*^{f00810} and *ago2*^{414} whole mutant flies relative to the wild type (Fig. 5C and fig. S12). We speculate that distinct consequences follow the loss of Hen1 and Ago2: In a *hen1* mutant, Ago2-bound esi-2.1 becomes tailed and trimmed, because it no longer possesses a protective 3′-terminal, 2′-*O*-methyl modification. Thus, for small RNAs such as esi-2.1, tailed and shortened species comprise both Ago1- and Ago2-loaded RNAs. In contrast, in an *ago2* mutant, the normally Ago2-bound small RNAs no longer exist, so the only remaining tailed and shortened species must derive from Ago1-bound esiRNAs. High-throughput sequencing data suggest that trimming of esi-2.1 occurs almost exclusively in the 3′-to-5′ direction (table S4).

A model for small RNA tailing and trimming in *Drosophila*. Our data suggest a model for the influence of target RNA complementarity on

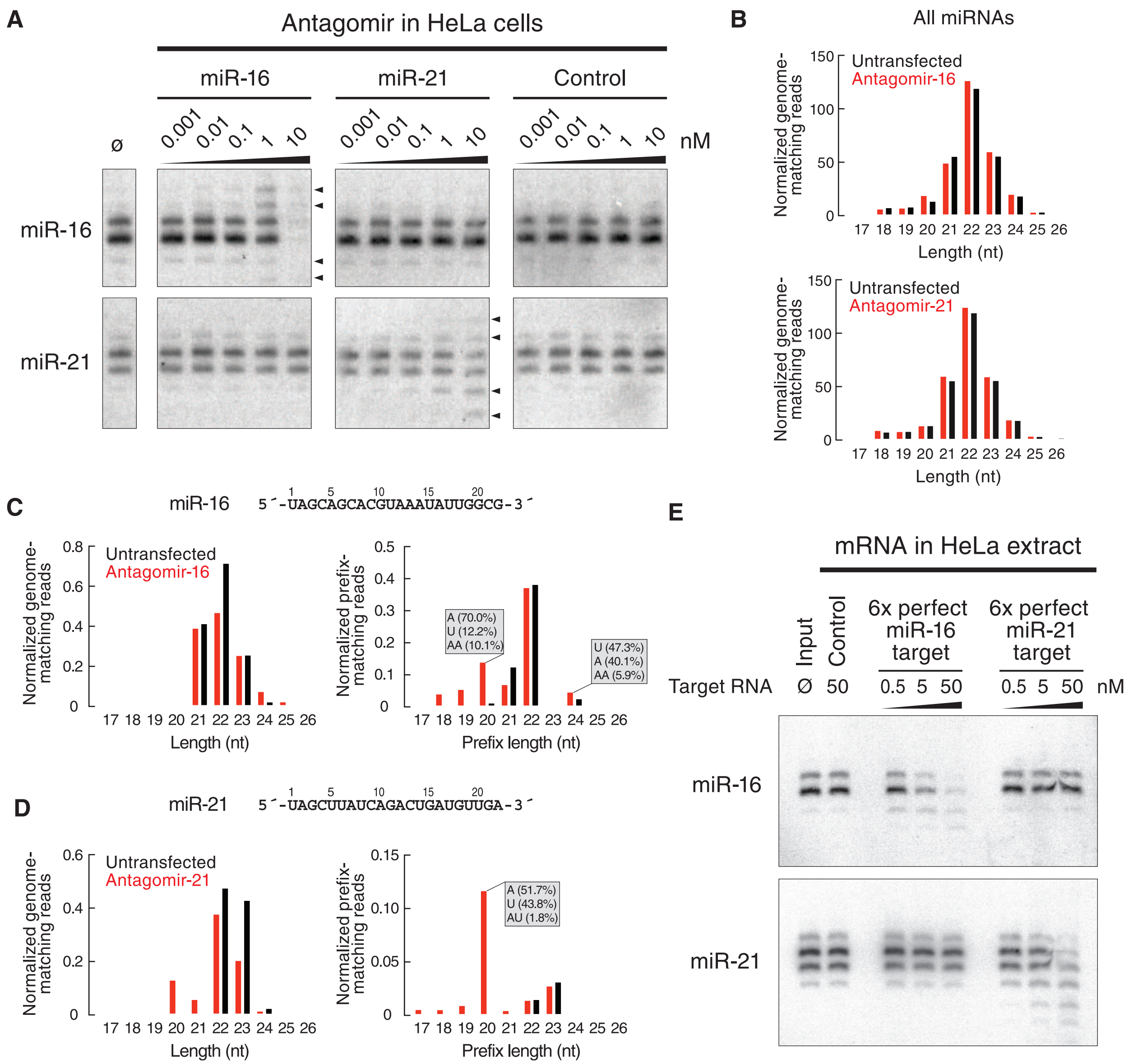

Fig. 6. Target-dependent small RNA remodeling and destabilization in cultured human HeLa cells. (**A**) Northern analysis of total RNA from HeLa cells transfected with increasing amounts of 21-nt target RNA analogs (antagomirs) fully complementary to miR-16 or miR-21. Arrowheads mark tailed or trimmed miRNAs. (**B**) Total miRNA length distribution in mock-transfected HeLa cells and in cells transfected with 1 nM antagomir targeting miR-16 (top) or 10 nM antagomir targeting miR-21 (bottom). (**C** and **D**) Small RNA profile from HeLa cells mock-transfected (black) or transfected (red) with 1 nM antagomir targeting miR-16 (C) or 10 nM antagomir targeting miR-21 (D). Left panels: Reads perfectly matching the miR-16-1 and miR-16-2 loci (C) or the miR-21 locus (D). Right panels: Reads with prefixes matching miR-16-1 and miR-16-2 (C) or miR-21 (D). Non–genome-matching nucleotides added to the 3′ end of the prefixes that most increased in response to antagomir transfection are shown (gray boxes). Reads are in ppm. (**E**) Endogenous miR-16 and miR-21 were destabilized when HeLa cytoplasmic extract was incubated with a fully complementary target mRNA but not with a control target. miR-16 and miR-21 were detected by Northern blotting.

small RNA abundance in *Drosophila* (fig. S13). miRNAs typically direct Ago1 to bind target RNAs and repress their translation and decrease their stability (*26*). Such binding is nearly always mediated by complementarity between the miRNA seed sequence and the target, with few additional base pairs tethering the two RNAs together. The presence of transcripts with extensive complementarity to Ago1-bound small RNAs results in small RNA remodeling, which our data suggest involves a terminal nucleotide transferase and a 3′-to-5′ exonuclease. In contrast, Ago2-associated small RNAs are 2′-*O*-methyl–modified by Hen1 as a final step of Ago2 loading. The methyl group blocks tailing and trimming; in *hen1* mutants, the unmethylated but Ago2-bound small RNAs are subject to target-directed tailing and trimming.

Homologs of the Hen1 methyltransferase are found in plants, fungi, and animals (*8*–*10*, *27*, *28*). In plants, miRNAs and siRNAs alike are methylated by Hen1, and the absence of Hen1 causes small RNAs to be 3′-uridylated and destroyed. In mammals, Hen1 methylates germ line–specific PIWI-interacting RNAs (piRNAs), but not miRNAs (*8*, *9*, *27*, *29*).

Stoffel and colleagues previously described the sequence-specific degradation of miRNAs in response to synthetic, chemically modified RNA-analogs, "antagomirs," designed to block miRNA function in vivo (*30*). In cultured HeLa cells, transfection of antagomirs to miR-16 or miR-21 triggered not only dose-dependent miRNA shortening, but also tailing (Fig. 6A and fig. S14). We sequenced 18- to 30-nt small RNAs from HeLa cells transfected with antagomirs against miR-16 or miR-21 and compared them to the small RNA profile of mock-transfected HeLa cells (tables S2 and S3). The profile of miRNA-matching reads in general did not change after transfection of either antagomir (Fig. 6B). However, we observed a sequence-specific decrease in full-length miR-16 (Fig. 6C, left panel) and miR-21 (Fig. 6D, left panel) in response to treatment with the corresponding antagomir. Like tailing in flies (Fig. 5), a decrease in genome-matching reads triggered by the antagomir was accompanied by an increased number of prefix reads for the antagomir-targeted miRNA, but not the control miRNA (Fig. 6, C and D, right panels, and fig. S15). The nontemplated nucleotides added to the 3′ end of the targeted miRNA were predominantly adenosine and uridine. As in *Drosophila*, target RNA–dependent trimming of small RNAs in HeLa cells was nearly always 3′-to-5′ (table S4). Moreover, we could recapitulate trimming of endogenous human miRNAs in HeLa cell cytoplasmic extract: Incubation of the extract with in vitro transcribed, 7-methylguanosine–capped and polyadenylated target mRNAs containing six sites fully complementary to miR-16 or miR-21 triggered shortening and loss of the corresponding miRNA (Fig. 6E). A control target did not alter miRNA length or abundance. These results suggest that target-dependent small RNA tailing and trimming is conserved between flies and mammals.

Discussion. In flies, RNA methylation by Hen1 enables Ago2 to bind and cleave highly complementary target RNAs; the exclusion of Hen1 from the Ago1-loading pathway restricts Ago1-bound small RNAs to regulate only partially complementary targets. Thus, the methyl group deposited by Hen1 allows specialization of *Drosophila* Argonaute proteins. The finding that Ago1-associated small RNAs are sensitive to target-directed tailing and destruction has likely shaped the evolution of miRNA target sites in *Drosophila* and perhaps other animals; most predicted miRNA binding sites lack substantial pairing to the small RNA 3′ end (*3*, *20*).

Even in *hen1*^{f00810} flies, small RNAs bound to Ago1 are more prone to target RNA–dependent tailing and trimming than those bound to Ago2 (Fig. 3). Ago1 is an inefficient ribonuclease whose catalytic rate is limited by the dissociation of its reaction products (*19*), whereas Ago2 is an efficient multiple-turnover enzyme (*31*). The ability of Ago2 to rapidly cleave its RNA targets may limit its susceptibility. In contrast, Ago1 likely resides on its target RNAs for longer than Ago2, making Ago1-bound small RNAs good substrates for target-directed tailing and trimming.

Uridylation of small RNAs as well as Ago2-cleaved, 5′ target RNA fragments has been linked to RNA turnover (*12*, *32*–*34*). The molecular basis for the tailing and trimming of Argonaute-bound small RNAs is unknown. The ends of small RNAs are anchored to Argonaute proteins through binding of the small RNA 5′ phosphate to a pocket composed mainly of residues from the Mid domain and binding of the small RNA 3′ end to the PAZ domain (*35*–*41*). Access to the 3′ end of the small RNA likely requires dislodging it from the PAZ domain. Recent crystal structures of a eubacterial Argonaute protein confirm earlier suggestions that extensive pairing of the 3′ half of a siRNA with its target releases its 3′ end from the PAZ domain (*42*, *43*). Our data are consistent with the idea that extensive 3′ pairing to a target RNA exposes a small RNA to nucleotidyl transferases and 3′-to-5′ exonuclease enzymes.

References and Notes

1. M. Ghildiyal, P. D. Zamore, *Nat. Rev. Genet.* **10**, 94 (2009).
2. S. M. Hammond, S. Boettcher, A. A. Caudy, R. Kobayashi, G. J. Hannon, *Science* **293**, 1146 (2001).
3. J. Brennecke, A. Stark, R. B. Russell, S. M. Cohen, *PLoS Biol.* **3**, e85 (2005).
4. K. Okamura, A. Ishizuka, H. Siomi, M. C. Siomi, *Genes Dev.* **18**, 1655 (2004).
5. S. Iwasaki, T. Kawamata, Y. Tomari, *Mol. Cell* **34**, 58 (2009).
6. M. W. Rhoades *et al.*, *Cell* **110**, 513 (2002).
7. A. Pélisson, E. Sarot, G. Payen-Groschêne, A. Bucheton, *J. Virol.* **81**, 1951 (2007).
8. M. D. Horwich *et al.*, *Curr. Biol.* **17**, 1265 (2007).
9. K. Saito *et al.*, *Genes Dev.* **21**, 1603 (2007).
10. B. Yu *et al.*, *Science* **307**, 932 (2005).
11. W. Park, J. Li, R. Song, J. Messing, X. Chen, *Curr. Biol.* **12**, 1484 (2002).
12. J. Li, Z. Yang, B. Yu, J. Liu, X. Chen, *Curr. Biol.* **15**, 1501 (2005).
13. L. F. Sempere, E. B. Dubrovsky, V. A. Dubrovskaya, E. M. Berger, V. Ambros, *Dev. Biol.* **244**, 170 (2002).
14. See supporting material on *Science* Online.
15. Y. Tomari, T. Du, P. D. Zamore, *Cell* **130**, 299 (2007).
16. B. Czech *et al.*, *Mol. Cell* **36**, 445 (2009).
17. K. Okamura, N. Liu, E. C. Lai, *Mol. Cell* **36**, 431 (2009).
18. M. Ghildiyal, J. Xu, H. Seitz, Z. Weng, P. D. Zamore, *RNA* **16**, 43 (2010).
19. K. Förstemann, M. D. Horwich, L. Wee, Y. Tomari, P. D. Zamore, *Cell* **130**, 287 (2007).
20. D. P. Bartel, *Cell* **136**, 215 (2009).
21. M. Ghildiyal *et al.*, *Science* **320**, 1077 (2008); published online 10 April 2008 (10.1126/science.1157396).
22. B. Czech *et al.*, *Nature* **453**, 798 (2008).
23. K. Okamura *et al.*, *Nature* **453**, 803 (2008).
24. K. Okamura, S. Balla, R. Martin, N. Liu, E. C. Lai, *Nat. Struct. Mol. Biol.* **15**, 581 (2008).
25. Y. Kawamura *et al.*, *Nature* **453**, 793 (2008).
26. P. Brodersen, O. Voinnet, *Nat. Rev. Mol. Cell Biol.* **10**, 141 (2009).
27. Y. Kirino, Z. Mourelatos, *Nat. Struct. Mol. Biol.* **14**, 347 (2007).
28. H. M. Kurth, K. Mochizuki, *RNA* **15**, 675 (2009).
29. T. Ohara *et al.*, *Nat. Struct. Mol. Biol.* **14**, 349 (2007).
30. J. Krützfeldt *et al.*, *Nature* **438**, 685 (2005).
31. B. Haley, P. D. Zamore, *Nat. Struct. Mol. Biol.* **11**, 599 (2004).
32. B. Shen, H. M. Goodman, *Science* **306**, 997 (2004).
33. T. E. Mullen, W. F. Marzluff, *Genes Dev.* **22**, 50 (2008).
34. J. C. van Wolfswinkel *et al.*, *Cell* **139**, 135 (2009).
35. J. J. Song *et al.*, *Nat. Struct. Biol.* **10**, 1026 (2003).
36. K. S. Yan *et al.*, *Nature* **426**, 468 (2003).
37. A. Lingel, B. Simon, E. Izaurralde, M. Sattler, *Nature* **426**, 465 (2003).
38. J. B. Ma, K. Ye, D. J. Patel, *Nature* **429**, 318 (2004).
39. A. Lingel, B. Simon, E. Izaurralde, M. Sattler, *Nat. Struct. Mol. Biol.* **11**, 576 (2004).
40. J. S. Parker, S. M. Roe, D. Barford, *Nature* **434**, 663 (2005).
41. J. B. Ma *et al.*, *Nature* **434**, 666 (2005).
42. Y. Tomari, P. D. Zamore, *Genes Dev.* **19**, 517 (2005).
43. Y. Wang *et al.*, *Nature* **461**, 754 (2009).

44. We thank S. Ma and A. Boucher for help with fly husbandry, G. Farley for technical assistance, E. Pfister for cloning of miR-16 and miR-21 reporter constructs, and members of the Zamore lab for advice, suggestions, and critical comments on the manuscript. Sequence data are available through the NCBI Short Read Archive (www.ncbi.nlm.nih.gov/sites/sra) as GSM278704 (*ago2*^{414}), SRA010045 (*hen1*^{f00810} National Institute on Aging NRSA grant F30AG030283 (M.D.H.), and HeLa cell data), and GSE18806 (Oregon R). Supported by EMBO long-term fellowship ALTF 522-2008, Austrian Science Fund (FWF) Erwin Schrödinger-Auslandsstipendium J2832-B09 (S.L.A.), and NIH grants GM62862 and GM65236 (P.D.Z.). P.D.Z. is a member of the scientific advisory board of Regulus Therapeutics.

Supporting Online Material

www.sciencemag.org/cgi/content/full/328/5985/1534/DC1
Materials and Methods
SOM Text
Figs. S1 to S15
Tables S1 to S5
References

14 January 2010; accepted 19 April 2010
10.1126/science.1187058

Bose-Einstein Condensation in Microgravity

T. van Zoest,[1] N. Gaaloul,[1] Y. Singh,[1] H. Ahlers,[1] W. Herr,[1] S. T. Seidel,[1] W. Ertmer,[1] E. Rasel,[1]* M. Eckart,[2] E. Kajari,[2] S. Arnold,[2] G. Nandi,[2] W. P. Schleich,[2] R. Walser,[3] A. Vogel,[4] K. Sengstock,[4] K. Bongs,[5] W. Lewoczko-Adamczyk,[6] M. Schiemangk,[6] T. Schuldt,[6] A. Peters,[6] T. Könemann,[7] H. Müntinga,[7] C. Lämmerzahl,[7] H. Dittus,[7] T. Steinmetz,[8] T. W. Hänsch,[8] J. Reichel[9]

Albert Einstein's insight that it is impossible to distinguish a local experiment in a "freely falling elevator" from one in free space led to the development of the theory of general relativity. The wave nature of matter manifests itself in a striking way in Bose-Einstein condensates, where millions of atoms lose their identity and can be described by a single macroscopic wave function. We combine these two topics and report the preparation and observation of a Bose-Einstein condensate during free fall in a 146-meter-tall evacuated drop tower. During the expansion over 1 second, the atoms form a giant coherent matter wave that is delocalized on a millimeter scale, which represents a promising source for matter-wave interferometry to test the universality of free fall with quantum matter.

The gedanken experiment of a freely falling elevator was crucial for the development of the theory of general relativity (GR) (*1*). In such an environment, there are locally no gravitational forces, an idea that gave birth to the equivalence principle. Whereas GR rules the macroscopic world, quantum mechanics (QM) dominates the microscopic scales and reveals the wave nature of matter. Bose-Einstein condensates (BECs) (*2*, *3*) exist on the border between quantum and classical physics; they are governed by the laws of QM but can take macroscopic dimensions. We took advantage of the absence of gravity in a freely falling elevator to follow the long-time (1-s) evolution of a BEC. In particular, we report the preparation and observation of a BEC during free fall in the 146-m-high drop tower of the Center of Applied Space Technology and Microgravity (ZARM) in Bremen, Germany, reaching expansion times up to 1 s that are difficult to reach in Earth-bound laboratories. The extended time of free fall allows us to observe the ultraslow expansion of the released BEC to a

[1]Institut für Quantenoptik, Leibniz Universität Hannover, Welfengarten 1, 30167 Hannover, Germany. [2]Institut für Quantenphysik, Universität Ulm, Albert Einstein Allee 11, 89081 Ulm, Germany. [3]Institut für Angewandte Physik, Technische Universität Darmstadt, Hochschulstrasse 4A, 64289 Darmstadt, Germany. [4]Institut für Laser-Physik, Universität Hamburg, 22761 Hamburg, Germany. [5]Midlands Ultracold Atom Research Centre, Birmingham B15 2TT, UK. [6]Humboldt-Universität zu Berlin, Hausvogteiplatz 5-7, 10117 Berlin, Germany. [7]Center of Applied Space Technology and Microgravity (ZARM), Universität Bremen, Am Fallturm, 28359 Bremen, Germany. [8]Max-Planck-Institut für Quantenoptik and Sektion Physik der Ludwig-Maximilians-Universität, Schellingstrasse 4, 80799 München, Germany. [9]Laboratoire Kastler-Brossel de l'Ecole Normale Supérieure, 24 rue Lhomond, 75231 Paris, France.

*To whom correspondence should be addressed. E-mail: rasel@iqo.uni-hannover.de

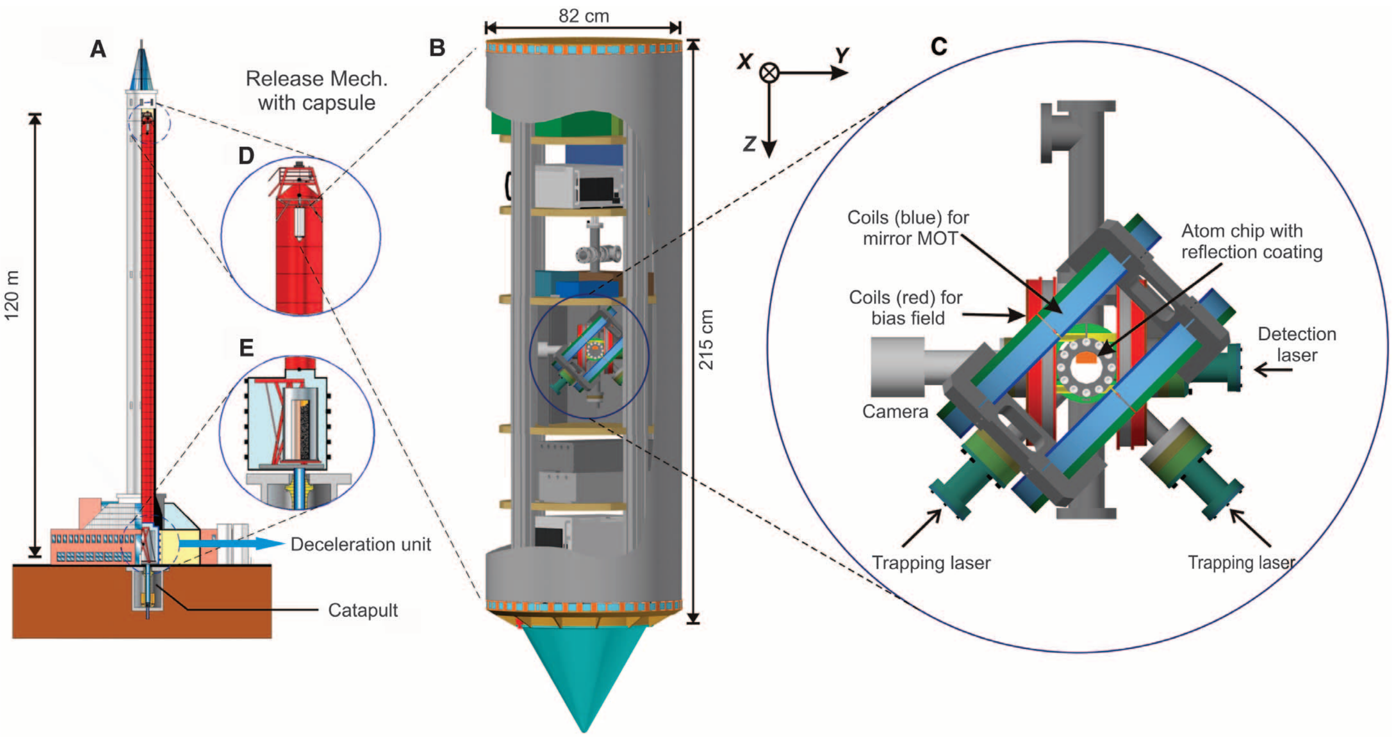

Fig. 1. Cuts through the ZARM drop tower facility in Bremen (**A**) and the capsule (**B**) containing the heart of the BEC experiment (**C**). The capsule is released from the top of the tower (**D**) and is recaptured after a free fall of 4.7 s through an evacuated stainless steel tube at the bottom of the tower by a 8-m-deep pool of polystyrene balls (**E**). In the process of recapturing the capsule, the experiment has to survive decelerations up to 500 m/s^2 (about 50 times the local gravitational acceleration). The facility permits up to three drops per day. The capsule contains all of the components necessary to prepare and observe a BEC, such as the laser systems for cooling the atoms, the ultrahigh-vacuum chamber with the atom chip, the current drivers and power supplies, a charge-coupled device (CCD) camera, and a control computer. The vacuum chamber is surrounded by two magnetic shields and allows us to include an atom interferometer in future experiments. Moreover, the catapult underneath the movable polystyrene pool offers the possibility of extending the time of free fall to 9 s.

macroscopic matter-wave packet, which provides us with a probe that is highly sensitive to magnetic and gravitational fields and represents a testing ground for physics at ultralow energy scales. We have performed more than 180 experiments to demonstrate the feasibility of coherent matter-wave experiments in microgravity (*4*), thus opening up a new avenue for high-precision measurements in space (*5*).

The drive for large expansion times of a BEC is motivated by the increase in sensitivity of an inertial sensor based on an atom interferometer with the square of the time (*6*) the atoms spend in the interferometer. As a result, cold atom–based sensors, such as gyroscopes or gravimeters (*7*), might reach an unprecedented sensitivity that is necessary to perform tests (*8*) of GR, such as the measurement (*9*, *10*) of the Lense-Thirring effect, which is a manifestation of gravitational forces induced by rotating masses (*11*). Moreover, recent advances in atom-optics technology have led to the preparation of tests of the equivalence principle with matter waves (*12*, *13*) rather than macroscopic systems, and these advances make the detection of gravitational waves feasible (*14*).

Unfortunately, the grip of gravity on matter makes it difficult in an Earth-bound laboratory to enable a BEC to expand freely over long periods. For example, during 1 s, a mass initially at rest would fall about 5 m. One way to circumvent this problem is levitation by electromagnetic forces counteracting gravity (*15*). However, only one class of atoms with specific magnetic properties or one species can be levitated at a time. This limitation serves as one motivating factor for our BEC experiment (*16*) in the drop tower (Fig. 1).

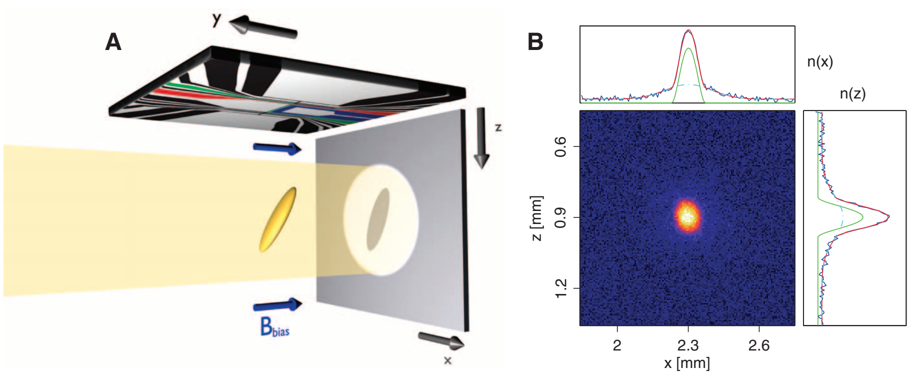

Fig. 2. Absorption imaging technique (**A**) used for the measurement of the two-dimensional spatial distribution of the BEC in microgravity (**B**). The BEC is initially confined by a combination of magnetic fields generated by the Z-shaped wire on the surface of the atom chip and a homogeneous bias field B_{bias}. After its release from the trap, the BEC is illuminated by a laser, and the shadow of the condensate is detected by a CCD camera (A). The resulting two-dimensional density distribution (B) corresponds to a BEC created and observed in free fall for an expansion time of 100 ms. Here, bright and dark colors indicate high and low atomic densities, respectively. At the top and on the right-hand side of this image, we show the *x* and *z* profiles, *n*(*x*) and *n*(*z*), of the integrated density distribution. Both consist of a central peak, representing the BEC, on top of a pedestal, formed by thermal atoms. A bimodal function (red line) is used to fit the BEC part and the thermal pedestal with the square of an inverted parabola (green line) and a Gaussian (blue line).

Here, the complete apparatus is in free fall, and the capsule provides an environment with residual accelerations that are as low as 1 part in 10^5 of terrestrial gravity, conditions that are difficult to reach in other microgravity platforms.

The realization of this experiment required the miniaturization of the setup, which was made possible by the development of atom chips (*17*–*19*). We combined this technology with a mirror magneto-optical trap (MOT), which was loaded with roughly 1.3×10^7 atoms of ^{87}Rb from the background gas. Loading was completed after 10 s, and the capsule was then released. During the first second of free fall, the atoms are held in the mirror MOT until the initial vibrations of the capsule have damped out. The atoms are further cooled in optical molasses and transferred to an Ioffe-Pritchard trap on the chip. A BEC of about 10^4 atoms in the hyperfine state $F = 2$, $m_F = 2$ (where F and m_F are the quantum numbers for the total angular momentum and the Zeeman sublevel, respectively) is routinely obtained within 1 s after compression of the trap and radio frequency–induced evaporation. The lifetime of our condensate inside the trap is 3 s, which is longer than the remaining time of free fall. The temperature and chemical potential of the BEC are lowered by adiabatically opening the trap. Finally, the BEC is released by switching off the currents through the atom chip, which defines the origin of time for the expansion.

We observed the BEC by using the absorption imaging technique (Fig. 2A). As an example, we show in Fig. 2B a BEC after a time of flight of 100 ms in free fall. Even for this expansion time, the observation of a BEC in an Earth-bound laboratory becomes difficult, because one has to adiabatically lower the trap frequencies to reduce the mean field energy and, consequently, reduce the speed of expansion. It is at this point that microgravity becomes crucial, because it allows us to reach trap frequencies in the hertz regime, giving rise to ground-state energies of the atomic ensemble in the nanokelvin range.

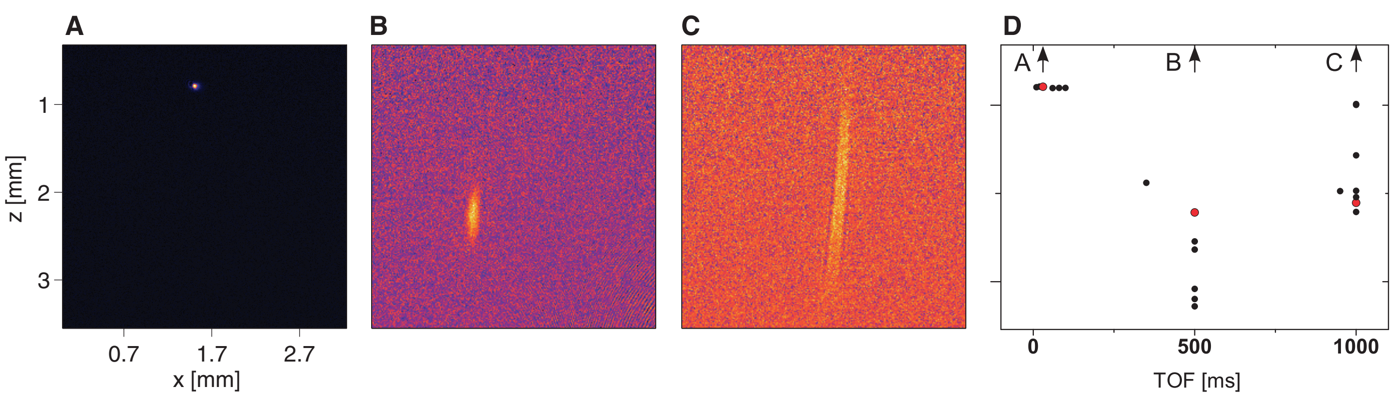

Fig. 3. Gallery of absorption images of BECs created and observed in free fall (**A** to **C**) together with the time dependence of the *z* coordinate of the center of mass of the BEC (**D**). The series starts with a time of flight of 30 ms (A), which is typical for Earth-bound laboratory experiments. The following two figures correspond to expansion times of 500 ms (B) and 1 s (C). In the latter case, the BEC extends over a distance of more than 2 mm in the *z* direction. In (D), we depict the *z* coordinates of the center of mass of more than 20 BECs as a function of the expansion time. The red dots correspond to the BECs presented in (A), (B), and (C). The *z* coordinate varies within a range of several millimeters, as discussed in (*23*).

In our experiment, the kinetic energy of the atoms is extremely low (9 nK), and the shadow of the BEC can even be observed after an expansion time of 1 s, when the BEC forms a delocalized wave packet extending over more than 2 mm.

In Figs. 3 and 4, we display the long-time evolution of a BEC during the extended free fall in the drop tower. Three absorption images corresponding to expansion times of 30 ms (Fig. 3A), 500 ms (Fig. 3B), and 1000 ms (Fig. 3C) are shown. The cases presented in Fig. 3, B and C, indicate a suppression of the expansion of the BEC in the x direction. Figure 3D shows that, during an evolution time of 1 s, the BEC moves within a range of about 3 mm in the z direction. Both effects, the suppression of the expansion and the motion of the center of mass, have their origins in the sensitivity of the BEC to any inhomogeneous stray magnetic fields during the expansion phase.

To provide a quantitative understanding of these observations, we compare and contrast in Fig. 4 the experimentally obtained half widths (solid squares) of the z and x profiles of the BEC with numerical simulations. The latter are based on scaling methods (*20*–*22*) and rely on a detailed modeling of the magnetic fields generated by the chip and the coils (*23*). The homogeneous stray field inside the vacuum chamber, which results, for example, from the vacuum pump, has been measured in the optical molasses phase in additional ground-based experiments. It is also included in the simulation, allowing us to estimate the trapping frequencies along the principal axes of the harmonic potential just before release to be 10, 22, and 27 Hz. We have also verified the validity of the scaling method by full three-dimensional simulations of the time-dependent Gross-Pitaevskii equation (*24*).

In the regime up to 100 ms (Fig. 4, A and C), which is at the limit of experiments in ground-based laboratories, both half widths display a systematic discrepancy between the observations (solid squares) and our simulations (black dashed curves) up to 75 ms. This deviation arises from a limitation in the optical resolution of the absorption imaging of the BEC, which we estimated to be approximately 20 μm. Taking this issue into account, our improved simulations (black solid curves) agree with the experimental observations.

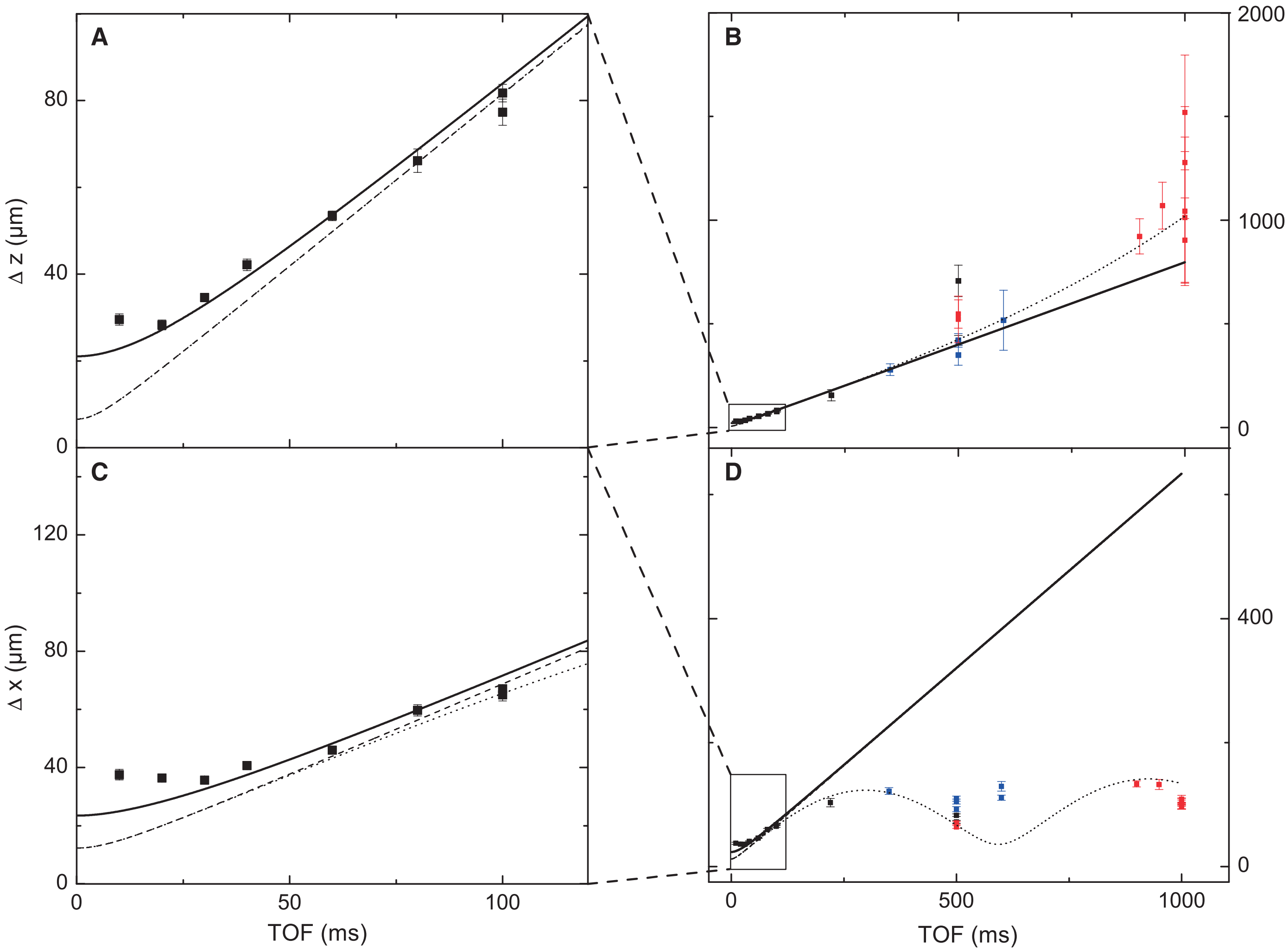

Fig. 4. Measured sizes of BECs in microgravity for short [(**A**) and (**C**)] and long [(**B**) and (**D**)] expansion times compared with numerical simulations. As a measure, we use the half widths Δz [(A) and (B)] and Δx [(C) and (D)] of the z and x profiles of the condensate extracted from the observed density distributions. The experimental data points (black, red, and blue solid squares) are shown with error bars due to density profile fittings; different colors indicate different detection configurations used in the absorption imaging of the BECs. Lines represent numerical simulations of the experiment based on the theory presented in (*20*–*22*) and summarized in (*23*). Up to 100 ms [(A) and (C)], the observed BEC sizes exceed the theoretical predictions (black dashed curves). By incorporating an estimated resolution limit of our optical imaging system of 20 μm, we find a good agreement between the corrected theoretical prediction (black solid curves) and the observed BEC sizes. For large expansion times [(B) and (D)], the observed expansion of the BEC does not obey the theoretically predicted linear growth for a vanishing magnetic field (black solid curves). However, by taking weak field curvatures of less than 1 μT/mm^2 into account, our simulations (black dotted curves) allow for a qualitative explanation of the observed data points.

Microgravity enables us to venture into the regime of unprecedented long time evolution of the BEC up to 1 s (Fig. 4, B and D) with our setup. Our measurements reveal the above-mentioned suppression of the expansion in the x direction. Although our theory (black solid curves) predicts a linear growth, we observe a saturation. In addition, the observed widths in the z direction are larger than expected.

The origin of both deviations can be traced back to the fact that, during the expansion phase, the atoms are in the $F = 2$, $m_F = 2$ hyperfine state. Because of the long expansion times, these deviations represent a sensitive probe of tiny magnetic field gradients and curvatures. By including magnetic field curvatures on the order of a few microtesla per square millimeter in our simulation (black dotted curves), we are able to provide a qualitative explanation of the observed half widths. A coherent transfer of the BEC into the magnetically insensitive hyperfine state $F = 2$, $m_F = 0$ would avoid the influence of parasitic effects, and the implementation of this transfer is currently under way.

We anticipate a multitude of new research directions for ultracold, dilute quantum gases in free fall. A spin-off from our experiment is the possibility of preparing an extremely dilute wave packet at the lowest energy scales. This limit is difficult to reach in standard BEC experiments but is relevant for the observation of quantum reflection (*25*) or Anderson localization (*26*, *27*). Future atom interferometers in space will probe the boundary between GR and QM.

References and Notes

1. C. W. Misner, K. S. Thorne, J. A. Wheeler, *Gravitation* (Freeman, San Francisco, 1973).
2. E. A. Cornell, C. E. Wieman, *Rev. Mod. Phys.* **74**, 875 (2002).
3. W. Ketterle, *Rev. Mod. Phys.* **74**, 1131 (2002).
4. G. Stern *et al.*, *Eur. Phys. J. D* **53**, 353 (2009).
5. E. Arimondo, W. Ertmer, W. P. Schleich, E. M. Rasel, Eds., *Proceedings of the International School of Physics "Enrico Fermi" Course CLXVIII "Atom Optics and Space Physics"* (IOS Press, Bologna, Italy, 2009).
6. P. R. Berman, Ed., *Atom Interferometry* (Academic Press, San Diego, CA, 1997).
7. A. Peters, K. Y. Chung, S. Chu, *Nature* **400**, 849 (1999).
8. W. P. Schleich, M. O. Scully, in *New Trends in Atomic Physics, Proceedings of the Les Houches Summer School 1982, Session XXXVIII*, G. Grynberg, R. Stora, Eds. (North-Holland, Amsterdam, 1984), pp. 995–1124.
9. I. Ciufolini, E. C. Pavlis, *Nature* **431**, 958 (2004).
10. I. Ciufolini, *Nature* **449**, 41 (2007).
11. I. Ciufolini, J. A. Wheeler, *Gravitation and Inertia* (Princeton Univ. Press, Princeton, NJ, 1995).
12. S. Fray, C. Alvarez Diez, T. W. Hänsch, M. Weitz, *Phys. Rev. Lett.* **93**, 240404 (2004).
13. S. Dimopoulos, P. W. Graham, J. M. Hogan, M. A. Kasevich, *Phys. Rev. Lett.* **98**, 111102 (2007).
14. S. Dimopoulos, P. W. Graham, J. M. Hogan, M. A. Kasevich, S. Rajendran, *Phys. Rev. D Part. Fields Gravit. Cosmol.* **78**, 122002 (2008).
15. A. E. Leanhardt *et al.*, *Science* **301**, 1513 (2003).
16. A. Vogel *et al.*, *Appl. Phys. B* **84**, 663 (2006).
17. W. Hänsel, P. Hommelhoff, T. W. Hänsch, J. Reichel, *Nature* **413**, 498 (2001).
18. R. Folman, P. Krüger, J. Schmiedmayer, J. Denschlag, C. Henkel, *Adv. At. Mol. Opt. Phys.* **48**, 263 (2002).
19. J. Fortágh, C. Zimmermann, *Rev. Mod. Phys.* **79**, 235 (2007).
20. Y. Kagan, E. L. Surkov, G. V. Shlyapnikov, *Phys. Rev. A* **54**, R1753 (1996).
21. Y. Castin, R. Dum, *Phys. Rev. Lett.* **77**, 5315 (1996).
22. P. Storey, M. Olshanii, *Phys. Rev. A* **62**, 033604 (2000).
23. Materials and methods are available as supporting material on *Science* Online.
24. G. Nandi, R. Walser, E. Kajari, W. P. Schleich, *Phys. Rev. A* **76**, 063617 (2007).
25. T. A. Pasquini *et al.*, *Phys. Rev. Lett.* **97**, 093201 (2006).
26. J. Billy *et al.*, *Nature* **453**, 891 (2008).
27. G. Roati *et al.*, *Nature* **453**, 895 (2008).

28. This project is supported by the German Space Agency Deutsches Zentrum für Luft- und Raumfahrt (DLR) with funds provided by the Federal Ministry of Economics and Technology (BMWi) under grant number DLR 50 WM 0346. We thank the German Research Foundation for funding the Cluster of Excellence QUEST Centre for Quantum Engineering and Space-Time Research.

Supporting Online Material
www.sciencemag.org/cgi/content/full/328/5985/1540/DC1
Materials and Methods
References

5 March 2010; accepted 10 May 2010
10.1126/science.1189164

Hot-Electron Transfer from Semiconductor Nanocrystals

William A. Tisdale,[1] Kenrick J. Williams,[2,3]* Brooke A. Timp,[2] David J. Norris,[1]† Eray S. Aydil,[1]† X.-Y. Zhu[2,3]*†

In typical semiconductor solar cells, photons with energies above the semiconductor bandgap generate hot charge carriers that quickly cool before all of their energy can be captured, a process that limits device efficiency. Although fabricating the semiconductor in a nanocrystalline morphology can slow this cooling, the transfer of hot carriers to electron and hole acceptors has not yet been thoroughly demonstrated. We used time-resolved optical second harmonic generation to observe hot-electron transfer from colloidal lead selenide (PbSe) nanocrystals to a titanium dioxide (TiO_2) electron acceptor. With appropriate chemical treatment of the nanocrystal surface, this transfer occurred much faster than expected. Moreover, the electric field resulting from sub–50-femtosecond charge separation across the PbSe-TiO_2 interface excited coherent vibrations of the TiO_2 surface atoms, whose motions could be followed in real time.

The maximum theoretical efficiency of a standard silicon solar cell in use today is limited to ~31%, in part by the loss of any photon energy that exceeds the semiconductor bandgap (*1*). Absorption of high-energy photons creates hot electrons and holes that cool quickly (within ~1 ps) to the band edges by sequential emission of phonons. There the carriers remain for hundreds of picoseconds or longer before slower processes such as radiative or nonradiative recombination occur. The goal of standard solar cells is to extract these band-edge electrons and holes to produce electrical current. However, because of the initial cooling process, a substantial amount of solar energy has already been irreversibly lost. If instead, all of the energy of the hot carriers could be captured, solar-to-electric power conversion efficiencies could be increased, theoretically to as high as 66% (*2*). We can envision the realization of such a hot carrier solar cell in a semiconductor device where scattering among photoexcited electrons and reabsorption of additional photons in the conduction band is faster than hot-electron cooling, resulting in a quasi-equilibrium characterized by an electron temperature much higher than the lattice temperature. This is coupled with equally fast hot-electron transfer to an electron conductor in a narrow energy window (to minimize additional energy loss in the latter). The same argument applies to the holes.

A potential route to the above hot carrier solar cell is to use semiconductor nanocrystals, or quantum dots (*3*). In these materials, the quasi-continuous conduction and valence energy bands of the bulk semiconductor become discretized owing to confinement of the charge carriers. Consequently, the energy spacing between the electronic levels can be much larger than the highest phonon frequency of the lattice, creating a "phonon bottleneck" in which hot-carrier relaxation is only possible via slower multiphonon emission (*4*). For example, hot-electron lifetimes as long as ~1 ns have been

[1]Department of Chemical Engineering and Materials Science, University of Minnesota, Minneapolis, MN 55455, USA. [2]Department of Chemistry, University of Minnesota, Minneapolis, MN 55455, USA. [3]Department of Chemistry and Biochemistry, University of Texas, Austin, TX 78712, USA.

*Present address: Department of Chemistry and Biochemistry, University of Texas, Austin, TX 78712, USA.
†To whom correspondence should be addressed: zhu@cm.utexas.edu (X.-Y.Z.), dnorris@umn.edu (D.J.N.), aydil@umn.edu (E.S.A.)

observed in quantum dots grown by molecular beam epitaxy (*5*). Even in colloidal quantum dots, which are coated with surfactant molecules that provide additional high-frequency vibrations for carrier relaxation, long lifetimes have been demonstrated through careful design of core-shell structures and control of interfaces (*6*). Such slowing of electron relaxation in core-shell quantum dots has recently been shown to allow the tunneling of hot electrons through the shells to surface trap states (*7*). Because of their ability to slow electronic relaxation, quantum dots can in principle enable extraction of hot carriers (to electron or hole conductors) before they cool to the band edges, leading to more efficient solar cells (*8*). However, hot-carrier transfer from nanocrystals to an electron or hole conductor has not yet been observed. Here, we show that electron transfer from the higher excited states of a colloidal semiconductor nanocrystal (PbSe) to a common electron acceptor (TiO_2) is indeed possible and, with appropriate chemical treatment of the nanocrystal surface, occurs on an ultrafast time scale (<50 fs).

Although heterogeneous electron transfer from molecular chromophores to metal-oxide semiconductors has been probed with femtosecond time-resolved absorption (*9*), extending this approach to quantum dots has proved challenging. Differentiating between transient spectroscopic signatures of the photoexcited quantum dot, the reduced TiO_2 substrate, and the trap states is difficult (*10*). Further, to generate adequate signal, porous samples with large surface area but poorly defined interfaces are used. Consequently, reported time scales have spanned from picoseconds to microseconds (*10*–*13*).

Optical second harmonic generation (SHG) (*14*) is a much better technique for studying quantum-dot–to–semiconductor electron transfer because it offers femtosecond time resolution with sufficient sensitivity for well-defined crystalline interfaces. In a centrosymmetric semiconductor such as rutile TiO_2, the second harmonic response originates only from the first few atomic layers near the surface (*15*). Thus, SHG should be extremely sensitive to changes in the local electronic environment resulting from interfacial electron transfer. Indeed, SHG has been used to probe ultrafast electron transfer at liquid-liquid interfaces (*16*). We show here that it can also be applied to semiconductor interfaces.

For fast electron transfer to occur, the nanocrystals should exhibit strong electronic coupling to the substrate. We chose colloidal PbSe quantum dots, as they are easy to prepare (*17*) and are better suited for electron transfer than other possible materials. In particular, PbSe has an extremely large exciton Bohr radius (46 nm) such that charge carriers in sub–10-nm diameter PbSe quantum dots are subject to strong quantum confinement effects (*18*), and their electronic wave functions will extend spatially well beyond the nanocrystal surface. This delocalization facilitates electron transfer if the nanocrystals are close to an electron accepting substrate. We chose rutile TiO_2 for this role because it not only is technologically relevant and available as a single crystal but also has a very large density of accepting states. Further, the (110) surface of rutile TiO_2 is one of the most studied metal oxide interfaces, and the surface nonlinear susceptibility tensor and the origins of the second harmonic response are known (*15*).

Each sample consisted of one or two monolayers of PbSe nanocrystals deposited on atomically flat single-crystalline (110) TiO_2 (Fig. 1, A and B). The films were chemically treated with either hydrazine or 1,2-ethanedithiol (EDT) (*19*) to respectively remove or substitute for the oleic acid present on the nanocrystal surface. Both treatments enhance electronic coupling to the TiO_2 substrate and within the film (*17*, *20*–*22*), but the bare surfaces produced by hydrazine result in stronger coupling (fig. S3). However, hydrazine can also leave many dangling bonds at the nanocrystal surface that can presumably act as scattering sites and accelerate electronic cooling within the quantum dot. In contrast, thiols such as EDT passivate the nanocrystal surface and slow hot-electron relaxation in colloidal nanocrystals (*6*).

We tested PbSe nanocrystals ranging in diameter from 3.3 to 6.7 nm. As with all strongly confined semiconductor nanocrystals, the energy of excited electron states in PbSe quantum dots increases with decreasing particle size. Thus, we first used ultraviolet photoelectron spectroscopy, in conjunction with optical absorption, to determine the energy of the lowest excited electronic state in our nanocrystals (*19*). We found that, regardless of particle size or chemical treatment, this state was always below the TiO_2 conduction band minimum (Fig. 1C). As a result, electron transfer from PbSe to TiO_2 should only be possible from hot electronic states of the quantum dot (*12*).

To study this electron transfer, we used 50-fs pulses of 810-nm (1.53-eV) light both to photoexcite (pump) the nanocrystals and detect (probe) the second harmonic response (*19*). The intensity of reflected second harmonic light at 405 nm ($I^{2\omega}$)

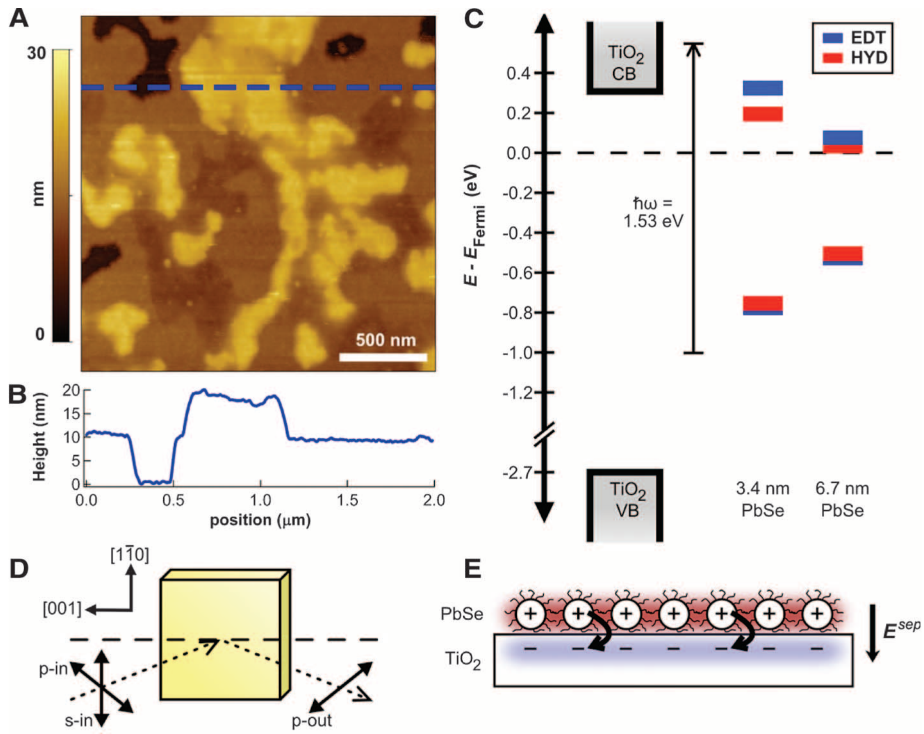

Fig. 1. (**A**) Atomic force micrograph showing the morphology of a ~1.5-monolayer film of 6.7-nm oleic acid–capped PbSe nanocrystals supported on atomically flat TiO_2. (**B**) Line height profile corresponding to the dashed blue line in (A). The height of a monolayer (~11 nm) is the diameter of a nanocrystal (~7 nm) plus the thickness of the passivating organic layer (~2 nm) both above and below. (**C**) Alignment of highest occupied and lowest unoccupied quantum dot energy levels relative to the TiO_2 conduction band edge after chemical treatment of the nanocrystal surface. Alignment is determined by ultraviolet photoelectron and near-infrared absorption spectroscopies and indicates that electron transfer from the lowest excited state of the quantum dot is not energetically possible. The vertical arrow depicts symmetric photoexcitation of the PbSe quantum dots with 810-nm light. Numerical values are available in table S1. VB, valence band; CB, conduction band; EDT, 1,2-ethanedithiol; HYD, hydrazine. (**D**) Illustration of the crystal orientation and optical polarization used for SHG in reflection from the rutile (110) surface. (**E**) Schematic representation of the interfacial electric field generated by separation of electrons and holes across the PbSe-TiO_2 interface. Red indicates positive charge density; blue, negative charge density.

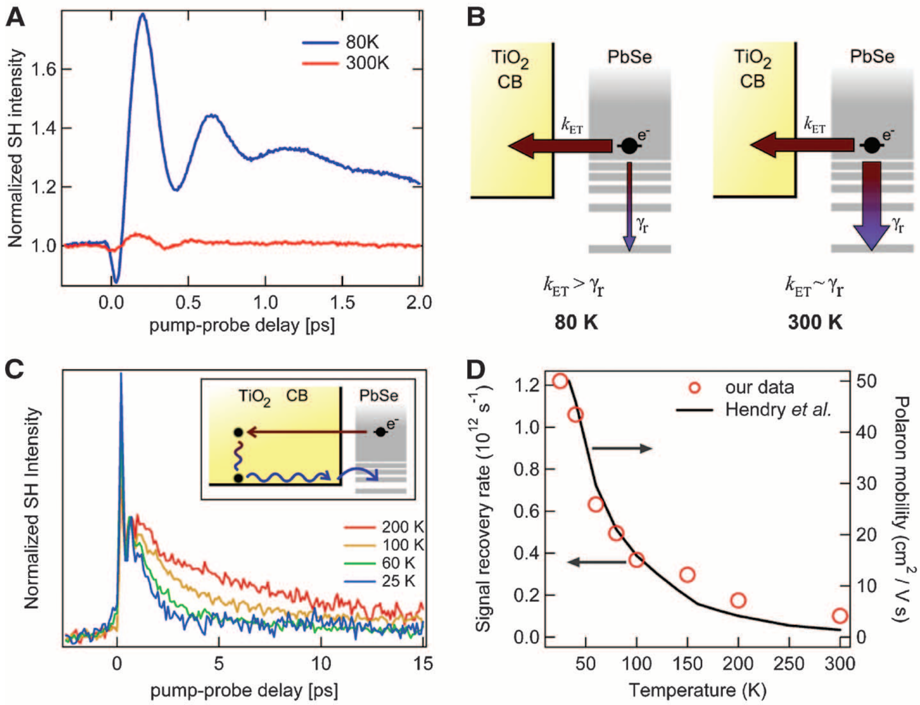

Fig. 2. (**A**) Time-resolved second harmonic response of the TiO_2 surface coated with 1.5 monolayers of hydrazine-treated 3.3-nm PbSe nanocrystals. The large rise in SHG intensity is indicative of efficient electron transfer from PbSe to TiO_2. (**B**) Illustration of the competing pathways of interfacial electron transfer and intra–quantum-dot relaxation. At higher temperatures, hot-electron relaxation (γ_r) becomes competitive with interfacial electron transfer (k_{ET}). (**C**) Temperature-dependent decay of the pump-induced SHG signal enhancement; the absolute intensity has been normalized for pump-induced change to better illustrate the temperature-dependent recovery rate. (Inset) Cartoon showing ballistic electron injection (straight arrow) followed by phonon scattering and polaronic transport back to the interface (wavy lines) and then transfer back to the nanocrystal (curved arrow). (**D**) Correlation of SHG signal recovery rate (red circles) with the temperature-dependent polaron mobility perpendicular to the *c* axis in TiO_2 measured previously (*29*) assuming a temperature-independent polaron effective mass (black line).

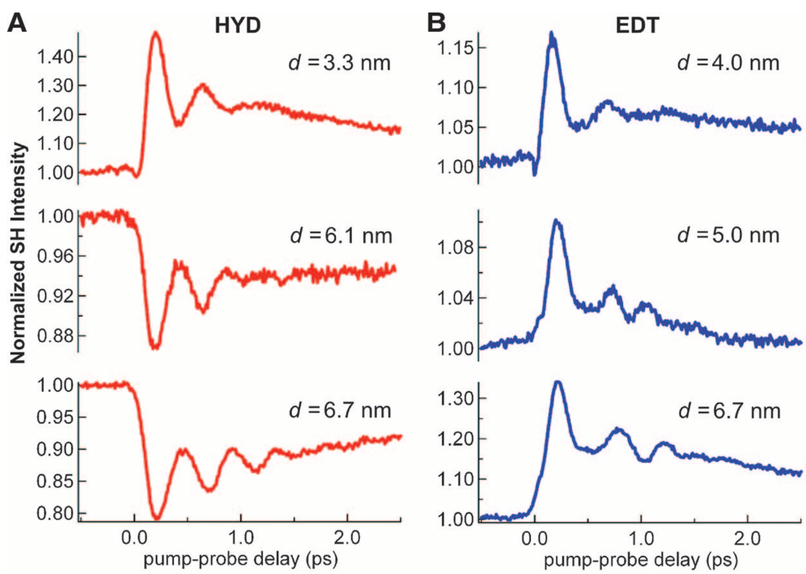

Fig. 3. Dependence of the time-resolved second harmonic response on nanocrystal size after treatment with (**A**) hydrazine (HYD) or (**B**) 1,2-ethanedithiol (EDT). The EDT-treated nanocrystals display efficient hot-electron transfer for all sizes studied, whereas substantial hot-electron transfer is only observed for smaller nanocrystals treated with hydrazine.

was recorded as a function of time delay between the pump and probe pulses. The polarization (p or s) of the fundamental was controlled and that of the second harmonic independently detected to isolate specific components of the nonlinear susceptibility tensor (Fig. 1D).

If electron transfer occurs, the separation of electrons and holes across the PbSe-TiO_2 interface generates an electric field, E^{sep}, oriented in the surface normal direction (Fig. 1E). SHG is highly sensitive to such slowly varying (relative to the optical frequency) electric fields because they can perturb the symmetry of the medium (*23*). This electric-field–induced second harmonic (EFISH) response has been used to study metal-electrolyte interfaces (*24*) and buried interfaces in field-effect transistors (*25*). When an interface already exhibits a large SHG signal, $I^{2\omega}$, even without an induced interfacial field [e.g., rutile (110) under the p-in/p-out configuration in Fig. 1D], the change in the SHG intensity, $\Delta I^{2\omega}$, due to electron transfer is proportional to E^{sep} as

$$\Delta I^{2\omega} = I^{2\omega} - I_o^{2\omega} \approx \eta (I^{\omega})^2 E^{sep} \qquad (1)$$

where $I^{2\omega}$ is the intensity of the probe beam at the fundamental frequency ω, and η contains the dependence on the dielectric function through linear and nonlinear Fresnel factors as well as the wavelength-, polarization angle–, and crystallographic orientation–dependent nonlinear susceptibility [see supporting online material (SOM) text 2] (*26*). If the charge-separated PbSe-TiO_2 interface is treated as a parallel-plate capacitor, then E^{sep} and the corresponding EFISH signal scale approximately linearly with the amount of separated charge. Consequently, electron transfer dynamics may be extracted directly from the time-resolved change in SHG intensity following photoexcitation of the PbSe film.

However, the analysis is complicated by the contribution to the SHG response from the quantum dots themselves. In particular, we expect photoexcitation of the quantum dots to lead to a decrease in SHG intensity, as is observed in molecular chromophores (*16*) and semiconductor nanowires (*27*). Indeed, we measure a drop in SHG intensity upon photoexcitation of our PbSe films supported on amorphous silica glass (at all quantum dot sizes, treatments, and temperatures). Because glass has a bandgap too wide to accept electron transfer from our quantum dots, we attribute this reduced intensity to their intrinsic SHG response (figs. S7 to S9).

In contrast to this drop, we observe a substantial rise in SHG intensity after photoexcitation of the quantum dots on TiO_2 at 80 K (Fig. 2A). This response is consistent with efficient hot-electron transfer from PbSe to TiO_2 for several reasons. First, the SHG signal rises on a time scale shorter than that of the laser pulse (50 fs). Such an ultrafast response would be expected for

the strong-coupling limit of electron transfer. Also, because the electronic relaxation time between the first two excited states in similar-sized PbSe quantum dots has been measured as 540 fs at 300 K (*28*), electron transfer must be appreciably faster than this to outpace the cooling process. Second, the magnitude of the ultrafast SHG response decreases with increasing temperature (Fig. 2A). As the PbSe quantum dots are warmed to 300 K, the time constant for electron transfer should be largely unaffected in the strong-coupling limit. However, the electronic relaxation rate is known to increase exponentially (*28*). Thus, at higher temperatures, cooling of hot electrons can compete with hot-electron transfer (Fig. 2B). Because cooled electrons cannot transfer to TiO_2 in our samples, accelerated cooling leads to a decrease in SHG signal. As a negative control, we observe no electron transfer when we decrease the pump photon energy to below the threshold necessary to reach the conduction band minimum of TiO_2 (fig. S10).

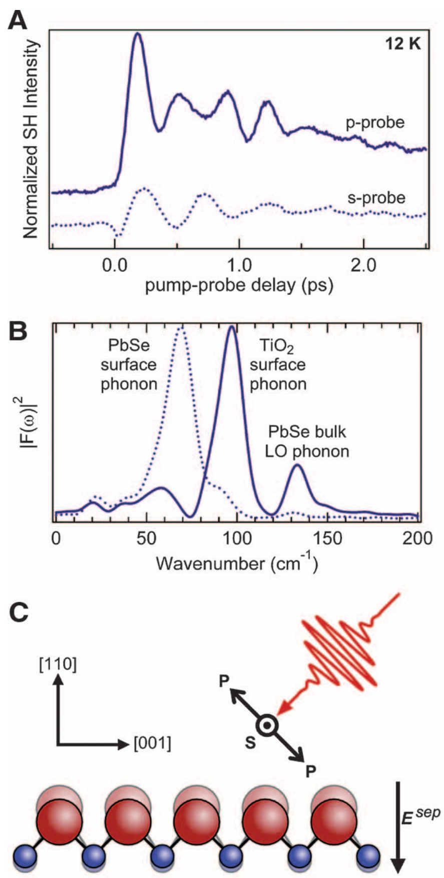

Fig. 4. Excitation of a coherent surface phonon by ultrafast electron transfer. (**A**) Time-resolved response at 12 K of the TiO_2 surface coated with 1.5 monolayers of EDT-treated 6.7-nm PbSe nanocrystals probed with either p- (solid) or s- (dotted) polarized light. (**B**) Fourier power spectrum of the oscillatory part of the SHG response curves shown in (A). With p-polarized light, a vibrational mode at 97 ± 5 cm^{-1} attributed to a rutile (110) surface-specific coherent transverse optical phonon is observed. (**C**) Coherent vibration of the Ti-O zigzag bonds running along the [001] direction of the rutile (110) surface excited by ultrafast switching-on of the interfacial electric field resulting from sub–50 fs electron transfer.

An analysis of the temperature-dependent decay of the pump-induced SHG signal on the picosecond time scale (Fig. 2C) is consistent with the temperature dependence of electron mobility in TiO_2. If an electron transfers from PbSe to a resonant energy level within the TiO_2 conduction band, this electron would have considerable kinetic energy. It would move ballistically into TiO_2, where electron-phonon scattering would bring it to the bottom of the conduction band, forming a polaron (*29*, *30*). The electric field would eventually return the electron back to the TiO_2 surface for recombination with the positively charged nanocrystal and quenching of the EFISH signal (Fig. 2C, inset). An alternative interpretation is that the injected electron diffuses deep into bulk TiO_2 and is thus screened, resulting in the decay in SHG signal. In this scenario, recombination occurs on a much longer time scale (between consecutive probe pulses). We favor the former interpretation because computational study on the single-crystal TiO_2(110) surface showed an order-of-magnitude faster time scale (~100 fs) for electron diffusion into the bulk TiO_2, whereas back electron transfer from the near-surface region of TiO_2 to electron acceptors on the surface occurs on picosecond time scales, in agreement with the SHG decay time observed here (*30*). Regardless of which mechanism is operative, the rate of decay of the interfacial electric field would be proportional to the mobility of the polaron (see SOM text 4). Previous optical measurements determined this mobility in single-crystalline rutile TiO_2 as a function of temperature (*29*). The strong correlation between the decay rate of pump-induced SHG signal enhancement and the temperature-dependent polaron mobility (Fig. 2D) supports the conclusion that we are observing hot-electron transfer to delocalized TiO_2 conduction band states.

Further evidence is provided by the influence of nanocrystal size on the SHG response at 80 K. The pump-induced SHG response has two opposite contributions: the positive response from electron transfer to TiO_2 and the negative contribution from photoexcited nanocrystals. In hydrazine-treated samples (Fig. 3A), only smaller PbSe nanocrystals (3.3 nm) exhibit a signal characteristic of efficient electron transfer. The larger quantum dots (6.1 and 6.7 nm) exhibit a sharp drop in the SHG signal at zero pump-probe delay, indicative of a dominant contribution from photoexcited nanocrystals (figs. S8 and S9). The electronic state energies in the nanocrystals are size dependent, and these observations are related to which excited states are resonant with the TiO_2 conduction band. In larger nanocrystals, this resonance occurs for highly excited electronic states (above $1P_e$) where ultrafast relaxation makes hot-electron transfer less competitive. In smaller nanocrystals, the resonance occurs for the second excited state ($1P_e$), and its relatively long lifetime makes hot-electron transfer to TiO_2 more efficient. Further, if the overall hot-electron relaxation rate could be slowed, electron transfer should compete effectively in all nanocrystal sizes. Indeed, for EDT-treated quantum dots, in which the overall electron relaxation is expected to be slower owing to effective surface passivation, we always observe the dominance of the positive SHG response from hot-electron transfer (Fig. 3B). The fluctuations in the magnitude of the pump-induced SHG signal intensity shown in Fig. 3 are representative of sample-to-sample variability in our data. We observe that these magnitude fluctuations arise primarily from batch-to-batch variations in the nanocrystals themselves and are presumably related to the structure and overall quality of the nanocrystal surface, which should play an important role in interfacial electron transfer.

One additional feature in our SHG data is the presence of large oscillations in the time-dependent response. For example, Fig. 2A shows a size-independent frequency of ~70 cm^{-1} (2.1 THz or 8.7 meV). These oscillations have larger amplitude and slower dephasing at 80 K than at 300 K and are observed with both s- and p-polarized light. Though they are not present before removal of oleic acid from the nanocrystal surface, observation of these oscillations does not require interfacial electron transfer because they occur in hydrazine- and EDT-treated PbSe films supported on SiO_2 (figs. S8 and S9). On the basis of the frequency, its invariance with quantum dot size, and the independence of substrate material, yet sensitivity to surface chemical treatment, we attribute these oscillations to a coherent surface optical phonon mode in electronically coupled two-dimensional PbSe quantum dot assemblies. Close inspection of the EDT data (Fig. 3B) reveals frequency beating in the oscillations, which becomes more apparent at lower temperatures (Fig. 4A). A frequency-domain analysis of the p-polarized SHG waveform in Fig. 4A reveals three dominant Fourier components (Fig. 4B): the previously identified PbSe surface optical mode at ~70 cm^{-1} (2.1 THz), the bulk PbSe longitudinal optical (LO) phonon at 133 ± 5 cm^{-1} (4.0 THz) (*31*), and a mode at 97 ± 5 cm^{-1} (2.9 THz) that dominates the p-polarized SHG signal but is much weaker for s-polarized probe light. The frequency of this last component is close to a predicted transverse optical phonon mode (104 cm^{-1}) of the rutile (110) surface of TiO_2, which involves the motion of Ti and O atoms in and out of the surface plane (*32*). Under the p-in/p-out configuration with our crystal orientation (Fig. 1D), the SHG response of the (110) surface originates from anharmonic polarizability of the Ti-O zigzag bonds running along the [001] direction (Fig. 4C) (*15*). As these bonds stretch and compress in phase, we observe a time-dependent modulation of the SHG intensity resulting from accompanying fluctuations of the bond hyper-

polarizability. By symmetry, this modulation should arise if the driving electromagnetic wave contains an electric-field component along the Ti-O bond. Consequently, it is only observed with a p-polarized probe beam. For the s-polarized case, the SHG response arises mainly from the PbSe quantum dots, and the coherent phonon mode at 70 cm^{-1} dominates.

We take the coherent surface phonon attributed to TiO_2 as further evidence for hot-electron transfer. Such vibrations can be excited when electric fields near the surface are activated by optical pulses shorter than the vibrational period (*33*). Electron transfer across the PbSe-TiO_2 interface within the 50-fs width of the excitation pulse establishes an interfacial electric field faster than the characteristic response time of the surface atoms. These atoms subsequently find themselves in a vibrationally excited state of the new electric-field–induced minimum energy surface configuration. Time-domain fitting of an appropriate model function to the data in Fig. 4A (see fig. S11) reveals that the initial phase of this vibration is a cosine, consistent with a displacive excitation mechanism (see SOM text 3). The phase coherence of these collective motions is then lost over time because of elastic and inelastic scattering with bulk phonons.

These results indicate that hot-electron transfer from semiconductor nanocrystals to a technologically relevant electron acceptor is possible. This effect is expected to be of general relevance to other semiconductor nanocrystals and electron and hole conductors, provided the hot electrons and holes possess sufficiently long lifetimes and the interfaces are properly controlled to enable ultrafast charge transfer. Moreover, if hot-electron (hole) transfer can be controlled to occur in very narrow energy windows to also minimize loss in the electron (hole) conductor, the highly efficient hot-carrier solar cell may be realized.

References and Notes

1. W. Shockley, H. J. Queisser, *J. Appl. Phys.* **32**, 510 (1961).
2. R. T. Ross, A. J. Nozik, *J. Appl. Phys.* **53**, 3813 (1982).
3. A. P. Alivisatos, *Science* **271**, 933 (1996).
4. A. J. Nozik, *Annu. Rev. Phys. Chem.* **52**, 193 (2001).
5. K. Mukai, M. Sugawara, in *Self-Assembled InGaAs/GaAs Quantum Dots* (Academic Press, San Diego, CA, 1999), vol. 60, pp. 209–239.
6. A. Pandey, P. Guyot-Sionnest, *Science* **322**, 929 (2008).
7. A. Pandey, P. Guyot-Sionnest, *J. Phys. Chem. Lett.* **1**, 45 (2010).
8. A. J. Nozik, *Physica E* **14**, 115 (2002).
9. N. A. Anderson, T. Q. Lian, *Annu. Rev. Phys. Chem.* **56**, 491 (2005).
10. J. L. Blackburn *et al.*, *J. Phys. Chem. B* **109**, 2625 (2005).
11. I. Robel, V. Subramanian, M. Kuno, P. V. Kamat, *J. Am. Chem. Soc.* **128**, 2385 (2006).
12. B. R. Hyun *et al.*, *ACS Nano* **2**, 2206 (2008).
13. S. Y. Jin, T. Q. Lian, *Nano Lett.* **9**, 2448 (2009).
14. Y. R. Shen, *Nature* **337**, 519 (1989).
15. M. Omote *et al.*, *J. Phys. Cond. Mat.* **17**, S175 (2005).
16. E. A. McArthur, K. B. Eisenthal, *J. Am. Chem. Soc.* **128**, 1068 (2006).
17. D. V. Talapin, C. B. Murray, *Science* **310**, 86 (2005).
18. F. W. Wise, *Acc. Chem. Res.* **33**, 773 (2000).
19. See supporting material on *Science* Online.
20. D. Yu, C. J. Wang, P. Guyot-Sionnest, *Science* **300**, 1277 (2003).
21. J. M. Luther *et al.*, *ACS Nano* **2**, 271 (2008).
22. K. J. Williams *et al.*, *ACS Nano* **3**, 1532 (2009).
23. T. F. Heinz, in *Nonlinear Surface Electromagnetic Phenomena*, H. Ponrath, G. Stegeman, Eds. (Elsevier, Amsterdam, 1991), pp. 353–416.
24. R. M. Corn, D. A. Higgins, *Chem. Rev.* **94**, 107 (1994).
25. O. A. Aktsipetrov *et al.*, *Phys. Rev. B* **60**, 8924 (1999).
26. A. Nahata, T. F. Heinz, *Opt. Lett.* **23**, 67 (1998).
27. J. C. Johnson *et al.*, *Nano Lett.* **4**, 197 (2004).
28. R. D. Schaller *et al.*, *Phys. Rev. Lett.* **95**, 196401 (2005).
29. E. Hendry, F. Wang, J. Shan, T. F. Heinz, M. Bonn, *Phys. Rev. B* **69**, 081101 (2004).
30. O. V. Prezhdo, W. R. Duncan, V. V. Prezhdo, *Prog. Surf. Sci.* **84**, 30 (2009).
31. R. N. Hall, J. H. Racette, *J. Appl. Phys.* **32**, 2078 (1961).
32. R. Lindsay *et al.*, *Phys. Rev. Lett.* **94**, 246102 (2005).
33. Y. M. Chang, L. Xu, H. W. K. Tom, *Phys. Rev. Lett.* **78**, 4649 (1997).

34. We thank K. S. Leschkies, A. Wolcott, C. Nelson, and G. Haugstad for assistance with PbSe nanocrystal synthesis and atomic force microscopy imaging. This work was supported by the U.S. Department of Energy (DE-FG02-07ER46468). Partial support from the NSF Nanoscale Interdisciplinary Research Team (NIRT) program (CBET-0506672) and the Materials Research Science and Engineering Center (MRSEC) programs (DMR-0819885) in the form of student assistantships to B.A.T. and W.A.T. are acknowledged. W.A.T. received support from a University of Minnesota Doctoral Dissertation Fellowship.

Supporting Online Material

www.sciencemag.org/cgi/content/full/328/5985/1543/DC1
Materials and Methods
SOM Text
Figs. S1 to S11
Table S1
References

3 December 2009; accepted 4 May 2010
10.1126/science.1185509

Crossover from Single-Step Tunneling to Multistep Hopping for Molecular Triplet Energy Transfer

Josh Vura-Weis,[1] Sameh H. Abdelwahed,[2] Ruchi Shukla,[2] Rajendra Rathore,[2]* Mark A. Ratner,[1]* Michael R. Wasielewski[1]*

Triplet energy transfer (TT), a key process in molecular and organic electronics, generally occurs by either strongly distance-dependent single-step tunneling or weakly distance-dependent multistep hopping. We have synthesized a series of π-stacked molecules consisting of a benzophenone donor, one to three fluorene bridges, and a naphthalene acceptor, and studied the rate of TT from benzophenone to naphthalene across the fluorene bridge using femtosecond transient absorption spectroscopy. We show that the dominant TT mechanism switches from tunneling to wire-like hopping between bridge lengths 1 and 2. The crossover observed for TT can be determined by direct observation of the bridge-occupied state.

The rapid and efficient transport of energy and charge over tens to hundreds of nanometers in molecules underlies the performance of devices such as organic photovoltaics, thin-film transistors, and light-emitting diodes. Charge and energy transport is also crucial to many biological processes, such as long-distance electron transfer in proteins (*1*) and the quenching of triplets in the bacterial photosynthetic reaction center by energy transfer cascades. (*2*) The study of charge transfer (CT) and triplet energy transfer (TT) in donor-bridge-acceptor (D-B-A) systems has demonstrated two general transport mechanisms—strongly distance-dependent single-step tunneling and weakly distance-dependent multistep hopping, which is also known as wire-like transport (*3*). Optimizing TT efficiency is particularly important for improving organic and polymer light-emitting diode (OLED/PLED) performance, because injection of charge into the active layer of these devices generally leads to a 3:1 ratio of triplet to singlet excitons through spin statistics (*4*, *5*), although the singlet exciton population may be higher in π-conjugated polymers (*6*). TT in PLEDs occurs both within and between chains (*7*), so that transport through noncovalent π-stacked molecules is important.

A major goal is to design molecules that exhibit multistep hopping in which charge or energy moves from a donor to the bridge and then later to the acceptor. Several CT studies have shown a crossover from tunneling to hopping as the bridge length increased, which

[1]Department of Chemistry and Argonne-Northwestern Solar Energy Research (ANSER) Center, Northwestern University, Evanston, IL 60208, USA. [2]Department of Chemistry, Marquette University, Post Office Box 1881, Milwaukee, WI 53201, USA.

*To whom correspondence should be addressed: rajendra.rathore@marquette.edu (R.R.); ratner@chem.northwestern.edu (M.A.R.); m-wasielewski@northwestern.edu (M.R.W.)

has shed light on the interplay between electronic coupling and D-B and B-A energy matching necessary for rapid charge transfer (*8–11*). Because the oxidized/reduced bridge molecules are generally poor chromophores (*12*), the crossover in mechanism has been deduced from a "kink" in plots of the transfer rate versus D-A distance or from a delay between the appearance of D^+ and the appearance of A^-, as opposed to direct spectroscopic measurements of the bridge-occupied state. Although synthetic analogs of the triplet energy cascades found in nature have been prepared (*13*, *14*), a switch in TT mechanism as a function of bridge length has not yet been demonstrated.

We present direct evidence for a change in mechanism from single-step tunneling to multistep hopping for TT determined by spectroscopic detection of the bridge-occupied state. As our D-B-A system, we have synthesized molecules with a benzophenone triplet energy donor (Bp), polyfluorene bridges (F_n, where $n = 1$ to 3), and a naphthalene acceptor (Nap) (Fig. 1A). These are constrained to a π-stacked geometry through methylene linkers. The cofacially arrayed polyfluorene bridges have been shown by ^{1}H NMR (nuclear magnetic resonance) spectroscopy to remain π-stacked in solution, and single-crystal x-ray crystallography has shown that the fluorenes are separated by ~3.0 Å at their closest contact (*15*). All of the molecules we report have been fully characterized by NMR and high-resolution mass spectrometry, and the structure of a representative triad was also confirmed by x-ray crystallography (Fig. 1B). Synthetic details are given in the supporting online material (*16*).

The triplet energy levels of Bp, F_n, and Nap (Fig. 1C) were determined from phosphorescence spectroscopy and Configuration Interaction Singles (CIS) calculations (*16*). The ^3F_n energy of 2.8 eV was always between that of ^{3}Bp (3.0 eV) and ^{3}Nap (2.6 eV). The ^3F_n energy was independent of the number of fluorenes, indicating weak coupling between the fluorene monomers and a lack of triplet delocalization. In contrast, the triplet energy level of linearly conjugated oligofluorene decreases from 2.86 to 2.25 eV as the length increases from one to three monomers because of increased delocalization of the wave function (*17*).

We monitored TT using femtosecond transient absorption spectroscopy. A 150-fs, 350-nm laser pulse selectively excited Bp, and transient spectra were measured with a white-light continuum probe pulse. The total instrument response function was 180 fs. The three-dimensional (3D) transient absorption spectra for each molecule are shown in Fig. 2. The initially created ^{1*}Bp state absorbed at 580 nm (*18*) and was converted by intersystem crossing to ^{3}Bp, which absorbed at 535 nm. In the Bp-F_n model compounds, the triplet energy then transferred from ^{3}Bp to the F_n bridge, as revealed by the absorptive feature at ~400 nm for all molecules and an additional peak at ~585 nm for F_2 and F_3. The lack of 585-nm absorption in $^3F_1$ is consistent with the $T_1 \rightarrow T_n$ spectra of linearly conjugated fluorenes, which show only a 385-nm peak for one fluorene but an additional 690-nm peak for longer oligomers (*17*).

Because overlapping spectral features are present, we determined the intersystem crossing time constant τ_{isc} (^{1*}Bp→^{3}Bp) and bridge injection times τ_{inj} (^{3}Bp→^3F_n) using a global fitting routine that incorporates a sequential kinetic model. The global fits of the Bp-F_n transient spectra (Fig. 2, A to C) gave $\tau_{isc} = 6$ ps and $\tau_{inj} = 156$, 119, and 104 ps for Bp-F_1, Bp-F_2, and Bp-F_3, respectively (*19*). The value of τ_{isc} is constant for all molecules studied and will be ignored for the remainder of the discussion, as it is much faster than all other processes studied. Also we report time constants instead of rate constants ($\tau = 1/k$) except in rate equations. In each of these fits, spectral and kinetic slices of the reconstructed data are nearly superimposable with the corresponding slices of the experimental data.

The rate of TT may be roughly described in the nonadiabatic, high-temperature Marcus formalism (*20–24*)

$$k = \frac{2\pi}{\hbar} V^2 \sqrt{\frac{1}{4\pi\chi k_B T}} e^{\frac{-(\Delta G^\circ + \chi)^2}{4\chi k_B T}} \tag{1}$$

where ΔG° is the free energy change, χ is the reorganization energy arising from Huang-Rhys factors associated with excitation transfer (*22*), and *V* is the electronic coupling between D and A, which depends on orbital overlap and therefore scales exponentially with distance. This scaling is influenced by the intervening medium and is characterized by a factor β such that $k \propto \exp(-\beta^* R_{DA})$, where R_{DA} is the donor-acceptor distance. The

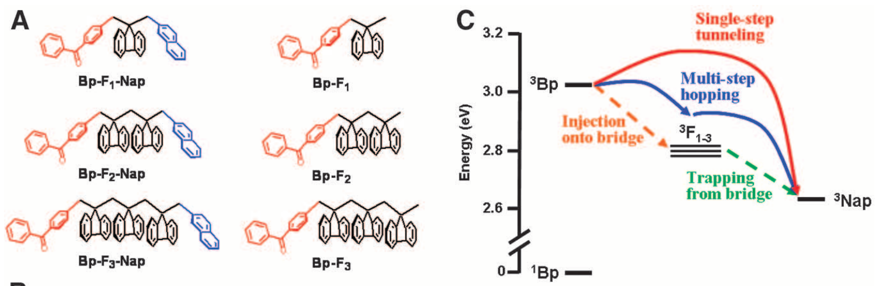

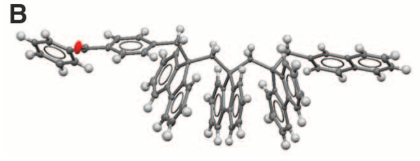

Fig. 1. (**A**) Structures of Bp-F_n and Bp-F_n-Nap molecules. (**B**) X-ray structure of Bp-F_3-Nap showing the cofacial π-stacked arrangement of all chromophores. (**C**) Energy level diagram of Bp-F_n-Nap showing two mechanisms of TT: single-step tunneling from Bp to Nap, or multistep hopping consisting of injection onto the F_n bridge followed by trapping by Nap. The triplet energy of the F_n bridges is independent of *n* to within 0.02 eV.

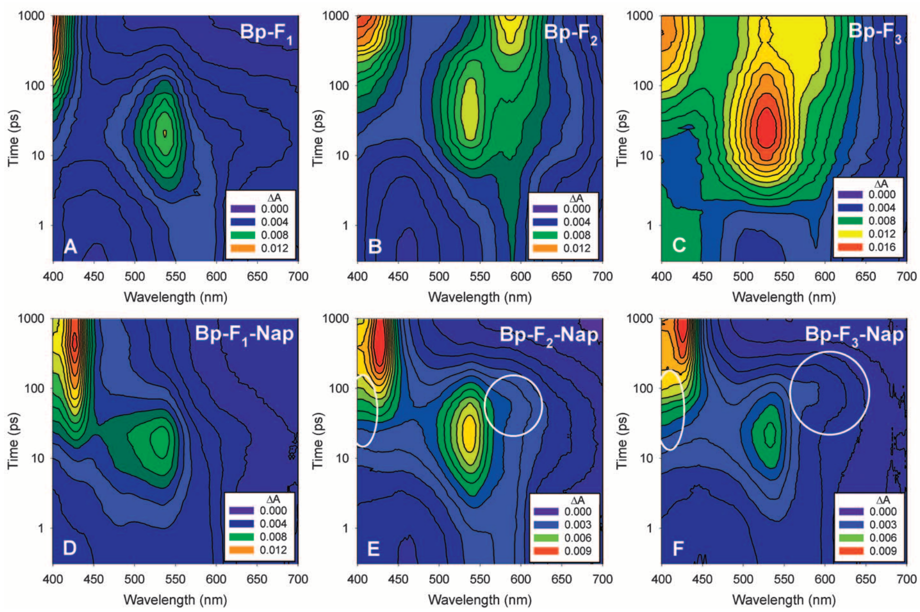

Fig. 2. Transient absorption spectra of Bp-F_n (**A** to **C**) and Bp-F_n-Nap (**D** to **F**). White ovals identify absorption due to the ^3F_n bridge-occupied state.

length dependence of τ_{inj} cannot be explained by differences in $\Delta G°$ or χ, because the bridge energies are nearly degenerate. Instead, we postulate that the Bp triplet can tunnel to any of the n bridge sites (i.e., to site 1 or 2 for Bp-F_2), with the observed rate for Bp-F_2 and Bp-F_3 being the sum of the two or three individual rates. As discussed in the supporting online text (*16*), such a model leads to a β value of 0.36 $Å^{-1}$. This is smaller than might be expected for a π-stacked system, although it is within the range observed for TT across conjugated bridges (*25–28*). We suspect that this low β value is due to the compressed π stack that leads to strong electronic coupling between the different sites; a similar effect has been seen for charge transfer through a benzene stack (*29*).

The transient spectrum of the Bp-F_1-Nap donor-bridge-acceptor molecule (Fig. 2D) showed the same ^{1*}Bp→^{3}Bp progression from 585 to 535 nm as Bp-F_n, followed by loss of the ^{3}Bp peak and growth of absorption at 425 nm that is characteristic of ^{3}Nap. We fitted the ^{1*}Bp→^{3}Bp→^{3}Nap process using the two-step model described above and obtained a total TT time τ_{tot} (^{3}Bp→^{3}Nap) of 62 ps, again with excellent agreement between the experimental and reconstructed data. This time is surprising, because it is much faster than the 156 ps triplet injection time for Bp-F_1. Full TT must occur at least partially through a single-step tunneling mechanism, and the observed rate k_{tot} will be the sum of the rates of hopping and tunneling processes ($k_{tot} = k_{tun} + k_{hop}$). Because there was no evidence for buildup of triplet on the F_1 bridge, we can assume that in Bp-F_1-Nap, the trapping rate k_{trap} was much faster than k_{inj}, and thus $k_{hop} \approx k_{inj}$. Using $\tau_{hop} = 156$ ps and $\tau_{tot} = 62$ ps, we calculated a tunneling time τ_{tun} of 104 ps, which results in quantum yields of 60% for single-step tunneling and 40% for hopping. The relative free energy changes of the two processes causes direct tunneling from Bp to Nap to be faster than triplet injection onto F_1. A straightforward application of Marcus theory can be used to explain this result (*16*).

Unlike the transient spectra of Bp-F_1-Nap, those of Bp-F_2-Nap and Bp-F_3-Nap could not be fit well using a two-step ^{1*}Bp→^{3}Bp→^{3}Nap model. The reconstructed spectra underestimate a 585-nm shoulder at intermediate times, as shown in Fig. 3A for Bp-F_2-Nap. Absorption from 400 to 420 nm is also underrepresented in the fit. Inspection of the average residual (data minus fit) from 50 to 200 ps shows a strong resemblance to the $^3F_2$ spectrum seen at long times in the transient absorption of Bp-F_2, with peaks at 585 and ~400 nm (Fig. 3B). This shows that the $^3F_2$ bridge state is occupied at intermediate times. The dips in the residual at 430 and 530 nm correspond to ^{3}Nap and ^{3}Bp absorption that is overrepresented in the fit.

We therefore extended the global fit to use a three-step ^{1*}Bp→^{3}Bp →^3F_n→^{3}Nap kinetic model, where the ^3F_n state represents the triplet localized on any of the spectroscopically indistinguishable bridge sites. Because of the large number of fitting parameters, the ^{3}Bp→^3F_n time constants were fixed at the values obtained from the Bp-F_n model complexes. The 400-nm and 585-nm absorption at intermediate times is now well represented in the fit (Fig. 3C). Trapping times τ_{trap} for the ^3F_n→^{3}Nap process were fit as 74 ps and 179 ps for Bp-F_2-Nap and Bp-F_3-Nap, respectively. The slower trapping time for Bp-F_3-Nap is consistent with the qualitative observation that the ^3F_n features at 400 and 585 nm are more prominent in its transient spectra because of a higher population of the bridge-occupied state. Because triplet injection preferentially populates the bridge sites closest to Bp, adding more sites necessarily slows τ_{trap}, either because the triplet takes time to migrate along the bridge or because direct trapping from the distant bridge site is slow. Although we have modeled the ^3F_n→^{3}Nap step as a simple rate process that depends on a single rate constant and the total population of all bridge sites, in reality this step is certainly more complex. Given the lack of information on the exact location of the triplet within the F_n bridge, we feel this is a reasonable approximation.

Finally, we constructed a plot showing the evolution of the total, hopping, and tunneling rates as a function of bridge length to illustrate the crossover between tunneling-dominated behavior and hopping-dominated behavior. Given the rates measured above, along with the calculated β value of 0.36$Å^{-1}$, we estimate tunneling times τ_{tun} for Bp-F_2-Nap and Bp-F_3-Nap as 310 and 900 ps, respectively. We calculate phenomenological hopping and total rates k_{hop} and k_{tot} by simulating the ^{3}Nap population as a function of time and fitting it to a single-exponential rise. For k_{hop} we omit the direct ^{3}Bp→^{3}Nap pathway, whereas for k_{tot} all pathways are included. Figure 4 shows the microscopic k_{tun}, k_{inj}, and k_{trap} and phenomenological k_{hop} and k_{tot} rates as a function of Bp-Nap distance and number of fluorenes n.

The crossover between tunneling and hopping as the dominant mechanism occurs between n = 1 and 2, where the percentage of population transferred by single-step tunneling drops from 60% to 28%. Two factors influence this crossover. The primary cause is the steep drop in k_{tun} that results from the exponential distance dependence of orbital overlap. In addition, k_{inj} rises because of the addition of a second bridge site to which the energy can transfer. Because k_{trap} falls more sharply than k_{inj} rises, the net hopping rate k_{hop} decreases slightly. At n = 3, the trapping rate becomes rate-limiting for k_{hop}. At this distance k_{tot} is further dominated by k_{hop}, with 90% of the TT going through the hopping pathway.

Our direct study of the crossover between single-step tunneling and multistep hopping as the bridge length increases shows that while the bridge is energetically accessible in all cases,

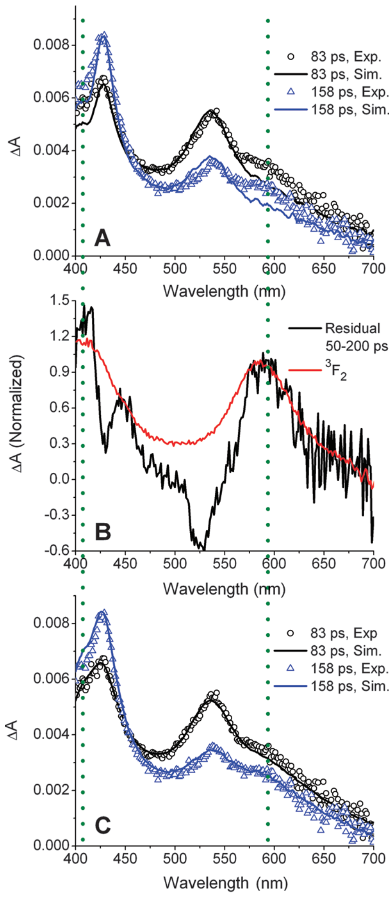

Fig. 3. (**A**) Experimental and reconstructed transient spectra of Bp-F_2-Nap at 83 and 158 ps using a two-step ^{1*}Bp→^{3}Bp→^{3}Nap model. The fit is poor at 400 and 585 nm, as highlighted by the dotted green line. (**B**) Average residual (data-fit) from 50 to 200 ps versus $^3F_2$ spectrum, both of which peak at 400 and 585 nm. (**C**) Experimental and reconstructed transient spectra of Bp-F_2-Nap at 83 and 158 ps using a three-step ^{1*}Bp→^{3}Bp→$^3F_2$→^{3}Nap model. Addition of the $^3F_2$ intermediate leads to excellent fits at those wavelengths.

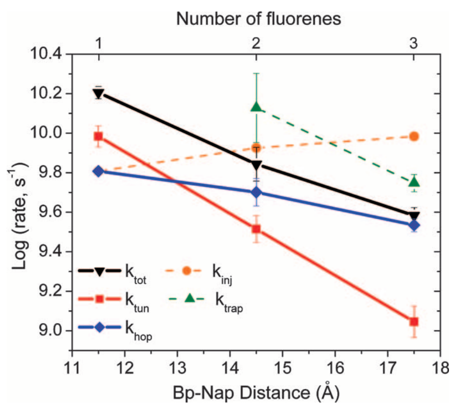

Fig. 4. Triplet energy transfer rates ($k = 1/\tau$) as a function of Bp-Nap distance. Single-step tunneling dominates for n = 1, whereas multistep hopping dominates for n = 2 or 3. Error bars are the standard deviation of three measurements (*16*).

tunneling is preferred for the shortest bridge length because of the large free-energy change between D and A. At longer distances, the poor scaling of direct tunneling favors a stepwise mechanism. Triplet energy transfer through π-stacked molecules is common in organic light-emitting diodes, and this intermediate regime between the strong distance dependence of tunneling and weak distance dependence of hopping may prove useful in understanding and designing energy transfer pathways in such devices.

References and Notes

1. H. B. Gray, J. R. Winkler, *Annu. Rev. Biochem.* **65**, 537 (1996).
2. L. Takiff, S. G. Boxer, *J. Am. Chem. Soc.* **110**, 4425 (1988).
3. P. F. Barbara, T. J. Meyer, M. A. Ratner, *J. Phys. Chem.* **100**, 13148 (1996).
4. M. A. Baldo, D. F. O'Brien, M. E. Thompson, S. R. Forrest, *Phys. Rev. B* **60**, 14422 (1999).
5. V. Cleave, G. Yahioglu, P. L. Barny, R. H. Friend, N. Tessler, *Adv. Mater.* **11**, 285 (1999).
6. M. Wohlgenannt, Z. V. Vardeny, *J. Phys. Condens. Matter* **15**, R83 (2003).
7. H. H. Liao *et al.*, *Phys. Rev. B* **74**, 245211 (2006).
8. W. B. Davis, W. A. Svec, M. A. Ratner, M. R. Wasielewski, *Nature* **396**, 60 (1998).
9. R. H. Goldsmith *et al.*, *Proc. Natl. Acad. Sci. U.S.A.* **102**, 3540 (2005).
10. E. A. Weiss *et al.*, *J. Am. Chem. Soc.* **126**, 5577 (2004).
11. F. D. Lewis *et al.*, *J. Am. Chem. Soc.* **128**, 791 (2006).
12. M. U. Winters, K. Pettersson, J. Mårtensson, B. Albinsson, *Chemistry - A European Journal* **11**, 562 (2005).
13. D. Gust *et al.*, *J. Photochem. Photobiol. B* **43**, 209 (1998).
14. R. E. Palacios *et al.*, *Chem. Phys. Chem.* **6**, 2359 (2005).
15. R. Rathore, S. H. Abdelwahed, I. A. Guzei, *J. Am. Chem. Soc.* **125**, 8712 (2003).
16. Materials and methods are available as supporting material on *Science* Online.
17. D. Wasserberg, S. P. Dudek, S. C. J. Meskers, R. A. J. Janssen, *Chem. Phys. Lett.* **411**, 273 (2005).
18. M. Montalti, A. Credi, L. Prodi, M. T. Gandolfi, *Handbook of Photochemistry, Third Edition* (Taylor & Francis, Boca Raton, FL, 2006).
19. Errors are shown in Fig. 4 and are about <5% for injection times and 10 to 30% for all other times. See table S1 for all times and errors.
20. R. A. Marcus, *Annu. Rev. Phys. Chem.* **15**, 155 (1964).
21. M. E. Sigman, G. L. Closs, *J. Phys. Chem.* **95**, 5012 (1991).
22. The Marcus treatment was developed to describe electron transfer but is also valid for TT, which is often described as a "double exchange" or "Dexter exchange" (*23*) process. Energy transfer arises from electron tunneling among sites due to two-electron exchange integrals, accompanied by reorganizational energy in the nuclear motion (Huang-Rhys factors). Note that we have used the variable χ for the reorganization term to distinguish this process from charge transfer, where λ is used. Other parallels between energy and electron transfer have been shown (*24*).
23. D. L. Dexter, *J. Chem. Phys.* **21**, 836 (1953).
24. J. J. Hopfield, *Proc. Natl. Acad. Sci. U.S.A.* **71**, 3640 (1974).
25. J. Andreasson, J. Kajanus, J. Mårtensson, B. Albinsson, *J. Am. Chem. Soc.* **122**, 9844 (2000).
26. A. C. Benniston, V. Grosshenny, A. Harriman, R. Ziessel, *Angew. Chem. Int. Ed. Engl.* **33**, 1884 (1994).
27. A. Harriman, A. Khatyr, R. Ziessel, A. C. Benniston, *Angew. Chem. Int. Ed.* **39**, 4287 (2000).
28. B. Albinsson, J. Mårtensson, *J. Photochem. Photobiol. Photochem. Rev.* **9**, 138 (2008).
29. Y. K. Kang, I. V. Rubtsov, P. M. Iovine, J. X. Chen, M. J. Therien, *J. Am. Chem. Soc.* **124**, 8275 (2002).

30. J.V.W. thanks R. H. Goldsmith for assistance with Matlab and helpful discussions. This work was supported by the Chemical Sciences, Geosciences, and Biosciences Division, Office of Basic Energy Sciences, Department of Energy, under grant DE-FG02-99ER14999 (M.R.W.), NSF Chemistry (R.R. and M.A.R.), and Office of Naval Research (M.A.R.). The crystal structure of Bp-F_3-Nap has been deposited at CCDC with accession number 772735.

Supporting Online Material
www.sciencemag.org/cgi/content/full/328/5985/1547/DC1
Materials and Methods
Figs. S1 to S9
Tables S1 and S2
References

9 March 2010; accepted 29 April 2010
10.1126/science.1189354

Subpolar Link to the Emergence of the Modern Equatorial Pacific Cold Tongue

Alfredo Martínez-Garcia,[1,2,3]* Antoni Rosell-Melé,[3,4] Erin L. McClymont,[5] Rainer Gersonde,[6] Gerald H. Haug[1,2]

The cold upwelling "tongue" of the eastern equatorial Pacific is a central energetic feature of the ocean, dominating both the mean state and temporal variability of climate in the tropics and beyond. Recent evidence for the development of the modern cold tongue during the Pliocene-Pleistocene transition has been explained as the result of extratropical cooling that drove a shoaling of the thermocline. We have found that the sub-Antarctic and sub-Arctic regions underwent substantial cooling nearly synchronous to the cold tongue development, thereby providing support for this hypothesis. In addition, we show that sub-Antarctic climate changed in its response to Earth's orbital variations, from a subtropical to a subpolar pattern, as expected if cooling shrank the warm-water sphere of the ocean and thus contracted the subtropical gyres.

The equatorial Pacific cold tongue is a vivid expression of the ocean's thermocline, the contact between the pools of warm surface water circulating within the subtropical gyres and the colder ocean below. The trade winds drive an east-to-west downward tilt in the thermocline, which causes the thermocline to contact the ocean surface in the eastern Pacific, producing the cold tongue. An "El Niño" occurs when weaker trades allow the thermocline tilt to relax toward the horizontal, causing the cold tongue to disappear (*1*, *2*). The cold tongue is also sensitive to the mean depth of the thermocline (*3*), which can change on longer time scales, deepening in response to reduction in the meridional temperature gradient (*4*–*6*). If the thermocline deepens from its present position, the eastern cold tongue might eventually disappear.

Several authors have suggested that the warm-water volume was greater and the cold tongue absent in warm Pliocene times (*5*–*9*), with the cold tongue emerging only after adequate cooling had occurred. The existing paleotemperature data sets from the equatorial Pacific indicate that the emergence of the cold tongue during the Pliocene-Pleistocene transition was probably a multistage process that involved a different temporal behavior and signature at different locations and latitudes. The sea surface temperature (SST) reconstructions from the eastern part of the present-day cold tongue [Ocean Drilling Program (ODP) Site 846] seem to indicate that the latitudinal temperature gradient along the equator started to emerge around 4.3 million years ago (Ma) (*10*). However, the multiproxy paleotemperature estimates (based on alkenones and Mg/Ca paleothermometers) from a record located several hundred kilometers toward the west (ODP Site 847) show very little change at that time (*7*, *11*), indicating that the cold tongue, if present, was probably smaller than today. Indeed, the paleotemperature data from ODP Site 847 suggest that the cold tongue expanded toward its present configuration in the interval from ~1.8 to ~1.2 Ma (*7*), during what would appear to be a time of relatively stable polar climate and glacial ice volume (*12*). If the development of the modern cold tongue was driven by thermocline shoaling, it should have been accompanied by an equatorward contraction of the thermocline's polar margins, which is a second expression of the volume of warm ocean water (*5*, *6*). However, the paleoceanographic

[1]Geological Institute, ETH Zürich, 8092 Zürich, Switzerland. [2]DFG-Leibniz Center for Surface Process and Climate Studies, Institute for Geosciences, Potsdam University, D-14476 Potsdam, Germany. [3]Institut de Ciència i Tecnologia Ambientals, Universitat Autònoma de Barcelona, Bellaterra, 08193 Catalonia, Spain. [4]Institució Catalana de Recerca i Estudis Avançats, Barcelona, 08010 Catalonia, Spain. [5]School of Geography Politics and Sociology, Newcastle University, Newcastle upon Tyne NE1 7RU, UK. [6]Alfred Wegener Institute for Polar and Marine Research, D-27568 Bremerhaven, Germany.

*To whom correspondence should be addressed. E-mail: alfredo.martinez-garcia@erdw.ethz.ch

test of this prediction has awaited the development of continuous high-latitude SST reconstructions, especially from the Southern Hemisphere, which is particularly important in the ventilation of the global thermocline. Here, we report two high-resolution Pliocene-Pleistocene paleotemperature records from the northern and southern subpolar regions, which provide strong evidence in favor of this contraction of the subtropical ocean. Such findings support the existence of a pervasive link between the cooling and equatorward expansion of subpolar and polar conditions and the emergence of the modern cold tongue in the equatorial Pacific at the beginning of the Pleistocene.

The two paleotemperature records presented in this study are based on the analysis of alkenone unsaturation indices (*13*, *14*) in sediments from ODP Sites 882 (sub-Arctic Pacific) and 1090 (sub-Antarctic Atlantic) (Fig. 1). The percentage of the $C_{37:4}$ alkenone relative to the total abundance of C_{37} alkenones (%$C_{37:4}$) in these records (Fig. 2, D and E) is an additional tracer that can be used to infer variations in the meridional extent of polar and subpolar conditions through time (*15*–*18*).

The long-term trend of the SST records reveals a major subpolar cooling from ~1.8 to ~1.2 Ma, with an average bipolar temperature drop of 4° to 5°C (Fig. 2, B and C). This coincides with an increase in the %$C_{37:4}$ alkenone in both sites, indicating a progressive expansion of the polar waters into the present-day sub-Arctic and sub-Antarctic regions (Fig. 2, D and E). These findings are in good agreement with the onset of a progressive increase in biogenic opal mass accumulation rates observed in the Southern Ocean around the Polar Front, the Polar Front Zone, and the Subtropical Front during this time interval (*19*). Micropaleontological data from the Southern Ocean indicate that a temperature drop of 5° to 6°C in the sub-Antarctic Atlantic during the Last Glacial Maximum (LGM) was associated with an expansion of winter sea ice in the Atlantic sector of the Southern Ocean from 55°S to ~47°S (*20*). If most of the Pliocene glacial SSTs were 4° to 5°C warmer than LGM temperatures, then Antarctic sea ice cover during Pliocene glacial stages may have been more similar to the present-day distribution than to the LGM distribution. In this sense, the end of the subsequent cooling transition around 1.2 Ma can be considered to mark the establishment of an Antarctic sea ice field comparable to that during the LGM.

The pronounced subpolar cooling and the associated sea ice expansion resulted in an increase in the meridional temperature gradient between the subpolar regions and the equatorial Pacific, changing from around 14° to 15°C in the Pliocene to the 19° to 20°C characteristic of the present-day ocean in the case of the western Pacific, and from 11° to 12°C in the Pliocene to the present gradient of 13° to 14°C in the eastern Pacific (Fig. 2F). A weaker meridional temperature gradient in the early Pliocene implies an expanded tropical warm pool and consequently a weakening and poleward expansion of the Hadley atmospheric convective cells (*6*). Our data suggest that this vast tropical warm pool persisted until the end of the Pliocene at 1.8 Ma.

Remarkably, our data show that the temporal evolution of the meridional temperature gradients between the subpolar regions and the equatorial Pacific mirrors the strengthening of the zonal (east-west) equatorial Pacific temperature gradient (from ~1.8 to ~1.2 Ma) that led to the expansion of the equatorial Pacific cold tongue toward its present-day configuration, and to the development of the modern mode of the Walker circulation system (*7*, *8*) (Fig. 2F). As recently shown by Brierley *et al.* (*6*), the meridional expansion of the warm pool provides a crucial mechanism to sustain a deeper thermocline in the equatorial Pacific during the Pliocene through its effect on the temperature of the thermocline waters in the subtropical subduction zones. Our findings indicate that, in fact, the subsequent expansion of the polar oceans and the associated contraction of the warm pool was closely coupled to the development of the modern cold tongue in the equatorial Pacific, providing strong empirical support for the existence of a direct link between the strengthening of the meridional temperature gradients and the shoaling of the thermocline in the eastern equatorial Pacific.

In addition, our data from ODP Site 1090 indicate that the subpolar cooling transition was linked to a major shift in the response of sub-Antarctic climate to Earth's orbital variations from a subtropical to a subpolar pattern, consistent with an equatorward expansion of the polar and subpolar frontal systems and an associated contraction of the subtropical gyres at the beginning of the Pleistocene. The record of glacial/interglacial sub-Antarctic Atlantic temperature variability during the past 800,000 years is in good agreement with the paleoclimatic reconstructions of the Antarctic ice core records (*21*–*23*), showing a dominant obliquity (41,000-year) cycle during the mid-Pleistocene, a progressive increase in the power of the 100,000-

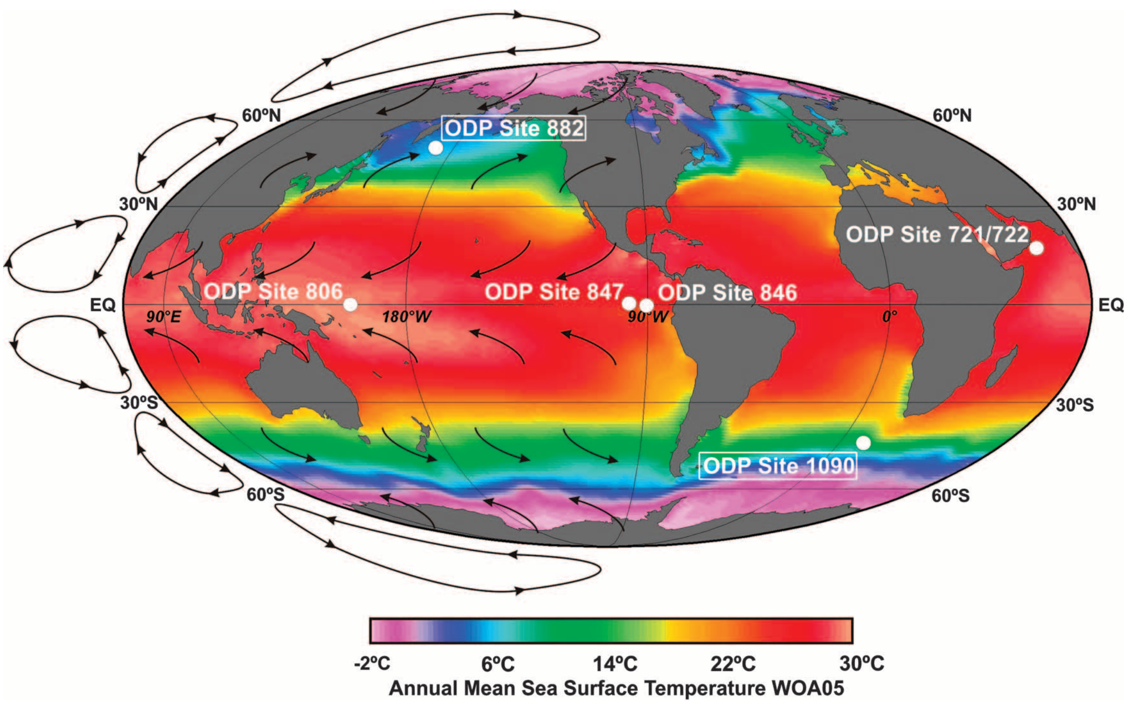

Fig. 1. Location of ODP Site 1090 (42°54.5′S, 8°54.0′E; water depth 3702 m), ODP Site 882 (50°21′N, 167°35′E, water depth 3244 m), and other records discussed in the text. Black arrows are schematic representations of the atmospheric convective cells and wind direction. Modern annual mean SST values are from the World Ocean Atlas 2005 (WOA05). [Map generated with Ocean Data View software, http://odv.awi.de]

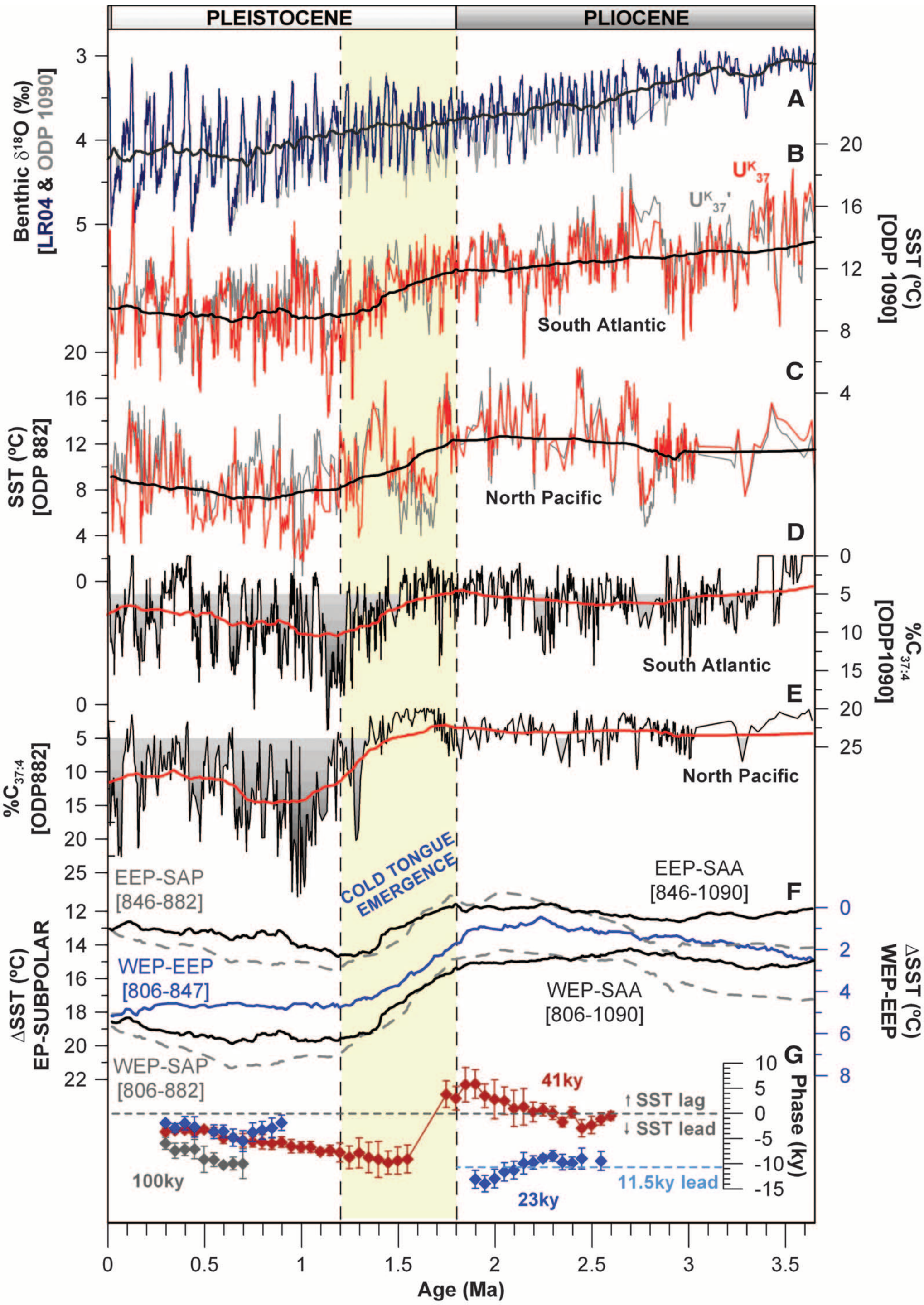

Fig. 2. Pliocene-Pleistocene evolution of the subpolar oceans, global ice volume, and meridional temperature gradients. (**A**) Lisiecki and Raymo (LR04) benthic $\delta^{18}O$ stack (*12*) (blue) and ODP Site 1090 benthic $\delta^{18}O$ reconstruction (*30*) (gray). (**B** and **C**) SST reconstructions using alkenone unsaturation indices, U^K_{37} (red line) and $U^{K'}_{37}$ (gray line), from ODP Site 1090 in the sub-Antarctic Atlantic (SAA) (B) and ODP Site 882 in the sub-Arctic Pacific (SAP) (C). (**D** and **E**) Latitudinal extension of the polar waters into the SAA (D) and the SAP (E), inferred from the percentage of tetra-unsaturated alkenone relative to the total abundance of unsaturated C37 alkenones (%$C_{37:4}$). (**F**) Evolution of the longitudinal and latitudinal SST gradients estimated by subtracting 400,000-year smoothed curves of ODP Site 806 for the western equatorial Pacific (WEP) (*7*), ODP Sites 846 (*10*) and 847 (*7*) for the eastern equatorial Pacific (EEP), ODP Site 882 for the SAP, and ODP Site 1090 for the SAA. (**G**) Phase relationships between ODP Site 1090 benthic $\delta^{18}O$ and alkenone SST for the intervals where the two series are coherent above the 80% confidence level. Phase, coherency estimates, and errors (± SD) were calculated using the iterative spectral feature of the Arand software package with a 600,000-year window and 300 lags. ky, thousands of years.

year cycle toward the present, and secondary precession (23,000- and 19,000-year) cycles (Fig. 3C). Moreover, variations in sub-Antarctic Atlantic temperatures lead changes in continental ice volume (inferred from $\delta^{18}O$) by around 3200 years at the precession frequency band. This likely corresponds to a phase lag of around 1600 years with respect to Northern Hemisphere insolation (*12*), in good agreement with the estimates obtained from the independently dated Antarctic ice cores [i.e., ~1800 years (*22*)]. However, before 1.6 Ma, the temperature variability of the sub-Antarctic Atlantic was distinctly different, with an increased power of precession with respect to obliquity (Fig. 3, B and C), a clear Southern Hemisphere insolation forcing of sub-Antarctic Atlantic temperature at the precession frequency band (*24*), and an in-phase behavior with respect to $\delta^{18}O$ at the obliquity band (Fig. 2G), which is indicative of a shift toward low-latitude insolation forcing of sub-Antarctic Atlantic climate during this period. These findings suggest that the equatorward contraction of the subtropical gyres at the beginning of the Pleistocene caused the sub-Antarctic Atlantic climate to become less sensitive to (precession-driven) variations in Southern Hemisphere low-latitude insolation forcing and more sensitive to (obliquity-driven) variations in Antarctic climate around 1.6 Ma (*25*). This interpretation is supported by a decrease in precession signal observed in African continental climate records subsequent

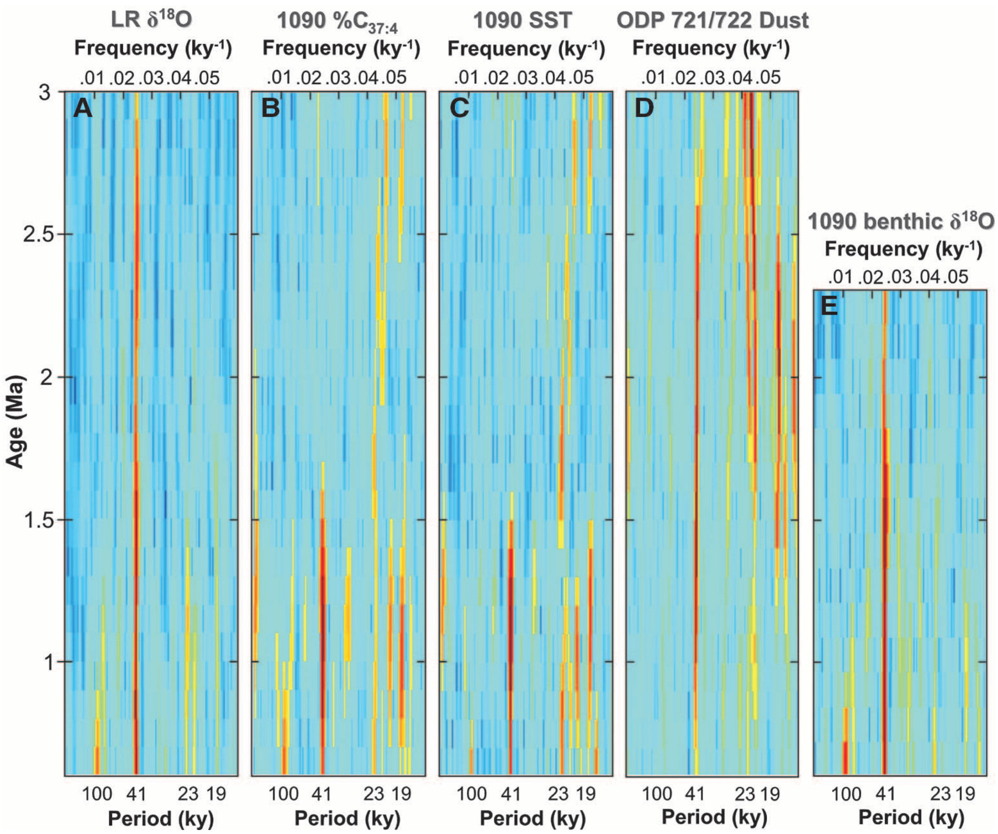

Fig. 3. Evolutionary Blackman-Tukey power spectra of (**A**) LR04 global benthic $\delta^{18}O$ stack (*12*), (**B**) ODP Site 1090 %$C_{37:4}$, (**C**) ODP Site 1090 SST, (**D**) ODP Site 721/722 dust flux reconstruction (*28*), and (**E**) ODP Site 1090 benthic $\delta^{18}O$ record (*30*). The evolutionary power spectra of all the records was computed using the short-time Fourier transform of overlapping segments with a 600,000-year Hamming window and 90% overlap. Before spectral analysis, all series were detrended, interpolated to 2000-year intervals (ky, thousands of years), and prewhitened to minimize the interference of low-frequency variability.

to 1.8 to 1.6 Ma (Fig. 3D) (*26*–*28*). A shift in Southern Ocean biology is also recorded around 1.6 Ma, marked by the onset of massive *Fragilariopsis kerguelensis* (diatom) deposition (*29*) and the development of extensive diatom mats between 47° and 50°S (*29*).

Why the cold tongue expanded toward its present-day configuration around 1.8 to 1.2 Ma, during what would appear to be a time of relatively stable polar climate and glacial ice volume, has been a long-standing question. Our data show that the tropics were not alone in changing at this time, with a bipolar cooling and equatorward expansion of the subpolar water masses also occurring. Thus, our data appear to confirm the hypothesis that the expansion of the subpolar oceans shoaled the thermocline and thus led to the emergence of the modern cold tongue. The converse causation, with the equatorial Pacific driving subpolar changes, lacks the same grounding in dynamical expectations (*4*).

Under anthropogenic forcing of climate, the high latitudes appear to be responding faster than elsewhere—a dynamic that fits with expectations. Given the close link demonstrated here between subpolar ocean climate and the equatorial Pacific, the cold tongue may also respond to the ongoing warming. Indeed, it seems plausible that a warming-driven deepening of the thermocline could result in a reduction or even loss of the cold tongue, initiating a warm state in the Pacific tropical ocean that is reminiscent of the Pliocene.

References and Notes

1. M. A. Cane, S. E. Zebiak, *Science* **228**, 1085 (1985).
2. S. G. H. Philander, *Nature* **302**, 295 (1983).
3. D. Gu, S. G. H. Philander, *Science* **275**, 805 (1997).
4. S. G. Philander, A. V. Fedorov, *Paleoceanography* **18**, 1045 (2003).
5. A. V. Fedorov *et al.*, *Science* **312**, 1485 (2006).
6. C. M. Brierley *et al.*, *Science* **323**, 1714 (2009); published online 26 February 2009 (10.1126/science.1167625).
7. M. W. Wara, A. C. Ravelo, M. L. Delaney, *Science* **309**, 758 (2005); published online 23 June 2005 (10.1126/science.1112596).
8. A. C. Ravelo, D. H. Andreasen, M. Lyle, A. Olivarez Lyle, M. W. Wara, *Nature* **429**, 263 (2004).
9. P. Molnar, M. A. Cane, *Paleoceanography* **17**, 1021 (2002).
10. K. T. Lawrence, Z. Liu, T. D. Herbert, *Science* **312**, 79 (2006).
11. P. S. Dekens, A. C. Ravelo, M. D. McCarthy, *Paleoceanography* **22**, PA3211 (2007).
12. L. E. Lisiecki, M. E. Raymo, *Paleoceanography* **20**, PA1003 (2005).
13. F. G. Prahl, S. G. Wakeham, *Nature* **330**, 367 (1987).
14. S. C. Brassell, G. Eglinton, I. T. Marlowe, U. Pflaumann, M. Sarnthein, *Nature* **320**, 129 (1986).
15. A. Rosell-Melé, *Paleoceanography* **13**, 694 (1998).
16. E. Bard, F. Rostek, J. L. Turon, S. Gendreau, *Science* **289**, 1321 (2000).
17. E. L. McClymont, A. Rosell-Melé, G. H. Haug, J. M. Lloyd, *Paleoceanography* **23**, PA4214 (2008).
18. See supporting material on *Science* Online.
19. G. Cortese, R. Gersonde, C. D. Hillenbrand, G. Kuhn, *Earth Planet. Sci. Lett.* **224**, 509 (2004).
20. R. Gersonde, X. Crosta, A. Abelmann, L. Armand, *Quat. Sci. Rev.* **24**, 869 (2005).
21. J. Jouzel *et al.*, *Science* **317**, 793 (2007); published online 5 July 2007 (10.1126/science.1141038).
22. K. Kawamura *et al.*, *Nature* **448**, 912 (2007).
23. A. Martínez-Garcia *et al.*, *Paleoceanography* **24**, PA1207 (2009).
24. This conclusion is directly derived from the observation that during this period sub-Antarctic Atlantic temperatures led benthic $\delta^{18}O$ at the precession band by around half of a precession cycle (Fig. 2G), which implies that SST variations were in antiphase with changes in Northern Hemisphere ice volume. In principle, this conclusion is independent of age model constraints because both SST and benthic $\delta^{18}O$ have been measured in the same sedimentary record. Thus, considering that changes in benthic $\delta^{18}O$ are paced by Northern Hemisphere insolation and that insolation changes at the precession band are anticorrelated between the two hemispheres, our results suggest that changes in sub-Antarctic Atlantic temperatures were forced by changes in Southern Hemisphere insolation before 1.6 Ma (Fig. 2G).
25. T. Naish *et al.*, *Nature* **458**, 322 (2009).
26. P. J. Hopley *et al.*, *Earth Planet. Sci. Lett.* **256**, 419 (2007).
27. R. Tiedemann, M. Sarnthein, N. J. Shackleton, *Paleoceanography* **9**, 619 (1994).
28. P. B. deMenocal, *Science* **270**, 53 (1995).
29. G. Cortese, R. Gersonde, *Mar. Geol.* **252**, 100 (2008).
30. K. A. Venz, D. A. Hodell, *Palaeogeogr. Palaeoclimatol. Palaeoecol.* **182**, 197 (2002).

31. We thank the Integrated Ocean Drilling Program (IODP) for providing the samples used in this study, and two anonymous reviewers for providing valuable comments that improved the final version of the paper. Supported by a FPU grant awarded by the Ministerio de Ciencia e Innovación, Spain (A.M.-G.).

Supporting Online Material
www.sciencemag.org/cgi/content/full/328/5985/1550/DC1
Materials and Methods
Tables S1 to S3
References

10 November 2009; accepted 6 April 2010
10.1126/science.1184480

Radiocarbon-Based Chronology for Dynastic Egypt

Christopher Bronk Ramsey,[1]* Michael W. Dee,[1] Joanne M. Rowland,[1] Thomas F. G. Higham,[1] Stephen A. Harris,[2] Fiona Brock,[1] Anita Quiles,[3] Eva M. Wild,[4] Ezra S. Marcus,[5] Andrew J. Shortland[6]

The historical chronologies for dynastic Egypt are based on reign lengths inferred from written and archaeological evidence. These floating chronologies are linked to the absolute calendar by a few ancient astronomical observations, which remain a source of debate. We used 211 radiocarbon measurements made on samples from short-lived plants, together with a Bayesian model incorporating historical information on reign lengths, to produce a chronology for dynastic Egypt. A small offset (19 radiocarbon years older) in radiocarbon levels in the Nile Valley is probably a growing-season effect. Our radiocarbon data indicate that the New Kingdom started between 1570 and 1544 B.C.E., and the reign of Djoser in the Old Kingdom started between 2691 and 2625 B.C.E.; both cases are earlier than some previous historical estimates.

Egyptian historical chronologies have been underpinned by relative dating derived from a variety of sources. Building on the surviving evidence from Manetho's *Aegyptiaca* (written in the third century B.C.E.) and the king lists dating from the pharaonic era, generations of scholars have used written and archaeological information to check, and in some instances revise, the sequence of kings and the lengths of their reigns. Undocumented years at the ends of some reigns and overlap between successive monarchs create uncertainties of the order of a few years (*1*).

The placement of this relative chronology on the absolute-calendar time scale, however, has been principally based on the interpretation of a small number of ancient astronomical observations in the Middle and New Kingdoms (MK and NK, respectively) and is therefore considerably less certain. Many of the relevant celestial and lunar phenomena repeat at regular intervals, giving different possible chronologies, and their timing is dependent on the location of the observer, which may also add to the uncertainty (*2*). In addition, much work has been done to synchronize the chronology of Egypt to that of neighboring civilizations (*3*–*5*), particularly with Mesopotamia, which also has a rich and detailed historical record and astronomically based datums; however, precise absolute-age synchronisms between them are only possible in the late NK (*6*). Radiocarbon dating, which is a two-stage process involving isotope measurements and then calibration against similar measurements made on dendrochronologically dated wood, usually gives age ranges of 100 to 200 years for this period (95% probability range) and has previously been too imprecise to resolve these questions.

Here, we combine several classes of data to overcome these limitations in precision: measurements on archaeological samples that accurately reflect past fluctuations in radiocarbon activity, specific information on radiocarbon activity in the region of the Nile Valley, direct linkages between the dated samples and the historical chronology, and relative dating information from the historical chronology. Together, these enable us to match the patterns present in the radiocarbon dates with the details of the radiocarbon calibration record and, thus, to synchronize the scientific and historical dating methods. We obtained short-lived plant remains from museum collections (e.g., seeds, basketry, plant-based textiles, plant stems, fruits) that were directly associated with particular reigns or short sections of the historical chronology. We avoided charcoal and wood samples because of the possibility of inbuilt

[1]Research Laboratory for Archaeology and the History of Art, University of Oxford, Dyson Perrins Building, South Parks Road, Oxford OX1 3QY, UK. [2]Department of Plant Sciences, University of Oxford, South Parks Road, Oxford OX1 3RB, UK. [3]Laboratoire de Mesure du Carbone 14, bat 450 Porte 4E, Commissariat à l'Energie Atomique (CEA)–Saclay, France-Université Paris VII-Diderot, 91191 Gif-Sur-Yvette, France. [4]Vienna Environmental Research Accelerator Laboratory, Fakultät für Physik, Isotopenforschung, Universität Wien, Währingerstrasse 17, A-1090 Wien, Austria. [5]The Recanati Institute for Maritime Studies, University of Haifa, Haifa 31905, Israel. [6]Centre for Archaeological and Forensic Analysis, Department of Applied Science, Security and Resilience, Cranfield University, Shrivenham, Swindon SN6 8LA, UK.

*To whom correspondence should be addressed. E-mail: christopher.ramsey@rlaha.ox.ac.uk

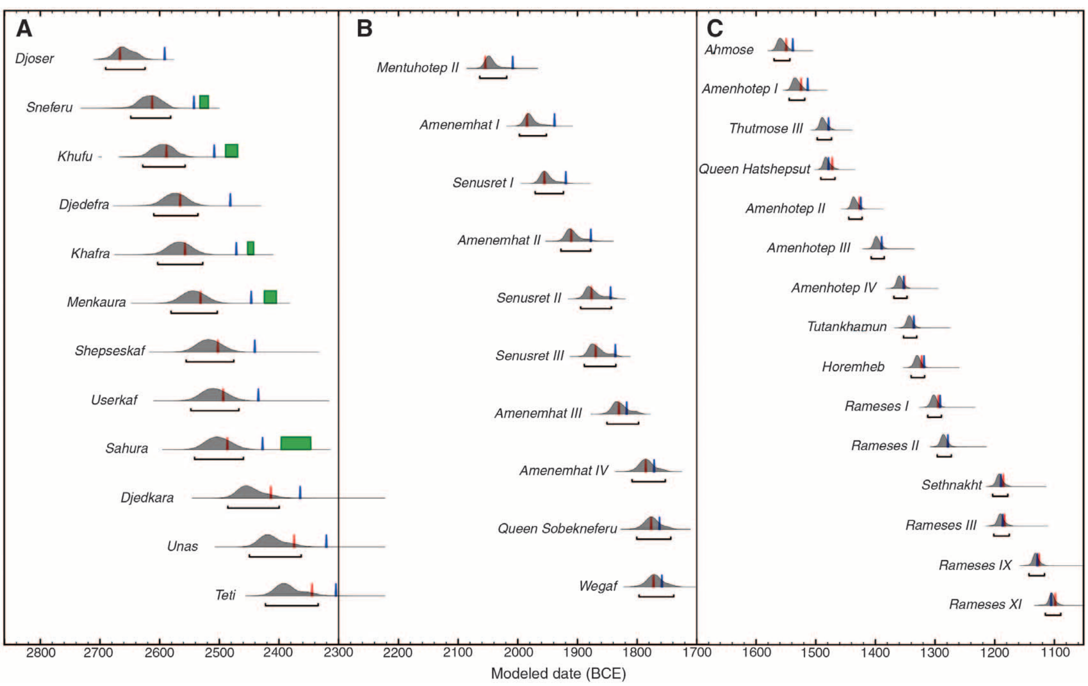

Fig. 1. A selection of the accession dates (first regnal year) for the (**A**) OK, (**B**) MK, and (**C**) NK derived from this research. The marginal posterior probability distributions are shown in gray, with their corresponding 95% probability ranges indicated below. Red, historical dates from Shaw (*18*); blue, from Hornung *et al.* (*21*); and green, from Spence (*24*). The accession intervals used for the model are from Shaw (*18*), and corresponding distributions using the intervals from Hornung *et al.* (*21*) are shown in fig. S4.

age. We also avoided mummified material because of concerns about contamination from bitumen or other substances used in the mummification process and human material because of the possibility of riverine or marine components in the diet (which might contain older carbon). We selected samples according to the security of their archaeological context and relation to a given king's reign, but in making the chronological associations, we were reliant on the judgement of excavators and curators and on the integrity of the collections themselves, because many of the excavations took place in the 19th or early 20th century. Most of the samples were taken from individual funerary contexts. In a few cases, we sampled different short-lived plant remains from a single context, allowing us to check the internal consistency of the measurements.

We prepared samples for radiocarbon analysis using standard acid-base-acid methods, in some cases preceded by solvent extraction of possible museum-based contaminants (*7–10*). Next, we converted treated samples to graphite (*11*) before radiocarbon measurement by accelerator mass spectrometry (AMS) (*12–14*). Calibration of the radiocarbon dates was against the InCal04 calibration curve (*15*) using OxCal v4.1.3 (*16*, *17*). In all, we obtained 211 AMS radiocarbon determinations (table S1). Where there were indications of conservation work, we attempted to avoid sampling the affected areas and used solvent pretreatment methods to remove potential contaminants, but the possibility remains that some cases of contamination may have escaped detection.

Fourteen of the ancient samples were actually from the first or second millennium C.E. and were thus clearly intrusive; we do not consider these further. Another small set of radiocarbon dates show offsets of a few hundred years (typically younger than expected). This is not surprising, as tomb contexts are often disturbed after being sealed, and some intrusion of younger material is always a possibility. Where we have multiple samples from single contexts, the internal agreement between the dates is usually good, except for two measurements on the same sample, where we suspect contamination, that are not included in the analysis (see table S1 for details).

In one case, although the internal consistency is satisfactory, seven dates from one single 19th Dynasty tomb are ~200 years older than the historical age ascribed to them (see dates ascribed to Ramses I/Seti I in table S1). In this instance, we have concluded that there must be an archaeological problem and have excluded the dates from the model. We included all other dates (188 in total), whether or not they appear to be outliers in our analysis. We have 128 dates from the NK, 43 from the MK, and 17 from the Old Kingdom (OK). The majority (~75%) of the measurements have calibrated age ranges that overlap with the conventional historical chronology, within the wide error limits that result from the calibration of individual dates.

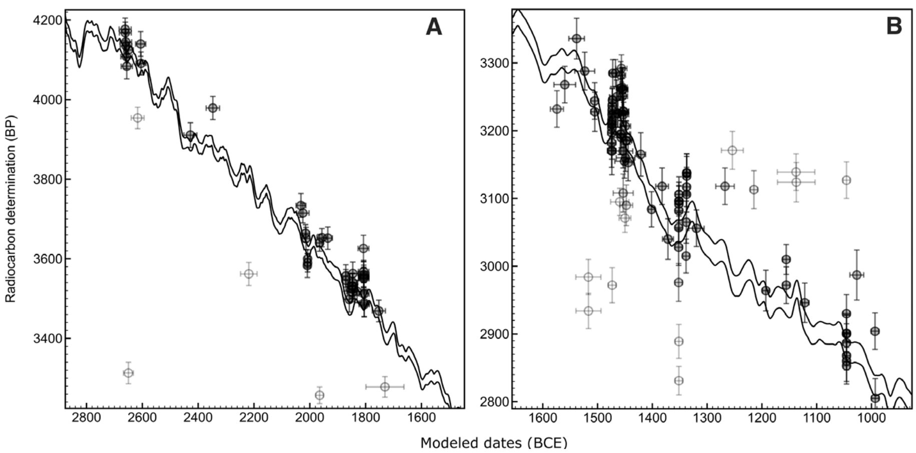

Fig. 2. This figure shows the distribution of uncalibrated radiocarbon dates against the modeled age. For each measurement, we show the mean and ±1σ of the radiocarbon and modeled calendar dates: Points that have a low likelihood of being an outlier are shown with a gray point and black error bars; those that are certain to be outliers are shown with gray error bars and white points (see table S1 for outlier probabilities). The calibration curve is shown as two black lines (±1σ). The dates from the OK [(**A**) up to ~2300 B.C.E.] are concentrated in particular parts of the chronology; most of the information comes from the start of the OK. For the MK [(A) from ~2100 B.C.E.], the pattern of radiocarbon dates clearly reflects the distribution in the calibration curve, picking up distinctive features present 1800 to 1900 B.C.E. and ~2000 B.C.E. (**B**) There are many more dates shown in the NK, most of which are superimposed on each other and overlie the calibration curve, picking up clear distinctive features of the curve, for example, around 1450 B.C.E. There is also a scatter of outliers (shown in gray), but these show no systematic pattern and have no single explanation.

To build a high-precision chronological sequence, we combined our radiocarbon measurements with the historical information relating to reign order and length. To do this, we adopted a Bayesian modeling approach using the program OxCal (*16*, *17*). For each major period (OK, MK, and NK), we constructed a separate multiphase model (*16*) with phase boundaries set at the accession dates for the individual rulers (or, in some cases, series of rulers). The order of the reigns was defined but no prior information was included on the absolute dating of the chronology. The dates for the samples were constrained to lie in particular reigns (or, in some instances, within several adjacent reigns), and their associated calibrated radiocarbon measurements were included as likelihoods in the Bayesian model. The radiocarbon dates thus provide the only linkage in the model to the calendar time scale.

We also included reign lengths as prior information relating to the intervals between the successive accession dates, using the consensus values from Shaw (*18*) as our estimates. Uncertainties in reign lengths are small, especially for the NK where they are typically 1 or 2 years, though larger in a few specific cases such as for Thutmose II and Horemheb. We quantify this uncertainty in our model, but rather than using the distribution $N(0,1^2)$, we use the Student's t distribution ($\nu = 5$), which has longer tails to provide a more robust result. For the MK, we use an uncertainty that is three times that of the NK [i.e., similar to a longer-tailed $N(0,3^2)$]; for the OK, the uncertainty is five times that of the NK. These uncertainties are somewhat subjective, so we tested the models for robustness under different choices of the scaling of these uncertainties (fig. S2).

We also used environmental information from a series of 66 AMS measurements on botanical specimens, with documented dates of collection from Egypt in the period 1700 to 1900 C.E. These show a small but significant depletion in radiocarbon levels relative to the calibration curve (*15*), equivalent to a shift to older radiocarbon dates of 19 ± 5 radiocarbon years (^{14}C yr) (*19*). This offset most likely reflects the unusual growing season in premodern Egypt, which was concentrated during the winter months after the annual inundation. Plants in Egypt sampled the atmosphere at a different time of the year than the trees measured for the calibration curve, and we might expect a slight depletion because of the annual fluctuation in the atmospheric radiocarbon activity. The size of the effect agrees well with the estimated peak-to-peak amplitude of the seasonal fluctuations in radiocarbon activity in the atmosphere of up to 4 per mil (<32 ^{14}C yr) for the pre-industrial era, produced by variations in the rate of transport of ^{14}C from the stratosphere to the troposphere (*20*). We used a single model parameter (ΔR) to model the environmental offset, with a prior of $N(19,5^2)$.

Because a proportion of the samples were expected to be out of context, we used *t*-type outlier-modeling (*17*) with a prior outlier probability of 5%; we also tested the outcomes of the model for robustness with a higher value of this prior probability (see supporting online material).

The modeling of the data provides a chronology that extends from ~2650 to ~1100 B.C.E. (Figs. 1 and 2 and Table 1). The benefits of using the reign order and length information together with the radiocarbon dates are greatest where density of dates is highest. In the NK (128 dates), the average calendrical precision is 24 years [95% highest posterior density (hpd) range] for accession dates (or 11 years for the 68% hpd range). In the MK, where dates are sparser and the uncertainty in the reign lengths is greater, the average calendrical precision is 53 years (95%); in the OK, where the number of dates is even lower, the precision is 76 years (95%) but is still markedly better than that possible with individual measurements. Because reign length has been included in our models, it is important to stress that the outputs of the models cannot be used to provide reign-length information.

The radiocarbon-based chronology for the NK resolves different possible historical chronologies (Fig. 1C). The radiocarbon dates chosen for the NK are on samples from the 17th to the 21st Dynasties, which provide brackets beyond the beginning and end of the NK. However, there are no dates for specific reigns before that of Thutmose III, and so dates earlier than this are based primarily on the reign-length information included in the model. The agreement is closest to the consensus chronology compiled by Shaw (*18*), in which the NK starts in 1550 B.C.E. and from which we take our reign lengths. It rules out some of the other interpretations proposed (*21*–*23*) that are somewhat later, even if different reign lengths and overlaps are considered (fig. S3A). The radiocarbon dates imply that the NK might have begun earlier by about a decade than the consensus date of Shaw, which would imply either shorter overlaps or a slight extension to some reigns in the sequence.

In the MK, the conventional (and earlier) historical chronology (*1*) is largely based on a single observation of the heliacal rising of the star Sothis (Sirius). Different interpretations of this and other astronomical observations are possible, depending on the supposed point of observation, and a chronology that is about 40 years younger has also been put forward, based more on lunar observations (*21*–*23*). The radiocarbon chronology favors the earlier interpretation, but it cannot be used to decide conclusively between these interpretations (Fig. 1B).

The results for the OK, although lower in resolution, also agree with the consensus chronology of Shaw (*18*) but have the resolution to contradict some suggested interpretations of the evidence, such as the astronomical hypothesis of Spence (*24*), which is substantially later, or the reevaluation of this hypothesis (*25*), which leads to a date that is earlier. The absence of astronomical observations in the papyrological record for the OK means that this data set provides one of the few absolute references for the positioning of this important period of Egyptian history (Fig. 1A).

Thus, the radiocarbon measurements provide a coherent chronology for ancient Egypt, which is in good agreement with some earlier attempts to tie down the floating chronology. In contrast, a previous large-scale radiocarbon study gave dates that were substantially earlier than the expected ages for the OK (*26*) and dates that are earlier than expected at Tell el-Dab^{c}a (*27*). These discrepancies probably reflect the choice

Table 1. Modeled accession dates (first regnal year) for selected kings and queens in the Egyptian historical chronology based on the new radiocarbon data (this paper) and reign accession intervals from Shaw (*18*) (see tables S7 and S8 for full lists) compared with other estimates (*18*, *21*). The number of radiocarbon dates for individual reigns included in the models is shown (full details are in table S1). 0, reigns for which we have no dates; ND, not determined.

King/queen	No. ^{14}C dates in models	Accession dates (B.C.E.)					
		Shaw (*18*)	Hornung *et al.* (*21*)	Modeled hpd ranges			
				68%		95%	
				from	to	from	to
			Old Kingdom				
Djoser	7	2667	2592	2676	2643	2691	2625
Sneferu	2	2613	2543	2634	2599	2649	2582
Khufu	0	2589	2509	2613	2577	2629	2558
Djedefra	0	2566	2482	2593	2556	2610	2536
Khafra	0	2558	2472	2586	2548	2604	2528
Menkaura	0	2532	2447	2564	2524	2581	2504
Shepseskaf	0	2503	2441	2538	2498	2556	2476
Userkaf	0	2494	2435	2530	2489	2548	2468
Sahura	0	2487	2428	2524	2482	2542	2460
Djedkara	1	2414	2365	2473	2432	2486	2400
Unas	0	2375	2321	2438	2397	2450	2363
Teti	0	2345	2305	2412	2370	2423	2335
	7	Further dates from the Second to Eighth Dynasties					
			Middle Kingdom				
Mentuhotep II	9	2055	2009	2057	2040	2064	2019
Amenemhat I	4	1985	1939	1991	1973	1998	1952
Senusret I	1	1956	1920	1965	1945	1971	1924
Amenemhat II	0	1911	1878	1922	1901	1928	1878
Senusret II	2	1877	1845	1890	1868	1895	1844
Senusret III	10	1870	1837	1884	1860	1889	1836
Amenemhat III	10	1831	1818	1844	1820	1851	1798
Amenemhat IV	0	1786	1772	1799	1773	1809	1753
Sobekneferu	0	1777	1763	1790	1764	1801	1744
Wegaf	0	1773	1759	1785	1758	1797	1739
	7	Further dates from the 11th to 13th Dynasties					
			New Kingdom				
Ahmose	0	1550	1539	1566	1552	1570	1544
Amenhotep I	0	1525	1514	1541	1527	1545	1519
Thutmose III	24	1479	1479	1494	1483	1498	1474
Hatshepsut	25	1473	1479	1488	1477	1492	1468
Amenhotep II	1	1427	1425	1441	1431	1445	1423
Amenhotep III	2	1390	1390	1404	1393	1408	1386
Amenhotep IV	17	1352	1353	1365	1355	1370	1348
Tutankhamun	7	1336	ND	1349	1338	1353	1331
Horemheb	0	1323	1319	1336	1325	1341	1318
Rameses I	0	1295	1292	1308	1297	1313	1290
Rameses II	2	1279	1279	1292	1281	1297	1273
Sethnakht	0	1186	1190	1198	1187	1204	1179
Rameses III	0	1184	1187	1196	1185	1202	1176
Rameses IX	2	1126	1129	1137	1127	1143	1117
Rameses XI	0	1099	1106	1110	1100	1116	1090
	48	Further dates from the 17th to 21st Dynasties					

Fig. 3. Systematic regional offset in radiocarbon dates from the calibration curve. (**A**) In our model, we have used a prior for the regional offset of 19 ± 5 ^{14}C yr, as shown by the light gray region; the posterior density for the NK (dark gray region) confirms the assumed value for this period. (**B**) If we use a much more neutral prior for this offset of 0 ± 10, the posterior for this parameter is almost unchanged, showing that the ancient data support such an offset independently.

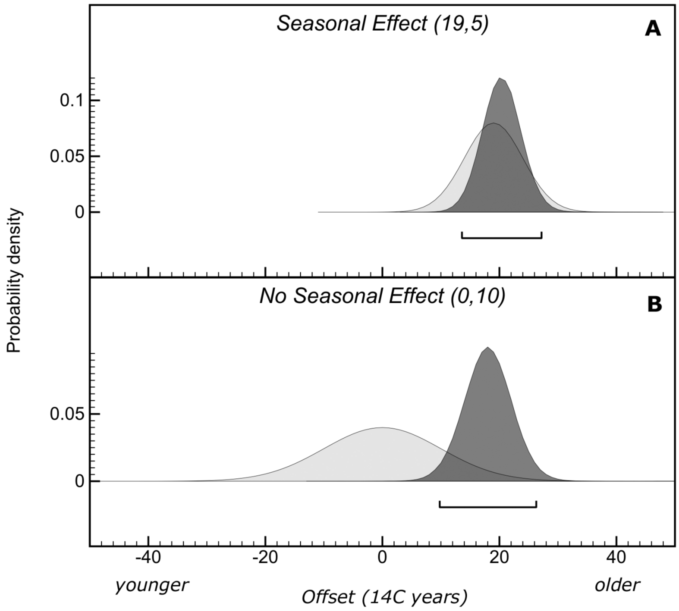

of samples for dating. Many of the sites in ancient Egypt were densely populated over long periods (a notable exception being Amarna). In addition, some resources, such as wood, were in short supply. Reuse of scarce resources can result in the incorporation of older organic material, particularly wood and charcoal, into younger deposits. The long use, revisiting, and robbing of some monuments also provide opportunities for later organic material to be discovered in earlier contexts. We were able to reduce, but not eliminate, such outliers by selecting only short-lived plants from secure contexts. Despite these precautions, we still found a significant number of young outliers among the dates measured, which we accounted for by using Bayesian outlier analysis.

To test the sensitivity of our analysis to the parameters of the model, we looked at the effect of altering the uncertainty in the reign lengths, alternative reign-length estimates (*21*), and the prior outlier probability (figs. S2 to S4). We also evaluated the effect of applying a different prior for ΔR. The main model uses a prior of $N(19,5^2)$, based on the environmental information (*19*). If we use a more neutral prior of $N(0,10^2)$ for the NK where we have most dates, the chronology is virtually unaltered (fig. S5), and the posterior for ΔR is also similar (Fig. 3). This shows that the ancient samples independently confirm a local offset in radiocarbon of 20 ± 5 years, because the pattern of radiocarbon dates found through the NK fits better with the calibration curve when such an offset is applied.

The confirmation of a small regional offset will need to be considered in the calibration of all radiocarbon dates from the Nile region. The small size of this offset implies that previous studies that have seen much larger offsets (*26*, *27*) are probably due to sample selection or context.

This radiocarbon-based chronology for the dynastic period allows direct comparison to the radiocarbon records of predynastic sites in Egypt, and those from the neighboring regions of Libya and Sudan, which is a prerequisite for understanding the speed and mechanisms of Egyptian state formation. This chronology also has implications for the wider Mediterranean and surrounding regions that rely on linkages to Egypt to anchor their own chronologies (*3*–*5*). For the second millennium B.C., for example, it will contribute to our understanding of the differences between the historical Aegean chronology, derived from linkages with Egypt (*27*), and the radiocarbon record for that region, and specifically, for the Minoan eruption of Santorini (*28*, *29*). More widely, Egypt and Mesopotamia are the only parts of the western Old World that have written records spanning the Bronze and Iron ages, and they are linked by trade with regions that stretch from Central Asia to the western Mediterranean and down into Nubia. Chronology is key to understanding the nature of these linkages, and the harmonization of the historical chronologies of Egypt with the calibrated radiocarbon time scale removes a fault line between regions dated scientifically and those tied into historical sequences.

References and Notes

1. W. A. Ward, *Bull. Am. Schools Orient. Res.* **288**, 53 (1992).
2. K. A. Kitchen, *World Archaeol.* **23**, 201 (1991).
3. M. Bietak, Ed., *The Synchronisation of Civilizations in the Eastern Mediterranean in the Second Millennium BC* (Verlag der Österreichischen Akademie der Wissenschaften, Vienna, 2001).
4. M. Bietak, Ed., *The Synchronisation of Civilizations in the Eastern Mediterranean in the Second Millennium BC II* (Verlag der Österreichischen Akademie der Wissenschaften, Vienna, 2003).
5. M. Bietak, E. Czerny, Eds., *The Synchronisation of Civilisations in the Eastern Mediterranean in the Second Millennium BC III* (Verlag der Österreichischen Akademie der Wissenschaften, Vienna, 2007).
6. K. A. Kitchen, in (*5*), pp. 163–171.
7. F. Brock, T. F. G. Higham, P. Ditchfield, C. Bronk Ramsey, *Radiocarbon* **52**, 103 (2010).
8. E. M. Wild *et al.*, *Radiocarbon* **50**, 1 (2008).
9. Q. Hua *et al.*, *Nucl. Instrum. Methods Phys. Res. B* **223–224**, 489 (2004).
10. F. Bruhn, A. Duhr, *Radiocarbon* **43**, 229 (2001).
11. M. Dee, C. Bronk Ramsey, *Nucl. Instr. Methods Phys. Res. B* **172**, 449 (2000).
12. C. Bronk Ramsey, T. Higham, P. Leach, *Radiocarbon* **46**, 17 (2004).
13. E. Cottereau *et al.*, *Radiocarbon* **49**, 291 (2007).
14. P. Steier, F. Dellinger, W. Kutschera, W. Rom, E. M. Wild, *Radiocarbon* **46**, 5 (2004).
15. P. J. Reimer *et al.*, *Radiocarbon* **46**, 1029 (2004).
16. C. Bronk Ramsey, *Radiocarbon* **51**, 337 (2009).
17. C. Bronk Ramsey, *Radiocarbon* **51**, 1023 (2009).
18. I. Shaw, Ed., *The Oxford History of Ancient Egypt* (Oxford Univ. Press, Oxford, 2000).
19. M. W. Dee *et al.*, *J. Archaeol. Sci.* **37**, 687 (2009).
20. B. Kromer *et al.*, *Science* **294**, 2529 (2001).
21. E. Hornung, R. Krauss, D. A. Warburton, Eds., *Ancient Egyptian Chronology* (Brill, Leiden, Netherlands, 2006).
22. D. Franke, *Orientalia* **57**, 113 (1988).
23. R. Krauss, *Sothis- und Monddaten*: *Studien zur astronomischen und technischen Chronologie altägyptens* (Gerstenberg, Hildesheim, Germany, 1985).
24. K. Spence, *Nature* **408**, 320 (2000).
25. D. Rawlins, K. Pickering, *Nature* **412**, 699 (2001).
26. G. Bonani *et al.*, *Radiocarbon* **43**, 1297 (2001).
27. M. Bietak, F. Höflmayer, in *The Synchronisation of Civilisations in the Eastern Mediterranean in the Second Millennium BC III*, M. Bietak, E. Czerny, Eds. (Verlag der Österreichischen Akademie der Wissenschaften, Vienna, 2007), pp. 13–23.
28. S. W. Manning *et al.*, *Science* **312**, 565 (2006).
29. W. L. Friedrich *et al.*, *Science* **312**, 548 (2006).

30. This project was funded by the Leverhulme Trust (grant no. F/08 622/A). The botanical specimens were from the Oxford University Herbaria and the Natural History Museum, London. Archaeological samples were from Ägyptisches Museum und Papyrussammlung, Berlin; Ashmolean Museum, Oxford; Bolton Museum and Art Gallery; British Museum, London; City Museum and Art Gallery, Bristol, UK; Cornell University, New York; Desert Research Institute, Las Vegas, Nevada; Kunsthistorisches Museum, Vienna; The Manchester Museum; Medelhavsmuseet, Stockholm; Metropolitan Museum of Art, New York; Musée du Louvre, Paris; Musées royaux d'art et d'histoire, Brussels; National Museums, Liverpool, UK; The Petrie Museum of Egyptian Archeology, London; The Pitt Rivers Museum, Oxford; Royal Botanic Gardens, Kew, UK; Staatliches Museum Ägyptischer Kunst, Munich; and the Victoria Museum of Egyptian Antiquities, Uppsala University, Sweden. The Oxford laboratory infrastructure was funded by the Natural Environment Research Council and software development by English Heritage. The Illahun, Heqanakht, and Hatshepsut measurements and research were funded by the German-Israeli Foundation for Scientific Research and Development (grant no. I-2069-1230.4/2004); preliminary background research was aided by the SCIEM2000 project. The dating at Saclay was performed at the LMC14 (funded by CNRS, CEA, Institut de Radioprotection et de Sûreté Nucléaire, Institut de Recherche pour le Développement, and Ministère de La Culture).

Supporting Online Material

www.sciencemag.org/cgi/content/full/328/5985/1554/DC1
Materials and Methods
SOM Text
Figs. S1 to S5
Tables S1 to S7
References

10 March 2010; accepted 3 May 2010
10.1126/science.1189395

Evolutionary Novelty Is Concentrated at the Edge of Coral Species Distributions

Ann F. Budd[1]* and John M. Pandolfi[2]

Conservation priorities are calculated on the basis of species richness, endemism, and threats. However, areas ranked highly for these factors may not represent regions of maximal evolutionary potential. The relationship between geography and evolutionary innovation was analyzed in a dominant complex of Caribbean reef corals, in which morphological and genetic data concur on species differences. Based on geometric morphometrics of Pleistocene corals and genetically characterized modern colonies, we found that morphological disparity varies from the center to the edge of the Caribbean, and we show that lineages are static at well-connected central locations but split or fuse in edge zones where gene flow is limited. Thus, conservation efforts in corals should focus not only on the centers of diversity but also on peripheral areas of species ranges and population connectivity.

Coral reefs are the most diverse of all marine ecosystems and are increasingly threatened by climate change (*1*, *2*), ocean acidification (*3*), and local anthropogenetic disturbance (*4*). Their structural framework is formed by scleractinian corals, 32.8% of which have been recently categorized as having an elevated risk of extinction (*5*). Current conservation priorities have been established using various approaches, such as biodiversity hotspots, ecoregions, wilderness areas, and megadiversity countries, that focus on areas that are high in biodiversity or endemism or are severely threatened (*6*–*8*). These priority-setting approaches assume that areas of high biodiversity have high levels of endemism, and they target areas that are under the most threat. However, managing reefs on the basis of these approaches alone has been questioned, in part because centers of species richness and endemicity do not coincide in reef corals (*9*, *10*). Moreover, these approaches do not incorporate evolutionary processes. Taxon richness and measures of phylogenetic diversity have been found to be decoupled in terrestrial floras, pointing in general toward the need for a more evolutionary process–based approach to conservation (*7*). Because the geography of evolutionary innovation in reef corals is unknown, we used data from fossil and extant reef corals to examine the distribution of evolutionary innovation across the biodiversity hotspot in the west-central Caribbean (*6*) relative to the edge of species distributions in the eastern Caribbean.

One evolutionary response that has been observed at the geographic margins of many different plant and animal species is introgressive hybridization, an increasingly recognized source of evolutionary innovation and adaptive radiation (*11*, *12*). In reef corals, hybridization has been found at the periphery of species ranges in both the Caribbean and Indo-Pacific regions (*13*–*15*). Although rare on ecological time scales, hybridization has thus been hypothesized to play an important role in reef corals in range expansion and adaptation to changing environments on geological time scales (*15*). Much of the evidence for this hypothesis is from genetic and reproductive data on living corals, which are limited to ecological time scales. Our investigation expands this research to geological time scales.

Under the assumption that genetic and morphological data are correlated, morphological data have been used successfully to distinguish genetically distinct morphospecies and trace patterns in lineages through geological time in marine invertebrates (*16*). We studied the *Montastraea annularis* coral species complex, because the correlation between genetic and morphological data is strongly supported (fig. S1), and hybridization has been recognized in the geological past by studying morphological intermediates between species (*17*). The *M. annularis* complex has been ecologically dominant on Caribbean reefs for >2 million years (*18*, *19*) and has a fossil record extending back >6 million years (*18*). Its geographic distribution is currently restricted to the Caribbean, Gulf of Mexico, and western Atlantic (Florida, the Bahamas, and Bermuda) (*20*) and, unlike that of many terrestrial organisms (*21*), has not changed throughout its history. Today the complex consists of three species: *M. annularis* s.s., *M. faveolata*,

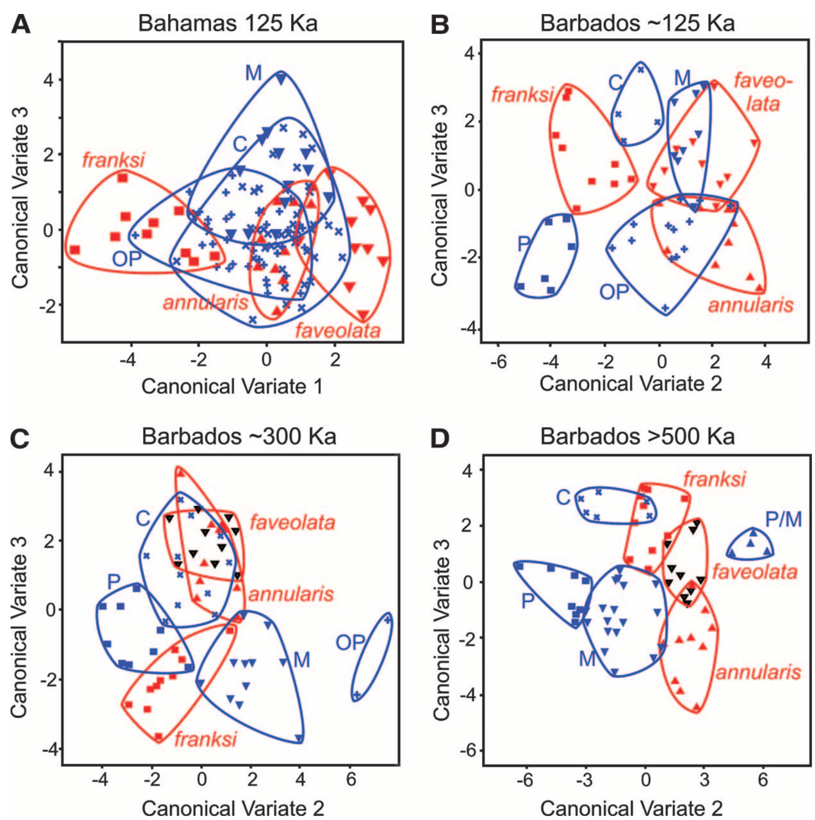

Fig. 1. Plots of scores on canonical variates comparing the three Recent species (red) with the fossil morphospecies (blue) aged (**A**) ~125 ka in the Bahamas, (**B**) ~125 ka in Barbados, (**C**) ~300 ka in Barbados, and (**D**) >500 ka in Barbados. The canonical variates show the maximum Mahalanobis distances among Recent Panama species along the *x* axis and fossil colony forms along the *y* axis (table S3). Each point represents one colony; polygons enclose the maximum variation within species or morphospecies. Correlations of canonical variates with original variables and other statistics are given in table S3. P, plate; M, massive; C, column; OP, organ-pipe; P/M, an additional massive species found only in the >500-ka Barbados assemblages.

[1]Department of Geoscience, University of Iowa, Iowa City, IA 52242, USA. [2]Centre for Marine Studies, School of Biological Sciences, and Australian Research Council Centre of Excellence for Coral Reef Studies, University of Queensland, Brisbane, Queensland 4072, Australia.

*To whom correspondence should be addressed. E-mail: ann-budd@uiowa.edu

and *M. franksi*, which are morphologically and genetically distinct in Panama and Belize but not in the Bahamas (fig. S1). Morphological features that distinguish the three species include both colony growth form and various measures of corallite architecture (*18*, *22*). Genetic and reproductive variability have been identified at three amplified fragment length polymorphism (AFLP) loci, the noncoding region of the mitochondrial genome, and internal transcribed spacer sequences, along with differences in spawning time and gamete compatibility (*23*, *24*). *M. faveolata* and *M. franksi* have a fossil record extending back >2.5 million years and belong to different subclades (monophyletic units) within the complex, whereas *M. annularis* s.s. extends back only ~0.5 million years and is more closely related to *M. franksi* (*18*, *23*, *25*).

Our fossil samples consist of a total of 432 colonies that were collected from three groups of Pleistocene terraces on the island of Barbados [dated at ~640 to 860 thousand years ago (ka) (referred to here as >500 ka); at ~250 to 500 ka (~300 Ka); and at ~80 to 250 Ka (~125 ka)] and from late Pleistocene coastal terraces (~125 ka) at four other Caribbean locations (Table 1). Morphospecies were recognized within each of these seven fossil units by comparing colony growth forms (plate, massive, column, and organ-pipe) using geometric morphometric techniques (*17*) and multivariate statistical analyses (canonical variates analysis) of the coordinates of 19 landmarks digitized in transverse thin section. Samples within each fossil unit were first analyzed separately to distinguish morphospecies. Thirty-two modern genetically characterized colonies from the San Blas Islands of Panama (*23*) were included in each analysis to provide a baseline for morphospecies recognition. *F* values corresponding with Mahalanobis distances were used to determine whether any of the fossil morphospecies were the same as the three modern species. In the three Barbados fossil units, morphospecies were also analyzed with a combined canonical variates analysis, and the resulting Mahalanobis distances were used to trace lineages through geological time. Finally, the Mahalanobis distances between all pairwise combinations of morphospecies within each fossil unit were standardized and compared among units to test for differences in morphological disparity. These distances were used to create an index of evolutionary novelty, which is calculated for each locality using the product of its species richness times the deviation of its mean distance from the global mean distance (*26*). Evolutionary novelty indices increase as morphological diversity increases.

Speciation and extinction rates were consistently higher in Barbados than in the other four Caribbean locations (see numbers of first and last occurrences in Table 1). Three or four morphospecies were found within each of the seven fossil units, indicating that diversity remained the same in the complex both spatially and temporally during the frequent climatic oscillations of the late Pleistocene (Fig. 1; Table 1). In each of the seven fossil units, one morphospecies was the same as *M. faveolata*; in all of the fossil units except Barbados, another morphospecies was the same as *M. annularis* s.s. *M. franksi* was found only in the Dominican Republic. An extinct organ-pipe form (*M. nancyi*) first appears at ~125 ka and was found at all five ~125-ka sites (*27*). An additional morphospecies (an extinct platy form, P) could also be traced through the three time units in Barbados. The remaining morphospecies in Barbados, which consist of massive (P/M), columnar (C1, C2, and C3) and organ-pipe (OP) forms, do not match the three modern species or morphospecies in the other fossil units and appear to be unique. In contrast, the species composition at the other four Caribbean locations was exactly the same at ~125 ka and in Recent times. The wider geographic distribution found in *M. faveolata* than in *M. annularis* s.s. during the Pleistocene conforms with population genetic divergence estimates made using 10 nuclear DNA loci (7 microsatellite and 3 single-copy restriction fragment length polymorphism), which show higher gene flow and greater population connectivity in *M. faveolata* (*28*).

Mahalanobis distances between all pairwise combinations of morphospecies within each fossil unit were significantly lower in the ~125-ka terrace in the Bahamas and significantly higher in the three Barbados fossil units (Fig. 2A), as compared with the other Caribbean locations. Moreover, these two peripheral locations (Barbados and the Bahamas) had higher indices of evolutionary novelty than all other locations (Fig. 2B). In the Caymans, Dominican Republic, and Florida, Mahalanobis distances between fossil morphospecies were low and evolutionary novelty indices were intermediate, in comparison with those observed in modern species from Belize and Panama. The extremely low disparity (high species overlap) and high evolutionary novelty index observed in the Bahamas were interpreted as lineage fusion that resulted from introgressive hybridization within the species complex since 125 ka (*17*), an interpretation that agrees with genetic data (fig. S1). In the genetic analyses, hybridization was found in only one AFLP locus in one species (*M. annularis* s.s.) and in only 15% of the

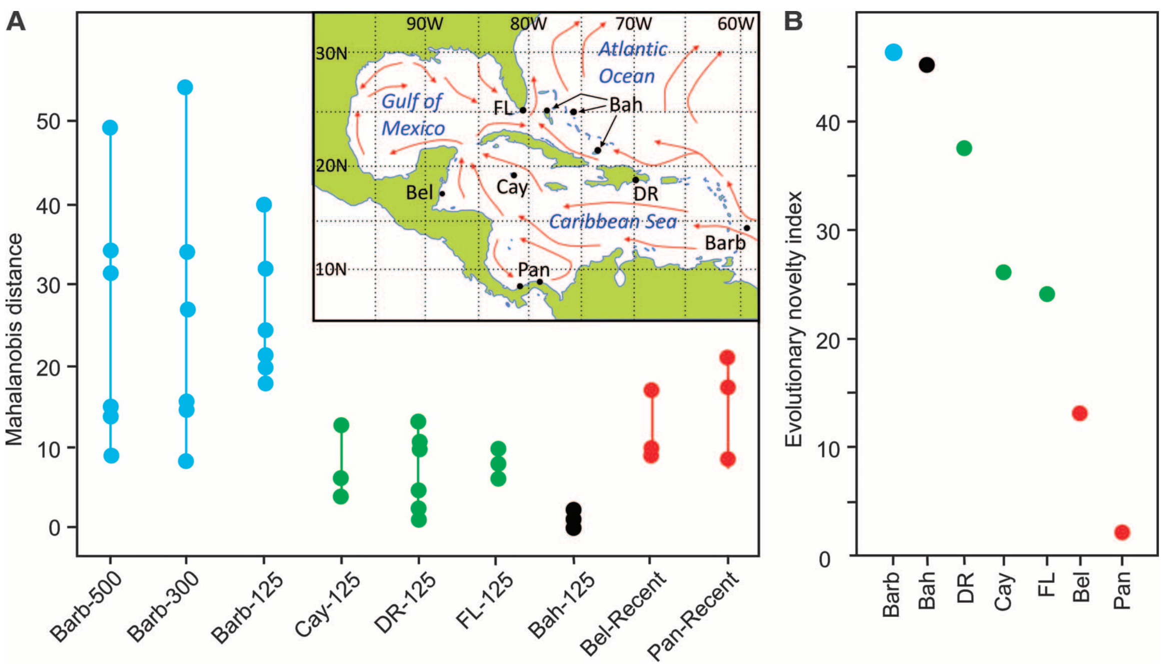

Fig. 2. Scatterplots showing (**A**) Mahalanobis distances between species at each locality (table S5) and (**B**) an index of evolutionary novelty defined as the product of species diversity and the absolute value of the deviation of the locality mean Mahalanobis distance from the global mean Mahalanobis distance. Mahalanobis distance values are high in the Pleistocene of Barbados (median = 23, blue), intermediate to high in the Recent of Belize and Panama (median = 13, red), intermediate in the Pleistocene of the central Caribbean (median = 8, green), and low in the Pleistocene of the Bahamas (median = 1, black). Mann-Whitney U tests performed on these distances show that the four groups are significantly different ($P \leq 0.05$).

Table 1. Summary of sampled morphospecies recognized within different fossil units. P, P/M, C1, C2, C3, and OP correspond with morphospecies shown in Figs. 1 and 2. The specimens that were analyzed are listed in appendix S1. na, not applicable.

Fossil unit	Total number of colonies sampled	Total number of morpho-species	Morpho-species with first occurrences	Morpho-species with last occurrences	Morpho-species corresponding with modern species	Extinct morpho-species that carry over to the next younger unit
Barbados >500 ka	36	4	P, P/M, C1	P/M, C1	*faveolata*	P
Barbados ~300 ka	33	4	C2, OP	C2, OP	*faveolata*	P
Barbados ~125 ka	32	4	C3, *nancyi*	P, C3, *nancyi*	*faveolata*	na
Cayman Islands ~125 ka	77	3	*nancyi*	*nancyi*	*faveolata, annularis* s.s.	na
Dominican Republic ~125 ka (*17*)	114	4	*nancyi*	*nancyi*	*faveolata, annularis* s.s., *franksi*	na
Florida ~125 ka	34	3	*nancyi*	*nancyi*	*faveolata, annularis* s.s.	na
Bahamas ~125 ka (*17*)	106	3	*nancyi*	*nancyi*	*faveolata, annularis* s.s.	na

colonies sampled, suggesting that this genetic signal may reflect an ancestral polymorphism rather than recent events (*23*, *24*). The significantly higher disparity observed in Barbados, where we do not have genetic data, may be interpreted as an evolutionary innovation (lineage splitting), which could have been caused by evolutionary mechanisms ranging from hybridization (resulting from increased gene flow between species) followed by ecological diversification, to parapatric or peripatric speciation (resulting from restricted or no gene flow between diverging peripheral populations). Studies of hybrids in land snails (*12*) have shown that novel morphologies may be caused by novel alleles or by the inheritance of a mosaic of morphological characters related to the geometry of shell coiling, which during growth can lead to novel adult morphologies. Hybridization could similarly lead to evolutionary novelty and adaptation in the *M. annularis* complex. Alternatively, evolutionary novelty could be caused by reproductive isolation associated with parapatric or peripatric speciation.

In addition to Caribbean members of the *M. annularis* complex, hybridization has been observed in modern Caribbean *Acropora*, but the hybrid *Acropora* morphotypes (*A. prolifera*) are not hybridizing species and have little evolutionary potential (*29*). In contrast, all three of the *M. annularis* species are vital and can be crossed under lab-controlled conditions, suggesting that they have the potential to hybridize. However, other pre- and post-mating isolation mechanisms must operate to maintain them as distinct species (*23*, *24*). Therefore, the outcome of hybridization is different between *Acropora* and *Montastraea* in the Caribbean.

Caribbean reef corals of the *M. annularis* species complex exhibited significant geographic differences in evolutionary response to Pleistocene climatic oscillations, despite the absence of the range shifts observed in many terrestrial organisms (*21*). Lineage splitting (Barbados) and fusion (the Bahamas) were concentrated at edge zones, which we hypothesize were characterized by limited larval supply and population connectivity, in contrast with well-connected interior locations near the Caribbean biodiversity center (the Dominican Republic, Cayman Islands, and Florida), which exhibited lineage stasis and had species whose morphologies are the same as those of modern species in Panama and Belize (Fig. 2A). Barbados apparently represents a source population from which larvae disperse, which lies along an edge of the geographic distribution of the complex, where currents first begin to move through the Caribbean and there are no extant external sources of larvae. The Bahamas were similarly isolated during the Pleistocene but represent a sink population into which larvae immigrate. During low Pleistocene sea level stands, larval flow through the Caribbean may have been diminished by restricted oceanic currents, and flow between the Bahamas platform and the rest of the Caribbean would have been limited. In addition, water movement across the Bahamas platform itself would have been reduced (*30*, *31*). The observed differences in evolutionary response between locations correspond with the genetic discontinuity in the Mona Passage between Puerto Rico and the Dominican Republic, which separates eastern from western Caribbean populations of reef fish and acroporid corals today (*32*, *33*). Moreover, empirical data for living *Acropora* also indicate that the Bahamas are isolated from the rest of the Caribbean (*33*).

Lower gene flow to edge locations would have altered population dynamics, thereby enhancing evolutionary innovation. In the Bahamas (the sink population), fewer immigrants would have led to hybridization during population decline, which resulted in genetic assimilation, reduced genetic variance, and overlapping morphology. In Barbados (the source population), geographic isolation would have led to genetic differentiation, causing evolutionary diversification and the creation of novel morphologies. One example of a speciation and range extension was *M. nancyi*, which may have arisen in Barbados as much as 250 ka and spread across the Caribbean before it ultimately became extinct between 82 and 3 ka (*25*, *27*).

Our work emphasizes the need to consider the fossil record in addition to genetic and physical data in order to obtain a more complete picture of factors influencing reef connectivity and evolutionary responses to environmental change. Our data suggest that species edge zones play an important role in evolutionary innovation, which may be caused by factors ranging from hybridization to parapatric or peripatric speciation, depending on population dynamics. These interpretations agree with recent results for reef fish (*34*) and hermit crabs (*35*). Edge zones are not only potential evolutionary cradles but are likely to be important sources of evolutionary innovation, especially as they migrate in the face of projected climate change. As such, we believe that species edge zones and peripheral areas, such as the eastern Caribbean, together with population connectivity, should play a prominent role in the future design (number, placement, and size) of marine reserves.

References and Notes

1. T. P. Hughes *et al.*, *Science* **301**, 929 (2003).
2. J. M. Lough, *Geophys. Res. Lett.* **35**, L14708 (2008).
3. O. Hoegh-Guldberg *et al.*, *Science* **318**, 1737 (2007).
4. J. M. Pandolfi *et al.*, *Science* **301**, 955 (2003).
5. K. E. Carpenter *et al.*, *Science* **321**, 560 (2008).
6. C. M. Roberts *et al.*, *Science* **295**, 1280 (2002).
7. F. Forest *et al.*, *Nature* **445**, 757 (2007).
8. T. M. Brooks *et al.*, *Science* **313**, 58 (2006).
9. S. R. Palumbi, *Coral Reefs* **16**, S47 (1997).
10. T. P. Hughes, D. R. Bellwood, S. R. Connolly, *Ecol. Lett.* **5**, 775 (2002).
11. M. L. Arnold, *Natural Hybridization and Evolution* (Oxford Univ. Press, New York, 1997).
12. S. Chiba, *Evolution* **59**, 1712 (2005).
13. M. Hatta *et al.*, *Mol. Biol. Evol.* **16**, 1607 (1999).
14. K. J. Miller, D. J. Ayre, *Heredity* **92**, 557 (2004).
15. B. L. Willis, M. J. H. van Oppen, D. J. Miller, S. V. Vollmer, D. J. Ayre, *Annu. Rev. Ecol. Evol. Syst.* **37**, 489 (2006).
16. J. B. C. Jackson, A. H. Cheetham, *Trends Ecol. Evol.* **14**, 72 (1999).
17. A. F. Budd, J. M. Pandolfi, *Paleobiology* **30**, 396 (2004).
18. A. F. Budd, J. S. Klaus, *J. Paleontol.* **75**, 527 (2001).
19. J. M. Pandolfi, A. F. Budd, *Mar. Ecol. Prog. Ser.* **369**, 89 (2008).
20. J. E. N. Veron, *Corals of the World* (Australian Institute of Marine Science, Townsville, Queensland, Australia, 2000).
21. G. M. Hewitt, *Philos. Trans. R. Soc. London Ser. B* **359**, 183, discussion 195 (2004).
22. N. Knowlton, E. Weil, L. A. Weigt, H. M. Guzmán, *Science* **255**, 330 (1992).

23. H. A. Fukami *et al.*, *Evolution* **58**, 324 (2004).
24. D. R. Levitan *et al.*, *Evolution* **58**, 308 (2004).
25. J. M. Pandolfi, C. E. Lovelock, A. F. Budd, *Evolution* **56**, 479 (2002).
26. Methodological details are provided in supporting information on *Science* Online.
27. J. M. Pandolfi, *J. Paleontol.* **81**, 472 (2007).
28. S. G. Severance, S. A. Karl, *Mar. Biol.* **150**, 57 (2006).
29. S. V. Vollmer, S. R. Palumbi, *Science* **296**, 2023 (2002).
30. P. Mann, in *Caribbean Basins, 4: Sedimentary Basins of the World*, P. Mann, Ed. (Elsevier, Amsterdam, 1999), pp. 3–31.
31. G. Draper, P. Mann, J. F. Lewis, in *Caribbean Geology: An Introduction*, S. K. Donovan, T. A. Jackson, Eds. (University of the West Indies Publishers' Association, Kingston, Jamaica, 1994), pp. 129–150.
32. I. B. Baums, M. W. Miller, M. E. Hellberg, *Mol. Ecol.* **14**, 1377 (2005).
33. H. M. Galindo, D. B. Olson, S. R. Palumbi, *Curr. Biol.* **16**, 1622 (2006).
34. L. A. Rocha, B. W. Bowen, *J. Fish Biol.* **72**, 1101 (2008).
35. M. C. Malay, G. Paulay, *Evolution* **64**, 634 (2010).
36. We thank T. Fadiga for assistance with measurements; N. Knowlton and H. Fukami for genetic analyses; and D. Carlon, N. Knowlton, and R. Steneck for comments. The specimens that were analyzed are listed in appendix S1. This research was supported by NSF grants EAR97-25273 and DEB-0343208 to A.F.B. and by Smithsonian Institution Marine Science Network and Biodiversity grants, a Smithsonian Tropical Research Institute Tupper Fellowship, and an Australian Research Council Centre of Excellence grant to J.M.P.

Supporting Online Material
www.sciencemag.org/cgi/content/full/328/5985/1558/DC1
Materials and Methods
Figs. S1 and S2
Tables S1 to S5
References
Appendix S1

1 March 2010; accepted 29 April 2010
10.1126/science.1188947

Identification of Germline Stem Cells in the Ovary of the Teleost Medaka

Shuhei Nakamura,[1] Kayo Kobayashi,[1] Toshiya Nishimura,[1,2] Shin-ichi Higashijima,[3,4] Minoru Tanaka[1,2]*

Germline stem cells continually produce sperm in vertebrate testes, whereas there is no direct evidence showing that germline stem cells are present in adult vertebrate ovaries. By using transgenic methods and clonal analysis, we identified germline stem cells that supported oogenesis and the production of offspring in the ovaries of adult medaka fish. Early-stage germ cells were localized in clusters along interwoven threadlike cords of *sox9b*-expressing somatic cells (termed germinal cradles) where the germ cells developed. Germline stem cells gave rise to germ cells that divided to produce cysts, which then underwent cell death or separated to form follicles. Our results provide insight into the germline stem cell biology of medaka and provide a model system for studying vertebrate stem cell niches.

Many organisms continually produce gametes from germline stem cells in specific niches within the testis (*1*). In contrast to the testes, the ovaries of most adult mammals contain only postmitotic germ cells and a finite number of mature eggs. Only a few examples of mammals are suggested to have stem-like germ cells and mitotic oogonia in adult ovary, which, however, remain controversial (*2*–*6*). Nevertheless, some species—including lower vertebrates that show high fecundity—may produce oocytes either cyclically or continually from mitotic oogonia (*7*–*9*). A stem cell–based mechanism and histological evidence to support this mechanism, however, have not been shown in adult ovaries.

Many studies have identified genes involved in gonadal sex differentiation. *Sox9*, for example, is essential for mammalian testicular development (*10*, *11*). In medaka (*Oryzias latipes*), a teleost fish, *sox9b* is expressed in the developing gonads, where it is thought to be the functional ortholog of mammalian *Sox9* (*12*).

We used EGFP (enhanced green fluorescent protein) fluorescence to visualize endogenous *sox9b*-expressing cells in the ovaries of transgenic adult medaka (*sox9b*-EGFP medaka) (*13*); the *sox9b*-expressing cells formed interwoven threadlike cords (Fig. 1, A and B, and fig. S2, A to D). Early germ cells were detected by using germ line–specific markers, OLVAS [medaka (*Olyzias latipes*) vasa] and tdrd1 (tudor domain containing 1) (*14*–*16*), components of a germ line–specific intracellular structure called nuage. These cells were nested in the cords of *sox9b*-expressing cells (Fig. 1B) and were connected by thin processes originating from the *sox9b*-expressing cells. Expression of *sox9b* by cells surrounding the germ cells in the ovary was confirmed by using in situ hybridization (fig. S2E). Hereafter, we refer to the nest of germ cells in the cord as the germinal cradle in the ovarian cord. Laminin staining (Fig. 1, C and D), three-dimensional tissue imaging (fig. S2F and movie S1), periodic acid–Schiff (PAS) staining (fig. S2, G and H), and electron micrographs (fig. S2, I and J) showed that the ovarian cords and germinal cradles were buried in the germinal epithelium, a thin multilayered tissue that covers the dorsal side of the stromal compartment (fig. S1, A and B). The germinal cradles lay between epithelial cells of the germinal epithelium and the basement membrane bordering the stromal compartment. Germinal epithelia from 3-month-old adult medaka contained 629 ± 22 germinal cradles (mean ± SEM; $n = 4$).

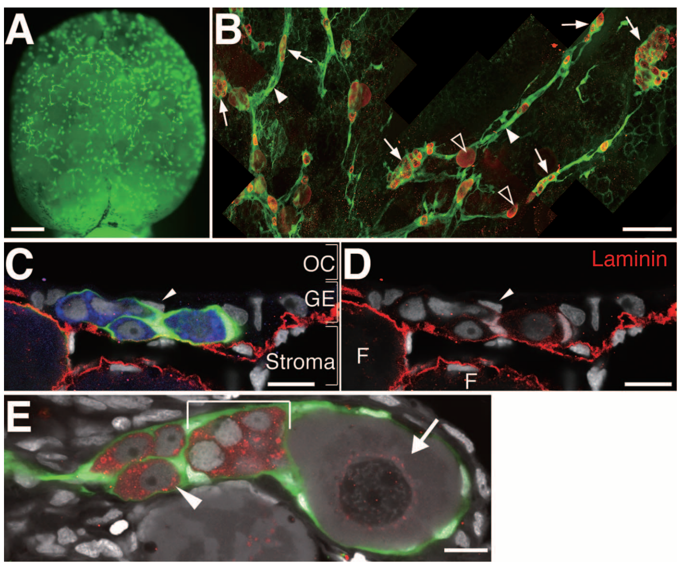

Fig. 1. Ovarian cords in adult medaka are composed of early-stage germ cells and *sox9b*-expressing cells. Scale bars indicate 1 mm (A), 100 μm (B), or 10 μm [(C) to (E)]. (**A**) A dorsal fluorescent image of an ovary from a *sox9b*-EGFP–expressing adult medaka. (**B**) An enlarged image of an immunostained ovary. Germ cells detected on the basis of OLVAS expression (red) are nested in germinal cradles (arrows) connected by cellular processes (arrowheads) that originate from *sox9b*-EGFP–expressing cells (green). Open arrowheads, isolated diplotene oocytes. (**C** and **D**) A cross section of the germinal epithelium. A germinal cradle composed of *sox9b*-expressing cells (green) and early-stage germ cells (blue, OLVAS) lies between dorsal epithelial cells (arrowheads) and basement membrane (red, laminin). OC, ovarian cavity; GE, germinal epithelium; Stroma, stromal compartment; F, follicle. Gray, 4´,6´-diamidino-2-phenylindole (DAPI). (**E**) A representative germinal cradle. Arrowhead, isolated Gs cells; bracket, Gcys cells; arrow, early-stage Gdip oocytes. Germ cells expressing tdrd1, red; *sox9b*-expressing cells, green; DAPI, gray.

[1]Laboratory of Molecular Genetics for Reproduction, National Institute for Basic Biology, Okazaki 444-8787, Japan. [2]Department of Basic Biology, the Graduate University for Advanced Studies (SOKENDAI), Okazaki, Aichi 444-8585, Japan. [3]National Institutes of Natural Sciences, Okazaki Institute for Integrative Bioscience, National Institute for Physiological Sciences, Okazaki, Aichi 444-8787, Japan. [4]Department of Physiological Sciences, the Graduate University for Advanced Studies (SOKENDAI), Okazaki, Aichi 444-8585, Japan.

*To whom correspondence should be addressed. E-mail: mtanaka@nibb.ac.jp

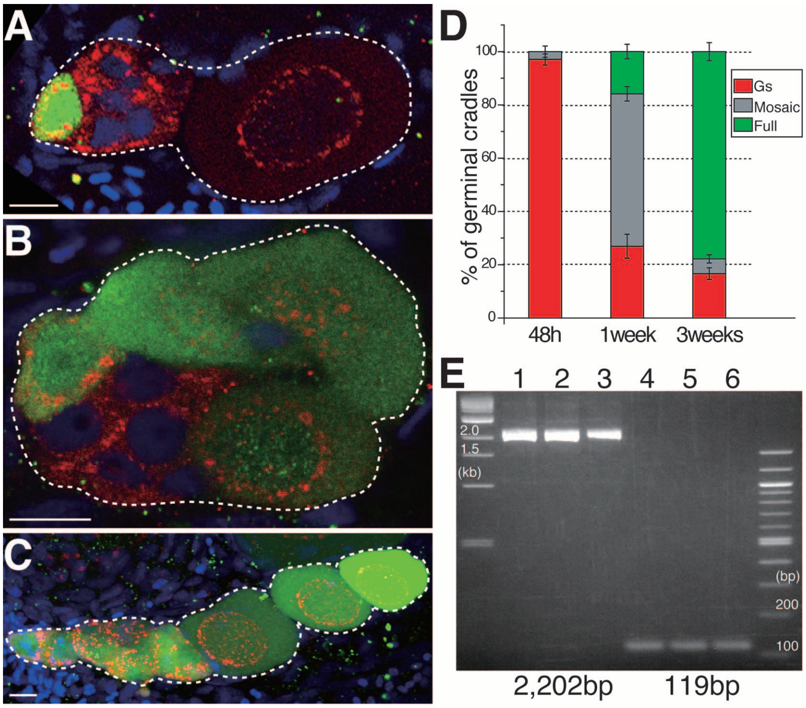

Fig. 2. *Nos2*-expressing Gs cells include ovarian germline stem cells. (**A** to **C**) A representative Gs clone (A), mosaic clone (B), and full clone (C). All germ cells were detected on the basis of tdrd1 expression (red). Germinal cradles are outlined by dotted lines. Green, anti-EGFP; blue, DAPI. Scale bars, 10 μm. (**D**) The percentages (mean ± SEM) of the various clone types at 48 hours (n = 7), 1 week (n = 6), and 3 weeks (n = 8) after heat treatment. (**E**) Genotyping of F1 offspring from heat-treated transgenic medaka. Some offspring showed *loxP*-mediated excision of the genomic region (lanes 4 and 5, 119–base pair (bp) bands].

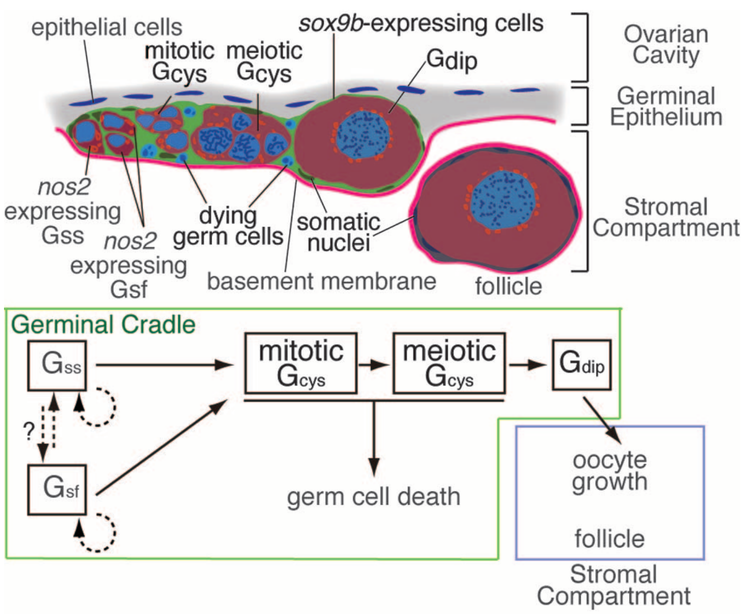

Fig. 3. A schematic representation of germ cell development in the germinal cradle. Germ cells are nested within germinal cradles in an interwoven threadlike ovarian cord of *sox9b*-expressing cells (green) in the germinal epithelium. Isolated *nos2*-expressing Gs cells (either Gss or Gsf cells), Gcys cells, and Gdip oocytes are present in the germinal cradle. After several synchronous mitotic divisions (mitotic Gcys), the Gcys cells enter meiosis (meiotic Gcys). Whereas some cyst-forming cells die and are eliminated, others develop into Gdip oocytes and exit the germinal cradles as follicles for further oocyte development. A population of Gs cells maintains the Gcys and Gdip oocyte populations, enabling the production of a large number of fertile eggs.

The germinal cradles contained three histologically distinct germ cell types (Fig. 1E): single isolated germ cells surrounded by *sox9b*-expressing somatic cells (referred to as Gs cells), connected clusters of germ cells that formed cysts (Gcys cells), and early-stage oocytes (Gdip oocytes) that were at the diplotene stage on the basis of the perinuclear localization of nuage (*16*), meiotic markers, and diffuse chromatin structures (fig. S4, E, F, I, and L). The germinal cradles contained four different combinations of these three germ cell types (Fig. 1E and fig. S3, A to C). No germinal cradles lacked Gs cells. In addition to the combinations of germ cells, relatively large, isolated Gdip oocytes were frequently observed in the ovarian cord (Fig. 1B).

To further characterize the different germ cell types, we used a medaka line (*nos2p*-EGFP) in which *nanos2* (*nos2*)-driven EGFP expression is observed in both oogonial and spermatogonial cells (*17*). By using the transgenic medaka, we detected *nos2* expression in Gs cells but not Gcys cells or Gdip oocytes (fig. S3, D to G). One to five Gs cells were detected in the germinal cradles of *nos2p*-EGFP transgenic medaka (n = 118 germinal cradles from three medaka; fig. S3H).

Incorporation of 5-bromo-2′-deoxyuridine (BrdU) and phosphorylated histone H3 (PH3) labeling, which marks mitotically dividing cells, suggested that Gcys cells undergo synchronous mitosis (fig. S4, A and B). Time-lapse analysis of cultured germinal epithelia identified a collection of germ cells that divided synchronously, consistent with the observations in the cysts (fig. S5, A to C, and movie S2). Additionally, some cysts contained SYCP1 and SYCP3, two components of the synaptonemal complex (*18*) (fig. S4, C and F). This indicated that the Gcys cell population could be further split into mitotic and meiotic cells. SYCP3 was detected in cysts composed of more than six germ cells, suggesting that Gcys cells enter meiosis after three to five rounds of synchronous mitotic division (table S1). A small number of adherent cells ruptured and were eliminated from the germinal cradle (figs. S4D and S5, D to F, and movie S3), which may explain why the number of germ cells within the cysts deviated from 2^n.

Gdip oocytes in the germinal cradles were surrounded by *sox9b*-expressing cells (Fig. 1E), suggesting that the clusters of meiotic Gcys cells become individual cells as meiosis in the cyst progresses to the diplotene stage (fig. S4, G to L). The Gdip oocytes were larger than Gs cells (Fig. 1E and figs. S2I and S3B). All germ cells were motile and changed their relative positions. Large germ cells, in particular, shuttled between the germinal cradles, and isolated Gdip oocytes in the ovarian cord may be cells in transit to another germinal cradle (fig. S5, G to I, and movie S2). Given these observations, we hypothesized that some or all of the *nos2*-expressing Gs cells in the germinal cradles function as ovarian stem cell–like germ cells, which can produce a population of Gcys cells and Gdip oocytes.

In some vertebrate tissues and plant meristems, stem cells cycle slowly or are quiescent (*19*–*21*).

To analyze the cell cycles of germ cells in the germinal cradles, we assessed the S-phase index, a measure of the percentage of nuclei in the S phase. Adult female medaka were exposed to BrdU for various periods of time (fig. S6A). After 24 hours, nearly 60% of the Gs cells were BrdU positive, and the rate of newly stained cells slowed over the following week such that about 75% of the Gs cells were BrdU positive. Thus, Gs cells appear to be heterogeneous. Piecewise linear regression analysis revealed two distinct populations: fast-dividing (Gsf) and slow-dividing (Gss) germ cells. BrdU pulse-chase experiments also identified label-retaining germ cells among the Gs cells (fig. S6, B to D). These experiments suggest that at least 60% of Gs cells are Gsf cells. In contrast, the percentage of BrdU-positive Gcys nuclei increased from about 35% after 1 hour of BrdU labeling to nearly 100% after 24 hours. Thus, no quiescent Gcys cells were present in the germinal cradles.

We next addressed the potential functions of the Gs cells. We conducted experiments to determine whether Gs cells facilitate the recovery of Gcys cells after busulfan treatment. Three- to 4-month-old female medaka were treated with 10 ng/ml busulfan for 1 week to eliminate mitotically active Gcys cells. The number of germinal cradles with Gcys cells was markedly reduced 1 month after treatment, before recovering to the numbers observed in untreated control samples 3 months after the treatment (fig. S7). These results suggest that the Gs cells present 1 month after oogenesis was disrupted are capable of regenerating Gcys cells in the germinal cradles.

To confirm that Gs cells in the ovary were stem cell–like germ cells, we conducted clonal analysis by using transgenic medaka harboring two distinct fluorescent constructs {*hsp*-cre:mCherry/*nos2p*-loxP[DsRed]-EGFP-*olvas*3′ untranslated region (UTR)} (fig. S8). In these medaka, heat treatment transiently induces EGFP expression only in *nos2*-expressing Gs cells, and EGFP transcripts are stabilized in all germ cells through the action of the 3′ UTR of *olvas* (*14*, *15*).

Adult transgenic fish ($n = 21$) were heated to 39°C for 2 hours, and immunohistochemistry was performed by using antibodies specific for GFP and the pan–germ cell marker tdrd1 (*16*). Several different combinations of EGFP fluorescent cells were found in the germinal cradles, including cradles in which the only EGFP-labeled germ cells were Gs cells (Gs clone type) (Fig. 2A and fig. S9, E and F), cradles containing fluorescent Gs cells as well as Gcys cells and/or Gdip oocytes (mosaic clone type) (Fig. 2B and fig. S9, G and H), and cradles entirely occupied by fluorescent germ cells (full clone type) (Fig. 2C and fig. S9, I and J). Forty-eight hours after heat treatment, most germinal cradles were the Gs clone type (97.0 ± 2.0%, mean ± SEM, $n = 7$), whereas 3 weeks later, the full clone type was the most prevalent germinal cradle structure (77.8 ± 3.3%, mean ± SEM, $n = 8$) (Fig. 2D). Thus, all of the germ cells in the germinal cradles were derived from the population of *nos2*-expressing Gs cells.

To confirm that the *nos2*-expressing Gs cells generated fertile eggs, F1 embryos from heat-treated transgenic medaka were genotyped (fig. S8 and table S2). Some embryos possessed an uncleaved *loxP* region, whereas others exhibited the characteristic pattern of successful *loxP*-mediated recombination (Fig. 2E). Embryos with the cleaved *loxP* region were produced for 3 months after heat treatment (table S2), indicating that the population of *nos2*-expressing Gs cells was capable of continuously generating fertile eggs.

We identified and characterized ovarian cords within the germinal epithelia of medaka ovaries. These cords were composed of *sox9b*-expressing cells and contained mitotic *nos2*-expressing Gs cells in discrete structures referred to as germinal cradles. These mitotic oogonia continually gave rise to germ cells that developed in the ovary, finally resulting in fertile eggs. Thus, we conclude that the ovarian cord harbors the histological niche within the ovary where germinal cradles are formed (Fig. 3). Moreover, these cradles contain oogonia characteristic of germline stem cells that contribute to the production of fertile eggs (Fig. 3).

The germinal cradle in the ovarian cord is reminiscent of the germarium from the *Drosophila* ovary (*1*); both promote the development of germ cells from germline stem cells to very early diplotene oocytes in a unique histological compartment within the ovary. These similarities might reflect a fundamental process governing oogenesis across animal species.

References and Notes

1. M. D. Wong, Z. Jin, T. Xie, *Annu. Rev. Genet.* **39**, 173 (2005).
2. T. C. A. Kumar, *Proc. R. Soc. London Ser. B* **169**, 167 (1968).
3. J. Johnson, J. Canning, T. Kaneko, J. K. Pru, J. L. Tilly, *Nature* **428**, 145 (2004).
4. K. Zou *et al.*, *Nat. Cell Biol.* **11**, 631 (2009).
5. J. Pacchiarotti *et al.*, *Differentiation* **79**, 159 (2010).
6. K. Eggan, S. Jurga, R. Gosden, I. M. Min, A. J. Wagers, *Nature* **441**, 1109 (2006).
7. R. R. Tokarz, in *The Vertebrate Ovary*, R. E. Jones, Ed. (Plenum, New York, 1978), pp. 145–179.
8. R. A. Wallace, K. Selman, *J. Electron Microsc. Tech.* **16**, 175 (1990).
9. C. Morinaga *et al.*, *Proc. Natl. Acad. Sci. U.S.A.* **104**, 9691 (2007).
10. V. P. I. Vidal, M. C. Chaboissier, D. G. de Rooij, A. Schedl, *Nat. Genet.* **28**, 216 (2001).
11. T. Wagner *et al.*, *Cell* **79**, 1111 (1994).
12. N. Klüver, M. Kondo, A. Herpin, H. Mitani, M. Schartl, *Dev. Genes Evol.* **215**, 297 (2005).
13. S. Nakamura *et al.*, *Mol. Reprod. Dev.* **75**, 472 (2008).
14. H. Kurokawa *et al.*, *Dev. Growth Differ.* **48**, 209 (2006).
15. M. Tanaka, M. Kinoshita, D. Kobayashi, Y. Nagahama, *Proc. Natl. Acad. Sci. U.S.A.* **98**, 2544 (2001).
16. Y. Aoki *et al.*, *Dev. Dyn.* **237**, 800 (2008).
17. Y. Aoki, S. Nakamura, Y. Ishikawa, M. Tanaka, *Zoolog. Sci.* **26**, 112 (2009).
18. T. Iwai *et al.*, *Exp. Cell Res.* **312**, 2528 (2006).
19. E. Passegué, A. J. Wagers, S. Giuriato, W. C. Anderson, I. L. Weissman, *J. Exp. Med.* **202**, 1599 (2005).
20. Y. Stahl, R. Simon, *Int. J. Dev. Biol.* **49**, 479 (2005).
21. J. W. Zhang *et al.*, *Nature* **425**, 836 (2003).

22. We thank M. Yamashita and T. Iwai for anti-medaka SYCP antibodies, T. Czerny for plasmids containing the hs promoter region, and S. Yoshida for helpful discussions. We are grateful to Y. Ichikawa and C. Kinoshita for maintaining the fish colony. This work was supported in part by Grants-in-Aid for Scientific Research on Innovative Areas, "Gamete Stem Cells" (grant 21116509) and for Young Scientists (B) (21770072) (to S.N.), and for Scientific Research on Priority Areas (B) (21370101); the National BioResource Project Medaka; and the Daiko Foundation and the Center for the Promotion of Integrated Science (CPIS) of SOKENDAI (to M.T.).

Supporting Online Material

www.sciencemag.org/cgi/content/full/science.1185473/DC1
Materials and Methods
SOM Text
Figs. S1 to S9
Tables S1 and S2
References
Movies S1 to S3

3 December 2009; accepted 5 May 2010
Published online 20 May 2010;
10.1126/science.1185473
Include this information when citing this paper.

Down-Regulation of a Host MicroRNA by a *Herpesvirus saimiri* Noncoding RNA

Demián Cazalla, Therese Yario, Joan Steitz*

T cells transformed by *Herpesvirus saimiri* express seven viral U-rich noncoding RNAs of unknown function called HSURs. We noted that conserved sequences in HSURs 1 and 2 constitute potential binding sites for three host-cell microRNAs (miRNAs). Coimmunoprecipitation experiments confirmed that HSURs 1 and 2 interact with the predicted miRNAs in virally transformed T cells. The abundance of one of these miRNAs, miR-27, is dramatically lowered in transformed cells, with consequent effects on the expression of miR-27 target genes. Transient knockdown and ectopic expression of HSUR 1 demonstrate that it directs degradation of mature miR-27 in a sequence-specific and binding-dependent manner. This viral strategy illustrates use of a ncRNA to manipulate host-cell gene expression via the miRNA pathway.

Herpesvirus saimiri (HVS) infects T cells and causes aggressive leukemias and lymphomas in New World primates (*1*). In transformed marmoset T cells, the most abundant HVS transcripts are seven small noncoding RNAs (ncRNAs) called HSURs (*H. saimiri* U-rich RNAs) (*2*–*4*). HSURs exhibit structural but little sequence similarity to cellular small nuclear RNAs (snRNAs).

HSURs are encoded by all HVS subgroups; HSURs 1 and 2 (Fig. 1A) are the most highly conserved and the only snRNAs expressed by the closely related *Herpesvirus ateles* (*5*). Because HSURs are dispensable for transformation in vitro (*6*, *7*), their strong conservation suggests an in vivo role in infected monkeys. HSURs 1 and 2 contain highly conserved AU-rich 5′-end sequences (Fig. 1A and figs. S1 and S2) that are similar to AU-rich elements (AREs) found in the 3′ untranslated regions (3′UTRs) of short-lived mRNAs (*8*–*10*). HSURs 1 and 2 are responsible for the up-regulation of a handful of host proteins that are hallmarks of T-cell activation (*11*) and may contribute to an enhanced growth rate (*7*) of transformed cells.

Comparisons of HSUR 1 (fig. S1) and HSUR 2 (fig. S2) between HVS strains identified stretches of perfectly or highly conserved sequences (Fig. 1A, bold nucleotides). Bioinformatic searches then revealed complementarity between these HSUR sequences and three microRNAs (miRNAs) expressed in T cells: miR-142-3p, miR-27, and miR-16 (Fig. 1A) (*12*).

Department of Molecular Biophysics and Biochemistry, Howard Hughes Medical Institute, Yale University School of Medicine, Boyer Center for Molecular Medicine, 295 Congress Avenue, New Haven, CT 06536, USA.

*To whom correspondence should be addressed. E-mail: joan.steitz@yale.edu

Coimmunoprecipitation experiments on extracts of virally transformed marmoset T cells using antibodies to Ago2 showed that HSURs 1 and 2 were selectively present as compared with control immunoprecipitates, whereas all other HSURs (Fig. 1B, lanes 3 and 5) and cellular small nuclear ribonucleoproteins (snRNPs) (fig. S3) did not detectably associate with micro-ribonucleoproteins (miRNPs). Immunoprecipitation was then performed on extracts from T-cell lines transformed with either the wild-type HVS strain A11 or a mutant deleted for HSURs 1 and 2 (*7*) by using antibodies to Sm proteins, which recognize both cellular and viral snRNPs (*3*). Figure 1C (lanes 5 and 10) reveals the association of miR-16, miR-27, and miR-142-3p, and not of the control miR-20, but only when HSURs 1 and 2 are present. Psoralen [aminomethyltrioxsalen (AMT)] crosslinking experiments (fig. S4) (*13*) confirmed the existence of in vivo interactions between miR-27 and HSURs.

We noticed a distinct difference in the overall level of miR-27 in the marmoset T-cell line transformed by wild-type HVS as compared with that of the mutant lacking HSURs 1 and 2 (Fig. 1C and fig. S5). The miR-27 family includes miR-27a and miR-27b, which are transcribed from different chromosomes and differ by only one nucleotide near the 3′ end. Quantitative real-time polymerase chain reaction (PCR) confirmed the higher abundance of both miR-27a and miR-27b in transformed T cells lacking HSURs 1 and 2 (Fig. 2A). Levels of miR-23a and miR-24, two miRNAs contained in the same primary transcript as miR-27a (*14*), were unchanged (Fig. 2A and fig. S5), which suggested posttranscriptional differences in the expression of miR-27 between these two cell lines. The abundance of the precursor miRNAs (pre-miRNAs) for miR-27a and miR-27b (fig. S6) did not differ between the two cell lines, nor did that of the passenger strand of the miR-27a duplex (Fig. 2A), which suggests that miRNA processing by Drosha and Dicer (*15*) is not altered.

To determine whether the difference in the abundance of miR-27 is due to a change in the stability of the mature miRNA, we designed a pulse-chase strategy using synthetic miRNA duplexes (*16*) in which only the guide strand was radioactively labeled. After nucleofection (the "pulse"), we monitored the miRNA remaining over time (the "chase"; Fig. 2B) in marmoset T cell lines transformed by either wild-type HVS or mutant HVS lacking HSURs 1 and 2. miR-27a was degraded more rapidly in the wild-type transformed cells, whereas no difference was observed for either miR-16, which is predicted to bind HSUR 2 (Fig. 1A), or for the control miR-20a (fig. S7).

HSURs 1 and 2 do not affect the steady-state levels of host mRNAs in virally transformed marmoset T cells, except for eight genes (*8*, *11*) that are not predicted targets of HSUR-bound

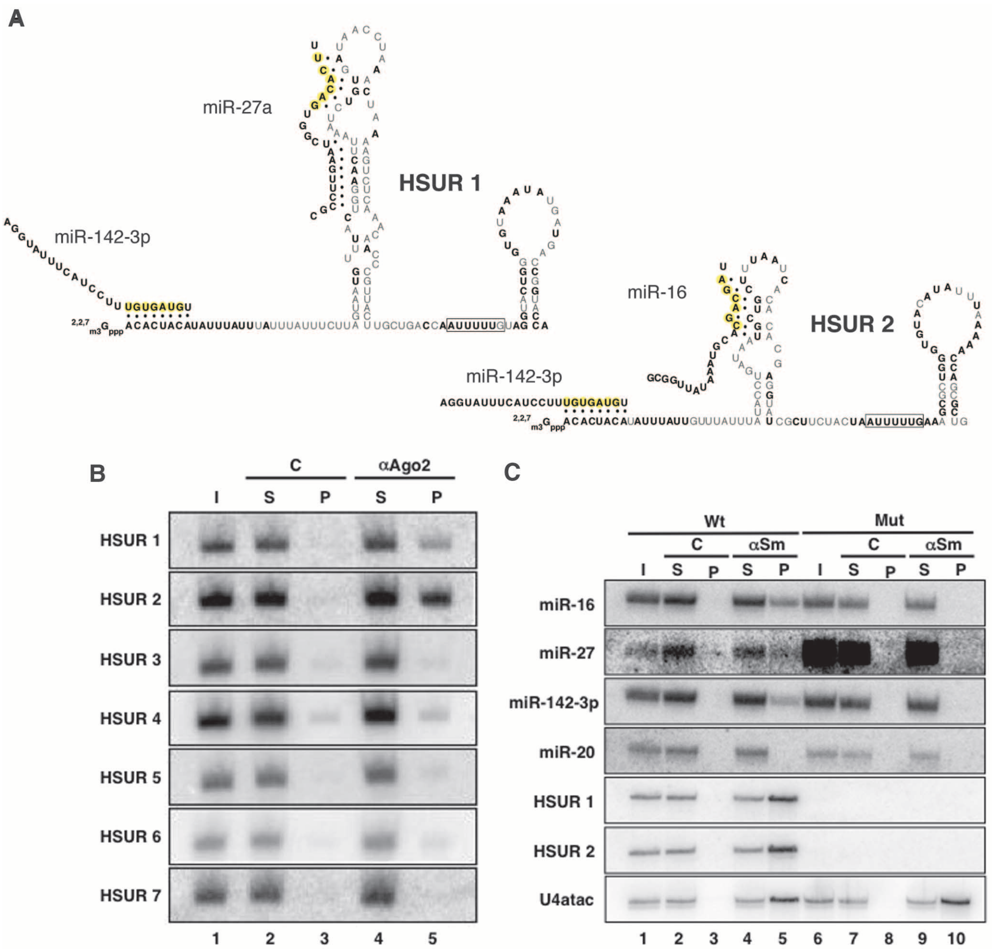

Fig. 1. HSURs 1 and 2 bind host miRNAs in virally transformed T cells. (**A**) Sequences and predicted secondary structures of HSURs 1 and 2. Bold nucleotides are perfectly conserved in all available genome sequences from independent isolates of HVS A, B, and C strains and also in *H. ateles* (figs. S1 and S2). Complementarity between HSURs and miRNAs is represented by dots; miRNA seed regions are in yellow. (**B**) Coimmunoprecipitation of HSURs from extracts of virally transformed marmoset T cells with antibody to Flag (lane 3) or antibody to Ago2 (lane 5). I, input (5%); S, supernatant (5%); P, pellet (100%). (**C**) Coimmunoprecipitation of miRNAs from extracts of virally transformed marmoset T cell lines expressing (Wt, lanes 1 to 5) or lacking HSURs 1 and 2 (Mut, lanes 6 to 10) with Y12 antibody (αSm, lanes 4, 5 and 9, 10) or nonimmune serum (C, lanes 2, 3 and 7, 8). I, input (2%); S, supernatant (2%); P, pellet (100%). Northern blots in (B) and (C) were probed for HSURs, miRNAs, or U4atac, as an αSm immunoprecipitation control.

miRNAs (*17*). We analyzed the levels of forkhead box 1 (FOXO1) protein, whose mRNA is a validated target of miR-27 (*18*). The difference in miR-27 abundance correlates with up-regulation of the FOXO1 protein (Fig. 2C) in the presence of HSURs 1 and 2, which suggests that these HVS ncRNAs perturb host gene expression via the miRNA pathway.

To confirm that the difference in miR-27 levels does not result from accumulated mutations in the two HVS-transformed T cell lines, we treated cells that contained wild-type HVS with chimeric oligonucleotides that effectively induce degradation of complementary nuclear RNAs (*19*). Knockdown of HSUR 1 but not of HSUR 2 correlated with higher levels of miR-27 (Fig. 3, A and B) and with lower levels of the miR-27 target protein, FOXO1 (Fig. 3C), which suggests that HSUR 1 is specifically involved in regulating miR-27.

Direct base-pairing between HSUR 1 and miR-27 is required to control miRNA abundance. Human Jurkat T cells were stably transfected with a plasmid containing HVS DNA that encodes all seven HSURs, including their endogenous transcription and processing signals (*7*). Precipitation of HSUR snRNPs with antibodies to Sm proteins confirmed their association with miR-27 in extracts of this cell line (Fig. 4B, lanes 1 to 5). In contrast, antibodies to Sm proteins did not coimmunoprecipitate miR-27 from extracts of Jurkat T cells stably transfected with a plasmid deleted for the HSUR 1 gene (Fig. 4B, lanes 6 to 10). Likewise, mutation of the conserved miR-27 binding site in HSUR 1 [Fig. 4A, HSUR 1 mutant (H1Mt)] abolished the immunoprecipitation of miR-27 (Fig. 4B, lanes 11 to 15). Furthermore, mutations in HSUR 1 that were designed to produce complementarity to miR-20a (Fig. 4A, H1m20) enabled a previously unknown interaction with miR-20 (Fig. 4B, lanes 16 to 20).

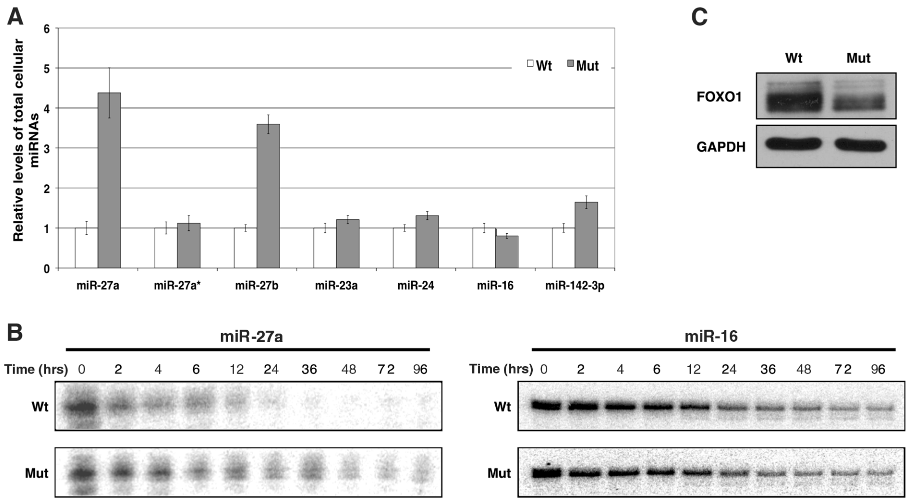

Fig. 2. The presence of HSURs 1 and 2 affects miR-27a abundance, decay, and target expression. (**A**) Relative levels of different mature miRNAs in virally transformed marmoset T cells expressing (Wt) or lacking (Mut) HSURs 1 and 2 were determined by means of quantitative real-time PCR. (**B**) Pulse-chase assay assessing the decay of radioactively labeled synthetic miR-27a and miR-16. (**C**) Western blot analysis of FOXO1 in marmoset T cells transformed by HVS expressing (Wt) or lacking (Mut) HSURs 1 and 2.

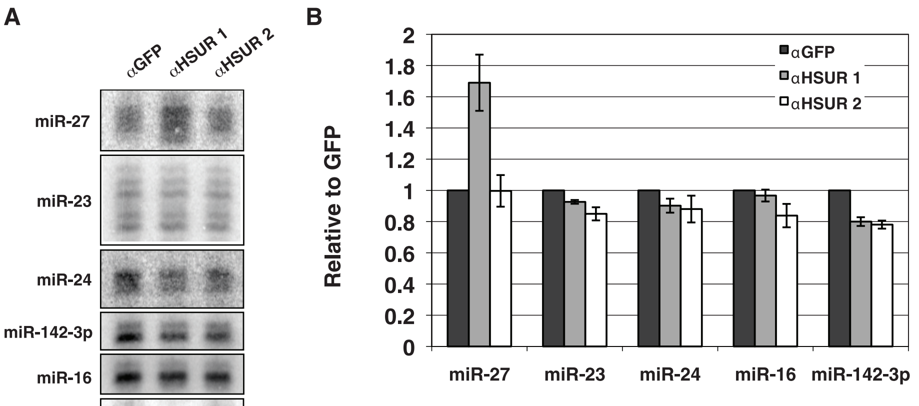

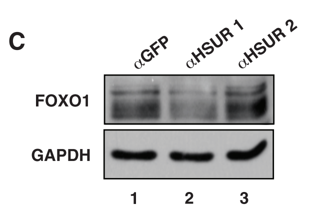

Fig. 3. HSUR 1 regulates the abundance of miR-27 in virally transformed T cells. (**A**) Northern blot analyses of miRNAs and HSURs after nucleofection with chimeric oligonucleotides antisense to GFP (lane 1), HSUR 1 (lane 2), or HSUR 2 (lane 3). (**B**) Quantification of miRNAs from three independent experiments performed as in (A). (**C**) Western blot of FOXO1 in HVS-transformed marmoset T cells nucleofected as described in (A).

Expression of wild-type HSUR 1 alone (fig. S8) in Jurkat T cells (fig. S9) is sufficient to down-regulate the level of miR-27a as compared with transfection with the empty vector [Fig. 4C; green fluorescent protein (GFP)]. Direct interaction between HSUR 1 and miR-27 is required because cells transfected with a H1Mt that is unable to bind miR-27 (Fig. 4B) have levels of miR-27 comparable with those of cells transfected with the empty vector. Moreover, the miR-20a level was substantially lower after transfection of the HSUR 1 mutant (H1m20) that binds this miRNA (Fig. 4B). Together, these results indicate that base-pairing to an internal site in HSUR 1 is both necessary and sufficient to direct a mature miRNA into a cellular degradation pathway.

The ARE-like sequence in HSUR 1 is known to induce in vivo decay of HSUR 1 itself (*9*), suggesting that the ARE could be involved in the HSUR 1–dependent decay of miR-27. We transfected Jurkat T cells with a mutant HSUR 1 containing two U→G substitutions in the ARE (H1M1) that were previously shown to stabilize and raise cellular levels of HSUR 1 (*9*). This mutation resulted in higher levels of HSUR 1 (fig. S9) and did not alleviate but produced a more pronounced down-regulation of the abundance of miR-27 as compared with wild-type HSUR 1 (Fig. 4C), indicating that HSUR 1 directs the degradation of miRNAs by an ARE-independent mechanism.

We have demonstrated that HSUR 1 and 2 snRNPs directly bind specific host miRNPs in virally transformed T cells. Whereas the interaction of miR-27 with an internal site in HSUR 1 results in the degradation of this miRNA, the binding of miR-142-3p and miR-16 to HSURs 1 and 2 does not result in their lowered levels (Fig. 2, A and B, and fig. S5). Nonetheless, mutational alteration of its binding site in HSUR 2 indicates that the interaction with miR-16 also occurs via base-pairing (fig. S10), and it is conceivable that if this base-pairing were stronger, decay would be induced. Because HSURs are comparable in abundance with the bound miRNAs in virally transformed T cells (table S1), it seems unlikely that they could effectively compete with mRNA targets and act as miRNA sponges (*20*) even though down-regulating the activity of these miRNAs might be advantageous for the virus. For instance, miR-16 is reported to target cell-cycle and apoptosis regulators such as Bcl-2 and cyclins D1 and E1 (*21*, *22*), but we do not observe differences in levels of miR-16 target proteins in the presence versus absence of HSURs 1 and 2 (fig. S11). The functional importance of the interaction

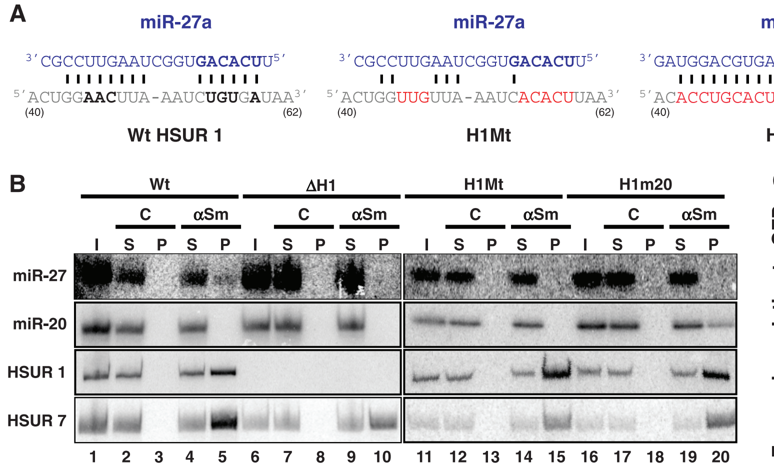

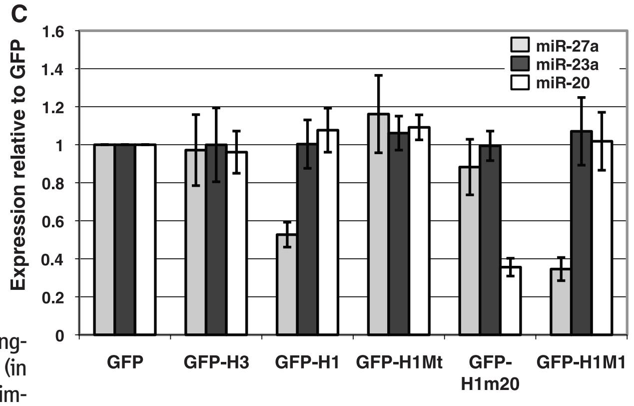

Fig. 4. HSUR 1 down-regulates mature miRNAs in a sequence-specific and binding-dependent manner. (**A**) Partial sequences of HSUR 1 (positions 40 to 62) and its mutants (in red) H1Mt and H1m20. Bold nucleotides are perfectly conserved (Fig. 1A). (**B**) Coimmunoprecipitation of miRNAs with αSm, as in Fig. 1C, from extracts of Jurkat T cells stably expressing HSURs 2 to 7 and either wild-type HSUR 1 (Wt, lanes 1 to 5), no HSUR 1 (ΔH1, lanes 6 to 10), mutant HSUR 1 H1Mt (lanes 11 to 15), or mutant HSUR 1 H1m20 (lanes 16 to 20). (**C**) miRNA levels in Jurkat T cells fluorescence-activated cell sorted for GFP after transient transfection with empty vector (GFP) or with plasmids expressing GFP and the following: HSUR 3 (GFP-H3), Wt HSUR 1 (GFP-H1), H1Mt (GFP-H1Mt), H1m20 (GFP-H1m20), or H1M1 (GFP-H1M1).

between HSURs 1 and 2 and miR-16 and miR-142-3p requires further investigation.

It is not yet clear how down-regulation of miR-27 benefits HVS. Down-regulation of the same host miRNA has been reported for another herpesvirus, murine cytomegalovirus, upon infection of cell lines and primary macrophages apparently also at the posttranscriptional level (*23*). Only a few targets of miRNA-27, including the transcription factors FOXO1, RUNX1 and PAX3, have been validated (*18*, *24*, *25*). Thus, identification of additional targets of miR-27 in T cells transformed with HVS is needed, as well as elucidation of the molecular mechanism by which association with HSUR 1 leads to miR-27 decay.

References and Notes

1. A. Ensser, B. Fleckenstein, *Adv. Cancer Res.* **93**, 91 (2005).
2. B. Biesinger, J. J. Trimble, R. C. Desrosiers, B. Fleckenstein, *Virology* **176**, 505 (1990).
3. S. I. Lee, S. C. Murthy, J. J. Trimble, R. C. Desrosiers, J. A. Steitz, *Cell* **54**, 599 (1988).
4. D. A. Wassarman, S. I. Lee, J. A. Steitz, *Nucleic Acids Res.* **17**, 1258 (1989).
5. J. C. Albrecht, *J. Virol.* **74**, 1033 (2000).
6. A. Ensser, A. Pfinder, I. Müller-Fleckenstein, B. Fleckenstein, *J. Virol.* **73**, 10551 (1999).
7. S. C. Murthy, J. J. Trimble, R. C. Desrosiers, *J. Virol.* **63**, 3307 (1989).
8. H. L. Cook, H. E. Mischo, J. A. Steitz, *Mol. Cell. Biol.* **24**, 4522 (2004).
9. X. C. Fan, V. E. Myer, J. A. Steitz, *Genes Dev.* **11**, 2557 (1997).
10. V. E. Myer, S. I. Lee, J. A. Steitz, *Proc. Natl. Acad. Sci. U.S.A.* **89**, 1296 (1992).
11. H. L. Cook *et al.*, *Curr. Biol.* **15**, 974 (2005).
12. P. Landgraf *et al.*, *Cell* **129**, 1401 (2007).
13. G. D. Cimino, H. B. Gamper, S. T. Isaacs, J. E. Hearst, *Annu. Rev. Biochem.* **54**, 1151 (1985).
14. M. Lagos-Quintana, R. Rauhut, W. Lendeckel, T. Tuschl, *Science* **294**, 853 (2001).
15. V. N. Kim, J. Han, M. C. Siomi, *Nat. Rev. Mol. Cell Biol.* **10**, 126 (2009).
16. H. W. Hwang, E. A. Wentzel, J. T. Mendell, *Science* **315**, 97 (2007).
17. Materials and methods are available as supporting material on *Science* Online.
18. I. K. Guttilla, B. A. White, *J. Biol. Chem.* **284**, 23204 (2009).
19. T. Ideue, K. Hino, S. Kitao, T. Yokoi, T. Hirose, *RNA* **15**, 1578 (2009).
20. M. S. Ebert, J. R. Neilson, P. A. Sharp, *Nat. Methods* **4**, 721 (2007).
21. A. Cimmino *et al.*, *Proc. Natl. Acad. Sci. U.S.A.* **102**, 13944 (2005).
22. Q. Liu *et al.*, *Nucleic Acids Res.* **36**, 5391 (2008).
23. A. H. Buck *et al.*, *RNA* **16**, 307 (2010).
24. O. Ben-Ami, N. Pencovich, J. Lotem, D. Levanon, Y. Groner, *Proc. Natl. Acad. Sci. U.S.A.* **106**, 238 (2009).
25. C. G. Crist *et al.*, *Proc. Natl. Acad. Sci. U.S.A.* **106**, 13383 (2009).

26. We thank A. Giraldez for initial bioinformatic searches, R. C. Desrosiers for plasmids and cell lines, R. Jobava for technical assistance, K. Tycowski and K. Riley for critical commentary, and A. Miccinello for editorial assistance. This work was supported by grant CA16038 from the NIH. The content is solely the responsibility of the authors and does not necessarily represent the official views of the NIH. J.S. is an investigator at the Howard Hughes Medical Institute.

Supporting Online Material
www.sciencemag.org/cgi/content/full/328/5985/1563/DC1
Materials and Methods
Figs. S1 to S11
Table S1
References

18 January 2010; accepted 14 April 2010
10.1126/science.1187197

MicroRNA-33 and the SREBP Host Genes Cooperate to Control Cholesterol Homeostasis

S. Hani Najafi-Shoushtari,[1,2] Fjoralba Kristo,[3] Yingxia Li,[4] Toshi Shioda,[1] David E. Cohen,[4] Robert E. Gerszten,[3,5] Anders M. Näär[1,2]*

Proper coordination of cholesterol biosynthesis and trafficking is essential to human health. The sterol regulatory element–binding proteins (SREBPs) are key transcription regulators of genes involved in cholesterol biosynthesis and uptake. We show here that microRNAs (miR-33a/b) embedded within introns of the SREBP genes target the adenosine triphosphate–binding cassette transporter A1 (ABCA1), an important regulator of high-density lipoprotein (HDL) synthesis and reverse cholesterol transport, for posttranscriptional repression. Antisense inhibition of miR-33 in mouse and human cell lines causes up-regulation of ABCA1 expression and increased cholesterol efflux, and injection of mice on a western-type diet with locked nucleic acid–antisense oligonucleotides results in elevated plasma HDL. Our findings indicate that miR-33 acts in concert with the SREBP host genes to control cholesterol homeostasis and suggest that miR-33 may represent a therapeutic target for ameliorating cardiometabolic diseases.

Cholesterol and other lipids play key roles in many physiological processes in metazoans, and aberrant cholesterol/lipid homeostasis has been linked to a number of diseases, including atherosclerosis, metabolic syndrome, and type II diabetes, underscoring the importance of understanding fully how cholesterol/lipid homeostasis is regulated (*1*, *2*).

The sterol regulatory element-binding protein (SREBP) transcription factors are critical regulators of cholesterol/lipid homeostasis, which act by controlling the expression of many cholesterogenic and lipogenic genes [e.g., low-density lipoprotein (LDL) receptor, 3-hydroxy-3-methylglutaryl coenzyme A reductase, and fatty acid synthase] (*3*–*6*). Although much is known about SREBP-dependent transcriptional mechanisms governing the biosynthesis and uptake of cholesterol and fatty acids, it is unclear how this regulatory circuit is coordinated with opposing pathways that mediate cholesterol/lipid efflux or degradation to achieve appropriate cholesterol/lipid levels to satisfy cellular and physiological demands.

In addition to classical transcription regulators, a class of noncoding RNAs termed microRNAs (miRNAs) has emerged as important modulators of numerous cellular processes that affect organism growth, development, homeostasis, and disease (*7*–*12*). Indeed, recent studies have revealed that a liver-restricted miRNA, miR-122, regulates cholesterol/lipid metabolism in mice and nonhuman primates, although the mechanism remains unclear (*13*–*16*). Data from these studies not only emphasize the important roles played by miRNAs in normal physiology but also point to the feasibility of antisense-based therapeutic targeting of miRNAs to treat human disease.

During our investigations of gene regulation by SREBPs (*17*), we noted the intriguing presence of a highly conserved miRNA family, miR-33, within intronic sequences of the SREBP genes in organisms from *Drosophila* to humans (Fig. 1, A and B, and fig. S1). Two isoforms of miR-33 exist in humans: miR-33b, which is present in intron 17 of the SREBP-1 gene on chromosome 17, and miR-33a, which is located in intron 16 of the SREBP-2 gene on chromosome 22 (Fig. 1, A and B). In mice, however, there is only one miR-33 isoform (which is conserved with human miR-33a), located within intron 15 of the mouse SREBP-2 gene, whereas intron 17 in the mouse SREBP-1 gene lacks sequence homology to the human intronic sequences harboring miR-33b (fig. S1).

Similar to miR-33, many mammalian miRNAs are located within introns of protein-coding genes rather than in their own unique transcription units (*18*). Intronic miRNAs are typically coordinately expressed and processed with the precursor mRNA in which they reside (*19*–*21*). Accordingly, the mature forms of miR-33a/b appear to be coexpressed with the SREBP host genes in a number of human and mouse tissues examined (Fig. 1, C to E, and figs. S2 to S4).

We wished to determine the potential function(s) of miR-33a/b and whether they exhibit functional association with the SREBP host genes. miRNAs have been shown to target mRNAs for posttranscriptional repression by base-pairing with mRNA sequences typically located in the 3′ untranslated regions (3′UTRs) and causing translational inhibition or mRNA cleavage (*22*). We initially employed commonly used bioinformatics tools that predict miRNA targets largely based on the ability of the miRNA sequence to undergo specific base-pairing with its putative 3′UTR target, known as "seed pairing" (*22*). The most prominent predicted conserved target for miR-33a/b among vertebrates is the adenosine triphosphate–binding cassette A1 (ABCA1) cholesterol transporter (table S1 and fig. S5A). ABCA1 is a key mediator of intracellular cholesterol efflux from liver to apolipoprotein A-I (apoA-I) for generation of high-density lipoprotein (HDL) (*1*, *23*, *24*). It is also important for HDL-cholesterol trafficking from peripheral tissues (e.g., macrophages) by the reverse cholesterol transport (RCT) pathway back to the liver for processing and excretion into bile and feces (*25*).

As SREBPs promote cholesterol uptake and synthesis through transactivation of the LDL receptor and cholesterol biosynthesis genes, we hypothesized that miR-33–mediated inhibition of ABCA1 and cholesterol efflux could potentially act in cooperation with SREBPs to boost intracellular cholesterol levels. To test this hypothesis, we first carried out RNA interference–mediated knockdown of components of the miRNA biogenesis pathway to determine whether ABCA1 protein expression is regulated by miRNAs. Indeed, transfection with siRNAs directed against the Drosha and Dicer miRNA processing enzymes resulted in a marked increase in ABCA1 protein expression in several human and mouse cell lines, including human HepG2 liver carcinoma cells, IMR-90 normal human fibroblasts, and the mouse macrophage cell line J774 (Fig. 2A). These results are thus consistent with regulation of ABCA1 by miRNAs. To evaluate the specific effect of miR-33 on ABCA1 expression, we transfected cells with synthetic miR-33 precursor oligonucleotides (pre-miR-33a/b) to increase the intracellular levels of miR-33a and b, respectively. These studies show that ABCA1 expression is repressed by excess miR-33, especially in mouse J774 macrophages and the human IMR-90 fibroblasts (Fig. 2B). To further determine whether miR-33a/b are specifically involved in regulating

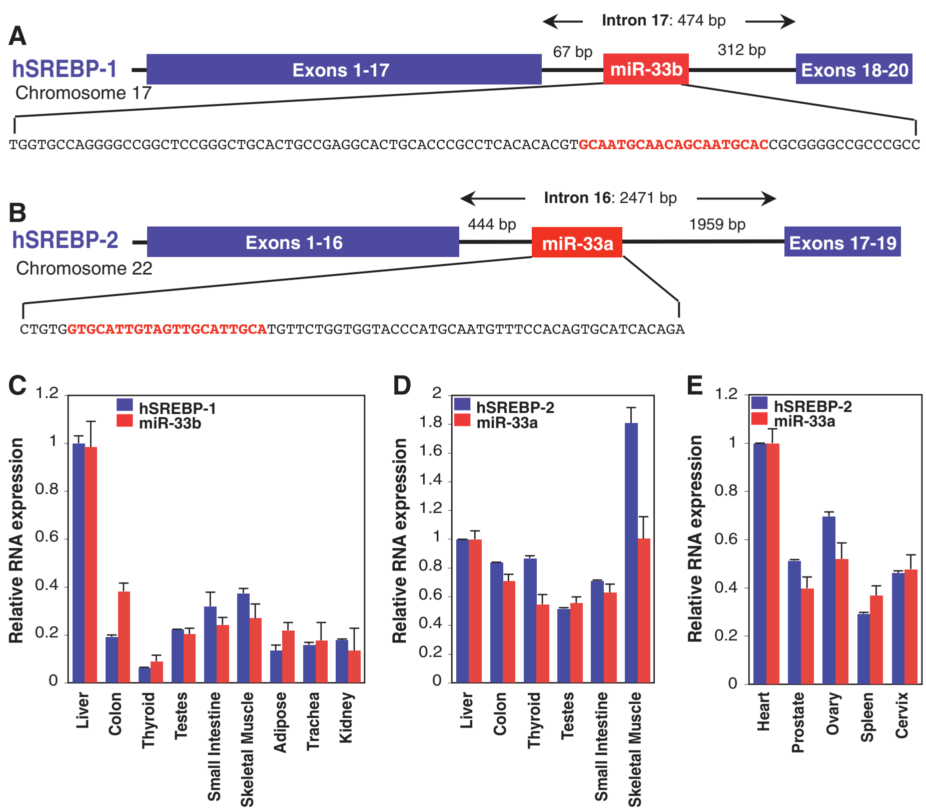

Fig. 1. SREBPs are host genes to conserved intronic miRNAs, miR-33a/b, which are coexpressed with SREBPs. Human SREBP-1 (**A**) and SREBP-2 (**B**) genes harbor related intronic miRNAs (miR-33b and miR-33a, respectively). The sequences encoding the pre-miRNAs are shown, with the mature miRNA sequences highlighted in red. (**C** to **E**) Expression profile of miR-33a/b and SREBP host genes in selected human tissues. Error bars represent experimental SD.

[1]Massachusetts General Hospital Cancer Center, Charlestown, MA 02129, USA. [2]Department of Cell Biology, Harvard Medical School, Boston, MA 02115, USA. [3]Center for Immunology and Inflammatory Diseases, Massachusetts General Hospital, Charlestown, MA 02129, USA. [4]Department of Medicine, Division of Gastroenterology, Brigham and Women's Hospital, Harvard Medical School, Boston, MA 02115, USA. [5]Cardiovascular Research Center, Massachusetts General Hospital, Charlestown, MA 02129, USA.

*To whom correspondence should be addressed. E-mail: naar@helix.mgh.harvard.edu

ABCA1 expression, we transfected the three cell lines with antisense oligonucleotides directed against miR-33a and/or b (anti-miR-33a/b). Introduction of anti-miR-33a/b indeed resulted in strongly increased levels of ABCA1 in the three cell lines (Fig. 2C). Taken together, these findings demonstrate that ABCA1 protein expression is regulated by miR-33a/b.

To determine whether miR-33a/b specifically target ABCA1 posttranscriptionally through its 3′UTR, we fused a fragment of the human ABCA1 3′UTR harboring the predicted miR-33 target sequences to a Luciferase reporter plasmid (fig. S5B). As shown in Fig. 2D, the Luciferase-ABCA1 3′UTR reporter was expressed at markedly lower levels in human embryonic kidney (HEK) 293 cells as compared with the Luciferase vector without insert. Introduction of excess wild-type human miR-33a/b precursor oligonucleotides resulted in further repression of the wild-type ABCA1 3′UTR reporter (Fig. 2E). By contrast, miR-33a/b precursors mutated in the seed base-pairing sequence had no effect, as compared with precursor control (PC) (Fig. 2E and fig. S5C). Together, these data show that miR-33a/b are capable of repressing expression from the ABCA1 3′UTR. Importantly, cotransfection with miR-33a/b antisense oligonucleotides caused complete derepression of the Luciferase-ABCA1 3′UTR reporter, consistent with regulation of ABCA1 3′UTR by endogenous miR-33a/b (Fig. 2F). Finally, mutations in the seed base-pairing sequences of the predicted miR-33 target sites in the ABCA1 3′UTR reporter abolished regulation by miR-33a/b precursors as well as anti-miR-33a/b (Fig. 2G). Together, these results suggest that miR-33a/b inhibit expression of human ABCA1 by targeting the ABCA1 3′UTR for translation repression or mRNA degradation.

Reverse cholesterol transport from atherogenic macrophages/foam cells is of clinical importance because of the prominent role played by foam cells in cardiovascular disease, and a number of studies have highlighted the biomedical implications of ABCA1-dependent cholesterol efflux and HDL biogenesis for atherosclerosis (*23*, *26*–*28*). We have investigated the potential biomedical and physiological relevance of the miR-33/SREBP/ABCA1 cholesterol regulatory circuit using the mouse J774 macrophage model (*29*). SREBPs are regulated in a classic negative feedback manner by cholesterol (*3*, *5*), and we find that depletion of cholesterol by lovastatin/β-cyclodextrin treatment results in increased expression of both miR-33a and the mSREBP-2 host gene in J774 macrophages, with a concomitant decrease in ABCA1 protein expression (Fig. 3, A to C). The strong suppression of ABCA1 protein levels in response to cholesterol depletion is at least partially reversed by miR-33a antisense oligonucleotides (Fig. 3D), consistent with the notion that miR-33a mediates cholesterol-regulated posttranscriptional control of ABCA1 levels in mouse macrophages. We also found that the high protein levels of ABCA1 observed in J774 macrophages cultured in the presence of serum/cholesterol are substantially suppressed by additional miR-33a precursor (Fig. 3E), in keeping with miR-33 regulation of ABCA1. By contrast with the apparent regulation of ABCA1 levels in J774 cells by miR-33a, expression of the intracellular cholesterol transporter NPC1 is unaffected by miR-33a precursor or antisense treatment (fig. S6), demonstrating specific regulation of ABCA1

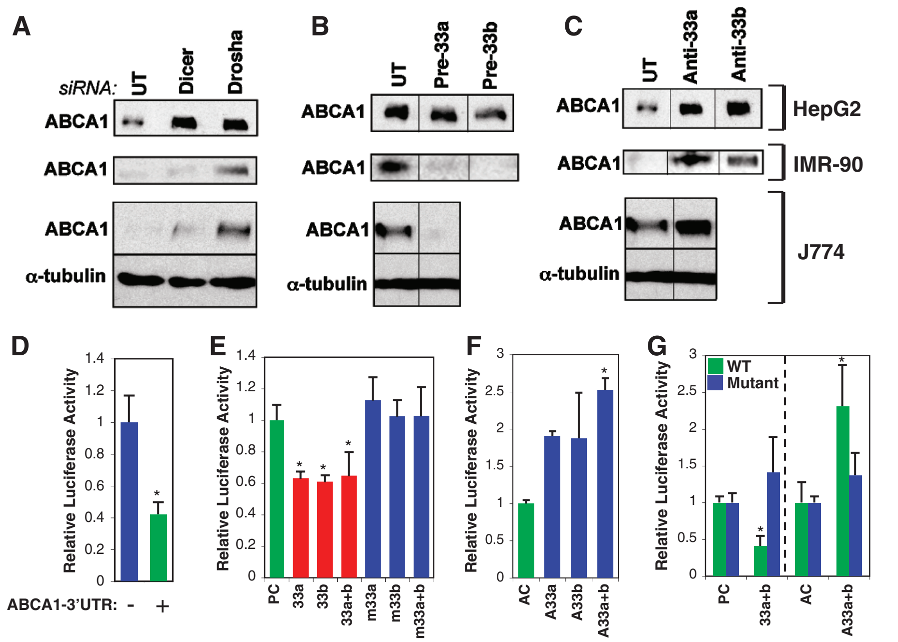

Fig. 2. miR-33 regulates the cholesterol transporter ABCA1. (**A**) Transfection of siRNA against Drosha and Dicer results in increased protein levels of ABCA1 in human HepG2 hepatoma cells (top row), human IMR-90 fibroblasts (middle row), and the mouse macrophage cell line J774 (bottom row). (**B**) Introduction of miR-33a or miR-33b precursors into the three cell lines represses ABCA1 protein levels. (**C**) miR-33a/b antisense oligonucleotides (A33a/b) increase ABCA1 levels. (**D**) Schematic representation of the Luciferase reporter vector harboring the ABCA1 3′UTR fragment (green) containing the two predicted miR-33 target sites. (**E**) Insertion of the ABCA1 3′UTR fragment into a Luciferase reporter results in decreased Luciferase expression in HEK293 cells. (**F**) Cotransfection with wild-type, but not mutated, miR-33a/b precursors causes further repression of the Luciferase-ABCA1 3′UTR reporter. A scrambled sequence was used as PC. (**G**) miR-33a/b antisense oligonucleotides result in derepression of the Luciferase-ABCA1 3′UTR reporter. A scrambled sequence was used as AC. Error bars represent SD. *, $P < 0.05$.

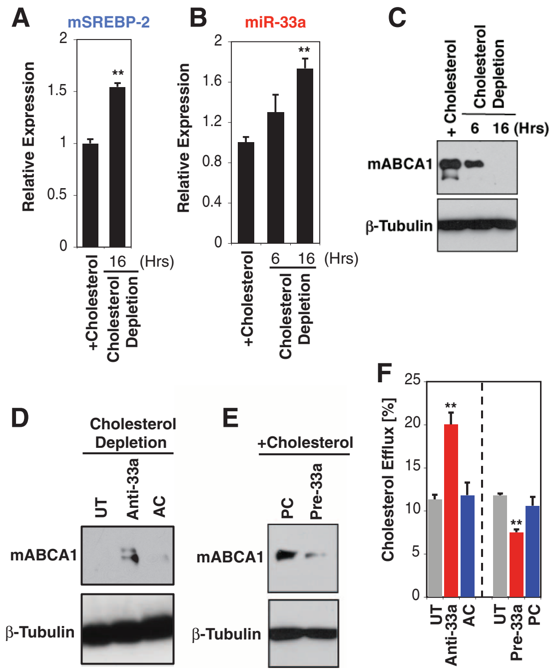

Fig. 3. Reciprocal regulation by cholesterol and SREBP/miR-33. Lovastatin/β-cyclodextrin-mediated depletion of cholesterol in J774 mouse macrophages results in increased expression of (**A**) SREBP-2 and (**B**) miR-33a, and (**C**) in decreased ABCA1 protein levels. (**D**) Cholesterol-depleted J774 mouse macrophages exhibit up-regulation of ABCA1 protein in response to miR-33a antisense inhibition. (**E**) Transfection of J774 macrophages cultured in the presence of serum/cholesterol with miR-33a precursor results in decreased levels of ABCA1. (**F**) Introduction of miR-33a antisense oligonucleotides into J774 macrophages loaded with radio-labeled cholesterol results in increased cholesterol efflux, whereas miR-33a precursors inhibit cholesterol efflux. Error bars represent SD. **, $P < 0.01$.

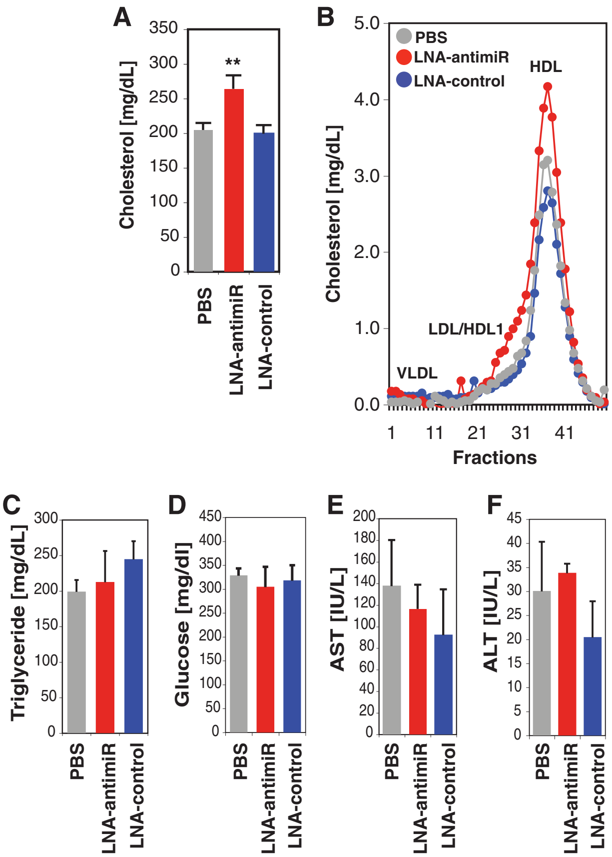

Fig. 4. Regulation of HDL by miR-33a in vivo. (**A**) Tail-vein injection of mice fed a western-type diet with LNA-antisense oligonucleotides directed against mouse miR-33a results in elevated total serum cholesterol. (**B**) Fast protein liquid chromatography analysis of pooled serum from five mice on a western-type diet revealed an increase in the magnitude of the HDL-cholesterol peak in the LNA-antimiR–treated animals. Elution of lipoprotein standards is indicated by the labels. Plasma triglycerides (**C**), glucose (**D**), AST (**E**), and ALT (**F**) were unaffected by the treatments. Error bars represent SEM. **, $P < 0.01$.

by miR-33a. Our data together show that mouse miR-33a and the SREBP-2 host gene are coregulated by cholesterol and suggest the existence of a reciprocal regulatory network of SREBP, miR-33, ABCA1, and cholesterol in macrophages.

Next, we examined the effects of miR-33 manipulations on cholesterol efflux from J774 macrophages. Cells were first labeled with [^{3}H]-cholesterol and then transfected with miR-33a precursor, miR-33a antisense, or control oligonucleotides, followed by measurements of the level of [^{3}H]-cholesterol efflux to serum/apoA-I. As shown in Fig. 3F, introduction of miR-33a antisense oligonucleotides into mouse macrophages caused a marked (two-fold) increase in [^{3}H]-cholesterol efflux, whereas miR-33a precursor treatment led to a significant decrease in [^{3}H]-cholesterol efflux, as compared with control oligonucleotides [antisense control (AC)/PC] or untransfected cells (UT). These findings demonstrate that miR-33 posttranscriptional repression of ABCA1 results in retention of intracellular cholesterol in macrophages and are in keeping with our hypothesis that miR-33 regulates cholesterol trafficking by controlling ABCA1 levels.

Based on our in vitro findings, we hypothesized that manipulation of ABCA1 levels by miR-33 antisense approaches might lead to augmented HDL-cholesterol levels in a mammalian in vivo model. Previous studies in mice and nonhuman primates have supported the feasibility of locked nucleic acid (LNA) antisense approaches to modulate miRNA pathways with important physiological consequences in vivo (*13*, *14*). We therefore performed tail-vein injections of mice on a western-type diet with phosphate-buffered saline (vehicle), LNA-miR-33a antisense, or LNA-control oligonucleotides. After three injections over 5 days, mice were killed and serum was collected. We find that plasma HDL-cholesterol concentrations were significantly increased in LNA-miR-33a antisense-treated animals as compared with LNA-control-treated mice (Fig. 4, A and B, and table S2). By contrast, there were no significant effects on plasma concentrations of LDL cholesterol, triglycerides, or glucose levels (Fig. 4, C to F, and table S2). In these experiments, there was also no apparent hepatotoxicity [as measured by plasma aspartate aminotransferase/alanine aminotransferase (AST/ALT)] (Fig. 4, E and F, and table S2). The observed elevation in plasma HDL cholesterol in response to LNA-miR-33a antisense treatment is consistent with regulation of ABCA1-dependent cholesterol efflux by miR-33a in vivo. Hepatic ABCA1 is a major contributor to HDL production in normal mice (*23*, *24*); however, we find only modest effects of miR-33a LNA-antimiR on hepatic ABCA1 mRNA/protein as compared with LNA-control (fig. S7). Based on these findings, we speculate that liver might not be the sole target tissue in mediating the effect of miR-33a LNA-antimiR on HDL production, with possible additional contribution of miR-33a regulation of reverse cholesterol transport from extrahepatic tissues/cells.

We have shown that members of the mammalian SREBP family of transcription factors, key regulators of cholesterogenic and lipogenic genes, are hosts to conserved miRNAs (miR-33a/b) that may function in concert with the SREBP host gene products to govern intracellular cholesterol levels and cholesterol homeostasis in vertebrates (fig. S8). Indeed, our data reveal that miR-33 exerts posttranscriptional control of the ABCA1 cholesterol transporter, with important consequences for cholesterol trafficking in vitro and HDL synthesis in vivo. Our findings also point to the possibility of antisense therapeutic targeting of miR-33a/b as a strategy to increase HDL in individuals suffering from cardiometabolic diseases.

References and Notes

1. F. R. Maxfield, I. Tabas, *Nature* **438**, 612 (2005).
2. D. E. Moller, K. D. Kaufman, *Annu. Rev. Med.* **56**, 45 (2005).
3. M. S. Brown, J. L. Goldstein, *J. Lipid Res.* **50**, (Suppl), S15 (2009).
4. T. F. Osborne, P. J. Espenshade, *Genes Dev.* **23**, 2578 (2009).
5. M. S. Brown, J. L. Goldstein, *Cell* **89**, 331 (1997).
6. J. D. Horton, J. L. Goldstein, M. S. Brown, *J. Clin. Invest.* **109**, 1125 (2002).
7. A. H. Williams, N. Liu, E. van Rooij, E. N. Olson, *Curr. Opin. Cell Biol.* **21**, 461 (2009).
8. M. V. Iorio, C. M. Croce, *J. Clin. Oncol.* **27**, 5848 (2009).
9. D. P. Bartel, *Cell* **116**, 281 (2004).
10. L. He, G. J. Hannon, *Nat. Rev. Genet.* **5**, 522 (2004).
11. J. Krützfeldt, M. Stoffel, *Cell Metab.* **4**, 9 (2006).
12. G. Stefani, F. J. Slack, *Nat. Rev. Mol. Cell Biol.* **9**, 219 (2008).
13. J. Elmén *et al.*, *Nature* **452**, 896 (2008).
14. J. Elmén *et al.*, *Nucleic Acids Res.* **36**, 1153 (2008).
15. C. Esau *et al.*, *Cell Metab.* **3**, 87 (2006).
16. J. Krützfeldt *et al.*, *Nature* **438**, 685 (2005).
17. F. Yang *et al.*, *Nature* **442**, 700 (2006).
18. A. Rodriguez, S. Griffiths-Jones, J. L. Ashurst, A. Bradley, *Genome Res.* **14**, (10A), 1902 (2004).
19. D. Wang *et al.*, *PLoS ONE* **4**, e4421 (2009).
20. S. Baskerville, D. P. Bartel, *RNA* **11**, 241 (2005).
21. Y. K. Kim, V. N. Kim, *EMBO J.* **26**, 775 (2007).
22. D. P. Bartel, *Cell* **136**, 215 (2009).
23. A. R. Tall, L. Yvan-Charvet, N. Terasaka, T. Pagler, N. Wang, *Cell Metab.* **7**, 365 (2008).
24. X. Wang, D. J. Rader, *Curr. Opin. Cardiol.* **22**, 368 (2007).
25. D. J. Rader, E. T. Alexander, G. L. Weibel, J. Billheimer, G. H. Rothblat, *J. Lipid Res.* **50**, (Suppl), S189 (2009).
26. R. R. Singaraja *et al.*, *J. Clin. Invest.* **110**, 35 (2002).
27. X. Wang *et al.*, *J. Clin. Invest.* **117**, 2216 (2007).
28. M. Van Eck *et al.*, *Arterioscler. Thromb. Vasc. Biol.* **26**, 929 (2006).
29. M. de la Llera-Moya *et al.*, *Arterioscler. Thromb. Vasc. Biol.* **30**, 796 (2010).

30. We thank S. Vasudevan and A. Walker for critical reading of the manuscript and K. Coser for technical assistance. This work was supported by the following funding sources: NIH R01GM071449 and R21DK084459 (A.M.N.), R01DK56626, R01DK48873, and P30 DK34854 (D.E.C.), American Heart Association Established Investigator Award (R.E.G.), the Fondation Leducq (R.E.G.), and Massachusetts Biomedical Research Corporation Tosteson Fellowship Award (S.H.N.-S.). A.M.N. and Massachusetts General Hospital have filed a patent application relating to the therapeutic use of antisense oligonucleotides directed against miR-33.

Supporting Online Material

www.sciencemag.org/cgi/content/full/science.1189123/DC1
Materials and Methods
Figs. S1 to S8
Tables S1 and S2
References

4 March 2010; accepted 5 May 2010
Published online 13 May 2010;
10.1126/science.1189123
Include this information when citing this paper.

MiR-33 Contributes to the Regulation of Cholesterol Homeostasis

Katey J. Rayner,[1,2]* Yajaira Suárez,[1]* Alberto Dávalos,[1] Saj Parathath,[1] Michael L. Fitzgerald,[2] Norimasa Tamehiro,[2] Edward A. Fisher,[1] Kathryn J. Moore,[1,2]†‡ Carlos Fernández-Hernando [1]†‡

Cholesterol metabolism is tightly regulated at the cellular level. Here we show that miR-33, an intronic microRNA (miRNA) located within the gene encoding sterol-regulatory element–binding factor–2 (SREBF-2), a transcriptional regulator of cholesterol synthesis, modulates the expression of genes involved in cellular cholesterol transport. In mouse and human cells, miR-33 inhibits the expression of the adenosine triphosphate–binding cassette (ABC) transporter, ABCA1, thereby attenuating cholesterol efflux to apolipoprotein A1. In mouse macrophages, miR-33 also targets ABCG1, reducing cholesterol efflux to nascent high-density lipoprotein (HDL). Lentiviral delivery of miR-33 to mice represses ABCA1 expression in the liver, reducing circulating HDL levels. Conversely, silencing of miR-33 in vivo increases hepatic expression of ABCA1 and plasma HDL levels. Thus, miR-33 appears to regulate both HDL biogenesis in the liver and cellular cholesterol efflux.

Cholesterol is an essential cell membrane component and precursor in metabolic pathways, including steroid hormone and bile acid synthesis. Control of cholesterol levels is essential to human health. In mammalian cells, the sterol-response element–binding protein (SREBP) transcription factors regulate the expression of genes involved in cholesterol biosynthesis and cellular uptake (*1*). In addition, the liver X receptor (LXR) nuclear hormone receptors are important transcriptional regulators of genes involved in the response to cholesterol excess (*2*), including those encoding the adenosine triphosphate–binding cassette (ABC) transporters ABCA1 and ABCG1, which promote cellular cholesterol efflux (*2*). The regulation of these pathways is complex and likely to involve posttranscriptional mechanisms as well.

MicroRNAs (miRNAs) are small (22-nt) endogenous double-stranded RNAs that have emerged as posttranscriptional regulators of physiological processes (*3*). miRNAs bind to complementary target sites in the 3′ untranslated regions (3′UTRs) of mRNAs, causing translational repression and/or mRNA destabilization (*3*). A single miRNA can have multiple targets, potentially providing simultaneous regulation of the genes involved in a physiological pathway. We explored whether miRNAs contribute to the maintenance of cholesterol homeostasis.

We undertook an unbiased genome-wide screen of miRNAs modulated by cellular cholesterol content. We identified a subset of 21 miRNAs differentially regulated in human macrophages by cholesterol depletion and cholesterol enrichment, including several whose predicted gene targets are involved in cholesterol uptake, transport, and efflux (table S1). Confirmation of these candidates identified miRNAs that were both up- and down-regulated by cellular cholesterol content (fig. S1A). Sequence alignment revealed that one of these candidates, hsa-miR-33a and its mouse homolog mmu-miR-33 (referred to here as miR-33), is encoded within intron 16 of *SREBF2,* a gene that encodes a key transcriptional regulator of cholesterol uptake and synthesis (Fig. 1A) (*1*). Furthermore, the pre-miRNA is highly conserved in mammals (Fig. 1A), prompting us to select miR-33 for further characterization of its role in cholesterol metabolism.

We found that in mouse peritoneal macrophages, miR-33 and *SREBF2* expression were coordinately down-regulated by cholesterol loading, suggesting that these gene regulatory elements are cotranscribed (Fig. 1B). Furthermore, macrophages

[1]Departments of Medicine and Cell Biology, Leon H. Charney Division of Cardiology and the Marc and Ruti Bell Vascular Biology and Disease Program, New York University School of Medicine, New York, NY 10016, USA. [2]Department of Medicine, Massachusetts General Hospital, Harvard Medical School, Boston, MA 02114, USA.

*†These authors contributed equally to this work.
‡To whom correspondence should be addressed. E-mail: kathryn.moore@nyumc.org (K.J.M.); carlos.fernandez-hernando@nyumc.org (C.F.-H.)

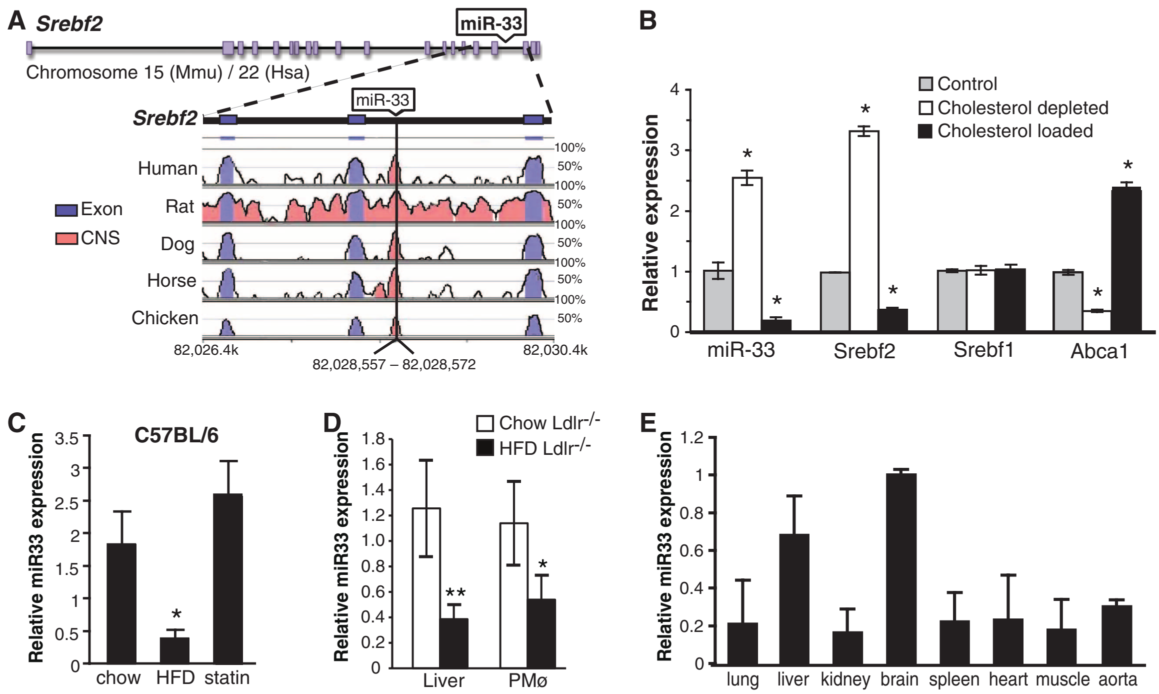

Fig. 1. Regulation of miR-33 is inversely correlated with cellular cholesterol levels. (**A**) Schematic representation of the *SREBF2* gene locus, demonstrating the miR-33 coding sequence within intron 16 and its conservation among species (reference: the mouse genome). (**B**) Quantitative real-time fluorescence polymerase chain reaction (QRT-PCR) analysis of miR-33, *SREBF2*, *SREBF1*, and *ABCA1* expression in control macrophages or macrophages loaded with cholesterol by AcLDL treatment or depleted of cholesterol by statin treatment. *$P \leq 0.05$. (**C**) QRT-PCR analysis of miR-33 in liver of C57BL6 mice ($n = 5$ per group) fed a chow diet, high-fat diet (HFD), or rosuvastatin-supplemented diet (statin) (**D**) QRT-PCR analysis of miR-33 in liver and peritoneal macrophages (PMø) from *Ldlr*$^{-/-}$ mice fed a chow or HFD for 12 weeks ($n = 6$ per group). **$P \leq 0.01$. (**E**) QRT-PCR analysis of miR-33 tissue expression in C57BL6 mice ($n = 3$). In (B) to (E), data are the mean ± SEM and are representative of ≥3 experiments.

depleted of cholesterol with the 3-hydroxy-3-methylglutaryl coenzyme A (HMG-CoA) reductase inhibitor simvastatin showed robust up-regulation of both miR-33 and *SREBF2*, but not *SREBF1* (Fig. 1B). Levels of miR-33 were inversely correlated with the expression of another cholesterol-responsive gene product, the cholesterol transporter ABCA1 (Fig. 1B). Analysis of the kinetics of miR-33 induction revealed a concomitant increase in miR-33 and SREBP2 levels with simvastatin treatment, consistent with their coregulation (fig. S1B). We next determined whether miR-33 is regulated under physiologic conditions by measuring its expression in mice fed a chow, rosuvastatin-supplemented, or high-fat diet. Consistent with our in vitro observations, hepatic miR-33 levels were inversely correlated with cholesterol levels and *ABCA1* expression and positively correlated with *SREBF2* mRNA levels, suggesting that miR-33 is regulated by dietary cholesterol in vivo (Fig. 1C and fig. S1, C and D). miR-33 levels were also regulated in two mouse models of hypercholesterolemia: *Ldlr*$^{-/-}$ and *Apoe*$^{-/-}$ mice. Hepatic and peritoneal macrophage miR-33 levels were markedly reduced in *Ldlr*$^{-/-}$ mice that were fed a high-fat diet (Fig. 1D). Similarly, miR-33 levels in peritoneal macrophages from hypercholesterolemic *Apoe*$^{-/-}$ mice correlated inversely with cellular cholesterol ester content and expression of ABCA1 (fig. S2A). We next examined miR-33 expression in mouse tissues and various cell lines. In addition to macrophages, miR-33 was highly expressed in mouse and human hepatic cells and to a lesser extent in endothelial cells (fig. S2B). Furthermore, miR-33 was widely expressed in mouse tissues and was particularly abundant in the brain and liver (Fig. 1E).

To gain insight into the function of miR-33, we analyzed its potential gene targets, using several miRNA target prediction algorithms (*3*). We identified putative binding sites for mouse miR-33

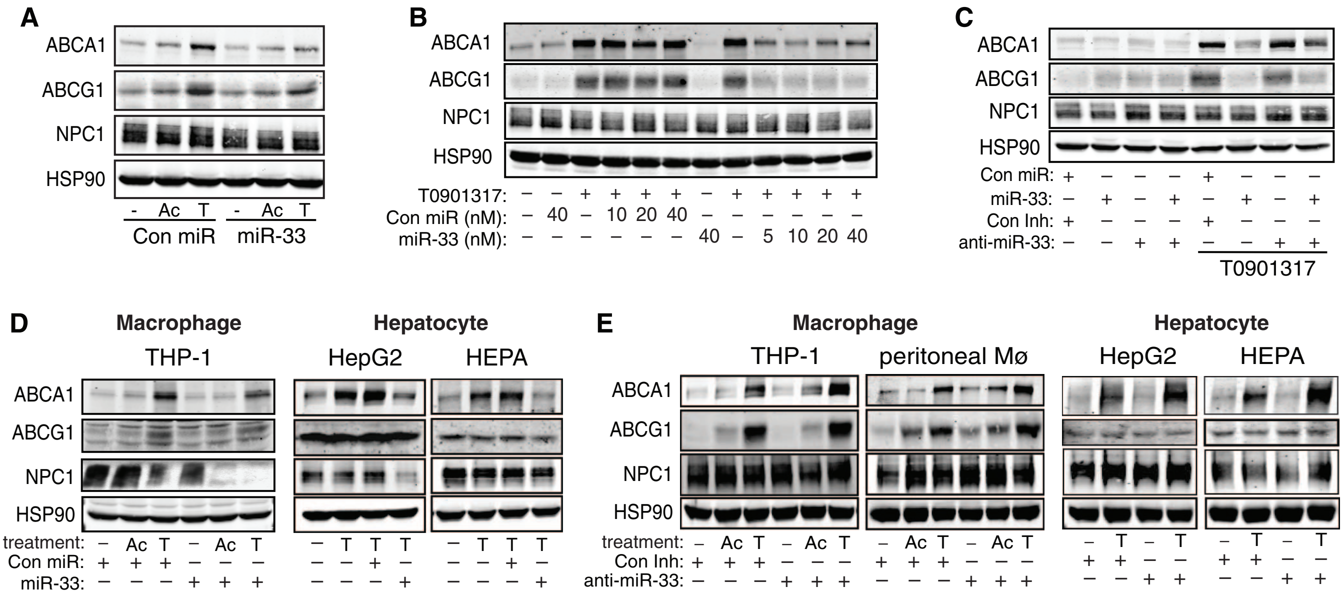

Fig. 2. Posttranscriptional regulation of ABCA1, ABCG1, and NPC1 by miR-33. (**A** to **C**) Western blot analysis of ABCA1, ABCG1, NPC1, and HSP90 in primary mouse macrophages transfected with (A) a control (Con) miR or miR-33, (B) increasing concentrations of control miR or miR-33, or (C) control miR or miR-33 in the presence or absence of a control inhibitor or anti-miR-33. Ac, AcLDL; T, T0901317. (**D**) Expression of ABCA1, ABCG1, and NPC1 expression in human (THP-1 and HepG2) and mouse (HEPA) cells of the indicated origin transfected with control miR or miR-33. (**E**) Expression of ABCA1, ABCG1, and NPC1 in human (THP-1 and HepG2) and mouse (peritoneal Mø and HEPA) macrophages and hepatic cells transfected with control inhibitor or anti-miR-33. Data are the mean ± SEM and are representative of ≥3 experiments.

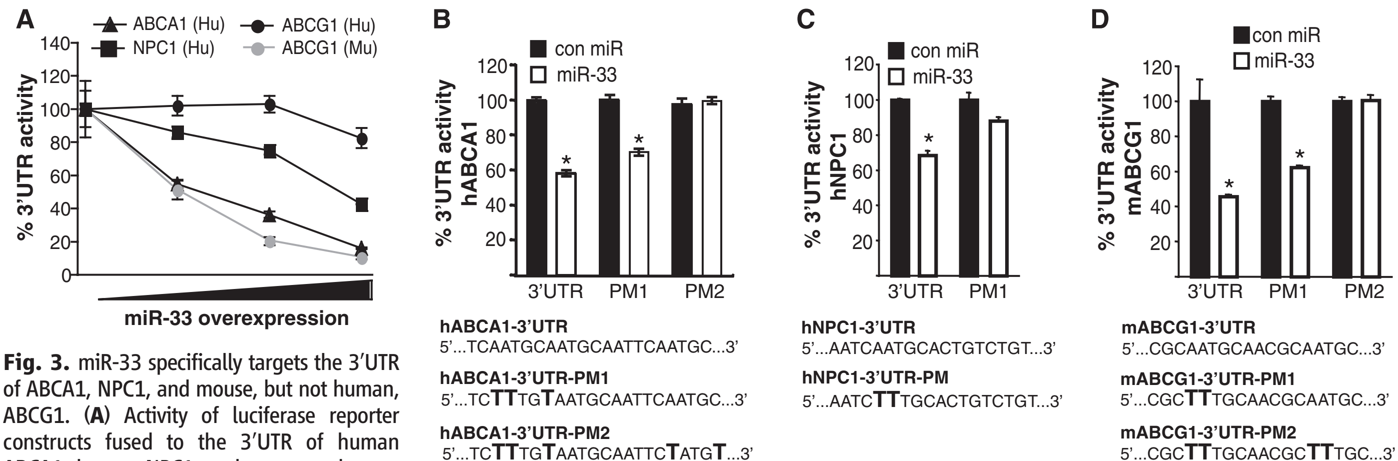

Fig. 3. miR-33 specifically targets the 3′UTR of ABCA1, NPC1, and mouse, but not human, ABCG1. (**A**) Activity of luciferase reporter constructs fused to the 3′UTR of human ABCA1, human NPC1, and mouse or human ABCG1 in HEK293 cells transfected with increasing concentrations (0, 5, 50, or 500 ng) of control miR or miR-33. (**B** to **D**) Luciferase reporter activity in COS-7 cells transfected with control miR or miR-33 of the (B) hABCA1, (C) hNPC1, and (D) mABCG1 3′UTRs containing the indicated point mutations (PM) in the miR-33 target sites. Data are expressed as mean % of 3′UTR activity of control miR ± SEM and are representative of ≥3 experiments. *$P \leq 0.05$.

in the 3′UTR of several genes involved in cellular cholesterol mobilization, including ABCA1 and ABCG1 and the endolysosomal transport protein NPC1 (fig. S3), suggesting that miR-33 coordinates cholesterol homeostasis through these pathways (*4*, *5*). To test this hypothesis, we determined the effect of miR-33 on the expression of ABCA1, ABCG1, and NPC1 in macrophages treated with acetylated low-density lipoprotein (AcLDL) (to enrich in cholesterol) or the LXR ligand T0901317 (to directly stimulate expression of the three genes) (*2*). Transfection of mouse peritoneal macrophages with miR-33 (but not a control miRNA) strongly decreased the stimulation of both ABCA1 and ABCG1 protein and mRNA (Fig. 2A and fig. S4A; quantification in fig. S5A). These effects of miR-33 were seen with concentrations of as little as 5 nM (Fig. 2B) and were reversible by co-incubation with an antisense inhibitor of miR-33 (anti-miR-33) (Fig. 2C; quantification in fig. S5, B and C). miR-33 also repressed ABCA1 and ABCG1 protein in mouse hepatic cells, indicating that its effects are not cell type–specific (Fig. 2D). Inhibition of endogenous miR-33 by anti-miR-33 increased the expression of ABCA1 and ABCG1 in macrophages and of ABCA1 in hepatocytes, which is consistent with the hypothesis that miR-33 has a physiological role in regulating the expression of these transporters (Fig. 2E; quantification in fig. S6).

Although we found that miR-33 comparably repressed ABCA1 in cells of mouse and human origin, this was not the case for NPC1 and ABCG1. miR-33 strongly suppressed NPC1 protein in cells of human origin (Fig. 2D), whereas in mouse cells, miR-33 suppressed NPC1 protein levels only modestly and had no effect on NPC1 mRNA levels (fig. S4A). Furthermore, transfection of human macrophage, hepatic, and endothelial cells with miR-33 had no detectable effect on ABCG1 protein (Fig. 2D and fig. S4B). Conservation map analysis revealed that although the predicted miR-33 target sites in the 3′UTR of mouse ABCA1 and NPC1 are highly conserved (fig. S3), the putative sites for miR-33 in the 3′UTR of ABCG1 are present only in mouse and rat. Moreover, a second miR-33–binding site was identified in human NPC1 (fig. S3C), highlighting the species-specific regulation of cholesterol metabolism genes by miR-33.

To assess the effects of miR-33 on the 3′UTR of human and mouse ABCA1, ABCG1, and NPC1, we used luciferase reporter constructs. miR-33 markedly repressed mouse, but not human, ABCG1 3′UTR activity (Fig. 3A). Furthermore, consistent with species-conserved miR-33 target sites, miR-33 significantly inhibited human ABCA1 (hABCA1) and hNPC1 3′UTR activity (Fig. 3A). Mutation of the miR-33 target sites relieved miR-33 repression of hABCA1, murine ABCG1 (mABCG1), and hNPC1 3′UTR activity, consistent with a direct interaction of miR-33 with these sites (Fig. 3, B to D). Mutation of both miR-33 sites in the 3′UTR of hABCA1 and mABCG1 was necessary to completely reverse the inhibitory effects of miR-33 (Fig. 3, B and D). miR-33 more strongly repressed hNPC1 as compared to mNPC1 3′UTR activity, which is consistent with the presence of an additional miR-33–binding site (fig. S4C). Together, these experiments identify ABCA1 and NPC1 as conserved targets of miR-33, whereas ABCG1 is a target only in the mouse.

To confirm the specificity of miR-33 targeting of ABCA1, ABCG1, and NPC1, we assessed the effect of miR-33 overexpression on other lipid metabolism–related genes in macrophages and hepatocytes. Whereas ABCA1 was predictably down-regulated in these cells, we observed few changes in the expression of non–miR-33 targets (fig. S7, A and B). Other genes containing putative miR-33–binding sites such as HMGCR and SCAP were modestly down-regulated at the mRNA level, but there was no detectable change in protein expression (fig. S8).

The ability of ABCA1 and ABCG1 to stimulate the efflux of cholesterol from cells in the periphery, particularly cholesterol-laden macrophages in atherosclerotic plaques, is an important antiatherosclerotic mechanism (*5*). Transfection of J774 murine macrophages with miR-33 attenuated cholesterol efflux to apolipoprotein A1 (apoA1) and high-density lipoprotein (HDL), in agreement with the known functions of ABCA1 and ABCG1, respectively (Fig. 4, A and B). miR-33 did not impair cholesterol efflux to HDL in human THP-1 macrophages, which is consistent with the lack of miR-33–binding sites in the human ABCG1 3′UTR (Fig. 4B). Similar results were seen in human and rat hepatocytes, where transfection of miR-33 reduced cholesterol efflux to apoA1 (fig. S9A). Antagonism of endogenous miR-33 increased ABCA1 protein and cholesterol efflux to apoA1 in both murine and human macrophages (Fig. 4C and fig. S9B). Under conditions in which miR-33 is increased (cholesterol depletion), anti-miR-33 significantly increased cholesterol efflux in both macrophages and hepatocytes (fig. S9C). Thus, manipulation of cellular miR-33 levels alters macrophage cholesterol efflux, a critical first step in the reverse cholesterol transport pathway for the delivery of excess cholesterol to the liver (*5*).

In addition to cellular cholesterol efflux, ABCA1 is responsible for initiating HDL for-

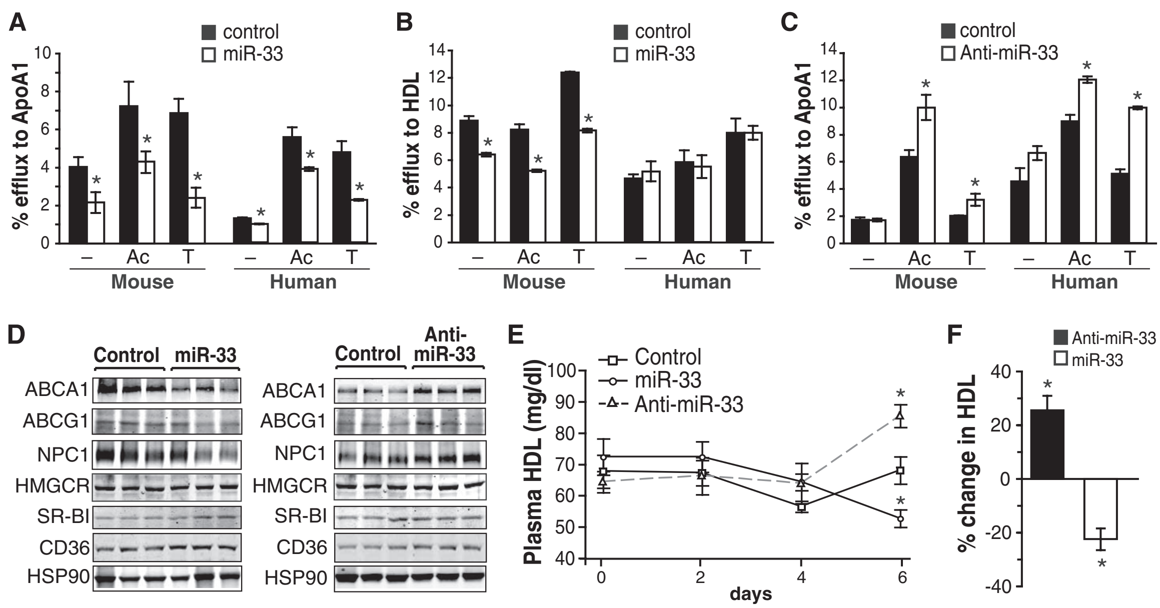

Fig. 4. Modulation of miR-33 regulates cellular cholesterol efflux and serum HDL levels. (**A** and **B**) Cholesterol efflux to (A) apoA1 and (B) HDL in mouse J774 and human THP-1 macrophages stimulated with AcLDL (Ac) or T0901317 (T) and expressing a control miR or miR-33. (**C**) Cholesterol efflux to apoA1 in mouse J774 and human THP-1 macrophages stimulated with AcLDL or T0901317 and expressing a control inhibitor or anti-miR-33. (**D**) Analysis of hepatic gene expression 6 days after infection with the control, miR-33, or anti-miR-33 lentiviruses. Western blots are of liver tissue from three representative mice per treatment. (**E**) Plasma HDL levels in mice infected with the control, miR-33, or anti-miR-33 lentiviruses. ($n = 6$). (**F**) Percentage change in serum HDL 6 days after lentiviral delivery of miR-33 or anti-miR-33 (relative to control). Data are the mean ± SEM. *$P \leq 0.05$

mation in the liver (*6*). Thus, we investigated the effect of manipulating miR-33 levels in vivo in mice using lentiviruses encoding pre-miR-33, anti-miR-33, or control. Efficient lentiviral delivery was confirmed by measuring green fluorescent protein in the liver (fig. S9D). Consistent with our in vitro results, miR-33 significantly reduced hepatic ABCA1 expression (Fig. 4D; quantification in fig. S9E). It also modestly decreased ABCG1 and NPC1 protein levels, although the effect was not statistically significant. No changes in SR-B1, a cognate receptor for HDL in the liver (*7*), or other cholesterol-related genes were observed (Fig. 4D). Moreover, an unbiased assessment of hepatic gene expression revealed few significant differences in the expression of other cholesterol metabolism–related genes in mice treated with miR-33 or anti-miR-33 lentiviruses (fig. S10). In vivo overexpression of miR-33 resulted in a progressive decline of plasma HDL, as expected from the requirement of ABCA1 for HDL formation (Fig. 4E), with a 22% decrease achieved after 6 days (Fig. 4F). Conversely, mice expressing anti-miR-33 showed a 50% increase in hepatic ABCA1 protein and a concomitant 25% increase in plasma HDL levels after 6 days (Fig. 4, D to F). Thus, manipulation of miR-33 levels in vivo alters ABCA1 expression and the mobilization of cholesterol to HDL.

To date, only one other miRNA, miR-122, has been shown to have a direct role in cholesterol metabolism (*8*–*10*). The expression of miR-122 is highly restricted to the liver, where it is believed to maintain the differentiated state. Silencing of miR-122 down-regulates genes implicated in cholesterol biosynthesis and triglyceride metabolism, increasing hepatic fatty acid oxidation and reducing plasma cholesterol, hepatic fatty acid, and cholesterol synthesis. In contrast, miR-33 is widely expressed in different cell types and tissues, consistent with the hypothesis that it has a more global effect on cellular cholesterol homeostasis. Moreover, we have shown that miR-33 specifically regulates cholesterol transport pathways that mobilize cholesterol from intracellular stores to HDL lipoproteins.

Although the pathways regulating the generation and uptake of LDL cholesterol are well characterized, the molecular mechanisms regulating circulating levels of HDL, the "good cholesterol," remain poorly defined. The identification of *ABCA1* as the gene mutated in Tangier disease, a condition characterized by a near-deficiency of plasma HDL, revealed its essential role in both HDL generation and reverse cholesterol transport (*11*–*13*). Subsequent studies have established that ABCA1 and ABCG1 probably act in a sequential fashion, with ABCA1 lipidating apoA1 to generate nascent HDL particles, which can then promote additional cholesterol efflux via ABCG1 (*5*). Despite these major advances, it has become clear that the regulation of these pathways is complex and influenced not only by genetic factors but also by posttranscriptional mechanisms (*14*). Our data provide evidence for a role for miR-33 in the epigenetic regulation of cholesterol homeostasis. We propose that miR-33 functions via a negative feedback loop triggered by the cholesterol content of the cell; under low sterol conditions, the coincident transcription of SREBF2 and miR-33 coordinate cellular cholesterol homeostasis by simultaneously initiating transcription of cholesterol uptake and synthesis pathways and posttranscriptionally repressing genes involved in cellular cholesterol export.

Our work identifies miR-33 as a potential regulator of two central pathways that control HDL cholesterol: (i) HDL biogenesis in the liver, as reflected by the impact of miR-33 manipulation on circulating HDL levels; and (ii) cellular cholesterol efflux from macrophages, the first step in the reverse cholesterol transport pathway through which HDL and apoA1 ferry excess cholesterol back to the liver for excretion. Because plasma HDL levels show a strong inverse correlation with atherosclerotic vascular disease, there has been intense interest in therapeutically targeting HDL and macrophage cholesterol efflux pathways. Our study suggests that antagonists of endogenous miR-33 may be a useful therapeutic strategy for enhancing ABCA1 expression and raising HDL levels in vivo.

References and Notes

1. J. D. Horton, J. L. Goldstein, M. S. Brown, *J. Clin. Invest.* **109**, 1125 (2002).
2. S. W. Beaven, P. Tontonoz, *Annu. Rev. Med.* **57**, 313 (2006).
3. D. P. Bartel, *Cell* **136**, 215 (2009).
4. D. S. Ory, *Trends Cardiovasc. Med.* **14**, 66 (2004).
5. A. R. Tall, L. Yvan-Charvet, N. Terasaka, T. Pagler, N. Wang, *Cell Metab.* **7**, 365 (2008).
6. J. F. Oram, A. M. Vaughan, *Curr. Opin. Lipidol.* **11**, 253 (2000).
7. M. Krieger, *J. Clin. Invest.* **108**, 793 (2001).
8. J. Elmén *et al.*, *Nature* **452**, 896 (2008).
9. C. Esau *et al.*, *Cell Metab.* **3**, 87 (2006).
10. J. Krützfeldt *et al.*, *Nature* **438**, 685 (2005).
11. M. Bodzioch *et al.*, *Nat. Genet.* **22**, 347 (1999).
12. A. Brooks-Wilson *et al.*, *Nat. Genet.* **22**, 336 (1999).
13. S. Rust *et al.*, *Nat. Genet.* **22**, 352 (1999).
14. C. L. Wellington *et al.*, *Lab. Invest.* **82**, 273 (2002).

15. We thank E. Hernando-Monje for assisting with lentiviral experiments and M. Freeman and L. Stuart for discussions. This work was supported by the American Heart Association (grant SDG-0835585D to C.F.-H., grant SDG-0835481N to Y.S., and grant 09GRNT2260352 to M.L.F.); NIH (grant R01AG02055 to K.J.M., grant R01HL074136 to M.L.F., grant R01HL084312 to E.A.F., and grant 1P30HL101270-01 to C.F.-H.); and the Heart and Stroke Foundation of Canada (K.J.R.). The authors (C.F.-H. and K.J.M) and New York University School of Medicine are preparing a patent application relating to the use of miR-33 as a therapeutic.

Supporting Online Material
www.sciencemag.org/cgi/content/full/science.1189862/DC1
Materials and Methods
Figs. S1 to S10
Table S1

11 January 2010; accepted 5 May 2010
Published online 13 May 2010;
10.1126/science.1189862
Include this information when citing this paper.

Development of the Hippocampal Cognitive Map in Preweanling Rats

Tom J. Wills,[1]*† Francesca Cacucci,[1,2]*† Neil Burgess,[3,4] John O'Keefe[1]

Orienting in large-scale space depends on the interaction of environmental experience and preconfigured, possibly innate, constructs. Place, head-direction, and grid cells in the hippocampal formation provide allocentric representations of space. Here we show how these cognitive representations emerge and develop as rat pups first begin to explore their environment. Directional, locational, and rhythmic organization of firing are present during initial exploration, including adultlike directional firing. The stability and precision of place cell firing continue to develop throughout juvenility. Stable grid cell firing appears later but matures rapidly to adult levels. Our results demonstrate the presence of three neuronal representations of space before extensive experience and show how they develop with age.

The hippocampal cognitive map has been proposed as a Kantian synthetic a priori system, partly or wholly formed genetically, to serve as a scaffold for representing experiential information about the external environment (*1*). This suggests that the basic constituents of the cognitive map develop independently of spatial experience, or might even precede it, and is supported by the early development of spatial cognition in weanling rats (*2*–*4*). We tested this idea by looking for place cells (*5*) in hippocampal region CA1, and for grid (*6*) and directional cells (*7*) in medial entorhinal cortex (MEC) as preweanling rats first began to leave the nest and to actively explore their environment (*8*) [typically on post-

[1]Cell and Developmental Biology, University College London, Gower Street, London WC1E 6BT, UK. [2]UC Institute of Behavioural Neuroscience, Division of Psychology and Language Sciences, University College London, London WC1H 0AP, UK. [3]UC Institute of Cognitive Neuroscience, University College London, London WC1N 3AR, UK. [4]UC Institute of Neurology, University College London, London WC1N 3BG, UK.

*These authors contributed equally to this work.
†To whom correspondence should be addressed: f.cacucci@ucl.ac.uk or t.wills@ucl.ac.uk

natal day 16 (P16) in our experiment] (*9*) (see fig. S1 for typical recording locations).

We recorded 567 hippocampal pyramidal cells and 1514 medial entorhinal cells from 42 male rats between the ages of P16 and P30 as they foraged for food in an enclosure, using miniaturized microdrives and recording locations matched across ages (*9*) (fig. S2, C to E). Cells were categorized as directional, place, or grid cells if their spatial firing characteristics exceeded the 0.05 significance level of the relevant measures [spatial information (*10*) for place cells, gridness (*6*, *11*) for grid cells, Rayleigh vector for directional cells] in spatially shuffled data for the corresponding age and region (*9*).

When do the three types of spatial firing first appear, and how do they develop with age? Representative examples of cells recorded across ages P16 to P29 are shown in Fig. 1A and, in

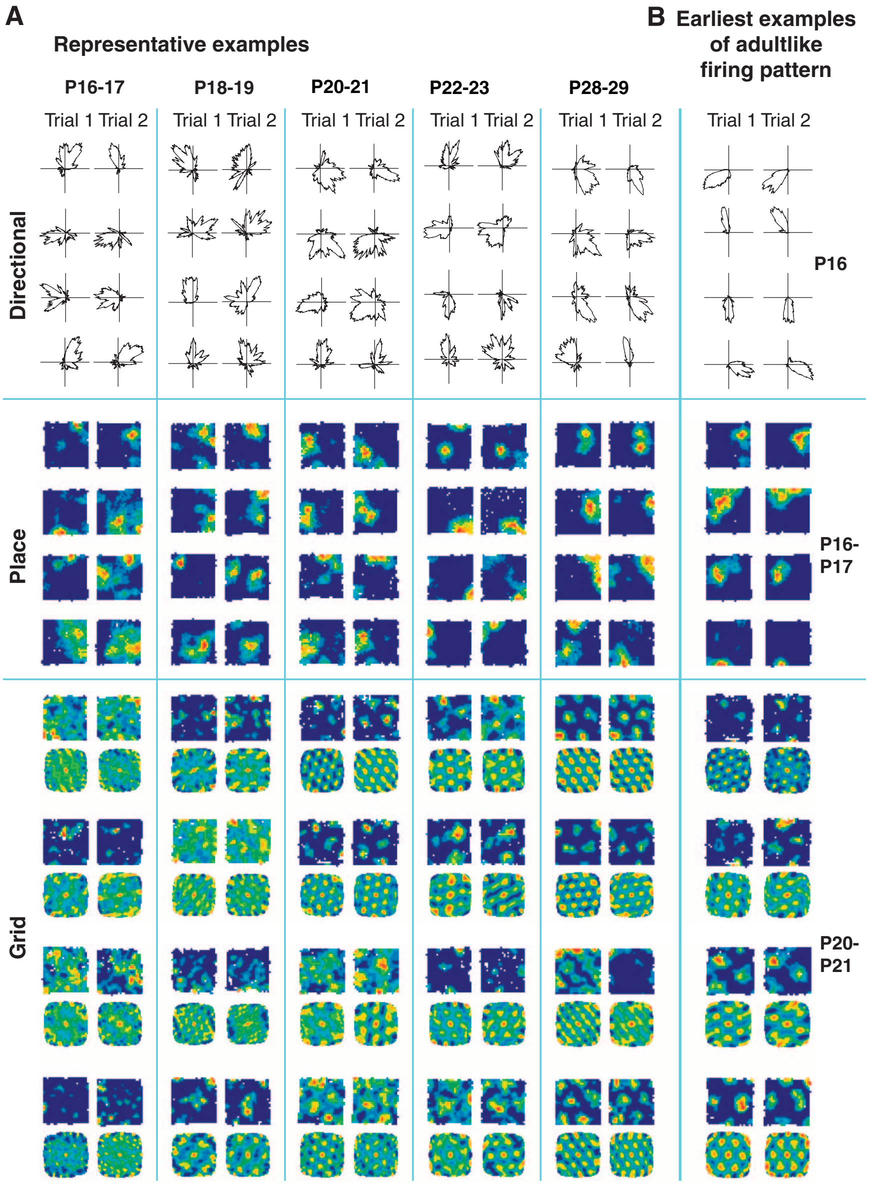

Fig. 1. Development of directional, place, and grid cell firing with age. (**A**) Four representative examples of each type of firing are shown across a range of ages for two consecutive trials (left and right columns): polar plots for directional firing, firing rate maps for place cells, firing rate maps (above) and spatial autocorrelograms (below) for grid cells. Example cells were chosen to have mean values of both the spatial firing criterion variable and intertrial stability within one standard deviation of the appropriate group mean. (**B**) The earliest examples of directional, place, and grid firing corresponding to the classical examples found in adults.

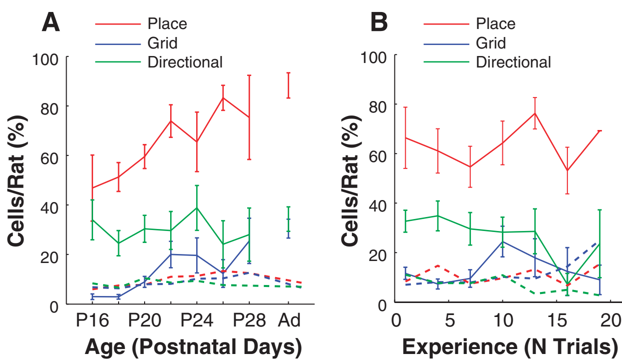

Fig. 2. The proportions of cells per rat fulfilling the criteria for directional (green), place (red), and grid (blue) cells as a function of age (**A**) or experience of the testing environment (**B**). Solid lines represent the mean percentage of cells per rat that fulfilled the spatial firing criteria; error bars represent ± SEM over all rats. Dotted lines represent the $P = 0.05$ significance level for the mean percentage of cells for each cell type, based on spike-shuffled data (see *9*).

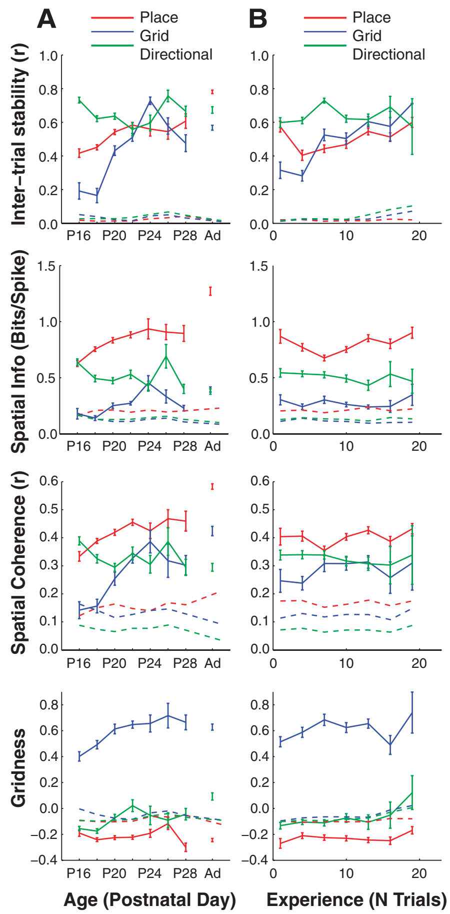

Fig. 3. Spatial firing properties of the directional (green), place (red), and grid cells (blue) as a function of age (**A**) and experience of the testing environment (**B**). Shown (from top to bottom) are the stability (spatial correlation trial-to-trial), quality (locational or directional spatial information per spike), spatial coherence, and gridness of firing of the three cell types. For summary statistics, see fig. S8A. Dotted lines represent the $P = 0.05$ significance level of expected mean value of spatiality for each cell type based on spike-shuffled data; solid lines represent the mean over cells (± SEM).

Fig. 1B the earliest examples of stable adultlike firing found in directional (P16), place (P16 to 17), and grid cells (P20 to 21). See figs. S3 to S6 for the complete data set and fig. S7 for the distributions of the relevant measures across all cells recorded in MEC and CA1.

Adultlike proportions of directional cells were present from the earliest age point, and these cells exhibited adultlike stability and quality (Figs. 2A and 3A, and see fig. S8, A and B, for statistical analysis). Somewhat higher proportions of directional cells were found near the border with parasubiculum (fig. S9) than in the heart of MEC, but did not increase with age in either region. It is noteworthy that directional tuning was also tighter in this border region (fig. S9C). This strong directional signal may originate in the presubicular head-direction cells, as preliminary recordings from this region revealed adultlike directional cells at very early ages (P14) there too (fig. S9, D and E).

Significant proportions of place cells are also present initially (Fig. 2) but continue to increase toward adult levels throughout development. Although cells with multipeaked firing were also found early in MEC, significant proportions of classical adultlike grid cells first appeared only at around P20 and increased rapidly to near-adult levels by P22 (fig. S8B).

A critical attribute of spatial representations is their stability over time, which provides a reliable environmental representation suitable for long-term memory (*12*). The correlation of firing rate maps from one trial to the next is typically 0.6 or higher for all three cell types in the adult (Fig. 3A). Stability measures during development show the same pattern as proportions of cells: Directional firing has adultlike stability from the earliest age; stable place cell firing is also present initially but continues to improve throughout development; and stable grid cell firing is initially almost nonexistent but develops rapidly at around P20 (Fig. 3A and fig. S8, A and B).

The quality of spatial encoding can be fairly compared across cell types by using the spatial information per spike [regarding location for place and grid cells and direction for directional cells (*10*)]. As with the proportions of cells and stability of firing, the quality of spatial encoding is adultlike from the earliest age in directional cells, significantly high in early place cell firing but increasing throughout development, and reaches adult levels in grid cells at P24 (Fig. 3A and fig. S8, A and B).

We are able to dissociate the effects of age from effects of experience in the testing environment because we began recording from different animals at different ages. Effects of experience on place cell stability at P18 to P19, and grid cell firing stability at P22 to P30 were seen, but these were weaker than the corresponding increases with age. All other effects reflect age alone (Figs. 2B and 3B and fig. S8A). (The independent effects of age and experience separately are shown in fig. S10.)

In adult rats, the firing of place and grid cells is carefully timed to the theta rhythm ["phase precession" (*13*, *14*)], and theta oscillations may play a role in the creation of place (*13*) and grid (*15*, *16*) firing. How does the temporal organization of the hippocampal formation develop? As the rat pups moved around the environment, theta activity was present in the local field potential at the earliest recording time point of P16. Theta frequency increased with age and with running speed [as in adults (*17*, *18*)]. Theta amplitude showed a similar profile (Fig. 4) (*19*). Both the slope and intercept of the frequency-speed relation increased with age ($P < 0.001$) (Fig. 4C). Significant proportions of cells in CA1 and MEC showed theta-modulated firing from the earliest ages. The proportions in each region were approximately equal, started from around 20% at P16, and were not significantly different from adult levels by P22 (Fig. 4D).

Finally, the frequency of modulation (indicated by the power spectrum of the spike-train autocorrelogram) of grid and place cell firing was slightly higher than the simultaneously recorded local field potential theta (Fig. 4, E and F); this finding is consistent with the presence of phase precession. We did not systematically record on the linear track to test for this, but can report one observation of phase precession in five CA1 cells as early as P17 (fig. S11).

Could any of our results reflect changes in behavior, such as speed of movement (*17*, *18*)? Speed of movement initially slows between P16 and P20 and then rises steadily, producing a U-shaped pattern with age (fig. S12A), mirrored by an inverted U-shaped pattern in the number and duration of periods of immobility (fig. S12, B to D). Coverage of the environment and distribution of heading directions did not vary across the recording period (fig. S13). The observed monotonic changes in spatiality seem unlikely to reflect these factors, which we confirmed by filtering the data to equate median speeds across all ages (fig. S12, E to G). Changes in the quality of tetrode recordings with age can also be discounted (fig. S2, F and G), as can

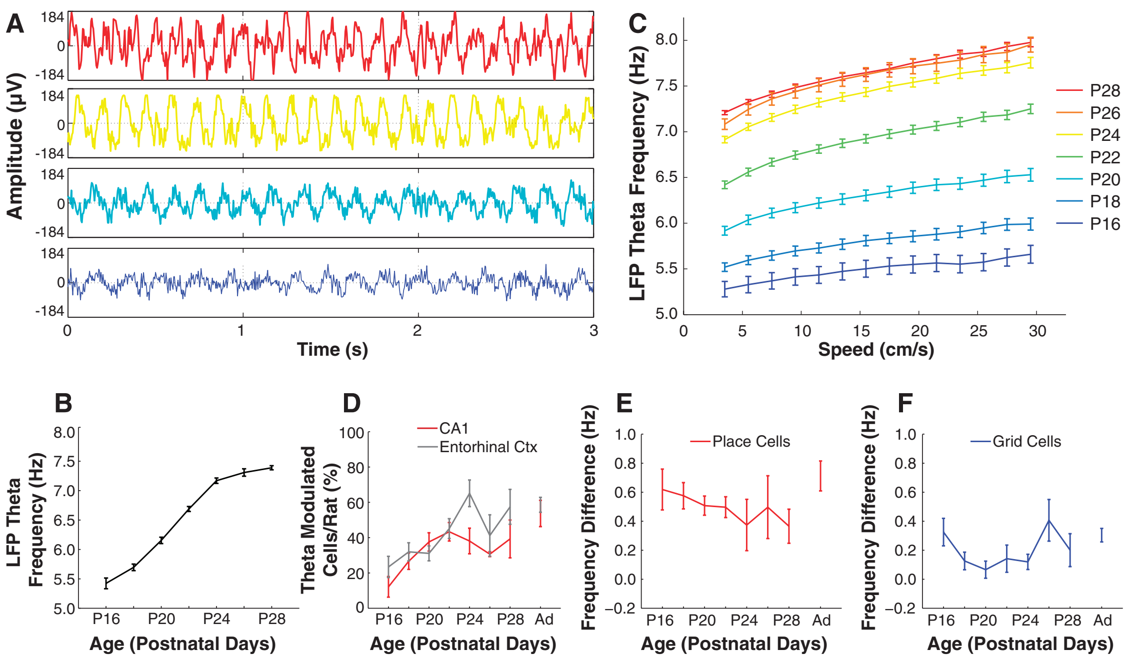

Fig. 4. Movement-related theta rhythmicity of the local field potential (LFP) and cell firing. (**A** to **C**) LFP theta oscillations are present at the earliest age recorded, increase in frequency with age (A) and (B), and increase with running speed at every age (C). (A) Samples of LFP from different ages. (B and C) Mean theta frequency for periods of translational motion are shown versus age (B) and running speed (C). Error bars show SEM; (A) and (C) are color coded by age. (**D**) Theta-modulated firing is present at the earliest ages in CA1 and MEC, and the proportions of theta-modulated cells increase with age in both areas (CA1: $r = 0.34$, $P = 0.01$; MEC: $r = 0.36$, $P < 0.001$) and are not significantly different from adult by P22 ($P = 0.74$, Tukey's post hoc test). The theta-band modulation of firing in CA1 place cells (**E**) and entorhinal grid cells (**F**) is higher in frequency than the ongoing LFP theta, and the frequency difference does not change significantly with age (place cells: $r = 0.05$, $P = 0.28$; grid cells: $r = 0.08$, $P = 0.32$).

changes in more general properties, such as firing rates or percentage of complex spikes (fig. S14).

Because early directional firing is stable relative to the environment, it must use environmental cues as well as interoceptive inputs. In addition, directional modulation remains parallel across the whole environment, even during the rat's first-ever exploration of the recording environment (fig. S15A), which indicates that, as in the adult (*7*), it does not reflect a simple association to a single cue. Furthermore, when tested in two visually different environments, the preferred directions of simultaneously recorded cells rotated together coherently (fig. S15, B and C). These observations suggest the presence of functional sensory input to MEC at P16 and that directional firing could not be produced solely by experience-dependent plasticity driven by movements within the nest before exploration. The timing of development of the different spatial cell types suggests that ontogeny recapitulates phylogeny insofar as the directional signal originates in the brainstem, the place signal originates in archicortex (i.e., hippocampus proper), and the grid cells originate in neo/transcortex.

Stable directional firing, place cell firing, and theta-band temporal organization occur before significant proportions of adultlike grid cells fire. These three factors may combine stable adultlike grid cell firing (*15*, *16*) with further physiological developments [e.g., of MEC stellate cell intrinsic membrane potential oscillations (*20*)], to create. Once formed, simultaneously recorded grids have similar wavelengths and orientations, as in the adult (*6*) (fig. S16); these findings are consistent with the presence of coherent ensembles (*21*). In addition, the appearance of place cell firing with trial-to-trial stability before stable grid cell firing implies that place cell firing can be driven by inputs other than those from grid cells, including environmental inputs, such as boundary vector cells (*22*–*24*) or local cues (*24*), acting together with the (highly stable) directional cells. Our results, together with evidence that place cell firing is not abolished by entorhinal cortex lesions (*25*), call into question the hypothesis that entorhinal cortex grid cells provide the only spatial input to the place cells. Both place and grid cell firing continues to develop after P20, more rapidly for grid than place cells. Although both systems appear to be interdependent in the adult (*26*), their differential developmental time courses suggest that interconnectivity develops after pups begin to explore. For example, the presence of theta-modulated firing in both regions at the earliest ages suggests that each area has oscillatory machinery, such as that required for phase precession (*16*, *27*). Controlled rearing studies will be required to further disentangle the dependencies of these different spatial representations on each other and on experiential and innate processes.

Our results put the development of the place and directional systems earlier than previously reported (*28*) and have general implications for the interaction of innate and experientially acquired knowledge in spatial cognition. The expression of some types of spatial learning ability continues to improve for a long time after the components of the cognitive map are relatively mature, which suggests that the rate-limiting step may be the use of spatial signals by the rest of the brain. However, some types of spatial behavior in rats, such as spatial orientation based on enclosure geometry (*29*), are likely directly controlled by head-direction cells, so that our evidence for an early, perhaps preconfigured, directional firing would be consistent with the early appearance of this behavior in humans (*30*).

References and Notes

1. J. O'Keefe, L. Nadel, *The Hippocampus as a Cognitive Map* (Oxford Univ. Press, Oxford, 1978).
2. F. Schenk, *Behav. Neural Biol.* **43**, 69 (1985).
3. J. W. Rudy, S. Stadler-Morris, P. Albert, *Behav. Neurosci.* **101**, 62 (1987).
4. L. Nadel, L. Wilson, E. M. Kurtz, in *Developmental Time and Timing*, G. Turkewitz and D. A. Devenny, Eds. (Erlbaum, Hillsdale, NJ, 2009), pp. 233–252.
5. J. O'Keefe, J. Dostrovsky, *Brain Res.* **34**, 171 (1971).
6. T. Hafting, M. Fyhn, S. Molden, M. B. Moser, E. I. Moser, *Nature* **436**, 801 (2005).
7. J. S. Taube, R. U. Muller, J. B. Ranck Jr., *J. Neurosci.* **10**, 420 (1990).
8. C. J. Gerrish, J. R. Alberts, *Dev. Psychobiol.* **29**, 483 (1996).
9. Materials and methods are available as supporting material on *Science* online.
10. W. E. Skaggs, B. L. McNaughton, K. M. Gothard, E. J. Markus, *Adv. Neural Inf. Process Syst.* **5**, 1030 (1993).
11. C. Barry, R. Hayman, N. Burgess, K. J. Jeffery, *Nat. Neurosci.* **10**, 682 (2007).
12. C. Lever, T. Wills, F. Cacucci, N. Burgess, J. O'Keefe, *Nature* **416**, 90 (2002).
13. J. O'Keefe, M. L. Recce, *Hippocampus* **3**, 317 (1993).
14. T. Hafting, M. Fyhn, T. Bonnevie, M. B. Moser, E. I. Moser, *Nature* **453**, 1248 (2008).
15. N. Burgess, C. Barry, J. O'Keefe, *Hippocampus* **17**, 801 (2007).
16. L. M. Giocomo, E. A. Zilli, E. Fransén, M. E. Hasselmo, *Science* **315**, 1719 (2007).
17. J. Rivas, J. M. Gaztelu, E. García-Austt, *Exp. Brain Res.* **108**, 113 (1996).
18. A. Jeewajee, C. Barry, J. O'Keefe, N. Burgess, *Hippocampus* **18**, 1175 (2008).
19. M. O. Leblanc, B. H. Bland, *Exp. Neurol.* **66**, 220 (1979).
20. B. G. Burton, M. N. Economo, G. J. Lee, J. A. White, *J. Neurophysiol.* **100**, 3144 (2008).
21. B. L. McNaughton, F. P. Battaglia, O. Jensen, E. I. Moser, M. B. Moser, *Nat. Rev. Neurosci.* **7**, 663 (2006).
22. C. Lever, S. Burton, A. Jeewajee, J. O'Keefe, N. Burgess, *J. Neurosci.* **29**, 9771 (2009).
23. T. Solstad, C. N. Boccara, E. Kropff, M. B. Moser, E. I. Moser, *Science* **322**, 1865 (2008).
24. F. Savelli, D. Yoganarasimha, J. J. Knierim, *Hippocampus* **18**, 1270 (2008).
25. T. Van Cauter, B. Poucet, E. Save, *Eur. J. Neurosci.* **27**, 1933 (2008).
26. V. H. Brun *et al.*, *Neuron* **57**, 290 (2008).
27. C. D. Harvey, F. Collman, D. A. Dombeck, D. W. Tank, *Nature* **461**, 941 (2009).
28. P. D. Martin, A. Berthoz, *Hippocampus* **12**, 465 (2002).
29. K. Cheng, *Cognition* **23**, 149 (1986).
30. L. Hermer, E. S. Spelke, *Nature* **370**, 57 (1994).

31. We thank C. Barry for use of adult grid cell data, A. Jeewajee and C. Barry for assistance with data analysis, S. Burton and R. Varriale for technical assistance, and C. Lever and J. Krupic for helpful discussions. This work was supported by the European Union SpaceBrain grant, the Wellcome Trust, the U.K. Medical Research Council, the U.K. Royal Society and a Research Councils U.K. academic fellowship to F.C.

Supporting Online Material

www.sciencemag.org/cgi/content/full/328/5985/1573/DC1
Materials and Methods
SOM Text
Figs. S1 to S16
References

11 February 2010; accepted 22 April 2010
10.1126/science.1188224

Development of the Spatial Representation System in the Rat

Rosamund F. Langston,[1]*† James A. Ainge,[1,2]* Jonathan J. Couey,[1] Cathrin B. Canto,[1] Tale L. Bjerknes,[1] Menno P. Witter,[1] Edvard I. Moser,[1]‡ May-Britt Moser[1]

In the adult brain, space and orientation are represented by an elaborate hippocampal-parahippocampal circuit consisting of head-direction cells, place cells, and grid cells. We report that a rudimentary map of space is already present when 2½-week-old rat pups explore an open environment outside the nest for the first time. Head-direction cells in the pre- and parasubiculum have adultlike properties from the beginning. Place and grid cells are also present but evolve more gradually. Grid cells show the slowest development. The gradual refinement of the spatial representation is accompanied by an increase in network synchrony among entorhinal stellate cells. The presence of adultlike directional signals at the onset of navigation raises the possibility that such signals are instrumental in setting up networks for place and grid representation.

The hippocampus and entorhinal cortex are key components of the brain's network for representing an animal's position in external space (*1*, *2*). In the hippocampus, place cells fire selectively when the animal visits a specific part of the environment (*3*). Cortical

inputs to place cells are likely to originate from entorhinal grid cells (*4*, *5*) one or two synapses upstream. These cells have multiple discrete firing locations that, for each cell, define a periodic hexagonal array across the full extent of any space available to the animal (*5*, *6*). Together with head-direction cells and border cells located in the same brain region (*7*, *8*), grid cells are thought to provide the key elements of a path integration–based spatial map in which the animal's position can be updated dynamically in accordance with its own movements (*9*–*11*).

The extended ontogenetic development of the hippocampal formation (*12*) prompted us to ask how space is represented when animals navigate for the first time. Previous work has suggested that, in the juvenile rat, place fields become progressively more adultlike between postnatal days 27 and 50 (P27 to P50) (*13*), but it has remained unclear whether rat pups form any representation of the local environment at the onset of outbound exploration, between P15 and P20, as would be expected if the spatial representation system is preconfigured (*14*). We implanted pups with miniature microdrives from the age of P13, generally before the eyelids unsealed (~P14 to P15) (*15*). The pups were returned to the home cage of their mother after the surgery. Tetrodes were moved toward pre- or parasubiculum, CA1, or medial entorhinal cortex (MEC) over the course of the next 2 to 3 days. Neural activity was then recorded in these regions while the young animals foraged individually in a high-walled square open field (50 cm × 50 cm × 50 cm, or 70 cm × 70 cm × 50 cm). The rat pups covered large segments of the open field from the beginning (fig. S1).

Recordings were first obtained from pre- and parasubiculum, where cells are strongly tuned to head direction in adult rats (*16*, *17*) (Fig. 1A). Directional tuning was quantified by computing, for each recorded cell, the length of the mean vector for the distribution of firing rates across the 360 degrees of possible head directions (*15*). Cells were classified as direction-modulated if the mean vector length was larger than the 95th percentile of a distribution of mean vector lengths based on shuffled data from the respective brain region and age group. Strong directional tuning was already apparent at P15 and P16 in pups exploring outside the nest for the first time (26 of 42 cells or 61.9%) (Fig. 1, B to D; fig. S2; and table S1) (*12*). The fraction of direction-modulated cells at P15 to P16 was substantially larger than expected with random selection from the shuffled distribution [$Z = 16.9$, $P < 0.001$, large-sample binomial test with expected P_0 of 0.05] and not significantly lower than in adult animals (756 out of 1182 pre- and parasubiculum cells, or 64.0%; $Z = 0.916$, $P > 0.15$) (*17*). The degree of directional tuning was not different from that of head-direction cells in adults [mean vector lengths: 0.679 ± 0.039 and 0.629 ± 0.008, respectively; $t(777) = 1.10$, $P > 0.25$] (Fig. 1D) (*12*). The modulation was stable within trials (angular correlation between first and second half: 0.695 ± 0.049) and between trials (0.801 ± 0.087) (*12*).

We next asked whether hippocampal cells have place fields at the onset of navigational experience. Spatially selective firing was apparent from the outset (Fig. 2; figs. S3 to S5; and table S2). In the youngest pups (P16 to P18), 24 out of 58 cells (41.4%) satisfied the criteria for place cells (spatial information above the 95th percentile of a distribution for randomly shuffled data from all hippocampal cells in that age group) (Fig. 2C and fig. S6). This is significantly more than expected by random selection from the shuffled distribution ($Z = 25.6$, $P < 0.001$) (Fig. 2D and fig. S6). These early cells were theta-modulated (fig. S7) and showed phase precession (*18*) and experience-dependent field expansion (*19*) from the outset (fig. S8). During the 2 weeks after the first exploration session, there was a small and gradual increase in the proportion of place cells (P16 to P24 versus P25 to P35: $Z = 2.80$, $P < 0.005$, binomial test) (Fig. 2, C and D). There was no further increase in information content and coherence in the subpopulation of neurons that passed the criteria for place cells ($r < 0.14$, $P < 0.05$) (Fig. 2E), but firing fields generally became more stable, both within and between trials

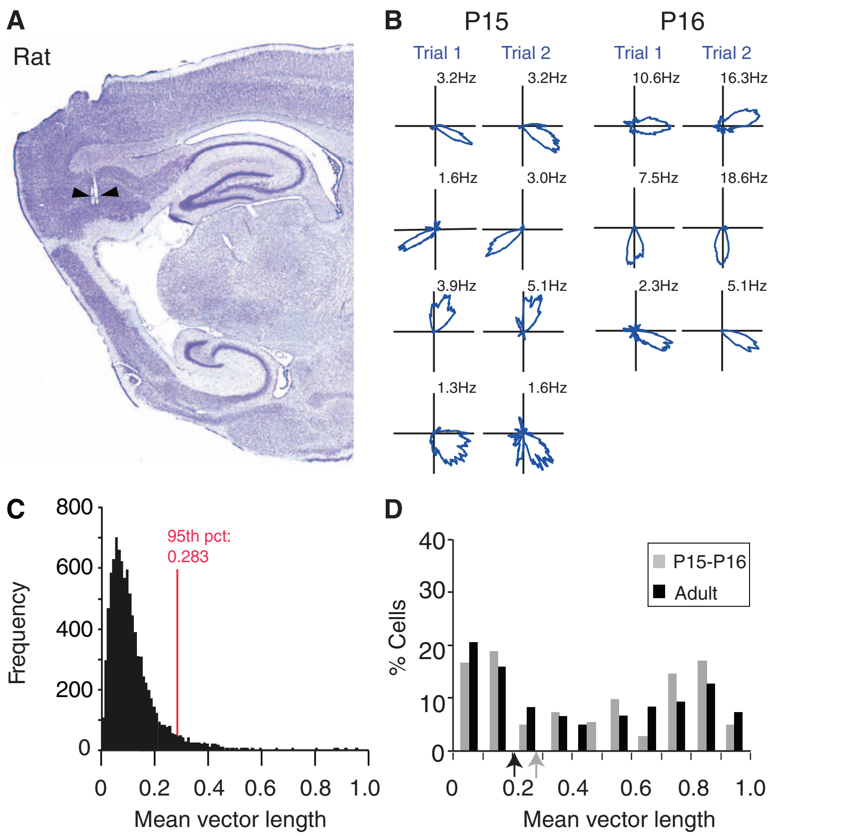

Fig. 1. Head-direction cells during first-time navigation. (**A**) Nissl-stained sagittal brain section showing representative recording location (arrowhead) in dorsal presubiculum. (**B**) Strong directional tuning of presubiculum cells on postnatal days P15 and P16. Traces show firing rate as a function of head direction on two trials. Postnatal day and peak firing rate are indicated. (**C**) Distribution of mean vector lengths (directional tuning) across 16,800 sets of randomly shuffled data from all P15 to P16 cells. Red line indicates 95th percentile (chance level). (**D**) Frequency distribution showing mean vector lengths in observations from pre- and parasubiculum cells at P15 to P16 (gray) and adult age (black). Arrows indicate chance levels [determined as in (C)].

[1]Kavli Institute for Systems Neuroscience and Centre for the Biology of Memory, Medical Technical Research Center, Norwegian University of Science and Technology, Olav Kyrres gate 9, 7489 Trondheim, Norway. [2]School of Psychology, University of St. Andrews, St. Mary's Quad, South Street, St. Andrews, Fife KY16 9JP, Scotland.

*These authors contributed equally to this work.
†Present address: Centre for Neuroscience, Division of Medical Sciences, Ninewells Hospital and Medical School, Dundee DD1 9SY, Scotland, UK.
‡To whom correspondence should be addressed. E-mail: edvard.moser@ntnu.no

[spatial correlation versus age: $r(159) = 0.272$, $P < 0.001$ and $r(137) = 0.356$, $P < 0.001$, respectively] (Fig. 2F). The changes could not be attributed merely to differences in behavior (fig. S1) and appeared to be more related to age than to the number of training trials (*12*). There was no difference between any of the spatial firing measures in the oldest group of juveniles (P31 to P35) and those of the adult group ($P > 0.05$).

The presence of spatially selective firing in CA1 of rat pups was mirrored in recordings from superficial layers of MEC, at positions known to contain large numbers of grid cells in adult rats (*4*–*7*) (Fig. 3; figs. S4, S9, and S10; and table S3). Cells with multipeaked firing fields were observed from the onset of exploration at P16 to P18, but these fields often lacked the strict periodicity of adult grid cells (Fig. 3B and fig. S9). Eleven out of 86 cells recorded in MEC at P16 to P18 (12.8%) passed the criterion for grid cells (rotational-symmetry scores exceeding the 95th percentile of a distribution of grid scores for shuffled data from all MEC cells of the respective age group; Fig. 3, C and D; and figs. S11 and S12). This is significantly more than expected by random selection from the shuffled distribution ($Z = 3.31$, $P < 0.001$) (Fig. 3D, figs. S12 and S13) (*12*). The fraction of cells that satisfied the grid-score criterion showed no significant change between the first and second block of 10 days (P16 to P25 versus P26 to P34: $Z = 1.03$, $P > 0.15$, Fig. 3, C and D) but increased between the young groups (P16 to P34) and the adults ($Z = 2.50$, $P < 0.01$). The periodic properties of the early gridlike cells evolved noticeably during the first 2 weeks of outbound exploration (Fig. 3, B and E). In the juvenile groups (P16 to P34), there was a significant age-related increase in grid scores within the population of cells that passed the criterion [$r(46) = 0.358$, $P = 0.01$] (figs. S9 and S12). There was no further increase in the grid scores of the grid cells after 4 weeks of age [P28 to P34 versus adults: $t(25) = 0.80$, $P > 0.40$]. The enhancement of spatial periodicity was accompanied by a growing number of theta-modulated neurons (fig. S7), as well as improved spatial stability of entorhinal firing fields [within trials: $r(319) = 0.236$, $P < 0.001$; between trials: $r(226) = 0.374$, $P < 0.001$] (Fig. 3F).

We asked if the entorhinal representation of young animals is directionally modulated, considering that most cells in layer III of the adult MEC have directional preferences (*7*). Twenty of the 86 entorhinal cells in the P16 to P18 group (23.3%) passed the criterion for direction-modulated cells (Fig. 3H and fig. S14). This is significantly more than expected by random selection from the shuffled distribution ($Z = 7.77$, $P < 0.001$, large-sample binomial test with expected P_0 of 0.05) (Fig. 3G and figs. S12 and S15). There was no further change in the proportion of direction-modulated neurons across age groups (P16 to P24 versus P25 to P34: $Z = 1.92$, $P > 0.05$) (Fig. 3H) but the tuning of those cells that satisfied the criterion became stronger [age versus mean vector length: $r(104) = 0.344$, $P < 0.001$; age versus directional information: $r(104) = 0.387$, $P < 0.001$] (Fig. 3I), and there was a significant increase in angular correlation within and between trials [$r(320) = 0.184$, $P = 0.001$ and $r(226) = 0.374$, $P < 0.001$, respectively, all MEC cells] (*12*) (Fig. 3J).

The gradual fine-tuning of the spatial and directional representation in MEC suggests that this network is still developing when rats explore the external world for the first time. To probe the maturity of the spatial representation circuit more directly, we made simultaneous whole-cell recordings from groups of three or four unconnected medial entorhinal stellate cells in horizontal brain slices from pups of the same litters as used for the in vivo study (Fig. 4A). Spontaneous subthreshold changes in membrane potential were then correlated across cell pairs (Fig. 4, B and C). At P16 to P21, significant correlations in membrane potential were observed during ~10% of the total time sampled. This percentage increased to 29% at P22 to P24 and remained at 30 to 40% at P25 to P29 [$F(4,101) = 20.2$, $P < 0.001$] (*12*). In contrast to the intrinsic MEC connections, the strong external inputs to layer II/III cells

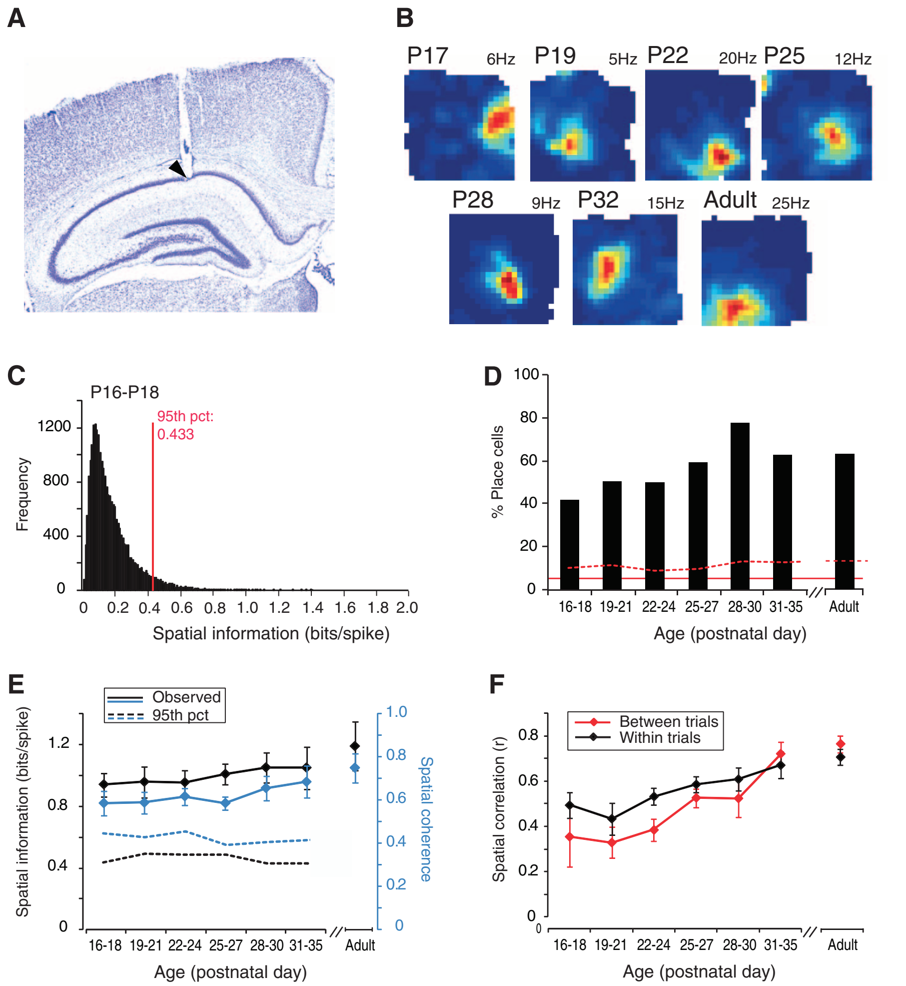

Fig. 2. Development of place cells. (**A**) Nissl-stained coronal brain section showing representative tetrode location in CA1. (**B**) Firing fields of CA1 place cells between P17 and P35. Rate maps are color-coded from blue to red; maximal rate is indicated. (**C**) Distribution of spatial information scores across 23,200 sets of randomly shuffled data from P16 to P18. Red line indicates 95th percentile. (**D**) Percentage of hippocampal cells passing the 95th percentile criterion for place cells in each age block. Red solid line indicates the proportion of cells, P_0, expected to pass the criterion in (C) by chance (5%). Red stippled line indicates upper limit of 95% confidence interval for P_0. (**E**) Spatial information (black) and spatial coherence (blue) as a function of age (means ± SEM; all hippocampal place cells). (**F**) Spatial correlation between rate maps on first and second half of each trial and between consecutive trials (all active CA1 cells).

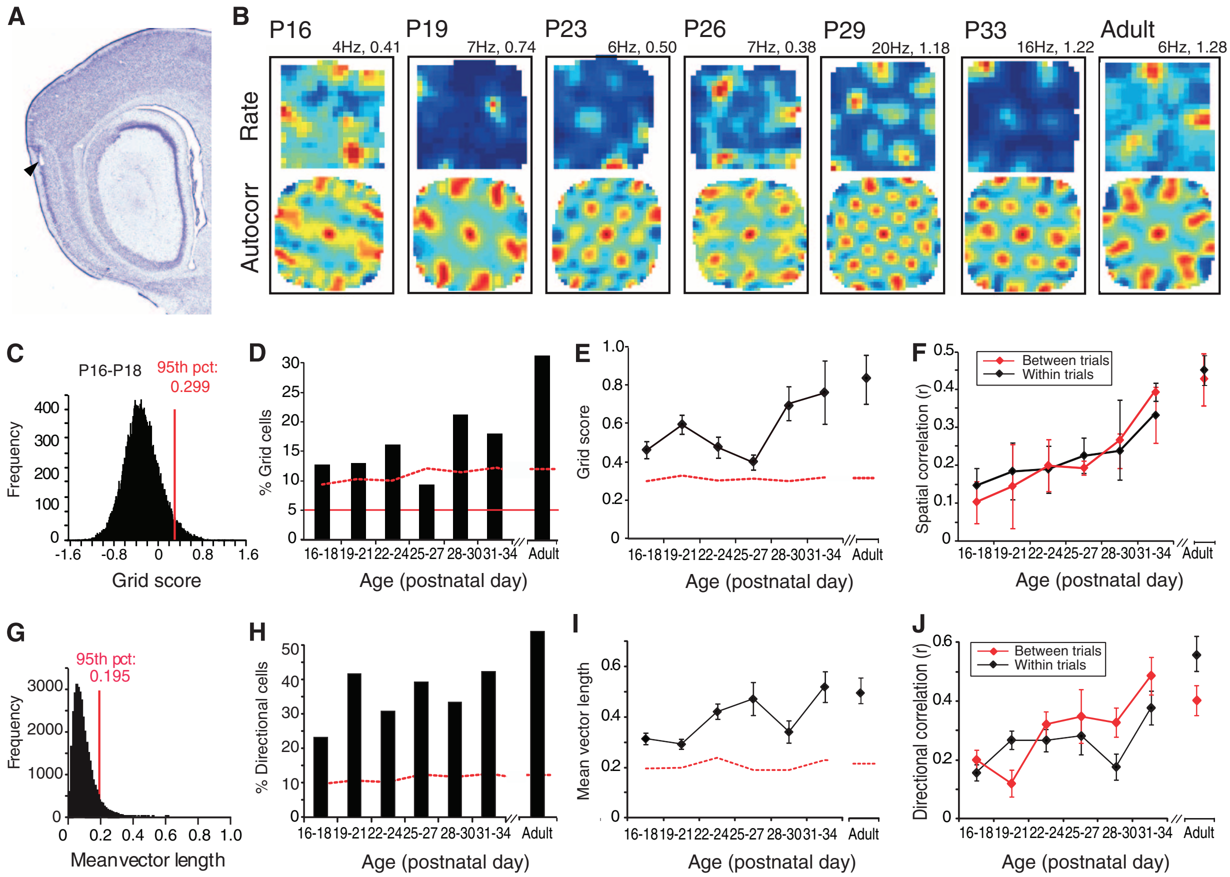

Fig. 3. Development of grid cells. (**A**) Nissl-stained sagittal brain section showing representative recording position in layer II of MEC. (**B**) Firing fields of entorhinal grid cells from P16 to P34: (top) rate maps, as in Fig. 2B; (bottom) spatial autocorrelations, color scale from blue ($r = -1$) to red ($r = +1$), grid scores are indicated. (**C**) Distribution of grid scores across 32,400 sets of shuffled data from P16 to P18. Red line indicates 95th percentile. (**D**) Percentage of cells that passed the 95th percentile criterion in (C). Solid and stippled lines as in Fig. 2D. (**E**) Grid scores as a function of age (grid cells only; means ± SEM). (**F**) Spatial correlation between rate maps (means ± SEM; all entorhinal cells, as in Fig. 2F). (**G**) Distribution of mean vector lengths across 34,400 sets of randomly shuffled data from all MEC cells. (**H**) Percentage of MEC cells with mean vector lengths above the chance level. (**I**) Mean vector length as a function of age (direction-modulated cells only; means ± SEM). (**J**) Stability of directional tuning as a function of age (angular correlations, all entorhinal cells; means ± SEM).

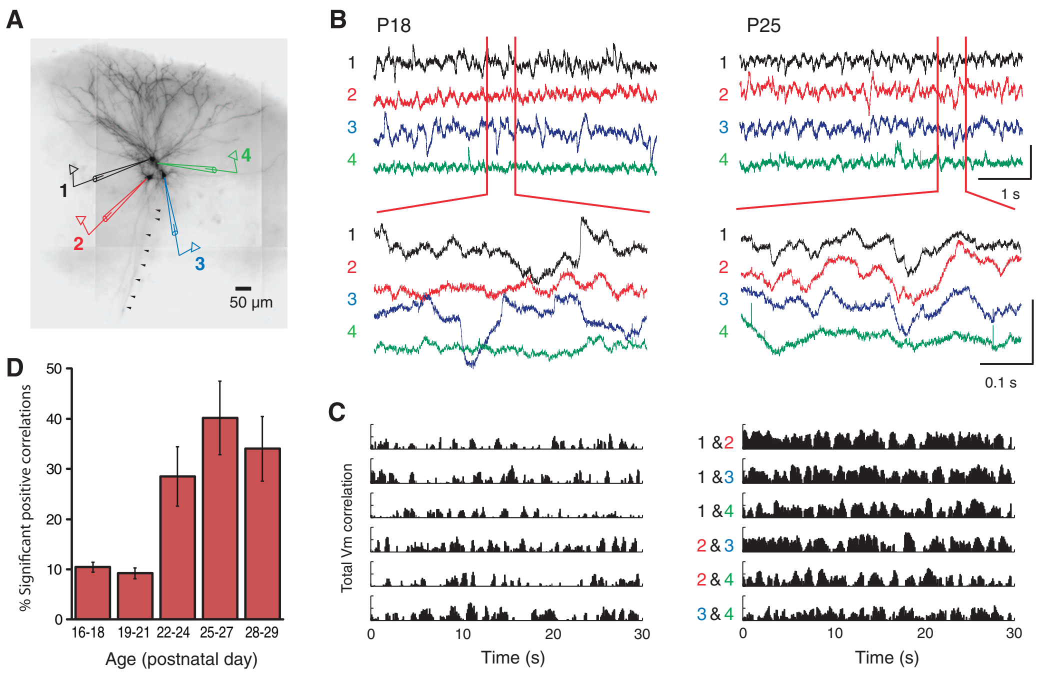

Fig. 4. Age-dependent synchrony in subthreshold membrane potential between layer II stellate cells. (**A**) Representative experimental setup. Four layer II stellate cells were filled with biocytin on P18; cell number is indicated by color; colors correspond to traces in (B and C). Arrowheads indicate descending axons. (**B**) Resting-membrane potential traces in four simultaneously recorded stellate cells from P18 and P25. Traces are shown at two time scales (upper versus lower). (**C**) Membrane voltage (V_m) correlation between sets of four cells at P18 and P25 measured over 30 s. Each row shows the correlation across time between the membrane voltage of one pair of cells (identities indicated with numbers and color in the center). Correlation values were calculated using a 250-ms sliding window moved in 50-ms increments. Only positive correlations are shown. (**D**) Percentage of significant positive correlations ($P < 0.001$) per age group (mean ± SEM).

from the presubiculum and parasubiculum (*20*) already had adultlike properties at 2 weeks of age (fig. S16). The stabilization of entorhinal and hippocampal spatial representations at about 3½ to 4 weeks of age largely coincides with the emergence of adultlike connectivity within the entorhinal microcircuit, which suggested that local network synchrony is instrumental in forming an accurate and precisely updated metric representation of self-position (*9*, *10*).

Our study has two main findings. First, head-direction cells, place cells, and grid cells were detected when rat pups navigated spaces outside the nest for the first times in their lives. The three cell types may interact from the outset, with rudimentary grid cells providing sufficiently patterned input to the hippocampus to generate place-specific firing in this region (*9*, *10*, *21*, *22*). Second, directional and positional components of the representation were found to mature at different rates. Head-direction cells in pre- and parasubiculum showed adultlike properties when the pups left the nest for the first time, often only hours after the eyelids had unsealed, whereas grid and place cells continued to evolve, with many grid cells not reaching adultlike levels of spatial periodicity until about 4 weeks of age. Because connections from pre- and parasubiculum to MEC were already functional at P16, the early representation of direction in pre- and parasubiculum may be instrumental in the subsequent development of adultlike grid and place maps in entorhinal cortex and hippocampus. The evolution of functional intrinsic connections in MEC during the fourth week may be essential not only for grid formation but also for reliable translation of the representation across the network in response to ongoing changes in the animal's speed and direction (*9*, *10*). Whether the formation of prototypical representations in the parahippocampal and hippocampal cortices requires translational or vestibular experience at younger ages, in the nest, remains to be determined.

References and Notes

1. J. O'Keefe, L. Nadel, *The Hippocampus as a Cognitive Map* (Clarendon Press, Oxford, 1978).
2. E. I. Moser, E. Kropff, M.-B. Moser, *Annu. Rev. Neurosci.* **31**, 69 (2008).
3. J. O'Keefe, J. Dostrovsky, *Brain Res.* **34**, 171 (1971).
4. M. Fyhn, S. Molden, M. P. Witter, E. I. Moser, M.-B. Moser, *Science* **305**, 1258 (2004).
5. T. Hafting, M. Fyhn, S. Molden, M.-B. Moser, E. I. Moser, *Nature* **436**, 801 (2005).
6. M. Fyhn, T. Hafting, A. Treves, M.-B. Moser, E. I. Moser, *Nature* **446**, 190 (2007).
7. F. Sargolini *et al.*, *Science* **312**, 758 (2006).
8. T. Solstad, C. N. Boccara, E. Kropff, M.-B. Moser, E. I. Moser, *Science* **322**, 1865 (2008).
9. M. C. Fuhs, D. S. Touretzky, *J. Neurosci.* **26**, 4266 (2006).
10. B. L. McNaughton, F. P. Battaglia, O. Jensen, E. I. Moser, M.-B. Moser, *Nat. Rev. Neurosci.* **7**, 663 (2006).
11. N. Burgess, C. Barry, J. O'Keefe, *Hippocampus* **17**, 801 (2007).
12. Supporting text and figures are available as supporting material on *Science* Online.
13. P. D. Martin, A. Berthoz, *Hippocampus* **12**, 465 (2002).
14. I. Kant, *Kritik der reinen Vernunft* (J. F. Hartknoch, Riga, Latvia, 1781).
15. Materials and methods are available as supporting material on *Science* Online.
16. J. S. Taube, R. U. Muller, J. B. Ranck Jr., *J. Neurosci.* **10**, 420 (1990).
17. C. N. Boccara *et al.*, *Soc. Neurosci. Abstr.* **34**, 94.9 (2008), presented 15 November 2008.
18. J. O'Keefe, M. L. Recce, *Hippocampus* **3**, 317 (1993).
19. M. R. Mehta, C. A. Barnes, B. L. McNaughton, *Proc. Natl. Acad. Sci. U.S.A.* **94**, 8918 (1997).
20. M. Caballero-Bleda, M. P. Witter, *Exp. Brain Res.* **101**, 93 (1994).
21. T. Solstad, E. I. Moser, G. T. Einevoll, *Hippocampus* **16**, 1026 (2006).
22. E. T. Rolls, S. M. Stringer, T. Elliot, *Network* **17**, 447 (2006).

23. We thank R. Skjerpeng for programming; C. N. Boccara for sharing adult pre- and parasubiculum data; and A. M. Amundsgård, K. Haugen, K. Jenssen, H. Waade, and T. Åsmul for technical assistance. Supported by Fondation Bettencourt-Schueller, Seventh Framework Programme of the European Commission (SPACEBRAIN), Kavli Foundation, and a Centre of Excellence grant from the Research Council of Norway.

Supporting Online Material

www.sciencemag.org/cgi/content/full/328/5985/1576/DC1
Materials and Methods
SOM Text
Figs. S1 to S16
Tables S1 to S3
References

10 February 2010; accepted 22 April 2010
10.1126/science.1188210

NEW PRODUCTS: IMAGING AND MICROSCOPY

HIGH-PERFORMANCE IMAGING

The Gel Logic 2200 Pro is an advanced optical imaging system aimed at in vitro scientific applications. Featuring a cooled 2.2-megapixel charge-coupled device camera and true 16-bit data capture, it can automate the process of capturing high-quality fluorescent, luminescent, and colorimetric images in sample formats such as gels, membranes, protein immunoblots, and 96-well plates. The system features intelligent software that enables researchers to identify a focal point on an image and press a button. The system then automatically adjusts to the perfect image focal point. The system is designed to combine high-quality images with easy-to-use software.

Carestream Molecular Imaging

For info: 877-747-4357 | www.carestreamhealth.com

LED FOR STEREOMICROSCOPES

New light emitting diode–based (LED) accessories for stereomicroscopes include cold light sources with high-power LEDs. For microscopes in the SteREO Discovery series, LED intermediate tubes are available to provide intensive fluorescence excitation. The light sources allow energy-saving, efficient work with high-quality results. The CL 6000 LED and CL 9000 LED cold light sources can be used on all stereomicroscope systems from Carl Zeiss for reflected light and transmitted light illumination, brightfield and darkfield applications, polarization contrast, and other illumination and contrasting techniques. High-power LEDs enable the use of short camera exposure times. The color temperature remains constant at each light intensity. The LEDs provide white light, daylight-quality illumination with high-intensity and homogeneous illumination of the object field. The flicker-free light guarantees vibration-free live images on the monitor.

Carl Zeiss

For info: +49-3641-64-2770 | www.zeiss.de

MICROSCOPE AUTOMATION SYSTEM

The ProScan III Microscope Automation System features a compact and modular design capable of controlling up to 16 axes, including a motorized stage, focused drive, three filter wheels, and three shutters with the speed, accuracy, and precision required by today's automated and demanding applications. The system also features a small footprint. The Interactive Control Center provides centralized manual control of all equipment. The screen provides positional feedback, while the joystick, buttons, and digital potentiometers control accessories such as a stage, focus drive, filter wheels, and shutters. New features allow the user to measure distances, label filter wheel positions with dye names, and take fine control of the stage for intricate movements. ProScan III is suited to demanding imaging applications that require high accuracy, speed, and repeatability, with the option to encode all axes.

Prior Scientific

For info: 800-877-2234 | www.prior.com

UPRIGHT MICROSCOPE SERIES

The BX3 line of upright clinical and research microscopes features ergonomic and imaging features that provide comfort, ease of use, and accuracy. The line offers outstanding optical performance, value, and reliability as well as eco-friendly operation. The line includes the BX43 System Microscope for clinical laboratory applications, the BX46 Clinical Microscope with ergonomic design and fast observation, and the BX53 System Microscope for research and clinical applications. All three systems feature the proprietary UIS2 optics, which deliver sharp, bright images and are manufactured from lead-free glass. New features allow users to record and share microscope magnification and setting information automatically for comparing, measuring, and scaling images. A handy exposure button makes it possible for researchers to capture digital images without taking their hands off the microscope. An optional tilting trinocular observation tube provides efficient operation when capturing photomicrographs.

Olympus

For info: 484-896-5107 | www.olympus.com/BX3

Electronically submit your new product description or product literature information! Go to **www.sciencemag.org/products/newproducts.dtl** for more information.

Newly offered instrumentation, apparatus, and laboratory materials of interest to researchers in all disciplines in academic, industrial, and governmental organizations are featured in this space. Emphasis is given to purpose, chief characteristics, and availability of products and materials. Endorsement by *Science* or AAAS of any products or materials mentioned is not implied. Additional information may be obtained from the manufacturer or supplier.